Surface chemistry of molecules of astrophysical interest : theory and simulations

Joan Enrique-Romero

Universitat Autònoma de Barcelona

Université Grenoble Alpes

THÈSE

Pour obtenir le grade de

DOCTEUR DE L'UNIVERSITE GRENOBLE ALPES

préparée dans le cadre d'une cotutelle entre **l'*Université Grenoble Alpes*** et **l'*Universitat Autònoma de Barcelona***

Spécialité : **Astrophysique et Milieux Dilues**

Arrêté ministériel : le 6 janvier 2005 – 25 mai 2016

Présentée par

Joan ENRIQUE-ROMERO

Thèse dirigée par **Cecilia CECCARELLI** et **Albert RIMOLA**

préparée au sein de **L'Institut de Planétologie et Astrophysique de Grenoble** et **Facultat de Ciències, Departament de Química de l'Universitat Autònoma de Barcelona**

dans **l'École Doctorale de Physique** et **l'Escola de Doctorat de l'Universitat Autònoma de Barcelona**

Surface chemistry of molecules of astrophysical interest: theory and simulations

Thèse soutenue publiquement le **18 Octobre 2021**,
devant le jury composé de :

M Pierre BECK
Professeur, Univerité Grenoble Alpes, Président
Mme Herma CUPPEN
Professeur, Radboud University, Rapporteur
M Alexander. G. G. M. TIELENS
Professeur, Leiden University, Rapporteur
Mme Mariona SODUPE
Professeur, Autonomous University of Barcelona, Examinateur
Mme Charlotte VASTEL
Professeur, *Institut pour la Recherche en Astrophysique et Planétologie (IRAP, Toulouse)*, Examinateur

Memòria presentada per aspirar al Grau de Doctor per:

Joan ENRIQUE-ROMERO

Vist i plau,

Cecilia CECCARELLI **Albert RIMOLA**

Grenoble, 10 Septembre 2021

To my parents, who have given me so much
A mis padres, que tanto me han dado
Als meus pares, que tant m'han donat
A mes parents qui m'ont tant donné

Preface

This thesis has the following structure: first, there are three introductory chapters, the first one is a general introduction, the second contains the theoretical background and tools needed to understand any of the results presented in chapters of results, and the third one exposes the state of the art of computational chemistry applied to astrochemistry.

At this point, the thesis is divided into three Parts of results, the first chapter of which is an introduction where the scientific context, the goals and novelties of the presented research, and a summary of the results are presented. Each of these three parts deal with different aspects of computational chemistry that I have applied to astrochemistry problems. The first one contains the results on static quantum chemical calculations on surface radical–radical reactions, the second one contains a chemical kinetics investigation on acetaldehyde formation from radical–radical surface reactions, and the last one contains the results of molecular dynamics simulations on the energy dissipation and possible chemical desorption after the formation of HCO and H_2 on water ice surfaces.

Finally, there is a chapter of conclusions and perspectives, the bibliography, and the appendixes. The latter contain supporting information for the chapters of results and a copy of the published and accepted articles that have resulted from this Thesis work.

Cette thèse a la structure suivante : d'abord, il y a trois chapitres d'introduction, le premier est une introduction générale, le deuxième contient le contexte théorique et les outils nécessaires pour comprendre n'importe lequel des résultats présentés dans les chapitres de résultats, et le troisième expose l'état de l'art de la chimie computationnelle appliquée à l'astrochimie.

A ce stade, la thèse est divisée en trois parties de résultats, dont le premier chapitre est une introduction où sont présentés le contexte scientifique, les objectifs et les nouveautés de la recherche présentée, et un résumé des résultats. Chacune de ces trois parties traite de différents aspects de la chimie computationnelle que j'ai appliqués à des problèmes d'astrochimie. La première contient les résultats de calculs de chimie quantique statique sur les réactions radicalaires de surface, la deuxième contient une étude de cinétique chimique sur la formation d'acétaldéhyde à partir de réactions radicalaires de surface, et la dernière contient les résultats de simulations de dynamique moléculaire sur la dissipation d'énergie et la désorption chimique possible après la formation de HCO et H_2 sur les surfaces de glace d'eau.

Enfin, il y a un chapitre de conclusions et de perspectives, la bibliographie, et les annexes. Ces dernières contiennent des informations complémentaires pour les chapitres de résultats et une copie des articles publiés et acceptés qui ont résulté de ce travail de thèse.

Note : des résumés détaillés en français sont disponibles à la fin de la thèse.

Acknowledgments

A thesis is sometimes a burden, others a gift, a vital goal or a dream. It brings you happiness and sadness, company and solitude, hard work and boredom, calm and anxiety. Therefore, one needs to be able to thrive through many situations, and having the support of other people is such a replenishing feeling. I wish I could thank everyone who has pushed me forward following my goals, all of those people who gave me their time, help, company and friendship. However the list could be longer than this whole thesis. Therefore, my friends and acquaintances, please feel included even if your name does not appear explicitly in this page.

I want to start thanking my two supervisors, Albert and Cecilia. It has been a real pleasure working with and learning from you. You have been excellent at guiding me through this PhD, not only in the scientific side, but also in the human one. Having a chemist and an astronomer as thesis supervisors has enriched my scientific and communicative capabilities, since many times, although working in the same field, the language with which one describes and understands the Universe can be so different, depending on the point of view.

I want to thank the funding agencies that have made this thesis possible. In particular the European Reserch Council for the European Union's Horizon 2020 research and innovation programme projects "The Dawn of Organic Chemistry" (DOC, grant agreement No 741002), "Quantum Chemistry on Interstellar Grains" (QUANTUMGRAIN, grant agreement No 865657) that have funded 3 and one year, respectively, of my research, and of course to their PIs, my supervisors, for their dedication and scientific quality that led them to win these very competitive funding schemes. In addition, these big European projects have allowed me to share my time as a PhD with wonderful senior and young researchers: Ana, Arezu, Bertrand, Cecile, Claudine, Ele, Fanny, Gemma, Juan, Marta (for so so much), Panta, Pedro, Berta, Chus, Eloy, Jessica; thank you all!

I cannot forget about our friends from the Marie Skodowska-Curie project "Astro-Chemical Origins" (ACO, grant agreement No. 811312) project, who are a lot, and I just list some of them: André (and his wife Thai), Layal, Lorenzo, Simon and Stefano; and our friends in UGA and UAB: Aina, Jiang, Jola, Junko, Ricardo, Robin, Van, Sergi, Javi, Ana, Iker... Working in such a highly international and interdisciplinary environment, plentiful with nice and clever people, has been a joy.

This has allowed us to take part in lots of activities, such as conferences and schools, and to set up many international collaborations, like our core team, prof. Gretobape, that brings together great scientists from France, Italy and Spain. I want to thank the seniors of this team, Dimitrios, Nadia and Piero, their students, like Luca and Lorenzo Z., and their local teams and the members of Master Up in Perugia for so many good memories and learnings, advises and beautiful memories.

I am very grateful to the powerful computers I have had access to, from the GRICAD infrastructure in Grenoble and the Picard structure in UAB, to the millions of hours in HPC resources we were awarded with by IDRIS (allocation 2019-A0060810797) attributed by GENCI (Grand Equipement National de Calcul Intensif).

I thank to the referees of this thesis manuscript, Herma Cuppen and Xander Tielens, for their time, pieces of advice, and good words. I am also very grateful to the other members of the jury, Nadia Balucani, Pierre Beck, Johannes Kaester, Mariona Sodupe, Piero Ugliengo, and Charlotte Vastel (especially for your fast availability) for agreeing to be part of the jury, even if in the end some of them had to take another formal role.

I want also to remember the nice people I met during my summer stays back when I was an undergraduate student: Josep Miquel, Robert, Rosario and Chema, from Universitat Autònoma de Barecelona and Universitat de Barcelona; and everyone I met in Mexico during my short stays at CRyA (later IRyA).

Finally, I thank from all my heart my family, my loving mother and father who so much have given for me, and my little brother.

Une thèse est parfois un fardeau, d'autres fois un cadeau, un objectif vital ou un rêve. Elle vous apporte bonheur et tristesse, compagnie et solitude, travail et ennui, calme et anxiété. Il faut donc être capable de s'épanouir dans de nombreuses situations, et le soutien d'autres personnes est un sentiment tellement vivifiant. J'aimerais pouvoir remercier tous ceux qui m'ont poussé à poursuivre mes objectifs, tous ces gens qui m'ont donné leur temps, leur aide, leur compagnie et leur amitié. Mais la liste serait plus longue que cette thèse. Par conséquent, mes amis et connaissances, sentez-vous inclus même si votre nom n'apparaît pas explicitement dans cette page.

Je tiens tout d'abord à remercier mes deux superviseurs, Albert et Cecilia. Ce fut un réel plaisir de travailler avec vous et d'apprendre de vous. Vous avez été excellents pour me guider tout au long de ce doctorat, non seulement sur le plan scientifique, mais aussi sur le plan humain. Avoir un chimiste et un astronome comme directeurs de thèse a enrichi mes capacités scientifiques et communicatives, car bien souvent, bien que travaillant dans le même domaine, le langage avec lequel on décrit et comprend l'Univers peut être si différent, selon le point de vue.

Je tiens à remercier les organismes de financement qui ont rendu cette thèse, et bien d'autres, possible. En particulier, le Conseil européen de la recherche pour les projets du programme de recherche et d'innovation Horizon 2020 de l'Union européenne "The Dawn of Organic Chemistry" (DOC, convention de subvention No. 741002), "Quantum Chemistry on Interstellar Grains" (QUANTUMGRAIN, convention de subvention No. 865657) qui ont financé respectivement 3 et 1 an de ma recherche, et bien sûr à leurs chercheurs principaux, mes superviseurs, pour leur dévouement et leur qualité scientifique qui leur ont permis de remporter ces programmes de financement très compétitifs. En outre, ces grands projets européens m'ont permis de partager mon temps de doctorat avec de merveilleux chercheurs seniors et jeunes : Ana, Arezu, Bertrand, Cécile, Claudine, Ele, Fanny, Gemma, Juan, Marta (pour beaucoup), Panta, Pedro, Berta, Chus, Eloy, Jessica ; merci à tous !

Je ne peux pas oublier nos amis du projet Marie Skodowska-Curie "Astro-Chemical Origins" (ACO, grant agreement No. 811312), qui sont nombreux, et je n'en cite que quelques-uns : André (et sa femme Thai), Layal, Lorenzo, Simon et Stefano ; et nos amis de l'UGA et de l'UAB : Aina, Jiang, Jola, Junko, Ricardo, Robin, Van, Sergi, Javi, Ana, Iker... Travailler dans un environnement aussi international et interdisciplinaire, riche en personnes sympathiques et intelligentes, a été une joie.

Cela nous a permis de participer à de nombreuses activités, comme des conférences et des écoles, et de mettre en place de nombreuses collaborations internationales, comme notre équipe centrale, le prof. Gretobape, qui réunit de grands scientifiques de France, d'Italie et d'Espagne. Je tiens à remercier les seniors de cette équipe, Dimitrios, Nadia et Piero, leurs étudiants, comme Luca et Lorenzo Z., ainsi que leurs équipes locales et les membres de Master Up à Perugia pour tant de bons souvenirs et d'apprentissages, de conseils et de beaux souvenirs.

Je suis très reconnaissant aux puissants ordinateurs auxquels j'ai eu accès, de l'infrastructure GRICAD à Grenoble et la structure Picard à l'UAB, aux millions d'heures de ressources HPC qui nous ont été attribuées par l'IDRIS (allocation 2019-A0060810797) attribuées par GENCI (Grand Equipement National de Calcul Intensif).

Je remercie les examinateurs de ce manuscrit de thèse, Herma Cuppen et Xander Tielens, pour leur temps, leurs conseils et leurs bons mots. Je suis aussi très reconnaissant aux autres membres du jury, Nadia Balucani, Pierre Beck, Johannes Kaester, Mariona Sodupe, Piero Ugliengo, et Charlotte Vastel (surtout pour votre disponibilité rapide) pour avoir accepté de faire partie du jury, même si finalement certains d'entre eux ont dû prendre un autre rôle formel.

Traduit avec www.DeepL.com/Translator (version gratuite)

Il y a quelques personnes en particulier que je veux remercier, même si elles ne sont pas directement impliquées dans cette thèse. Il s'agit de Josep Miquel, Robert, Rosario et Chema, de l'Universitat Autònoma de Barecelona et de l'Universitat de Barcelona ; et de toutes les belles personnes que j'ai rencontrées au Mexique pendant mes séjours de licence au CRyA (maintenant l'IRyA).

Enfin, je remercie du fond du coeur ma famille, ma mère et mon père qui ont tant donné pour moi, et mon frère.

Abstract

Abstract 

In this thesis I have investigated some of the critical points towards the formation of iCOMs on interstellar icy dust. In particular I have tackled the problem of the synthesis of iCOMs on the surfaces of interstellar dust grains from a theoretical point of view with quantum chemistry calculations. Such calculations have shown that radical—radical reactions on interstellar ice are (i) can have activation energy barriers mainly due to the radical—surface interaction, (ii) can have competitive channels other than the formation of iCOMs like that of direct hydrogen abstraction, in which one radical takes an H atom from the other and (iii) the occurrence of one channel or the other may entirely depend on their orientation upon encounter. These results have a strong impact in the astrochemistry community since in most cases it is usually assumed that radical–radical reactions are barrierless and that can only produce iCOMs. Another point that we have tackled in this thesis is the importance of binding energies when computing the efficiencies of radical—radical reactions, which strongly depend on the diffusion timescales, which in turn depend on the binding energies and on the diffusion-to-desorption activation energy ratio. We have shown for the formation of acetaldehyde from the coupling of CH_3 and HCO radicals the choice of the diffusion-to-desorption activation energy ratio strongly affects the conclusions, and that tunneling effects in direct H-abstraction reactions (in this case HCO + $CH_3 \rightarrow$ CO + CH_4) can be of great importance at low temperatures. The reaction rates related to the activation energies were obtained by means of the Rice-Rampsberger-Kassel-Marcus (RRKM) theory, i.e. the microcanonical counterpart of the classical transition state theory, while the desorption and diffusion rate constants were simulating using Eyring's equation. Finally, we have also tackled the problem of the fate of the energy after a chemical reaction on top interstellar ices. We have studied how does the energy released by H + CO $\rightarrow$ HCO and H + H $\rightarrow$ H_2 partition in between the product molecule and the surface by means of ab initio molecular dynamics. For the former reaction, the surface was modelled by a proton ordered Ih crystalline ice in order to limit the complexity of the system (in such an ordered surface, the number of binding sites is drastically reduced to a few that periodically repeat). We found that the energy released is very efficiently absorbed and dissipated by the ice structure in about 1 ps, so that the HCO product remains frozen on the ice surface. In the case of H_2, we have studied the reaction on crystalline and on three different spots on an amorphous ice model. In all cases the ice structure absorbs about one half of the energy released upon H_2 formation, which is still not enough for H_2 to remain frozen, so that its fate is probably leave into the gas phase with a certain amount of vibrational excitation (they were found to be vibrationally excited during the first ps). The region where the H_2 molecule was formed was observed to remain energized for about 100-200 fs, so that we cannot reject the idea that the energy released by such reactions might be used by other species with low binding energies to be ejected into the gas.

Keywords: *Interstellar medium, Surface chemistry, Computational chemistry, Theory, Simulations, Astrochemistry*

Résumée

Dans cette thèse, j'ai étudié certains des points critiques vers la formation d'iCOMs sur la poussière glacée interstellaire. En particulier, j'ai abordé le problème de la synthèse des iCOMs sur les surfaces des grains de poussière interstellaire d'un point de vue théorique avec des calculs de chimie quantique. Ces calculs ont montré que les réactions radicalaires sur la glace interstellaire (i) peuvent avoir des barrières d'énergie d'activation principalement dues à l'interaction radical-surface, (ii) peuvent avoir des canaux compétitifs autres que la formation d'iCOMs comme celui de l'abstraction directe d'hydrogène, dans lequel un radical prend un atome H à l'autre et (iii) l'occurrence d'un canal ou de l'autre peut dépendre entièrement de leur orientation lors de la rencontre. Ces résultats ont un fort impact dans la communauté astrochimique puisque dans la plupart des cas, on suppose que les réactions radicales-radicalaires sont sans barrière et qu'elles ne peuvent produire que des iCOMs. Un autre point que nous avons abordé dans cette thèse est l'importance des énergies de liaison lors du calcul des efficacités des réactions radicalaires, qui dépendent fortement des échelles de temps de diffusion, qui à leur tour dépendent des énergies de liaison et du rapport entre l'énergie d'activation de diffusion et de désorption. Nous avons montré que pour la formation d'acétaldéhyde à partir du couplage de radicaux CH_3 et HCO, le choix du rapport entre l'énergie d'activation de diffusion et de désorption affecte fortement les conclusions, et que les effets de tunnel dans les réactions directes d'absorption de l'hydrogène (dans ce cas, HCO + $CH_3 \rightarrow$ CO + CH_4) peuvent avoir une grande importance à basse température. Les taux de réaction liés aux énergies d'activation ont été obtenus au moyen de la théorie de Rice-Rampsberger-Kassel-Marcus (RRKM), c'est-à-dire la contrepartie microcanonique de la théorie classique des états de transition, tandis que les constantes de vitesse de désorption et de diffusion ont été simulées à l'aide de l'équation d'Eyring. Enfin, nous avons également abordé le problème du devenir de l'énergie après une réaction chimique sur les glaces interstellaires supérieures. Nous avons étudié comment l'énergie libérée par H + CO $\rightarrow$ HCO et H + H $\rightarrow$ H_2 se répartit entre la molécule du produit et la surface au moyen de la dynamique moléculaire ab initio. Pour la première réaction, la surface a été modélisée par une glace cristalline Ih ordonnée en protons afin de limiter la complexité du système (dans une telle surface ordonnée, le nombre de sites de liaison est drastiquement réduit à quelques uns qui se répètent périodiquement). Nous avons constaté que l'énergie libérée est très efficacement absorbée et dissipée par la structure de la glace en 1 ps environ, de sorte que le produit HCO reste gelé à la surface de la glace. Dans le cas de H_2, nous avons étudié la réaction sur des cristaux et sur trois points différents d'un modèle de glace amorphe. Dans tous les cas, la structure de la glace absorbe environ la moitié de l'énergie libérée lors de la formation de H_2, ce qui n'est toujours pas suffisant pour que H_2 reste gelé, de sorte que son destin est probablement de partir dans la phase gazeuse avec une certaine quantité d'excitation vibratoire (on a constaté qu'ils étaient excités vibratoirement pendant les premiers ps). On a observé que la région où la molécule de H_2 a été formée reste énergisée pendant environ 100-200 fs, de sorte que nous ne pouvons pas rejeter l'idée que l'énergie libérée par de telles réactions pourrait être utilisée par d'autres espèces avec de faibles énergies de liaison pour être éjectées dans le gaz.

Mots clés: *Milieu interstellaire, Chimie de surface, Chimie computationnelle, Théorie, Simulations, Astrochimie*

Resum

En aquesta tesi he investigat alguns dels punts crítics cap a la formació d'iCOMs en la pols gelada interestel·lar. Concretament, he abordat el problema de la síntesi d'iCOMs en les superfícies dels grans de pols interestel·lar des d'un punt de vista teòric amb càlculs de química quàntica. Aquests càlculs han demostrat que les reaccions radical-radical en el gel interestel·lar (i) poden tenir barreres d'energia d'activació degudes principalment a la interacció radical-superfície, (ii) poden tenir canals competitius diferents de la formació d'iCOMs com el de l'abstracció directa d'hidrogen, en què un radical pren un àtom d'H de l'altre i (iii) que la reacció segueixi un canal o un altre pot dependre totalment de la seva orientació a l'hora de trobar-se els dos radicals. Aquests resultats tenen un fort impacte en la comunitat astroquímica, ja que en la majoria dels casos se sol assumir que les reaccions radical-radical no tenen barrera i que només poden produir iCOMs. Un altre punt que hem abordat en aquesta tesi és la importància de les energies d'adsorció a l'hora de calcular les eficiències de les reaccions radical-radical, que depenen fortament de les escales de temps de difusió, que al seu torn depenen de les energies d'enllaç i de la relació entre l'energia d'activació de difusió i desorció. Hem demostrat que, per a la formació d'acetaldehid a partir de l'acoblament dels radicals CH_3 i HCO, l'elecció d'aquesta relació afecta sobre manera a les conclusions, i que l'efecte tunel en les reaccions d'extracció directa d'H (en aquest cas HCO + $CH_3 \rightarrow$ CO + CH_4) poden ser de gran importància a baixes temperatures. Les velocitats de reacció relacionades amb les energies d'activació es van obtenir mitjançant la teoria de Rice-Rampsberger-Kassel-Marcus (RRKM), és a dir, la contrapart microcanònica de la teoria clàssica de l'estat de transició, mentre que les constants de velocitat de desorció i difusió es van simular mitjançant l'equació d'Eyring. Finalment, també hem abordat el problema d'on va a parar l'energia alliberada després d'una reacció química en els gels interestel·lars. Hem estudiat com es reparteix l'energia alliberada per H + CO $\rightarrow$ HCO i H + H $\rightarrow$ H_2 entre la molècula producte i la superfície mitjançant dinàmiques molecular ab initio. Per a la primera reacció, la superfície es va modelar mitjançant un gel cristal·lí *Ih* amb protons ordenats per limitar la complexitat de sistema (en una superfície tan ordenada, el nombre de llocs d'adsorció es redueix dràsticament a uns pocs que es repeteixen periòdicament). Trobem que l'energia alliberada és absorbida i dissipada molt eficientment per l'estructura del gel en aproximadament 1 ps, de manera que el producte HCO roman congelat en la superfície de gel. En el cas de l'H_2, hem estudiat la reacció en el cristal·lí i en tres punts diferents d'un model de gel amorf. En tots els casos, l'estructura del gel absorbeix aproximadament la meitat de l'energia alliberada en formar-se el H_2, cosa que no és suficient perquè H_2 romangui congelat, de manera que el seu destí és probablement anar a la fase gasosa amb una certa quantitat d'excitació vibracional (s'ha comprovat que s'excita vibracionalment durant els primers ps). Es va observar que la regió on es va formar la molècula d'H_2 roman energitzada durant uns 100-200 fs, i per això no podem rebutjar la idea que l'energia alliberada per aquestes reaccions pugui ser utilitzada per altres espècies amb baixes energies d'enllaç per a ser expulsades al gas.

Paraules clau: *Astroquímica, Medi interestel.lar, Química de superficies, Química computacional, Teoria, Simulacions, Astroquímica*

Contents

Chapter 1
Introduction

Outline

The evolution of the physical conditions in the Universe is accompanied by the evolution of chemistry, from the formation of elements to the formation of molecules. In this Chapter, I introduce some of these concepts starting with the formation of elements in the Big Bang and stars (§ 1.1). Then the properties of the interstellar medium and its main components are shortly presented in § 1.2, followed by the processes responsible for the formation of low mass stars like our Sun, and the associated chemical evolution (§ 1.3). The two main paradigms trying to explain the formation of complex molecules in the ISM are presented in § 1.4, the importance of computational chemistry tools in astrochemistry is explained in § 1.5, and finally, the goals of this thesis are presented in § 1.6.

1.1 The chemical history of the Universe: the formation of elements (Johnson, 2019; Planck Collaboration et al., 2020)

According to the current cosmological model of the Universe (the ΛCDM[1] model), the Universe we live in can be traced back in time to a singularity. Approximately 14 Gyr ago, this singularity started to expand in an event called "the Big Bang", the starting point of time and space. A minuscule fraction of a second after the Big Bang, the Universe had undergone an extremely rapid period of expansion called inflation. In this extremely short period, the scales in the Universe grew exponentially. Such boosted evolution is believed to be responsible for the existence of structures in the Universe (like galaxies) and its fine-tuned (tridimensional) flatness. The history of the Universe from this point on is also the history of chemistry and matter, as seen in Figure 1.1.

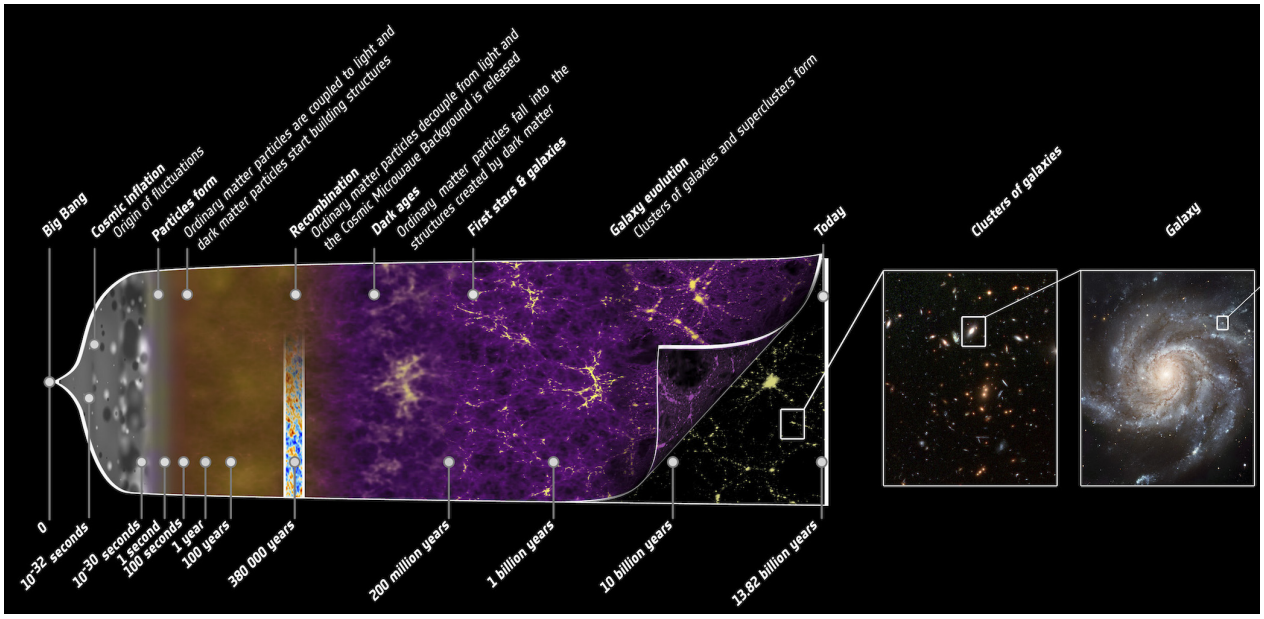

Figure 1.1: *Schematic of the history of the Universe, credit: ESA - C. Carreau, obtained here*

Before the first second, baryonic matter (the one forming ordinary matter particles) were formed. However, the extreme temperatures prevented atoms to be formed yet. As the Universe expanded the temperature decreased and about 3 minutes after the Big Bang the first light nuclei (mainly H, D and He nucelous) were formed. At that point, matter was still ionic, and it was found in thermodynamic equilibrium with photons. Thousands of years later, when the Universe was 250–400 kyr old, it cooled down to about 10^4 K and electrons could for the first time recombine with protons forming neutral H atoms for the first time. This is known as the "last scattering surface" as it is the last time matter and radiation had a strong coupling until the emergence of the first stars. From this moment on, light could freely travel through the Universe, this

[1] ΛCDM: Λ is related to the cosmological constant (connected to dark energy) and CDM stands for "cold dark matter".

light can still be observed as the *cosmic microwave background* (CMB)[2]. About 200 Myr after the Big Bang, the first stars appeared in proto-galaxies.

In present, galaxies appear associated in large clusters thanks to gravity, with hundreds to thousands of members, separated by large distances[3]. The main components of galaxies are stars, gas, dust and dark matter. Regarding us, approximately 4.5 Gyr ago the Solar System and the Earth formed within an arm of a spiral galaxy, the Milky Way.

The energy composition of the present Universe has recently been reevaluated by the *Planck collaboration*: most of the Universe is dark matter and dark energy (26.2% and 68.9% respectively), while only a 4.9% forms the (ordinary) matter. The latter is the most familiar component as it forms the "visible" budget of the Universe (e.g. stars, planets, gas, dust...), made of protons, neutrons and electrons. In contrast, the two dark components are still poorly understood (Planck Collaboration et al., 2014a,b, 2020).

The chemical elements generated in the Big Bang account mainly for H and He (and a bit of Li), which nowadays still represent the 98% in mass of ordinary matter (being the former the most abundant element). From the first stars, the successive generations of stars in galaxies have provided the Universe with heavier elements accounting for the remaining 2% of matter, thanks to the nuclear reactions going on in their cores and some more happening upon their death.

The Big Bang, and the life and death of stars are responsible for the formation of new atomic nuclei from simpler ones in a process called nucleosynthesis. Indeed, stars fuse light elements into heavier ones in their interiors though thermonuclear reactions. The first element to be fused in the core of stars is hydrogen, forming He. This stage is called main sequence and is the longest lasting one for all stars. However, the higher the mass of a star, the faster it evolves, and thus, smaller stars tend to have longer lives. The following stages in the evolution of a star strongly depends on its mass, which in turn affects their capacity of forming new elements.

Low ($0.08M_\odot < M < 3M_\odot$) and intermediate ($3M_\odot < M < 8M_\odot$) mass stars Once all H has been consumed, the He core contracts. This heats up the region surrounding the core, which stratifies in concentric shells and which are still rich in hydrogen. The ones closest to the core start to burn hydrogen into helium. This triggers a change in the stellar inner structure: the inert He core contracts while the outer layers expand, so that the star has become a red giant. The H-burning shells feed He into the core as it keeps contracting and heating up. For intermediate mass stars, the thermonuclear fusion reactions converting He into ^{12}C are switched on. Instead, the core of low mass stars keeps collapsing, until the electrons within become degenerate. Once the core is hot enough, He is suddenly burnt in a series of short and violent flashes, increasing the core's temperature until it is no longer degenerate, moment at which He burns under rather stable circumstances. The core expands and the overall size of the star shrinks because the energy production lowers, entering the so-called horizontal branch stage. Eventually, He is depleted in the center, leaving an inert core made of C and a fraction of O (formed by the reaction of C and He) surrounded by two successive shells where He and H, respectively, still burn. Again, the core contracts and the overall star expands, entering the asymptotic giant branch (AGB). The core will never reignite and the outer layers of the star are so far away that gravity can barely keep the star together. The energy production is pulsating and the outer layers are pushed away. In this stage there is some mixing of the material from the center into the outer layers (specially for more massive stars), triggering the formation of heavier elements through slow neutron capture processes. Additionally, the atmospheres are cold enough for some molecules to exist, e.g. CO, SiC... (depending on the relative amount of C and O).
At the end, all what is left is a white dwarf (the core of the dead star, made of C and O) surrounded by a "planetary" nebula (the expelled material).

Massive stars ($8M_\odot > M > 20M_\odot$) They are so massive that electron degeneracy cannot halt the core's collapse and the burning of heavy elements occurs successively. For this reason a stratified structure centered at the core of the star with successive burning layers of lighter elements builds up.

[2]The CMB constitutes a strong observational support for the CDM model. The CMB radiation was released at a temperature close to 3000 K, which nowadays, due to the expansion of the Universe, has a temperature of $\sim$ 2.7 K.

[3]The space between galaxies is not completely empty, it is filled with highly rarified, hot and ionized gas.

Eventually the star becomes a super giant with an inert ^{56}Fe[4] core stabilized by the electronic degeneracy pressure. Meanwhile, around the core there are successive layers where Si, O, Ne, C, He and H burn. At some point the iron core gets so massive that electronic degeneracy cannot prevent it from further collapse, which in turn makes the star to expand, yielding a significant mass loss.
The core gets denser until protons and electrons react forming neutrons and neutrinos. The neutron core halts its contraction once it reaches degeneracy, but the rest of the star is still collapsing. The collision of the in-falling material against the neutron core causes a rebound with so much energy that the subsequent expanding waves rip apart the star and spread its mass over large distances: it is a super nova type II. The energy is so high that heavy elements are produced through rapid neutron capture nuclear reactions. At the center, all that remains is the core: a neutron star. Stars with masses over $20M_{\odot}$, however, are so massive that not even neutron degeneracy can halt the collapse. In these cases, a black hole is formed instead.
As it can be seen, high mass stars play an important role as they form nuclei heavier than O.

Everything together shows that (i) the evolution of stars and the elemental chemical budget of the Universe are strongly linked and (ii) the abundance of heavy elements within a galaxy varies point to point, according to the stellar history of the region. The next step in chemical complexity are molecules. Low mass star atmospheres are known to contain simple species (e.g. NH, CH, OH, CN and CO, Asplund et al., 2009). But for higher chemical complexity one must look into more quiescent regions, like AGB stars and the space in between stars in a galaxy.

Such environments form the so called interstellar medium (ISM). In the coming section the ISM structure and properties is presented.

1.2 The interstellar medium (Tielens, 2010)

Approximately 90% of the (detected) mass of the Milky Way is in the form of stars. Most of the rest, gas (ions, atoms, molecules) and dust (namely silicates and carbonaceous materials with typical sizes of 0.1 μm), forms the interstellar medium (ISM). Of these two components, the former is more abundant. For example, in the solar neighborhood[5] the gas-to-dust ratio is about 100 in mass.

Matter in the ISM is inhomogeneously[6] distributed in a rather clumpy and filamentary fashion, forming structures that are generically called clouds, with sizes between 1–50 pc. It is typically classified into so-called "phases" (see below), according to the state of gaseous hydrogen (as it is the most abundant element, $\sim$70% in mass), and the local physical conditions, which are summarized in Figure 1.2 (McKee et al., 1977; Tielens, 2010; D. C. Whittet, 2002):

Coronal gas It is the hottest and most diffuse phase, formed by super nova shock waves and found all over the galactic halo covering large distances. This gas fills a large portion above and below the galactic disk. It is also known as hot interstellar medium.

HII gas It refers to ionized hydrogen, it is found in two forms, as diffuse gas covering large spatial scales in between denser clouds and as compact, dense, expanding gas around young massive stars (O-type) called HII regions.

Warm neutral medium It is similar to the diffuse HII phase, but hydrogen is found in atomic form and fills a significant part of the galactic disc, around a 40%.

Cold neutral medium (CNM) Formed by atomic (and very little molecular) hydrogen and is denser than the previous phases, but at difference to those, it occupies a small part of the ISM, few %.

[4] Iron is the most stable nucleolus as it has the highest binding energy per nucleon. Fusion reactions to form heavier elements are endothermic.

[5] Solar neighborhood: a cylindrical region around our Sun with 1 kpc of radius.

[6] These inhomogeneities are observed at all sorts of sizes, from 10^{-4} pc (the size of the Solar System) up to 10^{3} pc (the scales of spiral arms in the galaxy) D. C. Whittet, 2002.

Diffuse molecular gas Similar to CNM, but the column density is large enough to sport a self-protective shell preventing H_2 from photodissociation, mainly due to self-shielding.

Dense molecular gas These often gravitationaly bound clouds are characterized by their high densities, which, make them appear as dark patches in the visible over brighter stellar backgrounds due to the absorption and scattering of light by dust grains. Stars are formed within the densest and coldest regions of molecular clouds. In the coldest regions dust grains acquire thick ice mantles, which have a major role in the local chemical evolution, as will be seen.

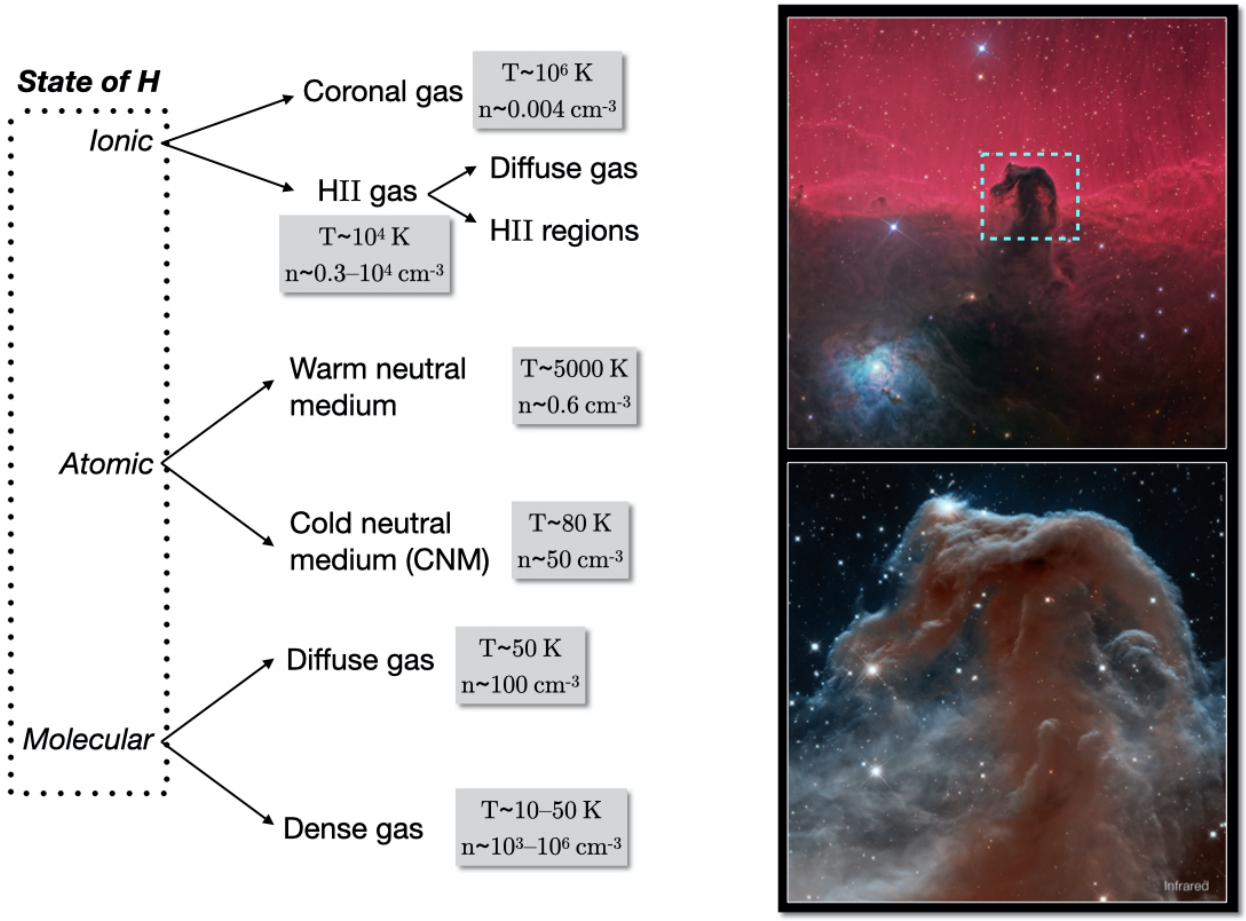

Figure 1.2: *Left hand side: Schematic description of the different phases of the ISM, according to the states of hydrogen. Right hand-side: Horsehead nebula and its surroundings (upper panel, using R-G-B, Hα and OIII filters, Author: Ken Crowford, Source: here) and a zoom towards the Horsehead nebula observed in the IR by Hubble's telescope (lower panel, Credit: NASA/ESA/Hubble Heritage Team, Source: here).*

In the right hand side of Figure 1.2 one can see two views of the Horsehead nebula, a dense star-forming region of the ISM in Orion's constellation. The upper figure shows three of the phases of the ISM: in the background, in red, one can see the emission of ionized hydrogen (IC 434 emission nebula), in the lower left side there is a reflection nebula in blue (NGC 2023, where the light of near by stars is reflected on the dusty component of the nebula) and, prominent in the foreground within a dashed box, there is the dark dense cloud known as the Horsehead nebula (B33), part of the L1630 dense cloud (seen in the bottom of the top panel). In the lower panel one can see a zoom in onto the Horsehead nebula in the infrared which allows to "see" further inside the dusty dark nebula.

As it can be seen, the ISM covers several orders of magnitude in both temperature and density, reflecting the radiative and mechanical energy input by massive stars. These phases are not static, but they are connected through the ISM life cycle, in which stellar evolution plays a major role. Stars form out of the

matter in the ISM. Part of it is modified by stellar nucleosynthesis, and once the star dies, it comes back to the ISM, either quietly in the form of stellar mass loss or by super nova explosions, with little mass lost in the process (e.g. white dwarfs, neutron stars and black holes) Tielens, 1998.

The most relevant phases, from a chemical point of view, are the densest ones. This is because high densities protect the interior of clouds from external interstellar radiation. This protection allows i) the survival of chemical species, preventing photodissociation and photoionisation, ii) very low temperatures, down below 10 K in the densest regions, and iii) the star formation process, which is accompanied by the chemical evolution of the cloud.

As regards the dust, despite of being a minor component ($\sim$1% in mass), it is a very important one. From a purely physical point of view, dust particles act as radiation filters, as they absorb and scatter radiation over a wide range of wavelengths, being specially efficient at short ones such as visible or UV. Such extinction (i.e. the combined effect of absorption and scattering) of light provides information about the nature of the interstellar dust grains. For example, back in the late 1970s Mathis et al. (1977) fitted the extinction interstellar curve of diffuse regions using different materials, providing a power law size distribution that goes approximately like $n(a)da \propto a^{-3.5}da$ (where 0.005 $\leq a \leq$ 0.3 μm is the radius of a dust grain assuming it to be spherical) with smaller grains being more abundant. The light absorbed by dust grains is radiated back as continuum emission in the mid/far IR, approximately following a black body. This re-emitted light may also be polarized according to the morphology of the dust particle (D. C. Whittet, 2002). Various studies of the gas and dust emission, in diffuse (e.g. extinction versus H-nuclei column density) and dense (e.g. CO versus dust continuum emission) strongly suggest that dust and gas are well mixed in the majority of the dense ISM.

It is usually assumed that the elemental abundances in the (local) ISM are close to the values of the solar photosphere (Asplund et al., 2009; Tielens, 2010). It turns out that in the ISM there is a depletion[7] of elements such as C, O, Mg, Si and Fe from the gas phase (Jenkins, 2009). Hence, one would expect dust grains to be composed of such elements. Indeed, the components of dust grains are: graphite-like *sp*^{2}-bonded carbon such as cationic poly-cyclic hydrocarbons (PAHs), graphitic carbon and fullerene-based compounds (Jones et al., 2017; Tielens, 2008); and amorphous and crystalline silicates[8] such as amorphous Mg-rich olivine ($Mg_{2x}Fe_{2-2x}SiO_4$) (Henning, 2010) with 0.5$\leq$ x $\leq$ 0.9 (Kemper et al., 2004; Min et al., 2007, 2008). These silicates lock up most of the Si in the ISM. Nevertheless, many other features remain unassigned.

Apart from this, dust grains grow amorphous molecular ice mantles in the cold and dense phases of the ISM (see the following section). These coatings are thought to be thick ices containing molecular species in solid form. They can be formed by the accretion of gas-phase species (e.g. CO) and by the formation of new molecules *in situ* (e.g. water and other simple hydrogenated molecules) Boogert et al., 2015; Tielens et al., 1982; D. C. Whittet, 2002. We know about their chemical composition thanks to features in the dust infrared extinction curves obtained by astronomers, see Figure 1.3 for an example. From such observations we know that the most abundant component in ices is amorphous solid water (ASW), followed by other species such as CO, CO_2, CH_4, NH_3, H_2CO and methanol (see the review by Boogert et al. (2015)).

In summary, (ice coated) dust grains are thought to have a central role in the chemistry of the ISM. Their importance is manyfold: (i) they act as radiation filters; (ii) they become the main cooling agents in very dense regions (see next section); (iii) heterogeneous catalysis can take place on their surfaces; (iv) they act as a "third body" by absorbing part of the nascent energy after association chemical reaction, opening chemical paths not possible in the gas phase; (v) their ice coatings act as molecular storage spots as they concentrate molecular species (see next section); and (vi) icy dust grains are thought to be present from the initial phases of stellar formation, passing though planet formation and even in the Solar System (SS). This last consideration points towards the possibility that interstellar ices may carry chemical inheritance from one phase to another, likely connecting the ISM and the origin of life in planetary systems (Paola Caselli et al., 2012).

[7] Depletion in the context of the ISM means a "lack" from the gas-phase. Sources of depletion may be: trapping of elements in the refractory dust cores and, at lesser extent, freeze out of volatiles onto dust grains, lose of chemical species in the gas due to chemical reactions...

[8] Mixtures of SiO_2, SiO and metal-oxides.

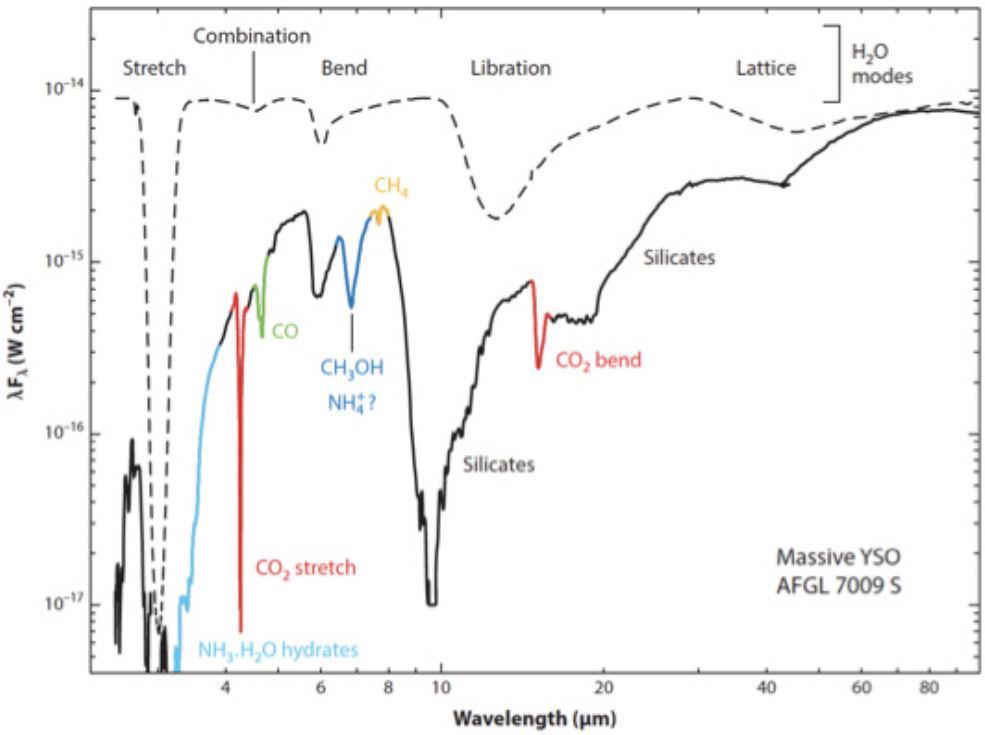

Figure 1.3: *Strongest features of ice-coated dust grains around the massive protostar AFGL 7009 S (Dartois et al., 1998), extracted from Boogert et al. (2015). A synthetic spectrum for small water ice spheres at 10 K is shown on the top as a dashed line indicating the different contributions of this molecule to the spectrum. Selected ice features are highlighted with different colors on top of the observed spectrum.*

1.3 Low mass star formation and chemical evolution

As it was said before, stars form within molecular clouds. Molecular clouds come in a variety of sizes, from few to $\sim$15 pc[9] and contain 10^3–10^5 times the mass of the sun ($M_\odot$) with mean densities around 50–10^4 cm^{-3} at temperatures close to 10–30 K, see Figures 1.2 and 1.3 for examples. Molecular clouds fragment into over-densities called dense cores where low-mass star formation actually takes place (Beichman et al., 1986). Dense cores have masses ranging 0.5–5 $M_\odot$ and have smaller sizes (0.03–0.2 pc) with higher mean densities ranging 10^4–10^5 cm^{-3} at temperatures between $\sim$6–12 K (Bergin et al., 2007; Crapsi et al., 2007; Keto et al., 2008). An example is the L1544 core in the Taurus molecular cloud (see the upper left inset in Figure 1.3). In the following, the physics and chemistry accompanying the star-formation process are explained. This process has different stages, starting from the prestellar core one, followed by the so-called Class `0`, `I`, `II` and `III` protostar stages, and ending in a planetary system.

Prestellar stage

Physics

Dense cores are but a small portion of the total mass of the molecular cloud with sizes of $\sim 10^4$ AU, and not all of them form stars. The main force towards the formation of stars is the self-gravity of the core, which may be counteracted at different scales by different forces such as turbulence, magnetic fields and thermal pressure; although in the case of dense cores, the internal energy of the gas is dominated by thermal motions (Bergin et al., 2007; Paola Caselli et al., 2012; Stahler et al., 2004). Collapse will take place from the inside out if one only takes into account the thermal pressure as a counter-force (Shu, 1977). Other

[9] A parsec is equivalent to $\sim$3.26 light years, $\sim 2.06\times10^5$ AU (astronomical units, the mean Sun–Earth distance), or $\sim 3.09\times10^{16}$ m.

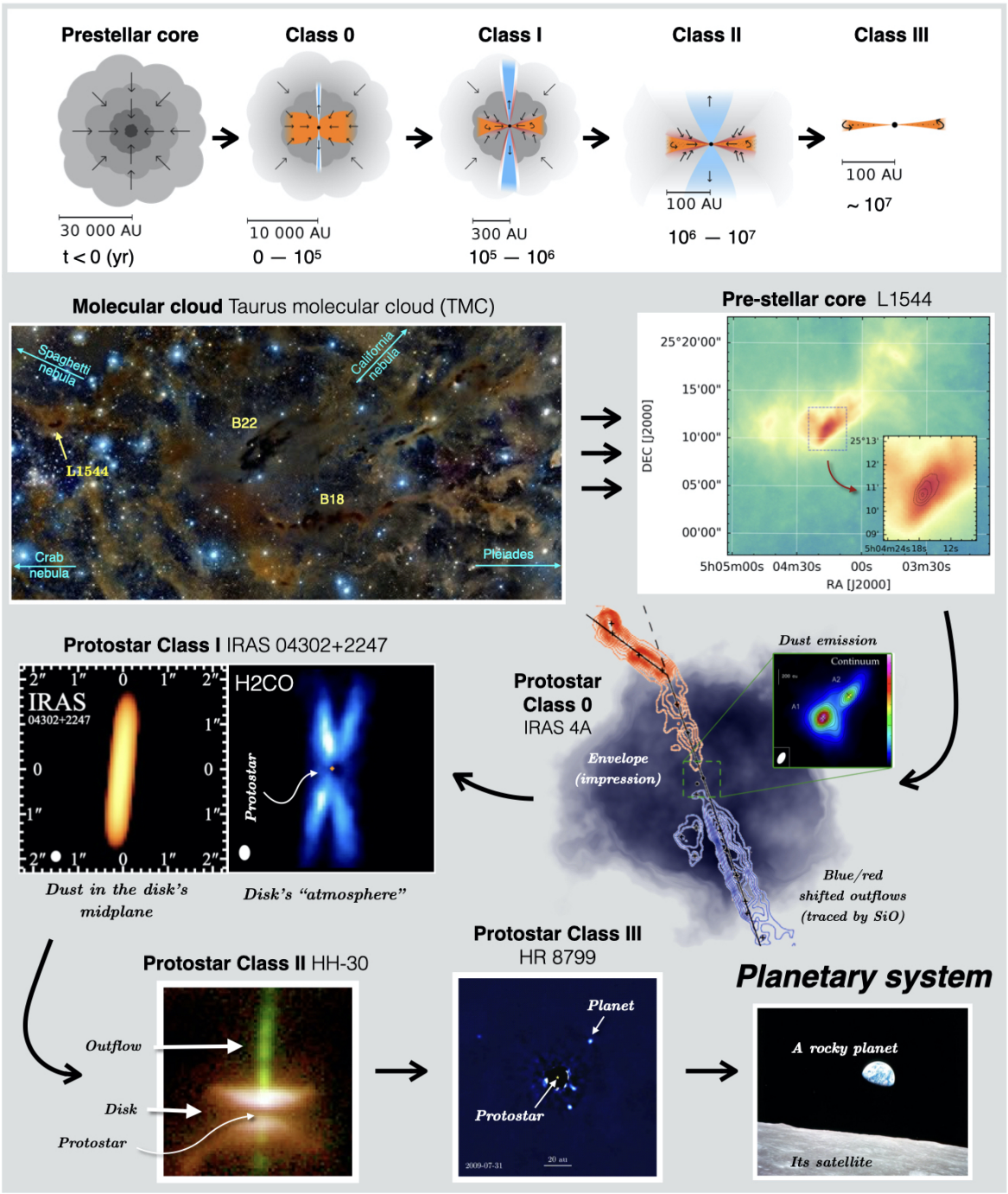

Figure 1.4: *Stages of low mass star formation. Upper panel: schemes with the physical structure of each stage adapted from Persson (2014) with their typical sizes and ages. Lower panel: real examples from actual observations, Taurus molecular cloud[a], L1544[b], IRAS 4A[c], IRAS 04302+2247[d], HH-30[e], HR 8799[f] and the Earth seen from the moon[g].*

[a]Rogelio Bernal, flickr page. [b]Herschel observations at 250 microns André et al. (2010) (data obtained from the ESA Herschel science archive with SPIRE/PACS parallel mode) and dust emission from Ward-Thompson et al. (1999) in contours on top of the closeup sub-panel. [c]Combination of the dust emission from A. López-Sepulcre et al. (2017) and the SiO gas emission by the bipolar jets from Choi (2005), the cloudy shape was added in order to emphasize the deep embedding of such protostars, composite figure by M. de Simone. [d]Continuum and H_2CO emission from disk of the protostar IRAS 04302+2247 Garufi et al. (2021). The disk midplane can be seen by the dust emission, while its atmosphere is traced by the molecular emission of H_2CO. For the latter, there is no central emission due to the dust opacity. [e]Hubble space telescope vista of HH-30, obtained from Burrows et al. (1996). Bright regions correspond to the reflected light from the central object. [f]Class III HR 8799 as observed from the Keck observatory, obtained from the APOD website, credits: J. Wang (UC Berkeley) & C. Marois (Herzberg Astrophysics), NExSS (NASA), Keck Obs). [g]The Earth seen from the moon by the Apollo 8 mission, Credits NASA, obtained from NASA's webpage.

collapse mechanisms can be pressure shocks initiated, for example, by supernovae explosions. When a core is in the verge of collapse it is called pre-stellar core, since, once collapse is started it will produce (one or more) stars. On the other hand, if it is dynamically stable, oscillating (Lada et al., 2003) or it is expanding (Tafalla et al., 2004), then it is called star-less core (Paola Caselli et al., 2012; Keto et al., 2008). The critical quantity is the density, with a threshold value around 10^5 cm^{-3} for a typical dense core with 1-10 $M_\odot$ and temperatures $\sim$10 K. Above this critical value the gas is mainly cooled by collisions with dust grains instead of molecular line emission (mainly CO, Burke et al., 1983; Goldsmith et al., 1978). The temperature of grains is determined by their interaction with the interstellar radiation field which is highly diminished in dense cores. Densities over the critical value are attainable at the center of the core as dense cores have radial temperature profile increasing towards the outside, with values as low as $\sim$ 6 K in the central region (Crapsi et al., 2007; Keto et al., 2008).

Chemistry

Prestellar cores show exotic chemistry and chemical fractionation: long unsaturated hydrocarbobs appear in these regions and, meanwhile dust and the abundance of D- and N-bearing species peak towards their centers, C-bearing molecules show a central hole, peaking right after. The reasons for this lie in the interesting and exotic chemistry taking place in these regions. Given the quiescent physical conditions, gas-phase chemistry is limited to be exothermic, barrierless and bimolecular at most (in the gas-phase). In other words, kinetics dominate over thermodynamics. In general, such cold regions are characterised by the presence of large unsaturated organics like the HC_n or HC_nN families, as a consequence of ion-molecule reactions (Herbst, 2017; Herbst et al., 1973), even though most carbon atoms are locked into CO molecules which become the second most abundant gas phase species after molecular hydrogen, a consequence of the kinetics rule.

Ion-molecule reactions include proton/H-additions (by reaction with H_3^+ or H_2), hydrocarbon chain elongation by C-addition reactions with C^+, N-addition to cations and neutralization (by dissociative recombination, which tends to favor fragmented products). Hydrocarbon chains tend to be unsaturated because, in general, proton/H-additions become less and less efficient as the hydrocarbon backbone grows. Somewhat more saturated molecules may form by condensation reactions[10] followed by dissociative recombination, e.g. $C_2H_2^+ + CH_4 \rightarrow C_3H_5^+ + H$ leading to CH_3CCH (see Herbst (2017) and references therein).

Neutral-neutral gas-phase reactions between a closed-shell and a radical are especially important as many of them are barrierless and can take place at very low temperatures. An example are the reactions between acetylene and C/CN/CCH leading to C_3H and $C_3/HC_2CN/HC_4H$.

On the other hand, the formation of saturated and O-bearing organics is thought to work out in a different way, dominated by grain chemistry and neutral-neutral gas-phase chemistry, with little contribution from ion-molecule chemistry and are more common in warmer regions, see below.

Grains in dense cores cores grow thick molecular ices as these are radiation-procteted regions, the cold conditions permit the accretion and storage of gas-phase species which can undergo surface chemical reactions (Figure 1.5). Chemical reactions on dust grains are of associative nature, e.g. the formation of molecular hydrogen from to H atoms. Here the dust grain acts as a catalyst and as a third body, absorbing the energy released by the reaction. This opens new chemical paths not accessible in the gas phase. Particularly important are hydrogenation reactions, due to the high mobility of hydrogen atoms (Tielens et al., 1982). Some of these reactions include the formation of water, formaldehyde and methanol, other less abundant hydrydes like methane and ammonia (formed from the hydrogenation of C and N) and CO_2 (formed by the association of CO and OH Ioppolo et al., 2011; Noble et al., 2011). The composition of the gas affects the one of the ices. Inside dense cores, C is converted into CO which becomes the most abundant gas-phase molecule. This means that less CH_4 is formed while CO_2 becomes more abundant in the ices (Boogert et al., 2015). Frozen CO undergoes hydrogenation leading to formaldehyde and methanol, in which tunneling reactions are very important (Andersson et al., 2011; Kenzo Hiraoka et al., 2002; Rimola et al., 2014). Deeper into the dense core, species heavier than He tend to disappear from the gas phase as they efficiently freeze out into ice mantles due to low temperatures and high densities ($>10^5$ cm^{-3}). Over a 90%

[10] Chemical reactions in which at least two reactants couple forming a larger molecule as main product and some smaller byproduct of reaction.

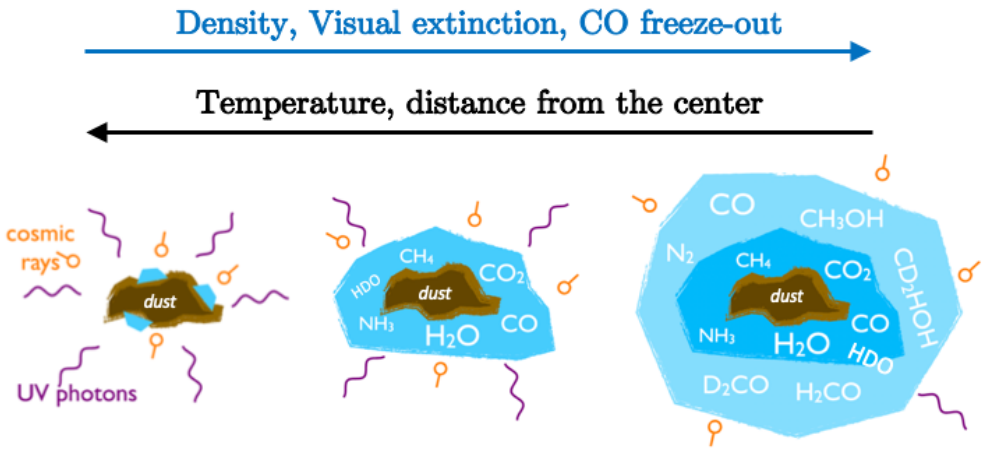

Figure 1.5: *Schematic description of the ice evolution in a dense core adapted from Paola Caselli et al. (2012).*

of CO depletion has been observed in the central zones of prestellar cores (Bacmann et al., 2002; P. Caselli et al., 1999). The increased abundance of CO in the ices has serious implications for the overall chemical structure. First, CO-derivatives appear in the ices (e.g. formaldehyde, methanol) together with intact CO; second, CO is the second most abundant species in the gas phase, and despite of being chemically inert, it can easily get protonated by H_3^+ forming HCO^+, which then returns to CO after electron recombination reactions, removing large amounts of H_3^+ from the gas phase. Therefore, the gradual disappearance of CO from the gas opens new chemical paths. Some of the consequences are (i) the increase of deuterated species (over a 10% with respect to the standard D/H ratio (Bacmann et al., 2003; P. Caselli et al., 2003; Ceccarelli et al., 2014; Crapsi et al., 2005)) as the destruction rates of H_2D^+ (the initiator of D-fractionation) with CO drop due to the depletion of the latter; and (ii) the increase in abundance of N_2H^+ as CO depletes (one of the major destruction channels of N_2H^+ is $N_2H^+ + CO \rightarrow HCO^+ + N_2$).

Despite the strong dimming of interstellar photons in dense cores (beyond visual extinctions $\sim$ 3 mag external UV photons are no longer important Hollenbach et al., 2009), photoprocesses are important at this stage. Secondary UV photons originated by the interaction of cosmic rays with H_2 (Gredel et al., 1989; Prasad et al., 1983) are able to break chemical bonds of frozen species, forming radicals (R. T. Garrod et al., 2006; K. I. Öberg et al., 2009), although these radicals may also be formed by partial hydrogenation of frozen species (V. Taquet et al., 2012). The coupling reactions of these radicals once the temperature rises (due to the evolution of the core) are thought to form most complex species (see §1.3).

Back in the 2010s, "interstellar complex molecules" (COMs or iCOMs[11]) were detected towards cold sources (e.g. Bacmann et al., 2012; Jiménez-Serra et al., 2016; Vastel et al., 2014) and cold protostellar envelopes (e.g. Cernicharo et al., 2012; Jaber et al., 2014; Karin I. Öberg et al., 2010). This stimulated the research on (i) non-thermal processes on the ice-coatings of dust grains like chemical desorption (Duley et al., 1993; R. T. Garrod et al., 2007; Minissale et al., 2014b, 2016b; Takahashi et al., 1999c; Vasyunin et al., 2013), UV-induced photodesorption (Bertin et al., 2013, 2016; Fayolle et al., 2011) and CR spot heating (T. I. Hasegawa et al., 1993; Juris Kalvāns, 2016; Leger et al., 1985), and (ii) new cold gas-phase chemistry in which neutral-neutral reactions lead to the formation of Earth-like organics like methyl formate and dimethyl ether, initiated by methanol reacting with OH forming CH_3O in the gas phase (Balucani et al., 2015).

[11] Defined as a molecule containing carbon and composed of at least six atoms Ceccarelli et al., 2017b; Herbst et al., 2009b

Class 0/I and hot corinos

Physics

The evolution from pre-stellar core towards stellar system is divided into different "classes" of protostars according to their spectral signatures[12]. An overview of the process with some real examples is shown in Figure 1.3. It must be taken into account, however, that the protostellar phase is actually very short (few Myr) in comparison to solar-type star lifetimes ($\sim 10^{10}$ yr).

From the prestellar core phase, the general picture reads as follows: once the collapse has started, matter falls towards the center feeding the central object. The gravitational energy of the collapse is released at the center into radiation. Initially, the collapse is isothermal, but as it proceeds, the inner part heats up. The protostar accretes mass from the envelope (which still extends to sizes comparable to those of dense cores, namely $\sim 10^4$ AU) through an accretion disk. Both the density and the temperature increase towards interior and so does the complexity of the observed gas-phase species. This sets two differentiated regions: the warm ($\gtrsim$100 K) vicinity to the protostar and the cold outer envelope. In particular, in a Class 0 protostar the central object is highly obscured by the thick collapsing envelope[13]. In order to remove the angular momentum in excess, a bipolar, highly collimated outflow emerges from the protostar. An example of Class 0 protostar is the binary system NGC 1333 IRAS 4A, shown in Figure 1.3. The two protostars of this binary system are traced by dust continuum and the outflows by their characteristic molecular emission of SiO. After $\sim 10^5$ years, the system protostar + disk + envelope enter the Class I phase. The parent envelope has grown thinner due to accretion and the cavities caused by the outflowing material. The disk is now visible in the IR as a consequence of the absorption and re-emission of the radiation coming from the protostar by the dust in the disk.
An example of a Class I protostar is the IRAS 04302+2247 object shown in Figure 1.3 as seen by ALMA.

Chemistry

The warm regions around Class 0/I protostars are called hot corinos, which, in practice, can be defined as warm ($\gtrsim$ 100 K) and dense regions ($\sim 10^7$ cm^{-3}) characterized by an enhanced gas-phase richness of iCOMs (Cazaux et al., 2003; Ceccarelli, 2004; Ceccarelli et al., 2000). Around the hot corino, other chemical zones appear as a consequence of the continuous changes in temperature and density until the core merges with the parent molecular cloud. In between, chemistry typical of prestellar cores (e.g. CO freeze-out) exists (e.g. J. Jørgensen et al., 2005). In those regions where temperature exceeds $\sim$ 30 K, methane (and CO) can be injected to the gas-phase from ices, where it can react *via* ion-molecule processes with C^+, forming so-called carbon chain molecules[14]. Meanwhile, less volatile molecules in the ices begin to gain mobility. This is particularly important for radicals formed in the prestellar stage. These radicals may have a chance to react forming iCOMs during this warm-up stage as gas-phase hydrogen atoms have too short residence times on interstellar ices to saturate radicals back. The coupling of radical species may form more saturated species such as alcohols, hydrocarbons, esters, and nitriles (R. T. Garrod et al., 2006; Robin T. Garrod et al., 2008; Herbst, 2017; Herbst et al., 2009b). They may then be released to the gas phase by either thermal or non-thermal processes. Nevertheless, it is not clear that surface radical-radical coupling reactions do actually account for the observed abundances of iCOMs in the ISM (Barger et al., 2020; V. Taquet et al., 2012).

In the hot corino region, once the dust temperature exceeds $\sim$100 K, grain mantles fully evaporate, releasing their molecular content into the gas-phase. A rich chemical diversity is observed, with both simple molecules and iCOMs. In the hot corino, neutral-neutral gas-phase reactions that posses energy barriers become available (Paola Caselli et al., 2012; Charnley et al., 1992; Herbst, 2017; D. Skouteris et al., 2017; Dimitrios Skouteris et al., 2018; Vianney Taquet et al., 2016; Vazart et al., 2020), which enhances even more the diversity of complex chemicals.

[12] The shape of the $\log(\lambda F_\lambda)$ *vs* λ, where F_λ is the emitted energy flux.

[13] In order to observe any of the properties of these objects one needs to use very long wavelengths, such as sub-millimeter.

[14] The presence of carbon chain molecules may be a signature of fast collapse, e.g. due to a shock, so that carbon had not enough time to form CO and froze out instead during the prestellar phase N. Sakai et al., 2008 (long chained hydrocarbons; Aikawa et al., 2008; Hassel et al., 2011, 2008; N. Sakai et al., 2010a,b)

Molecular shocks caused by outflows are chemically interesting regions too. The ejected material from the protostar creates shocks when it hits the surrounding quiescent medium. This forms chemically rich zones as ice-coated dust grains are sputtered[15], releasing their ice content into the gas phase (P. Caselli et al., 1997; Flower et al., 1994; Gusdorf et al., 2008a,b; Schilke et al., 1997), and new molecules are formed in the gas phase, making such objects unique astronomical "laboratories" where to constrain iCOM formation mechanisms (Paola Caselli et al., 2012; Codella et al., 2017, 2020; De Simone et al., 2020).

All in all, the chemical content of an early protostar is directly inherited from the prestellar phase thanks to interstellar ices which act as "time capsules", and then becomes the starting point of hot core/corino chemistry.

Despite of the increased chemical diversity and complexity, ion-molecule reactions followed by dissociative recombination destroy complex species, forming simpler ones. Nonetheless, part of the formed complex species may have a chance to be transferred to the following stages thanks to the cold midlplane of the disk, where they remain frozen on grains.

Class II/III and protoplanetary/debris disks

Physics

After $\sim 10^6$ years, the protostar enters in the Class II (or T-Tauri) phase. Most of the envelope has been accreted or blown away and the disk is now fully visible. Dust coagulation in the disk is efficient, so that planetesimals will form.

The protoplanetary disk will further evolve into a debris disk (Class III). Gas has been added to the star, gas planets or has been blown away due to the stellar radiation winds. The debris disk will keep evolving for millions of years, *via* collisions of planetesimals, forming planets. An example of Class II the HH 30 object and an example of a Class III protostar is the HR 8799 system, both shown in Figure 1.3.

Regarding the structure of the protoplanetary disk in the Class II stage, one can differentiate two directions, the radial and the vertical ones. The disk is symmetric about the mid-plane in the vertical direction, showing lower temperatures and higher densities in the region close to the mid-plane where gas species are depleted and ices grow thick, as opposed to the disk surface, which directly suffer the radiation of the protostar. On the radial direction, the temperature and density increase closer to the protostar, while lower temperatures are found further out. This implies that moving out from the protostar, the different species frozen in the mid-plane will sublimate at different spatial positions, generating the so-called snow-lines.

Chemistry

The chemical and physical structures of the disk are strongly entangled. The disk can be vertically divided into three regions: (i) the most UV-photon exposed region is dominated by photodissociation due to the radiation coming from the protostar and the interstellar UV field, (ii) a warm molecular layer where molecules survive, and (iii) the colder regions near the midplane, with temperatures close to those in prestellar cores, where additionally, densities rise up to 10^{11} cm^{-3} (Henning et al., 2013; Karin I. Öberg et al., 2021). It is in the mid-plane region where chemicals inherited from the preceding stages may survive, although this material could get mixed with processed one due to the settling and inwards drift of dust particles due to their growth and the inherent turbulence of the disk.

1.4 Complex Organic molecules: the two paradigms

iCOMs are important for at least two reasons: first, their formation in the harsh environments of the ISM is a real challenge for astrochemists, and second they represent the dawn of organic chemistry in space and could be involved in the emergence of life serving as the building bricks of more complex species, which could somehow be inherited through the different phases of star and planet formation (Paola Caselli et al., 2012; de Duve, 2011; De Duve, 2005).

[15] Gas–grain collisions.

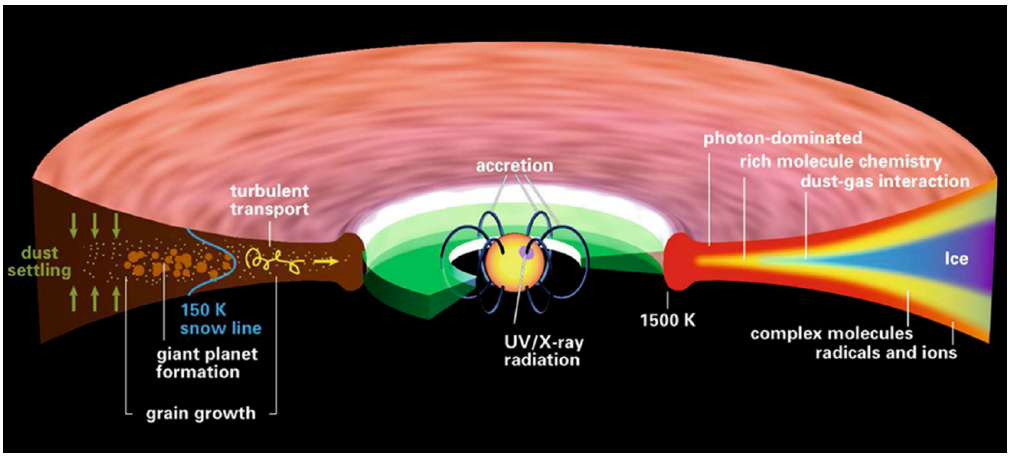

Figure 1.6: *Diagram of the physical and chemical structure of a protoplanetary disk. Taken from Henning et al. (2013). In the left hand side one can see a representation of the different physical processes taking place (e.g. the water snow line at 150 K, dust transport), and in the right hand side one can see the layered chemical structure of protoplanetary disks.*

From the astronomical side, among the more than 200 molecules detected in the ISM, about one third are iCOMs[16]. Indeed, since their discovery in the 70s (e.g. Rubin et al., 1971), they have been detected in a variety of interstellar sources like star formation regions (e.g. Belloche et al., 2017; Cazaux et al., 2003; Kahane et al., 2013; Ligterink et al., 2017; A. López-Sepulcre et al., 2015; McGuire et al., 2018; Mendoza et al., 2014; Rubin et al., 1971), the circumstellar envelopes of AGB stars (e.g. Cernicharo et al., 2000), shocked regions (Arce et al., 2008; Codella et al., 2017, 2020; De Simone et al., 2020; Lefloch et al., 2017), and external galaxies (Muller et al., 2013). Despite of this, there are intrinsic limitations to the level of chemical complexity that astronomers are able to detect. Indeed, the larger the molecule, the smaller its rotational constants and therefore the larger its rotational partition function, which implies that weaker line intensities are detected by astronomers.

Therefore, understanding how they are formed and destroyed is a great asset for understanding the ultimate organic complexity in the ISM. This complexity increment is the result of a tight interplay between gas-phase and grain surface chemistry, where the two can have a different importance in time and space for different molecules.

In present, there are two principal paradigms to explain the evolution of the chemical complexity observed in the ISM according to where interstellar complex organic molecules (iCOMs) are formed, either in the gas-phase (Caselli et al., 1993; Charnley et al., 1992; Millar et al., 1991) or in the ices coating insterstellar dust grains R. T. Garrod et al., 2006; Robin T. Garrod et al., 2008 (see Figure 1.7). They both share a common initial step, the formation of ices made of simple hydrogenated (e.g. water, methanol, formaldehyde, methane, ammonia...) and oxidized (e.g. CO_2) species on interstellar dust grains during the prestellar phase (§ 1.3) as a result of the accretion of gas-phase atomic and molecular species, and surface hydrogenation reactions. From this point on they diverge. The gas-phase paradigm says that, as the chemical content of these ices is sublimated in warm star-forming stages (e.g. at the hot corino, § 1.3), these molecules undergo hot gas-phase reactions leading to iCOMs (Charnley et al., 1992). On the other hand, the surface chemistry paradigm says that these simple ices are energetically processed[17] forming radical species that remain frozen in the ice. As the dust temperature slowly rises due to the evolution of the protostar, these radical species become mobile on the surface. They diffuse over the dust and eventually meet and react forming an iCOM as a result of their coupling, in a sort of LEGO-like fashion. These iCOMs remain frozen, so that at higher temperatures they sublimate and are observed in the hot corino R. T. Garrod et al. (2006).

The gas-phase model was in vogue during the 1990s up to the first half of the 2000s, when it was

[16] See, for example, Molecules in Space, link here, by the Cologne Database for Molecular Spectroscopy for a list of detected molecules in interstellar, circumstellar and extragalactic sources

[17] By the dim UV-field generated by the secondary photons resulting after the interaction of CR with hydrogen molecules, or the CR themselves.

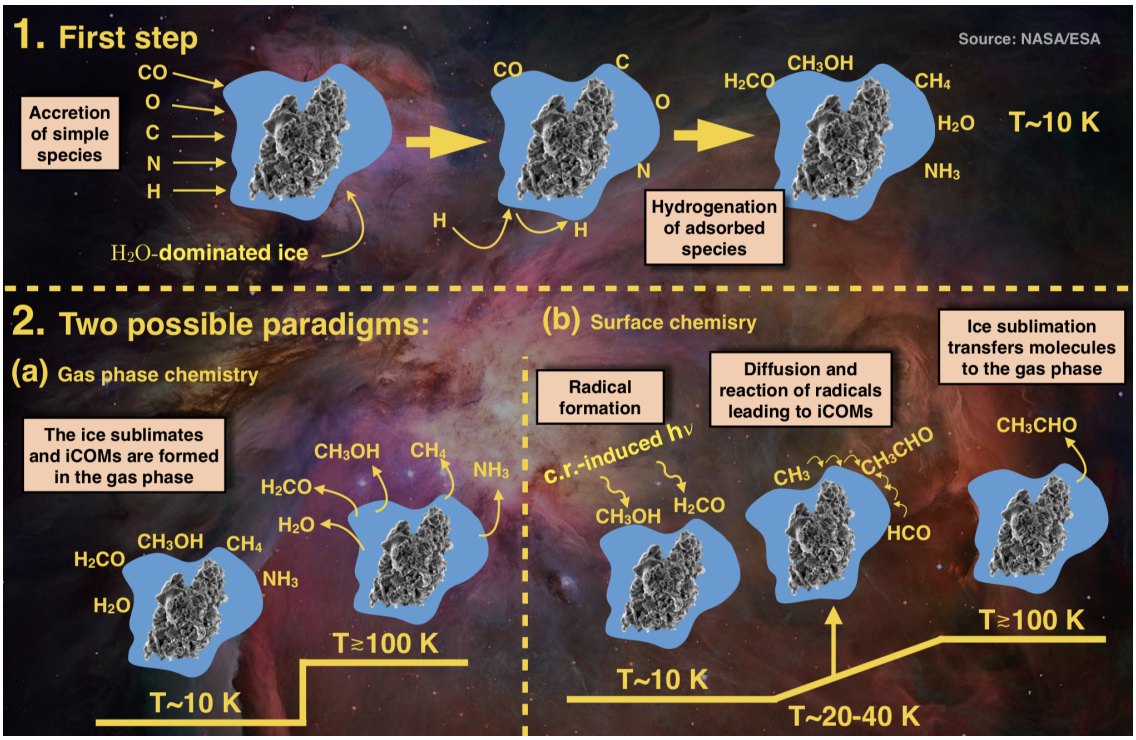

Figure 1.7: *Schematic description of the two main paradigms for iCOM formation in the ISM. Read the text for more information.*

realized that gas phase ion-molecule reactions alone cannot account for the observed iCOM abundances[18] (Geppert et al., 2005, 2006; Horn et al., 2004). At this point, gas phase "hot" chemistry lost its prevalence in astrochemical models. Since the gas-phase does not work, then iCOMs must be formed on dust grains, was the thought of many in the community after the many successes of laboratory studies in producing iCOMs when energetically processing interstellar ice analogues[19] (e.g. Hagen et al., 1979; Strazzulla et al., 1983; Tielens et al., 1987). This was the onset of the surface chemistry model by R. T. Garrod et al. (2006).

However, the surface chemistry paradigm has not been free of uncertainties and criticism. For example, despite its popularity due to its capacity to qualitatively explain the formation of iCOMs, it still fails at reproducing the observed absolute and relative abundances of many molecules[20]. Indeed, there there are still many details poorly understood, like photodissociation yields, the actual UV field produced by CRs, the

[18] These ion–molecule reactions involve the formation of cationic molecules (e.g. protonated dimethyl ether, $CH_3OCH_4^+$) as a consequence of protonation reactions. In order to form the neutral iCOM, the extra proton has to be eliminated. This step was thought to happen through an electron recombination step. However, this kind of reaction favors highly fragmented products, so that iCOM formation remains highly inefficient (Geppert et al., 2006). This is a big issue, which, however, could be attenuated by considering alternative paths for the elimination of the proton, like reaction with an ammonia molecule leading to the iCOM and an ammonium cation, NH_4^+, (Rodgers et al., 2001; Vianney Taquet et al., 2016). Nevertheless, while ammonia is abundant in ice mantles, it is not in the gas phase of hot cores/corinos.

[19] However, laboratory experiments on the energetic processing of ices show that a large variety of complex species can be formed as a consequence of an entangled network of chemical processes. This is due to the efficient production of hot radicals as a consequence of the photodissociation of molecules in the ice. These radicals can react with other radicals and molecules giving rise to the complex reaction network. In the end, there is no clear signature left about the formation process, since it is impossible to unravel the kinetics and relative importance of each process.

[20] For example, Vianney Taquet et al. (2015) found large deviations in the relative abundances of methyl formate ($HCOOCH_3$) and dimethyl ether (CH_3OCH_3) with respect to methanol (as large as 2 orders of magnitude) when employing the surface chemistry model by Robin T. Garrod (2013). Similarly, J. K. Jørgensen et al. (2016) found several mismatches between the predictions of Robin T. Garrod (2013) and the observed relative abundances of several iCOMs including methyl formate, glycolaldehyde, ethylene glycol ($(CH_2OH)_2$), acetaldehyde (CH_3CHO), and acetic acid (CH_3COOH), in both low mass and high mass protostars. Codella et al. (2017) found that the formation of formamide is better explained by gas phase reactions based on the neutral–neutral NH_2 + H_2CO reaction (V. Barone et al., 2015; D. Skouteris et al., 2017; Vazart et al., 2016). More recently Barger et al. (2020) found large deviations (of as much as 3 orders of magnitude) between simulated and observed abundances of acetaldehyde in the hot cores NGC 7538 IRS 1 and W3(H2O), while Vazart et al. (2020) propose that acetaldehyde can be a gas phase product, based on the ethanol tree synthetic sequence by Dimitrios Skouteris et al. (2018)

reactivity of radicals (is it really barrieless? are there more chemical paths available?), surface diffusion, the fate of chemical reaction energies...

Most importantly, in the 2010s, the surface chemistry paradigm was challenged by observations of iCOMs in regions of the ISM where the warm-up phase required for radicals to diffuse and meet cannot be at work due to the low temperatures, $\sim$10 K, (Bacmann et al., 2012; Cernicharo et al., 2012; Jaber et al., 2014; Jiménez-Serra et al., 2016; Vastel et al., 2014). Tn this context, alternative processes surch as non-thermal desorption, cosmic ray-induced cold chemistry and new cold gas phase chemical routes have been put forward to explain this (see more details in § 4.1)

In summary, there is not yet a clear "theory" of how iCOM are formed as many details related to interstellar ice surface chemistry remain unclear. In addition, we may have not seen the full picture yet, meaning that maybe gas phase reactions are more important than we thought.

In the following section I discuss what role can computational chemistry play in astrochemistry, and why it is so important, if not mandatory. Then I expose the objectives of this thesis.

1.5 Why computational chemistry?

Astrochemistry is a multidisciplinary field. Astronomy, experimental chemistry and models are part of the natural environment of this field, and computational chemistry has a definitive slot in it (see §4.1). All these fields have accompanied astrochemistry ever since its birth, in the 70s. However, computational methods have only become maturely available for large and accurate simulations in the two last decades, thanks to the increase in computational capabilities and the improvements of computational methods. In additon, there are some limitations related to experiments and astrochemical models, especially related to dust grain chemistry, which computational methods can tackle.

Laboratory experiments are key at guiding the community as they can tell us whether a mechanism works or not at conditions close to those of the ISM and they can provide exceptional physicochemical data on molecular and surface properties, but they have severe limitations. First, the time-scales of star formation processes in the interstellar medium is of tens of millions years, while that of an Earth-based laboratory experiment is of hours or days. This forces experimental astrochemists to use exaggerated fluxes of atomic and molecular species (e.g. 10^{12}–10^{13} H atoms cm^{-2} s^{-1}), energetic particles, and photons in order to be able to observe chemical changes in their samples within laboratory timescales. Regarding surfaces, they cannot exactly reproduce the properties of interstellar ices, like their size, chemical composition and most important, structure. Indeed, very often non realistic ice mixtures are used to keep the experimental conditions as simple as possible to avoid an overflow of experimental parameters. These limitations imply the build-up of large reactants concentrations on laboratory surface samples, and the artificial injection of energy in the system as a consequence of the large chemical fluxes with excess kinetic energy (Tielens, 2013; Vidali, 2013). Additionally, many microscopic aspects belonging to the atomic scale cannot be attained due to the "ensemble" detection methods (e.g. temperature programmed desorption followed by quadrupole mass spectrometry, TPD-QMS, of gas phase species or reflection absorption infrared spectra, RAIRS, which allows to directly probe ice surfaces *in situ*, see e.g. the reviews by Linnartz et al. (2015) and Cuppen et al. (2017)), i.e. one cannot detect a single molecule desorbing from a surface or a single reaction, something that is possible with computational chemistry.

Regarding astrochemical models, they are designed with more or less complexity focusing on particular problems related to astrochemistry, for example aiming at comparing the predictions of the abundance of particular molecules, with the final goal of reproducing and rationalizing astronomical observations. These models are fed with physicochemical properties, e.g. reaction rate coefficients, binding energies... sometimes obtained from solid phase experiments (which then need to be interpreted at atomic scale) or computational chemistry calculations, but quite often from gas phase experiments, or are just extrapolated from similar processes using chemical intuition (Cuppen et al., 2017; Linnartz et al., 2015). This renders the predictions of astrochemical models quite uncertain. In addition to this, the chemical networks utilized in these models can be incomplete and/or out-dated given the vast amount of chemical reactions included nowadays. Therefore, much is yet to be done.

Computational chemistry methods can tackle the weak points of both experiments and astrochemical models thanks to its unique capacity to provide physicochemical data like reaction rates, activation energies, structural properties... directly at the atomic level. It is therefore, a complementary tool to experiments,

and a source of physicochemical insights on microscopic processes. **Chapter 3** is dedicated to **reviewing computational chemistry works in the literature up to 2017** (when this thesis started), focused on surface chemistry, in order to present the state of the art of computational chemistry works. Additionally, **Chapter 2** contains a review of the **computational chemistry tools** used in this thesis.

1.6 Objectives of this thesis

In this PhD thesis I studied surface chemistry processes key for the surface chemistry paradigm in Figure 1.7. Specifically I focused on: (i) radical–radical surface reactions, and (ii) the fate of the energy released by two chemical reactions on water ices.

The first set of goals regards **radical–radical reactions** on interstellar ice surfaces. The questions I aim to answer for a sample of radical–radical reactions are: (i) Are radical–radical surface reactions actually barrierless as commonly assumed? (ii) In a reactive event, the products are always iCOMs? Or are there other channels? (iii) If there are other channels, do they compete with iCOM formation? and (iv) Does the surface environment affect the reactivity of radicals? These goals are investigated in **Parts I and II**. The former Part contains static quantum chemistry calculations in which the activation energy barriers of selected radical–radical reactions is investigated. In the latter, kinetic calculations are run for the formation acetaldehyde, and its formation efficiency is derived.

On the other hand, in **Part III** I tackle another important topic, the **fate of the energy liberated by surface reactions**. For this we investigated two key surface reactions: the formation of HCO and the formation of molecular hydrogen on water ice. The questions to answer are: (i) How is the energy partitioned among the surface and the product molecule? (ii) Are these reactions possibly leading to the desorption of the product as a result of the liberated energy? (iii) Could the energy absorbed by the ice be employed in the desorption of nearby, weakly adsorbed species?

Each one of these Chapters have their own short introduction with the scientific context, the specific goals of each one of them, the novelties, the methods and a summary of the results. Then, the research carried out in each part is presented in different Chapters. Finally, the **conclusions and the perspectives** of this doctoral thesis work are presented in **Chapter 13**. At the end the reader will find a copy of the published and accepted scientific articles that have derived from the research presented here.

Chapter 2
Theoretical background

Outline

This chapter contains a review of the methods and theoretical tools employed in this thesis. In sections 2.1, 2.2 and 2.3 the basics of wave function theory and density functional theory are presented and reviewed; in section 2.4 the broken (spin) symmetry aproximation is explained; section 2.5 presents the different ways of modeling surfaces using computational chemistry; section 2.6 reviews how potential energy surfaces can be used in order to derive kinetics within the transition state theory and the RRKM theory; section 2.7 briefly introduces how molecular dynamics simulations are run; and finally a short summary of this chapter can be found in § 2.8.

2.1 Molecules as quantum systems

The molecular Hamiltonian (F. Jensen, 2017; Szabo et al., 1996)

Chemical reactions can only be understood in detail if we understand what happens with the electronic structure during the chemical change. This can only be achieved hitherto with quantum mechanics. The fundamental basis is the *Schrödinger equation*[1]:

$$\hat{H}|\Psi(\mathbf{r},t)\rangle = i\hbar\frac{\partial}{\partial t}|\Psi(\mathbf{r},t)\rangle, \tag{2.1}$$

where $\hbar = h/2\pi$ with h is Planck's constant, $\hat{H}$ is the Hamiltonian operator and $|\Psi\rangle$ is the wave function that describes an instantaneous state of the whole system. This linear partial differential equation describes the wave-functions and energies of a set of N particles with positions $\mathbf{r} = \{\mathbf{r}_i\}$ with $i = 1, ..., N$ that can evolve over time.

The wave-function itself lacks of physical meaning, but $\langle\Psi|\Psi\rangle = \int d\mathbf{r}\Psi^*\Psi$ is the probability density of finding each particle at a given point and at a given time. Other physical properties can also be obtained from the wave-function by applying operators, since it contains all the information of the system. In the framework of quantum mechanics, any measurable property has an associated linear and Hermitian operator. For example, in the case of energy this operator is the Hamiltonian, $\hat{H}$:

$$\hat{H} = \underbrace{\sum_{i=1}^{N} -\frac{\nabla^2_{(i)}}{2\hbar^2 m_i}}_{\hat{T}} + \underbrace{\sum_{i=1}^{N}\sum_{j>i}^{N}\frac{q_i q_j}{4\pi\epsilon_0|\mathbf{r}_i - \mathbf{r}_j|}}_{\hat{V}}, \tag{2.2}$$

which includes the kinetic ($\hat{T}$) and potential ($\hat{V}$) energy terms. The former is the sum of one-particle kinetic energies (where m_i is the mass of the ith particle and $\nabla^2_{(i)}$ is the Laplacian operator acting on the coordinates of the ith particle) and the latter is the sum of two-particle Coulomb's interactions (where q_i is the charge of the ith particle).

Since Eq. 2.2 has no explicit dependence on time, the wave-function can be expressed as $|\Psi(\{\mathbf{x}_i\},t)\rangle = |\Psi_t(t)\rangle \times |\Psi_x(\{\mathbf{x}_i\})\rangle$, where $\Psi_t(t) = A\exp(-iEt)$, i.e. it is a phase and therefore it carries no information on the physics of the system. Therefore one can keep only the space-dependent part, reaching the *time-independent* (non-relativistic) Schrödinger equation:

$$\hat{H}|\Psi(\{\mathbf{x}_i\})\rangle = E|\Psi(\{\mathbf{x}_i\})\rangle, \tag{2.3}$$

from which one can get the energy: $E = \langle\Psi|\hat{H}|\Psi\rangle$.

Chemical systems consist of 2 different types of particles: electrons and nuclei. For a system with n electrons and $N - n$ nuclei, the kinetic energy contributions can be separated into the electronic and the nuclear terms, $\hat{T}_e$ and $\hat{T}_n$. Regarding the potential energy term, there are crossed terms: electron-electron, nucleus-nucleus and electron-nucleus potential energy terms (V_{ee}, V_{nn}, V_{en}). The last term couples electrons and nuclei, rendering the system not separable into electron-dependent and nuclei-dependent wave-functions. Thus, the *molecular Hamiltonian* (in atomic units) is:

[1] This equation is written in "bra-ket" (or Dirac's) notation. The wave-function is written as a vector or "ket", $|\Psi\rangle$, such that it has its dual "bra", $\langle\Psi|$.

$$\hat{H} = \hat{T}_e(\mathbf{r}) + \hat{T}_n(\mathbf{R}) + V_{ee}(\mathbf{r}) + V_{nn}(\mathbf{R}) + V_{en}(\mathbf{r},\mathbf{R}) = \\ -\sum_{i=1}^{n}\frac{\nabla^2_{(i)}}{2} - \sum_{K=n+1}^{N}\frac{\nabla^2_{(K)}}{2M_K} + \sum_{i=1}^{n}\sum_{j>i}^{n}\frac{1}{|\mathbf{r}_i - \mathbf{r}_j|} \\ + \sum_{K=n+1}^{N}\sum_{L>K}^{N}\frac{Z_K Z_L}{|\mathbf{R}_K - \mathbf{R}_L|} - \sum_{i=1}^{n}\sum_{K=n+1}^{N}\frac{Z_K}{|\mathbf{r}_i - \mathbf{R}_K|}, \quad (2.4)$$

where the nuclear charges have been changed by their atomic numbers ($q_K = +Z_K$) and the explicit electronic or nuclear coordinates dependence, $\mathbf{r}$ and $\mathbf{R}$ respectively, are used.

The non-separability of the wave-function into an electronic and a nuclear part limits the applicability of eq. 2.3, mainly for hydrogenoid atoms (i.e. atoms composed by nuclei and one electron). However, molecules are multielectronic systems and for this reason the following approximation will come in handy.

The Born-Oppenheimer approximation (BOA): the origin of the potential energy surface (F. Jensen, 2017)

Introduced in 1927 by Max Born and J. Robert Oppenheimer, this approximation introduces the following *ansatz* – "*the motion of electrons can be decoupled from that of nuclei given the higher mass of nuclei*" ($m_{proton} \sim 1836 \times m_e$). The mathematical realization of this statement starts by considering nuclei as classical, charged point-like particles. This removes the kinetic term related to nuclei and converts V_{nn} into a constant. In a first step the remaining terms of the Hamiltonian are grouped to solve the *electronic* Schrödinger equation:

$$\hat{H}_e(\mathbf{r};\mathbf{R})|\Psi_e(\mathbf{r};\mathbf{R})\rangle = \left[\hat{T}_e(\mathbf{r}) + \hat{V}_{ee}(\mathbf{r}) + \hat{V}_{en}(\mathbf{r};\mathbf{R})\right]|\Psi_e(\mathbf{r};\mathbf{R})\rangle = U_e(\mathbf{R})|\Psi_e(\mathbf{r};\mathbf{R})\rangle, \quad (2.5)$$

where $|\Psi_e(\mathbf{r};\mathbf{R})\rangle$ is the electronic wave-function with energy $U_e(\mathbf{R})$. These two quantities depend on the nuclear coordinates $\mathbf{R}$, at least parametrically, because one gets a unique $U_e(\mathbf{R})$ value at a given $\mathbf{R}$.

By adding the constant nuclear repulsion to this energy, one gets the so-called potential energy surface (PES): $E(\mathbf{R}) = U_e(\mathbf{R}) + V_{nn}(\mathbf{R})$. Thus, for each arrangement of nuclei, a different $E(\mathbf{R})$ value is obtained, giving rise to an energy (hyper)surface. Eq. 2.5 provides a set of solutions, each one is an electronic state. Therefore, there is a different PES for each of them, although one is normally only interested on the ground one. Minima in the PES correspond to stable equilibrium geometries of the chemical species, e.g. stable molecular geometries.

In a second step one solves the full Schödinger equation in order to get the solution for the full system (electrons and nuclei). Now, crossed terms appear, since $\hat{T}_n$ can act on $|\Psi_e(\mathbf{R})\rangle$ as it depends parametrically on nuclear coordinates. These terms are neglected in the BOA, leading to:

$$\left(\hat{T}_n + E(\mathbf{R})\right)|\Psi_n(\mathbf{R})\rangle = E_{tot}|\Psi_n(\mathbf{R})\rangle \quad (2.6)$$

where it now becomes apparent that nuclei move over the PES[2]. The solutions to the previous equation are the vibrational and rotational energy levels of the system. Nevertheless, in the end one further simplifies the PES locally introducing the harmonic oscillator and the rigid rotor models, e.g. to a minimum of the PES.

The BOA works fairly well in most of the cases, as long as the different electronic states are well separated surfaces. So far we have not taken into account some key quantum aspects of electrons, like their indistinguishably and their spin. The first topic will be the main focus of the next section and the latter will appear later on.

[2]This is but a simplified version of the actual BOA, which implicitly contains the adiabatic aproximation (i.e. the total wave-function is restricted to a single electronic state). For a full derivation reference (F. Jensen, 2017) is recommended.

Pauli exclusion principle and the electronic problem (F. Jensen, 2017)

Electrons are non-distinguishable particles. That is, any observable derived from the wave-function, like their probability density, must be invariant given any permutation of the electronic coordinates: $|\Psi(...,\mathbf{r}_i,...,\mathbf{r}_j,...)|^2 = |\Psi(...,\mathbf{r}_j,...,\mathbf{r}_i,...)|^2$.

Let's denote $\hat{P}$ the permutation operator of parity[3] p that permutes two electrons in the wave-function. It must be hold that $\hat{P}|\Psi\rangle = (-1)^p|\Psi\rangle$. This is the *Pauli exclusion principle*, which may be translated in words as – "*An acceptable wave-function for n electrons must be anti-symmetric with respect to the exchange of any two electrons*". Any electronic wave-function must obey this principle.

Yet, there is still an underlying problem: the shape of the electronic wave-function is in general not known. In fact it can only be exactly derived for single-electron systems, e.g. H_2^+. This is the so-called *electronic problem*.

In order to tackle it several approximate methods have been proposed. Some of them focus on the wave-functions (wave-function-based methods), while others focus on the electronic density, i.e. the squared modulus of the electronic-wave function. These methods are reviewed in the following sections.

2.2 Wave Function-Based Methods

Some basics and Hartree-Fock theory (F. Jensen, 2017)

The variational method stands out in computational chemistry. This method takes Eckart's theorem (eq. 2.7) as a starting point in order to obtain approximate ground-state wave-functions

$$\frac{\langle\Psi_{trial}|\hat{H}|\Psi_{trial}\rangle}{\langle\Psi_{trial}|\Psi_{trial}\rangle} = E \geq \frac{\langle\Psi_0|\hat{H}|\Psi_0\rangle}{\langle\Psi_0|\Psi_0\rangle} = E_0, \tag{2.7}$$

where the denominators ensure the normalization. It states that one may use a trial function (Ψ_{trial}) to compute an energy, E, which will always be an upper bound to the actual one, E_0. One may recursively apply this theorem variating in some way the trial wave-function to reach the lowest energy possible.

How is it possible to have a good trial wave-function? The state of a single electron depends on four variables: three for its position ($\mathbf{r} = (r_1, r_2, r_3)$) and one for its spin ($\sigma$). Since the Born-Oppenheimer (electronic) Hamiltonian has no explicit dependence on spin, the electronic wave-function can be separated into a spatial part, called orbital, $|\Psi(\mathbf{r})\rangle$, and a spin function, $|\omega(\sigma)\rangle$, which can take two values, spin up[4], $|\alpha\rangle$, or spin down, $|\beta\rangle$. The result is a *spin-orbital* function: $\chi(\mathbf{x}) = |\Psi(\mathbf{r})\rangle|\omega(\sigma)\rangle$, where $\mathbf{x} = (\mathbf{r}, \sigma)$. As an *ansatz* for a many-electron system, let's assume a system of N non-interacting electrons. The Hamiltonian would simply be a sum of one-electron terms, and the associated wave-functions a simple product of one-electron functions. This would, however, violate Pauli's principle as it is not antisymmetric. A better approach is the *Slater* determinant, eq. 2.8, made of one-electron spin-orbitals, which exploits the natural antisymmetric properties of determinants:

$$\Phi_{SD}(\mathbf{x}_1,...,\mathbf{x}_N) = |\chi_1...\chi_N| = (N!)^{-1/2}\begin{vmatrix} \chi_1(\mathbf{x}_1) & \chi_2(\mathbf{x}_1) & \cdots & \chi_N(\mathbf{x}_1) \\ \chi_1(\mathbf{x}_2) & \chi_2(\mathbf{x}_2) & \cdots & \chi_N(\mathbf{x}_2) \\ \vdots & \vdots & & \vdots \\ \chi_1(\mathbf{x}_N) & \chi_2(\mathbf{x}_N) & \cdots & \chi_N(\mathbf{x}_N) \end{vmatrix}. \tag{2.8}$$

This is the simplest way to put together a many-electron wave function, and it is the starting point of the Hartree-Fock theory, the simplest wave-function based method.

The Hamiltonian acts on Φ_{SD} giving

$$\langle\Phi_{SD}|\hat{H}|\Phi_{SD}\rangle = V_{NN} + \sum_{i=0}^{N_{elec}} h_i + \sum_{i=0}^{N_{elec}}\sum_{j>i}^{N_{elec}} J_{ij} - K_{ij}, \tag{2.9}$$

[3] Number of simple interchanges that characterize the permutation operator.

[4] Spin up/down functions are orthonormal, i.e. $\langle\alpha|\beta\rangle = \delta_{\alpha\beta}$.

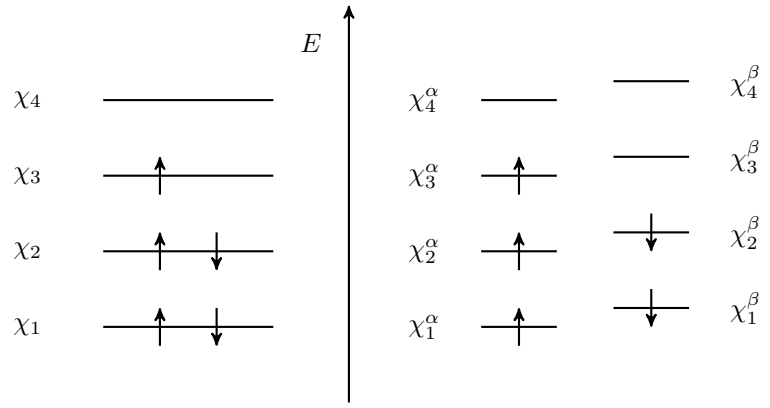

Figure 2.1: *A schematic of ROHF and UHF approaches.*

where one-electron terms were gathered into h_i and two-electrons one into $J_{ij} - K_{ij}$. These terms are defined as: $h_i = \langle\chi_i|\hat{T}_e + \hat{V}_{en}|\chi_i\rangle$, $J_{ij} = \langle\chi_i\chi_j|r_{ij}^{-1}|\chi_i\chi_j\rangle$ and $K_{ij} = \langle\chi_i\chi_j|r_{ij}^{-1}|\chi_j\chi_i\rangle$. The two latter terms come from $\hat{V}_{ee}$ acting on the wave-function, where r_{ij} is the distance between the ith and jth electrons. Here J_{ij} represents the Coulomb interaction between two charge densities $|\chi_i|^2$ and $|\chi_j|^2$, while K_{ij}, called the *exchange* term, arises from the anti-symmetric nature of the Slater determinant. Both J_{ij} and K_{ij} are positive, and therefore, if $i = j$ they vanish, preventing any self-interaction spurious effect which would come from J_{ii}. The core of the Hartree-Fock theory is to apply the variational method to this independent particle model. By proceeding this way, J_{ij} and K_{ij} integrals can be expressed as single-electron operators, defined by the spin-orbitals themselves: $J_j\chi_i(\mathbf{x}) = \chi_i(\mathbf{x})\int \frac{|\chi_j(\mathbf{x}')|^2}{|\mathbf{x}-\mathbf{x}'|}d\mathbf{x}'$ and $K_j\chi_i(\mathbf{x}) = \chi_j(\mathbf{x})\int \frac{\chi_j^*(\mathbf{x}')\chi_i(\mathbf{x}')}{|\mathbf{x}-\mathbf{x}'|}d\mathbf{x}'$.

However, this renders the HF theory as a mean-field theory, i.e. each electron feels the averaged effect of the rest by means of these one-electron operators.

Collecting these two terms plus h_i, one reaches the Fock operator, which may be defined for a given spin direction σ, either up or down (α, β), as:

$$\hat{F}^\sigma|\chi_i^\sigma\rangle = \left[\hat{h} + \sum_{j,\sigma'}\hat{J}_j^{\sigma'} - \delta_{\sigma\sigma'}K_j^\sigma\right]|\chi_i^\sigma\rangle = \epsilon_i^\sigma|\chi_i^\sigma\rangle, \tag{2.10}$$

where ϵ_i^σ are the energies associated with the ith spin-orbtial with spin σ.

These are the *unrestricted* HF (UHF) equations, in which each electron is allowed to occupy a different spatial orbital thanks to the separation into the electron's spin flavor. Nevertheless the two sets of orbitals are still coupled by the Coulomb's term. For a closed-shell molecule, i.e. same number of spin up/down electrons, the previous equation is $\hat{F}|\chi_i\rangle = (\hat{h} + \sum_j 2\hat{J}_j - K_j)|\chi_i\rangle = \epsilon_i|\chi_i\rangle$, in which each spin-orbital is filled by two electrons, one spin up and one spin down. This gives rise to the *restricted* HF (RHF) theory. One could also take a midway by forcing some of the orbitals to behave as RHF and others as UHF, which is the *restricted open-shell* HF (ROHF) method (see Fig. 2.1). The total RHF and ROFH wave-functions are also eigen-functions of the total squared spin operator $\hat{S}^2$, while the UHF ones are not. One feature of UHF wave-functions are their lower energy as they have more variational freedom than those of RHF or ROHF, and the possibility to better describe spin polarized systems (systems where the interaction of the spins of nearby electrons is important).

The realization of HF theory in computers is possible due to the self consistent field (SCF) algorithm, in which an initial guess wave-function is used to form the initial Fock matrices with elements $F_{ij}^\sigma = \langle\chi_i|\hat{F}^\sigma|\chi_j\rangle$ (note that there will be a single matrix for RHF). These matrices are diagonalized, providing a new set of spin-orbitals which are then used to form a new Fock matrix. This process is iteratively applied until the total electronic energy has converged according to a threshold. The converged HF wave-function is the Slater determinant formed with these final spin-orbitals.

In practice, each spin-orbital is taken to be a linear combination of atom-centered functions $\{\varphi_\mu\}$:

$$\chi_i(\mathbf{x}) = \sum_{\mu} c_{\mu,i}\varphi_{\mu}(\mathbf{x}), \tag{2.11}$$

so that the set of coefficients $c_{\mu,i}$ are the variational parameters that change at each iteration. These functions can, for example, be atomic orbitals (AO).

In summary, the HF method takes an independent particle model *ansatz* to solve the actual system of interacting electrons. By doing so, it reaches a set of *self-consistent* equations based on the Fock operator. This operator acts on spin-orbitals, each one describing the state of an electron (its position and its spin). The outcome are the energies of each spin orbital. This theory can take three flavors depending on how does spin enter in the solutions: UHF, RHF and ROHF. Yet, the HF method describes the movement of an electron which feels the field of the nuclei and the average field of all other electrons. Unsurprisingly, this method is far from giving the exact values of energy. HF misses some "electronic correlation" energy, as each electron only feels the averaged effect of the rest. This lack in electronic correlation energy is the energy required to reach the exact value:

$$E_{corr} = E_{exact} - E_{HF}, \tag{2.12}$$

where E_{HF} is the HF energy, and E_{corr} is always negative. More discussion on the electron correlation and how to retrieve it is provided in section 2.2, in which description of post-HF methods is provided.

Basis sets

As mentioned above, Slater determinants (eq. 2.8) are multi-electronic guess wave-functions made by one electron spin-orbitals (also called molecular orbitals), which are in turn made by linear combinations of atom-centered orbitals (e.g. atomic orbitals, eq. 2.11).

These atom-centered functions are actually made by linear combinations of other functions, called basis functions. A collection of basis functions forms a basis set.

Basis functions are normally Gaussian functions, so that their linear combination reproduce the shapes of atomic orbitals, which is much more efficient from the computational point of view. In order to reach a good representation of atomic orbitals one should have as many basis functions as possible, but in practice one must find a balance between computational effort and and a reduced number of basis functions in order to give good representations of AOs. There are extra basis function can be used, like polarization and diffuse functions. The former are high angular momentum (e.g. p, d, f atomic AOs) which add directionality to electron density of valence[5] electrons, especially important for anions and the latter are basis functions extended in space important for the description of bonding, dipolar moments and also loosely bound electrons, like it is the case for anions and radicals.

Other types of basis sets exists. Such as Slater-type and natural atomic orbital. For the case of systems with periodic boundary conditions, valence electrons can be described by plane waves (periodic functions in nature that are not localized but diffuse uniformly in space) or mixtures of plane waves and Gaussian functions (see § 2.5).

Electron correlation and Post-HF methods (F. Jensen, 2017)

Correlation energy, defined in the previous section (eq. 2.12), can be classified in two ways: (i) as Coulomb's and Fermi's correlation, or (ii) as static and dynamic correlation.

The first classification accounts for the different interaction of electrons with parallel (Fermi correlation) or antiparallel (Coulomb correlation) spins. Taking RHF theory, due to the Pauli principle, a given spin-orbital can only be populated by two electrons with antiparallel spins. Therefore Coulomb correlation can take place between electrons in both the same spatial orbital and different ones. On the other hand, Fermi correlation can only happen between electrons in different orbitals, and consequently, it is smaller. The second classification (into dynamic and static correlation) is analogous to the previous one, but has some conceptual

[5] Valence electrons: these are the electrons on the top layer of the electronic structure of a given system, the ones that will participate in chemical reactions.

differences. Dynamic correlation takes into account the *instantaneous* correlation of electrons while the static one is associated to near-degenerate states (spin-orbitals of similar energy). The dynamic correlation is more important for electrons in the same orbital, while static one is more important between electrons in different orbitals. In this sense, UHF can retrieve more static correlation than RHF.

There are several ways to recover the energy associated with electronic correlation. In general, they consist in expanding the total wave-function into a leading term given by the HF solution followed by linear combinations of other determinants. The latter are built from the HF solution by considering excitations of electrons into higher energy states, i.e. Slater determinants in which some spin-orbital(s) which were occupied in the HF wave-function have been exchanged by higher energy non-occupied ones:

$$\Psi(\mathbf{x}_1, ..., \mathbf{x}_N) = |\Phi_{HF}\rangle + \sum_{ia} C_i^a |\Phi_{i^a}\rangle + \frac{1}{4}\sum_{ijab} C_{ij}^{ab} |\Phi_{ij}^{ab}\rangle + ... \tag{2.13}$$

where the $i, j, k, l...$ indexes indicate the original position of electrons in $|\Phi_{HF}\rangle$ that have been excited to the $a, b, c, d...$ positions, which where unoccupied in the HF reference. In the end, the expansion is normally truncated at some point due to the high computational cost.

Different post-HF methods appear depending on how the expansion coefficients are obtained. For example, if the variational method is used, then the method is the *configuration interaction* (CI). Other options are to determine them by using the *perturbation theory* or the *coupled cluster theory*. All of them are described below. These methods can retrieve more or less electron correlation, often more of one kind than the other. Taking the classification of electronic correlation into dynamic and static, perturbative and coupled cluster methods usually retrieve more dynamic than static correlation, while CI-like methods retrieve more static than dynamic correlation. Combinations of these method families can be done to retrieve larger amounts of both, at the expense of an even higher computational cost.

Many-body perturbation theory

In this theory, one takes a reference Hamiltonian, e.g. the HF one ($H^{(0)}$), and adds a (small) perturbation ($\hat{H}'$), e.g. the missing correlation. The usual method is the Møller-Plesset (MP) formalism, with $\hat{H}' = \hat{H}_{BO} - \hat{H}^{(0)}$, where the last term is the HF Hamiltonian: $\hat{H}^{(0)} = \sum_i \hat{F}_i$. The perturbed Schrödinger equation is $(\hat{H}^{(0)} + \lambda\hat{H}')\Psi = E\Psi$. The energy and solution of this equation is a continuous function of λ, so that it can be expanded in a Taylor series: $E(\lambda) = E^{(0)} + \lambda^1 E^{(1)} + \lambda^2 E^{(2)} + ...$ and $\Psi(\lambda) = \Psi^{(0)} + \lambda^1\Psi^{(1)} + \lambda^2\Psi^{(2)} + ...$, where each term of the expansion is an order of the correction, and the terms of the wave-function are orthogonal between them. Substituting these terms in the Schrödinger equation one gets

$$(\hat{H}^{(0)} + \lambda\hat{H}')(\Psi^{(0)} + \lambda^1\Psi^{(1)} + \lambda^2\Psi^{(2)} + ...) = (E^{(0)} + \lambda^1 E^{(1)} + \lambda^2 E^{(2)} + ...)(\Psi^{(0)} + \lambda^1\Psi^{(1)} + \lambda^2\Psi^{(2)} + ...),$$

Then, separating by orders of $\lambda^{(i)}$ (the ith order perturbation equations):

$$\begin{aligned}
\lambda^0 :&\quad \hat{H}^{(0)}\Psi^{(0)} = E^{(0)}\Psi^{(0)} \\
\lambda^1 :&\quad \hat{H}^{(0)}\Psi^{(1)} + \hat{H}'\Psi^{(0)} = E^{(0)}\Psi^{(1)} + E^{(1)}\Psi^{(0)} \\
\lambda^2 :&\quad \hat{H}^{(0)}\Psi^{(2)} + \hat{H}'\Psi^{(1)} = E^{(0)}\Psi^{(2)} + E^{(1)}\Psi^{(1)} + E^{(2)}\Psi^{(0)} \\
... :&\quad ...
\end{aligned}$$

In order to compute the successive corrections one may use the knowledge of the previous ones by using the energy of the unperturbed (zeroth order) equation. In the MP formalism it is just the sum of the energies of the occupied spin-orbitals (which counts the electron-electron twice). It can be shown that the nth correction to the energy is $E^{(n)} = \langle\Psi^{(0)}|\hat{H}'|\Psi^{(n-1)}\rangle$. Then, the first order correction removes the electron-electron interaction once, and therefore the sum of zeroth and first order is just the HF energy. Hence, MP does not recover any correlation until second order. Higher order solutions adds excited Slater determinants.

However the expansion in excited determinants is normally truncated to a certain order, at least second. Møller-Plesset methods are labeled as MPn where n is the order of the correction where the expansion is truncated. The usual ones are MP2, MP3 and MP4. Since this family of methods are not variational, the

energy is not an upper bound to the real one, and therefore, it may actually be lower than the actual one. These methods are not suitable for systems where the ground state needs to be described by a more than one Slater determinant (e.g. diradicals) as high correction orders would be required for it. For such systems one would prefer multireference methods like CASPT2 (see below).

Configuration interaction (CI) and Multi-configurational self-consistent field wave-functions (MCSCF)

In the CI method, one takes the HF wave-function and generates new Slater determinants by exchanging one, two, three, four... spin-orbitals that are occupied in the HF reference by non-occupied ones (i.e. excited states), following single (S), double (D), triple (T), quadruple (Q)... excitations:

$$\Psi(\mathbf{x}_1, ..., \mathbf{x}_N) = C_0|\Phi_{HF}\rangle + \sum_S C_S|\Phi_S\rangle + \sum_D C_D|\Phi_D\rangle + \sum_T C_T|\Phi_T\rangle + \sum_Q C_Q|\Phi_Q\rangle + ..., \tag{2.14}$$

where each one of these additional Slater determinants are also referred to as configurations and the factors C_K are determined variationally. Normally the HF term carries the highest weight. When all possible configurations are included and the set of spin-orbitals are described by an infinite number of basis functions, we have the *full-CI* wave-function. This is the exact solution to the BO Hamiltonian when using the one-electron basis set expansion. However the number of configurations increases factorially (it is a binomial coefficient of the number of basis functions and the number of electrons). Therefore, in practice one truncates the expansion into certain configurations. For example the "CI singles and doubles" (CISD) would include all configurations up to the double excitation terms. The more basis functions and the more configurations, the better the results, but it is also more computationally demanding.

Another approach is, additionally to the configuration coefficients in the CI expansion, to simultaneously optimize the basis function coefficients. These are the *multi-configurational self-consistent field* (MCSCF) methods. The main drawback is the higher computational cost. But they become mandatory for systems in which the single-determinant HF wave-functions cannot even give the correct qualitative wave function (such as biradical systems).

A popular MCSCF method is the *complete active space SCF* (CASSCF). In this method only a portion of spin-orbitals are used to generate different configurations. In general, those involving core electrons (those that do not belong to the valence shells) and high excited states, since they do not take part in chemical reactions. In CASSCF, the set of spin-orbitals are divided into *active* and *inactive* (which may be populated with 2 electrons if they are core orbitals or empty if they are high energy levels). Inside the active space, a full-CI is performed, i.e. all excitations are allowed. This method is very sensitive to the active space, which very often has to be chosen manually. The common notation for this method is CASSFC$[n, m]$ where n, m are the number of electrons and spin-orbitals in the active space.

A generalisation of CASSCF is the *restricted active space SCF* (RASSCF), in which the active space is divided into three sections (RAS1–3). Each section has its own restrictions: RAS2 is equivalent to the CASSCF active space, while RAS1 and RAS3 are used to generate more configurations outside the RAS2 space, for example a certain number of excitations from RAS1/2 into RAS3 are allowed. If one allows excitations of two electrons from RAS1 to RAS3, the full RASSCF would be a combination of a full-CI in RAS2 and a CISD in RAS1→RAS3. A representation of these two methods is shown in Fig. 2.2.

So far, the reference state was the HF one. But one could scale this idea up by considering a MCSCF function like CASSCF as the reference. This gives rise to the multi-reference configuration interaction (MRCI) family. For example, consider making a CISD-like wave-function out of a MCSCF reference. It would take single and double excitations of all determinants in the MCSCF function. Of course this is an even more expensive sub-family of methods, very often not practicable. Another example is the use of a CASSCF wave-function as a reference, and then apply many-body perturbation theory, reaching the CASPT2 method (in this case up to second order perturbations).

Coupled Cluster (CC)

In this method, one defines a *cluster* operator ($\hat{T} = \hat{T}_1 + \hat{T}_2 + \hat{T}_3 + ... + T_{N_{elec}}$), which generates all excitations by acting on the reference HF wave-function. Each T_i exchanges i electrons from occupied spin-orbitals to i

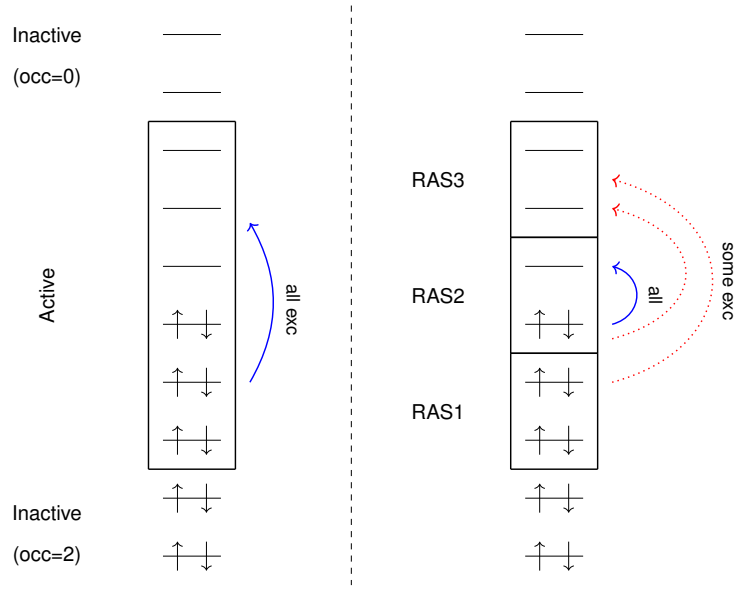

Figure 2.2: *Scheme the of CASSCF (left) and the RASSCF (right) approaches. Blue arrows indicate that all excitations are taken into account within the active space (or RAS2), and the red dashed ones that only some are allowed, up to a certain number.*

excited ones. It is applied on the reference wave-function as: $\Psi_{CC} = e^{\hat{T}}\Psi_{HF}$. The exponential is expanded in a Taylor series. Using the definition of $\hat{T}$, the $\hat{T}_i$ operators are organized by excitation orders:

$$e^{\hat{T}} = \sum_{k=0}^{\infty} \frac{1}{k!}\hat{T}^k = 1 + \hat{T}_1 + (\hat{T}_2 + \frac{1}{2}\hat{T}_1^2) + (\hat{T}_3 + \hat{T}_2\hat{T}_1 + \frac{1}{6}\hat{T}_1^3) + ...$$

The first term is the HF reference, the second are all single excitations, the first parenthesis are double excitations, classified as connected ($\hat{T}_2$) or disconnected ($\hat{T}_1^2$), the second parenthesis contains triple excitations (true ones $\hat{T}_3$ and product ones, e.g. $\hat{T}_2\hat{T}_1$). Then the Schrödinger equation becomes: $\hat{H}e^{\hat{T}}\Psi_{HF} = E_{CC}e^{\hat{T}}\Psi_{HF}$. At this point, a variational approach for the energy is unpractical and one, instead, projects the energy on the reference wave-function: $E_{CC} = \langle\Psi_{HF}|\hat{H}|e^{\hat{T}}\Psi_{HF}\rangle$. Nevertheless, the expansion of $\hat{T}$ is truncated to a certain point. For instance if only single and double excitations ($\hat{T} = \hat{T}_1 + \hat{T}_2$) are considered, then we are using the CCSD method. Higher orders are computationally very expensive, but third order excitations can be added perturbationally giving rise to the CCSD(T) method, which is very often used as a reference methodology and referred to as the *computational chemistry golden standard* (Sherrill, 2010), although it basically recovers dynamic correlation. The good part of CC methods is that excitations of orders higher than the truncation one enter in the wave-function, e.g. in the CCSD model, quadruple excitations rise thanks to $\hat{T}_2^2$. This method can also be included in the multi-reference family if the reference is, e.g. a MCSCF wave-function instead of the HF.

2.3 Density Functional Theory (DFT) (F. Jensen, 2017; Neese, 2009)

So far, I have presented wave-function based methods, which require to know or approximate the wave-function. The latter is a very complex entity that depends on $4N$ variables (positions and spin, with N the number of electrons). DFT, on the other hand, relies on a much simpler quantity: the electron density, which just depends on three spatial variables and may be derived from a wave-function:

$$\rho(\mathbf{r}) = N \int \cdots \int ds_1 d\mathbf{x}_2 \cdots d\mathbf{x}_N \Psi^*(\mathbf{x}_1, ..., \mathbf{x}_N)\Psi(\mathbf{x}_1, ..., \mathbf{x}_N). \tag{2.15}$$

The objective of DFT is to write the energy of a system of electrons that fulfills the BOA as a functional[6] of the electron density, like

$$E[\rho] = V_{NN} + E_e[\rho] = V_{NN} + V_{Ne}[\rho] + J_e[\rho] + T_e[\rho] + E'_{XC}[\rho], \tag{2.16}$$

where $V_{Ne}[\rho] = -\sum_{K=0}^{N} Z_K \int \rho(\mathbf{r}) r_{iK}^{-1} d\mathbf{r}$ is the electron–nucleous interaction, $J_e[\rho] = \frac{1}{2}\iint \rho(\mathbf{r}_1)\rho(\mathbf{r}_2) r_{12}^{-1} d\mathbf{r}_1 d\mathbf{r}_2$ is the electron–electron interaction, $T_e[\rho]$ is the electronic kinetic energy, and $E'_{XC}[\rho]$ a term accounting for exchange and correlation effects, which is known.

It may seem somewhat unnatural that the molecular BO Hamiltonian can be fully specified from a quantity that does not describe two-particle distributions but one-particle instead. However, it can be intuitively shown that the system can be completely defined by the electron density in its ground state. The BO Hamiltonian is completely determined by the number of electrons and the potential V_{Ne}, often called "external" potential in DFT. Both quantities can be derived from the electron density: its integral over the whole volume is the number of electrons, the cusps of the density are the positions of nuclei, and their heights define the nuclear charges, these two, in turn, define V_{Ne}. Finally, the Hamiltonian determines the energy, the wave-function and the associated properties. Therefore, there must be a one-to-one correspondence of the electron density and the energy of the system.

This was mathematically proved in the first Hohenberg and Kohn theorem (Hohenberg et al., 1964), which ensures the existence of a universal energy functional of the electronic density. Additionally they showed in their second theorem that the energy can be obtained by means of the variational principle, starting with a trial density, $\tilde{\rho}$, so that $E[\tilde{\rho}] \geq E[\rho]$. Furthermore, the unrestricted scheme (Fig. 2.1) can be introduced to DFT by simply splitting the total electron density into the electron density for α and β electrons ($\rho = \rho_\alpha + \rho_\beta$).

The only problem is that, although $E[\rho]$ is proved to exist and to be universal, it is unknown. The reason lies in the kinetic ($T[\rho]$) and the electron-electron interaction that have no classical analogues, i.e. the exchange and correlation energy contribution, ($E'_{XC}[\rho]$) in eq. 2.16, which cannot be directly written in terms of $\rho(\mathbf{r})$. If they were known, DFT would return the exact ground-state energy.

As a workaround, Kohn and Sham (Kohn et al., 1965) took some elements from HF theory and incorporated them in DFT in order to approximate the kinetic energy functional. It consists on considering a fictitious system of non-interacting electrons moving inside an "external" potential (V_{eN}). Such a system can be exactly described by a Slater determinant made up by auxiliary *Kohn-Sham* (KS) spin-orbitals[7]. As a constraint, it is then required that the electron density derived from these auxiliary functions is the same as the one of DFT i.e., $\rho_{KS}(\mathbf{r}) = \sum_i \int |\chi_i(\mathbf{x})|^2 d\sigma = \rho(\mathbf{r})$. The (small) difference in kinetic energy between the real and the fictitious ($T_s[\rho]$) system is added to the exchange-correlation term, which becomes: $E_{XC}[\rho] = E'_{XC}[\rho] + T[\rho] - T_s[\rho]$, and is now the only unknown term. The design of different $E_{XC}[\rho]$ functionals has led to the rise of several hundreds of methods, which make possible the realization of DFT. In the end, energy is obtained by minimizing the energy using a SCF-like algorithm as a function of the KS orbitals, which may be summarized as

$$E = \min_{\{\chi_k\}} \left[E_{KS-DFT}(\{\chi_k\}, \mathbf{R}) \right]. \tag{2.17}$$

DFT methods

It is customary to separate $E_{XC}[\rho]$ into a term for exchange and another for correlation, $E_{xc}[\rho] = E_x[\rho] + E_c[\rho]$. Then each DFT method relies on certain approximations to compute each part. Several hundreds DFT methods exist (e.g. (F. Jensen, 2017; Mardirossian et al., 2017)), and there is no systematic way to improve functionals. Often, researchers willing to use DFT methods that are not familiar with computational

[6] The energy is said to be a functional of the electron density. A functional is a prescription that produces a number from a function, instead of a set of coordinates, as a function would do.

[7] I put emphasis on *auxiliary* spin-orbitals in order to differentiate them from those in wave-function based methods like HF. The key is that these KS spin-orbitals are functionals of the electronic density and cannot be used both as a zeroth order function for perturbative improvement nor as the starting point to create multiple configurations. In plain words: the SD arising from KS spin-orbitals cannot be used as a wave function for the real system. Rather, it can be used to determine properties that depend on the electronic density.

chemistry, face the problem of having to pick a functional out of a disordered soup of DFT methods. Fortunately, one can devise a sort of classification in five families, introduced by Perdew and Schmidt (e.g. (John P. Perdew et al., 2001)), according to the fundamental ingredients in each method. This classification is called the *Jacob's ladder* of DFT, and connects the "hell" of non-interacting electrons to the "heaven" of chemical accuracy. The higher in the ladder, the higher in accuracy, at the expenses of higher computational efforts (although not always, see e.g. (Goerigk et al., 2017)). The rungs of the ladder (and therefore the subcategories of DFT methods), in order of complexity are: (i) *local spin density approximation* (LSDA) where the electronic density is assumed to be a slowly changing function, so that the uniform electron gas model can locally describe the non-uniform density system, (ii) the *generalized gradient approximation* (GGA), in which corrections accounting for the non-uniformity of ρ through the gradient of the electron density are introduced, (iii) meta-GGA family, which adds higher order corrections based on higher order derivatives of the electronic density (and in some cases the kinetic energy from the auxiliary orbitals), (iv) *hybrid* DFT methods, which improves the highly local nature of the previous families (they care about the electronic density at specific points and their close vicinity) by mixing some "exact" exchange energy (computed following the HF method with the KS auxiliary spin-orbitals), which is non-local, to the GGA and meta-GGA rungs, and finally (v) one can also mix in some (dynamical) correlation by mixing in some energy from perturvative methods like MP2, leading to double-hybrid methods, at the expenses of a higher computational cost. Nevertheless, one is often forced to choose a method which may not be the best one for general purposes, but that is good enough for the property or system of interest.

Some common problems in DFT methods (F. Jensen, 2017; Mardirossian et al., 2017)

DFT methods' popularity exploded in the beginning of this century mainly thanks to their cost-effectiveness, i.e. low computational cost and acceptable accuracy. However this does not mean that DFT methods are flawless. Indeed, they have several weak points, which are in general tackled in the successive rungs of the Jacob's ladder. These blind spots are:

- Reactivity: LSDA methods normally underestimate activation energies. GGA methods improve this affection significantly, but hybrid methods are the best cost-accuracy option.
- Self-interaction: it is the error in which an electron wrongly interacts with itself. In HF theory this does not happen as J_{ii} is canceled by K_{ii}. This does not necessarily happen in DFT methods, since $J[\rho]$ and E_{xc} may not cancel each other when deling self-electrons. A consequence of this bad cancellation of the self-interaction is that electron delocalized[8] systems are artificially over-stabilized.
- Pure DFT methods fail at describing weak inter-molecular interactions like dispersion forces. Indeed LDA and GGA approximations predict exponential fall-offs instead of the expected asymptotic $\sim r^{-6}$ behavior. Hybrids do not improve this picture, as the inclusion of HF-like exact exchange may end up in repulsive forces. Double-hybrids instead do improve the picture by the addition of correlation from the perturbative correction. Anyhow, it is customary to correct DFT functionals in order to properly describe London forces. Different strategies have arisen (Goerigk et al., 2019): (i) adding a functional-dependent correction in an *a posteriori* fashion, (ii) correcting it at the root *via* a non-local *kernel* (e.g. (Vydrov et al., 2010)), the use of effective core potentials (quite abandoned for this purpose) or the development of DFT methods with a large number of empirically fitted parameters to account for this effect, like the M06-2X method (Zhao et al., 2008), although for a proper description of London interactions they may need more corrections.

  The most popular strategy is the first one, due to its simplicity and almost zero computational cost. These additive corrections depend on the system's geometry. The first successful corrections called D and D2, were presented by Stefan Grimme (Grimme, 2004, 2006) and accounts for two-body interactions with empirically determined coefficients. The next generation are D3 (Grimme et al., 2010; D. G. Smith et al., 2016) and D3(BJ) (Grimme et al., 2011) corrections. These improve the descriptions of medium range interactions with respect to D2, are less empirical and incorporate dependence on the chemical environment of each atom by accounting for the number of directly bonded atoms. The

[8] Delocalized electrons are not associated to a single nuclei or bond, rather to a collection of them.

D3(BJ) flavor includes the Becke-Johnson damping function, which controls the overlap between short and long-range interactions, as the former is governed by the DFT method.

The general equation for the D3 correction is given by

$$\Delta E_{disp}^{D3} = -\frac{1}{2}\sum_{n=6,8}\sum_{A\neq B} s_n \frac{C_n^{AB}}{R_{AB}^n} f_{\text{damp}}(R_{AB}), \tag{2.18}$$

where s_n is a functional-dependent scaling factor, C_n^{AB} are the nth order dispersion parameters for each AB atom pair, R_{AB} are the AB inter-nuclear distances and

$$f_{\text{damp}}(R_{AB}) = 1/[1+\exp(-\gamma(R_{AB}/s_{r,n}R_0^{AB}-1))]$$

are damping functions where R_{AB}^0 are cut-off radii, $s_{r,6}$ are DFT method-dependent scaling factors, $s_{r,8}$ is set to 1 for all functionals and γ are constants, set to 14 for $n=6$ and 16 for $n=8$.

In the particular case of D3(BJ) expression 2.18 changes to

$$\Delta E_{disp}^{D3(BJ)} = -\frac{1}{2}\sum_{n=6,8}\sum_{A\neq B} s_n \frac{C_n^{AB}}{R_{AB}^n + f_{\text{damp}}^n(R_{AB}^0)}, \tag{2.19}$$

with $f(R_0^{AB}) = a_1 R_{AB}^0 + a_2$ where a_i are fit parameters (the BJ parameters) and $R_{AB}^0 = \sqrt{C_8^{AB}/C_6^{AB}}$.

For either D3 and D3(BJ), the fit parameters ($s_{r,6}$ and s_8, and a_1, s_8 and a_2, respectively) are determined in least-squares fit to a set of 130 dispersion interaction energies (Grimme et al., 2011, 2010; D. G. Smith et al., 2016).

- Multi-configurational character: DFT methods use, like HF theory, a single Slater Determinant (and therefore a single configuration, see 2.2). Consequently, DFT methods do not properly treat systems that need a multi-configurational description (with large static electron correlation). An example are singlet biradical systems. Luckily, one may use approximations like Broken (Spin) Symmetry (BS) in order to treat such systems with DFT methods (see below). In short, the idea of BS is to mix a triplet state in a singlet solution.

2.4 The broken (spin) symmetry approach (F. Jensen, 2017; Neese, 2004, 2009)

A radical is a chemical species (atom, molecule or ion) containing one (or more) unpaired electron, each with its own spin quantum number $S = 1/2$ and magnetic components $m_s = \pm 1/2$.

Spin multiplicity is given by $2S+1$, systems with spin multiplicities 1, 2, 3, 4... are called singlets, doublets, triplets, quartets... A monoradical is, therefore, a doublet. Triplet species arise from systems with two parallel (and) unpaired electrons. Open-shell singlets are, however, more complex. At variance with the closed-shell systems, where two antiparallel electrons occupy the same spin orbital, the open-shell ones are more exotic situations, in which two electrons with antiparallel spins occupy different spin-orbitals.

Systems with two unpaired electrons, i.e. triplet and open-shell singlet molecules are called biradicals[9] (Chalk, 2019). Examples of monoradicals in the ISM are the H atom and "normal radicals" like HCO, CH_3O and C_2H_5; examples of biradicals in the ISM are carbenes and nitrenes like CH_2, c-C_3H_2 and NH, and some resonant structures of PAHs that can be multiradicals. A pair of monoradicals close to each other can be understood as a biradical system.

Chemically speaking, the main feature of singlet biradicals is that the orbitals holding the unpaired electrons are close in energy, e.g. the H_2 dissociation curve (see below), and this is troublesome for computational methods relying on a single Slater determinant, like DFT.

[9] There are, in reality, two categories: di- and biradicals. The former are chemical systems with some interaction between the unpaired electrons, while biradicals are a special case of the latter where there is little or no interaction (each unpaired electron acts rather independently) (Abe, 2013)

Therefore there is plenty of interstellar chemical systems which are actually biradicals, and this can be a problem for computational chemists, since biradical species need a special treatment, where cost-effective methods that rely on a single Slater determinant to describe the many electron wave-function provide wrong energetics and geometries for the open-shell states. This is illustrated in the following lines, but the truth is that, only computationally demanding methods based on multiconfigurational methods like CI, MC-SFC and their multireference variants can actually tackle this sort problems properly.

As a matter of fact, however, one can resort to an approach consisting in a cost-effective method, the broken (spin) symmetry (BS) approach. In order to illustrate better all the concepts introduced in the lines above, the H_2 dissociation example is used. The starting point is the stable H_2 molecule, composed of two nuclei, A and B, with a minimal electronic wave function made of two molecular orbitals, $\chi_{+,-}$, made of the linear combinations of two atomic orbitals, $\phi_{A,B}$ (eq. 2.20):

$$\chi_{+,-} = N_{+,-}\left[\phi_A \pm \phi_B\right]. \tag{2.20}$$

where $N_{+,-} = (2 \pm 2S_{a,b})^{-1/2}$ are normalization constants with $S_{a,b}$ the overlap of the two atomic orbitals (if they are very far away, they will not overlap and thus $N_{+,-} = 1/\sqrt{2}$).

Upon dissociation one expects that each H atom keeps one electron, so that the final state are two H atoms with degenerate spin-orbitals, i.e. a singlet (open-shell) biradical system (see bottom right inset in Figure 2.3).

The ground-state solution from single Slater determinant methods is the singlet $\Psi_{GS} = |\chi_+^\alpha \chi_+^\beta|$, i.e. the two electrons lay on the spin-orbital of lowest energy (χ_+) and have antiparallel spins.

Moving to a CI-like point of view, one can build 5 more states by exciting one or the two electrons from the previous ground state (see top panel of Figure 2.3). Exciting the two electrons one gets $\Psi_{S1} = |\chi_-^\alpha \chi_-^\beta|$. Exciting just one electron we can build two triplet states $\Psi_{T1} = |\chi_+^\alpha \chi_-^\alpha|$, ${}^3\Psi_{T2} = |\chi_+^\beta \chi_-^\beta|$ and two more functions which are not eigenfunction of the squared spin operator[10], $\hat{S}^2$, but their combination gives rise to a singlet and a triplet states: $\Psi_{S2} = \frac{1}{\sqrt{2}}\left(|\chi_+^\alpha \chi_-^\beta| - |\chi_+^\beta \chi_-^\alpha|\right)$ and $\Psi_{T3} = \frac{1}{\sqrt{2}}\left(|\chi_+^\alpha \chi_+^\beta| + |\chi_+^\beta \chi_-^\alpha|\right)$, respectively. In order to get the physical meaning of these states, one can expand them over the atomic orbitals. Using the properties of determinants one gets:

$$\Psi_{GS} = 2^{-1}\left(|\phi_A^\alpha \phi_A^\beta| + |\phi_B^\alpha \phi_B^\beta| + |\phi_A^\alpha \phi_B^\beta| - |\phi_A^\beta \phi_B^\alpha|\right), \tag{2.21}$$

$$\Psi_{S1} = 2^{-1}\left(|\phi_A^\alpha \phi_A^\beta| + |\phi_B^\alpha \phi_B^\beta| - |\phi_A^\alpha \phi_B^\beta| + |\phi_A^\beta \phi_B^\alpha|\right), \tag{2.22}$$

$$\Psi_{S2} = 2^{-1/2}\left(|\phi_A^\alpha \phi_A^\beta| - |\phi_B^\alpha \phi_B^\beta|\right), \tag{2.23}$$

$$\Psi_{T1} = N_{T1}\left(\phi_A\phi_B - \phi_B\phi_A\right)(\alpha\alpha), \tag{2.24}$$

$$\Psi_{T2} = N_{T2}\left(\phi_A\phi_B - \phi_B\phi_A\right)(\beta\beta), \tag{2.25}$$

$$\Psi_{T3} = 2^{-1/2}\left(|\phi_A^\alpha \phi_B^\beta| + |\phi_A^\beta \phi_B^\alpha|\right). \tag{2.26}$$

$$\tag{2.27}$$

The expansion of Ψ_{GS} has resulted in the sum of 4 terms, which can be organized into a purely ionic and a purely neutral (biradical) singlet wave-functions:

$$\Psi_{ion} = 2^{-1/2}\left(|\phi_A^\alpha \phi_A^\beta| + |\phi_B^\alpha \phi_B^\beta|\right), \tag{2.28}$$

$$\Psi_{neu} = 2^{-1/2}\left(|\phi_A^\alpha \phi_B^\beta| - |\phi_A^\beta \phi_B^\alpha|\right), \tag{2.29}$$

meaning that the single Slater determinant methods predict a ground state mixture of 50% an ionic state and 50% a neutral one[11]. A CI-like wave-function is able to mix in different Slater determinants, and therefore its ground state would be $\Phi_{GS} = a_0\Psi_{GS} + a_1\Psi_{S1}$. For $a_0 = 1$ and $a_1 = 0$ one retrieves the single SD

[10] In this 2 electrons system, the total spin operator is given by: $\hat{\mathbf{S}} = \hat{\mathbf{S}}_1 + \hat{\mathbf{S}}_2$, and therefore $\hat{S}^2 = \hat{S}_1^2 + \hat{S}_2^2 + 2\hat{\mathbf{S}}_2\hat{\mathbf{S}}_2$.

[11] Note, however, that for the stable H–H bonded molecule this is the correct description.

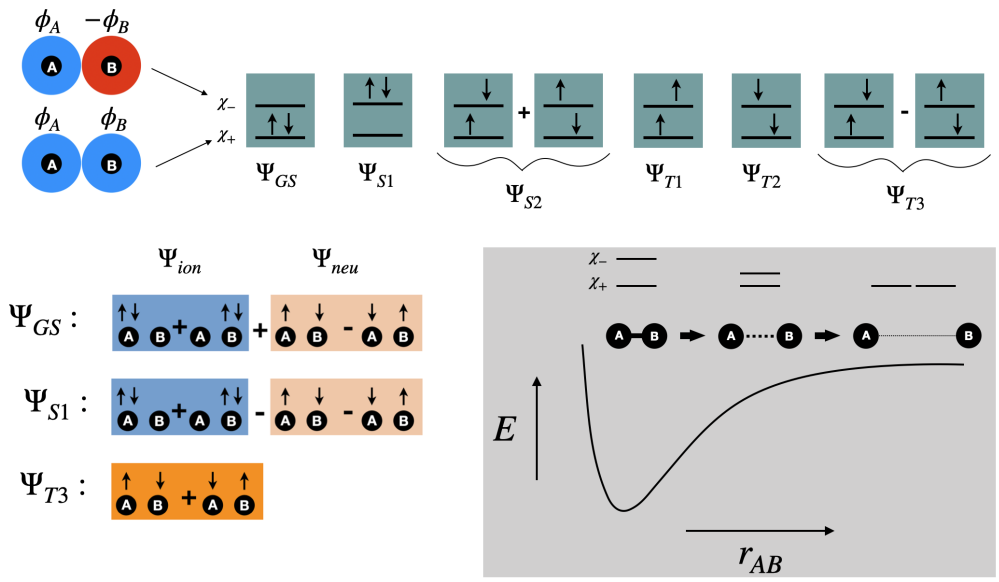

Figure 2.3: *Scheme with the CI states for the H_2 molecule in a 2 level basis (top), the expansion of the functions that contain some neutral character (bottom left) and the H_2 dissociation curve together (bottom right).*

ground-state, while for $a_0 = 1/\sqrt{2}$ and $a_1 = -1/\sqrt{2}$ one gets the pure biradical state. The a_0, a_1 factors are variationally determined, therefore CI-like calculations can naturally resolve the biradical state. This result for H_2 can be generalized for bigger systems containing two unpaired electrons and other core electrons that are well paired in spin orbitals of lower energy. In this case one would define $\phi_{A,B}$ as the orbitals containing the unpaired electrons, found on top fragments A and B. The wave-functions are now $\Psi_{GS} = |(\text{core})\chi_+^\alpha \chi_-^\beta|$, ${}^3\Psi_{T1} = |(\text{core})\chi_+^\alpha \chi_-^\alpha|$, etc.

The underlying idea of broken (spin) symmetry is to mix up χ_+ and χ_- in order to recover a CI-like behavior from a single SD. The mixing of $\chi_{+,-}$ gives rise to two "magnetic" spin-orbitals $\eta_{A,B}$:

$$\eta_{A,B}(\theta) = \cos(\theta)\chi_+ \pm \sin(\theta)\chi_-,$$

where θ is a mixing parameter. For $\theta = n\pi$ and $\theta = n\pi/2$ (with n an integer) one recovers Ψ_{GS} and Ψ_{S1}, respectively, while for $\theta = n\pi/4$ one gets $\eta_{A,B}(\pi/4) = 2^{-1/2}(\chi_+ \pm \chi_-)$, so that $\eta_{A,B}$ are essentially localized spin orbitals. The main difference with $\phi_{A,B}$ is that η_A has a tail extending from A to B, and *vice versa* for η_B. Then the guess wave-function of the BS approach is defined as:

$$\Psi_{BS}^{\text{guess}} = |(\text{core})\eta_A^\alpha \eta_B^\beta|,$$

which has the (qualitatively) correct shape of a neutral wave-function, but a wrong spin distribution: in a real singlet the total spin density should be zero in every point of space, but in this BS guess wave-function one has a region of positive spin density around fragment A and another of negative spin density around B, the total integral value being zero. The physical significance of this guess wave-function can be obtained by going back to the $\Psi_{+,-}$ spin-orbitals and comparing to the H_2 CI-like solutions we derived above. One gets:

$$\Psi_{BS}^{(\text{guess})} = A(\theta)|(\text{core})\Psi_+^\alpha \Psi_+^\beta| + B(\theta)|(\text{core})\Psi_-^\alpha \Psi_-^\beta| + C(\theta)\left[|(\text{core})\Psi_+^\alpha \Psi_-^\beta| - |(\text{core})\Psi_+^\beta \Psi_-^\alpha|\right] = A(\theta)\Psi_{GS} + B(\theta)\Psi_{S1} + D(\theta)\Psi_{T3}, \quad (2.30)$$

where now it becomes explicit the mixing of the Ψ_{T3} triplet state, which also describes a neutral situation (see eq. 2.26). One can also rewrite everything in terms of the ionic and neutral components:

$$\Psi_{BS}^{(\text{guess})} = \frac{\cos(2\theta)}{\sqrt{2}}\Psi_{ion} + \frac{1}{\sqrt{2}}\Psi_{neu} + \frac{\sin(2\theta)}{\sqrt{2}}\Psi_{T3}. \tag{2.31}$$

Here the neutral biradical function ${}^1\Psi_{neu}$ has a constant weight, at difference from the CI-like solution. The relative proportion of ionic and neutral character is instead given by balancing the ionic and triplet components, which is determined by the variational principle. The completely neutral solution is a 1:1 mixture of a singlet and a triplet states, which is qualitatively correct except for its spin density, although its charge density is correct (as good as the DFT method can provide). $\Psi_{BS}^{(\text{guess})}$ is the guess wave-function, which upon application of the variational principle relaxes into the final BS wave-function $\Psi_{BS} = |(\text{core})\tau_A^\alpha \tau_B^\beta|$. Here the magnetic orbitals have relaxed into their final forms, $\tau_{A,B}$, which will be orthogonal on their spin part but not necessarily in their spatial one. This gives more flexibility to the variational calculation related to the Kohn-Sham orbitals.

2.5 Modeling of solid surfaces (Martin, 2004; Marx et al., 2009)

Simulating solid state surfaces with computational chemistry techniques can be done by adopting two strategies: with the cluster approach and the periodic approach.

Clusters are finite-sized systems in which a collection of atoms/molecules are taken to simulate the surface. This approach is commonly used for molecular solids, like water ice. These surface models can be considered as "super" molecules, and therefore, computational methods usually employed for molecular systems (e.g. DFT, and even post-HF) can be adopted (depending on the size of the cluster).

Their main drawback is that clusters cannot properly represent some characteristic features of solids like their rigidity, specially at the edges, and long-range effects. Nevertheless, physico-chemical properties tend to converge as the size of the model increases, at the expense of the computational cost increment. An example of such cluster models is presented in Figure 2.4, where a cluster is cut from a proton ordered Ih periodic ice bulk structure (also known as XI ice). If one needs an amorphous structure, instead, one could optimize the geometry of the cut model. Larger models can be built, for example, by combining smaller clusters. Which can also be amorphized if needed. The two final amorphous ice models in Figure 2.4 are the ones used in most of my works (Parts I and II).

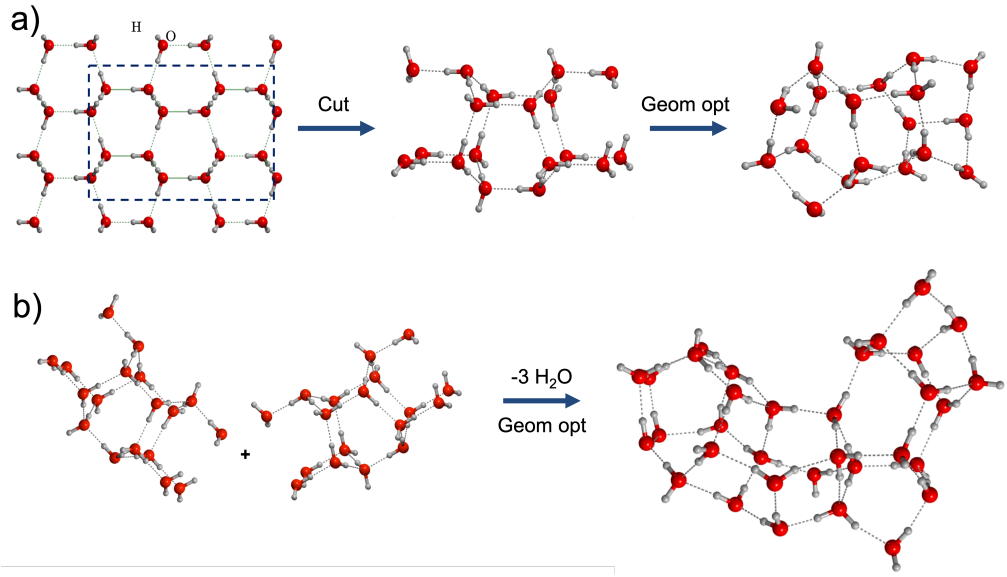

Figure 2.4: *Examples of how cluster-like surface models can be made out of a bulk structure, from Rimola et al. (2014). One starts by cutting out a cluster from a bulk structure, which can be amorphised, for example, by optimizing its geometry reaching a minimum of potential energy (case (a)). Larger clusters can be made by combining smaller ones (case (b)). See also 4.2.*

On the other hand, periodic simulations are based on the application of periodic boundary conditions (PBC). They rely on the translational symmetry of a collection of atoms contained in a "primitive" unit cell

over space in order to represent the system. The simplest example is that of a crystalline solid bulk, in which one takes the unit cell and repeats it over the three directions of space. But this technique can be used for other type of chemical systems, depending on how many repetition directions are taken: 1 direction would correspond to unidimensional systems like polymers, 2 directions to surfaces and 3 directions to material bulks. All of this can be done by exploiting (and imposing) translational symmetries, which permits the simplification of infinite-sized problems into a set of smaller problems (one would need infinite basis functions to represent an infinite system). In order to realize this, Bloch's theorem (see below) is essential.

Periodic boundary conditions (PBC) and Bloch's theorem

In PBC, the potential $V(\mathbf{r})$ is periodic over the translations of the primitive unite cell. These translations, in 3D space, are defined by the vector

$$\mathbf{T} = n_1\mathbf{a}_1 + n_2\mathbf{a}_2 + n_3\mathbf{a}_3, \tag{2.32}$$

where n_i are integers and $\mathbf{a}_i$ are three non-coplanar vectors. The periodic potential fulfills $V(\mathbf{r}+\mathbf{T}) = V(\mathbf{r})$, sot that it can be expressed as a Fourier series:

$$V(\mathbf{r}) = \sum_{\mathbf{G}} C_{\mathbf{G}} \exp\left(i\mathbf{G}\mathbf{r}\right), \tag{2.33}$$

where $C_{\mathbf{G}}$ are the expansion coefficients and $\mathbf{G}$ are vectors in the reciprocal space, often called "k-space", because these vectors have units of wave vectors ($\propto 1/l$, where l has units of length). These reciprocal vectors are defined as

$$\mathbf{G} = m_1\mathbf{A}_1 + m_2\mathbf{A}_2 + m_3\mathbf{A}_3, \tag{2.34}$$

which, from the periodicity of the potential, accomplish $\mathbf{G}\cdot\mathbf{T} = 2\pi \times$ integer and therefore $a_iA_j = 2\pi\delta_{ij}$. The k-space is also periodic, meaning that all information is contained in its unit cell, called the *first Brillouin zone*.

The Bloch theorem states that the solution of the Hamiltonian with the periodic potential can be chosen to be a plane wave times a function, $u_{\mathbf{k}}(\mathbf{r})$, which contains the periodicity of the lattice ($u_{\mathbf{k}}(\mathbf{r}+\mathbf{T}) = u_{\mathbf{k}}(\mathbf{r})$):

$$\Psi_{\mathbf{k}}(\mathbf{r}) = e^{i\mathbf{k}\mathbf{r}}u_{\mathbf{k}}(\mathbf{r}). \tag{2.35}$$

One can apply the Born-von Kármán boundary conditions: $\Psi_{\mathbf{k}}(\mathbf{r}+N_j\mathbf{a}_j) = \Psi_{\mathbf{k}}(\mathbf{r})$, where j runs from 1 to 3 (the three directions of space), and N_j are the number of repeated cells in the j direction in the real space. These boundary conditions imply that $\exp(iN_j\mathbf{k}\mathbf{a}_j) = 1$, or $\mathbf{k}\mathbf{a}_j = 2\pi\frac{p_j}{N_j}$, where p_j is an integer. This indicates that there are as many $\mathbf{k}$ as cells are considered, so that in the limit of infinite crystals (i.e. large number of repetitions in real sapace), there is an infinite number of $\mathbf{k}$'s. For each one of them, there is a solution of Schrödinger's equation, so that in principle, the total energy should be calculated as $E = \int d\mathbf{k}\,\epsilon(\mathbf{k})$. Assuming $\epsilon(\mathbf{k})$ to smoothly vary with $\mathbf{k}$ (this is actually the common situation, except for metals), one can simply sample some finite number of $\mathbf{k}$: $E = \sum_{\mathbf{k}}\epsilon(\mathbf{k})$. In practice, one runs some test calculations using different number of $\mathbf{k}$'s, until the property of interest converges. Indeed, there are special $\mathbf{k}$'s, which represent regions of the reciprocal space with high symmetry. The simplest of them is the so-called "Γ point", which is simply the origin of coordinates for the reciprocal space.

There are some strategies that computational chemists can use to decrease the computational effort for PBC-based calculations. For example, (i) if the primitive cell is very large, the reciprocal space cell will be very small, so that few $\mathbf{k}$'s will suffice, or (ii) if the atoms in the primitive cell actually reproduce an amorphous system (i.e. the cell contains an amorphous system, which is then repeated over space), then the periodicity of the the whole system is just an approximation, so that one would not excessively care about having a good k-space sampling. Often, a single k-point is enough (the Γ point).

Surfaces in PBC

Modeling surfaces in PBCs is not an easy task for computational chemists. In general, one has to set up a large simulation cell that contains a slab representing the surface. Most simulation softwares cannot simply simulate 2D periodicity, so that 3D periodicity has to be used instead. In this case, one makes large simulation cells with empty spaces in the z-direction over the surface slab, see Figure 2.5.

The thickness of this slab has to be chosen carefully, as the inner atoms should be a good approximation of the bulk (in a surface, the bottom of the z-direction would contain virtually infinite atoms). This can be checked by calculating the surface formation energy (Fiorentini et al., 1996), E_S, and see how it converges with the slab thickness:

$$E_S = \frac{E(n)_{SLAB} - nE_{BULK}}{2A} \tag{2.36}$$

where $E(n)_{SLAB}$ is the energy of the slab with n layers, E_{BULK} is the energy of the bulk and A is the area of the slab.

Additional requirements are that the dipole moment should be as close as possible to zero (otherwise calculations can fail due to have a periodic array of dipole moments, leading to instabilities in the electronic energy), and that the charge in the cell has to be zero. If these two conditions are not fulfilled, the result would be a conducting material and an infinite charge.

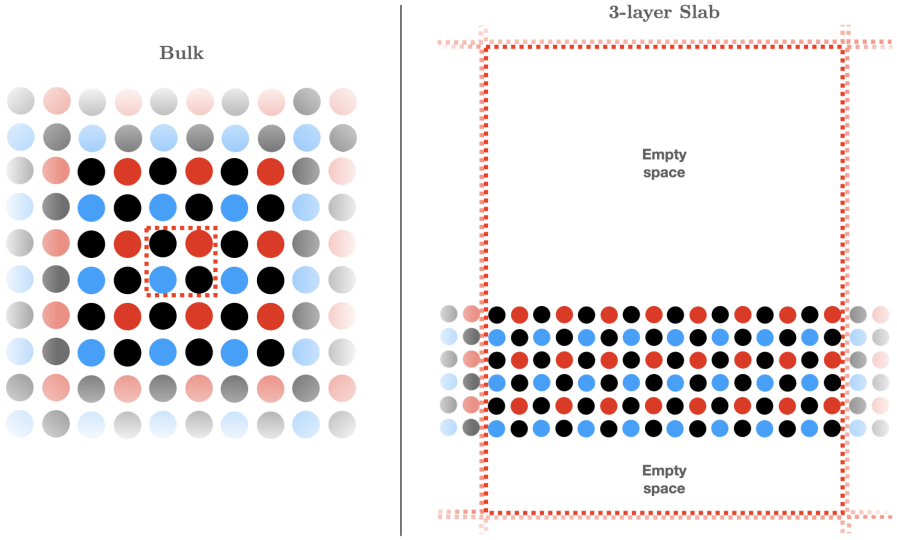

Figure 2.5: *Bulk (left) and slab schemes. Simulation cells are dashed red boxes.*

2.6 Potential energy surfaces (PES) and chemical kinetics

PES and transition state theory (TST) (Henriksen et al., 2018)

As introduced in § 2.1, the PES is a geometry-dependent energy hyper-surface consequence of the BOA. It depends on the specific configuration of the nuclei, so that for each set of nuclear positions one gets an energy value, which contains the electronic (kinetic + potential) and nuclear (potential) energies. All of the methods described above give the ways to calculate the electronic energy, with more or less detail, at a given nuclear configuration. For a system of N atoms, the PES depends on the number of atomic degrees of freedom, i.e. a subset of $3N-6$ nuclear coordinates ($3N-5$ for linear molecules) also known as internal coordinates. Motion along the PES represents the process to be followed by a chemical process, i.e. how the nuclei move in space according to what happens to electrons (e.g. bond formation/break, electrostatic interactions, bond polarization, dispersion interactions...) as seen in Figure 2.6.

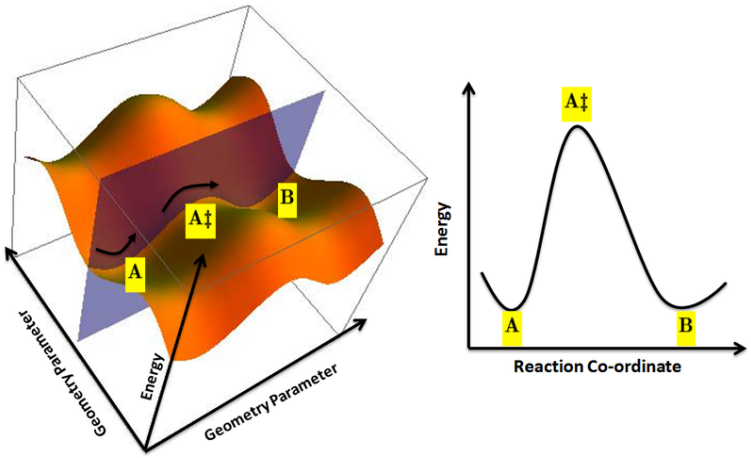

Figure 2.6: *Sketches of a hypothetical potential energy surface with only two coordinates (geometric parameters) containing two minima (A, B) and and a saddle point ($A^{\ddagger}$). This is an idealized case where the reaction coordinate coincides with one of the geometry parameter. Credit: AimNature, from Wikimedia Commons.*

Stationary points appear all over PESs. The two most important types of stationary points are minima and saddle points. Local minima represent atomic arrangements corresponding to energetically stable molecular geometries. In a reaction, reactants and products lie in minima. Saddle points, on the other hand, are points which are minima for all internal coordinates except for one, for which it is a maximum. The energetic barrier for reaction corresponds to the energy difference of this saddle point with respect to the energy of reactants. The relative energy between reactants and products is the reaction energy, which tells us about the exo- endothermicity of the reaction. All transient geometries between two minima are "transition states", however, in the chemical jargon when one simply says the transition state (TS), it is tacitly assumed that it is the one on top of the saddle point as it is more important than the rest. Motion along the potential energy surface tells us about the reaction mechanism (how many energy barriers there are, how many intermediates, etc), molecular geometries, vibrations, rotations... The latter two are normally approximated by simple models like the harmonic oscillator and the rigid rotor, respectively.

Conventional transition state theory (TST) is the theoretical framework used to derive reaction rates for chemical reactions by connecting motion on the PES with canonical statistical physics and thermodynamics. The key assumptions are: (i) there is chemical equilibrium between reactants and the "activated complex" (the high energy species formed corresponding to the saddle point, the TS), (ii) once a molecule has reached the TS it may either come back to reactants or evolve into products, and (iii) if it crosses the TS, the system can only evolve into products. For a single step reaction like $A + B \rightarrow P$, the rate of change of the abundances of either reactants and products is called the reaction rate law: Rate $= d[P]/dt = k[A][B]$, where $[A]$, $[B]$ $[P]$ are the abundances of species A, B and P and k is the reaction rate constant. The experimental relation for k is given by the Arrhenius equation (eq. 2.37), where k is related to the energy required to surpass the barrier, E_a, which is an experimental parameter:

$$k(T) = Ce^{-E_a/k_bT}, \tag{2.37}$$

with k_B the Boltzmann constant and T the temperature. The goal of TST is to provide a theoretical expression to arrive at the Arrhenius equation using the concept of TS. From now on, any quantity labelled by the $\ddagger$ symbol refers to the TS. The previous reaction, in TST language is $A + B \rightleftharpoons AB^{\ddagger} \rightarrow P$.

TST prediction crystallizes in the Eyring equation:

$$k(T) = C^0 \frac{k_BT}{h} \frac{q^{\ddagger}}{q_Aq_B} e^{-\Delta E_0^{\ddagger}/k_BT} = C^0 \frac{k_BT}{h} e^{\Delta S^{\ddagger}/k_B} e^{-\Delta H^{\ddagger}/k_BT} = C^0 \frac{k_BT}{h} e^{-\Delta G^{\ddagger}/k_BT}, \tag{2.38}$$

where C^0 is a standard concentration (needed because the reaction is bimolecular, i.e. has two reactants), q_i are the partition functions, $\Delta E_0^{\ddagger}$ is the energy barrier (including zero point energies), $\Delta S^{\ddagger}$ is the entropy change from reactants to the TS (which can be obtained from the partition functions), $\Delta H^{\ddagger}$ is the change

in entropy and $\Delta G^{\ddagger}$ is the change in free energy. Multiplicative corrections in order to include quantum tunneling and barrier recrossing can be included to improve TST predictions. For a unimolecular reaction like $A \rightleftharpoons A^{\ddagger} \rightarrow B$ the previous equation becomes

$$k(T) = \frac{k_B T}{h} \frac{q^{\ddagger}}{q_A} e^{-\Delta E_0^{\ddagger}/k_B T} = \frac{k_B T}{h} e^{\Delta S^{\ddagger}/k_B} e^{-\Delta H^{\ddagger}/k_B T} = \frac{k_B T}{h} e^{-\Delta G^{\ddagger}/k_B T}. \tag{2.39}$$

RRKM theory (Baer et al., 1996; Henriksen et al., 2018)

RRKM (after Rice, Ramsperger, Kassel and Marcus, their developers (Kassel, 1928; Marcus, 1952; Rice et al., 1927)) is the microcanonical version of TST. This chemical kinetics theory was born to be applied to unimolecular reactions, in which there is an energized reactant which passes through an activated complex state and then into products, following reaction

$$A^* \rightleftharpoons A^{\ddagger} \longrightarrow B, \tag{2.40}$$

where A^* is the energized reactant and B the product. As it can be seen, similarly to conventional TST, one assumes that there is equilibrium between reactants and the activated complex $A^{\ddagger}$. The decay of A follows the typical unimolecular rate law

$$\frac{-d[A]}{dt} = k(T)[A] \qquad \Longrightarrow \qquad [A](t) = [A](t=0)\exp[-k(T)t], \tag{2.41}$$

with $k(T)$ the unimolecular rate constant. In RRKM, all the assumptions of TST still hold, and additionally, it is assumed that the phase space is statistically populated[12].

Thus, the microcanonical rate constant is given by the following expression

$$k(E) = \frac{N^{\ddagger}(E - E_0)}{h\rho(E)} = \frac{\int_0^{E-E_0} d\epsilon^{\ddagger} \rho^{\ddagger}(E - E_0 - \epsilon^{\ddagger})}{h\rho(E)}, \tag{2.42}$$

where $N^{\ddagger}(E - E_0)$ is the sum of all states from 0 to $E - E_0$ for the TS, $\rho(E)$ is the density of states of reactants (i.e. the number of states per unit of energy, in quantum mechanics is the degeneracy, $g(E)$), E_0 is the energy barrier containing the vibrational ZPEs of reactants and the TS. The sum of states of the TS can be expressed as an integral of its density of states over the translational energy of the reaction coordinate $\epsilon^{\ddagger}$. Tunnelling effects can be included by introducing the transmission probability, $T(\epsilon^{\ddagger})$, inside the integral in eq. 2.42:

$$k(E) = \frac{\int_{-E_0}^{E-E_0} d\epsilon^{\ddagger} T(\epsilon^{\ddagger}) \rho^{\ddagger}(E - E_0 - \epsilon^{\ddagger})}{h\rho(E)}, \tag{2.43}$$

where the integration range expands to energies below the barrier and not just above it.

In a final step, $k(E)$ is converted into $k(T)$ by populating energy levels according to the Boltzmann distribution, $P(E) = g(E)\exp(-E/k_B T)/Q(T)$ (where $g(E)$ is the level degeneracy and $Q(T)$ is the partition function[13]):

$$k(T) = \int_{E_0}^{\infty} k(E) \times P(E) dE, \tag{2.44}$$

this equation leads to eq. 2.39, recovering TST.

[12] This is equivalent to say that fast intramolecular vibrational relaxation takes place. This means that given an excitation on a particular vibrational mode, the extra energy will be scrambled towards the rest of modes faster than the reaction itself. This ensures that the rate constant can be obtained from statistical mechanics principles. Otherwise, the rate constant would be time dependent.

[13] The partition function can be obtained from the density of states (i.e. the degeneracy), by means of a Laplace transform.

Tunneling for the RRKM theory (Atkins et al., 2013; Baer et al., 1996)

Quantum tunneling plays an important role in interstellar chemistry because of the very low temperatures and the involvement of light species such as hydrogen. For example it is needed for the formation of simple hydrogenated species on the surfaces of interstellar ices, e.g. CO + H $\rightarrow$ HCO, the first step towards the formation of important interstellar species like formaldehyde (H_2CO) and methanol (CH_3OH), e.g. (Andersson et al., 2011; Kenzo Hiraoka et al., 2002; Rimola et al., 2014).

Tunnelling probability depends on several factors of the saddle point, such as its height, its width and the mass associated with the reaction coordinate. Within the TST (and RRKM) theory, the reaction coordinate is separated from all the others, so that regarding tunneling, one needs to solve a uni-dimensional problem. As seen in eq. 2.43 we need a transmission probability, $T(E)$.

Analytical expressions for $T(E)$ can be obtained by using certain potential shapes. Some traditional examples are the squared barrier (described by a single step) or the parabolic barrier (function of the squared reaction coordinate). For this thesis we have used the unsymmetric Eckart potential (Equation 2.45 (Eckart, 1930)):

$$V(x) = \frac{Ae^{\tilde{a}x}}{1+e^{\tilde{a}x}} + \frac{Be^{\tilde{a}x}}{(1+e^{\tilde{a}x})^2}, \tag{2.45}$$

where $1/\tilde{a}$ is the length scale of the barrier, $A = V_1 - V_2$ and $B = (\sqrt{V_1} + \sqrt{V_1})^2$, with V_1 and V_2 the barriers from reactants to the TS and from products to the TS, so that $A \leq 0$ and $B > 0$. The transmission probability for such a barrier is given by (Henriksen et al., 2018):

$$T(E) = \frac{\cosh(a+b) - \cosh(a-b)}{\cosh(a+b) + \cosh(\sqrt{4\alpha_1\alpha_2 - \pi^2})}, \tag{2.46}$$

where $a = 2(\alpha_1\zeta)^{1/2}(\alpha_1^{-1/2} + \alpha_2^{-1/2})^{-1}$, $b = 2[(\zeta-1)\alpha_1 + \alpha_2]^{1/2}(\alpha_1^{-1/2} + \alpha_2^{-1/2})^{-1}$, $\alpha_1 = 2\pi V_1/h\nu^{\ddagger}$, $\alpha_2 = 2\pi V_2/h\nu^{\ddagger}$ and $\zeta = E/V_1$ with V_1 the reactants to saddle point barrier, V_2 that of products to the saddle point and $\nu^{\ddagger}$ the frequency of the transition state in absolute value.

A particular case of this barrier is the so-called symmetric Eckart's potential: $V(x) = 4V_0e^{\tilde{a}x}/(1+e^{\tilde{a}x})^2$, where V_0 and $1/\tilde{a}$ are the height and width of the barrier. For this particular case a simpler expression of the transmission probability is obtained (Atkins et al., 2013):

$$T(E) = \frac{\cosh(x_1) - 1}{\cosh(x_1) + \cosh(x_2)} \tag{2.47}$$

with $x_1 = 4\pi\frac{\sqrt{2mE}}{\hbar\tilde{a}}$ and $x_2 = 2\pi\frac{\sqrt{8mV_0 - (\hbar\tilde{a}/2)^2}}{\hbar\tilde{a}}$, where m is the mass associated to the reaction coordinate.

In RRKM, the transmission probability can directly be inserted in the final calculation of $k(E)$ (see eq. 2.43). The idea is to use the data obtained from computational chemistry calculations to derive $T(E)$. Under the harmonic oscillator approximation, the motion related to the reaction coordinate comes from the (imaginary[14]) frequency ($\omega^{\ddagger} = 2\pi\nu^{\ddagger}$) of the transition state, which carries the information of both its associated mass and the barrier's width: $\frac{m}{\tilde{a}^2} = \frac{V_0}{2}\omega^{-2}$.

Note: in the case of conventional TST, tunneling can be included by multiplying the rate constant times a correction factor $\kappa(T)$, which is calculated as

$$\kappa(T) = \frac{e^{V_0/k_BT}}{k_BT}\int_0^{\infty} dE\; T(E)\exp(-E/k_BT).$$

2.7 *Ab Initio* Molecular Dynamics (AIMD) simulations (Marx et al., 2009)

So far, the discussion on computational chemistry methods has focused on static calculations. The aim of this section is to introduce molecular dynamics simulations. The goal of such simulations is to describe the time evolution of chemical systems.

[14] The second derivative of the PES at the saddle-point on the reaction coordinate is negative (it is a maximum), therefore in the harmonic oscillator approximation, the frequency related to this coordinate at this point is an imaginary number.

One could treat chemical systems by means of classical mechanics, i.e. atoms are particles described by the Newton laws of motion. Atoms interact with each other by means of interatomic potentials (defining the force field), which may consist of numerous parameters in order to describe the wide amount of intra- and intermolecular interactions. In this picture electrons are not explicitly treated. These parametric potentials not only change with the elements involved, but also according to their chemical nature, e.g. a carbon bonded to another carbon by a double bond will experience a “stiffer spring force” than a carbon connected to a another one by a single bond. This may become cumbersome, but the strongest disadvantage is their intrinsic difficulty to describe chemical reactions and other process that require a precise treatment of electrons. *Ab Initio* molecualr dynamics (AIMD) simulations work out this niche by incorporating quantum chemistry methods within the BOA (§ 2.1, e.g. DFT) in order to include the electronic structure in the simulations, as an alternative to parametric potentials, while nuclei are still described by classical mechanics. The main drawback of AIMD simulations (apart of those arising from the quantum chemistry method and the BOA) is the higher computational effort required. This means that the simulation time-scale and number of simulations that one can run for a given system are much shorter/smaller than for classical mechanics-based simulations. Therefore, statistically meaningful samples are often not possible. Nevertheless, AIMD techniques are the methods of choice for processes like reactivity, or changes in the electronic properties. Therefore, in BOA-based AIMD one needs to solve the electronic Hamiltonian (eq. 2.5) and apply the variational principle to minimize the energy and the orbitals at each step of the simulation. The Lagrangian to be solved is:

$$\mathcal{L}_{BO}(\mathbf{R},\dot{\mathbf{R}}) = \sum_{L=1}^{N_{atoms}} \frac{M_L}{2}\dot{\mathbf{R}} - \min_{\{\chi_k\}} \left[E_{KS-DFT}\left(\{\chi_k\},\mathbf{R}\right)\right], \tag{2.48}$$

where $\mathbf{R}$, $\dot{\mathbf{R}}$ are the positions and velocities of nuclei, M_L is the mass of the Lth nucleus, $\{\chi_k\}$ are the Kohn-Sham orbitals and $min\{E_{KS-DFT}\}$ is the energy obtained from DFT (containing electronic energy and nuclear repulsion). This Lagrangian leads to the following equations of motion:

$$M_L\ddot{\mathbf{R}}_L = -\nabla_{\mathbf{R}_L} \min_{\{\chi_k\}} \left[E_{KS-DFT}(\{\chi_k\},\mathbf{R})\right], \tag{2.49}$$

where $\nabla_{\mathbf{R}_L} = \sum_{i=1}^{3} \partial/\partial R_{i,L}$ is the Gradient operator, so that $\nabla_{\mathbf{R}_K} E_{KS-DFT}$ are the forces, $\mathbf{F}$. The equations of motion are then integrated, typically using the velocity Verlet algorithm:

$$\mathbf{R}_L(t+\delta t) = \mathbf{R}_L(t) + \delta t\dot{\mathbf{R}}_L(t) + \frac{\delta t^2}{2M_L}\mathbf{F}_L(t) \tag{2.50}$$

$$\dot{\mathbf{R}}_L(t+\delta t) = \dot{\mathbf{R}}_L(t) + \frac{\delta t}{2M_L}\left[\mathbf{F}_L(t) + \mathbf{F}_L(t+\delta t)\right] \tag{2.51}$$

2.8 Summary

This section intends to offer a general overview of the theoretical tools discussed above. Regarding quantum chemical methods, there are two main paradigms aiming to solve the molecular electronic Hamiltonian (eq. 2.4): the wave-function and the density functional theories (WFT and DFT). The former family focuses on the wave function of the system, while the latter on its electron density.

The simplest approximation in wave function theory is the Hartree-Fock (HF) method (§ 2.2), which takes as an *ansatz* that the total wave function of a many electron system can be approximated by a Slater determinant (eq. 2.8), the simplest expression for a many electron wave function that satisfies the Pauli exclusion principle, mandatory for fermions. This method yields a set of one electron non-linear coupled equations. Their solution provides an approximated wave function in which each electron is free to move under the mean field potential created by the rest.

The HF method is limited, as it misses most of the effects from electronic correlation (i.e. how the instantaneous motion of one electron affects the others). In order to obtain a better treatment of the electronic correlation, several “post-Hartree-Fock" methods exist. In general, they consist on adding more Slater determinants to the HF wave function *ansatz*, which can be done in different ways (see § 2.2). Their main

drawback is their prohibitive computational cost for large systems. Alternative methods are those based on the Density Functional Theory (DFT), which rely on the electron density and not on the total wave function. These methods usually offer cost effective and accurate results, and are, therefore, very popular in the Computational Chemistry community. DFT has a large number of functionals, often with funny names like BLYP, BHLYP, M062X... each one with different capabilities and usually designed for specific purposes. The main differences among this plethora of functionals lie in how the so-called exchange–correlation energies are described (see eq. 2.16), which cannot be derived in an exact manner and have to be approximated, and hence the different existing approaches (see 2.3). In general, DFT calculations need to be corrected for long-range interactions (e.g. van der Waals interactions), which is usually done using empirical potentials on top of the DFT energy.

I note that for both WFT and DFT, one needs to provide an initial guess for the wave function (or the electronic density). This is done by combining basis functions forming a “basis set" aimed to represent molecular orbitals (§ 2.2).

In this thesis a particular set of systems has been investigated. These are biradical systems, that is, systems with two unpaired electrons of opposite electronic spin. To describe properly such systems one needs to have enough electronic correlation; otherwise, metastable states mixing ionic and biradical character appear. A suitable post-Hartree-Fock method for biradicals is CASPT2, which combines (i) the inclusion of excited states by adding Slater determinants (the CASSCF method) with (ii) perturbation theory (§ 2.2), ending up in a retrieval of enough electron correlation to properly describe such systems (see § 2.2). DFT methods together with the broken (spin) symmetry approximation (see § 2.4) offers a much less computationally demanding alternative. In this kind of calculation one mixes a triplet state in the overall singlet state to obtain enough electronic correlation as to properly describe the open shell singlet.

The methodologies presented above are used to derive the electronic energy related to a certain arrangement of atoms. Therefore, one can combine them with optimization algorithms to find stationary points in the potential energy (hyper)surface over the atomic coordinates. These stationary points can be minima (e.g. reactants, products, intermediates) or maxima (transition states) along a reaction path (see Figure 2.6). Molecular rotation and vibration are then usually approximated with the rigid rotor and harmonic oscillator models. With all of this information, one can obtain further insight on the chemical process of interest by investigating the kinetics of the reaction (see § 2.6).

In addition, these methods can also be used to simulate the dynamics of a given system. Usually a DFT method is used in such simulations, so that one can calculate the forces acting on each atom and propagate the system’s evolution in time following some algorithm (see § 2.7).

Finally, a word on surface modeling. In order to simulate processes taking place on surfaces, like reactions on interstellar ices, one needs to somehow take surfaces into account.

There are two principal strategies: the cluster and the periodic boundary conditions approaches. The first one considers few atoms forming a surface, and given its contained size, this approach is commonly used for studying reactions with computationally demanding and accurate methodologies. On the other hand, the latter approach considers a set of atoms in a simulation cell that repeats over space following periodic boundary conditions. This strategy is very useful for simulating solid crystals, e.g. one defines a small cell that repeats over the three directions of space producing the crystalline structure. One can also study more complex systems like amorphous solids (or liquids), at the expense of using a larger simulation cell (the larger the cell, the higher the computational cost). Similarly, surface processes can also be investigated by considering a large simulation cell that is partly filled with atoms forming a slab while the rest of its volume is empty. See more details in § 2.5.

Chapter 3
Works in the literature up to 2017

Outline

The first applications of computational chemistry methods to solve astrophysical problems can be tracked back to the 1970s. In those times, quantum chemistry methods were employed in the determination of molecular properties like spectroscopic parameters for the interpretation/characterization of microwave observations (e.g. Goddard, 1984; S. Green et al., 1974; Sheldon Green et al., 1976; Herbst et al., 1974; Pearson et al., 1974; Tucker et al., 1974b; Wilson, 1978, see also Vincenzo Barone et al., 2015, Fortenberry, 2017 for recent reviews on the topic), or in the study of gas-phase photoprocesses (e.g Caballol et al., 1976; Hayes et al., 1972; Jaffe et al., 1974). The field has evolved to the point that computational chemistry can nowadays be routinely applied in the investigation of more complex processes like gas phase reactions, e.g. V. Barone et al., 2015; Horn et al., 2004; Huang et al., 2000; J. C. Loison et al., 2015; J.-C. Loison et al., 2014a, 2010, 2012, 2014b; Redondo et al., 2013; Skouteris et al., 2017; Vazart et al., 2016; Walch et al., 2001 or surface reactions. For the latter, different types of surfaces have been studied, like silicates, graphite (simulating bare dust grain surfaces, e.g. Germán Molpeceres et al., 2019; Javier Navarro-Ruiz et al., 2015; Navarro-Ruiz et al., 2016), and interstellar ice surfaces. For the latter, water surfaces are the main focus as this molecule is the dominant component of interstellar ices (Boogert et al., 2015).

In this chapter I briefly review the literature on chemical processes on interstellar ice surfaces earlier to this thesis (before 2017, included), putting the focus on those works employing *ab initio* and DFT methods, although some works employing classical molecular dynamics have also been included due to their relation to the work presented in this thesis. The first related computational chemistry works are rather modern, about three–two decades ago, in which the name of David Woon repeatedly appears in the fields of *ab initio* and density functional theory (David E Woon, 2002a, 1999, 2001a,b), although other authors had important contributions in the field of classical molecular mechanics somewhat earlier (e.g. Buch et al., 1991; Takahashi et al., 1999a, see below). For a recent review on the topic I recommend the work by Zamirri et al. (2019), in which works focusing on solar system ices are also represented.

I have divided this chapter into different sections according to the kind of reaction or process of interest. In fact, some surface reactions are known to be key for the formation of important chemical species in the ISM like molecular hydrogen (§ 3.1), CO hydrogenation leading to formaldehyde and methanol (§ 3.2) and water (§ 3.3) Tielens et al., 1982. Others, like complex molecules formation, have not received as much attention as the previous reactions until more recently. For this reason complex molecule formation processes have been gathered into a single section (§ 3.4). Finally, there are some key aspects of interstellar ices that do not regard reactivity itself but related processes such as adsorption, diffusion and the dissipation of chemical energy. These were also gathered in another section (§ 3.5).

3.1 Hydrogen atom mobility and formation of molecular hydrogen

The formation of molecular hydrogen has been long known to be a surface process (e.g. Hollenbach et al., 1970, 1971; Smoluchowski, 1983; van de Hulst, 1946, see also the recent review by Valentine Wakelam et al. (2017)). Therefore, it does not come by surprise that processes related to H_2 formation are among the first applications of computational chemistry methods to problems involving astrophysical surfaces. This includes the investigation of H atom mobility on interstellar ices as well as H_2 formation.

The first works used classical molecular mechanics methods in order to simulate such processes. For example, Buch et al. (1991) studied the sticking probability of H and D atoms on an amorphous molecular cluster ice model of 115 water molecules and provided a simple formula to describe it. Masuda et al. (1998) did a similar simulation, this time using a slab model rather than a cluster one, and found higher sticking probability values than Buch et al., 1991, something that was reproduced later on by Al-Halabi et al. (2007) and Veeraghattam et al. (2014) who used a more modern set of parameters and more water molecules in their ASW models. The sticking coefficient of H atoms depends on several factors like the incoming H atom velocity (the fastest, the smallest the sticking), its angle to the surface (the closer to normal direction, the higher the sticking) and an increased sticking probabilities on ASW ices with respect to crystalline ices (e.g. Al-Halabi et al., 2002).

The above-mentioned theoretical works, however, cannot explain if quantum tunneling affects the diffusion of H atoms on ASW ices, as they rely on force field methods. Nevertheless, experiments by Hama et al. (2012) found that thermal hopping on ASW better explains H diffusion than tunneling, after observing

a weak kinetic isotope effect (KIE), while experiments by Kuwahata et al. (2015) suggested that H tunneling is more relevant on poly-crystalline ices due to the much more periodic surface potentials.

In this context, recent calculations have been carried out to better understand these phenomena at the atomic level. Senevirathne et al. (2017) studied the hopping of H atoms on fixed crystalline and amorphous ice models (taken from Andersson et al., 2006). They scan the potential energy surfaces on each ice model characterizing each minimum and saddle-point on them. They apply different schemes to include tunneling, including the Wigner and Eckart corrections as well as the instanton theory. They found similar results for the Eckart and instanton schemes, while for the Wigner not. The ASW model has a wide distribution of binding energies and therefore a wide distribution of hopping rate constants. They found that quantum tunneling is actually important, but only at temperatures below 10 K (the previous experimental works were performed at $\geq$ 8 K temperatures). Nevertheless, diffusion is slower on ASW (in accordance to previous experiments Hama et al., 2012; Kuwahata et al., 2015; Naoki Watanabe et al., 2010) as a consequence of the wider binding energy distribution that extends to higher values than on the crystalline one. Ásgeirsson et al. (2017) run a similar study as Senevirathne et al., 2017. They took a crystalline and an ASW ice models and located the minima and transition states of its potential energy surface. They used this energetic data to calculate desorption and diffusion rates, correcting for tunneling with the WKB correction[1]. This information was used as input parameters in kinetic Monte carlo simulations, allowing the investigation of quantum tunneling and long-time diffusion within the same framework. Their results are analogous to those by Senevirathne et al. (2017) regarding the importance of tunneling below 10 K, but for the long time diffusion thermal hopping is much more important on ASW, due to the deep binding energy wells, compared with the crystalline model.

The direct simulation of H_2 formation has a much smaller representation in the literature. Indeed, Takahashi et al. Takahashi et al., 1999a,b studied this reaction by means of classical molecular dynamics on amorphous ice in order to study the sticking probability of H atoms, their diffusion, reaction and desorption. They simulated the arrival of two H atoms on the surface and followed their evolution. They observed that the arriving H atoms can diffuse for about 60–140 Å and that once they loose all of their energy, they remain trapped for the whole simulation time. In those cases where H_2 was formed it was ejected into the gas phase with high vibrational states as the ice surface was found to not dissipate enough energy. In their latest work Takahashi et al., 2000, they studied the effects of H_2 formation on CO chemical desorption in order to asses if the energy liberated by H_2 was enough to locally warm up the ice allowing the sublimation of closeby CO molecules. They found that the closest vicinity of the reaction site (distances smaller than 4 Å) gains about 20 K and about 10 K for distances in between 4 and 6 Å. However, they observed that the heating lifetime was smaller than the one required for CO desorption on large grains, and therefore it is not efficient unless considering very small grains.

3.2 Hydrogenation of CO, formation of H_2CO and methanol

The successive hydrogenation of CO, leading to H_2CO and methanol (CH_3OH) was early proposed to be a surface process in the ISM Tielens et al., 1982. This chain reaction has been the subject of several experimental works, e.g. Chuang et al., 2016; Fedoseev et al., 2015; Fuchs et al., 2009; Hidaka et al., 2004; K. Hiraoka et al., 2001; Kenzo Hiraoka et al., 1994, 1998; Minissale et al., 2016c; Pirim et al., 2011, 2010; N. Watanabe et al., 2007; Naoki Watanabe et al., 2002a, 2003), as well as theoretical studies. Among these theoretical works, we find some of the earliest in the ice surface subset. Indeed, David E. Woon (2002b) investigated the effect of water molecules in the hydrogenation of CO up to CH_3OH and H abstraction from H_2CO. In this case the ice is modeled by a small number of water molecules (≤ 4) together with a polarized continuum model, and in another set of calculations they increased the number of explicit water molecules to 12, three of which were treated with an expensive electronic structure method (those belonging to the position where the reaction takes place) while the rest were described with a much less computationally expensive method. This author found that the water molecules have little effect on the activation barrier of the H + CO $\rightarrow$ HCO reaction, while they do lower the barrier for H + H_2CO $\rightarrow$ CH_3O by $\sim$4 kJ mol^{-1} and hinders the H + H_2CO $\rightarrow$ H_2 + HCO reaction. Additionally, the deuteration reactions of CO and H_2CO are slightly enhanced over the regular hydrogenation reactions. Therefore, water surfaces are not expected to

[1] WKB stands for Wentzel–Kramers–Brillouin, it is a semi-classical method to obtain an approximated tunneling probability, in whch it is assumed that the potential is a slowly varying function of the de Broglie wavelength.

be particularly good catalytic surfaces for these reactions, although they are have been shown to have a strong catalytic effect in the isomerization of *trans*-HCOH into formaldelyde by Peters et al. (2011).

Rimola et al. (2014) studied the CO and H_2CO hydrogenation reactions by means of density functional methods, employing much larger ASW ice surface models consisting of 3, 18 and 33 water molecules. They observed that the CO bond gets slightly polarized as a consequence of the interaction of the molecule with the surfaces, in which lower barriers were found by increasing the number of water molecules, a trend that was already noticed by Goumans et al. Goumans et al., 2008, 2007 who theoretically studied these hydrogenation processes on silica. Rimola en co-workers used their data in an astrochemical model and found good agreement with dark cloud observations. These authors also tried to simulate the hydrogenation sequence of a CO molecule belonging to a pure CO ice, and found similar results to those in the gas phase, hence indicating the importance of water as polar molecules in the surface.

More recently, Korchagina et al. (2017) studied the Eley-Rideal (ER) hydrogenation of CO by using the semiempirical SCC-DFTB method (a much less demanding methodology than pure DFT but at the expense of a much reduced accuracy) with the aim to assess the influence of the number of water molecules in this reaction. The surfaces were simulated by small amorphous molecular clusters with $\leq$5 and 10 water molecules. They run molecular dynamics at 70 K where an H atom (also at $\sim$ 70 K) was shot to the "cluster + CO" system. They obtained values for the formation efficiency of HCO and the efficiency of is desorption right after its formation, i.e. efficiencies for its chemical desorption. They find that HCO formation energy is dissipated by clusters with more than two water molecules, and that HCO remains attached to the surface for clusters larger than 3 water molecules. However, as the cluster size increases, the H atom gets stuck on the water molecules diminishing the efficiency of HCO formation. Therefore, the product yield increases for intermediate cluster sizes, drops for the smallest ones and diminishes for larger ones.

Song et al. (2017) studied the reactivity of H_2CO + H. On ASW ice models and using a hybrid methdology to describe it as used in David E. Woon, 2002b (namely, a region is described at a high theory level while the rest at a much lower one), they found three possible reactive channels for this reaction: formation of i) CH_3O, ii) CH_2OH and iii) H_2 + HCO. They provide the rate constants for ER and Langmuir-Hinshelwood (HL) mechanisms of these reactions including quantum tunneling by using the instanton[2] theory down to 59 K. They found that CH_2OH formation (the thermodynamically most stable species) has a much lower formation rate than the other two and that the ASW ice model has an important catalytic effect on CH_3O formation as it lowers its barrier but increases those for CH_2OH and H_2 + HCO. These effects can be seen in the branching ratios for each product, being about 0.8–0.9 for CH_3O, 0.1–0.2 for H_2 + HCO and $\sim$ 0 for CH_2OH formation. Additionally, strong KIEs were found for all three reactions, i.e. the deuterated forms of these reactions have much smaller tunneling rate constants than those for hydrogen.

3.3 H_2O formation

Different mechanisms exist for the surface formation of water, all of them based on the hydrogenation of surface species: (i) H + O $\rightarrow$ OH, H + OH $\rightarrow$ H_2O, (ii) H + O_2 $\rightarrow$ HO_2, H/H_2 + HO_2 $\rightarrow$ H_2O_2, H + H_2O_2 $\rightarrow$ H_2O + OH or H + HO_2 $\rightarrow$ 2OH and OH radicals can lead to H_2O following the first mechanism, and (iii) O_3 + H $\rightarrow$ OH + O_2 followed by the hydrogenation of OH (e.g. F. Dulieu et al., 2010; Kenzo Hiraoka et al., 1998; Oba et al., 2012; Tielens et al., 1982).

Lamberts et al. (2016) studied the H + H_2O_2 $\rightarrow$ H_2O + OH reaction. The reaction is first studied in the gas phase and then water molecules were added to the system, up to three molecules. Rate constants including tunneling by means of the instanton theory were reported for the reaction above and also the H-abstraction leading to HO_2 + H_2. The latter was found to have no relevance since the formation of water is much more efficient. A dependence on the number of water molecules was found, with the activation barrier being higher when more molecules are added because the transition states become more product-like. They also checked the differences of tunneling corrections when adopting the Eckart barrier or the instanton theory. Large KIE differences arise as the Eckart method underpredicts the kinetic constants at low temperatures.

As it was seen above, OH is a key species in this set of reactions, and the particular case of OH reactions with molecular hydrogen there is an activation barrier. Meisner et al. (2017) investigated the H_2 + OH $\rightarrow$ H_2O + H reaction by means of a hybrid scheme in which the reactants and some water molecules from the ice

[2] An instanton is the tunneling path itself at a given temperature.

surface are described at DFT level, while the rest of the ice is treated at a lower theory level. The ice surface is based on the a hexagonal crystalline ice. They studied the LH and ER kinetics of the reactions including quantum tunneling by means of instanton theory and the Eckart barrier. They found that the ice surface barely affects the activation energies (something also noted by Lamberts et al. (2017b) when considering the reverse reaction substituting the O atom by an S one, i.e. H + $H_2S \rightarrow H_2$ + HS), and a strong kinetic isotopic effect is observed when the reactive H atom is exchanged by a deuterium one. Additionally, the rate of reaction is almost temperature independent below 80 K.

3.4 Formation of complex molecules

Formation of iCOMs

Woon devised an alternative path to the formation of methanol, other than the successive hydrogenation of CO (§ 3.2). In 2011, David E. Woon (2011) explored the possibility that CH_3^+ and HCO^+ cations could react with water molecules from the ice. The ice was modeled with a molecular cluster made of 17 water molecules. He found that, similarly to the gas phase, these ions react with a water molecule without any activation energy barrier, but at difference from the gas phase, a proton is lost into the water ice surface leading to a neutral product: HCOOH and methanol plus a H_3O^+ cation stabilized by the rest of water molecules.

Another molecule that has received significant attention in the last years has been formamide due to its pre-biotic relevance (a recent review on this molecule has been recently published, by Ana López-Sepulcre et al. (2019)).

The successive hydrogenation of HNCO was thought to be responsible for the formation of formamide on ASW surfaces. However, experiments by Noble et al. (2015) and Fedoseev et al. (2016) ruled out this process. In this context Song et al. (2016) performed quantum chemistry calculations in order to retrieve the rate constants of these processes including tunneling with the instanton theory. The hydrogenation reactions on the ASW ice model were found to be about 4 kJ mol^{-1} lower than in the gas phase (where the barrier is about 36 kJ mol^{-1}). The barriers on the ice model were found to be rather independent from the chosen binding site. The quantum tunneling effects on the rate constants were found to be very small. This is due to the broad width of the activation energy barrier, which lowers the tunneling probability, and hence the low efficiency of HNCO hydrogenation.

Bredehöft et al. (2017) used computational chemistry methods in order to analyze the results of their experiments. They performed low energy electron irradiation of CO:NH_3 ices, and density functional calculations were employed to better understand the results of electron-impact products, although the ice effects were not included. The impact of electrons on molecules can form anionic, cationic or neutral radicals through electron attachment, electron impact ionization or neutral dissociation. The occurrence of one or another depends on (i) the energy of the incoming electron with respect to the ionization energy of the target molecule and (ii) the cross-section of the process. They find that the electron attachment to NH_3 is the most likely process. The $NH_3^{-,\bullet}$ leads to the formation of formamide by a sequential number of steps: the barrierless NH_2 + H^- followed by the barrier-free attack of NH_2 to CO ending in the abstraction of a H atom by the NH_2CO radical to NH_3. This last step has a high energy barrier ($\sim$65 kJ mol^{-1}), and the energy liberated by the electron attachment is assumed to help in surpassing it.

Finally, the coupling of radical species in interstellar ices have been proposed to be a plausible channel to form iCOMs (e.g. R. T. Garrod et al., 2006; Robin T. Garrod et al., 2008, see also § 4.1). This is one of the topics of this thesis, and as I already mentioned above, there was a single work investigating the presence of activation energy barriers for radical–radical reactions on interstellar ices: J. Enrique-Romero et al. (2016). In that pioneering work, we investigated the reactivity of HCO + CH_3 on interstellar ice surfaces leading to acetaldehye. The ice surfaces were modeled by molecular clusters of 18 and 33 water molecules using density functional theory. We found that the surface reaction of radicals does not necessarily lead to the formation of acetaldehyde, but there are competing channels producing CO + CH_4. These reactions were found to be barrierless. This, however, is a consequence of the methodology employed, which did not take into account the initial open-shell singlet biradical state.

Earlier on, Woods et al. (2013) explored the possibility that glycolaldehyde was a product of the dimerization of HCO on ices followed by two hydrogenation steps, for which they used astrochemical modeling

and quantum chemical calculations in which the BHLYP density functional combined with a double-ζ quality basis function with polarization were employed. The ice surface was modeled as a proton disordered Ih crystalline ice. These authors calculated the barrier for diffusion of HCO ($<$2 kJ mol^{-1}) and the barrier for the hydrogenation of glyoxal (HCOCHO, of 9.2 kJ mol^{-1}) but not the one for HCO + HCO reactions. Indeed, all radical–radical reactions were assumed to be barrierless. Butscher et al. (2017) experimentally investigated this same radical–radical reaction (i.e HCO dimerization) and employed quantum chemical calculations following J. Enrique-Romero et al., 2016 in order to interpret experimental results. In their experiments, glyoxal (HCOCHO) was not detected. They proposed that HCO + HCO reactions preferentially lead to CO + H_2CO as a consequence of the HCO + HCO $\rightarrow$ CO + H_2CO and HCO + HCO $\rightarrow$ HCOCHO $\rightarrow$ CO + H_2CO reactions. The latter is further displaced to the right due to experimental conditions (T$\sim$35 K) as CO molecules tend to sublimate. They also tentatively detected formaldehyde oligomers. They suggested that this signal arises from glyceraldehyde ($HCOCH_2CH_2OH$), formed by (i) the reaction of H_2CO with HCO, forming gycolaldehyde ($HCOCH_2OH$) and (ii) further reaction with another HCO radical forming glyceraldehyde. This last reaction happens as the temperature rises, since it has a relatively high energy barrier of 25 kJ mol^{-1}.

Formation of amino acids

The formation of these complex species on astrophysical ices has been investigated by computational chemists since the decade of the 2000s. The first works were carried out by D. Woon. Back in 2002, David E. Woon (2002c) studied the formation of the amino acids glycine (NH_2CH_2COOH), alanine and serine following the experimental results of Bernstein et al. (2002) who investigated the UV irradiation of H_2O ice doped with methanol, ammonia and HCN. Woon run calculations in which the water ice was modeled by a polarizable continuum model (i.e. PCM, in which water is modeled by a continuum dielectric so that the effect of water molecules is included in an implicit way). The formation of the COOH and CH_2NH_2 radicals was studied. For the former species, *trans*-COOH was shown to be the main product (assuming full energy dissipation by the ice surface) at variance with the gas-phase route, which yields CO_2 + H instead. The formation of the second radical (CH_2NH_2) due to HCN hydrogenation follows a similar trend as the hydrogenation of CO, namely activation energy barriers for odd H-additions and barrier-free reactions for even-numbered ones, with the added complexity that there are other hydrogenation products: HCN + H $\rightarrow$ CH_2N/HCNH, CH_2N/HCNH + H $\rightarrow$ CH_2NH, and finally, CH_2NH + H $\rightarrow$ CH_3NH/CH_2NH_2 (one more hydrogenation step would yield methylamine, CH_3NH_2). It was found that CH_2N formation was more favored than HCNH due to its lower barrier ($\sim$25.5 *vs* $\sim$53.5 kJ mol^{-1}), while the barriers to form CH_3NH/CH_2NH_2 radicals were found to be more comparable ($\sim$19.2 and $\sim$30.5 kJ mol^{-1}) being the first one more favorable. In summary, the activation energy barriers of COOH and the chain reactions leading to CH_3NH/CH_2NH_2 were found to be significantly high, between $\sim$13.8 and 30.5 kJ mol^{-1}. Thus, the plausibility of these reactions was related to the generation of "hot" H atoms after UV irradiation of laboratory ices, as they may retain most of the excess energy (about 250 kJ mol^{-1}) in the form of kinetic energy. This extra kinetic energy could either be used to promote such reactions or it could absorbed by the ice after several collisions. The formation of amino acids is initiated by the formation of glycine through the coupling of CH_2NH_2 and COOH radicals previously formed. Glycine could then refragment into secondary radicals, which could react with CH_3 and CH_2OH radicals present in the ice, this way forming alanine and serine. This mechanism however, requires the diffusion of radicals which is only possible at high temperatures. Therefore, Woon states that this mechanism is only possible in thermally shocked ices or in comets.

In 2010, Rimola et al. (2010) studied the formation of Glycine following a Strecker-like sythesis[3] on an ASW ice model made of 18 water molecules embedded in a PCM medium simulating the ice bulk. These authors found that the first step of the reaction has a low activation energy barrier (formation of NH_2CH_2OH, $\sim$ 8.4 kJ mol^{-1}), but a very high one for the second step (formation of H_2C=NH, $\sim$88 kJ mol^{-1}) thus hindering the formation of glycine. Fortunately, David E. Woon (2002c) found that H_2C=NH can be formed from HCN hydrogenation. Therefore, if H_2C=NH is formed following David E. Woon, 2002c, since the first step of the Strecker synthesis works (formation of NH_2CH_2OH) glycicine could be still formed following this

[3]Strecker synthesis: a multiple step synthetic pathway leading to amino acids. It starts with the condensation of an aldehyde (e.g. H_2CO) with an amine (e.g. NH_3) leading to an aminoalcohol (e.g. NH_2CH_2OH) which then forms an imine (e.g. H_2C=NH) by losing a water molecule in sufficiently acidic conditions, then a nucleophylic attack by a cianyde ion leading to an aminonitrile (e.g. NH_2-CH_2-C$\equiv$N), and finally a hydrolysis step, producing ammonia and an amino acid.

combined synthetic path. Rimola and co-authors studied this hypothesis and found barriers in the range of ∼33–38 kJ mol^{-1}, so that the combined synthetic route could work. The high barriers involved, however, will make it inefficient. Nevertheless, if NH_2CH_2CN is accumulated and delivered to the Earth by comets it may be an important precursor to glycine.

Later on, Rimola et al. (2012) studied the possibility to form glycine from CO and $NHCH_2$ on ices that had undergone the formation of a H_3O^+/OH cation–radical surface defect. Water ices are modeled by molecular clusters made of 3–6 and 8 water molecules. They found a relatively high energy barrier in the coupling of CO with the surface OH radical leading to COOH radical (16–20 kJ mol^{-1}). The COOH + $CHNH_2$ coupling was found to sport a very high energy barrier ($\sim$ 50 kJ mol^{-1}), but if $CHNH_2$ reacts first with H_3O^+ producing $CH_2NH_2^+$, the formation of either $NH_2CHC(OH)_2^+$ radical cation and $NH_2CHCOOH$ radical are possible. These reactions, however, are hampered at the low temperature conditions of the dense ISM due to the high barriers of the COOH formation, although it could take place at higher temperatures if the ices survive.

Ion chemistry

In some works, ions are very important, as they allow the lowering or disappearance of activation energy barriers (e.g. Rimola et al., 2012; David E. Woon, 2011). In these works, it is usually assumed that ions are formed in the gas phase and that land on the surface, or that are locally formed thanks to the effect of external UV/particle irradiation. However, there are chemical reactions that produce ions like acid–base reactions, and some theoretical works have focused on this topic too. For example, Park et al. (2004) investigated the deprotonation reactions of both HOCN and HNCO with ammonia and water on water ices (modeled following different strategies, including the polarized continuum model and the explicit inclusion of 2–6 water molecules). They found that the proton transfer reactions leading to OCN^-/NH_4^+ and OCN^-/H_3O^+ are catalyzed by water-assisted mechanism so that they become barrierless for clusters with more than three water molecules. Park et al. (2006) investigated the formation of ammonium (NH_4^+) and formate ($HCOO^-$) cations on water ices (simulated with clusters of $\leq$15 water molecules) and found that the proton transfer was barrierless. Kayi et al. (2011) studied the charge transfer reaction between CO_2 and CH_3NH_2, which was found to be more favorable on ice surfaces (modelled by clusters of $\leq$20 water molecules), forming the $CH_3NH_2^+CO_2^-$ zwitterionic complex[4]. Finally, David E Woon (2012) investigated the protonation of ammonia by CH_3COOH, HCN and HNC with water clusters made of 2–6 water molecules. In all cases, the ammonium cation (NH_4^+) was found to be formed in a barrierless fashion for ice clusters larger than three water molecules.

3.5 Other surface processes

A part from reactivity, there are other surface processes that are important in the ISM that have been simulated with computational chemistry, like diffusion, adsorption/accretion and the capacity of interstellar surfaces to dissipate the energy arising from chemical reactions.

Regarding the two first topics, very few works are available for species other than atomic hydrogen (see § 3.1). Some of the works reviewed above provide binding energy values as a by-product of their research, e.g. J. Enrique-Romero et al., 2016; Korchagina et al., 2017; Meisner et al., 2017; Rimola et al., 2014; Song et al., 2016, 2017. However, at the time that this thesis started, one work dealing with the binding energies of astrophysically relevant species on interstellar ices appeared. It was V. Wakelam et al. (2017) who proposed an alternative method to calculate binding energies. It is based on the interaction of different molecules and radicals with a single water molecule as it is assumed that the interactions with a whole ASW ice surface follows a proportionality law with this number. This last step is taken into account as an *a posteriori* correction to the calculated interaction. This correction is based on the dependency of the calculated values and those from temperature programmed desorption. This correction is, however, assumed to be the same for all species. This limits its actual applicability as this is not taking into account possible surface defects nor the specific features of each adsorbate.

[4] A zwitterionic complex is a overall neutral species with localized and opposite charges in its structure. These complexes are stable in contact with water thanks to solvation effects.

Using a much different methodology, Sameera et al. (2017) studied the binding energies of the OH, CH_3 and HCO radicals on a periodic crystalline hexagonal ice (Ih). They found that the dangling O and H groups from the water surface are key to understand the binding of these species, so that when both dangling groups are present in a certain surface binding site, the binding energies are large. They report binding energies for OH, HCO and CH_3 radicals in the ranges of $\sim$ 19–65, 11–41 and 11–25 kJ mol^{-1}, in agreement with the values reported by V. Wakelam et al. (2017) ($\sim$ 38, 20 and 13 kJ mol^{-1}, respectively).

Ghesquière et al. (2015), on the other hand, employed classical molecular dynamics to simulate bulk diffusion at temperatures between 90 and 170 K. In particular, they simulated the diffusion of H_2O, NH_3, CO_2, CO, and H_2CO in a box of water molecules that simulate laboratory low density amorphous water ice. They calculated the bulk diffusion coefficients at different temperatures as well as the activation energies for this process for each of the aforementioned molecules. They additionally suggest that the whole bulk diffusion mechanism is driven by the self-diffusion of water.

Regarding the energy dissipation capability of interstellar ices, Fredon et al. (2017) (and a follow up work in 2018, Fredon et al., 2018) studied the capacity of water ice surfaces (first on a crystalline ice model, and later on an ASW one) to absorb the energy from translationally excited molecules on their surfaces by means of classical molecular dynamics calculations. 70 and 10 binding sites for the crystalline and for the amorphous models are selected as initial positions for the following simulations. The admolecules[5] were given an initial kick corresponding to energies ranging between 50 and 500 kJ mol^{-1}, i.e. it is assumed that these admolecules were created after a chemical reactions and that the liberated energy went into their translational degrees of freedom. They found that the desorption of the excited species depends on the initial kick and on the binding energy of each species, which is also provided. They suggest that non-thermal diffusion (also as a consequence of the energy released by a chemical reaction) may induce further chemical reactions, although the traveled distances on the amorphous ice was found to be about a factor 2 shorter than in the crystalline case. A part from surface diffusion, penetration into the ice structure remains a possibility. They also found that in some cases a water molecule of the amorphous ice model can be ejected after collision with the translationally excited admolecule, especially for CH_4.

[5] Adsorbed molecules.

Part I

Static quantum chemical calculation on radical–radical surface chemistry

Chapter 4
Introduction to this part

Outline

4.1 Context

In the 1990s, the evolution of interstellar complex organic molecules (iCOMs) in hot cores/corinos was thought to be mainly driven by gas-phase reactions (e.g. Caselli et al., 1993; Charnley et al., 1992; Millar et al., 1991, paradigm 1 in Figure 1.7), in which the species forming the ice-coatings of dust grains would evaporate rapidly once the protostar heats up, stimulating rich chemistry (Brown et al., 1988; Charnley et al., 1992). However, the inefficiency of key reactions in the route to iCOMs (Geppert et al., 2005, 2006; Horn et al., 2004) revealed the need for other synthetic mechanisms leading to complex organics in the ISM. Back in the 1960–1970s, several experimental studies proposed the possibility that radicals could be formed in interstellar ices as a consequence of UV photon and cosmic ray (CR) exposure (Hagen et al., 1979; Strazzulla et al., 1983; Tielens et al., 1987). In this context, Allen et al. (1977) provided a list of plausible exothermic reactions that could take place on ice-coated dust grains which included radical-radical coupling reactions. Later on, R. T. Garrod et al. (2006) proposed an astrochemical model that predicted large amounts of methyl formate, formic acid and dimethyl ether during the protostellar *warm-up* phase from OH, HCO, CH_3, and CH_3O. This model was inspired by the works of Viti and collaborators Collings et al., 2004; Viti et al., 1999, 2004 that first introduced the concept of “warm-up" and with this information, R. T. Garrod et al., 2006 introduced the species-dependent diffusion of heavy radicals (e.g. HCO, CH_3O...) into their model when the temperature is larger than about 20–30 K. These authors also incorporated the photo-processing of ices as a source of radical species, apart from the partial hydrogenation of simple ice components V. Taquet et al., 2012, the photon sources of which being the heavily extinguished UV interstellar radiation field, and most importantly, the cosmic-ray (CR) induced UV radiation field Gredel et al., 1989; Prasad et al., 1983. Their physical model consisted of two successive physical phases, the collapse of a diffuse cloud (cold stage), followed by the switch on of the protostar (warm-up phase). This work, therefore, proposed that radical–radical reactions on interstellaer ices could be a very efficient pathway towards the formation of iCOMs.

Follow-up works such as Robin T. Garrod et al. (2008) extended the reaction network incorporating coupling reactions between H, OH, HCO, CH_3, CH_3O, CH_2OH, NH, and NH_2 (primary radicals, see Figure 4.1). They also included other radical–radical reactions involving different generations of radicals as well as reactions between radicals and aldehydes (containing the -COH group). They found that second generation radicals have little importance given the comparatively low abundances of their parent species and their larger binding energies, which imply that hydrogenation reactions may take place first.

E_b(K)	225	557	588	800	1189	1250	1425	1978	2254
Radical	**H**	**CO**	**CH_3**	**HCO**	**NH**	**CH_3O**	**OH**	**NH_2**	**CH_2OH**
H	H_2								
CO	HCO	x							
CH_3	CH_4	CH_3CO	C_2H_6						
HCO	H_2CO	x	CH_3CHO	OHCCHO					
NH	NH2	HNCO	CH_3NH	HNCHO	N_2H_2				
CH_3O	CH_3OH	CH_3OCO	CH_3OCH_3	$HCOOCH_3$	CH_3ONH	$(CH_3O)_2$			
OH	H_2O	COOH (CO_2 + H)	CH_3OH	HCOOH	HNOH	CH_3OOH	H_2O_2		
NH_2	NH_3	NH_2CO	CH_3NH_2	NH_2CHO	$HNNH_2$	CH_3ONH_2	NH_2OH	$(NH_2)_2$	
CH_2OH	CH_3OH	$CH_2(OH)CO$	C_2H_5OH	$CH_2(OH)CHO$	$CH_2(OH)NH$	CH_3OCH_2OH	$CH_2(OH)_2$	$CH_2(OH)NH_2$	$(CH_2OH)_2$
E_A (K)	2500	1500 (80)							

Figure 4.1: *Table taken from Robin T. Garrod et al., 2008. When combining a radical from the left with another of the right one gets a new iCOM. In the original paper they included CO in the list of radicals even if it is not. Notice the activation energies (bottom row, related to dark boxes) and binding energies (top row) utilized in the original article, two very important parameters in astrochemical models. Crosses mean “not included” in the reaction set of the model.*

Despite the success of such works in the community, this iCOM formation paradigm holds some problems. The first one is related to the reactivity of radical species on ice surfaces. It is assumed that radical–radical surface reactions take place in absence of activation energies, like if the radicals were in the gas phase, and additionally it is assumed that there is a single product channel leading to the formation of

iCOMs. This is motivated by experiments where iCOMs formation is observed after the energetic processing of interstellar ice analogues grown in the laboratory. Such experiments, however, can say little about the elementary processes taking place at atomic level. Additionally, they are far from the conditions found in the interstellar medium given that they work at much higher pressures, surface coverage and particle/photon fluxes than those found in the ISM in order to reproduce chemical and physical events within laboratory time-scales (Tielens, 2013). The second problem regards the mobility of species on surfaces. In order to simulate the surface diffusion and sublimation of frozen species, astrochemical models need a key quantity: the BE of the species to the surface. This quantity is usually poorly defined (as it depends on the molecule and the surface site) and in many cases it is simply extrapolated according to the functional groups present in each chemical species. The diffusion energy is usually taken to be a fraction of that of desorption, i.e. the BE (e.g. R. T. Garrod et al., 2006; Robin T. Garrod et al., 2008; Tatsuhiko I. Hasegawa et al., 1992; S. S. Jensen et al., 2021; M. Ruaud et al., 2015; Ruffle et al., 2000a; Vasyunin et al., 2017). Finally, the rates, branching ratios and yields of photodissociation processes forming radicals are also loosely defined: photodissociation rates are usually assumed to be equal to those in the gas phase and CR-induced UV fluxes strongly depend on the CR energy spectrum and the penetration of UV photons in ices (see V. Taquet et al., 2012 and references therein).

It is worth mentioning that with time, several improvements to these "gas-grain" models have been made. Aikawa et al. (2008) incorporated the spatial distribution and Awad et al. (2010) the evolution of the collapsing cloud. V. Taquet et al. (2012) introduced the multilayered and porous structure of interstellar ices into their model, assuming that only the outermost layer is chemically active while the bulk acts as a chemical storage. They predicted (i) a structured ice with the presence of relatively complex CO-derivatives (H_2CO and CH_3OH) being more abundant in higher layers, (ii) an important effect of the layered structure of ices, in which some of the produced radicals (formed by partial hydrogenation reactions rather than photolytic processes) remain trapped in the mantle with a reduced role of photolysis and (iii) a small effect on the overall chemistry due to the porous structure.

With the discovery of iCOMs in cold prestellar cores ($\leq$ 10 K) (e.g. Bacmann et al., 2012; Cernicharo et al., 2012; Jiménez-Serra et al., 2016; Vastel et al., 2014), new routes were put forward trying to explain these observations. These findings challenge the iCOM formation grain-surface paradigm, as the latter needs the warm up of interstellar grains at $\geq$ 20 K in order to allow the diffusion of radicals. In this context, Vasyunin et al. (2013) used the concept of reactive desorption as a possible process to release precursor molecules into the gas phase. In their model CH_3O is released into the gas phase by this mechanism where it may undergo, among other destruction reactions, radiative association with CH_3 at temperatures as low as 10 K forming dimethyl ether (however, they used a route that previous works (Duley et al., 1993) showed to be inefficient, see Balucani et al., 2015). In addition, the efficiency of reactive desorption is hideous and more complex than it seemed initially (see § 10). On another front-line, M. Ruaud et al. (2015) incorporated the Eley-Rideal mechanism in which landing C atoms react with frozen species via the formation of Van der Waals complexes in the cases where a high activation energy barrier exists. However this mechanism cannot account for the large abundances of dimethyl ether and methyl formate in cold cores (Herbst, 2017). As an alternative to surface chemistry, "cold" gas phase neutral–neutral reactions was also proposed by Balucani et al. (2015), who also assumed methoxy to be formed on the grain surfaces.

Recently, alternative pathways invoking the collision of CR with interstellar ices have been proposed using Monte Carlo simulations Herbst, 2017; Shingledecker et al., 2018a,b. This new paradigm is not actually new in the community, since experiments characterizing the irradiation products of laboratory ice analogues representing interstellar and Solar system media conditions were already been explored for decades (e.g. Baratta et al., 2004; Bennett et al., 2007, 2005; Hudson et al., 1999, 2001; Strazzulla et al., 1983, 1995). However, these are the first astrochemical models to provide a method to take into account the CR irradiation of ices. In this model, CRs are responsible for the formation of ions and electrons within the ice structure, which can become a source of electronically excited ice species. Such energized species are able to undergo chemical reactions with substantial activation energy, leading to the formation of several chemical species including iCOMs. Therefore this model proposes that CR would not only be crucial for gas phase reactions, as they are the main formation mechanism of gaseous H_3^+ (Herbst et al., 1973), and the formation of the secondary UV field in the densest parts of the ISM, but also the formation of iCOMs in ices *via* the formation of these ions and/or secondary electrons.

The crucial assumption and problem common to all the above models of grain-chemistry iCOM formation

is that radicals on the surface combine barrierless, namely with efficiency equal to unity. Is this assumption correct?

4.2 Goals, methods and novelty of the research in this part

In this Part, I present the results obtained in J. Enrique-Romero et al. (2020) and Joan Enrique-Romero et al. (2019, 2021a) (Chapters 6, 5 and 7, respectively). The first Chapter (5) presents the importance of using broken symmetry in DFT, the second one (6) is a "proof of concept" study in which the formation of acetaldehyde and formamide from HCO + CH_3 and HCO + NH_2 on ASW[1] ices is investigated, and the third one (7) is a systematic study on different radical radical reactions.

The goals of this research are (i) to find out whether radical–radical reactions on ASW ice surfaces are actually barrierless or not, (ii) to understand if such reactions have a single product channel, (iii) in the case to have different reaction channels, if they are in direct competition, and (iv) to understand how the surface environment affects the reactivity.

The set of radical–radical reactions to study were taken from Fig. 1 of Robin T. Garrod et al., 2008 (reproduced here in Figure 4.1), so that we investigate a subset of them, namely some of the reactions between CH_3, HCO, NH_2, CH_3O and CH_2OH, marked in red in Figure 4.1. Two ASW ice models of different sizes were employed (taken from Rimola et al., 2014). The smallest one presents a rather flat external surface and consists of 18 water molecules. The larger one, is composed by 33 water molecules and sports a cavity structure where radicals can establish more inter-molecular interactions. Both are shown in Figure 4.2. With this later model we aim to better represent the surfaces of interstellar ices. It also has a flat region which was found to be not suitable for our systematic study (Joan Enrique-Romero et al., 2021a) since some radical–radical reactions were found to end up in the collapse of the whole surface model.

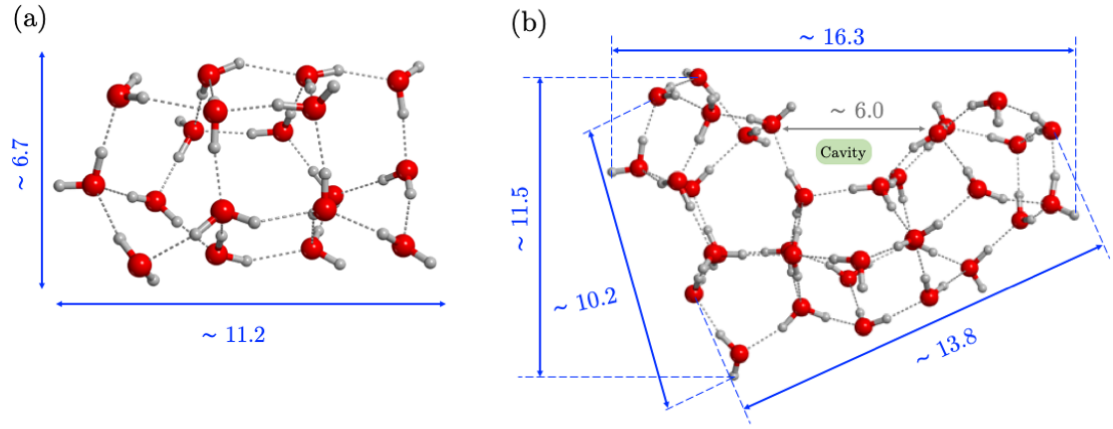

Figure 4.2: *The two main ASW models used in this Thesis, the one to the left is made of 18 water molecules (W18), and that to the right of 33 water molecules (W33). The molecular geometries shown in this figure were minimized at BHLYP-D3(BJ)/6-31+(d,p) level of theory. Distances are in Å. Notice the hemispherical cavity structure in the largest ice model in the right hand side.*

The novelty of my works presented in this chapter with respect to previous studies resides on the fact that these are the first ever studies of radical–radical reactivity on ASW ices at an atomic scale and by means of computational chemistry simulations. This kind of studies have not been tackled before[2] for several reasons. One is the general belief that radical–radical reactions are barrierless, which, as will be seen, is not always true, especially on polar molecular surfaces like ASW ices. Another reason is the intrinsic complexity of running these calculations: from the technological view point, one cannot afford to run the highly accurate and demanding calculations needed to describe singlet open shell systems (e.g. two radical species on the surface ready to react) on explicit surfaces, and the other one is the lack of theoretical works employing the broken symmetry approximation in the astrochemistry community.

[1] Amorphous solid water.

[2] There are two exceptions: J. Enrique-Romero et al. (2016) and Rimola et al. (2018).

To this end, we used DFT theory combined with the unrestricted and broken (spin) symmetry approaches in order to properly describe the singlet biradical state of reactants and transition states. This broken symmetry approach relies on partially mixing some triplet in order to retrieve a physically sound wave function solution to the singlet system (see § 2.4) with the drawback that it is more time consuming than normal DFT for (i) the usage of the mandatory unrestricted scheme and (ii) the need to make sure that the initial guess wave-function is is an actual open-shell singlet state[3], and that it is the minimum energy solution. Regarding the density functional, we have relied on BHLYP combined with the "D3" Grimme's dispersion correction[4] as it provides accurate binding energies and sports a 1:1 mixing of the pure DFT and exact exchange contributions. These two factors are important for us since (i) the activation energy barriers of surface radical–radical reactions come mostly from the radical–surface interaction and (ii) because such a high DFT-to-exact exchange ratio alleviates the effects of the electron self-interaction error inherent in DFT calculations.

In our calculations all electrons and atoms in the system are treated at the same level of theory. Minima and maxima in the PESs were characterized by frequency calculations. Zero point vibrational energies were calculated, and intrinsic reaction coordinate calculations were run when necessary (or possible) in order to ensure the connection between reactants and products to the transition state. We employed double- and triple-ζ basis sets from the Pople family, depending on the nature of the calculation, e.g. optimization and frequency calculations are more time consuming than single-point energy calculations, therefore the smaller basis set was employed for the former cases.

Binding energy calculations for each radical on each surface model were also carried out. In this case the final energies were corrected for dispersion, deformations, basis set superposition errors and zero-point energies.

4.3 Summary of the results

Radical–radical reactions are found to very often have energy barriers typically below $\sim$7 kJ mol^{-1} (equivalent to 840 K), although some specific cases can have much higher energy barriers. In general these barriers are a consequence of the interaction of the radicals to the ice surface, i.e. they come from the break of radical–surface interactions.

Two possible reaction channels are possible: (i) radical coupling. i.e. the formation of a chemical bond between both radicals leading to iCOMs, and (ii) direct H-abstraction reactions, where one of the radicals transfers an H atom to the other. These two reactions often present similar activation energy barriers, and therefore are, possibly, in competition. Hence, the assumption that a reaction between any two given radicals will necessarily produce iCOMs is not warranted and should be taken with caution in astrochemical modeling.

The effects of the surfaces are best represented by the values of the binding energies (BE). For both surface models the order in BE is the same: $CH_3 < HCO < NH_2 < CH_3O < CH_2OH$. However, BEs in the cavity of our larger model are found to be higher than on the surface of the 18 water molecules model. These differences arise as a consequence of the different chemical environment, given that the number of interactions in the cavity is larger.

Regarding more specific aspects, some conclusions for each radical can be derived:

- We found that HCO is a very efficient H-donor in direct H-abstraction reactions and, accordingly, this channel competes with radical coupling reactions, likely setting a 1:1 branching ration for each process.
- Due to the low BE of CH_3 to the adopted ASW surface, in many cases its reaction mechanisms comprise a low energy torsion, so that it is frequent to find reactions with this radical to be barrierless

[3] Open-shell means that not all electrons are paired. The case of biradicals is clear, with either singlet or triplet open shell states, i.e. there are two unpaired electrons with anti-parallel/parallel spins.

[4] See more details in each article since the introduction of this correction varied from our first work Joan Enrique-Romero et al., 2019, in which it was introduced as single point energies on top of the BHLYP optimized molecular structures, to the most recent oneJoan Enrique-Romero et al., 2021a, in which energies during the optimization process are also corrected, and moreover we use a more modern implementation, namely the one with the Becke-Johnson damping. See § 2.3 for more details on dispersion corrections.

(or almost). There are some exceptions on the cavity of our larger model, where CH_3 mobility is much more restricted, so that activation energy barriers can rise up to $\sim$7 kJ mol^{-1}.

- The strong interaction of the OH group in CH_2OH with the water molecules of the surface makes this radical to show a particular interaction pattern, in which its OH group is locked by H-bonds, while its C atom (containing the radical) is far from the surface and free to react. This makes this radical to have very low activation energy barriers for reactions on its C atom but very high ones for direct H-transfer ones where CH_2OH is the H-donor.

  The binding pattern of CH_2OH would imply that this radical is efficiently destroyed by reactions with other molecular radicals or H atoms.

- CH_3O has its radical electron on the O atom, which in turn establishes H-bonds with the surface water molecules. This makes this radical to be slightly less reactive than expected and therefore high energy barriers appear for CH_3O + CH_3O reactions. On the other hand, it can still perform direct H-abstraction reactions as a donor, but the high energy barriers due to its intrinsic H–C bond stability (and for the cavity, the higher number of intermolecular interactions) indicate that they are efficient only when considering quantum tunneling effects.

Finally, in our last work (Joan Enrique-Romero et al., 2021a, Chapter 7) we discuss what iCOMs from our sample could actually be formed, which ones will be in competition with the direct H-abstraction products, and which cannot be formed, based on a rough estimation of their reaction efficiency. This efficiency tells us about the competition between reaction and diffusion/desorption away from the reaction site (see Chapters 8 and 9 for its definition).

Those iCOMs that can be formed are: ethane (C_2H_6), methylamine (CH_3NH_2) and ethylene glycol (CH_2OHCH_2OH). Those that will have to compete with the direct H-abstraction channel are: glyoxal (HCO-CHO, against CO + H_2CO), formamide (NH_2CHO, against NH_3 + CO), methylformate (CH_3OCHO, against CH_3OH + CO) and glycolaldehyde (CH_2OCHO, against CH_3OH + CO). And those that will not be formed are: acetaldeyde (CH_3CHO) and dimethyl peroxyde (CH_3OOCH_3).

Chapter 5

Revisiting the reactivity between HCO and CH_3 on interstellar grain surfaces

The research presented in this Chapter has resulted in a scientific article:
Enrique-Romero, J.; Álvarez-Barcia, S.; Kolb, F. J.; Rimola, A.; Ceccarelli, C.; Balucani, N.; Meisner, J.; Ugliengo, P.; Lamberts, T.; Kästner, J.
Published in Monthly Notices of the Royal Astronomical Society, 2020.
DOI: 10.1093/mnras/staa484

Outline

The formation of interstellar complex organic molecules is currently thought to be dominated by the barrierless coupling between radicals on the interstellar icy grain surfaces. Previous standard DFT results on the reactivity between CH_3 and HCO on amorphous water surfaces showed that formation of CH_4 + CO by H transfer from HCO to CH_3 assisted by water molecules of the ice was the dominant channel. However, the adopted description of the electronic structure of the biradical (i.e., CH_3/HCO) system was inadequate (without the broken-symmetry (BS) approach). In this work, we revisit the original results by means of BS-DFT both in gas phase and with one water molecule simulating the role of the ice. Results indicate that adoption of BS-DFT is mandatory to describe properly biradical systems. In the presence of the single water molecule, the water-assisted H transfer exhibits a high energy barrier. In contrast, CH_3CHO formation is found to be barrierless. However, direct H transfer from HCO to CH_3 to give CO and CH_4 presents a very low energy barrier, hence being a potential competitive channel to the radical coupling and indicating, moreover, that the physical insights of the original work remain valid.

5.1 Introduction

As it was explained in §1.4 of this Thesis, iCOMs have been observed in a wide variety of astronomical objects like star forming regions (e.g. Belloche et al., 2017; Cazaux et al., 2003; Kahane et al., 2013; Ligterink et al., 2017; A. López-Sepulcre et al., 2015; McGuire et al., 2018; Mendoza et al., 2014; Rubin et al., 1971), in the circumstellar envelopes of AGB stars (Cernicharo et al., 2000), shocked regions (Arce et al., 2008; Codella et al., 2017; Lefloch et al., 2017) and even in external galaxies (Muller et al., 2013). Nevertheless, how they are formed is still an open question (see §1.4 and §4.1).

The main model trying to explain their formation routes assumes that whenever two radicals (e.g., created by UV photon and/or cosmic rays incidences) are in close proximity on the surface of interstellar ices (e.g., because of their diffusion) they can react to form iCOMs in a barrierless way.

However, a first theoretical study of the reactivity of HCO and CH_3 on an amorphous water surface (AWS), which is the bulk of the ices that envelope interstellar grains in cold objects, showed that the combination of these two radicals does not necessarily lead to the formation of the iCOM acetaldehyde (CH_3CHO) (J. Enrique-Romero et al., 2016). This unexpected result called for and was followed by other studies of different systems and with different computational methods. First, Rimola et al. (2018) and Joan Enrique-Romero et al. (2019) (find it in Chapter 6) studied the formation of formamide (NH_2CHO) and acetaldehyde by reactions between HCO and NH_2 and HCO and CH_3 on a AWS model by means of static quantum chemical calculations. Subsequently, Lamberts et al. (2019) studied the formation of acetaldehyde by reaction between of HCO and CH_3 on a CO-pure ice model by means of *ab initio* molecular dynamics (AIMD) simulations. The three works confirmed the main finding by J. Enrique-Romero et al., 2016, namely, that the reactivity between the radical pairs does not lead exclusively to the formation of the iCOMs, but formation of CO + NH_3 and CO + CH_4 via direct H abstraction can also take place. In view of these results, formation of iCOMs via the barrierless radical-radical combination scheme needs still to be validated.

Here, we aim to revise the first calculations carried out on the CH_3 + HCO system (J. Enrique-Romero et al., 2016) which were based on the standard DFT approach. Since then, it has become clear that an improved treatment of the radicals spins is necessary (Joan Enrique-Romero et al., 2019; Rimola et al., 2018). This Chapter is organised as follows: in § 5.2 we review the treatment of the spins of a biradical system, in § 5.3 we provide the details of the new computations carried out in this Chapter, in § 5.4 we show the results and in § 5.5 we discuss the conclusions.

5.2 Why a better treatment of the biradical wave-function is needed

In a work previous to this Thesis (J. Enrique-Romero et al., 2016), the reactivity between HCO and CH_3 in the gas phase and on AWS, modelled by H_2O ice clusters, was theoretically studied with standard DFT calculations. In the gas-phase model[1], different synthetic channels were identified, namely, the formation of acetaldehyde (CH_3CHO), CO + CH_4 and the carbene-ether CH_3OCH, the occurrence of which is determined

[1]We loosely use the term "gas-phase" to refer to systems where no water molecule are involved. The reader has to bear in mind that these reactions cannot take place in the gas phase of the ISM unless the excess energy is dissipated, for example by a third body, like a grain, that absorbs the nascent chemical energy.

by the relative orientation of the radicals. In contrast, on the AWS models, a hydrogen-atom relay mechanism assisted by water molecules of the ice led to the exclusive formation of CO + CH_4.

The electronic ground state for the CH_3CHO, CO + CH_4 and CH_3OCH products is a singlet wave function as they are closed-shell systems. Conversely, the HCO and CH_3 radicals are open-shell doublet systems due to their unpaired electron, while a system consisting of the two radicals (i.e., HCO and CH_3 together) can be either in triplet or singlet electronic states (the spins of the unpaired electrons can be of the same sign or of opposite signs, respectively). The triplet state is electronically non-reactive due to the Pauli repulsion. In contrast, the singlet state (usually referred to as a "biradical" system) is reactive because of the opposite spin signs. The description of the electronic structure of biradical states requires a wave function composed of more than a single Slater determinant (eq. 2.8 in § 2.2) to recover static correlation. In the wave function-based post-Hartree-Fock (post-HF) realm, this can be described by multi-configurational self consistent field (MCSCF) methods, such as the complete active space self-consistent field (CASSCF), or the so-called multi-reference methods like the complete active space perturbation theory (CASPTn) ones. In CASSCF, a particular number of electrons (N) are distributed between all possible (namely, ground and excited) configurations that can be constructed from M molecular orbitals, i.e., an (N, M) active space. It is worth mentioning that one has to pay special care when deciding the orbitals to include in the active space, since the resulting wave-function could erroneously describe the system under study. CASPTn is an improvement over CASSCF(N, M) where a perturbative expansion is further performed in order to retrieve more dynamic electron correlation (see § 2.2 for more information on wave function-based methods, in particular § 2.2). On the other hand, such multi reference character cannot be obtained from normal Kohn-Sham density functional theory (DFT, § 2.3). Instead, the electronic structure of biradicals can be approximated by an unrestricted open-shell wave function with the broken-(spin)-symmetry *ansatz* (§ 2.4), where a triplet state is mixed with a combination of ground and excited singlet states in order to obtain an electron-correlated wave-function (Neese, 2004; Noodleman, 1981; Noodleman et al., 1984, see).

Calculations by J. Enrique-Romero et al., 2016 were performed in an open-shell formalism, but after publication it was realised that the initial guess wave functions remained in a metastable, symmetric state with spin-up and spin-down orbitals being equally mixed (i.e., spin analysis indicated 50% of spin up and 50% of spin down in each radical and the total spin density being zero), thus resembling a closed-shell solution. Compared to that, the actual broken-symmetry wave function leads to a significant stabilization of the reactants, which changes the results qualitatively. Thus, the present work aims to revise some of the original results using the DFT broken-symmetry solution, showing moreover that it agrees reasonably well with those at the CASPT2 level.

5.3 Computational details

All DFT calculations were performed using the GAUSSIAN09 package (Frisch et al., 2009), while post-HF multi-configurational and multi-reference calculations were carried out with the OpenMolcas 18.09 software (Aquilante, Francesco et al., 2010, 2016; Fernandez Galván et al., 2019; Karlström et al., 2003).

DFT geometry optimisations and transition state searches were carried out with i) the M06-2X (Zhao et al.,) and ii) BHLYP-D3 (i.e. BHLYP, Becke, 1993a; C. Lee et al.,) including the Grimme's D3 dispersion correction (Grimme, 2006; Grimme et al., 2010) functionals, in combination with a def2-TZVPD basis set. Structures with triplet electronic states were simulated with open-shell calculations based on an unrestricted formalism. Singlet biradical systems were calculated adopting an unrestricted broken-symmetry (BS) approach. For the sake of comparison, for some cases, single point energy calculations adopting standard (i.e., non-BS) unrestricted (U) formalisms have also been carried out.

CASSCF geometry optimisations and transition state searches were performed using a (2,2) active space, corresponding to the radical unpaired electrons in their respective orbitals. Reaction energetics were refined by performing CASPT2 single point energy calculations on the CASSCF(2,2) optimised geometries. In both cases the cc-pVDZ basis set was employed. For the sake of clarity, here we only show the CASPT2 results. CASSCF(2,2) energetic values are available in the annex A, together with input examples. The XYZ molecular structure data files are avaliable in the online supporting information file of the publication related to this Chapter (here).

Since the scope of this work is to revise the electronic structure of the biradical systems, only electronic energy values are reported and accordingly zero-point energy corrections were not accounted for here.

5.4 Results

Reactions in the gas phase

In the gas phase, in agreement to the previous work J. Enrique-Romero et al., 2016, the nature of the final product depends on the relative initial orientations of the reactants. When the C atoms of the two radicals are pointing one to each other (i.e. $H_3C\cdots CHO$), they couple to form CH_3CHO, similarly, when the H atom of the HCO is pointing to the C atom of CH_3 (i.e. $OCH\cdots CH_3$), H is transferred to form CO + CH_4. Both processes have been found to be barrier-less, irrespective of the method (i.e., BS-DFT and MCSCF, see the left hand side of Figure 5.1).

On the other hand, when the O atom of HCO points towards the C atom of CH_3 (i.e. $HCO\cdots CH_3$), the carbene CH_3OCH species can form. For this case, however, BS-DFT calculations indicate that the biradical system is metastable. Consequently, formation of CH_3OCH is not spontaneous but requires overcoming an energy barrier of 31.3 and 51.0 kJ mol^{-1} at the (BS)UM06-2X and (BS)UBHLYP-D3 levels, respectively. The same trend is found for CASPT2 calculations with an energy barrier of 11.5 kJ mol^{-1} (see right hand side of Figure 5.1). It is worth mentioning that, for the formation of CH_3OCH, U single point calculations on the (BS)UM06-2X optimized geometries (without considering the BS approach) result in spontaneous formation of CH_3OCH, leading to the same result as for the restricted situation (see singlet_UM06-2X energies in Figure 5.1 represented by blue crosses). This is because the singlet UM06-2X initial guess wave function does not consider the reactant as an actual biradical system but the unpaired electrons are localized 50% spin-up and 50% spin-down in one radical and the same for the other radical, resembling an electronic closed-shell situation. This excited initial guess wave function is about 173.9 kJ mol^{-1} less stable than the asymptote (0.0 kJ mol^{-1}, corresponding to the situation where the radicals are infinitely separated) and hence the system rolls down to the most stable closed-shell situation. Similarly, single points at the triplet UM06-2X level on the (BS)UM06-2X optimized geometries are also shown in Figure 5.1 (represented by blue diamonds). We want to stress out that triplet-state wave-functions do not require the use of the broken-symmetry *ansatz* as single-reference methods like UDFT already provide good descriptions of such open shell systems thanks to Pauli's exclusion principle.

Reactions in the presence of one water molecule

For the reactivity between CH_3 and HCO in the presence of one water molecule, we have studied the reactions of CH_3CHO formation through a radical-radical coupling (Rc) and the formation of CO + CH_4 through both a direct hydrogen abstraction (dHa), i.e., the H transfer is direct from HCO to CH_3, and a water-assisted hydrogen transfer (wHt), i.e., the H transfer is assisted by the water molecule which allows a successive H-transfer mechanism $OC{\cdot\cdot}H\cdots HO{\cdot\cdot}H\cdots CH_3$.

In J. Enrique-Romero et al., 2016 it was shown that, in the presence of $(H_2O)_{18}$ and $(H_2O)_{33}$ water cluster models, the wHt was found to be barrierless, i.e., the assisted H transfer occurred spontaneously during the optimization process, a finding that led the authors to conclude that this channel was the dominant one over the others. However, we identified that such a spontaneous process is a consequence of the limitation of standard DFT to describe the electronic structure of biradical systems if the BS approach is not adopted.

By adopting BS-DFT, we have found here that for the both (BS)UM06-2X and (BS)UBHLYP-D3 methods, Rc is a barrierless process (see Figure 5.2).

The PESs for the dHa and wHt processes at the different theory levels are shown in Figure 5.3. At (BS)UM06-2X and (BS)UBHLYP-D3 levels, dHa presents a small energy barrier (2.4 and 5.1 kJ mol^{-1}, respectively). In contrast, wHt presents a high energy barrier (58.2 and 73.3 kJ mol^{-1}, respectively), indicating that it is not spontaneous. Similar findings are provided by CASPT2, which predicts energy barriers of 1.3 and 36.1 kJ mol^{-1} for dHa and wHt, respectively. In contrast, U single point energy calculations on the (BS)UM06-2X optimized geometries without considering the BS approach describe both dHa and wHt as spontaneous processes (see singlet_UM06-2X energies in Figure 5.3 represented by blue crosses), in which the reactant structures lay above the actual reactants by more than 200 and 250 kJ mol^{-1}, respectively. This is because the singlet UM06-2X calculation starts from a non-symmetry broken initial guess wave function, hence yielding the same wave function as a restricted (i.e., closed-shell) M06-2X calculation. This calculated closed-shell wave function can be understood as an electronically excited state, in which the electronic structure has a signifcant contribution of an ionic state: a protonated CO molecule (HCO^+)

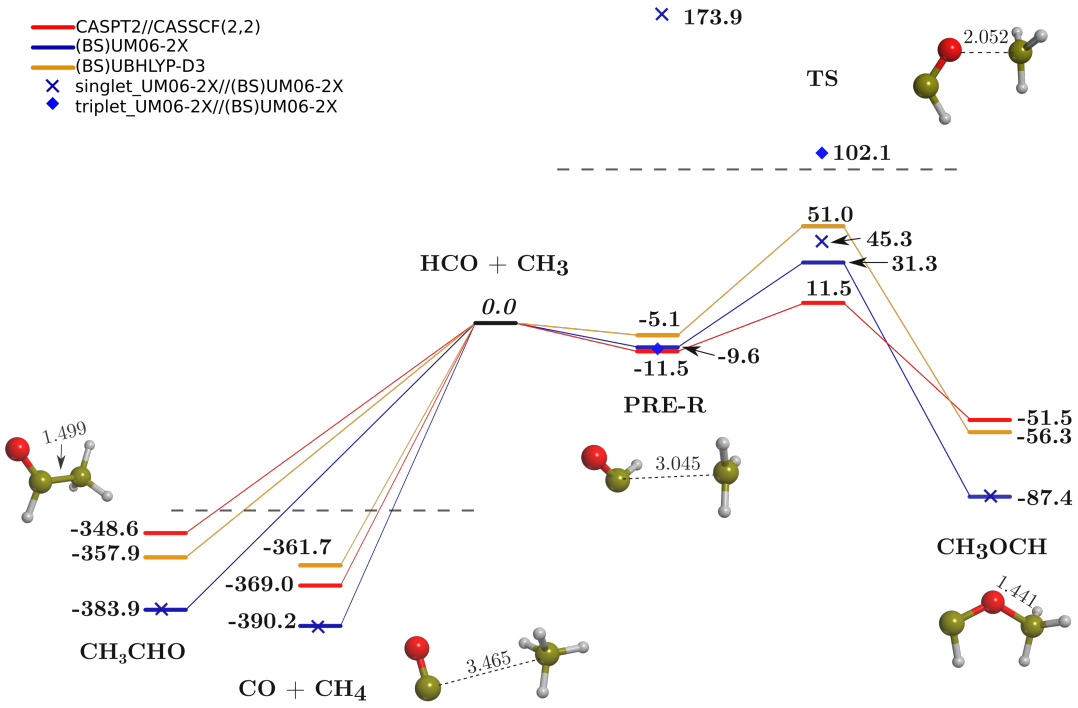

Figure 5.1: *PESs at different DFT levels and at CASPT2 for the reactivity between CH_3 and HCO to form CH_3OCH (right side panel) or CO + CH_4 and CH_3CHO (left side panel). The energy reference (0.0) is the HCO + CH_3 asymptote. Dashed horizontal lines indicate broken vertical axis. PRE-R refers to the prereactant complexes and TS to the transition states. Single point energies at singlet and triplet UM06-2X levels on the (BS)UM06-2X optimised geometries are also shown. The presented structures correspond to the (BS)UM06-2X optimized geometries except for PRE-R, wich is the triplet UM06-2X optimized geometry. Energy units are in kJ mol^{-1} and distances in Å. We have also checked the triplet state of the CH_3OCH product resulting 80 kJ mol^{-1} higher in energy than the singlet state and an energy barrier for its formation about 55 kJ mol^{-1} higher than the singlet case, (UM06-2X theory level).*

and a negatively charged CH_3 species (CH_3^-). This ionic state is an ideal situation to trigger a Grotthus-like mechanism, in which the "extra" proton of HCO^+ is transferred through the assisting water molecule to the "proton-defective" CH_3^-. These results confirm again the need to use the BS-DFT approach to properly describe biradical systems.

5.5 Conclusions

This work is a revision note of a previous work by some of us J. Enrique-Romero et al., 2016, in which the reactivity of the same system, i.e., CH_3 + HCO, has been studied using DFT methods adopting an unrestricted broken-symmetry approach (i.e., (BS)UM06-2X and (BS)UBHLYP-D3) as well as post-HF multi-configurational and multi-reference methods (i.e., CASSCF(2,2) and CASPT2). In the original work, the DFT broken-symmetry formalism was not adopted, hence seriously affecting the description of the electronic structure of the CH_3/HCO biradical system. The main conclusions of the present work are summarized as follows:

- When the unrestricted DFT formalism is used without adopting the broken-symmetry approach to describe the electronic structure of biradical systems, the initial guess wave function may collapse into a restricted closed-shell solution. If this occurs, the reactivity between two radicals is likely to be wrongly described. In the particular case of the CH_3 + HCO reactivity on water ice, calculations indicate that the water assisted H transfer process is spontaneous.
- Unrestricted broken-symmetry DFT calculations for biradical systems show qualitatively similar results as those obtained at post-HF multi-configurational and multi-reference levels, indicating the suitability of this DFT approach to describe the reactivity of biradical systems.

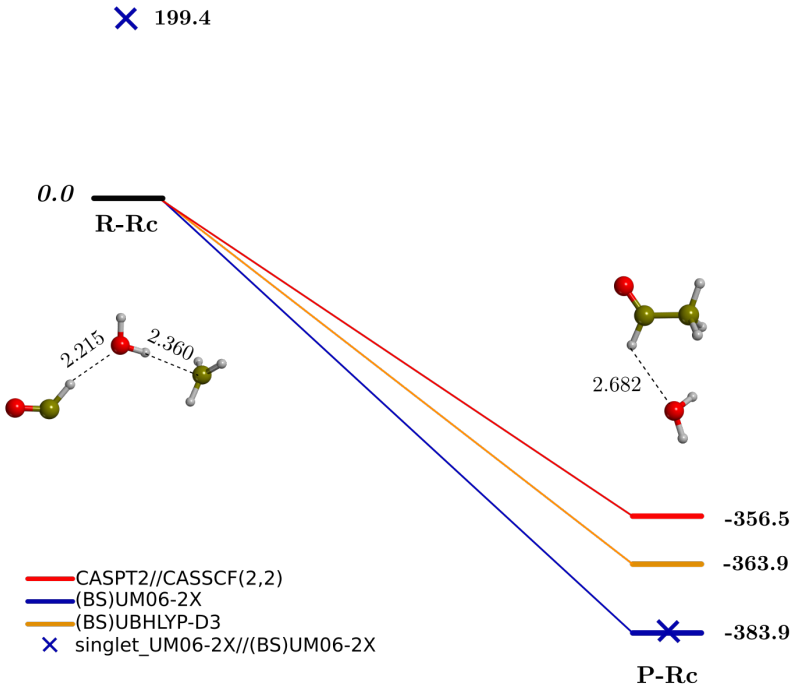

Figure 5.2: *PESs at different DFT levels and at CASPT2 for the Rc reaction between CH_3 and HCO in the presence of one water molecule. The 0th energy reference correspond to the prereactant complex (R-Rc). Single point energies at the singlet UM06-2X UM06-2X level on the (BS)UM06-2X optimised geometries are also shown. The structures presented in this figure are those corresponding to the (BS)UM06-2X optimised geometries. Energy units are in kJ mol^{-1} and distances in Å.*

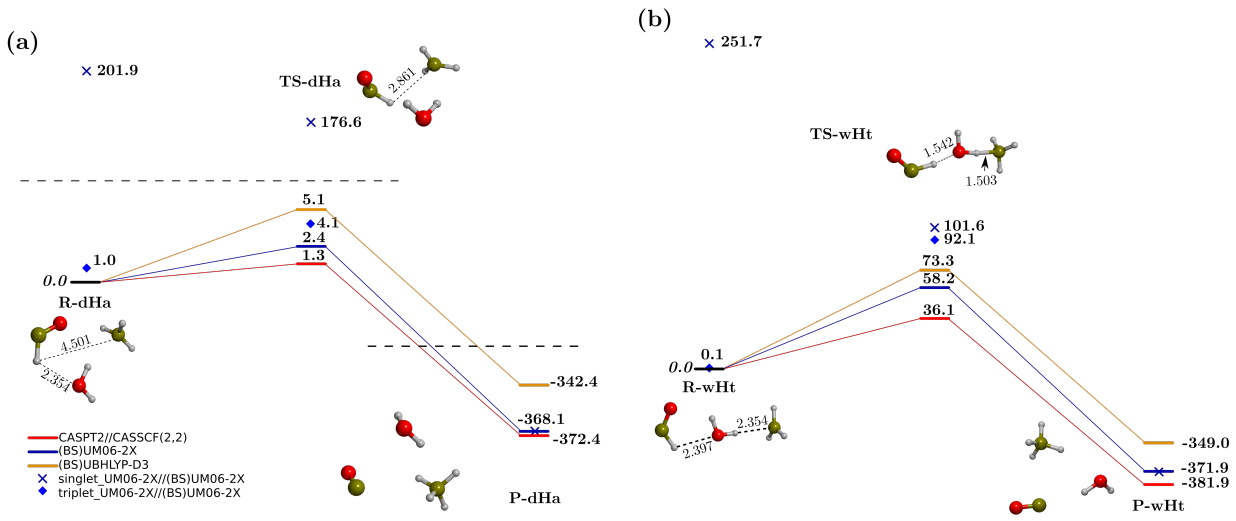

Figure 5.3: *PESs at different DFT levels and at CASPT2 for the reactions of dHa (a) and wHt (b) between CH_3 and HCO in the presence of one water molecule. The 0th energy references are the prereactant complexes: R-dHA (a) and R-wHt (b). Single point energies at the singlet UM06-2X and triplet UM06-2X levels on the (BS)UM06-2X optimised geometries are also shown. Dashed horizontal lines indicate broken vertical axis. The presented structures correspond to the (BS)UM06-2X optimised geometries. Energy units are in kJ mol^{-1} and distances in Å.*

- In the gas phase, both CH_3CHO and CO + CH_4 formations are found to be barrierless. In contrast, formation of the carbene CH_3OCH species has a noticeable barrier.
- In the presence of one water molecule, the water assisted hydrogen transfer reaction is not spontaneous but, in contrast, it has a high energy (58 and 73 kJ mol^{-1} at the (BS)M06-2X and (BS)BHLYP-D3 levels). Accordingly, its occurrence is unlikely under the interstellar conditions. In contrast, the radical-radical coupling is barrierless and the direct hydrogen abstraction presents a very small energy barrier ($\sim$5 kJ mol^{-1} at the most). Similar results have been obtained using larger cluster models mimicking the surface of interstellar water ice Joan Enrique-Romero et al., 2019 (see the following Chapter).

Finally, it is worth mentioning that, despite the limited description of the biradical system in J. Enrique-Romero et al., 2016, the physical insights provided by that work remain still valid, since it is shown that the biradical reactivity does not necessarily result in the radical-radical coupling product (i.e., the iCOM). Indeed, it is found here that the direct hydrogen abstraction can actually be a competitive channel, giving the same product as that for the water assisted hydrogen transfer. This finding is in agreement with recent theoretical works dealing with the reactivity of biradical systems on interstellar ice surfaces (Joan Enrique-Romero et al., 2019; Lamberts et al., 2019; Rimola et al., 2018).

Chapter 6

Reactivity of HCO with CH_3 and NH_2 on Water Ice Suraces. A Comprehensive Accurate Quantum Chemical Study

---

The research presented in this Chapter has resulted in a scientific article:
Enrique-Romero, J., Rimola, A., Ceccarelli, C., Ugliengo, P., Balucani, N., and Skouteris, D.
Published in ACS Earth and Space Chemistry, 2019.
DOI: 10.1021/acsearthspacechem.9b00156

Outline

Interstellar complex organic molecules (iCOMs) can be loosely defined as chemical compounds with at least six atoms in which at least one is carbon. The observations of iCOMs in star-forming regions have shown that they contain an important fraction of carbon in a molecular form, which can be used to synthesize more complex, even biotic molecules. Hence, iCOMs are major actors in the increasing molecular complexity in space and they might have played a role in the origin of terrestrial life. Understanding how iCOMs are formed is relevant for predicting the ultimate organic chemistry reached in the interstellar medium. One possibility is that they are synthesized on the interstellar grain icy surfaces, via recombination of previously formed radicals. The present work focuses on the reactivity of HCO with CH_3/NH_2 on the grain icy surfaces, investigated by means of quantum chemical simulations. The goal is to carry out a systematic study using different computational approaches and models for the icy surfaces. Specifically, DFT computations have been bench-marked with CASPT2 and CCSD(T) methods, and the ice mantles have been mimicked with cluster models of 1, 2, 18 and 33 H_2O molecules, in which different reaction sites have been considered. Our results indicate that the HCO + CH_3/NH_2 reactions, if they actually occur, have two major competitive channels: the formation of iCOMs CH_3CHO/NH_2CHO, or the formation of CO + CH_4/NH_3. These two channels are either barrierless or present relatively low ($\leq$ 10 kJ mol^{-1} equal to about 1200 K) energy barriers. Finally, we briefly discuss the astrophysical implications of these findings.

6.1 Introduction

It has been long demonstrated that star forming regions are places with a rich organic chemistry (e.g. Belloche et al., 2017; Paola Caselli et al., 2012; Cazaux et al., 2003; Herbst et al., 2009a; McGuire et al., 2018; Rubin et al., 1971).

Although there are no proofs that organic molecules formed in the interstellar medium (ISM) did play a role in the emergence of terrestrial life, there is mounting evidence that they were inherited by the small objects of the Solar System: for example, carbonaceous chondrites and comets contain a wide variety of organic molecules, some of them probably being a direct heritage of the ISM based on their relative abundances and ratio of deuterated versus hydrogenated species (e.g. Bianchi et al., 2018; Bockelée-Morvan, 2011; Paola Caselli et al., 2012; Ceccarelli et al., 2014).

Therefore, the processes responsible for the formation and destruction of iCOMs are key in order to understand what is the ultimate organic chemistry complexity in the ISM. The reason behind of this lies on the intrinsic limitations in large molecule detection (excluding linear chains) by radioastronomy as a consequence of the larger number of rotational transitions, with respect to smaller species, leading to weaker line intensities.

As a result, the numerous and weak lines of large iCOMs produce a “grass” of lines in the spectra, which makes the identification of a large molecule eventually impossible. Therefore, there is a limit to the largest detectable iCOM, and this has a direct consequence: we need to rely on our knowledge of the processes to predict which large molecules are synthesized in the ISM.

It has been already introduced (§ 4.1 and § 1.4) that the processes by which iCOMs are formed in the ISM are still an open question. Nevertheless, it seems that the “exclusive grain-surface" paradigm, in which iCOMs are formed on interstellar ice surfaces as a consequence of radical–radical coupling reactions during the so-called warm-up phase (at T$\sim$30 K) R. T. Garrod et al., 2006 (see paradigm 2 in Figure 1.7), still dominates in astrochemical models (e.g. Acharyya et al., 2015; Drozdovskaya et al., 2016; Robin T. Garrod et al., 2008; M. Ruaud et al., 2015; Vasyunin et al., 2017), despite of its several downfalls, like its inability to explain the presence of iCOMs in cold ($\sim$10 K) regions of the ISM (see §4.1 and 1.4). Finally, models based on the “exclusive grain-surface" paradigm are unable to reproduce the observed abundance of several iCOMs (e.g. Coutens et al., 2016; Ligterink et al., 2018; Müller et al., 2016).

However, there are still many uncertainties that make the last paradigm not fully validated, like the assumption that radicals react in a barrierless fashion on interstellar ice surfaces, and that radical–radical reactions always lead to iCOMs.

In this work, we focus on two reactions occurring on amorphous solid water (ASW) surfaces: HCO + CH_3 and HCO + NH_2. In the “exclusive grain-surface" paradigm mentioned above, it is expected that the radical coupling produces two iCOMs: CH_3CHO (acetaldehyde) and NH_2CHO (formamide).

Previous works by some of us J. Enrique-Romero et al., 2016; Rimola et al., 2018 showed that other reactive channels can compete with the iCOM formation. Specifically, the two reactions can lead to the

formation of CO + CH_4 and CO + NH_3, respectively, in which the H atom of HCO is transferred to the radical partner. Similar processes were identified computationally when HCO reacts with CH_3 on surfaces of CO-pure ices Lamberts et al., 2019.

The goal of the present work is to carry out a systematic study of two reactions, i.e., HCO + CH_3 and HCO + NH_2, considered here as prototype reactions for the formation of iCOMs, using different approximations for the calculations and models of ASW with the aim to: (1) understand how the different methods and models affect the results, (2) individuate the most convenient methods and models to use in future calculations of other similar radical-radical systems, and (3) identify the products of the reactions under different conditions. To this end, the present work focuses on the following three points:

1. *Methodology benchmark:* (i) The energy barriers for reactions between the two couples of radicals in the presence of 1 and 2 water molecules are computed with two DFT methods (B3LYP and BHLYP) and compared to the values calculated with the multi-reference CASPT2 method; (ii) The interaction of the three radicals (CH_3, HCO and NH_2) with 1 and 2 water molecules is studied and bench-marked taking as reference the binding energies computed at the CCSD(T) level.

2. *Radical-surface binding enthalpies:* We study the binding of the three radicals (CH_3, HCO and NH_2) to an ASW cluster model of 18 water molecules and to a larger cluster of 33 water molecules sporting two different morphological sites, a cavity and its side.

3. *Radical-radical reactivity:* The reactivity of the two radical couples is studied (i) on the 18 water molecules cluster, and (ii) on the two different morphological sites of the 33 water molecules cluster.

It is worth mentioning that the systems to deal with here sport an additional complexity from an electronic structure point of view. That is, two radicals interacting with water ice, in which the unpaired electrons have opposite signs, constitute a singlet biradical system.

As it was seen in Chapter 5, describing this electronic situation with quantum chemistry calculations is delicate. On the one hand, the preferred methodologies in order to study such systems, like *ab initio* multi-reference methods, are prohibitively too expensive and, accordingly, unpractical for large systems. On the other hand, however, one can achieve a good compromise between accuracy and computational cost by using the DFT broken-symmetry approach Abe, 2013, which not only requires an open shell electronic structure, but also a good initial biradical state, i.e. one electron on each radical with opposite spin.

This Chapter is organized as follows. First the adopted methods are presented (§ 6.2), then the results are provided following the 3 objectives described above, § 6.3, and finally a discussion, including the astrophysical implications, and the conclusions are presented in § 6.4 and 6.5, respectively.

6.2 Methods

All DFT and CCSD(T) calculations were performed using the GAUSSIAN09 Frisch et al., 2009 software package, while the multi-reference calculations were carried out with the OpenMolcas 18.09 Aquilante, Francesco et al., 2010, 2016; Fernandez Galván et al., 2019; Karlström et al., 2003 program.

Stationary points of the potential energy surfaces (PESs) were fully optimized using two hybrid density functional theory (DFT) methods: B3LYP and BHLYP. These methods have the same Lee, Yang, Parr correlation functional (LYP)C. Lee et al., but differ on the exchange functional: the Becke's three parameter (B3), which includes a 20% of exact exchange in its definition, Becke, 1993b and the Becke's half-and-half (BH), which mixes the pure DFT and the exact exchange energy in a 1:1 ratio Becke, 1993a. For B3LYP calculations, the Grimme's D3 dispersion term Grimme et al., 2010 was accounted for during the geometry optimizations. In contrast, for BHLYP, both the D2 Grimme, 2006 and D3 dispersion terms were included in an *a posteriori* way onto the pure BHLYP optimized geometries (see § 2.3 for a theoretical background on DFT).

A calibration study was first carried out for (i) the NH_2 + HCO and CH_3 + HCO reactivities in the presence of 1 and 2 water molecules (W1 and W2, respectively) and (ii) the interaction of each radical with W1 and W2. For this calibration study, the DFT methods were combined with the Pople's 6-311++G(2df,2pd) basis set. As reference for the reactivity results we used single point energy calculations at the multi-reference

CASPT2 level combined with the Dunnning's cc-pVTZ basis using as initial guess the orbitals generated at CASSCF(2,2) level. In the same way, single point energy calculations at the CCSD(T)/aug-cc-pVTZ level were also carried out in order to compare them to CASPT2 values. Regarding the interaction energies, the same DFT methods were compared to CCSD(T)/aug-cc-pVTZ level. All the single point energy calculations for this benchmark study were carried out on the B3LYP-D3 optimized geometries.

Radical-radical reactivity was also studied more realistically on two amorphous solid water (ASWs) ices modelled by molecular clusters consisting of 18 (W18) and 33 (W33) water molecules, which were also used in previous works J. Enrique-Romero et al., 2016; Rimola et al., 2014, 2018.

The optimized structures are shown in Figure 4.2. Interestingly, W33 exhibits a hemispherical cavity and, accordingly, we studied the surface processes considering both this cavity and an extended side of the ice surface (see Figure 4.2(b)), as they exhibit different surface properties. In order to make the calculations computationally affordable, for these cases the DFT methods were combined with the Pople's 6-31+G(d,p) basis set.

All stationary points were characterized by the analytical calculation of the harmonic frequencies as minima (reactants, products and intermediates) and saddle points (transition states). Intrinsic reaction coordinate (IRC) calculations at the same level of theory were carried out when needed to ensure that the transition states connect with the corresponding minima. Thermochemical corrections to the potential energy values were carried out using the standard rigid rotor/harmonic oscillator formulas McQuarrie, 1976 to compute the zero point energy (ZPE) corrections.

Adsorption energies of HCO, CH_3 and NH_2 on W18 and W33 were refined with single point energy calculations combining the DFT methods with the extended 6-311++G(2df,2pd) basis set and corrected for the basis set superposition error (BSSE). Considering *A* as the adsorbate and *B* as the surface cluster model, the BSSE-non-corrected adsorption energy was computed as $\Delta E_{ads} = E^{AB}_{AB}(AB) - E^{A}_{A}(A) - E^{B}_{B}(B)$, where superscripts denote the basis set used and the subscripts the geometry at which the calculation was done. BSSE-corrected energies were calculated as:

$$\Delta E^{CP}_{ads}(AB) = \Delta E_{ads} + BSSE(A) + BSSE(B) + \delta^A(A) + \delta^B(B) \tag{6.1}$$

where the BSSE values were calculated following the Boys and Bernardi counterpoise correction method ($BSSE(A) = E^{AB}_{AB}(A) - E^{A}_{AB}(A)$, Boys et al., 1970), and where the deformation of each monomer was also accounted for ($\delta^A(A) = E^{A}_{AB}(A) - E^{A}_{A}(A)$)[1].

Inclusion of ZPE corrections allowed us to obtain adsorption enthalpies at 0 K:

$$\Delta H_{ads}(AB) = \Delta E^{CP}_{ads}(AB) + \Delta ZPE \tag{6.2}$$

In the sign convention followed in this work, the adsorption energy is the negative of the binding energy, i.e. $\Delta E_{ads} = -\Delta E_{bind}$.

The systems containing two radical species were first optimized in the triplet electronic state, and then subsequently in the singlet state to describe the biradical system. Structures with doublet and triplet electronic states were simulated with open-shell calculations based on the unrestricted formalism. Singlet biradicals systems were calculated adopting the unrestricted broken symmetry (BS) approach, in which the most stable initial wave function was found using the *stable=opt* keyword in Gaussian09.

Following the International System Units, all energy units are given in kJ mol^{-1}, whose conversion factor to K is 1 kJ mol^{-1} = 120.274 K.

6.3 Results

In this section, results of the calibration study devoted to the reactivity and interaction of HCO with CH_3 and NH_2 in the presence of 1 and 2 water molecules are first presented. Then, results on adsorption properties and the radical-radical reactions on W18 and W33 are reported.

[1] After the publication of this article we realized that 6.1 contains an error: the deformation energies are already included in ΔE_{ads}, and therefore adding them again is not correct. The correct and updated values are 11.7, 28.5 and 42.8 kJ mol^{-1} for CH_3, HCO and NH_2, respectively. A further revision of these values are available in Chapter 7.

Table 6.1: *ZPE- and BSSE-non-corrected binding energies computed with different methods for the interaction of CH_3, HCO and NH_2 with 1 and 2 water molecules (W1 and W2) at the B3LYP-D3 and BHLYP levels. None, D2 (accounting for 2-body interactions) and D3 (accounting for 2- and 3-body interactions) dispersion corrections were considered for the latter. BHLYP-based and CCSD(T) values were calculated as single points on the B3LYP-D3 optimised geometries. Energy units are in kJ mol^{-1}.*

	B3LYP-D3	BHLYP	BHLYP-D2	BHLYP-D3	CCSD(T)
CH_3/W1	9.5	5.2	11.3	8.1	6.9
HCO/W1 (H)	12.9	10.9	13.6	13.1	12.0
HCO/W1 (O)	11.7	9.7	12.5	12.1	11.5
NH_2/W1 (H)	14.1	12.0	14.9	14.4	12.8
NH_2/W1 (N)	23.4	21.5	24.3	23.6	21.6
CH_3/W2	8.6	3.1	11.3	8.0	7.1
HCO/W2	14.8	9.2	16.1	15.1	13.2
NH_2/W2	41.6	36.6	44.5	41.9	38.3

Methodology benchmark

This section aims to be a calibration study to check the reliability of the B3LYP and BHLYP methods for (i) the radical-water interactions and (ii) the activation energy of the reactions of CH_3/HCO and NH_2/HCO, in both cases with one and two water molecules (W1 and W2 hereafter) as minimal models representing an ice surface. The references used for the study of the binding and activation energies are CCSD(T) and CASPT2, respectively. In all cases, single point energies were computed onto the B3LYP-D3 optimised geometries. The relative errors can be found in appendix B[2].

Table 6.1 contains the binding energies for the three radicals involved in this study (namely CH_3, NH_2 and HCO) interacting with W1 and W2. The systems where a radical interacts with W1 have been based on those presented by Valentine Wakelam et al. (2017), where the initial structures were built in a chemical-wise manner following the ability of each component of the radical to establish a hydrogen bond to a single water molecule, e.g. in the cases where NH_2 and HCO interact with W1 two possibilities were considered: the radicals acting as either H-bond donors (through one of their H atoms), or acting as H-bond acceptors (through the N and O atoms, respectively). The initial geometries of the systems with W2 were built similarly, with the radicals having the maximum number of hydrogen bonds to the two water molecules.

It can be seen that CH_3 is the species having the weakest interaction with the water molecules (6.9-7.1 kJ mol^{-1} at the CCSD(T) level). HCO and NH_2, instead, can form intermediate and strong H-bonds respectively, and, accordingly, they show higher binding energies (11.5-13.2 kJ mol^{-1} for the former and 12.8-38.3 kJ mol^{-1} for the latter at the CCSD(T) level). This trend is in agreement with that found by Valentine Wakelam et al. (2017), in which the binding energies of these species with W1 were 13, 19-23 and 23-38 kJ mol^{-1} for CH_3, HCO and NH_2 respectively, computed at the M062X/aug-cc-PVTZ level. Note, however, that the quoted values are not the final values used in the model by Valentine Wakelam et al. (2017), as they also use binding energies from other sources in the literature in order to fit experimental data.
Regarding the performance of the methods, the best ones are B3LYP-D3 and BHLYP-D3, with a relative error of 2-39% and 5-18% respectively. The pure BHLYP method systematically underestimates the binding energies, providing strong deviations for CH_3 and HCO, specially on W2. BHLYP-D2 dramatically overestimates the binding energies of CH_3-containing systems (relative errors of $\sim$ 60%), indicating that the D2 term probably accounts for dispersion in excess for this kind of weakly bound complexes.

Table 6.2 shows the calculated energy barriers of CH_3/HCO and NH_2/HCO on W1 and W2. Three different possible reactions have been identified: i) radical-radical coupling, leading to formation of the iCOMs (i.e. CH_3CHO and NH_2CHO); ii) direct hydrogen abstraction, in which the H atom of HCO is transferred to the other radicals, forming CO + CH_4 and CO + NH_3, respectively; and iii) water assisted hydrogen transfer, the same as ii) but the H transfer is assisted by the water molecules adopting a H relay mechanism. These reactions will be referred to as *Rc*, *dHa* and *wHt*, respectively, along the work.

[2] Additionally, in the online supporting information (SI) of the publication related to this Chapter, the reader can find all the XYZ data files (here).

Table 6.2: *ZPE-non-corrected energy barriers ($\Delta E^{\ddagger}$), computed with different methods, for radical-radical coupling (Rc), direct hydrogen abstraction (dHa) and water assisted hydrogen transfer (wHt) reactions of NH_2 + HCO and CH_3 + HCO in the presence of 1 and 2 water molecules computed at the B3LYP-D3 and BHLYP-based levels. For the latter two dispersion corrections have been considered: D2 (which considers all 2-body interactions) and D3 (which considers 2- and 3-body interactions). BHLYP-based, CCSD(T) and CASPT2 values were calculated as single point energy calculations on the B3LYP-D3 optimised geometries. Energy units are in kJ mol^{-1}. NB stands for "No Barrier" and means that the process is found to be barrierless.*

System	Process	*B3LYP -D3*	*BHLYP*	*BHLYP -D2*	*BHLYP -D3*	*CCSD(T)*	*CASPT2*
NH_2/HCO ··· W1	Rc	NB	NB	NB	NB	NB	NB
	dHa	3.5	6.1	4.1	5.1	5.3	4.2
	wHt	10.9	48.6	46.2	48.8	43.8	48.3
CH_3/HCO ··· W1	Rc	NB	NB	NB	NB	NB	NB
	dHa	3.1	6.9	3.3	5.1	5.0	1.5
	wHt	23.5	59.4	55.5	58.6	60.0	52.2
NH_2/HCO ··· W2	Rc	6.5	8.5	6.1	6.8	6.3	6.1
	dHa	NB	NB	NB	NB	NB	NB
	wHt	15.5	65.8	62.5	65.1	52.3	52.9
CH_3/HCO ··· W2	Rc	NB	NB	NB	NB	NB	NB
	dHa	1.6	4.0	1.5	1.6	1.6	1.0
	wHt	30.7	65.8	62.5	65.1	64.0	52.0

According to these values, two general trends are observed: (i) Rc and dHa are either barrierless (meaning that the initial biradical structures were not stable) or have relatively low energy barriers (1.0-6.1 kJ mol^{-1} for CASPT2), and (ii) wHt are the processes presenting the highest energy barriers (around 50 kJ mol^{-1} for CASPT2).

For those Rc and dHa reactions having an energy barrier, one can see that the worst performance is given by the pure BHLYP method compared to CASPT2. The rest of the methods perform similarly, BHLYP-D2 and B3LYP-D3 being the best ones, which are followed by BHLYP-D3. Regarding the wHt reactions, B3LYP-D3 dramatically underestimates the energy barriers (errors of $\sim$ 40-80%), while BHLYP-based methods perform reasonably well with errors below $\sim$ 25%. CCSD(T) performs similarly to the BHLYP-based methods, presenting moderate energy barrier deviations compared to the CASPT2 values.

In summary, BHLYP-D3 provides the most reliable binding energies, B3LYP-D3, BHLYP-D2 and BHLYP-D3 show good performances for energy barriers related to Rc and dHa processes, while BHLYP-D2 and BHLYP-D3 perform good for wHt energy barriers. Accordingly, and with the aim to be consistent, in the following sections (devoted to the binding and potential energy profiles on the W18 and W33 cluster models) we provide the results at the BHLYP-D3 level of theory, while results based on BHLYP-D2 (on both W18 and W33) and on B3LYP-D3 (on W18) are reported in the appendix B.

Radical-surface binding enthalpies

Here we present the ZPE- and BSSE-corrected binding energies of the radicals on the *W18* and *W33* cluster models and their comparison with recent literature. These values are important because binding energies are essential parameters in astrochemical modelling studies.

As it was stated in the previous section, the binding of the radicals on the water ice surfaces are mainly dictated by hydrogen bonds (H-bonds) and dispersion interactions. The clusters exhibit several potential binding sites (Figure 4.2) and, accordingly, different radical/surface complexes can exist. Here, for the sake of simplicity, we choose those complexes in which the inter-molecular interactions between the two partners are maximized. The underlying assumption is that radicals on the water ice surfaces have had enough time to thermalize and establish the largest number of inter-molecular interactions with the surface, as very probably is the case in the interstellar conditions. Figure 6.1 shows the BHLYP-D3 fully optimised complexes on W18 and on the two differentiated W33 sites: its side (W33-side) and its cavity (W33-cav). The corresponding BSSE-corrected binding enthalpies (at 0 K) are also shown. The same information at BHLYP-D2 and B3LYP-D3 is available in appendix B.

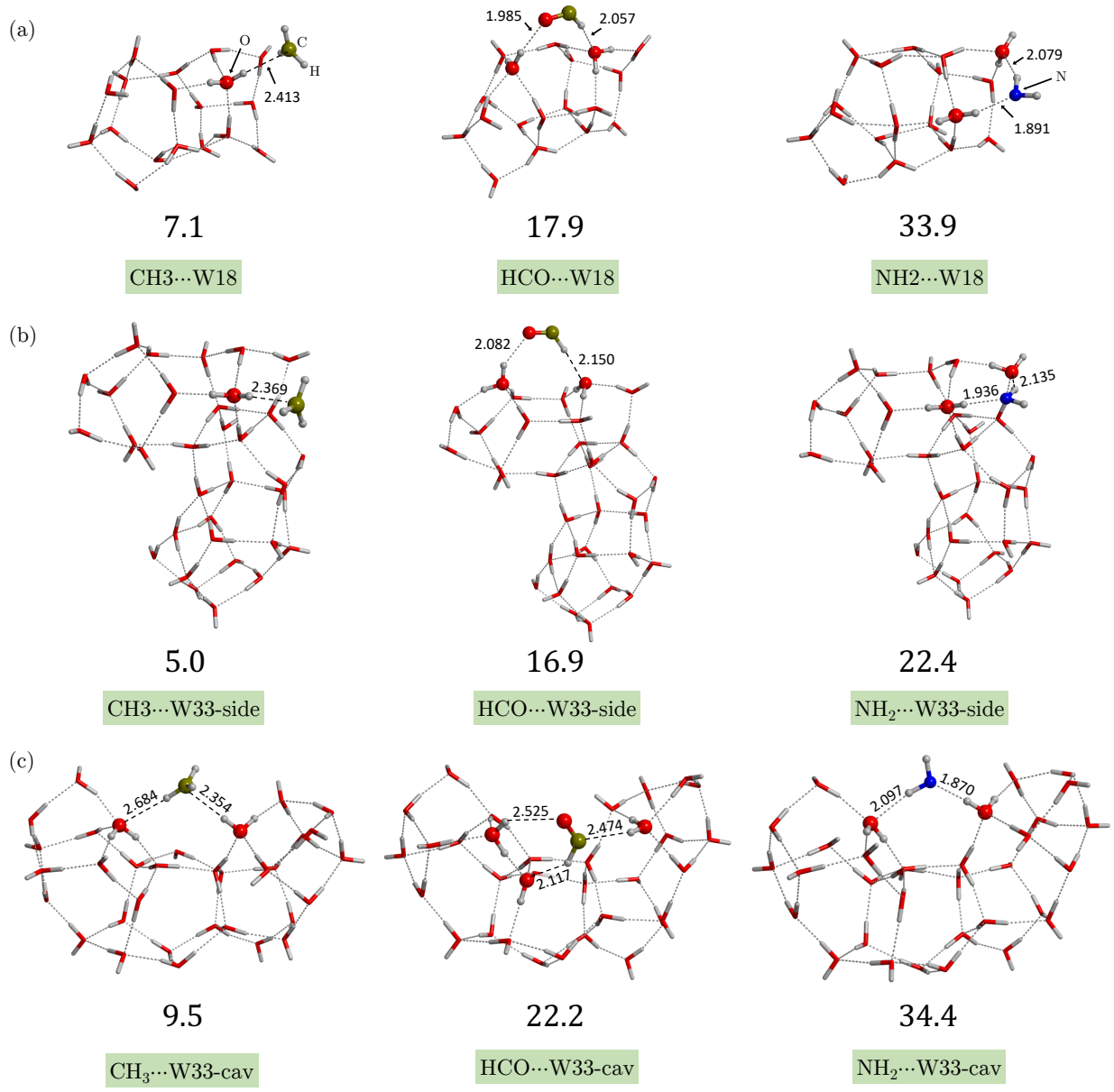

Figure 6.1: *Fully optimized geometries for the binding of CH_3, HCO and NH_2 on (a) W18, (b) W33-side and (c) W33-cav at BHLYP-D3/6-31+G(d,p). Bond distances are in Å. Binding enthalpies (at 0 K) values (in kJ mol^{-1}) are corrected for BSSE and are shown below their respective structures.*

The binding enthalpy trend is $NH_2 > HCO > CH_3$, irrespective of the cluster model and surface morphology, in agreement with the results of the previous section. Specifically, the binding enthalpy ranges are: 22.4-34.4, 16.9–22.2 and 5.0–9.5 kJ mol^{-1} for NH_2, HCO and CH_3, respectively. These values compare well with those previously computed by J. Enrique-Romero et al. (2016) for HCO and CH_3 on the W18 cluster (19 and 6 kJ mol^{-1}) and by Rimola et al. (2018) for NH_2 and HCO on the W33-cav cluster (33.5 and 17.5 kJ mol^{-1}). In the model presented in Valentine Wakelam et al. (2017), the authors reported binding energies of 27, 20 and 13 kJ mol^{-1} for NH_2, HCO and CH_3, respectively, in rough agreement with our results. Sameera et al. (2017) have recently computed the binding energies of HCO and CH_3 adsorbed on hexagonal ice slabs[3]. They found HCO binding energies ranging between 12–40 kJ mol^{-1}, and 11–25 kJ mol^{-1} for HCO and CH_3, respectively. These values are similar or moderately larger than the values found in our W33-cav cluster.

Finally, it is worth mentioning that these complexes do not present hemi-covalent bonds, as it was the case for CN in Rimola et al. (2018). Attempts to identify this type of binding in the current systems have been made but the initial structures collapsed to the complexes presented here upon geometry optimization. Therefore, for these systems, the interaction of the radicals with the ice surfaces is essentially dictated by H-bonds and dispersion forces.

Radical-radical reactivity

In this section, the reactivity of HCO with CH_3 and NH_2 on W18, W33-side and W33-cav are investigated. Given that the chemical environment between W18 and W33-side is similar (note that the surface morphology of W33-side is very similar to that of W18 because W33 was built up by joining two W18 unitsRimola et al., 2018), the comparison of the results between these two models will allow us to assess the effects introduced by the ASW model size. On the other hand, comparison between the reactivity on W33-side and W33-cav will allow us to assess the effects due to different surface environments, namely the presence of a higher number of radical/surface interactions. Please note that the cavity sites are probably more representative of the interstellar conditions than the side sites, as the vast majority of radicals are trapped in the bulk of the ice.

Figures 6.2, 6.3 and 6.4 show the PESs of the reactivity of CH_3/HCO and NH_2/HCO calculated at BHLYP-D3 on top of W18, W33-side and W33-cav, respectively. Based on the results for the reactivity in the presence of W1 and W2 (see §3.1), the same three reaction paths, i.e., *Rc*, *dHa* and *wHt*, have been investigated. However, as the later processes are those exhibiting the highest activation enthalpies (as high as 100.6, 78.8, 92.5 and 79.1 kJ mol^{-1} for CH_3/HCO$\cdots$W18, CH_3/HCO$\cdots$W33-cav, NH_2/HCO$\cdots$W18 and NH_2/HCO$\cdots$W33-cav, respectively), for the sake of clarity and with the aim of focusing only on the reactions that might play a role in interstellar chemistry, all results related to wHt can be found in appendix B, this section only showing the Rc and dHa reactions calculated at BHLYP-D3. In the same way, the reader can also find in appendix B the results for all systems computed at BHLYP-D2 and, for W18, also at B3LYP-D3.

The initial structures of these systems were built according to the interaction patterns present in the single adsorbed radical complexes (see reactant structures of Figures 6.2-6.4). The Rc and dHa reactions, forming acetaldehyde or formamide and CO+CH_4 or CO+NH_3, respectively, both take place through a single step. That is, the bond formation between the two radicals for Rc, and the H transfer for dHa. The only exception is the dHa reaction of CH_3/HCO$\cdots$W18, which displays first a submerged activation energy step where HCO breaks its H-bonds with the surface to facilitate the H transfer (see dHa-TS1 of Figure 6.2(a)). By comparing the Rc and dHa reactions on these three cluster models, the general trend is that Rc activation enthalpies are lower than the dHa ones, between 0.5 - 4 kJ mol^{-1} lower. This was already observed in the presence of W1 and W2, where most of the Rc reactions are barrierless while the dHa present physical (although low) energy barriers. It should be noticed that the HCO/CH_3 reactions on W33-side (Figure 6.3a) are barrierless due to the ZPE correction, as opposed to the the W1 and W2 cases where the lack of barrier is because of the unstable singlet evolving directly towards products. Indeed, all the stationary points shown in Figure 6.3(a) have been identified as stable structures in the pure PESs (i.e., without ZPE corrections) but after

[3]these authors used either full DFT with a double-ζ basis set or the ONIOM approach combining DFT with force fields. They reported several values owing to the different adsorption modes of these two species adopting the two computation approaches. This allowed them to report the wide range of binding energies reported here.

Table 6.3: *Highest activation enthalpies (at 0 K) for Rc, dHa and wHt reactions on W18, W33-side and W33-cav at the BHLYP-D3 level. Note that NB stands for "No Barrier". Units are in kJ mol^{-1}.*

	W18			W33-side			W33-cav		
Sys	Rc	dHa	wHt	Rc	dHa	wHt	Rc	dHa	wHt
HCO + CH_3	2.6	5.2	100.6	NB	NB	-	6.8	10.2	78.8
HCO + NH_2	3.1	5.0	92.5	5.1	5.4	-	2.1	1.6	79.1

introduction of ZPE corrections, the transition state becomes lower in energy than the reactants, and hence the barrierless character.

Another interesting point is that results for W18 and W33-side present some differences, particularly for the HCO + CH_3 reactions: on W33-side, both Rc and dHa are barrierless while on W18 they present energy barriers. This is indicative of the fact that the size of the cluster for this radical-radical reactivity is important. Finally, no clear trends related to the effect of the ASW ice morphology can be obtained by comparing the W33-side results with the W33-cav. That is, for HCO+CH_3 reactions, activation enthalpies are higher on W33, while the opposite occurs for HCO+NH_2 ones.
In the following section, a comprehensive discussion of all these results is provided.

6.4 Discussion

Reaction channels and competition to iCOMs formation

Our computations show that if HCO + CH_3 and HCO + NH_2 react on top of an ASW ice, they have two sets of possible reaction products: i) formation of iCOMs (*Rc* process), where the two radical species meet and couple, and ii) the formation of the hydrogenated CH_4/NH_3 species, where the H atom of HCO migrates to CH_3/NH_2, which can happen either directly (*dHa* process) or through the ice water molecules adopting a H transfer relay mechanism (*wHt* process). The energetics associated with each process at the BHLYP-D3 level are summarised in Table 6.3.

The *Rc* and *dHa* reactions show, in all the studied systems, similar energetic features, i.e., they are either barrierless or exhibit relatively low energy barriers. The highest pair of energy barriers concerns the HCO + CH_3 reactions on W33-cav, i.e., 6.8 and 10.2 kJ mol^{-1} for *Rc* and *dHa*, respectively. As a general trend, *dHa* reactions have slightly higher activation energies than *Rc* (by as much as 3.4 kJ mol^{-1} for HCO/CH_3 and 1.9 kJ mol^{-1} for HCO/NH_2). In some cases, like HCO/CH_3 $\cdots$ W33-side, HCO/NH_2 $\cdots$ W33-side and HCO/NH_2 $\cdots$ W33-cav both Rc and dHa can be considered as competitive reactions given the small activation energy differences. In contrast, the lowest energy barriers for wHt HCO + CH_3 and HCO + NH_2 reactions are $\sim$ 80 kJ mol^{-1}, respectively. These values are larger than any *Rc* and *dHa* energy barrier and, accordingly, *wHt* reactions cannot be considered by any means as competitive channels. The explanation of these energetic differences is provided by the reaction mechanisms. Rc and dHa reactions take place, in most of the cases, in a concerted way, in which the radicals, in essence, have to partly break the interactions with the surface to proceed with the reaction. In contrast, most of the *wHt* reactions adopt a multi-step mechanism since the H transfer, which is assisted by different ice water molecules, involves different breaking/formation bonds. In these cases, high energy intermediates consisting of the coexistence of HCO and an OH radical are involved (see appendix B).

In previous works by some of us, (e.g. J. Enrique-Romero et al., 2016) the *wHt* reactions between CH_3 + HCO on the W18 cluster model were observed to spontaneously occur during geometry optimization, i.e. they were found to be barrierless. The difference with the computations presented in this work resides on the fact that, in the previous work J. Enrique-Romero et al., 2016, the initial wave function did not describe a singlet biradical system but a metastable singlet closed-shell-like one, and hence the spontaneous evolution to form CO+CH_4. In this work, as well as in Rimola et al. (2018), the initial wave function is actually describing a singlet biradical situation, which leads to a significant stabilization of the reactants and hence the presence of high energy barriers.

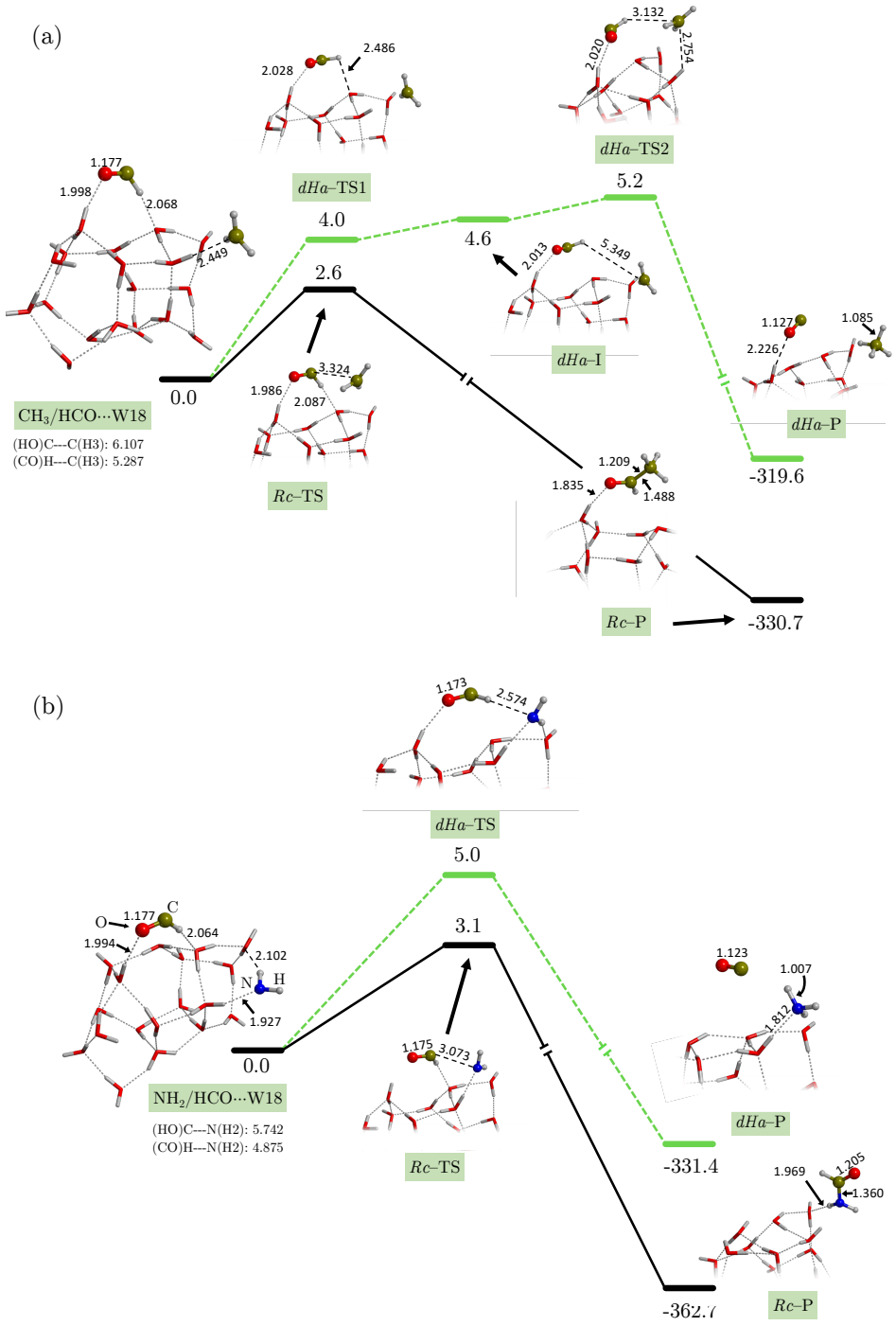

Figure 6.2: *ZPE-corrected Rc (solid black line) and dHa (dashed green lines) PESs for (a) HCO/CH_3 · · · W18 and (b) HCO/NH_2 · · · W18 calculated at the BHLYP-D3/6-31+G(d,p). Energy units are in kJ mol^{-1} and distances in Å. Notice that dHa-TS1 for (a) HCO/CH_3 · · · W18 lies below the intermediate dHa-I, due to the ZPE correction, setting effectively a single energy barrier: dHa-Ts2.*

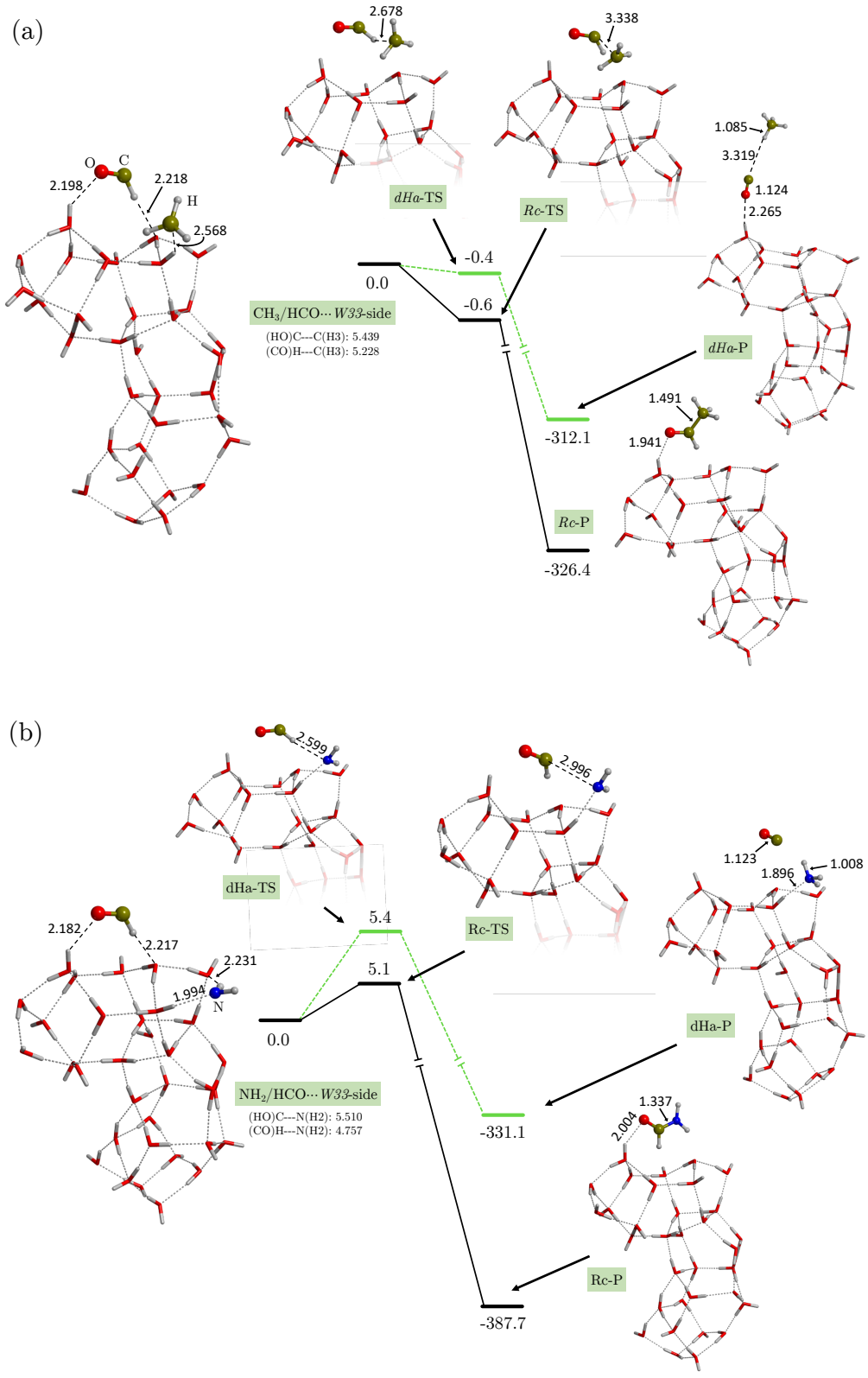

Figure 6.3: *ZPE-corrected Rc (solid black lines) and dHa (green dashed lines) PES for the HCO/CH_3 · · · W33-side (a) and HCO/NH_2 · · · W33-side (b) systems optimized at the BHLYP-D3 theory level. Energy units are in kJ mol^{-1} and distances in Å. Notice that both Rc and dHa TS for CH_3/HCO lie below the energy of reactants due to the ZPE correction.*

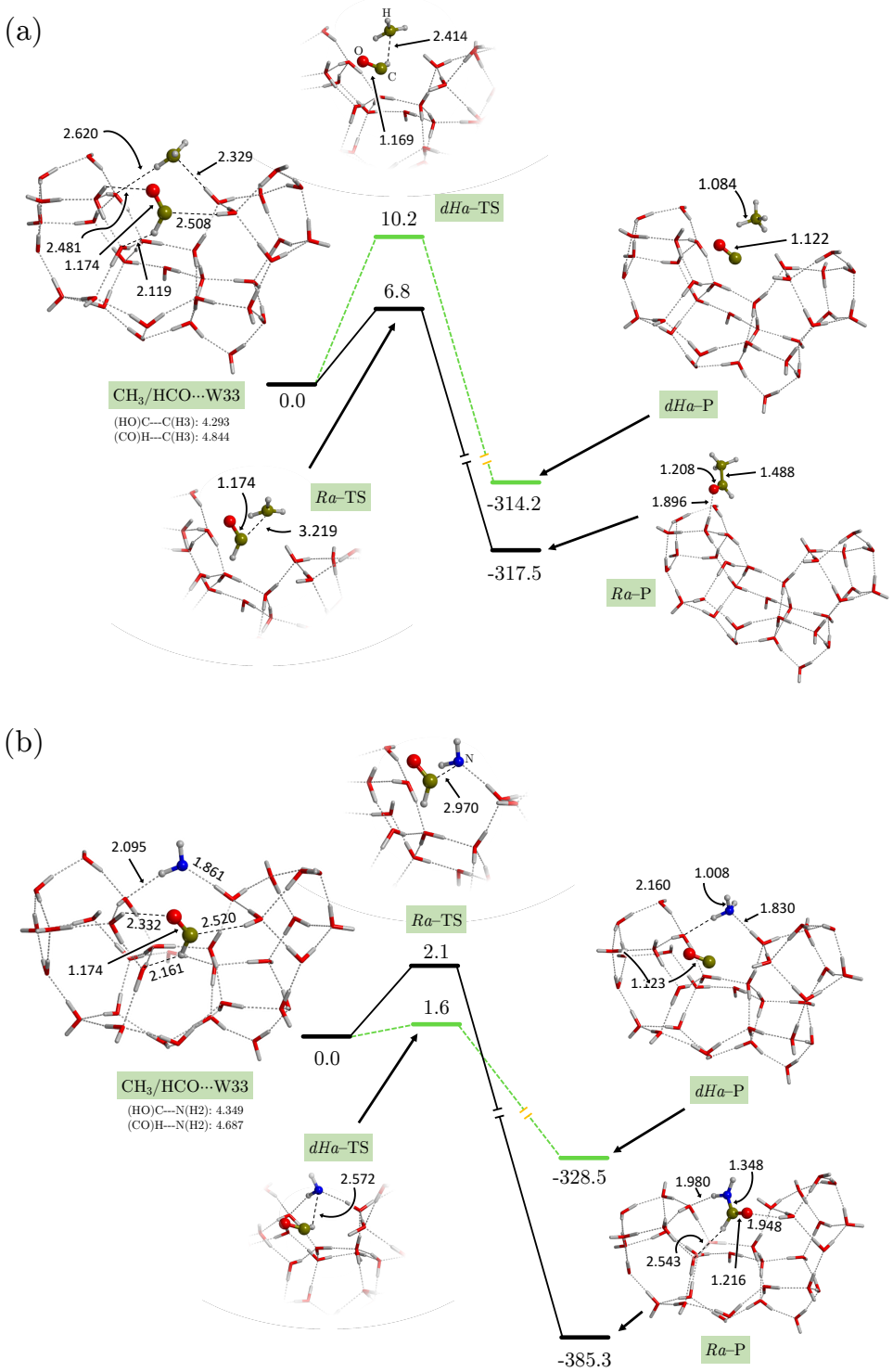

Figure 6.4: *ZPE-corrected Rc (solid black lines) and dHa (green dashed lines) PES for the $HCO/CH_3 \cdots W33$-cav (a) and $HCO/NH_2 \cdots W33$-cav (b) systems optimized at the BHLYP-D3 theory level. Energy units are in kJ mol^{-1} and distances in Å. BHLYP-D2 values can be found in appendix B.*

Finally, some words related to the chemical role played by the ice on these reactions are here provided. The *Rc* and *dHa* processes in the gas-phase (namely, in the absence of the icy grain) are, in both cases, barrierless. In contrast as explained above, in the presence of the surface, they exhibit, although low, energy barriers. Accordingly, from a rigorous chemical kinetics standpoint, the grains slow down the reactions. This leads us to think that a major role played by the grains is as that of third bodies, by quickly absorbing the nascent energy associated with the reactions, hence stabilising the products. This aspect is particularly appealing in the iCOMs formation processes via radical recombination since in the gas phase iCOMs can redissociate back to reactants if they are not stabilised through three-body reactions. As we will discuss below, the water morphology plays a role in the reaction energetics, although it does not change the essence of our conclusions.

Influence of the water ice surface model

Clear differences arise when comparing W33-side and W33-cav, as radicals on the latter exhibit more inter-molecular interactions with the surface. This can be seen for example in the binding energies (higher on W33-cav than on W33-side, see Figure 6.1). But also on the Rc and dHa energy barriers, for which a different behaviour is observed. Indeed, for HCO + CH_3 these reactions are barrierless on W33-side, while on W33-cav they present energy barriers of 7 (Rc) and 10 (dHa) kJ mol^{-1}. On the other hand, for HCO + NH_2 the opposite behaviour is observed: the energy barriers are higher on W33-side than on W33-cav (see Table 6.3). This might be indicating that the different polarity of the radicals, i.e., CH_3/apolar and NH_2/polar, is important when several polar-based inter-molecular interactions surround the reaction sites, like it is the case of W33-cav.

Finally, the size difference between the W18 and W33 models does not seem to provide a consistent trend, neither for binding energies nor for the PESs. This is probably due to the modest energetics of reactions of interest, which are the result of many intermingled effects, i.e. H-bond and dispersion interaction strength, small charge transfer and polarization. All these components are affected by the nature and size of the water adopted clusters without a definite and predictable structure-properties relationship.

Astrophysical implications

A major goal of this study is to understand whether iCOMs can be formed on the icy grain surfaces by the direct combination of radicals, a process assumed to be efficient in the majority of current astrochemical models (see Introduction). The present computations show that (i) there is a feasible channel leading to iCOM formation through radical-radical combination, (ii) this channel may possess a barrier, and (iii) there is at least a competitive reaction where radicals exchange a hydrogen atom, the outcome of which is somewhat a step backwards in chemical complexity as the products are simple hydrogenated species (CH_4 and NH_3 in the current work) and CO.

The present computational data does not allow us to definitively exclude the presence of a barrier in the radicals combination. Indeed, although common sense would indicate a lack of barrier, calculations show that the presence of the ice water molecules introduces an inter-molecular interaction that depends on where the radicals are placed and on the radical polarity. This interaction probably necessitates energy to be broken: it is not obvious that this energy is available in the ISM environments. In fact, according to Garrod et al. model R. T. Garrod et al., 2006, once the radicals are formed, they remain frozen on the ice and subsequently more ice layers build up on top. The radicals remain imprisoned in cavity structures inside the mantle and once the temperature reaches $\sim$ 30 K due to the evolution of the central protostar, they diffuse and react. Among the 3 reactions sites discussed in this article (W18, W33-side and W33-cav), the one best resembling this picture is given by W33-cav (see Figure 4.2) due to the larger number of inter-molecular interactions. The Rc and dHa energy barriers in the cavity have been shown to be larger for HCO + CH_3 than for HCO + NH_2, due probably to the different polarity of CH_3 and NH_2. If converted to Kelvin, the Rc and dHa barriers for HCO + CH_3 and HCO + NH_2 on W33-cav are about 800, 1200, 250 and 190 K, respectively (see Table 6.3). Thus, the efficiency of these reactions is not expected to be very high, especially for HCO + CH_3.

It has also to be noted that the starting points from where we study the reactivity in W33-cav (see reactant geometries from Figure 6.4) contain both radicals very close by and in the same cavity site (given

the computational cost of higher quality calculations we cannot simulate much larger clusters). However, in a more realistic situation each radical would be stored in different cavities and thus the actual barriers to overcome would not only involve breaking the radical/ice inter-molecular interactions, but also surmounting the ice surface diffusional barriers, decreasing in this way the efficiency of Rc and dHa reactions, even if they were ultimately barrierless.

We conclude this part mentioning that astronomical observations can also bring useful constraints to the formation routes of iCOMs showing alternative routes to the ones explored in this study. For example, high spatial resolution observations of formamide line emission towards the protostellar shock site L1157-B1 have demonstrated that the formation of formamide is dominated by the gas-phase reaction NH_2 + H_2CO Codella et al., 2017, a reaction theoretically studied by V. Barone et al., 2015; Skouteris et al., 2017. On the same line, observations of the deuterated forms of formamide (namely containing D rather than H atoms) also provide strong constraints on the formation route of this species in the hot corino of the solar-type protostar IRAS 16293-2422. The comparison of the measured NHDHCO/NH_2CHO and NH_2CDO/NH_2CHO abundance ratios Coutens et al., 2016 with those predicted by theoretical quantum chemical calculations Skouteris et al., 2017 strongly favors a gas-phase origin of formamide also in this source. Therefore, it is very likely that both grain-surface and gas-phase reactions contribute to the enrichment of iCOMs in the ISM, playing different roles in different environments.

6.5 Conclusions and perspectives

In this work, we have carried out an accurate study of the chemistry of two couples of radicals, HCO + CH_3 and HCO + NH_2, on icy surfaces. Our goal was to understand the possible reactions between the two radicals on water ice mantles, and how the results depend on the accuracy of the employed quantum chemical methods and on the adopted surface models. To this end, we used different quantum chemistry methods, in particular two hybrid DFT methods, B3LYP and BHLYP, plus the wave function based CCSD(T) and multi-reference-based CASPT2 ones. In addition, we adopted different cluster models simulating the water surfaces: we started with the simple cases of one and two water molecules to identify the basic processes and to test the methodology, and then using two different, large molecular cluster models for the ASW surfaces, of 18 and 33 water molecules, respectively. The conclusions of this work are the following:

1. If the reaction occurs, two channels are possible: (i) the combination of radicals into acetaldehyde/formamide and (ii) the formation of CH_4/NH_3 plus CO, where the H atom of HCO is passed to CH_3/NH_2 via H abstraction.
2. The two reaction channels are either barrierless or have relatively low energy barriers, from about 2 to 10 kJ mol^{-1}, as summarized in Table 6.3.
3. Comparison of the results obtained with B3LYP-D3 and BHLYP (the latter in its pure definition and including both D2 and D3 dispersion corrections) with those provided by CASPT2 for activation energies and those provided by CCSD(T) for binding energies, using one and two water molecules plus the radicals as test systems, indicates that B3LYP-D3 underestimates the energy barriers, while BHLYP-based methods show a reasonably good performance. For the computations relative to the 18 and 33 water clusters, we adopted BHLYP-D3 as it has been found, in the test systems, to properly deal with both the radical/surface binding and the radical-radical activation energies.
4. The morphology of the water cluster used for the simulations definitely affects the results of the computations. In particular, radicals would interact differently depending on whether they sit on a cavity structure, where they can establish several weak inter-molecular interactions with the icy water molecules, in addition to the H-bond.
5. Taking into account the results described in points 1, 2 and 4, the mechanism that radical combination necessarily produces iCOMs is still to be validated, and should be taken with care in astrochemical models.

In order to make progresses, more accurate computations would be needed, but they are not yet within the reach of the current computational capacities. On the other hand, dynamical simulations would help to understand the effect of the relative orientation of radicals upon encounter.

Chapter 7

A systematic study of radical–radical chemistry on interstellar ice surfaces

The research presented in this Chapter has resulted in a scientific article:
Enrique-Romero, J., Rimola, A., Ceccarelli, C., Ugliengo, P., Balucani, N., and Skouteris, D.
Submitted to the Apstrophysical Journal Supplement Series.

Outline

The formation of the interstellar complex organic molecules (iCOMs) is a hot topic in astrochemistry. In addition to be possible bricks of more complex prebiotic molecules, iCOMs formation in the ISM represents a challenge. One of the main paradigms trying to reproduce the observations postulates that iCOMs are formed on the ice mantles covering the interstellar dust grains as a result of radical-radical coupling reactions. In this Chapter, this iCOM formation mechanism is investigated by means of computational quantum mechanical methods. Specifically, the goal is to compute the properties and provide estimates of the efficiencies of the iCOM formation and the competitive channels, namely, the direct H-abstraction from one of the two radicals.

We study a set of radical-radical reactions involving the HCO/CH_3 + X systems, where X = NH_2, CH_3, HCO, CH_3O, CH_2OH, plus the CH_2OH + CH_2OH and CH_3O + CH_3O systems. The activation energy barriers of the radical-radical coupling and H-abstraction reactions for each studied system have been computed, as well as the binding energies of all the studied radicals, by means of density functional theory (DFT) calculations combined with the unrestricted and the broken symmetry approaches. The reaction efficiency of each reaction has also been estimated using the reaction activation, desorption and diffusion energies employing the Eyring equation to describe the kinetic constants. Following Chapter 6, all computations are carried out on two ice water models, which are clusters of 33 and 18 water molecules, respectively, the first one presenting a cavity while the later one a flat surface.

We find that radical-radical chemistry on surfaces is not as straightforward as usually assumed. In some cases, direct H abstraction reactions can compete with radical-radical couplings, while in others they may contain large activation energies. Specifically, we found that (i) ethane, methylamine and ethylene glycol are the only possible products of the relevant radical-radical reactions; (ii) glyoxal, methyl formate, glycolaldehyde, formamide, dimethyl ether and ethanol formation is likely in competition with the respective H-abstraction products, and (iii) acetaldehyde and dimethyl peroxide do not seem a likely grain surface products.

Our new computations shed some light on these aspects, even if we use rather simplistic descriptions of the icy surfaces and diffusion rates of the radicals. The main message from this work is that radical-radical combination forming iCOMs is not so obvious as usually assumed and dedicated studies on each specific system are mandatory.

7.1 Introduction

Among the more than 200 molecules detected in the ISM, about one third contains at least six atoms, whose one or more are carbon. This class of molecules is called interstellar Complex Organic Molecules in the literature (COMs, or iCOMs: Ceccarelli et al., 2017a; Herbst et al., 2009a) and are prevalently, but not exclusively, detected in star forming regions. Additionally, they could be related to the origin of life, and their formation mechanisms represent a scientific challenge (see § 1.4).

As already presented before (§ 1.4 and 4.1), iCOMs are either synthesized on the interstellar grain surfaces or in gas-phase by reactions involving smaller grain surface-chemistry products. In the first paradigm it is postulated that, during the cold pre-protostellar stage, the ice components are partially photo-dissociated by UV photons, generated by the interaction of cosmic-rays (CR) or X-rays with the hydrogen atoms in the gas phase, creating radicals that remain trapped into the ices. As the protostar gradually warms up its surroundings Viti et al., 2004, these radicals can diffuse over the ice, meet and react forming iCOMs R. T. Garrod et al., 2006; Robin T. Garrod et al., 2008; Herbst et al., 2009a; J. Kalvāns, 2018 (§ 1.4).

Additional processes have been considered to boost the iCOMs formation on the icy grain surfaces, such as the the reactivity of gas-phase C atoms (M. Ruaud et al., 2015) or CN (Rimola et al., 2018) landing on the icy surfaces, the formation of glyoxal by the coupling of two HCO radicals formed one next to the other on CO ices, followed by its hydrogenation that leads to glycoaldehyde and ethylene glycol Simons et al., 2020, or the reactions induced by landing cations (Rimola et al., 2021).

Following the research carried out in Chapters 5 and 6, here we focus on the reactivity on the grain icy surfaces between a larger set of radical species, arguably the most crucial step of this theory. Specifically, we present new *ab initio* quantum chemistry calculations on nine systems postulated to synthesize iCOMs, observed in the ISM, such as dimethyl ether, methyl formate and ethanol. Our aim is not only to supply the Potential Energy Surfaces (PES) and an approximate efficiency of the studied reactions but also to provide

hints on the possible expected output of other radical-radical systems of relevance in the formation of iCOMs on the icy surfaces.

This Chapter is organized as follows. In § 7.2, we present the systems studied in this work; in § 7.3 and 7.4 we describe the adopted methodology and the results of the new computations, respectively; and § 7.6 concludes the Chapter.

7.2 Studied systems

Here we expand the number of systems studied in Chapter 6 (Joan Enrique-Romero et al., 2019) adding nine more cases. Specifically, we selected a subset of the radical species considered by Robin T. Garrod et al., 2008 and that are the photolysis products of the closed-shell species formaldehyde, methane, methanol and ammonia: CH_3, HCO, CH_3O, CH_2OH and NH_2. Among those radicals, we focus on the CH_3/HCO + X reactions, where X is one of the above radicals. The list of studied systems and the possible products (from radicals combination and direct H-abstraction, respectively) are summarized in Table 7.1.

Our first goal here is to provide the potential energy surface (PES) of the reactions of the above systems, namely the energetics of the radical-radical coupling (hereinafter Rc) reaction, leading to the formation of an iCOM, as well as the possible competitive channels. On this respect, the previous studies mentioned above have shown that the H-abstraction reactions can potentially be more energetically favorable than the simple combination of the two radicals. In general, for H-abstraction reactions to take place, an H-donor and an H-acceptor radicals are needed. In some cases, such as CH_3 + CH_3, it does not happen. In others cases, such as HCO + CH_3O, both radicals can act as either H-acceptors/donors so that two direct H-abstraction channels might exist with different products.

In Chapter 6, we carried out the calculations considering two models for the amorphous water surfaces (AWS): with 18 (W18) and 33 (W33) waters, respectively. The W33 model is large enough to possess a geometrical cavity where radicals can lie, whereas the W18 model is too small for that purpose and only a "flat" surface is possible. These two models are obviously rough analogues of the ices that cover the interstellar grains. Nonetheless, they allow to have estimates of the energetics of reactions of radicals sitting on flat surfaces and inside a cavity, respectively. The latter is particularly interesting to describe the likely situation of most frozen radicals, as they are believed to be formed by the UV irradiation of the ice bulk. In other words, reactions among radicals are much more likely to occur in situations where they are surrounded by water molecules than on a flat surface exposed to the gas-phase. Actually, it is even possible that our W33 cavity description provides an optimistic view, as radicals may even be trapped in frozen water cages. For this reasons, in this work, we will pay special attention to the reactions occurring in the W33 cavity.

Providing the energetics of the process is a first mandatory step but it is not the end of the story. As it will be seen in the following Chapters 8 and 9 (Joan Enrique-Romero et al., 2021b), further insight can be obtained by calculating kinetic rate constants. Then, one can estimate the iCOM formation efficiency on the icy grain surfaces *via* the radical-radical coupling, as well as the H-abstraction competitive products. This study on the kinetics is postponed to a forthcoming work, but a rough estimate is provided.

7.3 Methods

In this section the methods employed for: the electronic structure calculations, the ASW ice models utilized and finally, how binding energies were calculated, are presented.

Electronic structure calculations

All DFT calculations were run with the GAUSSIAN16 software package (Frisch et al., 2016). Following previous chapters, the BHLYP functional (Becke, 1993a; C. Lee et al.,) was used, in which the Grimme's 3-body dispersion correction alongside the Becke-Johnson damping function (D3(BJ)) (Grimme et al., 2011, 2010) was introduced in an *a posteriori* manner.

The radical-radical reactions were studied both on amorphous solid water surface models (ASW) and in the absence of water molecules[1]. For the former, demanding calculations like geometry optimisations

[1] I.e. the reaction between the two radicals alone, in order to assess whether radicals are able to directly react or not.

Table 7.1: *Summary of the systems and reactions studied in this work.*

System	Radical coupling (Rc)	Direct H-abstraction product 1	Direct H-abstraction product 2
CH_3 + CH_3	C_2H_6 (Ethane)		
CH_3 + NH_2	CH_3NH_2 (Methylamine)		
CH_3 + CH_3O	CH_3OCH_3 (Dimethyl ether)	CH_4 + H_2CO	
CH_3 + CH_2OH	CH_3CH_2OH (Ethanol)	CH_4 + H_2CO	
HCO + HCO	HCOCHO (Glyoxal)	CO + H_2CO	
HCO + CH_3O	$HC(O)OCH_3$ (Methyl formate)	CO + CH_3OH	H_2CO + H_2CO
HCO + CH_2OH	$HC(O)CH_2OH$ (Glycolaldehyde)	CO + CH_3OH	H_2CO + H_2CO
CH_3O + CH_3O	CH_3OOCH_3 (Dimethyl peroxide)	H_2CO + CH_3OH	
CH_2OH + CH_2OH	$CH_2(OH)CH_2OH$ (Ethylene glycol)	H_2CO + CH_3OH	

or frequency calculations were run by using the double-ζ Pople's basis set 6-31+G(d,p) (Hariharan et al., 1973; Hehre et al., 1972), which were later refined by single point calculations with the 6-311++G(2df,2pd) (Krishnan et al., 1980) basis set. For the latter, due to their less demanding computational effort, all geometry optimizations were performed with the 6-311++G(2df,2pd) basis set.

All stationary points were characterized by the analytical calculation of the harmonic frequencies as minima (reactants, products, and intermediates) and saddle points (transition states). Intrinsic reaction coordinate (IRC) calculations at the same level of theory were carried out (when needed) to ensure that the transition states connect with the corresponding minima. Thermochemical corrections to the potential energy values were carried out using the standard rigid rotor/harmonic oscillator formulas to compute the zero point energy (ZPE) corrections McQuarrie, 1976. In order to properly simulate singlet electronic state biradical systems, we used the unrestricted formalism alongside the broken (spin) symmetry approach (e.g. Neese, 2004, see also § 2.4), which has been proven to be a cost-effective methodology to properly describe the electronic structure of this kind of systems (J. Enrique-Romero et al., 2020). The spin densities of each radical at the reactant structures can be found in appendix C.

Finally, we also calculated the tunneling crossover temperatures (T_c) following Fermann et al., 2000 (see appendix C) for those reaction steps where a hydrogen atom is transferred.

Water ice models

In the Chapter the same two ice cluster models employed in Chapter 6 (W18 and W33, see Figure 4.2) have been used. However, for the W33 model, only the cavity structure has been considered. The main reason of this choice relies on the fact that, as shown in Joan Enrique-Romero et al., 2019, results provided by W18 and by W33 elongated side are very similar. Additionally, we have also found that, for some radical-radical reactions, dramatic structural changes occurred on the W33 cluster model, in which the cavity collapsed when reactions between highly bound species were simulated. Therefore, W33 was used to simulate reaction occurring only in the cavity, while W18 on the flat surface.

Binding energies

The calculations of the radical–surface binding energies adopted the same electronic structure methodology as for reactivity. That is, for each radical–surface complex and isolated components (i.e. radicals and

surfaces), geometry optimizations and frequency calculations (and hence ZPE corrections) were computed at the BHLYP-D3(BJ)/6-31+G(d,p) level, which were followed by single point energy calculations at the improved BHLYP-D3(BJ)/6-311++G(2df,2pd) level to refine the potential energy values. With the obtained values we calculated the dispersion and deformation corrected interaction energies (ΔE_{ads}).

Subsequently, basis set superposition error (BSSE) corrections were obtained by running single point energy calculations at the BHLYP-D3(BJ)/6-311++G(2df,2pd) theory level. The final, corrected, interaction energy (ΔE_{ads}^{CP}) was calculated using the following equation:

$$\Delta E_{ads}^{CP}(AB) = \Delta E_{ads} + BSSE(A) + BSSE(B) + \Delta ZPE \tag{7.1}$$

Note that we used the same sign convention as in Chapter 6 (Joan Enrique-Romero et al., 2019), namely $\Delta E_{ads}^{CP} = -\Delta E_{bind}^{CP}$.

Reaction efficiencies

Astrochemical models compute the abundance of species by solving time-dependent equations that equate formation and destruction rates for each species. For grain-surface reactions, the formation rate is determined by the rate of encounters of the two reactants on the reaction site multiplied by the efficiency of the reaction, ε, which is the probability that when the two reactants meet they also react (R. T. Garrod et al., 2006; Tatsuhiko I. Hasegawa et al., 1993).

In order to provide a rough estimate of ε, we used the activation energy barriers and binding energies, following the schemes commonly used in astrochemical models (see Chapter 9, or Joan Enrique-Romero et al., 2021b, for a detailed discussion):

$$\varepsilon = \frac{k_{aeb}}{k_{aeb} + k_{diff,1} + k_{des,1} + k_{diff,2} + k_{des,2}} \tag{7.2}$$

where k_{aeb} are the rate constants related to the activation energy barrier and $k_{diff,i}$, $k_{des,i}$ are the diffusion and desorption rate constants of the species i.

All of these rate constants were derived using the Eyring equation:

$$k = (k_B T/h) \exp(-E_a/k_B T) \tag{7.3}$$

where k_B and h are the Boltzmann and Planck constants, T is the (surface) temperature and E_a is the activation energy of the process, i.e. the activation energy barrier for reactions or the diffusion E_{diff} and desorption E_{des} energies. It is worth noting that in Eq. 7.2, entropic effects are neglected, which is consistent with the very low temperature at which the processes (chemical reaction, diffusion, desorption) take place. The desorption energy, responsible of the $k_{des,1/2}$ terms, is just the opposite of the binding energy of each species, while the diffusion energy is taken to be a fraction of the desorption one.

In the literature, the E_{diff}/E_{des} ratio is usually assumed to be in the range of 0.3 and 0.4 for molecules (e.g. Aikawa et al., 2020; Tatsuhiko I. Hasegawa et al., 1992; Jin et al., 2020; Karssemeijer et al., 2014; Penteado et al., 2017; Maxime Ruaud et al., 2016). Recently, He et al. (2018) were able to measure the diffusion barrier of a number of molecules on ASW ices. They found E_{diff}/E_{des} ratios ranging between $\sim$0.3 and 0.6, depending on the coverage of admolecules, so that little coverage (sub monoloayer, ML, of admolecules) corresponds to the lower end of the E_{diff}/E_{des} ratio range, while higher coverages ($>$1ML) correspond to the higher end of the ratio range. Larger values of E_{diff}/E_{des} are normally assumed for atomic species (e.g. Minissale et al., 2016c found experimentally a E_{diff}/E_{des} value of 0.55 for N and O), and in the literature there is a fairly large amount of work in which a value of 0.5 is assumed, e.g. R. T. Garrod et al., 2006, 2011; Robin T. Garrod et al., 2008; S. S. Jensen et al., 2021; M. Ruaud et al., 2015; Vasyunin et al., 2017. This can, however, cause surface reactions to be much more efficient than using the recommended 0.3–0.4 range, as shown and discussed in detail by Joan Enrique-Romero et al., 2021b. For this reason, we used an intermediate value for E_{diff}/E_{des} of 0.35 in order to calculate the efficiency of the radical-radical reactions presented in this work.

7.4 Results

Binding energies

The computed binding energies (BEs) of the studied radicals with W33 and W18 are reported in Table 7.2. Optimized geometries for W33 are reported in Figure 7.1 while those for W18 are available in appendix C. For CH_3, HCO and NH_2, complexes in the previous Chapter (Joan Enrique-Romero et al., 2019) were re-optimized at the current theory level. For CH_3O and CH_2OH, the initial structures were constructed by maximising the inter-molecular interactions between the radicals and the cluster models.

Computed BEs follow the order of $CH_3 < HCO < NH_2 < CH_3O < CH_2OH$.

Differences with respect to BE values in Chapter 6 (Joan Enrique-Romero et al., 2019) arise from the different dispersion terms used in the two works, namely, D3(BJ) here versus D3 in Chapter 6, in which the former is understood to be more accurate as the components defining the D3(BJ) term enter in an optimisation processes in agreement with the particular system to simulate. Nevertheless, the same BE trends are obtained for the CH_3, HCO and NH_2 cases. Interestingly, BEs on W33 are about a 12–76 % higher than on W18, showing the importance of the larger number of inter-molecular interactions formed in the former cluster, as well as the larger dispersion interactions originated when the radicals adsorb in the cavity.

ΔE_{bind}^{CP}	CH_3	HCO	NH_2	CH_3O	CH_2OH
W33	14.3	29.4	44.3	38.1	51.3
W18	8.1	20.5	31.8	26.1	45.9

Table 7.2: *Computed corrected binding energies (ΔE_{bind}^{CP}) for the radicals interacting with the W18 and W33 cluster models. Units are in kJ mol^{-1}.*

The reliability of our methodology in computing these BE values is evidenced by comparing the results at BHLYP-D3(BJ)/6-311++G(2df,2pd) with those at CCSD(T)/aug-cc-pVTZ level (single point energy calculations on the BHLYP-D3(BJ) optimized geometries), in which a very good correlation between values is obtained (see appendix C).

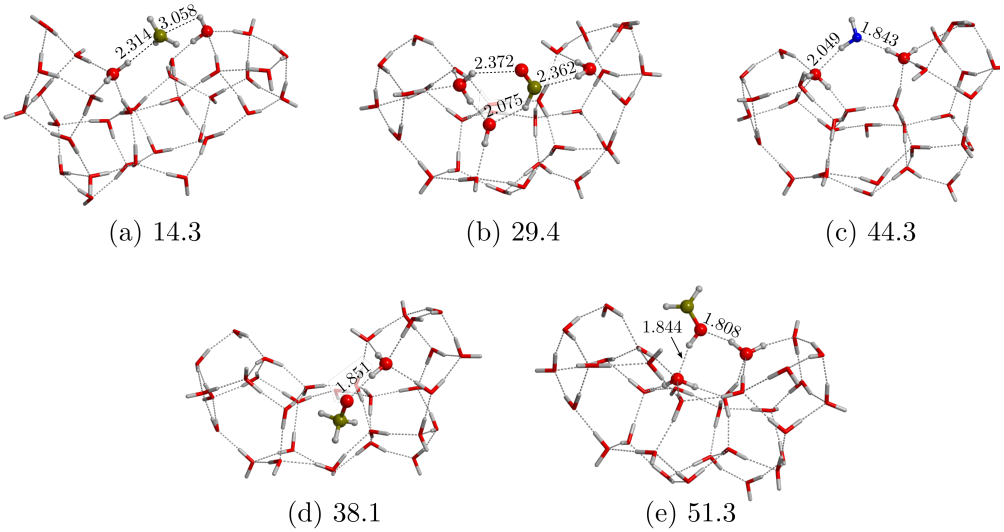

(a) 14.3 (b) 29.4 (c) 44.3

(d) 38.1 (e) 51.3

Figure 7.1: *Geometries of the five studied radicals, CH_3 (a), HCO (b), NH_2 (c), CH_3O (d) and CH_2H (e); adsorbed on W33 fully optimized at the UBHLYP-D3(BJ)/6-31+G(d,p) theory level. Energy values in kJ mol^{-1} are those refined at BHLYP-D3(BJ)/6-311++G(2df,2pd) level with the ZPE- and BSSE- corrections. Distances in Å.*

Radical-radical reactivity

In this section, the reactivity of the different sets of radical pairs on the W33 and W18 surface cluster models is presented. For the sake of clarity and brevity, along this section only structures involving W33 are shown. However, all computed structures (i.e., all the stationary points for both W33 and W18) are available in appendix C.

Remarkably, we showed in Chapters 5 and 6 (J. Enrique-Romero et al., 2020; Joan Enrique-Romero et al., 2019) that water assisted hydrogen transfer reactions present multiple steps and exceedingly high activation energies to be surmountable at interstellar conditions, so that these paths have been excluded in this work. Therefore, here we focus on the radical-radical coupling (Rc) leading to the formation of iCOMs (e.g. CH_3 + $CH_3O \rightarrow CH_3OCH_3$), and the direct hydrogen abstraction (hereinafter dHa) leading to simpler products (e.g. CH_3 + $CH_3O \rightarrow CH_4$ + H_2CO).

It is worth reminding that dHa reactions are not possible in the cases of CH_3 + CH_3 and CH_3 + NH_2, since none of these radicals can behave as H-donor (i.e. these reactions would be endothermic). In contrast, radical pairs in which both reactants exhibit properties of H-acceptors and H-donors, such as HCO, CH_3O and CH_2OH, two possible dHa processes are investigated (from each species, respectively). However, here we only show the most energetically favorable Rc and dHa channels. The corresponding computed energetics are summarized in the appendix C. The energetic data of all the computed reactions are also available in the appendix.

In the following, we will discuss the results separating the reactions into three groups, for better clarity: (i) reactions of CH_3 + X, (ii) reactions of HCO + X, and (iii) reactions of CH_3O + CH_3O and CH_2OH + CH_2OH.

CH_3 + X reactions

In general, this kind of reactions have very low energy barriers unless CH_3 is trapped by water molecules in the ice structure, or the reaction partner is not reactive enough, like dHa reactions with CH_3O/CH_2OH, which are largely prevented by either steric effects or strong surface interactions, blocking the H-atom that has to react.

CH_3 + CH_3 This reaction, which can only lead to ethane formation through the Rc channel, is barrierless on W18. In contrast, on W33, despite that the CH_3/surface interactions are essentially via dispersive forces (Joan Enrique-Romero et al., 2019), the reaction has a net energy barrier of 4.6 kJ mol^{-1}. The origin of this energy barrier arises from the interaction of one CH_3 with the water molecules of the surfaces. Indeed, in the reactant structure, one CH_3 is trapped by two dangling water surface H atoms, this way establishing weak H-bond interactions and reinforcing the dispersion interaction contribution. Thus, the coupling between the two CH_3 radicals requires breaking these interactions, which has an energy cost. Interestingly, these two weakly C–H$\cdots$O interactions are only possible on W33 due to the surface morphology of the cluster. Conversely, on W18, these interactions are not established (the two C–H$\cdots$O dangling bonds are missing) and, accordingly, the Rc reaction proceeds in a barrierless fashion.

CH_3 + NH_2 As in the previous case, reaction between CH_3 and NH_2 only leads to the formation of the iCOM (Rc channel), in this case methylamine (CH_3NH_2). For this radical pair, product formation presents very low energy barriers (0.4/1.6 kJ mol^{-1} on W33/W18). This is because the transition states mainly involve a translation/rotation of CH_3 towards NH_2.

CH_3 + CH_3O The formation of dimethyl ether (CH_3OCH_3) through the Rc channel on W18 has a barrier 0.2 kJ mol^{-1} while on W33 of 3.1 kJ mol^{-1}. This reaction is barrierless when we do not consider any ASW model (as in practice on W18), therefore, the origin of the barrier on W33 is caused by the morphology of the cluster model, similarly to what happens to the CH_3 + CH_3 case. Indeed, also in this case, the CH_3 establishes weakly H-bond interactions, which have to be broken to couple with the O of CH_3O. It is worth mentioning that a reactant structure in which the CH_3O radical is engaged by these H-bond interactions, the reaction is expected to have higher energy barriers, since the H-bonds will be stronger because of the participation of the O atom of CH_3O as H-bond acceptor. The dHa channel leading to CH_4 + H_2CO presents activation barriers of 9.5 and 1.0 kJ mol^{-1} on W33 and W18, respectively. In the absence of water molecules

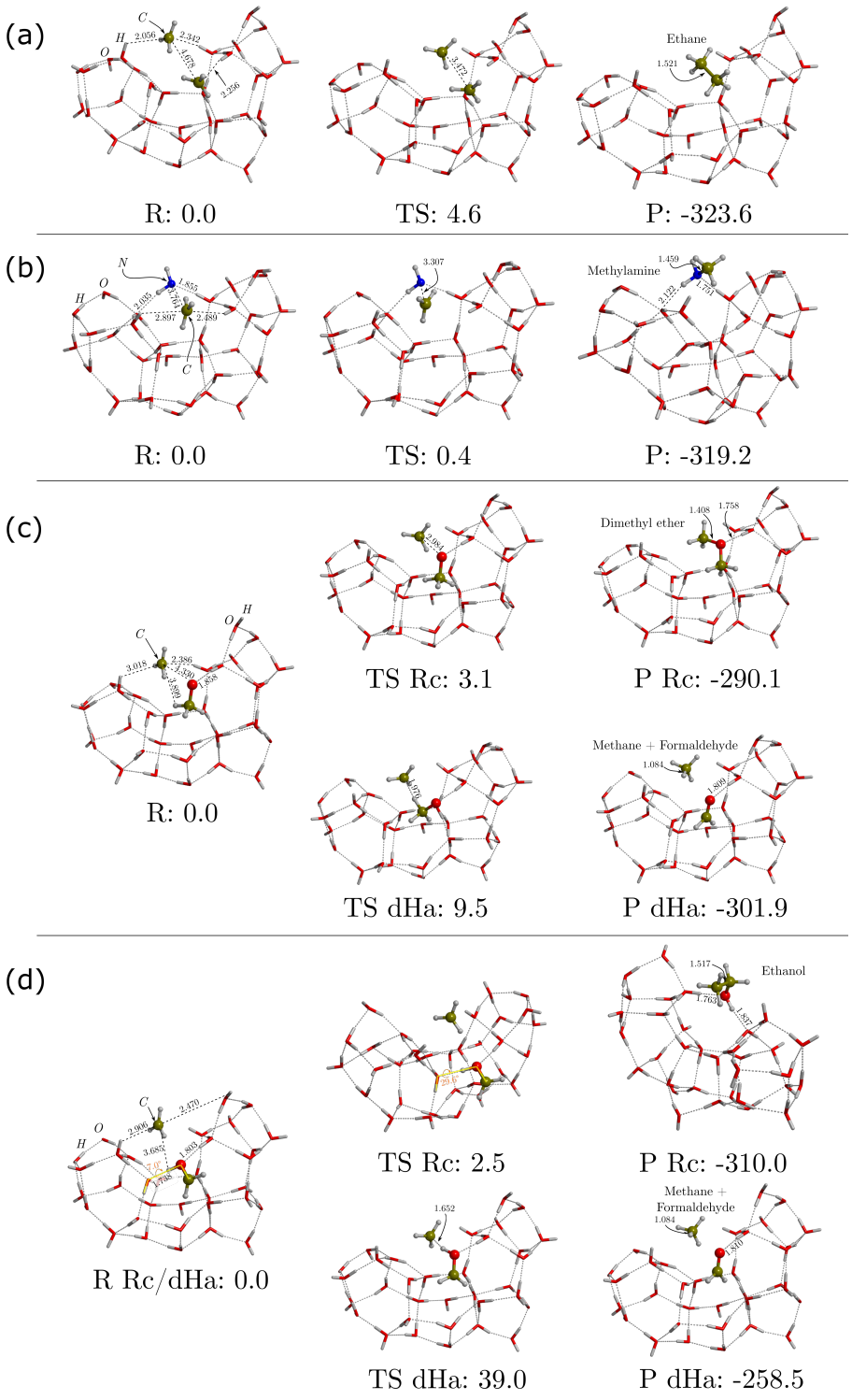

Figure 7.2: *ZPE-corrected PESs for (a) CH_3/CH_3, (b) CH_3/NH_2, (c) CH_3/CH_3O and (d) $CH_3/CH{-}2OH$ on W33-cav fully optimized at the BHLYP-D3(BJ)/6-31+G(d,p) theory level. DFT energies where further refined at BHLYP-D3(BJ)/6-311++G(2df,2pd) theory level. Energy units are in kJ mol^{-1} and distances in Å.*

this reaction has a barrier of 1.7 kJ mol^{-1} associated with the H–CH_2O bond breaking. This indicates that the energy barrier on W18 arises from this bond breaking, while on W33 it also has contributions from cavity effects, in this case, to overcome the dispersion forces between the –CH_3 moiety of CH_3O and the surface in order to reach a proper orientation allowing the H transfer.

CH_3 + CH_2OH This radical pair presents very low energy barriers in the Rc channel to form ethanol (CH_3CH_2OH), of 2.5 and 1.9 kJ mol^{-1} on W33 and W18, respectively. The opposite occurs for the dHa channel to form CH_4 + H_2CO (39.0 and 32.2 kJ mol^{-1} on W33 and W18, respectively). Although the interaction of CH_2OH with the surface is strong due to stable H-bonds, these H-bonds do not affect the Rc channel. Since the unpaired electron is on the C atom, it is freely accessible for the coupling. Accordingly, the Rc channel only requires overcoming the CH_3/surface dispersion interactions to form the C–C bond. In contrast, for the dHa channel, the strong CH_2OH/surface H-bond interactions inhibit the reaction since the H to be transferred is participating in the H-bonds, requiring the breaking of these interactions. The cost of this action is reflected by the fact that, in the absence of water molecules, the dHa channel has a lower energy barrier, of 9.8 kJ mol^{-1}.

HCO + X

At difference from the previous set of reactions, HCO + X have slightly higher energy barriers due to the higher binding energy of HCO. Nevertheless, HCO is a relatively good H-donor, and therefore, dHa reactions in which HCO donates its H atom have similar energy barriers as those of Rc.

HCO + HCO The energy barriers for Rc forming glyoxal (HCOCHO) and for dHa forming CO + H_2CO are very similar, i.e. 4.1 and 4.0 kJ mol^{-1} for Rc, and 4.0 and 2.7 kJ mol^{-1} for dHa, on the W33 and W18 surfaces, respectively. Here, the energy barriers are very similar because in both paths the structural reorganization of the reactants leading to products is also similar. Indeed, the reactions mainly involve the rotation of one of the two HCO radicals to arrive at the proper orientation to form either HCOCHO or CO + H_2CO, with a similar energy cost.

HCO + CH_3O For this system, the Rc and dHa channels (forming methyl formate and CO + CH_3OH, respectively) on W33 and W18 present similar energy barriers, of 3.5 and 5.1 and 2.0 and 3.2 kJ mol^{-1}, respectively. This is because the reactions proceed either through the translation (Rc) or the rotation (dHa) of the HCO radical, which present a similar energy cost. It is worth mentioning that this biradical system can also present another dHa channel, in which the CH_3O transfers its H atom to HCO to form H_2CO + H_2CO. However, this channel has a higher energy barrier (13.3/9.6 kJ mol^{-1} on W33/W18) because the orientation of CH_3O to transfer its H requires the breaking of the CH_3O/surface interactions. This was also observed in other radical pairs in which CH_3O is the H-donor in dHa processes (e.g., CH_3 + CH_3O).

HCO + CH_2OH The reactivity of this biradical system is similar to the previous one. That is, both the Rc channel (forming glycolaldehyde) and the dHa channel (in this case forming CO + CH_3OH due the H transfer from HCO to CH_2OH) present energy barriers below $\sim$2 kJ mol^{-1}, irrespective of the surface model where they are calculated. The explanation is the same: since CH_2OH is firmly attached by H-bonds on the surface, the reactions are driven by the motion of HCO, which in practice does not present any energy cost. Similarly to the previous biradical system, another dHa channel has been identified: that in which the H transfer takes place from CH_2OH to HCO forming H_2CO + H_2CO. Also in this case, the energy barriers are as high as $\sim$18 kJ mol^{-1} (on W33, see appendix C) due to the energy cost to break the CH_2OH/surface interactions, which is mandatory to transfer the H atom. The same reaction in the absence of water presents a barrier of 8.8 kJ mol^{-1}, indicating that the this structural reorganization is hindered by the CH_2OH/surface H-bonds.

CH_3O + CH_3O and CH_2OH + CH_2OH

As it was seen in above, the reactivity of CH_2OH + X and CH_3O + X (where X = CH_3 and HCO) share some similar aspects, namely Rc and dHa (where neither CH_3O nor CH_2OH act as an H donor) reactions tend

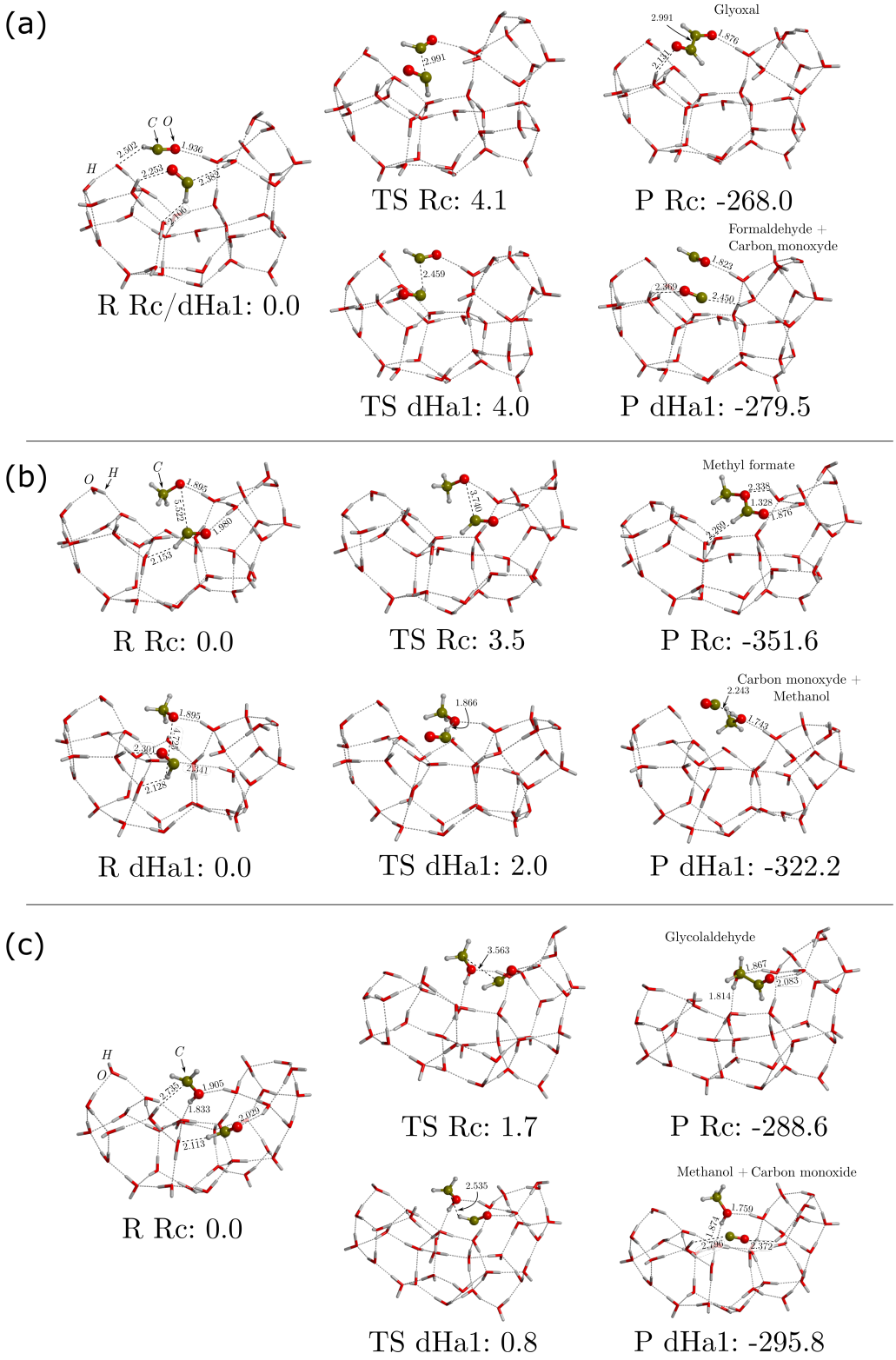

Figure 7.3: *ZPE-corrected PESs for (a) HCO/HCO, (b) HCO/CH_3O and (c) HCO/CH_2OH on W33-cav fully optimized at the BHLYP-D3(BJ)/6-31+G(d,p) theory level. DFT energies where further refined at BHLYP-D3(BJ)/6-311++G(2df,2pd) theory level. Energy units are in kJ mol^{-1} and distances in Å.*

to have low energy barriers. However, high energy barriers appear when either CH_3O or CH_2OH act as H-donors in dHa reactions.

In the CH_3O + CH_3O and CH_2OH + CH_2OH cases, we observed a clear different reactivity for their coupling reactions. In the CH_3O + CH_3O system, the Rc channel presents high energy barriers, given that the unpaired electrons on the O atoms are less reactive as a consequence of the H-bonding interaction with the surface, while for the CH_2OH + CH_2OH case, very low activation energies are obtained for the Rc channel on either surface models as a consequence of CH_2OH binding mode. Regarding their dHa reactions, we observe high energy barriers for both systems, as observed for CH_2OH + CH_3/HCO and CH_3O + CH_3/HCO where CH_2OH/CH_3O act as the H-donor.

CH_3O + CH_3O The Rc channel between two CH_3O radicals on W33 has a higher energy barrier than the dHa one (20.1 and 11.7 kJ mol^{-1}, respectively). This is because, in the reactant structure, both CH_3O radicals establish H-bond interactions with the surface through their O atoms. Since the Rc channel involves the coupling of the unpaired electrons of the two O atoms, the reaction requires the breaking of these H-bonds in both species. The contribution of these H-bond interactions in this energy barrier is demonstrated by the calculated value of the barrier in absence of water, of 1.8 kJ mol^{-1}. In the dHa channel, in contrast, a H atom is transferred from one CH_3O to the other without the need to break these H-bonds. In this case, the reorientation of the radicals is enough to facilitate the H transfer.

However, on W18 we observe the opposite trend: the Rc channel presents a lower energy barrier than the dHa one (10.3 and 15.9 kJ mol^{-1}, respectively). This is because in the reactant structure there are less intermolecular interactions and the two radicals are well oriented for the coupling, something that cannot take place in the cavity model due to its size and the lack of well oriented binding sites.

CH_2OH + CH_2OH This system is a paradigmatic case in which Rc channel has a low energy barrier while the dHa ones do not. Indeed, the lowest energy path is the Rc one, with 2.6/4.4 kJ mol^{-1} on W33/W18. On both clusters, the reaction involves a simple rotation around the intermolecular C–C dihedral angle (e.g. see Rc path in Figure 7.4(b)) in such a way that once the C atoms of each radical are faced one to each other the system easily evolves to form $CH_2(OH)CH_2OH$ (ethylene glycol) as a product.

In contrast, dHa reactions present higher energy barriers, about 9.1/20.6 kJ mol^{-1} on W33/W18, and often have multiple reorientation steps before the actual H-abstraction takes place, see for example the dHa1 and dHa2 channels on W33 shown in appendix C and and Figure 7.4(b), respectively. These are the consequences of the intrinsic stability of the CH_2OH radical (in the absence of water molecules, two CH_2OH radicals are able to form stable dimers), and the high capacity of this radical

Summary of radical-radical reactivity

The results on the activation energy barriers and reaction energies for each biradical system and each reaction studied, are summarized in Table 7.3. We do this according to two conditions: (i) if a reaction has more than a single step (e.g. dHa2-CH_2OH/$CH_2OH\cdots$W33, Fig. 7.4), we only report the highest energy barrier (in the example it would be the first barrier, of 9.0 kJ mol^{-1}); and (ii), for those biradical systems that have two dHa reactions channels, we only report the energetically most favorable one.

Reaction efficiencies

As described in Sect. 7.3, we computed a rough estimate of the efficiency of the reactions, ε, following the Eq. 7.2, using the computed binding energies of the radicals (Tab. 7.2, assuming a E_{diff}/E_{des} ratio of 0.35) and the activation energy barriers of the reactions (Tab. 7.3). Quantum tunneling effects are included in a qualitative manner on dHa reactions *via* their crossover temperatures (T_c, see appendix C).

With these calculations we aim to provide a simple means to discriminate which radical-radical processes are likely efficient from those that are not. In order to do this, we provide the efficiency values at the highest temperature possible for each reaction. In the absence of a full astrochemical model, we calculate this upper limit temperature as the temperature at which one would expect radicals to disappear from the surface due to thermal desorption. This is achieved by matching the desorption time-scale (proportional to $1/k_{des}$) to a value of 1 Myr (corresponding to the typical age expected for a protostar), which provides us with a

Table 7.3: *Summary of the theoretical results for radical-radical reactivity. First column reports the radical-radical system and column (2) the ice model to which the computations apply, i.e. W33 or W18 ice models or absence of water molecules (noW). Columns from (3) to (5) report the Radical coupling (Rc) product (col. 3) with the (ZPE-corrected) activation energy ($\Delta H^{\ddagger}$: col. 4) and the reaction energy (ΔH^{reac}: col. 5). Columns from (6) to (9) report the Direct H-abstraction (dHa) product (col. 6) with the (ZPE-corrected) activation energy ($\Delta H^{\ddagger}$: col. 7), the reaction energy (ΔH^{reac}: col. 8) and the crossover temperature (T_c: col. 9, see appendix C). The last column reports the category to which the reaction belongs (see text), based on the the efficiencies computed in Eq. 7.2 (assuming a diffusion-to-desorption barrier ratio of 0.35) and the crossover temperatures: (1) Rc plausible & dHa not plausible/possible; (2) Rc–dHa competition; (3) Rc–dHa competition at low temperatures thanks to tunneling; (4) Rc not plausible, dHa only plausible at low temperatures thanks to tunneling. Energy units are kJ mol^{-1}, temperatures in K.*

System	Ice	Radical-radical coupling			Direct H-abstraction				Reaction
	Model	Product	$\Delta H^{\ddagger}$	ΔH^{reac}	Product	$\Delta H^{\ddagger}$	ΔH^{reac}	T_c [K]	category
CH_3 + CH_3	W33	CH_3CH_3	4.6	-323.6					1
	W18		NB	-333.4	None				1
	noW		NB	-338.1					
CH_3 + NH_2	W33	CH_3NH_2	NB	-319.2					1
	W18		NB	-316.8	None				1
	noW		NB	-309.1					
CH_3 + CH_3O	W33	CH_3OCH_3	3.1	-290.1	CH_4 + H_2CO	9.5	-301.9	47.1	1, 3
	W18		NB	-299.5		1.0	-302.7	36.1	2
	noW		NB	-298.3		1.7	-297.5		
CH_3 + CH_2OH	W33	CH_3CH_2OH	2.5	-310.0	CH_4 + H_2CO	39.0	-258.5	242.0	1, 3(?)
	W18		1.9	-320.4		23.9	-255.1	295.7	1, 3(?)
	noW		NB*	-327.5$^{\nabla}$		9.8	-273.1		
HCO + HCO	W33	CHOCHO	4.1	-268.0	CO + H_2CO	4.0	-279.5	28.4	2
	W18		4.0	-260.3		2.7	-272.7	10.8	2
	noW		NB	-275.2$^{\nabla}$		NB	-278.5$^{\nabla}$		
HCO + CH_3O	W33	CH_3OCHO	3.5	-351.6	CO + CH_3OH	2.0	-322.2	34.6	2
	W18		5.1	-358.5		3.2	-323.4	57.8	2
	noW		NB*	-358.6$^{\nabla}$		NB*;#	-326.3		
HCO + CH_2OH	W33	$CHOCH_2OH$	1.7	-288.6	CO + CH_3OH	NB*	-295.8	-	2
	W18		1.6	-286.2		NB*	-290.2	-	2
	noW		NB*	-303.8$^{\nabla}$		NB*;#	-297.8		
HCO + CH_3	W33	CH_3CHO	5.5	-324.5	CH_4 + CO	7.2	-328.9	40.0	4
	W18		1.8	-329.5		5.0	-321.5	8.0	1
	noW		NB	-326.1$^{\nabla}$		NB	-340.4$^{\nabla}$		
HCO + NH_2	W33	NH_2CHO	2.1	-385.7	NH_3 + CO	1.4	-335.0	28.8	2
	W18		3.8	-364.9		4.9	-338.4	7.3	2
	noW		NB	-388.4$^{\nabla}$		NB?	-344.0$^{\nabla}$		
CH_3O + CH_3O	W33	$(CH_3O)_2$	20.1	-58.3	CH_3OH + H_2CO	11.7	-292.3	225.7	4
	W18		10.3	-64.1		15.9	-312.5	212.9	4, 3(?)
	noW		1.8	-75.0		8.1	-284.1		
CH_2OH + CH_2OH	W33	$(CH_2OH)_2$	2.6	-299.5	CH_3OH + H_2CO	9.0	-245.8	296.2	1
	W18		4.4	-288.7		27.6	-226.3	394.3	1
	noW		10.7	-295.1		6.0	-241.0		

Note: CH_3/HCO and NH_2/HCO values on W18 and W33 were recalculated from those in Chapter 6 (Joan Enrique-Romero et al., 2019). The main difference is on the dispersion correction used in this work (see also Joan Enrique-Romero et al., 2021b, or Chapter 9).

NB* indicates that the reaction has no effective barrier (< 1 kJ mol^{-1}), although a transition state was found, which after correcting for ZPE goes below the energy of the reactants.

$^{\#}$ Regarding the dHa reactions of HCO + CH_3O/CH_2OH in the absence of water molecules we report those for the dHa1 channel (i.e. HCO transfers its H atom to the partner radical). The dHa2 channels where CH_3O or CH_2OH transfer its H atoms to HCO have higher barriers, of 5.3 and 8.8 kJ mol^{-1}, respectively, similar to CH_3 + CH_3O/CH_2OH.

$^{\nabla}$ Calculated with respect to the asymptote (i.e. the sum of the energy of both radicals alone).

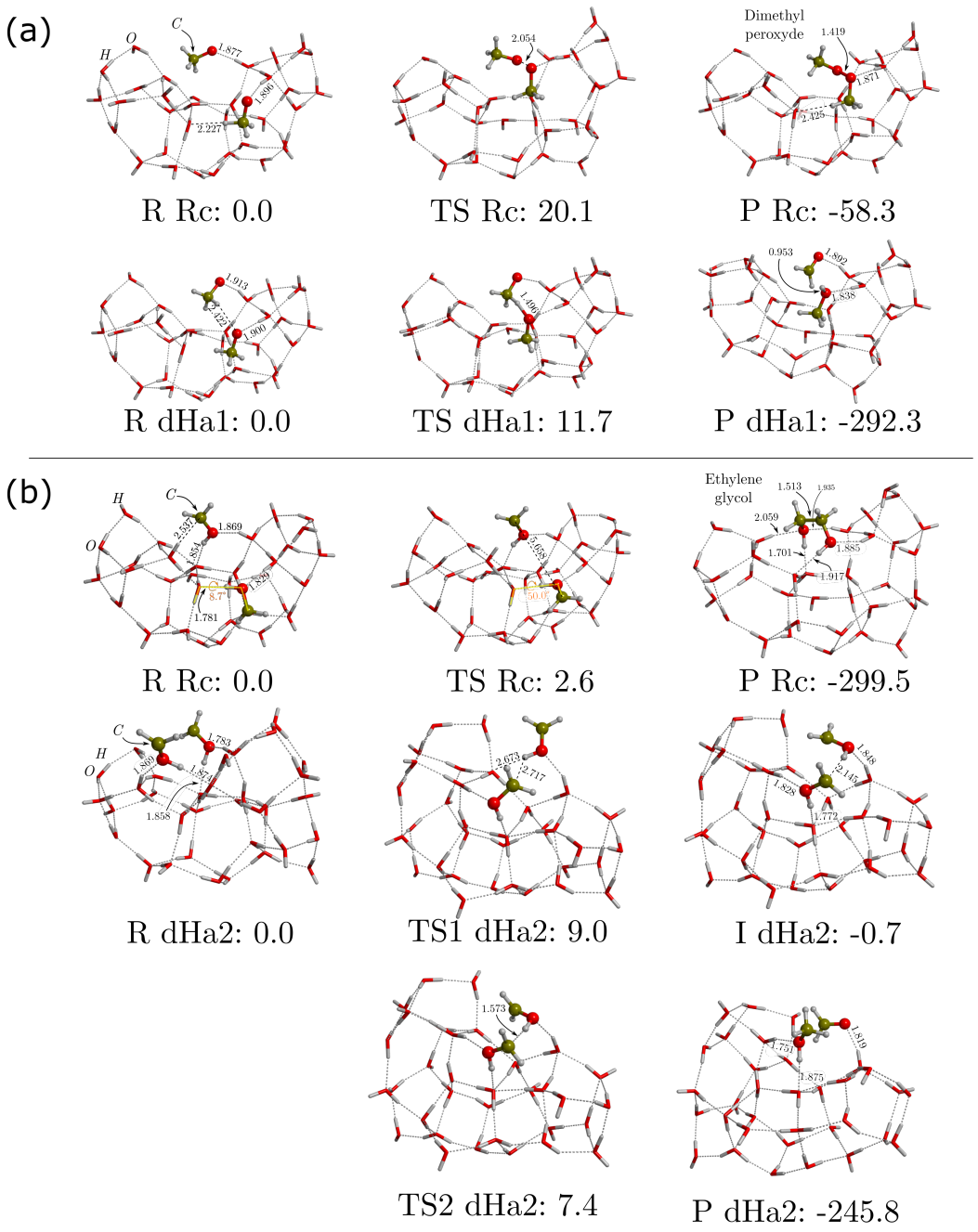

Figure 7.4: *ZPE-corrected PESs for (a) CH_3O/CH_3O and (b) CH_2OH/CH_2OH on W33-cav fully optimized at the BHLYP-D3(BJ)/6-31+G(d,p) theory level. DFT energies where further refined at BHLYP-D3(BJ)/6-311++G(2df,2pd) theory level. Energy units are in kJ mol^{-1} and distances in Å.*

temperature value. We label these temperatures by T_{des}, and they are listed in Tabs. 7.4 and 7.5 for the W33 and W18 ice models, respectively, together with the efficiencies for the radical coupling and direct H-abstraction reactions at these temperatures, and at 10 K.

Please note that Tabs. 7.4 and 7.5 also report the efficiencies and T_{des} of the HCO + CH_3/NH_2 systems. The first one, leading to acetaldehyde, has been fully studied in J. Enrique-Romero et al., 2020; Joan Enrique-Romero et al., 2021b, while the energetics of second system, leading to formamide, was presented in (Rimola et al., 2018).

Finally, it must be noted that the reported efficiencies are not the same as branching ratios. The latter take into account the rate at which radicals meet on the surface together with the efficiencies themselves, and provide a perspective of the relative importance of the different reaction channels that two reactants can follow (e.g. Joan Enrique-Romero et al., 2021b). On the other hand, the efficiencies tell us what is the probability that two reactants will react in a given reaction site on the surface before one of the two reactants diffuses or ultimately desorbs.

W33 ice ASW model Table 7.4 shows that out of the eleven reported systems, nine iCOMs forming reactions have efficiencies close to 1 by the end of the shortest radical residence on the ice surfaces, namely at temperatures T_{des}, while two (forming dimethyl peroxide and acetaldehyde) have efficiencies less than 0.1. Similarly, out of the nine systems where H-abstraction reactions are possible, five have efficiencies close to 1 at T_{des} (basically those with the form HCO + X $\rightarrow$ CO + HX, thanks to the low energy barriers involved). On the contrary, the efficiency of four H-abstraction reactions (CH_3 + CH_3O, CH_3 + CH_2OH, HCO + CH_3, CH_3O + CH_3O) fall below 1. Notice that if instead of using $E_{diff}/E_{des} = 0.35$, a value of 0.3 is used, all efficiencies are lowered, on the contrary, an increment to 0.4 makes them to increase. In fact, increasing this ratio one allows the radicals to stay longer in a given binding site, increasing the reaction efficiency. For example, the efficiency of the CH_3 + CH_3 $\rightarrow$ C_2H_6 reaction would go down from 0.7 (using a ratio of 0.35) to $\sim$0.1 for a ratio of 0.3 and up to $\sim$1 for a ratio of 0.4. On the same vein, setting the E_{diff}/E_{des} ratio equal to 0.5 makes almost all reactions to have an efficiency of 1, due to the longer time that radicals would remain together as a result of the lower diffusion. Changing the temperature at which ε is computed has, in most cases, no effect, indicating that the reaction and diffusion processes are not competitive even at such low temperatures. The exceptions are those reactions that have a small efficiency at T_{des} in Table 7.4.

Table 7.4: *Efficiencies, ϵ, of radical-radical reactions on the W33 ASW ice model. They are calculated using Equation 7.2, setting the temperature to T_{des} and 10 K, respectively, and considering that the diffusion barriers are equal to 0.35 times those of desorption. Note that the quoted values do not take into account quantum tunnelling, which could make efficiency larger at very low temperatures.*

			T=T_{des}			T=10 K		
System	Fastest hopper	T_{des} [K]	Rc efficiency	dHa case 1 efficiency	dHa case 2 efficiency	Rc efficiency	dHa case 1 efficiency	dHa case 2 efficiency
CH_3 + CH_3	CH_3	29	0.7	–	–	1.0	–	–
CH_3 + NH_2	CH_3	29	1.0*	–	–	1.0*	–	–
CH_3 + CH_3O	CH_3	29	1.0	0.0	–	1.0	0.0	–
CH_3 + CH_2OH	CH_3	29	1.0	0.0	–	1.0	0.0	–
HCO + HCO	HCO	60	1.0	1.0	–	1.0	1.0	–
HCO + CH_3O	HCO	60	1.0	1.0	2.9×10^{-3}	1.0	1.0	0.0
HCO + CH_2OH	HCO	60	1.0	1.0*	**	1.0	1.0*	**
CH_3O + CH_3O	CH_3O	77	1.3×10^{-5}	0.9	–	0.0	1.0	–
CH_2OH + CH_2OH	CH_2OH	103	1.0	**	**	1.0	**	**
HCO + CH_3	CH_3	29	0.1	1.1×10^{-4}	–	2.6×10^{-3}	0.0	–
HCO + NH_2	HCO	60	1.0	1.0	–	1.0	1.0	–

* Barrierless, therefore efficiency is 1 and no crossover temperature can be calculated.
** Multiple steps and high barriers, therefore very little efficiency. No crossover temperature is listed, as only the very last step will actually benefit from tunneling.

W18 ASW ice model The reaction efficiency calculations were also carried out for the systems on the W18 ice ASW model, where radical mobilities are higher due to the overall lower binding energies, and the simpler reaction mechanisms (usually single step reactions). The results are reported in Tab. 7.5. Both at T_{des} and 10 K, all iCOMs forming reactions have efficiencies close to 1, except the one from the CH_3O + CH_3O system, which due to its high barrier has an efficiency of the order of 10^{-2}. On the contrary, five H-abstraction reactions have efficiencies close to 1, while four have efficiencies close to zero, both at T_{des} and 10 K.

Table 7.5: *Efficiencies, ϵ, of radical-radical reactions on the W18 ASW ice model. They are calculated using Equation 7.2, setting the temperature to T_{des} and 10 K, respectively, and considering that the diffusion barriers are equal to 0.35 times those of desorption. Note that the quoted values do not take into account quantum tunnelling, which could make efficiency larger at very low temperatures.*

			$T = T_{des}$			$T = 10$ K		
System	Fastest hopper	T_{des} [K]	Rc efficiency	dHa case 1 efficiency	dHa case 2 efficiency	Rc efficiency	dHa case 1 efficiency	dHa case 2 efficiency
CH_3 + CH_3	CH_3	17	1.0*	–	–	1.0*	–	–
CH_3 + NH_2	CH_3	17	1.0*	–	–	1.0*	–	–
CH_3 + CH_3O	CH_3	17	1.0*	1.0	–	1.0*	1.0	–
CH_3 + CH_2OH	CH_3	17	1.0	0.0	–	1.0	0.0	–
HCO + HCO	HCO	42	1.0	1.0	–	1.0	1.0	–
HCO + CH_3O	HCO	42	1.0	1.0	9.6×10^{-4}	1.0	1.0	0.0
HCO + CH_2OH	HCO	42	1.0	1.0*	0.0	1.0	1.0*	0.0
CH_3O + CH_3O	CH_3O	53	0.03	0.0	–	0.0	0.0	–
CH_2OH + CH_2OH	CH_2OH	92	1.0	0.0	**	1.0	0.0	**
HCO + CH_3	CH_3	17	1.0	0.0	–	1.0	0.0	–
HCO + NH_2	HCO	42	1.0	1.0	–	1.0	1.0	–

* Barrierless, therefore efficiency is 1 and no crossover temperature can be calculated
** Multiple steps and high barriers, therefore very little efficiency. No crossover temperature is given, as only the very last step will actually benefit from tunneling.

7.5 Discussion

iCOMs formation versus H-abstraction

In this work, two radical-radical surface reactions-types have been investigated: radical coupling (Rc) and direct hydrogen abstraction (dHa). The former leads to the formation of iCOMs, while the latter does not lead to a increase in chemical complexity as the products are as simple as the reactants. Using the binding energies (Tab. 7.2), activation energy barriers (Tab. 7.3) and the reaction efficiencies ε (Tabs. 7.4), here we discuss which radical-radical reaction will likely take place and if there will be a competition between the Rc and dHa channels.

Depending on the values of the efficiencies and the crossover temperature for the Rc and dHa reactions (Tabs. 7.4 and 7.5), we can define four categories:
(1) Rc plausible and dHa not plausible/possible: the reaction will lead to the iCOM with no competition channel.
(2) Rc–dHa competition: both reactions are possible and are in competition.
(3) Rc–dHa competition at low temperatures because of the tunneling taking over in the dHa reactions.
(4) Rc not plausible and dHa only plausible at low temperatures thanks to tunneling: the reaction will not form the iCOM and, except at low temperatures, not even the competing channel will occur.

Based on these reaction categories, here we briefly discuss, in a qualitative manner, which iCOMs are likely to be formed, and in which cases the Rc processes may be in direct competition with the dHa ones.

In three cases (CH_3 + CH_3, CH_3 + NH_2 and CH_2OH + CH_2OH), the only possible product is the iCOM (namely ethane, methylamine, and ethylene glycol, respectively). We have categorized these reactions as category 1 on both W33 and W18 ASW ice model surfaces given their high efficiencies even at low temperatures ($\varepsilon >$0.7).

In four cases, (HCO + HCO, HCO + CH_3O, HCO + CH_2OH and HCO + NH_2), the formation of the iCOM (glyoxal, methyl formate, glycolaldehyde and formamide) and the dHa products are likely competing processes on both the W33 and W18 ice models. In practice, all reactions involving HCO (except HCO + CH_3; see Joan Enrique-Romero et al., 2021b, or Chapter 9) have Rc and dHa (of the HCO + X $\rightarrow$ CO + HX type) as competitive channels. Therefore, while iCOMs can be formed, a significant part of the reactants could be lost *via* these dHa reactions.

In other two cases (CH_3 + CH_3O and CH_3 +CH_2OH), iCOM formation (dimethyl ether and ethanol) are the dominant process except at low temperature, where H-abstraction can take over and become competitive thanks to quantum tunneling.

Finally, in two systems (HCO + CH_3 and CH_2OH + CH_2OH), iCOM formation (acetaldehyde and dimethyl peroxide) are unlikely to be formed.

In summary, assuming that radicals have already diffused and have encountered in a specific place similar to those represented by our ASW model ices, most iCOMs in the systems studied in this work are likely to be formed on the icy surfaces. However, while ethane, methylamine and ethylene glycol are the only possible products, glyoxal, methyl formate, glycolaldehyde, formamide, dimethyl ether and ethanol are likely in competition with the respective H-abstraction products. On the other end, acetaldehyde and dimethyl peroxide do not seem a likely grain surface products.

Finally, we caution that this just represents one part of the Langmuir-Hinshelwood reactivity. As discussed also in Joan Enrique-Romero et al., 2021b (Chapter 9), the binding and diffusion energies are crucial parameters. In this study, we assumed (computed) a single value for the binding energy but it is now clear that it depends on the site where the species lands (e.g. Bovolenta et al., 2020; Ferrero et al., 2020). Also, as already mentioned, the diffusion energy is poorly known. Since both parameters enter in an exponential way in the computation of the efficiencies, more theoretical studies are necessary to firmly draw a conclusion, which depends on the fraction of sites with low or high binding and diffusion energies. Nonetheless, this study shows that these computations are absolutely necessary in order to have quantitative and reliable astrochemical models.

Where do barriers come from?

There are two factors affecting the energy barriers of the reactions. The first one is related to the adsorption of the radicals on the surface, i.e., the way how they adsorb and the strength of this adsorption. All the studied radicals in this work interact with the water molecules exposed on the ice surfaces *via* H-bond and dispersion interactions, in which CH_3 and CH_2OH present the weakest and the strongest binding, respectively. Because of these interactions, radical-radical reactions on water ice surfaces exhibit energy barriers, as the reactions require the breaking of these radical/surface interactions. Remarkably, since the radical/surface interactions dictate the geometries of the adsorbed radicals, these interactions have also repercussions on the structural reorganization of the reactants necessary for the occurrence of the reactions. Take for example the dHa channels in which CH_2OH transfers its H atom. CH_2OH interacts with the surface mainly through two strong H-bonds involving the –OH group. Accordingly, dHa reactions require a large re-orientation, including the breaking of the CH_2-OH/surface H-bonds, to proceed with the reaction, which is accompanied by a high energy barrier. The second factor is related to the intrinsic feasibility of the reactions, that is, how stable against reaction are the biradical systems. To assess this point, we have investigated the reaction in absence of the water cluster, in this way to know the intrinsic energy cost (i.e., without the presence of external agents like the water clusters) of the reactions (see Sec. Methods). Results are shown in Table 7.3 ("noW" rows), while the structures of the optimized geometries are available in appendix C. We have detected that dHa channels involving either CH_3O or CH_2OH in which they transfer the H atom, irrespective of the other radical, all present energy barriers. This means that the H transfer from these two radicals is intrinsically associated with an energy cost. In contrast, this is not the case for dHa channels in which HCO transfers its H atom, since all these processes are barrierless in absence of the water clusters. Thus, HCO is a better H atom donor than CH_3O and CH_2OH and, accordingly, dHa channels involving HCO are more favourable than those involving CH_3O and CH_2OH. This is indeed reflected in the energy barriers of the dHa processes on W33/W18, which are lower for cases with HCO than for those with CH_3O or CH_2OH.

For Rc channels in the absence of water molecules, those in which either HCO or CH_3 participate, irrespective of the other radical, are barrierless, indicating that couplings involving these two radicals are largely favorable. This is reflected in the energy barriers on W33/W18, which are in most of the cases very low. In contrast, the Rc channels of CH_3O + CH_3O and CH_2OH + CH_2OH in the absence of water molecules do have energy barriers, showing that these two couplings are intrinsically less favourable than those involving HCO and CH_3. The reason why the CH_3O + CH_3O and CH_2OH + CH_2OH Rc reactions are not barrierless in the absence of an ice surface is the high stability of their biradical van der Waals complexes, i.e., $CH_3O\cdots CH_3O$ and $CH_2OH\cdots CH_2OH$. On the W33/W18 ASW ice models, these van der Waals cannot be formed as a consequence of the interaction with the surface. Indeed, the CH_2OH + CH_2OH Rc reactions on W33/W18 have similar energy barriers to those of HCO + X and CH_3 + X, because the coupling does not

require neither a strong structural reorganization nor the breaking of the CH_2OH/surface interactions, this way rendering the C–C bond formation energetically easy. And for the case of CH_3O + CH_3O Rc channel on W33/W18, energy barriers are much higher than in the absence of water molecules, due to the energetic cost of breaking the CH_3O/surface interactions and re-orientate the radicals to reach the coupling.

CH_3O and CH_2OH: who stays and who goes?

CH_3O and CH_2OH radicals are chemical isomers but exhibit different adsorption features and different radical-radical reactivity on ASW surfaces. Both radicals present high binding energies (CH_2OH larger than CH_3O) due to their capability to establish strong H-bonds with the surfaces. Nevertheless, the way how they are established (i.e., atoms involved and number of H-bonds formed) is rather different, and this yields differences in their reactivity. CH_2OH interacts with the surface through two strong H-bonds involving only the –OH group, this way leaving its C atom (namely, the radical center) unprotected and available to react. This has important consequences on the reactivity of the CH_2OH radical. Indeed, most of the CH_2OH + X reactions (X = CH_2OH, CH_3 and HCO) are Rc plausible as they present smaller energy barriers and often have less reaction steps than dHa. The unique exception is the CH_2OH + HCO reaction, which belongs to the Rc–dHa competition category due to the intrinsic ease of HCO to transfer its H atom (see above).

In contrast, the unpaired electron in CH_3O is on the O atom, which in turn is the atom through which the radical establishes H-bonds with the surface. Because of that, the O atom is blocked toward chemical reactivity and this is shown by the trends in the CH_3O + X reactions (X = CH_3O, CH_3 and HCO). CH_3O + CH_3O presents very high energy barriers, irrespective of the reaction channel and the ASW model. This is because CH_3O radicals have to reorganize structurally (namely, to break the interactions with the surface) in order to be ready to react. Reactions with CH_3 and HCO show in general Rc-dHa competition, except for the CH_3 + CH_3O case on W33 (Rc plausible) due to the high dHa barrier (9.5 kJ mol^{-1}) caused by the structural reorientation of CH_3O. Nevertheless, at very low temperatures ($<$ 40 K) they could be in competition due to the increased tunneling probability.

Interestingly, these trends gain relevance if we extrapolate them in the plausible scenario of hydrogenation of CH_2OH and CH_3O, both cases leading to the formation of methanol (CH_3OH). According to our results, an incoming H atom will react easier with CH_2OH than with CH_3O, since the C atom of the former is available while the O atom of the later is blocked. Remarkably, the propensity of the radicals to react is dictated by the geometrical constraints imposed by their interaction with the surface. Thus, in the presence of H atoms, CH_2OH would consume better than CH_3O, which could partly explain why CH_3O is detected and CH_2OH is not (e.g. Cernicharo et al., 2012).

Influence of the water ice surface model

The W33 ASW ice surface model presents a $\sim$6 Å wide cavity where both radicals can be adsorbed. In contrast, the W18 model does not exhibit a cavity, resembling instead a rather flat surface. As shown in § 7.4, the binding energies on W33 (i.e., adsorption on the cavity) are larger (by a 12–76%) than on W18, due to the larger number of radical/surface interactions formed on the former cluster model.

These effects are particularly important in those reactions in which the CH_3 radical participates. Indeed, in different reactions on W33, CH_3 is engaged by two weakly H-bonds, this way either hampering its motion towards the other radical (hence disfavouring Rc channels) or inhibiting its capability to receive an H atom from the other radical (hence disfavouring dHa channels: see Fig. 7.2). Indeed, the average energy barriers for Rc reactions involving CH_3 + X $\rightarrow$ X–CH_3 on W33 is 3.1 kJ mol^{-1}. In contrast, on W18, CH_3 adsorbs essentially through dispersion forces and accordingly it is relatively free to translate/rotate to favour the Rc and dHa channels, so that CH_3 + X Rc reactions have a barrier of 0.7 kJ mol^{-1} on average.

For the other radicals, we did not find so clear effects on the energy barriers due to the water ice surface morphology. These are indeed more complex cases than the CH_3 ones, since the reacting radicals can adsorb in different ways, establish different radical/surface interactions with different efficiencies, and require different structural reorganizations to react. Yet, we find that HCO + X $\rightarrow$ X–CHO Rc reactions have average barriers of 3.4/3.3 kJ mol^{-1} on W33/W18 and average dHa HCO + X $\rightarrow$ CO + HX reaction energy barriers of 2.9/3.2 kJ mol^{-1} on W33/W18.

Finally, some words related to our cluster models deserve to be mentioned. The first aspect is that they are rather small, although they are capable to host two small radicals on the surface. However, the limited sizes infer that, in the initial states, the reacting radicals are in close proximity. Thus, the predicted energy barriers concern only the chemical reactions between the radicals and not other surface phenomena like diffusion. In real systems, the two radicals will be likely separated by longer distances and, thus, diffusion is necessary. The second aspect is that the clusters composition is purely water, while actual ice mantles will contain other species. Thus, the interaction of the radicals with the surface can be different, affecting the diffusion, the reaction energies and the survival of the radicals against hydrogenation reactions. Therefore, the energy barriers reported in this work are constrained within these two aspects, assuming that ice composition plus extensive radical diffusion are actually needed for a more realistic modelling.

Predictions for other radical-radical systems

There are several other radical-radical systems proposed in the literature e.g. Robin T. Garrod et al., 2008 that we did not study in the present work, for example: OH/NH + X (X = CH_3, HCO, OH, NH, NH_2, CH_3O, CH_2OH), NH_2 + Y (Y = NH_2, CH_3O, CH_2OH) and CH_3O + CH_2OH. Here we propose to use the trends for the studied reactions and the classification in categories 1 to 4 discussed in § 7.5 as a predictive tool to estimate a likely category of these other radical-radical reactions.

As for the reactions studied in this work, the category classification is based on the reaction efficiency (§ 7.3), which depends on the reaction energy barrier, radical binding and diffusion energies. In order to guess the reaction category, we apply the following set of considerations:

- If the reaction mechanism only involves translations/rotations without the need to break the radical/surface interactions (e.g., the Rc reactions on W18 of the type CH_3 + X with X = CH_3, NH_2, HCO, CH_3O, CH_2OH), then we estimate the energy barriers to be low (lower than about 4 kJ mol^{-1}).
- If the reaction involves the breaking of strong radical/surface interactions (e.g., Rc and dHa for CH_3O + CH_3O), or the translation of a radical somehow trapped by the ice (e.g., CH_3 in CH_3 + CH_3/CH_3O on W33), then we estimate the energy barriers to be high (higher than about 10 kJ mol^{-1}).
- For dHa channels only, if the reaction involves the cleavage of intrinsically stable chemical bonds (e.g., the CH_2O–H bond), then we consider the energy barriers to be high (≥ 10 kJ mol^{-1}). If the reaction involves the opposite situation (e.g., the H–CO bond), then we consider the energy barriers to be low (≤ 4 kJ mol^{-1}).

Given the fundamental role that the binding energies play in such surface reactions, we have calculated the binding energies of NH (in its triplet electronic ground state) and OH radicals on the water ice clusters. They are: 13.0 and 24.2 kJ mol^{-1} on the W18 model, and 32.5 and 44.7 kJ mol^{-1} on the cavity of the W33 model, for NH and OH respectively (see appendix C). Thus, NH has a binding energy that lies between HCO and NH_2, while OH is almost the same as NH_2. With this information, we obtain the E_a– and T– dependent efficiencies (of either Rc and dHa reactions) for each system with OH + X, NH + X (X = CH_3, HCO, OH, NH_2, CH_3O, CH_2OH), NH_2 + Y (Y = NH_2, CH_3O, CH_2OH) and CH_3O + CH_2OH. Figure 7.5 contains a subset of them: OH + CH_3, HCO, CH_3O on both W33 and W18. The figures relative to the other systems are available in appendix C.

It can be rapidly noticed that there is a limit under which the efficiencies take values of unity; this is the point at which the reaction energy barriers coincide with the value of the diffusion barrier of the fastest hopper from each couple (i.e. E_{diff} =0.35$\times E_{des}$) and it is surface and radical dependent. Of course, the higher the binding energy (CH_3 < HCO < CH_3O < OH < CH_2OH) the higher this limit, meaning that for activation energy values below this threshold, radicals have enough time to react before they separate due to thermal hopping. On the contrary, above this energetic limit, the dependence on temperature becomes more and more important, so that at higher temperatures, higher efficiencies are obtained. Eventually, for sufficiently high activation energies, the reactivity between two radicals become inefficient.

While these plots are very informative, they lack three key points in the Langmuir-Hinshelwood-like surface reactions: (i) the temperature limit after which radicals will certainly not be available on the surface anymore (e.g. a theoretical limit can be set at the "desorption temperature", see § 7.3 for more details, while it could also be the point at which some of the two radicals has been consumed), (ii) the effects of quantum

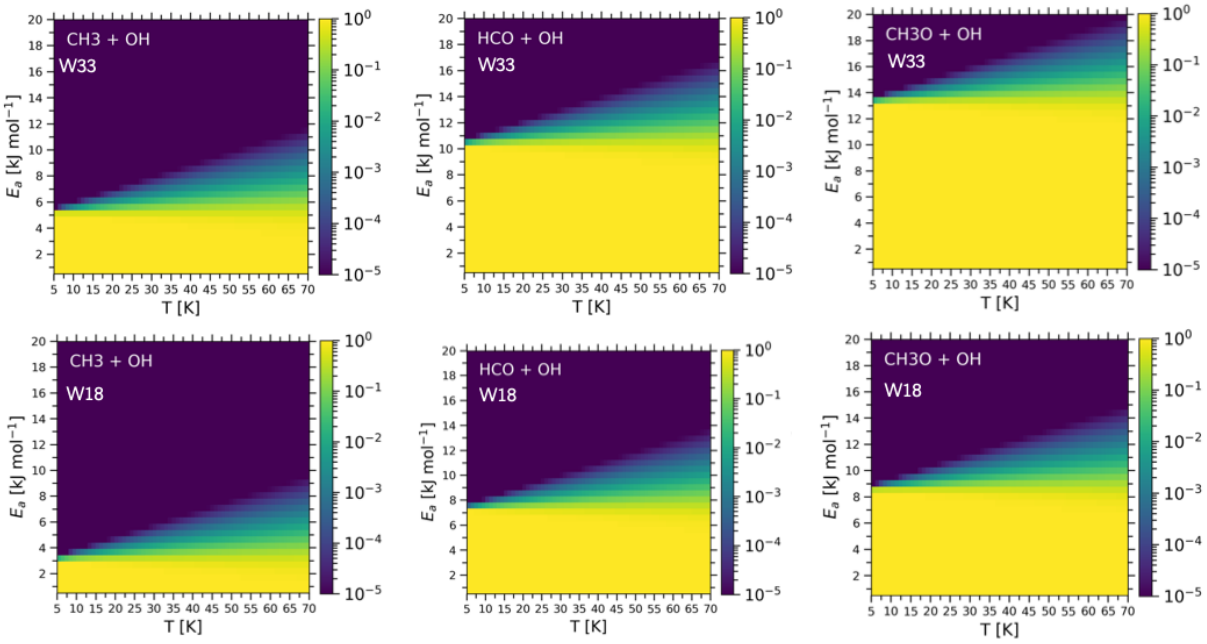

Figure 7.5: *Reaction efficiencies on W33 (upper panels) and W18 (lower panels) as a function of the activation energy and temperature of a subset of the radical-radical systems in Robin T. Garrod et al., 2008 not explicitly studied in this work and for which we guess their efficiency (see text). These calculations do not include tunneling effects.*

tunneling, that may be important for direct H-abstraction reactions, so that the rate constants related to the activation energy barriers become less dependent on temperature and, finally, (iii) the meeting rates, which will modulate the efficiency according to the meeting probability of radicals on the grain surfaces. Such effects are only attainable by more detailed, dedicated modelling.

In summary, in addition to the three considerations from above, one must also consider that the higher the binding energies of the radical couple, the higher the range of activation energy barriers that the reaction can have in order to present high efficiencies, at the expense of a lower meeting rate.

With this information, and bearing in mind the three above considerations, we propose the guessed reactivity properties for each one of these systems in the following paragraphs.

Radical coupling reactions

OH + X: (X = CH_3, HCO, OH, NH, NH_2, CH_3O, CH_2OH) OH has a high binding energy on W33 (44.7 kJ mol^{-1}) and an intermediate one on W18 (24.2 kJ mol^{-1}). Therefore, its diffusion barrier is rather high. For reactions with a radical X that have small diffusion barriers, like CH_3 or NH (the latter only on W18) reactions will take place only if they have small activation energy barriers. For such low binding energy radicals, this might hold as long as they do not experience trapping. On the other hand, if the radical X has also a high diffusion barrier, the reaction efficiencies will be unity even for relatively high activation energy barriers. There might be two cases where reactions could have very high reaction energies, and as a consequence low efficiencies: X=OH/CH_3O, since they both have their radical atom (oxygen) establishing H-bonding.

NH + X: (X = CH_3, HCO, OH, NH, NH_2, CH_3O, CH_2OH) NH has an intermediate to low binding energy depending on the surface environment (13.0 kJ mol^{-1} on W18 and 32.5 kJ mol^{-1} on W33). Therefore, one would expect low energy activation energy barriers on flat surfaces where NH can easily reorient, meaning high efficiencies. On the contrary, the high binding energy on W33 renders NH + X reactions efficient as long as the barrier is not very high, a scenario which is likely not given by any of the possible X radicals based on the experience with the systems we have studied.

NH_2 + X: (X = NH_2, CH_3O, CH_2OH) The NH_2 radical sports high binding energy regardless of the surface environment. Therefore, reactions with other radicals need to have very high energy barriers in order to have low efficiencies. Hence, we expect high efficiencies for any radical X.

CH_3O + CH_2OH Given the special binding structure of CH_2OH with its C atom free from surface interaction, we expect these reactions to have high efficiencies, also given their high binding energies.

Direct H-abstraction reactions

From the list of reactions, only HCO, CH_3O and CH_2OH can donate an H atom. From our experience with the systems in Tab. 7.3, we know that HCO is a very good H-donor, while CH_3O and CH_2OH are not. Reactions where HCO is the H-donor will most likely sport competition between Rc and dHa channels, while tunneling effects will be much more important for reactions where CH_3O is the H-donor. Regarding CH_2OH, its high stability makes energy barriers to be high and mechanisms to be more complex, likely with many energetic reorientation steps. Therefore, overall it is expected to be a non efficient process.

7.6 Conclusions

In this work, we have carried out DFT computations of the reactions on icy surfaces between nine radical-radical systems, postulated to lead to the formation of iCOMs by several astrochemical models based on the R. T. Garrod et al. (2006) scheme. The set of studied systems are HCO + X and CH_3 + X, where X is equal to CH_3, HCO, NH_2, CH_2OH and CH_3O, plus the systems CH_3O + CH_3O and CH_2OH + CH_2OH. We considered both the combination between radicals, leading to the iCOM, and the H-abstraction from one of them, leading to simpler molecules.

In order to simulate the interstellar icy surfaces, we employed two ice cluster models made of 18 and 33 water molecules (W18 and W33), respectively, which we tested in previous works (Joan Enrique-Romero et al., 2019, 2021b; Rimola et al., 2014). The W33 ice model presents a cavity structure, which likely makes it a better representation of interstellar ices than the W18 ice model, which only possesses a rather flat surface because of its limited size. Therefore, in the following, we will only report the conclusions based on the results obtained with the W33 model.

We computed the binding energy of the involved radicals and, for all the possible reactions between the nine radical-radical systems, the reaction energy barriers. We also computed the diffusion energy of each radical, assuming that it is 0.35 times the binding energy. Then, using the definition of reaction efficiency that takes into account the reaction activation energy barrier as well as the radicals diffusion and desorption timescales (Joan Enrique-Romero et al., 2021b), we provided a rough estimate of the reaction efficiency of each reaction using the Eyring equation approximation. The computed reaction efficiencies allows to predict which reactions will lead to iCOMs or to a competition with the H-abstraction channels, or to nothing.

The main conclusions of this work are the following.

(1) radical-radical reactions on icy surfaces are not straightforward nor barrierless in most of the studied systems. Very often, we find that two channels, radical coupling and H-abstraction, are in competition. In a few cases, we find that no reaction can occur between the two radicals. Specifically:

(i) Ethane (C_2H_6), methylamine (CH_3NH_2) and ethylene glycol (CH_2OHCH_2OH) are the only products of their respective radical-radical reactions.

(ii) The formation of glyoxal (HCOCHO), formamide (NH_2CHO), methyl formate (CH_3OCHO) and glycolaldehyde (CH_2OHCHO) is in competition with the H-abstraction products (CO + H_2CO, NH_3 + CO, CH_3OH + CO and CH_3OH + CO, respectively). Very likely, the branching ratio is 1:1, thanks to the capacity of HCO to become an H-donor in the H-abstraction reactions.

(iii) Acetaldehyde (CH_3CHO) and dimethyl peroxide (CH_3OOCH_3) are unlikely to be formed.

(2) The effect of the surface structure on the reaction output is best represented by the different binding energies on the two ice models. On the cavity structure of the W33 model, the binding energies are $\sim$10–80% higher than on the W18 model, due to the larger number/efficiency of intermolecular interactions. This effect is higher for weakly bound species like CH_3, evidencing its capacity to get trapped. Nevertheless, the same

trend on the binding energy of the different radicals is observed on both ice models: $CH_3 < HCO < NH_2 < CH_3O < CH_2OH$.

In addition, some radicals present features worth to emphasize.

(3) CH_3 is usually a very reactive species due to its low binding energy (in many cases its reaction mechanisms comprise a low energy torsion), although there are some exceptions where the mobility of CH_3 is much restricted by the cavity in W33, so that the activation energy barriers can rise up to $\sim$7 kJ mol^{-1}.

(4) CH_2OH presents an interesting binding pattern to the ice surface, which makes its C atom very reactive. The strong interaction of its OH group with the water molecules of the surface fixes its adsorption geometry, leaving the C atom unprotected and highly reactive. We predict that its reactivity with other radicals (with very low energy barriers) and specially with atomic hydrogen will be a major destruction route for this radical on the icy surfaces.

(5) CH_3O has its radical electron on the O atom, which in turn establishes H-bonds with the surface water molecules. This makes this radical to be slightly less reactive than expected and, therefore, high energy barriers appear for the CH_3O + CH_3O reactions. On the other hand, CH_3O can still perform direct H-abstraction reactions as a donor in other situations. However, the likely high reaction energy barriers, due to its intrinsic H–C bond stability (and for the cavity, the higher number of intermolecular interactions), suggest that the H-abstraction reactions are efficient only when considering quantum tunneling effects.

(6) Here we have studied in detail only a subset of radical-radical reactions present in Robin T. Garrod et al. (2008) scheme. For the systems involving the same set of radicals investigated in this work (CH_3, HCO, NH_2, CH_2OH, CH_3O) and, additionally, those involving OH and NH, we have discussed the possible outcomes, based on what we learned from the in-depth studied systems.

As conclusive remarks, we emphasize again that the assumption of the radical-radical combination leading exclusively and always to iCOM is far to be correct and the need to carry out dedicated studies on each radical-radical system in order to assess the outcome of its possible reactions. Also, the present study uses simplistic models of the ice structure as well as a very limited number of binding and reaction sites. More realistic computations should include larger icy grains as well as molecular dynamics simulations involving the encountering plus the reaction of the two radicals, probably possible in a near future thanks to the fast increase of the high performance super-computing facilities. In conclusion, our study probably just scratched the surface of the surface-chemistry on the icy interstellar grains.

Part II

Kinetic calculations on acetaldehyde formation *via* radical–radical surface chemistry

Chapter 8
Introduction to this part

Outline

8.1 Context

Astrochemical models usually assume that radical–radical coupling reactions on the icy dust grains are barrierless, which means that their reaction efficiency upon encounter on the ice surface is unity (i.e. if they meet, they will couple to form the molecule) R. T. Garrod et al., 2006; Robin T. Garrod et al., 2008. However, as it was seen in part I, activation energy barriers may exist and additionally the radical–radical coupling is not the only reaction channel, but direct H-abstraction reactions are also possible. One of such cases is the reaction between CH_3 + HCO, presented in part I by means of static quantum calculations.

Having unity reaction efficiencies in radical–radical surface reactions means that the rate at which radicals meet on the surface controls the reaction rate. In order to calculate the encountering timescale, it is usually assumed that the two reactants need to scan the whole surface before they meet (Tatsuhiko I. Hasegawa et al., 1992). Therefore, the meeting rates depend on the diffusion barriers, and these are assumed to be a fraction f of the barriers of desorption.

In the literature one can find values of f (diffusion-to-desorption barrier ratio) ranging from 0.3 to $\sim$0.8 (e.g. Tatsuhiko I. Hasegawa et al., 1992; Ruffle et al., 2000a), so that some authors use the middle value f=0.5 (R. T. Garrod et al., 2006, 2011; Robin T. Garrod et al., 2008; S. S. Jensen et al., 2021; M. Ruaud et al., 2015; Vasyunin et al., 2017). In the past few years, however, theoretical and experimental works on the diffusion on ices have provided constraints to the f value. For example, Karssemeijer et al. (2014) theoretically showed that the range for f can be narrowed down to 0.3–0.4 for molecules like CO and CO_2. Minissale et al. (2016a) experimentally found that the f ratio of atomic species like N and O is about 0.55, while He et al. (2018) showed that f is 0.3–0.6, being the lower values more suitable for surface coverage lower than one mono-layer, and recently **Kouchi2020_diff_diff** measured the fraction f of CO to be about 0.3 on amorphous solid water. Therefore, values in the range of 0.3–0.4 might be more suitable for molecular species.

8.2 Goals, methods and novelty of the research in this part

In this Part, I present the results obtained in Joan Enrique-Romero et al. (2021b) (Chapter 9). The goals of this research are (i) to do a step forward in acetaldehyde/CO + CH_4 formation from CH_3 + HCO radical coupling reaction and direct H abstraction by studying these reactions from a kinetics viewpoint, (ii) to evaluate the efficiencies of these two reactions, and (iii) to understand the effect of changing the diffusion-to-desorption ratio (f) on these efficiencies.

The main novelty of this work has been the production of chemical kinetics data for radical–radical reactions, for which we have employed RRKM theory (see §2.6). In RRKM theory the whole system, surface + radicals, is considered as a "supermolecule" undergoing a unimolecular reaction (e.g. Rimola et al., 2018), like if the reaction is understood as a conformational change of the supermolecule. This methodology also includes tunneling effects *via* the unsymmetric Eckart potential for H-abstraction reactions.

As a basis, we used our previous results on acetaldehyde/CO + CH_4 formation in Joan Enrique-Romero et al. (2019) in the cavity of the large ice model made of 33 water molecules (Figure 4.2(b)), as it is the most stable adsorption site in our models and we assume that radicals will react in stable sites like this one.

Kinetic calculations require quantum chemical energetic data as much accurate as possible, since the energy barriers enter in an exponential and, therefore, any error on this will be magnified. For this reason, we have performed a benchmark study in order to choose the density functional method that performs better using as a reference CASPT2 calculations. The BHLYP-D3(BJ) functional combined with a triple-ζ quality basis set resulted to be the best method, with errors below 5% at the most, and in 3% average. Therefore, in comparison to Joan Enrique-Romero et al. (2019) we improved (i) the dispersion correction, from D3 with zero-damping to D3 with the Becke-Johnson (BJ) damping, and (ii) the raw electronic energies by performing single point energy calculations at triple-ζ basis set level on the double-ζ optimized geometries for the sake of computational cost.

We also recomputed the radical–surface binding energies and used them to calculate the desorption and diffusion rates. Regarding the latter, we assumed the diffusion barriers to be a fraction (f) of those for desorption. Given the uncertainty on the choice of this fractions, three values for f were used: 0.3, 0.4 and 0.5.

The kinetics for desorption were calculated using the Eyring formula (see eq. 2.39 in §2.6). In order to include entropic effects, the partition functions of the desorption process were calculated: for the situation *prior* to desorption, only the vibrational degrees of freedom were accounted for, while for the situation *post* desorption, the vibrational degrees of freedom were included for the surface and the radical, and the rotational and translational ones were only taken into account for the radical in the gas phase. Thermal corrections following this same scheme were also included for the enthalpies. These entropies and enthalpies were multiplied times the diffusion-to-desorption fraction f when calculating the diffusion rate constants.

Finally, we computed the reaction efficiencies (ϵ) according to eq. 8.1 as follows (see Chapter 9):

$$\epsilon = \frac{k_{aeb}}{k_{aeb} + k_{diff}(i) + k_{des}(i) + k_{diff}(j) + k_{des}(j)}, \tag{8.1}$$

where k_{aeb} is the reaction rate constant calculated with RRKM theory (aeb stands for activation energy barrier) and $k_{diff}(i)$ and $k_{des}(i)$ are the diffusion and desorption rate constants for species i. This equation takes into account the competition between the reaction event and the possibility that reactants diffuse away or are desorbed.

8.3 Summary of the results

The CH_3 + HCO radical coupling reaction has a slightly lower barrier (5.5 kJ mol^{-1}) than that of the direct H-abstraction (7.2 kJ mol^{-1}). Translating this into kinetic terms, we find higher rate constant values for the former reaction at higher temperatures, while at lower temperatures tunneling for the H-abstraction takes over and this reaction becomes much faster than the coupling one.

Constraints to the highest possible temperatures at which these two reactions can take place are derived using the desorption time-scales. We derive the temperature at which each radical would desorb, assuming a time-scale of 10^6 yrs for the process. Since CH_3 has a much lower binding energy than HCO ($\sim$14.2 and $\sim$29.4 kJ mol^{-1}), CH_3 has a temperature limit of 30 K while HCO has it at 68 K. This means that the acetaldehyde/CO + CH_4 formation reactions from CH_3 + HCO can only be operative at temperatures below 30 K in our model.

Regarding the efficiencies, the choice of the diffusion-to-desorption ratio f has dramatic consequences for both reactions:

- For f=0.5 we have constant values of ϵ=1.0 for both reactions.
- For f=0.4, the efficiency of the coupling reaction lies between $\sim$0.8–0.9, and that of the direct H-transfer is equal to 1.0 up to $\sim$22 K, when it starts to decrease.
- Finally, for f=0.3 the efficiencies of both reactions are strongly temperature dependent. At low temperatures and due to the effect of quantum tunneling on the rate constant in the direct H-abstraction reaction, its efficiency is unity under $\sim$14 K and it drops as temperature increases, down to $\sim 10^{-3}$ at 30 K. On the other hand, the efficiency for the radical coupling reaction is negligible at low temperatures, and at 30 K it increases to a maximum value of about 0.01.

In summary, the efficiencies of radical coupling and direct H-abstraction reactions on our ice model are a complex function of the temperature, the diffusion energy of CH_3 and the factor f. For $f \geq$0.4 the efficiencies are close to unity, therefore resulting with a $\sim$1:1 competition between acetaldehyde and CO + CH_4 formation. In contrast, for f=0.3 acetaldehyde formation presents $\epsilon \leq$0.01 and CO + CH_4 formation ϵ lies between unity and 0.001. Therefore, alternative mechanisms towards acetaldehyde are needed. These results have also important consequences in astrochemical modeling.

Chapter 9

Theoretical Computations on the Efficiency of Acetaldehyde Formation on Interstellar Icy Grains

The research presented in this Chapter has resulted in a scientific article:
Enrique-Romero, J., Ceccarelli, C., Rimola, A., Skouteris, D., Balucani, N. and Ugliengo, P.
Published in Astronomy and Astrophysics, 2021.
DOI: 10.1051/0004-6361/202141531

Outline

Interstellar grains are known to be important actors in the formation of interstellar molecules such as H_2, water, ammonia and methanol. It has been suggested that the so-called interstellar complex organic molecules (iCOMs) are also formed on the interstellar grain icy surfaces by the combination of radicals via reactions assumed to have efficiency equal to unity.

In this work, we aim to investigate the robustness or weakness of this assumption. In particular, we consider the case of acetaldehyde (CH_3CHO), one of the most abundant and commonly identified iCOMs, as a starting study case. In the literature, it has been postulated that acetaldehyde is formed on the icy surfaces via the combination of HCO and CH_3. Here we report new theoretical computations on the efficiency of its formation.

To this end, we coupled quantum chemical calculations of the energetics and kinetics of the reaction CH_3 + HCO, which can lead to the formation of CH_3CHO or CO + CH_4. Specifically, we combine reaction kinetics computed with the RRKM (tunneling included) method with diffusion and desorption competitive channels. We provide the results of our computations in the format used by astrochemical models to facilitate their exploitation.

Our new computations indicate that the efficiency of acetaldehyde formation on the icy surfaces is a complex function of the temperature and, more important, of the assumed diffusion over binding energy ratio f of the CH_3 radical. If the ratio f is $\geq$0.4 the efficiency is equal to unity in the range where the reaction can occur, namely between 12 and 30 K. However, if f is smaller the efficiency dramatically crashes: with f=0.3 it is at most 0.01. In addition, the formation of acetaldehyde is always in competition with that of CO + CH_4.

Given the poor understanding of the diffusion over binding energy ratio f and the dramatic effect it has on the formation or not of acetaldehyde via combination of HCO and CH_3 on icy surfaces, model predictions based on the formation efficiency equal to one should to be taken with precaution. The latest measurements of f suggest f=0.3 and, if confirmed for CH_3, would rule out the formation of acetaldehyde on the interstellar icy surfaces. We recall the alternative possibility, recently reviewed, that acetaldehyde could be synthesised in the gas-phase starting from ethanol. Finally, our computations show the paramount importance played by the micro-physics involved in the interstellar surface chemistry and call for extensive similar studies on different systems believed to form iCOMs on the interstellar icy surfaces.

9.1 Introduction

Interstellar dust grains are known to be an essential component of the interstellar medium (ISM) for a large variety of reasons. Among them, dust grains provide the surfaces for chemical reactions that are difficult (or impossible) to take place in the gas phase. An emblematic example is the formation of the most abundant molecule in the universe, H_2, which largely occurs on the grain surfaces (e.g. Hollenbach et al., 1970; Vidali, 2013; Valentine Wakelam et al., 2017). Other important examples are the formation of water (e.g. (F. Dulieu et al., 2010; He et al., 2014; Lamberts et al., 2017a; G. Molpeceres et al., 2018)) and methanol (e.g. Rimola et al., 2014; Tielens et al., 1982; Naoki Watanabe et al., 2002a), which are also abundant molecules predominantly synthesized on the grain surfaces. As a matter of fact, in cold regions, the refractory core of the grains, made up of silicate or carbonaceous material, are coated by icy mantles mostly formed by amorphous water ice synthesized on these surfaces (e.g. Boogert et al., 2015).

As it has been seen in Part I, it has also been suggested that more complex molecules like iCOMs can also be a grain-surface chemistry product as a result of radical–radical coupling reactions (e.g. (Aikawa et al., 2020; Barger et al., 2020; R. T. Garrod et al., 2006, 2009; Herbst et al., 2009b; M. Ruaud et al., 2015)). One crucial step of this theory is the formation of iCOMs from the combination of two radicals when they meet on the grain icy surfaces. In the majority of the current astrochemical models, the reaction is assumed to proceed barrierlessly and without competitive channels.

In Chapters 6 and 7 it was showed that the formation of acetaldehyde (CH_3CHO) on the icy surfaces *via* the coupling of HCO and CH_3 radicals is in competition with the formation of CO + CH_4 *via* direct H-abstraction, with similar activation energy barriers governed by the interactions created between the surface water molecules and the two radicals.

Here, we pursue the above theoretical studies and present new computations to evaluate the efficiency of the radical–radical combination and H-abstraction reactions as a function of the temperature of the icy surfaces with the goal to provide values that can be easily incorporated in astrochemical models. In particu-

(1) $HCO + CH_3 \rightarrow CH_3HCO$
(2) $HCO + CH_3 \rightarrow CH_4 + CO$

lar, here we focus on acetaldehyde (CH_3CHO), one of the most abundant and common iCOM (e.g. Bianchi et al., 2018; Blake et al., 1987; Cazaux et al., 2003; Csengeri et al., 2019; C.-F. Lee et al., 2019; Lefloch et al., 2017; T. Sakai et al., 2018; Scibelli et al., 2020; Vastel et al., 2014), as a study case.

Following Chapters 5, 6 and 7, we here consider the two competing reactions that can arise from the reactivity between HCO and CH_3:

The goal is to evaluate the efficiency of each of the two reactions occurring on the interstellar icy surfaces. To this end, we compute the kinetics of the two reactions, using the previous energetic calculations by Joan Enrique-Romero et al., 2019 (Chapter 6) as a base. In these calculations we we assume that the two radicals are in the most stable energetic configuration prior to reaction, an assumption motivated by the long surface residence timescale (1–10 Myr, the molecular life timescale: e.g. Chevance et al., 2020) that radicals would experience before they become mobile and react with each other.

This Chapter is is organized as follows. The definition of the reaction efficiency and our choices for the various assumptions entering in the computations are discussed in § 9.2. § 9.3 describes the adopted methodology. The results are reported in § 9.4 and we discuss the implications of our new calculations in § 9.5.

9.2 Efficiency of radical-radical reaction products on icy surfaces

Surface-reaction rate definition

Generally, astrochemical models solve the time-dependent equations of the species densities by computing the formation and destruction rates of each species at a given time, both for species in the gas and on the grain surfaces. In particular, the rate R_{ij} of the formation reaction from two reactant species i and j is expressed as $R_{ij} = k_{ij} n_i n_j$, where n_i and n_j are the densities of species i and j, and k_{ij} is the rate constant at a given temperature. For surface reactions the latter is given by (Tatsuhiko I. Hasegawa et al., 1992):

$$k_{ij} = \varepsilon_{ij} \times \frac{R_{\text{diff},i} + R_{\text{diff},j}}{n_d}, \tag{9.1}$$

where ε_{ij} is an efficiency factor which accounts for chemical barriers, n_d is the dust grain density and $R_{\text{diff},i}$ and $R_{\text{diff},j}$ are the diffusion rates for species i and j, respectively. These diffusion rates are defined as $1/t_{\text{diff},k}$, where $t_{\text{diff},k}$ is the time it takes the species k to scan the whole grain (e.g. R. T. Garrod et al., 2006). Thus, the sum $R_{\text{diff},i} + R_{\text{diff},j}$ gives the rate at which species i and j meet on the surface.

Regarding the efficiency factor ε_{ij}, different approaches exist in order to derive it. Tatsuhiko I. Hasegawa et al. (1992) set it to either 1, in barrierless reactions, or to the tunnelling probability, if the reaction has an activation energy barrier and one of the reactants is light enough to tunnel through it. Later models include also the thermal probability for reaction, if there is an activation energy barrier (e.g. R. T. Garrod et al., 2006). However, in the presence of an activation energy barrier, reactants need to be close to each other for a certain amount of time for the reaction to occur (Tielens et al., 1982). In order to take this into account, Chang et al. (2007) redefined the efficiency taking into account the competition between diffusion and desorption of the most mobile species, as follows:

$$\varepsilon_{ij} = \frac{k_{aeb}(ij)}{k_{aeb}(ij) + k_{diff}(i) + k_{des}(i)} \tag{9.2}$$

where $k_{aeb}(ij)$ is the rate constant accounting for the reaction activation energy barrier, which is described by either classical thermal kinetics or quantum tunnelling; (i.e. a frequency times a Boltzmann factor or the tunnelling probability); $k_{diff}(i)$ is the rate constant for the diffusion of the most mobile species and $k_{des}(i)$ is its desorption rate constant. R. T. Garrod et al. (2011) further modified Eq. (9.2) by removing the desorption term and adding the diffusion of the other reaction partner, j, in the denominator.

For reactions involving radicals, ε_{ij} is normally assumed equal to 1 (e.g. R. T. Garrod et al., 2006), as they are considered to react via barrierless exothermic channels.

In this work, we include diffusion and desorption rates of the two reactants, which takes into account both the Chang et al. (2007) and R. T. Garrod et al. (2011) recipes:

$$\varepsilon_{ij} = \frac{k_{aeb}(ij)}{k_{aeb}(ij) + k_{diff}(i) + k_{des}(i) + k_{diff}(j) + k_{des}(j)} \tag{9.3}$$

In practice, the efficiency for the reaction is equal to unity only when the time scale for the reaction to occur ($1/k_{aeb}$) is shorter than the timescales at which reactants remain on the reaction site (the smallest between $1/k_{diff}$(i) and $1/k_{diff}$(j)).

A novel treatment of surface radical-radical reactions rate constants

The novelty of the present work is the estimate of the $k_{aeb}(ij)$ coefficient of radical-radical reactions via statistical kinetics calculations based on the Ramsperger-Rice-Kassel-Marcus (RRKM) microcanonical transition state theory. Briefly, RRKM computations provide unimolecular rate constants, namely the rate at which a system A becomes A′ passing through a transition state (only once). In our case, the system A is the ice-water molecules plus the two adsorbed radicals, namely we consider the water-cluster plus the radicals as a super-molecule isolated from its surrounding. The system A′ is the product of the radical-radical reaction on the icy surface, namely the water-cluster plus either the radical-radical recombination (e.g. React. I) or the H-abstraction (e.g. React. II) products.

Note that, in order to apply the RRKM theory, we implicitly assume that the intra-molecular energy redistribution of the reaction energy is faster than the reaction itself. This assumption is supported by recent ab initio molecular dynamics (AIMD) computations that show that a large fraction (≥50%) of the reaction energy is absorbed by the water ice in less than 1 ps (Pantaleone et al., 2020, 2021). We have checked a posteriori that the timescale of the reactions studied here is indeed longer that 1 ps.

Finally, the specific computational details of our proposed RRKM method are reported in § 9.3.

Desorption and diffusion energies

Equation 9.3 shows that, in addition to the probability $k_{aeb}(ij)$ for radicals i and j to react when they meet on a surface site, the efficiency factor ε_{ij} also depends on k_{des}^{-1} and on k_{diff}^{-1}, which are related to the residence time of the radicals on the surface and on the diffusion timescale of the radicals on the ice, respectively. The diffusion/desorption timescales $t_{\text{diff/des}}$ are given by the classical Eyring transition state theory (TST), in which $t_{\text{diff/des}}$ is inversely proportional to their rate constant, $t_{\text{diff/des}} \propto k_{\text{diff/des}}^{-1}$. According to TST, the general expression of the rate constant k for a unimolecular reaction in thermodynamic equilibrium conditions (like thermal diffusion and desorption) is given by the Eyring equation (eq. 2.38 in § 2.6), which I reproduce here:

$$k = \frac{k_B T}{h} \frac{Q^{\neq}}{Q_R} \exp(-\Delta V^{\neq}/k_B T) \tag{9.4}$$

where $\Delta V^{\neq}$ is the zero point energy-corrected energy barrier, $Q^{\neq}$ and Q_{R} are the total partition functions of the transition state and the initial state (namely, the reactants), respectively, k_B is Boltzmann's constant, T is the surface temperature and h is Planck's constant. Note that we use the classical Eyring equation because, since we are not dealing with light atoms but molecular radicals, tunneling is negligible.

By proper manipulation of equation 9.4, the rate constant becomes expressed as a function of the free energy barrier $\Delta G^{\neq}$ (usually referred to as free energy of activation) at a given temperature:

$$k = \frac{k_B T}{h} \exp(-\Delta G^{\neq}/k_B T) \tag{9.5}$$

in which $\Delta G^{\neq}$ = $\Delta H^{\neq}$ - T$\Delta S^{\neq}$ and where $\Delta H^{\neq}$ is the enthalpy of activation and $\Delta S^{\neq}$ the entropy of activation. These terms contain translational, rotational, vibrational and electronic contributions as they arise partly from the total partition functions Q.

With the adopted quantum chemical approach, the application of the Eyring TST allows us to compute desorption-related data (e.g., desorption activation energies and desorption rate constants) for each radical

through the outcome of these calculations (electronic energies, vibrational frequencies, partition functions, energy contributions, etc.). It is worth mentioning that, since the radicals are physisorbed on the ice surfaces, the energy barriers of the desorption processes coincide with the desorption energies. In the present case, we only account for the electronic and vibrational contributions to both $\Delta H^{\neq}$ and $\Delta S^{\neq}$ to arrive at the radical desorption energies as follows:

$$\Delta H = \Delta E_{electronic} + \Delta ZPE + \Delta E_{vib}(T) + \Delta H_{rot} + \Delta H_{trans} \tag{9.6}$$

and

$$\Delta S = \Delta S_{vib} + \Delta S_{rot} + \Delta S_{trans} \tag{9.7}$$

where the terms are the energy difference between the desorbed and the adsorbed states for the total electronic energy ($\Delta E_{electronic}$), for the zero point vibrational energy corrections (ΔZPE), for the thermal vibrational energy corrections ($\Delta E_{vib}(T)$), for the vibrational entropy (ΔS_{vib}), and for the rotational and translational contributions to enthalpy (ΔH_{rot} and ΔH_{trans}, respectively) and entropy (ΔS_{rot} and ΔS_{trans}, respectively). In this case, since we are dealing with the desorption of the radicals, the translational and rotational contributions arise from only the desorbed (free) radicals. Specific details on the calculation of some of these terms are provided in the appendix D, specifically § D.2. For the sake of simplicity, we will refer to this final desorption energy as E_{des}.

In contrast to desorption, obtaining diffusion-related data with the present calculations is a daunting task, as it requires localizing a large number of transition states for the radical hoping between the different binding sites. Moreover, the use of a relatively small cluster model dramatically constraints the validity of these results because of its limitation in terms of size and surface morphology. Therefore, to obtain a value for the diffusion energy of each radicals, which by analogy we will refer to as E_{diff}, we resorted to what is usually done in astrochemical modeling, that is, E_{diff} is taken to be a fraction f of E_{des}. However, deriving the value of f has proven to be difficult, both theoretically and experimentally. In the published astrochemical models, one can find a quite wide range of adopted f values, from 0.3 to $\sim$0.8 (e.g. Tatsuhiko I. Hasegawa et al., 1992; Ruffle et al., 2000a). Some authors have taken a middle point by setting this ratio to 0.5 (e.g. R. T. Garrod et al., 2006, 2011; Robin T. Garrod et al., 2008; S. S. Jensen et al., 2021; M. Ruaud et al., 2015; Vasyunin et al., 2017).

In the past few years, theoretical and experimental works on the diffusion process of species on ASW surfaces have provided constraints to the f value (see also the more extensive discussion in Sect. 9.5). In a theoretical work, Karssemeijer et al. (2014) showed that the range for the E_{diff}/E_{des} ratio can be narrowed down to 0.3–0.4 for molecules like CO and CO_2. Minissale et al., 2016c experimentally found that the f ratio of atomic species like N and O is about 0.55, while He et al., 2018 showed that f is 0.3–0.6, being the lower values more suitable for surface coverage lower than one mono-layer.

Given the uncertainty on the E_{diff}/E_{des} ratio for CH_3 and HCO, we carried out our calculations for three values: 0.3, 0.4 and 0.5.

Ice model

Regarding the amorphous solid water (ASW) model, there is still little knowledge that constrains the actual internal structure of interstellar ices. Observations suggest that the interstellar water ice is predominantly in the amorphous form (e.g. Boogert et al., 2015; Robert G. Smith et al., 1989, with some exceptions: e.g. Molinari et al., 1999). Many laboratory studies have been carried out to characterise the possible porosity of the interstellar ices. Typically, laboratory experiments produce porous ices of different densities by condensation of water vapour, even though they probably do not reproduce the interstellar water ice, in which water is believed to form *in situ* by hydrogenation reactions of frozen O, O_2 and O_3 (e.g. F. Dulieu et al., 2010; Hama et al., 2013; He et al., 2018; Potapov et al., 2021). In general, porous ices are detected in laboratory via the infrared (IR) signature of dangling OH groups, which are, however, missing in interstellar samples (Bar-Nun et al., 1987; Keane et al., 2001, see also the discussion in e.g. Hama et al., 2013; Zamirri et al., 2018). Several hypothesis have been suggested to explain the absence of the OH dangling signature (Oba et al., 2009; Palumbo, 2006; Palumbo et al., 2010), so that, at the end, there is consensus in the community that interstellar water ices are amorphous and porous in nature, even though many details are missing and we do not have a precise picture of the degree of porosity (e.g. Hama et al., 2013; Isokoski et al., 2014; Potapov et al., 2021).

In order to simulate the interstellar icy surfaces, Joan Enrique-Romero et al. (2019) considered a cluster of 33 water molecules (Figure 4.2(b)). This ice model possesses two major types of surface with respect to the binding capability: a cavity, where species are in general more strongly bonded to the surface, and an elongated side (Joan Enrique-Romero et al., 2019; Rimola et al., 2014, 2018). In this work, we only report the analysis of the reaction occurring in the cavity for the following reason. In astrochemical models, the vast majority of radical-radical reactions take place inside the bulk of the ice (e.g. R. T. Garrod et al., 2006). Therefore, the cavity site is a better representation of the sites where radical-radical reactions occur than that on the elongated side, which would at best describe the ice layer exposed to the gas and where just a tiny fraction of the reactions can occur, considering that the ice is constituted by more than 100 layers (e.g. Aikawa et al., 2020; V. Taquet et al., 2012).

Therefore, in this work, we use the Joan Enrique-Romero et al. (2019) ice model and methodology, but we improve the calculations for a better accuracy of the computed energetics, including dispersion, as described in detail in § 9.3.

9.3 Methodology

Electronic structure calculations

Given the importance of inter-molecular interactions in radical-radical reactions, we recomputed the stationary points of the potential energy surfaces (PES) previously reported by (Joan Enrique-Romero et al., 2019) using the Grimme's D3 dispersion term including the Becke-Johnson damping (D3(BJ)) (Grimme et al., 2011, 2010), this way improving the description of the dispersion forces with respect to the previous work.

All calculations were performed with the GAUSSIAN16 program package (Frisch et al., 2016). A benchmark study showed that the BHLYP hybrid density functional method is the best suited DFT method to study these reactions, with an average error of 3%, and a maximum error of 5.0% with respect to benchmark multi-reference CASPT2 calculations (see appendix D). Thus, stationary points were fully optimised using BHLYP (Becke, 1993a; C. Lee et al.,) combined with the standard 6-31+G(d,p) Pople basis set alongside the D3(BJ) dispersion term (Grimme et al., 2011, 2010). When needed, intrinsic reaction coordinate (IRC) calculations at the optimization theory level were carried out to ensure that the transition states connect with the corresponding minima. To balance the computational cost and chemical accuracy, reaction energetics were then refined by performing full BHLYP-D3(BJ)/6-311++G(2df,2pd) single-point energy calculations on the BHLYP-D3(BJ)/6-31+G(d,p) optimized stationary points. Improving chemical accuracy is a fundamental aspect when aiming at providing kinetic calculations and rate constants (including tunneling effects) (Álvarez-Barcia et al., 2018), as in the present work. Additionally, as shown in (Rimola et al., 2018) and J. Enrique-Romero et al., 2020; Joan Enrique-Romero et al., 2019 (Chapters 6 and 5), DFT is a cost-effective methodology with which a correct description of biradical systems can be achieved by using the unrestricted broken (spin)-symmetry approach (e.g. Neese, 2004, see § 2.4).

All optimized stationary points were characterized by the analytical calculation of the harmonic frequencies as minima and saddle points. Thermochemical corrections computed at BHLYP-D3(BJ)/6-31+G(d,p) were included to the single point BHLYP-D3(BJ)/6-311++G(2df,2pd) potential energy values using the standard rigid-rotor/harmonic oscillator formulae in order to obtain the zero-point vibrational energy (ZPE) corrections.

Kinetic calculations

In order to compute the rate constants for the chemical reactions between the radical pairs, we adapted our in-house kinetic code, based on the RRKM scheme for gas-phase reactions (Dimitrios Skouteris et al., 2018), to the surface plus adsorbed radicals case. First, we obtained the microcanonical rate constant $k_{aeb}(E)$ at a given energy E as:

$$k_{aeb}(E) = \frac{N(E)}{h\rho(E)} \tag{9.8}$$

where $N(E)$ is the sum of states for the active degrees of freedom in the transition state, $\rho(E)$ is the density of states for the active degrees of freedom in the reactant, and h is the Planck constant. Since we aim to simulate a reaction taking place on a solid surface, only vibrational degrees of freedom are taken

into account. Second, the obtained rate constants were Boltzmann-averaged in order to derive the rate constants as a function of the temperature.

For the H abstraction reaction, we took into account tunneling effects adopting the Eckart scheme via the unsymmetric potential energy barrier approach. In order to have a chemical system of reference to compare with, we applied the same method to the well studied reaction H + CO $\rightarrow$ HCO. In this case, the initial structures of the reaction were taken from the theoretical study by Rimola et al., 2014, which were re-optimized at the present work computational level. Here, from the optimized transition state, intrinsic reaction coordinate (IRC) calculations were run assuming a Langmuir-Hinshelwood (LH) like reaction, contrarily to the Rimola et al., 2014 original computations. All stationary points were characterized by frequency calculations, obtaining their (harmonic) vibrational modes and their zero-point energies. More details of these computations can be found in appendix D, specifically § D.4.

9.4 Results

Energetics of the reactions

Table 9.1 presents the 0 K enthalpies (i.e. potential energies plus ZPE corrections) of the studied reactions and Figures 9.1 and 9.2 show the PESs with the molecular structures.

The improvement in the dispersion correction and the refinement of the DFT energy slightly decrease the energy barriers of each one of the reactions to form acetaldehyde and CO + CH_4 by less than 2.5 kJ mol^{-1} with respect to the values quoted by Joan Enrique-Romero et al. (2019). Inversely, the H + CO $\rightarrow$ HCO reaction has a higher barrier, 13.5 kJ mol^{-1}, than that quoted by Rimola et al. (2014), 9.2 kJ mol^{-1}, for two reasons: (i) Rimola et al. assumed an Eley-Rideal reaction (namely, the H atom comes from the gas phase and reacts with frozen CO), while here we have considered a LH mechanism (§ 9.3), and (ii) they did not consider dispersion corrections.

Table 9.1: *Energetics and related parameters of the reactions and desorption and diffusion of the radicals. Top half: Activation ($\Delta H^{\ddagger}$) and reaction (ΔH^{RX}) enthalpies (in kJ/mol) at 0 K (i.e. sum of electronic energies at BHLYP-D3(BJ)/6-311+G(2df,2pd)//BHLYP-D3(BJ)/6-31+G(d,p) and ZPE at BHLYP-D3(BJ)/6-31+G(d,p)) for each radical-radical reaction. Values for the the H + CO $\rightarrow$ HCO reference reaction are also shown. Bottom half: Desorption energies (E_{des}) and desorption (T_{des}) and diffusion (T_{diff}) temperatures (in K) derived using the E_{des} assuming diffusion-to-desorption energy ratios of 0.5, 0.4 and 0.3, see § 9.2.*

Product	$\Delta H^{\ddagger}$	ΔH^{RX}
CH_3CHO	5.5	-324.5
CO + CH_4	7.2	-328.9
HCO	13.5	-91.6
Quantity [K]	CH_3	HCO
E_{des}	1715	3535
T_{des}	30	68
T_{diff} (0.5)	15	32
T_{diff} (0.4)	12	25
T_{diff} (0.3)	9	19

Rate constants

Figure 9.3 shows the rate constants as a function of the temperature of the reactions that form CH_3CHO and CO + CH_4 from the coupling and direct H-abstraction of CH_3 + HCO, respectively. The figure also reports the case of HCO formation from H + CO, for the sake of reference.

The rate constants of the reactions leading to CO + H_2CO and HCO take tunneling into account, which is evidenced by their deviation from linearity. It is also evident the strong temperature dependence of the radical-radical reactions studied, as compared to HCO formation.

The rate constants of the acetaldehyde formation are larger than those of CO + CH_4 formation at temperatures above $\sim$24 K. This is due to its lower barrier and the almost negligible quantum tunnelling contribution to HCO + CH_3 $\rightarrow$ CO + CH_4 at such temperatures. However, as the temperature decreases the tunnelling

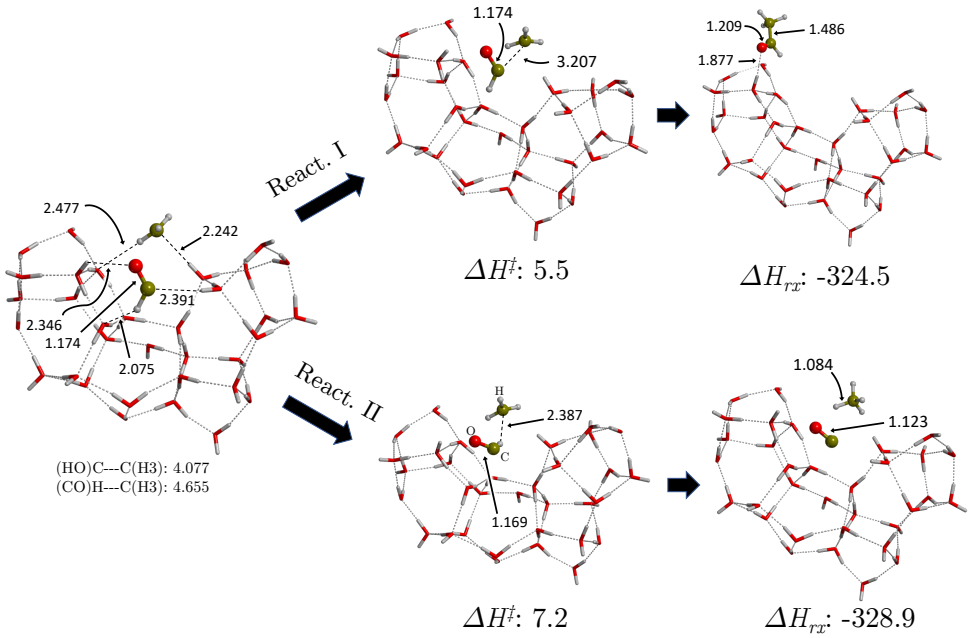

Figure 9.1: *Potential energy surfaces Reacts.* I *and* II. *Geometries and ZPE energy correction was obtained at UBHandHLYP-D3(BJ)/6-31+G(d,p) level, DFT energy was refined at UBHandHLYP-D3(BJ)/6-311++G(2df,2pd) level. Energy units are in kJ mol*$^{-1}$.

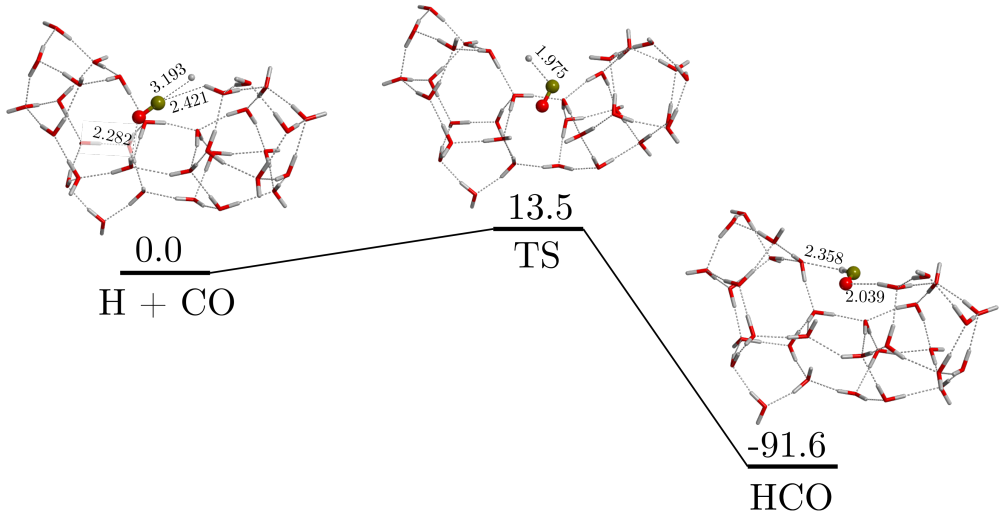

Figure 9.2: *Potential energy surface of the H + CO → HCO reaction, in kJ mol*$^{-1}$. *Energies are corrected for dispersion and ZPE. Geometries and ZPE energies were obtained at UBHandHLYP-D3(BJ)/6-31+G(d,p) level and DFT energies were refined at UBHandHLYP-D3(BJ)/6-311++G(2df,2pd) level. Reactants and products were obtained by running intrinsic reaction coordinate calculations.*

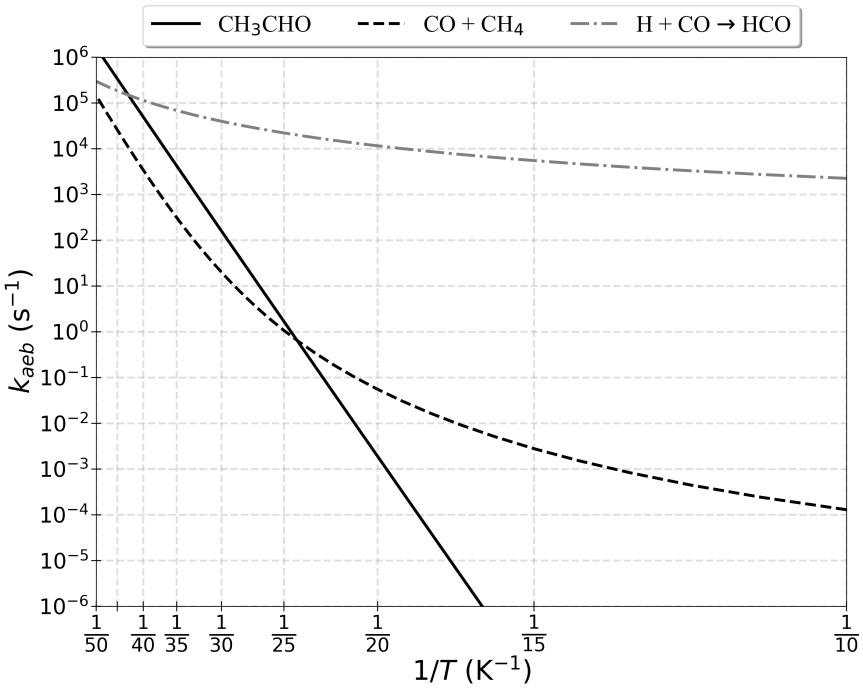

Figure 9.3: *Arrhenius plots, namely rate constants as a function of the inverse of temperature, for the reaction CH_3 + HCO forming acetaldehyde (black solid line) or CO + CH_4 (black dashed line), and for the reaction H + CO → HCO (grey dotted-dashed line), described in the main text.*

probability takes over deviating the rate constant of CO + CH_4 formation from linearity, becoming faster than the formation of acetaldehyde. On the contrary, HCO formation has a much weaker temperature dependence and higher rate constants over the considered temperature range. This is the result of the dominant strong quantum tunnelling of the H atom through the reaction barrier, in agreement with the literature results (e.g. Andersson et al., 2011; Rimola et al., 2014).

In order to facilitate the introduction of the new rate constants in astrochemical models, we fitted the reactions rate constants with the standard formula:

$$k_{aeb}(T) = \alpha \left(\frac{T}{300K}\right)^{\beta} \exp(-\gamma/T) \tag{9.9}$$

The values of α, β and γ are listed in Table 9.2.

Desorption and diffusion temperatures

Table 9.1 reports the computed E_{des} and the temperature for desorption T_{des} and diffusion T_{diff} derived assuming a half-life of 1 Myr. E_{des} values are obtained at BHLYP-D3(BJ)/6-311++G(2df,2pd)//BHLYP-D3(BJ)/6-31+G(d,p) level following the procedure explained in § 9.2, which moreover are corrected for deformation and basis set superposition energy. The T_{des} and T_{diff} values are obtained by using the standard equation for the half-life time, $t_{1/2}=\ln(2)/k_{diff/des}(T)$. These timescales provide an estimation of the characteristic temperatures for desorption and diffusion of the two radicals, CH_3 and HCO, involved in the formation of acetaldehyde on the icy surface.

Finally, note that our E_{des} are consistent with those computed by Ferrero et al., 2020 on a substantially larger ASW ice model. Specifically, our E_{des} in Table 9.1 lies in the high end of the Ferrero et al. range. On the contrary, and as already discussed in Ferrero et al., 2020, our E_{des} are different than those reported in the astrochemical databases KIDA[1] and UMIST[2], often used by modellers. Unfortunately, no experimental

[1] http://kida.astrophy.u-bordeaux.fr/
[2] http://udfa.ajmarkwick.net/

Table 9.2: *Rate constants k_{aeb} (in s^{-1}) and efficiency ε of the two possible reactions between HCO and CH_3. For each reaction, we report the values of α, β and γ of the rate constant k_{aeb} and the efficiency ε calculated assuming E_{diff}/E_{des} equal to 0.5, 0.4 and 0.3 (first column). The last three columns report the values of k_{aeb} and ε at 9, 20 and 30 K.*

E_{diff}/E_{des}	Rate constant	Temperature [K]	α [s^{-1}]	β	γ [K]	9 K	20 K	30 K
			Reaction (1): HCO + CH_3 $\rightarrow$ CH_3CHO					
	k_{aeb}					2.7×10^{-21}	1.9×10^{-3}	160.5
		9–30	3.1×10^{12}	0.70	663			
	ε					1.0	1.0	1.0
0.5		9–19	1.0	0.0	0.0			
		19–26	0.99	-3.4×10^{-3}	0.06			
		26–30	0.98	-0.01	0.28			
	ε					0.88	0.81	0.81
0.4		9–13	0.43	-0.21	0.28			
		13–30	1.0	0.14	-3.4			
	ε					4.9×10^{-8}	7.6×10^{-3}	0.01
0.3		9–30	3.3	0.12	161.2			
			Reaction (2): HCO + CH_3 $\rightarrow$ CH_4 + CO					
	k_{aeb}					6.8×10^{-5}	0.05	20.1
		9–15	6.1×10^{9}	10.4	-39.7			
		15–30	1.7×10^{23}	25.9	-274			
	ε					1.0	1.0	1.0
0.5		9–24	1.0	0.0	0.0			
		24–28	0.83	-0.12	2.79			
		28–30	0.53	-0.44	11.4			
	ε					1.0	1.0	0.35
0.4		9–21	1.0	0.0	0.0			
		21–25	7.4×10^{-11}	-13.8	278.8			
		25–30	3.2×10^{-6}	-5.8	53.3			
	ε					1.0	0.02	1.5×10^{-3}
0.3		9–15	0.96	-0.01	0.02			
		15–19	2.4×10^{-76}	-84.9	1205.1			
		19–30	2.4×10^{7}	19.9	-660.4			

data on the CH_3 and HCO E_{des} desorption energy exist, to our best knowledge.

9.5 Discussion

Formation of acetaldehyde versus CO + CH_4

We used the results of our new calculations (Sect. 9.4) of the CH_3 + HCO reaction kinetics, desorption and diffusion rate constants to compute the efficiency ε (Eq. 9.3) of the two channels leading to the formation of either CH_3CHO or CO + CH_4. As discussed in Sect. 9.2, given the uncertainty on its value, we considered three cases for the E_{diff}/E_{des} ratio f: 0.3, 0.4 and 0.5. Figure 9.4 shows the resulting ε as a function of the temperature and Table 9.2 reports the α, β and γ values obtained by fitting the ε curves with Eq. (9.9), for the three cases of f.

Note that, although we computed the efficiency of the reactions in the 5–100 K range, they will only take place as long as one of the two radicals can diffuse and scan the ASW sites and both radicals stay on the reaction site, namely they do not desorb (see Table 9.1). Consequently, the upper limit to the temperature where the CH_3CHO and CO + CH_4 formation reactions take place is set by the desorption of CH_3, as it has a lower desorption energy than HCO (30 and 68 K, respectively, see Table 9.1). Likewise, the lower limit is also set by the CH_3 diffusion energy only, which is equal to 15, 12 and 9 K for f equal to 0.5, 0.4 and 0.3, respectively. In the case of f equal to 0.5, HCO starts to be mobile when CH_3 has already sublimated, so that the efficiency of the reaction depends on CH_3 E_{diff} only. Conversely, for f equal to 0.4 and 0.3, the

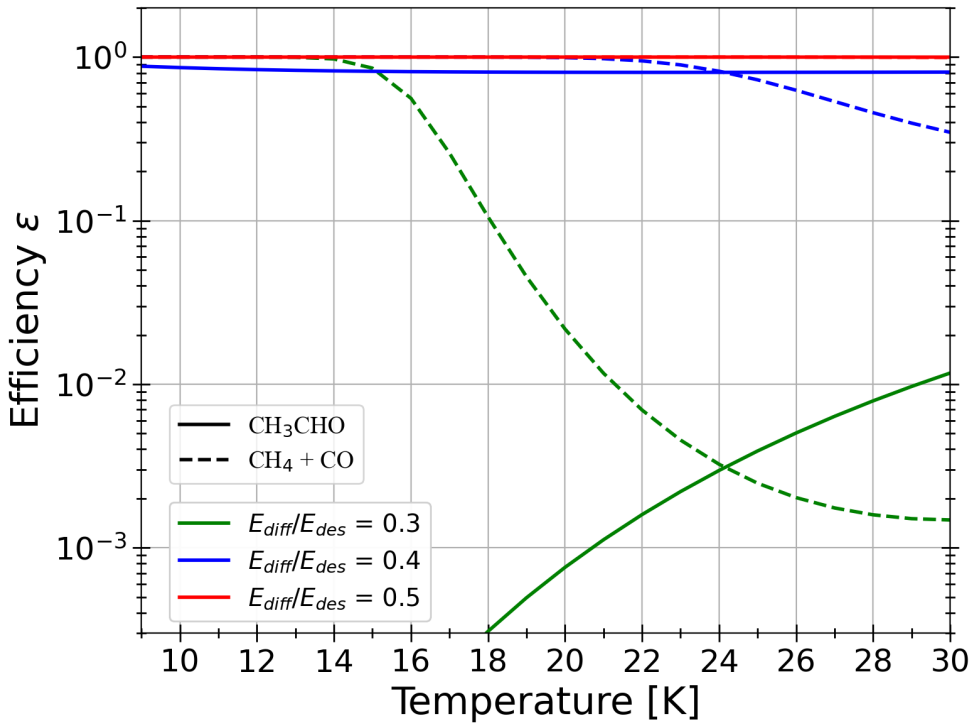

Figure 9.4: *Reaction efficiency ε (Eq. 9.3) of the reaction CH_3 + HCO leading to either CH_3CHO (solid lines) or CO + CH_4 (dashed lines) as a function of the temperature. The computations were obtained adopting three different E_{diff}/E_{des} ratios: 0.3 (green), 0.4 (blue) and 0.5 (red). Note that, for E_{diff}/E_{des}=0.5 the CH_3CHO and CO + CH_4 (red) curves overlap, namely they are constant and equal to 1.*

temperatures at which HCO and CH_3 can diffuse overlap, so that both species contribute to the denominator of Eq. (9.3).

Formation efficiency: For both reactions, formation of CH_3CHO and CO + CH_4, the efficiency ε is about 1 in the 9–15 K range regardless of the f value (between 0.3 and 0.5) with one exception, acetaldehyde formation with f=0.3, which starts at very low efficiency values and monotonically increases. For f=0.5, either reactions have efficiencies of about unity in the whole range of temperatures (up to 30 K). For f=0.4, formation of CO + CH_4 distances from unity at temperatures above $\sim$ 22 K, going into lower values so that at 30 K it reaches ε $\sim$0.3, while the efficiency of acetaldehyde formation stays about unity up to 30 K, where it takes a value of $\sim$0.8. On the other hand, for f=0.3 things are very different. The efficiency of CO + CH_4 crashed at higher temperatures, reaching values of about 0.001 at 30 K, while that of acetaldehyde never goes above $\sim$ 0.01.

This is because, for relatively large f values ($\geq$0.4), the most mobile radical, CH_3, moves slowly and the two radicals have plenty of time to react when they meet before one of them moves away: ε is, therefore, close to unity. However, when the timescale for diffusion becomes smaller than the reaction timescale (i.e. $k_{diff} \gg k_{aeb}$), CH_3 moves away before having the time to react and the efficiency drops below unity. In practice, the smaller the E_{diff}/E_{des} ratio, the faster CH_3 moves and the smaller ε. However, since both k_{diff} and k_{aeb} have an exponential dependence on the temperature, a change in behavior occurs when the reaction activation energy γ (Eq. (9.9)) is similar to E_{diff} and the efficiency ε strongly depends on the temperature. For the formation of acetaldehyde, γ=663 K (Table 9.2) and, therefore, the change of behavior occurs when E_{diff}/E_{des} $\sim$0.40. In these cases, the lower the temperature, the larger k_{diff} with respect to k_{aeb} and the smaller ε, as shown in Fig. 9.4. Similar arguments hold also for the HCO + CH_3 $\rightarrow$ CO + CH_4 reaction. The only difference is that, at low temperatures, k_{aeb} deviates from the exponential law because of the kicking in of the tunneling effect that greatly increases k_{aeb} (giving a negative γ values: see Table 9.2).

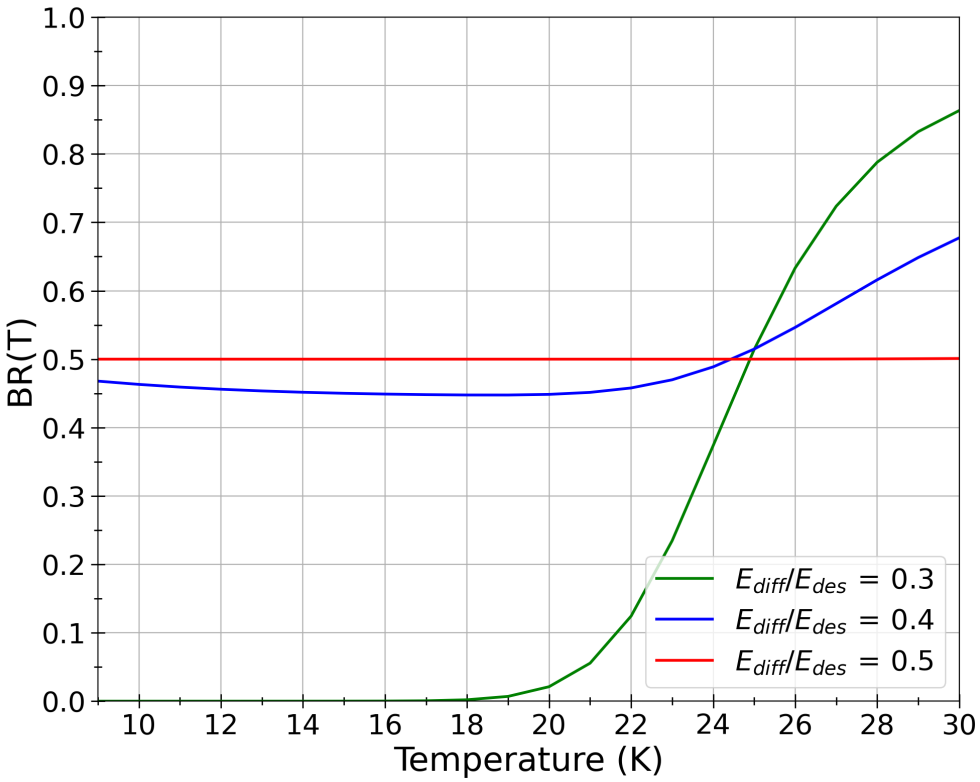

Figure 9.5: *Branching ratio $BR(T)$ of the formation rate of the CH_3CHO over CO + CH_4 (Eq. 9.10) as a function of the temperature in the range where the reactions can occur, namely below 30 K (see text), for E_{diff}/E_{des} equal to 0.3 (green), 0.4 (blue) and 0.5 (red).*

Since the tunneling is more efficient for decreasing temperature, the k_{aeb}/k_{diff} ratio decreases at increasing temperatures and, consequently, ε decreases.

Branching ratio: Figure 9.5 shows the branching ratio BR of the formation rate of CH_3CHO over CO + CH_4 as a function of the temperature, for the three f values (0.5, 0.4 and 0.3). The BR is obtained integrating Eq. (9.1) from the temperature at which CH_3 starts to be mobile T_0, a value that depends on the assumed f (see above), to the temperature T. It holds:

$$BR(T) = \frac{\int_{T_0}^{T} dT' \, \varepsilon_{CH_3CHO} \times (R_{diff,CH_3} + R_{diff,HCO})}{\int_{T_0}^{T} dT' \, (\varepsilon_{CH_3CHO} + \varepsilon_{CO+CH_4}) \times (R_{diff,CH_3} + R_{diff,HCO})} \tag{9.10}$$

The different effects commented above can be clearly seen in Fig. 9.5 and can be summarised as follows. For $f = 0.5$, the branching ratio BR is constant and equal to 0.5, namely the HCO + CH_3 reaction leads to acetaldehyde and CO + CH_4 in equal quantities. For $f = 0.4$, BR lies in the range 0.4–0.5 up to 25 K and then it becomes larger, because the the tunneling gain in the CO + CH_4 production at low temperatures vanishes. For $f = 0.3$ (and, in general, ≤ 0.4), BR is <0.5 at temperatures less than ∼25 K and rises to ∼0.9 at 30 K.

In other words, for $f \geq 0.4$, acetaldehyde and CO + CH_4 are in approximately equal competition in the range of temperatures where the HCO + CH_3 reaction can occur. However, for $f < 0.4$, acetaldehyde is a very minor product for temperatures lower than about 25 K and flips to be a major product above it.

The experimental point of view

Experiments studying the formation of acetaldehyde from radical-radical coupling date back to the 1990s (Hudson et al., 1997). They are mainly based on energetic (UV or particles) irradiation of different H_2O,

CO, CH_3OH and CH_4 ice mixtures e.g. Bennett et al., 2005; Martıín-Doménech et al., 2020; Karin I. Öberg et al., 2010. In relation to experimental acetaldehyde formation on grain surfaces, Bennett et al. (2005), after irradiation of a CO:CH_4 ice mixture, detected acetaldehyde and predicted that the orientation of the CH_3 and HCO radicals are crucial in the efficiency of the reaction. On the other hand, Martıín-Doménech et al. (2020) conducted laboratory experiments on the formation of acetaldehyde via the CH_3 + HCO reaction, concluding that this channel is not efficient enough to reproduce the astronomical observations.

As discussed by various authors, although laboratory experiments are primordial in suggesting possible mechanisms operating in the ISM and, specifically, the possible formation routes of molecules on the interstellar grain surfaces, they cannot provide the exact ISM conditions or a detailed description of the mechanisms at the atomic level. Despite this, the improvement of radical detection methods, such as the electron paramagnetic resonance (EPR) technique, will help to clarify the role of radicals generated in interstellar ice analogues (e.g. Zhitnikov et al., 2002). In this respect, therefore, theoretical computations as those reported in this work constitute a complementary, if not unique, tool to understand the interstellar surface chemistry.

Astrophysical implications

In astrochemical models, it is generally assumed that reactions between radicals on the surface of interstellar ices are barrierless and, consequently, that their efficiency is equal to 1 (Sect. 9.2). In addition, it is also often assumed that there are no competition channels to the production of iCOMs. At variance with these simple assumptions, our new calculations presented in Sect. 9.5, indicate that, at low ($\leq$ 15 K) temperatures, the efficiency of the acetaldehyde formation is close to unity, for a E_{diff}/E_{des} ratio f $\geq$0.40. However, there is a competing channel leading to CO + CH_4, for which the efficiency is also equal to 1, so that, at low temperatures and for f $\geq$0.40 the two channels are equally probable. The acetaldehyde formation efficiency remains close to unity in the temperature range where the reaction can occur, namely at $\leq$ 30 K, for f $\geq$0.40. However, the situation drastically changes for f $<$0.40. Specifically, for $f = 0.3$, the efficiency of acetaldehyde formation crashes to very low values and increases with temperature to a maximum of 0.01 at 30 K. Similarly, the formation of CO + CH_4 drops to 1.5×10^{-3} at 30 K.

Therefore, two major messages come out from our calculations: (1) the efficiency of the formation of acetaldehyde from the HCO + CH_3 reaction on icy surfaces is a complex function of the temperature and of the CH_3 diffusion energy E_{diff} (Fig. 9.4) and (2) the acetaldehyde formation receives competition with CO + CH_4 formation, which cannot be neglected and whose efficiency is also a complex function of temperature and E_{diff} (Fig. 9.5).

While the dependence on the temperature and the importance of the competition of other products were already recognised (Joan Enrique-Romero et al., 2019), the paramount importance of the diffusion energy E_{diff} in the radical-radical reactions efficiency was not appreciated, at least not at the extent indicated by this study (because of the assumption of astrochemical models that the efficiency of the radical-radical reactions on grains is 1). Penteado et al., 2017, for example, carried out an extensive study of the surface chemistry on the binding energies (namely, our E_{des}) showing how critical they are. Our new study suggests that E_{diff} is as much if not more crucial in the reactions involving two radicals on ASW.

What makes the situation actually critical is that, while studies of the binding energy of radicals can and have been estimated in experimental and theoretical works (e.g. see the recent works by Ferrero et al., 2020; Penteado et al., 2017), evaluating the diffusion energy of multi-atomic radicals on cold icy surfaces has proven to be extremely complicated and, to the best of our knowledge, no experimental or theoretical studies exist in the literature (see also e.g. Cuppen et al., 2017; Potapov et al., 2021). Indeed, as mentioned above, obtaining E_{diff} experimentally is hitherto hampered by technical limitations on the instrumentation used to detect the radicals (i.e., EPR measurements). In relation to theoretical investigations, this lacking in bibliography is due to the convergence of methodological difficulties that make the study of diffusion with computational simulations intrinsically complex (but also compelling). Diffusion can currently be studied by means of molecular dynamics (MD) or kinetic Monte Carlo (kMC) simulations. With the first, to obtain a sufficient representativeness of the species diffusion, long simulation time-scales are mandatory. This in practice means to adopt classical force fields, in which the electronic structure of the systems is missing. However, radicals are open-shell species (with at least one unpaired electron) and accordingly electrons have to be accounted for. Thus MD simulations should be grounded within the quantum mechanics realm,

which are much more expensive than the classical ones, making the MD simulations unfeasible. The alternative would be the adoption of kMC simulations. However, these simulations require building a complete network of the site-to-site radical hopping, in which for each hopping the corresponding rate constant has to be known *a priori*. This actually means to localize for each hopping the corresponding transition state structure (at a quantum chemical level), in which by using a realistic ASW model (i.e., large, amorphous and accordingly plenty of binding sites) makes the problem unpractical.

Usually, astrochemical models assume that the radical E_{diff} is a fraction f of E_{des} and the value f is derived from computations and experiments on species such as CO, CO_2, H_2O, CH_4 and NH_3 (e.g. Cooke et al., 2018; Ghesquière et al., 2015; He et al., 2017, 2018; Karssemeijer et al., 2014; Kouchi et al., 2020; Lauck et al., 2015; Maté et al., 2020; Mispelaer et al., 2013; Pedersen et al., 2015). These studies give a value for f between 0.3 and 0.6, as mentioned in Sect. 9.2. However, rigorously speaking, the experiments do not necessarily measure the same diffusion processes as in interstellar conditions, for at least the reasons of the surface coverage (He et al., 2018) and its dependence of the nature of the ice, specifically its degree of porosity (Maté et al., 2020), which is poorly known in the case of interstellar ices. As a matter of fact, using experimental and a theoretical Monte Carlo code, Maté et al., 2020 found that "the microscopic diffusion is many times faster than the macroscopic diffusion measured experimentally". Most recently, Kouchi et al., 2020 obtained a direct measurement of the diffusion energy of CO and CO_2 on ASW, using the transmission electron microscopy (TEM) technique, which allows a direct measurement of the surface diffusion coefficients (against the often used technique of IR spectroscopy, which only indirectly estimates the diffusion energy). Kouchi and coworkers found an f ratio equal to 0.3.

We have seen that, in the case of acetaldehyde, this uncertainty on f has a dramatic effect. If f is $>$0.4, the efficiency of acetaldehyde formation is equal to 1 and it is about equal to that of the CO + CH_4 formation. On the contrary, if f is equal to 0.3, then the efficiency of acetaldehyde formation (and CO + CH_4) crashes, to a maximum value of 0.02. The most recent measurements by Kouchi et al., 2020 point out the latter case as the most probable. If the value f=0.3 is confirmed, then acetaldehyde is unlikely to be formed on the interstellar icy grain surfaces.

One could be tempted to use the astronomical observations against the astrochemical model predictions to add constraints to the f value in (real) interstellar ices. Of course, given the large number of parameters associated with the astrochemical models it could be a dangerous exercise. Nonetheless, we can analyse two cases, as illustrative examples. Barger et al. (2020) compared the predictions of their model, where the formation of acetaldehyde is dominated by the reaction CH_3 + HCO assumed to have ε=1, with the observations towards various hot cores and found that in two of them, NGC 7538 IRS 1 and W3(H_2O), their model overproduces the acetaldehyde column densities by more than a factor 10^3 with respect to the observed ones. If f is equal to 0.3, introducing our new values for ε could possibly cure this mismatch. On the contrary, J. K. Jørgensen et al. (2016) found a good agreement between the observed abundances of acetaldehyde in IRAS16293B and SgrB2(N) and those predicted by the Robin T. Garrod (2013) model. In this case, the agreement would point to $f \geq 0.4$. In other words, our new computations might solve the mismatch observed towards NGC 7538 IRS 1 and W3(H_2O) if $f = 0.3$, but they would create a mismatch on the observations towards IRAS16293B and SgrB2(N), or viceversa. Alternatively, it is possible that f varies in different sources, belonging to different environments. For example, one could think that sources in cold quiescent regions have ices different, more or less porous, from those in warm and chaotic ones. The two examples discussed above, unfortunately, do not lead to a coherent behavior, as, for example, IRAS16293B and SgrB2(N) could not belong to more different environments.

In conclusion, the acetaldehyde formation by radical-radical recombination on the ices is such a strong function of the diffusion energy, likely linked to the nature of the ice, that a little variation of the E_{diff}/E_{des} (by 0.1) value can shift the efficiency from 1 to less than 0.01. The most recent estimates of E_{diff}/E_{des} suggest a value of 0.3 (Kouchi et al., 2020), which would make the formation of acetaldehyde on the grain surfaces unlikely. Anyway, the important message here is that astrochemical model predictions should be taken with a certain precaution. On the contrary, our new computations clearly show the huge importance of better knowing the microprocesses involved in the radical-radical chemistry on the icy interstellar grains and the urgent need of extensive studies, similar to the one presented here, on different systems believed to form iCOMs on the interstellar icy surfaces.

For the sake of completeness, the formation of acetaldehyde via radical-radical reactions on surfaces with lower binding energies such as solid CO could have a higher efficiency, due to the low radical–surface

interactions (Lamberts et al., 2019). Finally, it is worth reminding that acetaldehyde can alternatively be synthesised in the gas-phase (e.g. Charnley, 2004; De Simone et al., 2020; Vastel et al., 2014). Recently, Vazart et al., 2020 reviewed the gas-phase routes leading to acetaldehyde and found that, very likely, the dominant one is that starting from ethanol, the so-called ethanol tree (Dimitrios Skouteris et al., 2018). In particular, the ethanol tree route reproduces quite well both the acetaldehyde and glycolaldehyde abundances in the sources where ethanol was also observed, including IRAS16293B (Vazart et al., 2020).

9.6 Conclusions

In this work, we report new computations on the energetics and kinetics of the reaction HCO + CH_3, which can lead to the formation of either acetaldehyde or CH_4 + CO. Specifically, we compute the rate constants of both reactions as a function of temperature as well as the efficiency of the formation of acetaldehyde and CH_4 + CO, respectively, combining reaction kinetics at RRKM (tunneling included) with diffusion and desorption competitive channels. We provide analytical formulae so that the computed rate constants and efficiency can be easily introduced in astrochemical models.

The main conclusions of our study are the following.

1. The HCO + CH_3 reaction can only occur when the surface temperature is lower than 30 K, because CH_3 desorbs at larger temperatures.

2. Our computations suggest that acetaldehyde is not the dominant product for the reaction HCO + CH_3. The efficiency ε of its formation strongly depends on the E_{diff}/E_{des} ratio, providing dramatic variations between 0.3-0.5 values, the most usually used values in astrochemical models.

3. At low ($\leq$ 15 K) temperatures, ε is close to unity for both the formation of acetaldehyde and its competing CO + CH_4 channel for $f \geq$0.4, while only the efficiency of CO + CH_4 is unity at these temperatures for $f = 0.3$ thanks to quantum tunnelling. The efficiency of acetaldehyde formation remains unity in the range of temperatures where the reaction can occur ($\leq$30 K) for $E_{diff}/E_{des} \geq$0.40. For lower E_{diff}/E_{des} ratios, ε becomes $\ll$1 and increases with increasing temperature: in the case of E_{diff}/E_{des}=0.3, it reaches a maximum of $\sim$0.01 at 30 K. Conversely, the efficiency of the formation of CO + CH_4 increases with decreasing temperature because of the tunneling.

4. These variant ε values as a function of E_{diff}/E_{des} go against the assumption made in many astrochemical models, in which ε is equal to 1. This might have a substantial impact on the acetaldehyde abundance predicted by these models, which may overestimate it by a few orders of magnitude.

5. We discussed the example of IRAS16293B and suggested that, in this object, acetaldehyde is likely synthesized by a gas-phase reaction route that starts from ethanol.

Finally, this new study calls for specific similar computations on the radical-radical reactions assumed to form iCOMs in astrochemical models as assuming that they have efficiency ε equal to 1 and are the only reaction product could be highly misleading.

Part III

Reaction energy dissipation simulations

Chapter 10
Introduction to this part

Outline

10.1 Context

The detection of iCOMs in cold ($\sim$ 10 K) bodies of the ISM (Bacmann et al., 2012; Cernicharo et al., 2012; Jaber et al., 2014; Jiménez-Serra et al., 2016; Vastel et al., 2014) has challenged the surface chemistry paradigm for iCOM formation (mechanism 2 from Figure 1.7) as it needs warm conditions ($\sim$ 30 K) in order to allow the diffusion of radicals on ice surfaces (R. T. Garrod et al., 2006). One of the proposed alternatives is that simple ice components like methanol are released into the gas phase, where they participate in cold gas phase chemistry, thanks to some non-thermal mechanism (Balucani et al., 2015; Vasyunin et al., 2013).

One of such mechanisms is chemical desorption (CD) (Duley et al., 1993; R. T. Garrod et al., 2007; Minissale et al., 2014b, 2016c; Takahashi et al., 2000), which is proposed to play a major role in cold core complex chemistry over other non-thermal desorption mechanisms[1] (Vasyunin et al., 2017). The idea is rather simple: the energy released by an exothermic reaction can induce the desorption of the newly formed product. Ice surfaces can act as third bodies, and therefore absorb and dissipate part of the nascent reaction energy leaving some that could be used to break the bonds of the new molecule with the surface. However, if the ice surface absorbs too much energy, this could hinder the desorption of the formed species or could induce the desorption of volatile molecules belonging to the ice found nearby the reaction site. In other words, the reaction energy is generally partitioned among the product and the surface, and the degree of such a partitioning can eventually drive the CD of the formed species. Astrochemical models typically use CD efficiencies (i.e. the fraction of molecules non-thermally desorbed per chemical reaction) in the range of 1–10% (e.g. R. T. Garrod et al., 2007; Vasyunin et al., 2013, 2017), although the values for these efficiencies are highly controversial.

CD has been experimentally characterized on a number of surfaces and for a number of reactions, realizing that its efficiency depends on the nature of the product and the surface where it is formed. Indeed, in some cases this efficiency was found to be high. For example, Oba et al. (2018) found CD desorption efficiencies of $\sim$60 % for H_2S formation on ASW ices and François Dulieu et al. (2013) found very high CD efficiencies for water formation *via* hydrogenation of OH radicals on silica surfaces ($<$90 %). On the contrary, other studies show that CD can actually be very inefficient. For example, François Dulieu et al. (2013) also found very low chemical desorption efficiencies ($<$ 10%) for other hydrogenation reactions in the water formation reaction sequence on silica: O_2 + D $\rightarrow$ DO_2, DO_2 + D $\rightarrow$ D_2O_2, D_2O_2 + D $\rightarrow$ D_2O + OD. Similarly, He et al. (2017) found that the H-addition reaction to O_3 producing OH and O_2 on non-porous ASW ices causes little O_2 desorption ($\leq$11%). Regarding the formation of formaldehyde and methanol through the successive hydrogenation of CO, Chuang et al. (2018) found almost no CD per incident H atom (lower than 2%) on CO, H_2CO and CH_3OH ices.

Minissale et al. (2016b) reviewed and performed experiments on CD of a number of reactions, including O + O_2 $\rightarrow$ O_3 Minissale et al., 2014a,b, 2013, 2016b, the different steps of water formation (Chaabouni et al., 2012; François Dulieu et al., 2013), N + N $\rightarrow$ N_2, among others, exploring different surfaces (when possible) like non porous amorphous solid water ice, amorphous silicates and oxidized graphite. They showed that the CD efficiency depends on three major factors: the reaction formation energy, the binding energy of the adsorbate and the nature of the substrate. CD is more efficient for small molecules with low binding energies. Additionally, CD on hard surfaces like oxidized graphite can be qualitatively understood as an elastic collision between the excited product and the surface, while on water ice it is much more complex and less efficient. The reduced CD on water ices is attributed to the fast energy transport of water thanks to its H-bonding network, for which the elastic collisions model cannot be applied.

Fewer theoretical works have studied the dissipation and the CD process. Fredon et al. (2018, 2017) studied the relaxation of translationally excited (50–500 kJ mol^{-1}) CO_2, water and methane molecules on crystalline and amorphous water ices, in order to investigate the chemical desorption and non-thermal diffusion of this species. It was assumed that these kinetically excited molecules where readily been formed, so that the reaction energy has been entirely channeled into translation degrees of freedom. These authors found that the desorption probability depends on the injected energy and the species binding energies (see also §3.5), and not on the mass of the species as suggested by Minissale et al. (2016b).

[1] Other non-thermal mechanisms are CR spot heating (Tatsuhiko I. Hasegawa et al., 1992; Leger et al., 1985) and UV-induced photodesorption (Bertin et al., 2013, 2016; Fayolle et al., 2011).

Takahashi et al. (1999a,b) investigated the formation of H_2 on ASW ices by means of classical molecular dynamics. They simulated many processes involved in the formation of molecular hydrogen on surfaces, including the sticking probability of H atoms, their diffusion, their reaction and their desorption as a consequence of the liberated energy (i.e. following CD). H atoms from the gas phase can diffuse for about 60–140 Å, and if they loose enough kinetic energy they can remain trapped in deep binding wells. In those cases where H_2 was formed, the product was observed to be ejected into the gas phase quickly (in 400–600 fs) with high vibrational states (6–9 vibrational levels for ice temperatures of 10 K) as the ice surface was found to dissipate little energy ($\sim$3–5% of the total H_2 formation energy, about 458.1 kJ mol^{-1} in their simulation). Later on, the same authors (Takahashi et al., 2000) studied the possibility that a CO molecule could be non-thermally desorbed as a consequence of a H_2 molecule formed nearby. They found that the closest vicinity of the reaction site (distances less than 4 Å) increases its temperature by about 20 K and about 10 K for distances of 4–6 Å. This temperature gain, however, was observed to be too small compared with the time required for CO desorption on large grains (0.1 μm radius). Therefore, it was found that this process was not efficient unless a very small grain is considered, for which higher temperatures could be reached.

Korchagina et al. (2017) studied the hydrogenation of CO on water ice molecular clusters made of $\leq$5 and 10 water molecules through the Eley-Rideal mechanism at 70 K. They found that the HCO formation energy can be dissipated by the water cluster leading to a stable HCO molecule for clusters larger than 3 water molecules. This work, however, has two main weaknesses, the first one is the small water ice models, and the other is related to the low accuracy of the methods employed. More recently, Kayanuma et al. (2019) have studied the CD for the HCO + H reaction through the Eley-Rideal mechanism, where HCO is adsorbed on graphene. They found efficient CD for the products (H_2 and CO) when HCO is chemisorbed, while they found no CD when it is physisorbed (in this case H_2CO is produced).

In this Part, I focus on the capacity of water ice surfaces to dissipate the nascent energy of two key surface reactions in astrochemistry: H + CO $\rightarrow$ HCO and H + H $\rightarrow$ H_2. Two reaction extensively studied both experimentally (e.g. Kenzo Hiraoka et al., 2002; Naoki Watanabe et al., 2002b for HCO and Hama et al., 2012; Hornekær et al., 2003; Roser et al., 2003; Naoki Watanabe et al., 2010 for H_2) and theoretically (see §3.2 and §3.1).

10.2 Goals, methods and novelty of the research in this part

In this Part, I present the results obtained in Pantaleone et al. (2020) and Pantaleone et al. (2021), in which the fate of the HCO and H_2 formation energy is studied with *ab initio* molecular dynamics (AIMD) simulations (Chapters 11 and 12, respectively). This work was carried out in collaboration with S. Pantaleone, who had a post-Doc in our team of Grenoble. We worked hand-to-hand when running the simulations, and then I designed a python code in order to analyze results. We were awarded with two projects in the French National supercomputer network, GENCI, with the dossier numbers A0060810797 and A0080811498, of 1.7 and 6 million hours respectively. Finally, we wrote the two articles together, and shared our work.

The goals of this research are (i) to understand from an atomistic viewpoint how the energy released by HCO and H_2 formation is transferred toward the water surface and to quantify it, (ii) to understand if the product leaves or will leave the surface, (iii) in the case it does, to quantify how much energy is retained in the product (HCO or H_2) and, for the H_2 formation case, (iv) to quantify if the ice is locally warmed up enough to allow to allow the desorption of a nearby H_2 and CO molecule.

The novelty of this work is that (i) we simulate the process accounting for the actual reaction (instead of, for example, assuming a certain amount of initial energy once the products are already formed as often done in previous similar works; see §10.1) and (ii) we do so by means of AIMD simulations using large water ice surface models (containing 192 and 576 water molecules for HCO and H_2 formation, respectively), which is fundamental to reliably represent the energy dissipation. For the first work (Pantaleone et al., 2020), we used a proton ordered crystalline Ih water ice model as it limits the number of possible binding modes and sites making the overall analysis process much easier. For the second one Pantaleone et al., 2021, we have used both a crystalline and an amorphous ice.

The calculations were run using the CP2K package with the PBE-D3 density functional combined with a triple-ζ quality basis set with polarization functions for the valence electrons. In the case of HCO formation, the H + CO $\rightarrow$ HCO PES was previously characterized so that the simulation does not start from the reac-

tants but from the transition state (TS) structure. In contrast, for the formation of H_2, the simulation starts with the two H atoms sitting in close proximity and, since the reaction is found to be barrierless at these initial positions at the considered temperature (10 K), no TS search was necessary.

The crystalline surfaces were derived from the proton ordered bulk hexagonal ice (ice XI) structure. Cuts along the [001] direction were done in order to generate slab models with low dipole moment and plenty of binding sites (e.g. Zamirri et al., 2018). The slabs were then thermalized at 10 K by running a simulation in the canonical ensemble (NVT, i.e. the number of particles, N, the volume, V, and the temperature, T, are constant magnitudes).

The amorphous model was obtained by running a classical molecular dynamics (MD) simulation at 300 K on the crystalline one, and then abruptly lowering the temperature at 10 K followed by a geometry optimization and a thermalization run at 10 K[2].

The sizes of the periodic boxes for the HCO and H_2 formation simulations are: $17.544 \times 21.2475 \times 35.0$ and $26.318 \times 28.330 \times 50.0$ Å, where the slab thicknesses are about 13 and 21 Å (corresponding to 4 and 7 layers of crystalline ice, i.e. 192 and 576 molecules of water), respectively[3].

The dissipation energy simulations were run in the microcanonical ensemble (NVE, i.e. the number of particles, N, the volume, V, and the total energy, E, are constant magnitudes). In order to keep the total energy constant (in the canonical ensemble the thermal bath would artificially remove energy from the system). A single initial surface site was used for HCO formation, while for H_2 we took one site on the crystalline and three on the amorphous one.

In order to analyze the energy dissipation process I used my own python code. In this code the surface slab is separated into different regions in which the energy content of each region can be measured as a function of time. Similarly, the energy content of the HCO or H_2 products can be separated from the rest of the system.

10.3 Summary of the results

This section is divided into two parts, one for HCO and one for H_2 formation.

HCO formation

Regarding HCO formation, we did not observe chemical desorption, in line with experimental evidence (Chuang et al., 2018; Minissale et al., 2016c). Indeed, the crystalline water ice was found to dissipate most ($\sim$90%) of the nascent energy (i.e. reaction + TS potential energy, as the initial point is the TS structure) in less than a picosecond. We found that at the end of the simulation, HCO remains attached to the surface establishing 3 non-bonding interactions with the water molecules of the surface, and its total kinetic energy ($\sim$15 kJ mol^{-1}) is well below its binding energy (30 kJ mol^{-1}). This configuration was found to be independent of the initial H + CO orientation on the ice surface. All of this indicates that, for our system, HCO is doomed to rest on the surface thanks to its coupling with the surface due to its capacity of establishing H-bonds.

The energy dissipation process through the ice structure was followed over space by dividing the ice slab into concentric, evenly spaced shells (by 2.8 Å). The first one is a hemisphere of 4 Å radius centered at the reaction site (the C atom from HCO) that contains 6 water molecules. This first region suffers a kinetic excitation as a result of the reaction with peaks of $\sim$ 1 kJ mol^{-1} ($\sim$120 K) per water molecule above the initial energy, for about 1 ps. The second shell (containing 20 water molecules) has a lower excitation peak, roughly half of the previous one, of $\sim$ 0.4 kJ mol^{-1} per water molecule above the initial energy, and for about the same timescale. By the end of the simulation (at t=20 ps) all the ice has the same kinetic energy, indicating that the system has reached equilibrium.

[2]Credits to Stefano Ferrero, member of the ITN "AstroChemical Origins", ITN-ACO grant agreement No 811312. This European project is the “sibling” of the projects I have worked in during my PhD, the ERC “Dawn of Organic Chemistry”, P.I, C. Ceccarelli and the ERC QUANTUMGRAIN, P.I. A. Rimola, grants number 741002 and 865657, respectively

[3]The code that we have employed constrains us to use periodic boundary conditions along the 3 dimensions of space. In order to simulate a surface an empty space in the Z direction was left in order to avoid the interaction between vertical replicas ($\sim$ 20 Å for HCO and $\sim$ 30 Å for H_2).

H2 formation

The formation of H_2 from two H atoms is a much more exothermic reaction than that of HCO ($\sim$440 and $\sim$132 kJ mol^{-1} in our calculations, respectively) and, additionally H_2 has a much lower binding energy (about 10 kJ mol^{-1} in our calculations). This reaction is studied on top of a proton ordered crystalline ice, as for HCO formation, but also on an amophous one, in which three initial positions Pos1–3 are explored.

We found that, irrespective of the ice model or initial position of the two H atoms, the ice absorbs up to 50% of the liberated energy (at difference from Takahashi et al. (1999a,b), who reported a $<$5% energy dissipation capacity), showing little surface environmental dependence. The H_2 molecule is found to either desorb or diffuse non-thermally as a consequence of the reaction, always keeping more kinetic energy than its binding energy to the surface. Accordingly, H_2 is doomed to be desorbed sooner or later.

On the crystalline ice it is found that H_2 starts to diffuse following the electrostatic potential "channels" of the surface[4]. On the amorphous cases, on the other hand, we found either non-thermal diffusion (Pos2 and Pos3, this time not constrained to one direction, but over the whole surface) or direct desorption (Pos1). In the amorphous Pos1 simulations there is a strong collision against one of the ice water molecules, inferring this water molecule to be excited up to 40 kJ mol^{-1} for a period of 100–200 fs. As a consequence of this collision the H_2 molecule is expelled into the gas phase (it reaches 10 Å away with respect to the surface).

Making the same analysis of the energy dissipation as we did for HCO formation, we found that the water molecules in the closest vicinity of the H_2 formation site ($<$ 4 Å) can be excited between 3 and 14 kJ mol^{-1}. We argue that this energy could potentially be used to non-thermally desorb another H_2 molecule and, more interesting, a CO molecule. Finally, the vibrational state of the H_2 molecule upon formation is found to be high ($\nu < 6$), except in the case of the amorphous ice Pos1, which, after its strong collision with the surface water molecule, leaves the surface with a low vibrational state (ν=1–2).

[4]The surface has alternating dangling O and H atoms, which make its electrostatic potential to be periodic in one direction.

Chapter 11

Chemical Desorption versus Energy Dissipation: Insights from Ab Initio Molecular Dynamics of HCO Formation

The research presented in this Chapter has resulted in a scientific article:
Pantaleone, S., Enrique-Romero, J., Ceccarelli, C., Ugliengo, P., Balucani, N., and Rimola, A.
Published in The Astrophysical Journal, 2020.
DOI: 10.3847/1538-4357/ab8a4b

Outline

Molecular clouds are the cold regions of the Milky Way where stars form. They are enriched by rather complex molecules. Many of these molecules are believed to be synthesized on the icy surfaces of the interstellar submicron-sized dust grains that permeate the Galaxy. At 10 K thermal desorption is inefficient and, therefore, why these molecules are found in the cold gas has tantalized astronomers for years. The assumption of the current models, called chemical desorption, is that the molecule formation energy released by the chemical reaction at the grain surface is partially absorbed by the grain and the remaining one causes the ejection of the newly formed molecule into the gas. Here we report an accurate *ab-initio* molecular dynamics simulations aimed to study the fate of the energy released by the first reaction of the H addition chain on CO, CO + H $\rightarrow$ HCO, occurring on a crystalline ice surface model. We show that about 90% of the HCO formation energy is injected towards the ice in the first picosecond, leaving HCO with an energy content (10-15 kJ mol^{-1}) more than a factor two lower than its adsorption energy (30 kJ mol^{-1}). As a result, in agreement with laboratory experiments, we conclude that chemical desorption is inefficient for this specific system, namely H + CO on crystalline ice. We suspect this behavior to be quite general when dealing with hydrogen bonds, which are responsible of both the cohesive energy of the ice mantle and the interaction with adsorbates, as the HCO radical, even though *ad hoc* simulations are needed to draw specific conclusions on other systems.

11.1 Introduction

Following the context presented in § 10.1, the detections of iCOMs in cold ($\sim$10 K) sources (e.g. Bacmann et al., 2012; Cernicharo et al., 2012; Jiménez-Serra et al., 2016; Vastel et al., 2014) are important for (at least) two reasons: first, they challenge the idea that iCOMs are synthesized on the lukewarm (30-40 K) grain surfaces by radical-radical combination (R. T. Garrod et al., 2006; K. I. Öberg et al., 2009; M. Ruaud et al., 2015), and, second, if for whatever reason they are formed on the grain surfaces, the mechanism that lifts them off into the gas (where they are detected) must be non-thermal.

Different non-thermal mechanisms have been invoked in the literature to explain the presence of gaseous iCOMs in cold environments (see § 10.1). One of such mechanisms is chemical desorption (CD), whose underlying idea is that the energy released by strongly exothermic chemical reactions occurring on the grain surfaces is only in part absorbed by the grain while the remaining one is used to break the bonds of the newly formed species with the surface, so that a fraction of the synthesized species is injected into the gas phase. Therefore, CD and the dissipation of the surface-reaction energy are two faces of the same medal, intrinsically linked.

As explained in § 10.1, from an experimental point of view, it is extremely difficult, if not impossible, to quantify the energy dissipation. Overall, laboratory experiments showed that CD can be more or less efficient depending on the adsorbate and the substrate.

On the other hand, theoretical calculations are, in principle, capable to simultaneously study the energy dissipation and CD. As it was seen in § 10.1, the employed methods include molecular dynamics based on classical mechanics (e.g. Fredon et al., 2018, 2017) or self-consistent-charge density functional tight binding (SCC-DFTB) (Korchagina et al., 2017). Such simulations allow for the calculation of up to thousands of trajectories, which can then be statistically analyzed. However they present some weak points due to their intrinsic limitations or the adopted assumptions: (i) the limits of force field-based methods in dealing with chemical reactions in classical mechanics-based molecular dynamics; (ii) in Fredon et al., 2018, 2017, the injected energy of the admolecule which is only translational, while, after a reaction occurs, the energy should be partitioned also into vibrational and rotational levels; (iii) the relatively small size of the used water clusters, whose temperature may rise for high energy injections, thus resulting in an overestimation of the admolecule mobility.

As a more computationally demanding alterantive, one can use *ab-initio* Molecular Dynamics (AIMD) simulations, which do not allow for a statistical analysis of the results, but in which the system is more accurately described, typically using DFT methods, which in turn allows the direct study of chemical reactions. For example, Kayanuma et al. (2019) studied the reaction of H with adsorbed HCO on a graphene surface by means of AIMD simulations, showing that in the case of HCO chemisorption (i.e. chemical bond between the adsorbate and the surface), the products H_2 + CO are desorbed, while in the case of HCO physisorption (the interaction with the surface is of dispersive nature), formaldehyde is formed without chemical desorption.

In this Chapter, I present new AIMD simulations of the reaction H + CO on a large periodic crystalline water-ice surface assuming the Langmuir-Hinshelwood mechanism. This reaction is the first step towards the formation of methanol on the grain surfaces, one of the most studied both theoretically and experimentally (e.g. Andersson et al., 2011; Kenzo Hiraoka et al., 2002; Rimola et al., 2014; N. Watanabe et al., 2007; Naoki Watanabe et al., 2002b; David E. Woon, 2002b); therefore, in this context, it can be considered as one of the most important reactions in astrochemical studies. In addition, it is representative of the class of reactions with a relatively low reaction energy (less than 2 eV) to dissipate. Our scope is to understand from an atomic point of view how the energy released by the HCO formation is transferred towards the water surface, without any *a priori* assumption on how the reaction energy is distributed over the system. We emphasize that our approach is substantially different from the one used by Fredon et al., 2017 and Fredon et al., 2018, described above. In our case, we do not need to address a statistical behavior (depending on the species trajectory), because we simulate the reaction itself and how its energy is dissipated by the formed HCO. This does not depend on the initial H trajectory because the energy of the H atom is thermal (at 10 K, specifically) and, therefore, negligible with respect to the energy released by the reaction (about 1.4 eV). The result could, in principle, depend on the initial position of the CO on the crystalline ice, for which there are a few possibilities, and we will discuss this point in the article. In summary, our AIMD simulations allow us to quantify whether the newly formed species has enough energy to break its interactions with the water surface and, consequently, to be injected into the gas-phase.

Last, despite it is well known that interstellar ice is often amorphous, we chose a crystalline model because tuning the computational setup is easier. Once the system is carefully tested, our future works will focus on amorphous ice models. It is important to notice, however, that crystalline water ice has been detected in the ISM (Molinari et al., 1999) and, particular relevant for the planet formation studies, in protoplanetary disks (Terada et al., 2012), so that our simulations will be directly applicable in those environments.

The article is organized as follows. In § 11.2 we present the computational methodology, in § 11.3 the results and in § 11.4 we discuss these results in view of astrochemical implications. Finally, in § 11.5, we summarize the most important conclusions.

11.2 Computational Details

Methods

All the calculations have been carried out with the CP2K package (Goedecker et al., 1996; Hartwigsen et al., 1998; Hutter et al., 2014; Lippert et al., 1997; VandeVondele et al., 2003, 2005). The atoms have been treated as follows: core electrons have been described with the Goedecker-Teter-Hutter pseudopotentials (Goedecker et al., 1996; Hartwigsen et al., 1998), while valence electrons with a mixed Gaussian and Plane Wave (GPW) approach (Lippert et al., 1997). The PBE functional has been used for all the calculations (J. Perdew et al., 1996) combined with a triple-ζ basis set for valence electrons plus 2 polarization functions (TZV2P). The cutoff for plane waves has been set to 600 Ry. The *a posteriori* D3 Grimme correction has been applied to the PBE functional to account for dispersion forces (Grimme et al., 2011, 2010). During the optimization procedure, only the H, C, and O atoms (the ones belonging to the HCO·) were free to move, while the atoms belonging to the ice surface have been kept fixed to their thermalised positions.All calculations were carried out within the unrestricted formalism as we deal with open-shell systems. The spin density was checked for reactive, TS and product and it remains always well localized either on H atom (reactant) and on HCO for the product.

Two sets of convergence criteria were used: (i) for geometry optimizations to energy minima the energy threshold of the self-consistent field (SCF) procedure was set to ΔE = 10^{-7} a.u., while the thresholds on gradients and displacements were set to their default values (4.5×10^{-4} Ha Bohr^{-1} and 3.0×10^{-3} Ha Bohr^{-1}, respectively) and (ii) for transition state search, tighter parameters were adopted (ΔE = 10^{-10} for the SCF and 4.5×10^{-5} Ha Bohr^{-1} and 3.0×10^{-4} for gradients and displacements, respectively). These choices ensure good starting geometries for the *ab-initio* molecular dynamics (AIMD) simulation.

During the simulation, no spread of spin density through the ice was detected (see Figures E.1, E.2, and E.3 in appendix E.

The binding energy (BE) of HCO· were calculated according to the following formula:

$$BE_{HCO} = E_{CPLX} - (E_{Ice} + E_{HCO}) \tag{11.1}$$

where E_{CPLX} is the energy of the HCO/Ice system, E_{Ice} that of the bare ice surface, and E_{HCO} the energy of the HCO· alone, each one optimized at its own minimum. The BE_{HCO} will be used later on to compare with the residual kinetic energy of the HCO formation.

In order to reproduce the ISM conditions, the reaction was carried out in the microcanonical ensemble (NVE), where the total energy (*i.e.* potential + kinetic) is conserved. Moreover, we run an equilibration AIMD in the NVT ensemble (using the CSVR thermostat, with a time constant of 20 femtoseconds) at 10 K for 1 ps (with a time step of 1 fs) for the bare ice surface, to obtain a thermally equilibrated ice. Accordingly, the equilibrated velocities of the ice surface were used as starting ones for the NVE production, while the H and C velocities of HCO were manually set according to the H–C bond formation. The evolution of the system was followed for 20 ps, using a timestep of 1 fs.

Benchmark

In this subsection we present results obtained from a benchmark study on the reaction of HCO formation on a small cluster of 3 H_2O molecules (H + CO/3H_2O $\longrightarrow$ HCO/3H_2O), similarly to the work by Rimola et al. (2014). The structures are shown in Figure 11.1, while energetic values and harmonic frequencies are reported in Tables 11.1 and 11.2, respectively. Some of the calculations were run on the GAUSSIAN16 suite of programs Frisch et al., 2016.

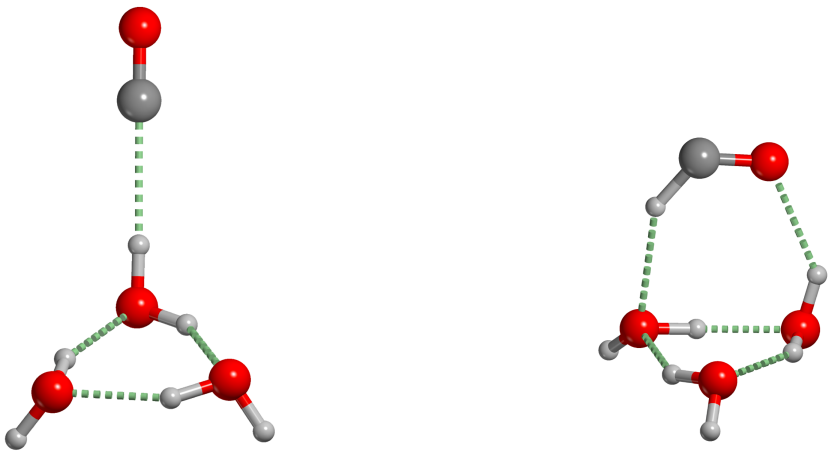

(a) CO/3H_2O (b) HCO/3H_2O

Figure 11.1: *PBE-D3/TZV2P optimized structures of reactant (a) and product (b) of the H + CO/3H_2O $\longrightarrow$ HCO/3H_2O reaction.*

It is clear from Table 11.1 that PBE energies are quite far from those calculated at higher levels of theory, in particular with respect to B2PLYPD3 and CCSD(T) methods. Hence, PBE results overestimate the chemical desorption, which as will be seen, is not a problem in our simulations as there is no CD observed.

Table 11.1: *Energetic data of the reaction (H + CO/3H_2O $\longrightarrow$ HCO/3H_2O) calculated at different levels of theory. 1: (CP2K) PBE-D3/TZV2P, 2: (Gaussian) PBE-D3/6-311++G(d,p), 3: (Gaussian) BHLYP-D3/6-311++G(d,p), 4: (Gaussian) BHLYP/6-311++G(d,p), 5: (Gaussian) MP2/aug-cc-pvtz, 6: (Gaussian) B2PLYPD3/aug-cc-pvtz, 7: (Gaussian) CCSD(T)/aug-cc-pvtz//B2PLYPD3/aug-cc-pvtz.*

Method	1	2	3	4	5	6	7
Energy (kJ mol^{-1})	-132.1	-122.6	-121.0	-108.0	-45.5	-91.3	-90.9

Harmonic frequencies computed at PBE level, on the other hand, show very good agreement with those calculated at the B2PLYPD3 level ($\sim$ 10% of difference), which is the most accurate method used in the

frequency-calculation benchmark (CCSD(T) is excluded here because frequency calculations are computationally too expensive and we can not perform then). This means that the vibrational coupling of HCO with the water molecules is correctly described, and hence, also the energy dissipation.

Table 11.2: *Harmonic frequencies of the reaction H + CO/3H_2O $\longrightarrow$ HCO/3H_2O calculated at different levels of theory, with their percentage differences with respect to the method adopted in the present work. 1: (CP2K) PBE-D3/TZV2P, 2: (Gaussian) PBE-D3/6-311++G(d,p), 3: (Gaussian) BHLYP-D3/6-311++G(d,p), 4: (Gaussian) BHLYP/6-311++G(d,p), 5: (Gaussian) MP2/aug-cc-pvtz, 6: (Gaussian) B2PLYPD3/aug-cc-pvtz, 7: (Gaussian) CCSD(T)/aug-cc-pvtz//B2PLYPD3/aug-cc-pvtz.*

Method	1	2	3	4	5	6	Diff % (1-2)	Diff % (1-3)	Diff % (1-4)	Diff % (1-5)	Diff % (1-6)
Frequencies (cm^{-1})	450	434	388	406	386	395	-4	-14	-10	-14	-12
	473	443	431	434	411	422	-6	-9	-8	-13	-11
	536	509	471	483	471	481	-5	-12	-10	-12	-10
	624	601	588	562	573	572	-4	-6	-10	-8	-8
	753	753	721	716	677	684	0	-4	-5	-10	-9
	994	974	877	915	880	891	-2	-12	-8	-11	-10
	1115	1108	1183	1183	1137	1146	-1	6	6	2	3
	1611	1583	1667	1670	1635	1640	-2	4	4	1	2
	1627	1593	1683	1686	1648	1655	-2	3	4	1	2
	1641	1623	1718	1712	1668	1673	-1	5	4	2	2
	1841	1847	2011	2014	1904	1871	0	9	9	3	2
	2690	2643	2897	2867	2858	2804	-2	8	7	6	4
	3196	3232	3707	3680	3509	3480	1	16	15	10	9
	3425	3474	3843	3846	3658	3643	1	12	12	7	6
	3465	3507	3876	3869	3698	3683	1	12	12	7	6
	3676	3703	4011	3996	3846	3821	1	9	9	5	4
	3762	3785	4060	4051	3899	3885	1	8	8	4	3
	3772	3795	4065	4063	3906	3892	1	8	8	4	3

Ice model

Ordinary ice is proton disordered and, accordingly, its crystal structure cannot be simply modeled by adopting relatively small unit cells. A possible alternative is to adopt P-ice, a proton ordered ice already successfully used in the past to simulate ice features (Pisani et al., 1996). P-ice bulk belongs to the $Pna2_1$ space group and from the bulk we cut out a slab to simulate the (100) surface, shown in Figure 11.2. The size of the surface was chosen according to the amount of energy to be dissipated. Given that the HCO· radical formation is strongly exothermic (132.5 kJ mol^{-1}; see Figure 11.3), a sufficiently large water ice slab is needed to absorb most of the nascent energy (see more details in the next section). Therefore, the periodic cell parameters have been set to $a = 17.544$ Å and $b = 21.2475$ Å with a slab thickness of ~ 13 Å (which corresponds to 4 water layers). The model consists of 192 water molecules in total. In the CP2K code, the electron density is described by plane waves, and, accordingly, the surface is replicated also along the non-periodic direction. To avoid interactions between the fictitious slab replicas, the *c* parameter (*i.e.*, the non-periodic one) was set to 35 Å.

11.3 Results

To study the CO hydrogenation on the ice surface, we simulated the reaction adopting a Langmuir-Hinshelwood (LH) surface mechanism, *i.e.* with both the reactants (H· and CO) adsorbed on the surface. Accordingly, we first optimized the geometries of the reactants (H· + CO), transition state (H$\cdots$CO) and product (HCO·) in order to obtain the potential energy surface of the reaction. As reported in Figure 11.3, the activation barrier (5.2 kJ mol^{-1}, 622.1 K) is quite high if we consider the sources of energy available in the ISM. Indeed, it is well known that this reaction proceeds mostly through H-tunneling (Andersson et al., 2011; Kenzo Hiraoka et al., 2002; Rimola et al., 2014). However, as AIMD operates within the Born-Oppenheimer approximation, *i.e.* the nuclei motion is driven by classical equations, quantum phenomena of atoms (such as tunneling effect) cannot be taken into account. Since our aim is not to simulate the reaction itself, but to understand where does the liberated energy go, we run the simulation starting from the transition state structure (Figure

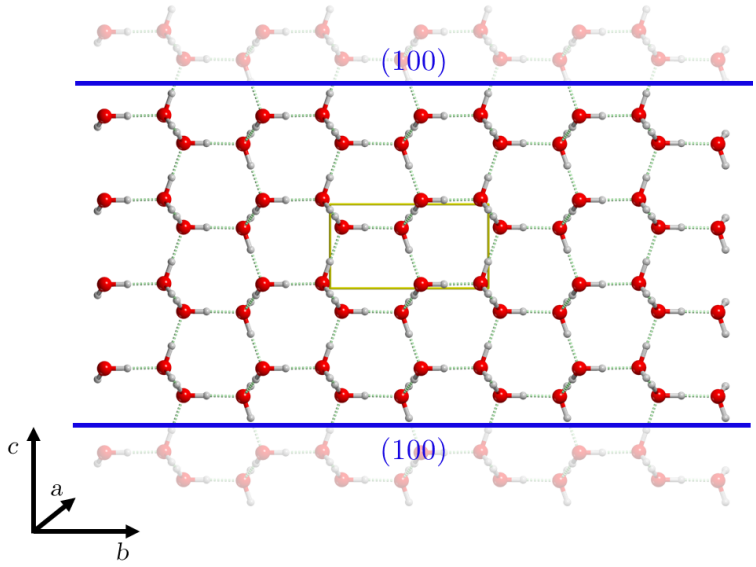

Figure 11.2: *PBE-D3/TZV2P optimized structure of the hexagonal ice bulk. The blue lines correspond to the bulk cut along the (100) plane.*

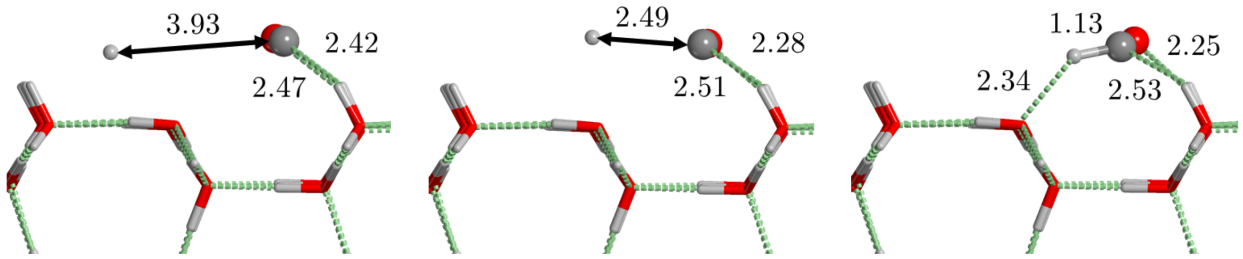

(a) Reactant (0.0) (b) Transition state (5.2) (c) Product (-132.5)

Figure 11.3: *PBE-D3 optimized geometries of reactant, transition state and product of the HCO· reaction formation on the ice surface. The numbers in parenthesis correspond to the relative energy in kJ mol^{-1} with respect to the reactant. Distances are in Å. H atoms in white, C atom in gray, O atoms in red.*

11.3(b)). In this way, we force the system to evolve in the direction of the product. Therefore, the total energy to be dissipated is the sum of the energy barrier and of the reaction energy (5.2 + 132.5) kJ mol^{-1} = 137.7 kJ mol^{-1}. Therefore, it is possible to estimate the expected temperature increase of the whole system after the reaction by invoking the equipartition theorem:

$$T = \frac{1}{3}\frac{E_{nasc}}{R\ N_{at}} \tag{11.2}$$

where E_{nasc} is the nascent energy due to the H–C bond formation (*i.e.* 137.7 kJ mol^{-1}), N_{at} is the whole system atoms number (3 for HCO· and 3 $\times$ 192 for the ice), and R the gas constant. Thus, the energy dissipation trough an ice slab containing 192 water molecules should produce a global temperature increase of about 19 K (which is in perfect agreement with the very first spike in T of Supplementary Figure E.6, reaching $\sim$10 K so that the final temperature will lie around 20 K. Then, when the simulation equilibrates, the temperature oscillates around this valuue 20 K. This very simple calculation is useful to have an idea of the atom number needed to avoid the nascent energy to artificially rise the total temperature.

Figure 11.4 shows the most interesting geometrical parameters of the system during the AIMD simulation. Both the temperature and potential energy oscillate around a stable value and they reach the equilibrium within 1 ps (see also Supplementary Figures E.6 and E.7). As one can see in Figure 11.4, the H–C bond forms in the first tens of fs of the simulation (keeping in mind that we are starting from the transition

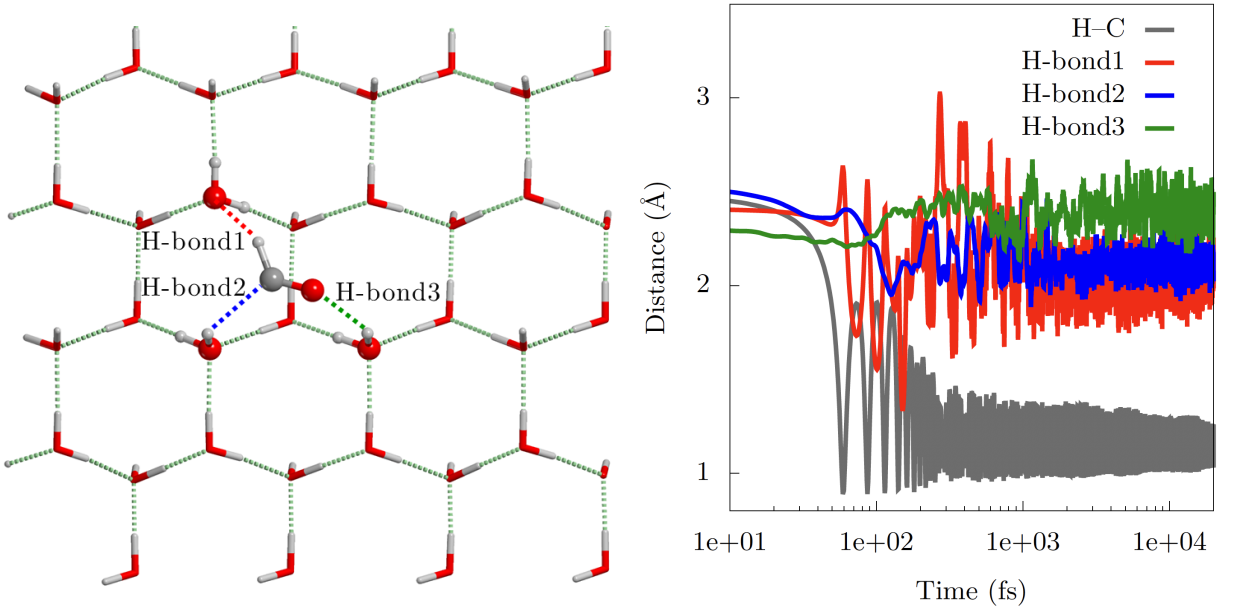

Figure 11.4: *Structure of the HCO· adsorbed on the ice surface at the last point of the AIMD simulation (left) and evolution of the most relevant geometrical parameters during the AIMD simulation (right). H-bonds colors in the chart correspond to the H-bonds in the figure depicted as dotted lines. H atoms in white, C atom in gray, O atoms in red.*

state). After the H–C bond formation, the HCO· radical moves on the surface in the sense of maximizing the H-bond contacts with the surrounding water molecules (Figure 11.4) and it lies in its most stable position after 1 ps, which corresponds to the equilibration of both the potential energy and the temperature. After this period, the HCO· stays in this stable position, without diffusing anywhere.

In Figure 11.5, the kinetic energy dissipation due to the H–C bond formation is reported. As expected, the kinetic energy released from the H–C bond formation rapidly drops (in less than 100 fs) and it is, simultaneously, absorbed by the water molecules of the surface. As one can see, at the beginning of the simulation, before 200 fs, the red line (T_{HCO}) is complementary to the green line (V_{TOT}). As the AIMD was executed in the NVE ensemble, when the kinetic energy drops, the potential one rises by the same amount. However, after 300 fs, when the HCO· starts to exchange energy with the surface, the red (T_{HCO}) and blue (T_{Ice}) lines become symmetric, *i.e.* the energy loss of HCO· is equal to the energy gain of the surface, in terms of kinetic energy. The most important message from Figure 11.5 is that, within the first ps, HCO· looses 90% of its initial kinetic energy, which is immediately transferred to the ice. Later, along the simulation, HCO· continues to transfer energy to the ice at a slower rate. After 20 ps, its kinetic energy is around 15 kJ mol^{-1}, at least twice lower than its binding energy. Therefore, it is unlikely that the HCO· will desorb. This is corroborated by Figure 11.4, where the H-bonds of HCO· to the surface lie in a rather steady fashion after its formation (they essentially vibrate around their equilibrium position).

In order to give a detailed analysis of the energy dissipation on the ice surface, we used the atomic simulation environment (ASE) python module (Bahn et al., 2002; Larsen et al., 2017). The energy dissipation was analyzed by dividing the slab of water molecules in concentric shells centered on the reaction center (*i.e.* the C atom). Note that the HCO radical has been excluded from this analysis because we are interested in the dissipation across the ice itself. The concentric shells were defined as follows: i) the first one is a hemisphere with 4 Å of radius and contains the closest water molecules to the CO molecule; ii) the other shells are equally spaced from each other by 2.8 Å (average closest O–O distance between water molecules), up to a distance of 18 Å in order to include also the farthest water molecules from the reaction center. We emphasize that only a single unit cell was used for this analysis, which means that no water molecules from periodic replicas are included in the energy dissipation analysis. The sketch showing the water shells is reported in Supplementary Figure E.9.

The results on the energy dissipation analysis are shown in Figure 11.6. The kinetic energy was normalized per water molecule, in order to remove the dependence on the number of water molecules (as each

shell contains different number of waters). One can see, from the two first shells (0.0-4.0 and 4.0-6.8 Å), that the energy is rapidly transferred from HCO to the ice, which is later uniformly distributed to outer shells: within ∼2 ps all shells have the same kinetic energy.

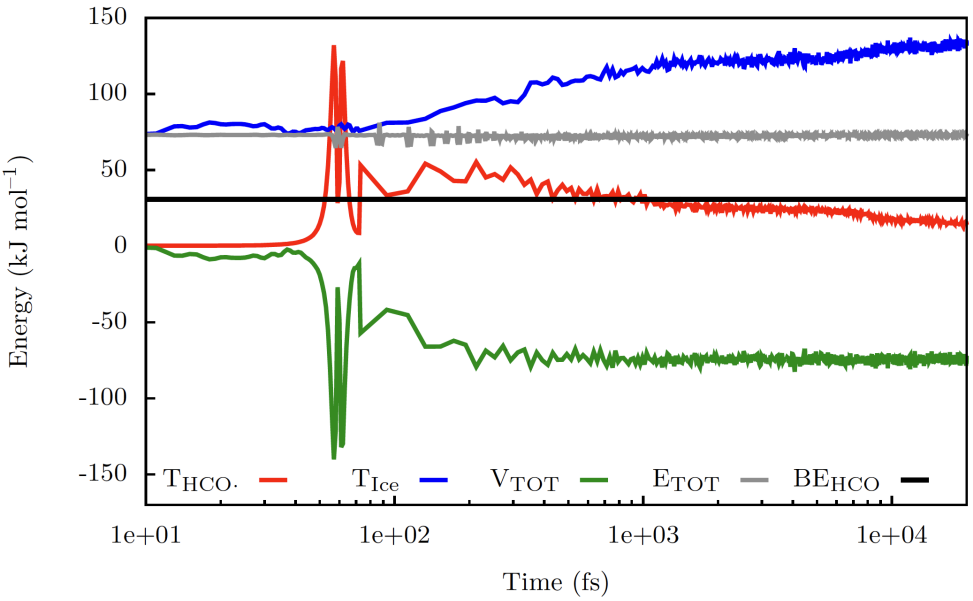

Figure 11.5: *Evolution of the most relevant energetic components (in kJ mol^{-1}) of the HCO·/Ice system during the AIMD simulation. E_{TOT} is the total energy (i.e. potential + kinetic, gray line). V_{TOT} is the potential energy (green line). $T_{HCO\cdot}$ and T_{Ice} are the kinetic energies of HCO· (red line) and ice (blue line), respectively. $BE_{HCO\cdot}$ is the binding energy of the HCO· (black line). Gray line shows very good energy conservation.*

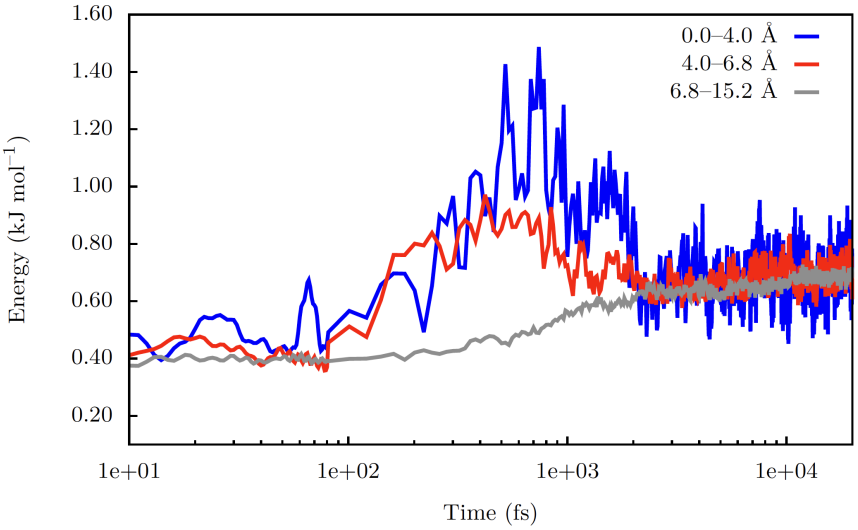

Figure 11.6: *Kinetic energy evolution (in kJ mol^{-1} per water molecule) of the ice surface. The ranges in the legend refer to the shells the water molecules belong to.*

11.4 Discussion

In the present work, the HCO· formation reaction on an ice surface model has been used as a test case in order to study the kinetic energy dissipation due to a bond formation (in the specific case the H–C bond).

This is particularly important because the energy released by the formation of a chemical bond may be a hot spot that makes possible other processes, like the desorption of the newly formed molecule or other molecules nearby. A crucial parameter is the timescale of the process: the main question is whether the released energy is available (and if yes, for how long) and whether it can be used by other adsorbed species, or, in contrast, it is immediately dissipated through the ice surface. From Figure 11.5, the answer is very clear: the slab of water molecules absorbs $\sim 90\%$ of nascent energy, which is equally distributed among all the water molecules of the ice surface within the first ps after the bond formation, and it is no longer available to assist other processes. In particular, and importantly, the residual HCO kinetic energy after 1 ps is almost half of the HCO binding energy, which implies that HCO will remain stuck on the surface and will not desorb.

Our simulations are based on three assumptions: (i) the starting position of the CO adsorbed on the ice is the most energetically favorable one; (ii) the surface of the ice is crystalline; (iii) the reaction follows a LH mechanism. In the following, we discuss the validity limits of each assumption.

(i) CO position The first assumption is based on the fact that, as molecules in cold molecular clouds move at low, thermal ($\sim$10 K) velocities, landing on grain surfaces is slow enough for them to feel the electrostatic potential generated by the surface. Consequently, they have sufficient time to accommodate on the icy mantle, maximizing their interactions with the ice surface itself. In other words, the main driving forces of the adsorption process in cold molecular clouds are long range forces. Nonetheless, a few other starting positions may exist with respect to the one that was chosen for this study. For this reason, we have explored two other starting configurations, namely the Pos2 and Pos3 reported in Figure E.5 in appendix E. Both of them lead to the HCO radical in the same position of that reported in Figures 11.3 and 11.4, after either geometry optimization or short AIMD simulation. In other words, whether CO is in the position we chose for the full AIMD simulations or in the other two positions, HCO ends up having the same position, which means the same bonds with the surface and, consequently, the evolution of the system is the same.

(ii) Crystalline ice As already mentioned in the Introduction, the major reason for choosing the crystalline ice structure is a computational one. In this respect, we would like to caution about the role of crystalline versus amorphous ice, because of the possibility that the symmetric electrostatic potential of the crystalline case can hinder the formed species to escape from the surface and, in crystalline systems, the vibrational coupling might be more efficient than in amorphous ones, thus allowing a faster dissipation of the energy and, consequently, underestimating the desorption rate. Further studies need to be carried out in order to understand if the crystalline nature of the ice affects and how the behavior of the formed species because of the crystal symmetry compared to the random nature of the amorphous ice. Having said that, our simulations are valid and applicable in the environments where crystalline ice has been detected (e.g. Molinari et al., 1999; Terada et al., 2012).

(iii) LH mechanism It is possible, and even probable, that the H atom will not arrive directly from the gas but rather is an atom that randomly grazes the ice surface. In this case, since the velocity of the H is even smaller than the one if it landed from the gas, the results of our simulations would not change. So, this choice is, after all, irrelevant for the purpose of our study.

In summary, we conclude that chemical desorption is not efficient in the H + CO reaction on crystalline ice, and this is a robust result. Laboratory experiments have proven to be difficult to obtain for this specific reaction. To our best knowledge, no experiment simulates it on crystalline ices. Minissale et al. (2016b) obtained a measure of the H + CO CD when the reaction occurs on oxidized graphite. They found a CD efficiency equal to 10$\pm$8 percent. Chuang et al., 2018 studied the CO hydrogenation process using as substrate gold, over which CO was deposited forming a thick layer of solid CO, subsequently bombarded with H atoms. They found that the global CD efficiency of the whole process up to the formation of CH_3OH is low, $\leq$0.07 per hydrogenation step, assuming an identical efficiency for each reaction in the hydrogenation process (Chuang et al., 2018). As already mentioned, the surface where the CO is adsorbed and the reaction occurs is certainly of paramount importance, so that it is not obvious to make a direct comparison between our computations and the above experiments. Yet, it seems that then latter agree on a small CD efficiency, if any, as our computations predict.

Finally, it is possible that for more exothermic reactions (like for example the last step to CH_3OH, which is much more exothermic than H + CO) and weakly bound systems (like H_2), chemical desorption can take place. This could also be the case for reactions occurring on grain surfaces of different nature, such as silicates or carbonaceous materials, as their heat capacities are very different from those of H_2O-dominated ices. Dedicated simulations should be carried out to assess it in these systems.

11.5 Conclusions

We studied the first step of the hydrogenation of CO on the interstellar grain icy surfaces by means of ab-initio Molecular Dynamics simulation. We studied the H + CO reaction occurring on a crystalline ice. Our goal was to understand from an atomistic point of view and to quantify the possibility that the energy released in the reaction is just partially dispersed on the crystalline substrate and the residual one is used to desorb the product, HCO.

The main conclusions of the present study are:

1. The reaction energy dissipation through thermal excitation of water molecules is extremely fast: after the first picosecond most of the reaction energy (137.7 kJ mol^{-1}) is dissipated away through the ice, leaving HCO with a kinetic energy of 10–15 kJ mol^{-1}, more than twice lower than its binding energy (30 kJ mol^{-1}).

2. As a consequence, the HCO product is doomed to remain attached to the crystalline ice and no desoprtion can occur.

The astrophysical implications are that, in the environments where crystalline ices are present, like for example some protoplanetary disks, chemical desorption does not occur for the reaction H + CO. We suspect that this may be a general behavior for reactions dealing with hydrogen bonds, as they are responsible for both the cohesive energy and the interaction with the crystalline ice. However, in order to assess whether this is true, ad hoc simulations similar to those presented here are mandatory.

Chapter 12

H_2 formation on interstellar grains and the fate of reaction energy

The research presented in this Chapter has resulted in a scientific article:
Pantaleone, S., Enrique-Romero, J., Ceccarelli, C., Ferrero, S, Balucani, N., Rimola, A, and Ugliengo, P.
Published in Astronomy and Astrophysics, 2021.
DOI: 10.3847/1538-4357/ac0142

Outline

Molecular hydrogen is the most abundant molecular species in the Universe. While no doubts exist that it is mainly formed on the interstellar dust grain surfaces, many details of this process remain poorly known. In this work, we focus on the fate of the energy released by the H_2 formation on the dust icy mantles, how it is partitioned between the substrate and the newly formed H_2, a process that has a profound impact on the interstellar medium. We carried out state-of-art *ab-initio* molecular dynamics simulations of H_2 formation on periodic crystalline and amorphous ice surface models. Our calculations show that up to two thirds of the energy liberated in the reaction ($\sim$300 kJ/mol $\sim$3.1 eV) is absorbed by the ice in less than 1 ps. The remaining energy ($\sim$140 kJ/mol $\sim$1.5 eV) is kept by the newly born H_2. Since it is ten times larger than the H_2 binding energy on the ice, the new H_2 molecule will eventually be released into the gas-phase. The ice water molecules within $\sim$4 Å from the reaction site acquire enough energy, between 3 and 14 kJ/mol (360–1560 K), to potentially liberate other frozen H_2 and, perhaps, frozen CO molecules. If confirmed, the latter process would solve the long standing conundrum of the presence of gaseous CO in molecular clouds. Finally, the vibrational state of the newly formed H_2 drops from highly excited states ($\nu = 6$) to low ($\nu \leq 2$) vibrational levels in a timescale of the order of ps.

12.1 Introduction

Molecular hydrogen is the most abundant molecule in the Universe. Its formation is also the first step of the interstellar chemistry and, therefore, a fundamental reaction. In molecular clouds, H_2 is mainly formed via the H + H association reaction on the interstellar dust grain surfaces, which act as a third body capable to partially absorb the energy ($\sim$440 kJ/mol $\sim$4.56 eV) released by the chemical reaction and, consequently, stabilise the newly formed H_2 molecule (e.g. Hollenbach et al., 1970, 1971; Smoluchowski, 1983; van de Hulst, 1946). Although no doubts exist on the occurrence of this process, many specific details remain poorly known (see e.g. Vidali, 2013; Valentine Wakelam et al., 2017).

Here, we focus on the fate of the energy released by the reaction, which has been source of debate for decades. Specifically: how much of the reaction energy is absorbed by the dust grain and in what timescale? What fraction of the chemical energy does go into the kinetic energy of the newly formed H_2? Is this energy large enough as H_2 breaks the interaction with the surface and leaves into the gas-phase? How much energy does the H_2 molecule possess when it leaves the grain surface and in what ro-vibrational state? And, finally, is the energy transmitted to the dust grain enough for locally warming it up and make adjacent frozen molecules sublimate? These points have a profound impact on several aspects of astrochemistry and, more generally, the physics and chemistry of the interstellar medium (ISM) (Duley et al., 1993).

Answers to the above questions largely depend on the nature of the substrate, namely the specific dust grain surface or, in practice, the interstellar environment where H_2 forms. Here we focus on cold ($\sim$ 10 K) molecular clouds. In these environments, the grain refractory cores are coated by water-dominated icy mantles either in polycrystalline (PCI) or amorphous (ASW for amorphous solid water) phases, the latter dominating over the former (Boogert et al., 2015; Robert G Smith et al., 1988; D. C. B. Whittet, 1993).

Unfortunately, laboratory experiments cannot entirely reproduce the interstellar conditions so that, while they can suggest routes and processes, they cannot provide definitive answers to the above-exposed questions (see e.g. Vidali, 2013). For example, obtaining experimentally how the H_2 formation nascent energy is partitioned is very difficult (Hama et al., 2012; Hornekær et al., 2003; Roser et al., 2003; Naoki Watanabe et al., 2010). Computational chemistry methods can be regarded as a complementary tool and, sometimes, as a unique alternative to laboratory experiments. So far, a limited number of studies devoted to the energy dissipation of the H_2 formation reaction on icy grains has appeared in the literature (Herbst et al., 2006; Takahashi et al., 1999a, 2001).

Here, we present a new theoretical study on the dissipation of the energy released by the $2H \rightarrow H_2$ reaction on water ice using *ab-initio* molecular dynamics simulations (AIMDs). We simulated the reaction adopting a Langmuir-Hinshelwood (LH) mechanism (*i.e.* both reactants are adsorbed on the surface in neighboring sites) both on amorphous and crystalline periodic models of interstellar icy mantles.

12.2 Computational details

Methods

All our calculations were carried out with the CP2K package (Hutter et al., 2014). Core electrons were described with the Goedecker-Teter-Hutter pseudopotentials (Goedecker et al., 1996) and valence ones with a mixed Gaussian and Plane Wave (GPW) approach (Lippert et al., 1997). The DFT (Density Functional Theory) PBE (Perdew-Burke-Ernzerhof) method was adopted (J. Perdew et al., 1996), combined with a triple-ζ basis set for valence electrons with a single polarization function (TZVP), and the *a posteriori* D3 Grimme correction to account for dispersion forces (Grimme et al., 2011, 2010). The plane-wave cutoff was set to 600 Ry. Ice surfaces were thermalized (see § 12.2), and during the geometry optimization only the reacting H atoms (those forming H_2) were allowed to move, keeping the water molecules fixed at their thermalized positions. All calculations were carried out within the unrestricted formalism as we deal with open-shell systems. The binding energy (BE) of H_2 was calculated as:

$$BE_{H_2} = E_{CPLX} - (E_{Ice} + E_{H_2}) \tag{12.1}$$

where E_{CPLX} is the energy of the H_2/Ice system, E_{Ice} that of the bare ice surface, and E_{H_2} the energy of the H_2 alone.

We have checked the quality of our results by compring the H_2 formation reaction energies and the $H\cdots H_2O$ binding energies calculated at PBE with those at CCSD(T) levels in the gas phase, shown in Table 12.1. The latter where calculated with the GAUSSIAN16 package Frisch et al., 2016. The difference between the two methodologies is acceptable, considering the energy released by the reaction.

As regards the AIMD simulations, we run an equilibration AIMD in the NVT ensemble (using the CSVR thermostat, with a time constant of 20 femtoseconds) at 10 K for 1 ps (with a time step of 1 fs) only for the bare ice surface. This ensures an initial thermally equilibrated ice. Then the velocities of the equilibrated ice surfaces are used as input for the NVE production runs. Those velocities, correspond to the initial kinetic energy of the ice, as presented in Figure 12.3. The H velocities, instead, were manually set to favor the H–H bond formation respecting the 10 K limitation.

Table 12.1: *Comparison of adsorption and reaction ($H + H \longrightarrow H_2$) energies at PBE and CCSD(T) levels.*

	Reaction energy (kJ mol^{-1})
Crystalline	-438.9
Pos1	-436.2
Pos2	-435.9
Pos3	-440.3
H_2 CP2K[a]	-440.6
H_2 Gaussian[b]	-457.4
	Binding energy (kJ mol^{-1})
CP2K[a]	4.1
Gaussian[b]	2.6

[a] PBE-D3/TZVP level
[b] CCSD(T)/aug-cc-pv5z level

AIMDs were carried out within the NVE (N = number of particles, V = volume, E = energy) ensemble, where the total energy V_{TOT} (*i.e.* potential + kinetic) is conserved. The evolution of the system was followed for 5 ps for the crystalline model and for 1 ps for the amorphous model, using time-steps of 0.2 fs.

Table 12.2: *Results of the AIMD for the H_2 formation on the crystalline (first row) and the ASW three positions (Fig. 12.1) (bottom three rows) ices. Second and third columns report the fraction of kinetic energy of the ice and the newly formed H_2, respectively, at the end of the simulation (5 and 1 ps for crystalline and ASW ices, respectively). Fourth column reports the H_2 binding energy (in kJ/mol) at the reaction site. Fifth and sixth columns report the vibrational state averaged over 0.2–1 ps and 1–5 ps, respectively (the latter can be computed only for the crystalline case). Last column reports the peak energy (in kJ/mol) of an ice-molecule neighbor (i.e. at ~ 3 Å) to where the reaction occurs.*

Model	$\frac{K_{ice}}{K_{ice}+K_{H_2}}$	$\frac{K_{H_2}}{K_{ice}+K_{H_2}}$	BE_{H_2} [kJ/mol]	$\nu^{0.2--1}$	ν^{1--5}	E_{peak} [kJ/mol]
Crys.	0.45	0.55	9.0	4–5	1–2	12.0
Pos1	0.65	0.35	9.7	1–2	–	43.0
Pos2	0.46	0.54	10.6	6	–	7.0
Pos3	0.47	0.53	12.4	5	–	7.0

Ice models

For the crystalline ice model, a periodic slab cut from the hexagonal ice bulk structure was used. The periodic cell parameters defining the system are: $a = 26.318$ Å and $b = 28.330$ Å, while the slab thickness is ~ 21 Å (corresponding to seven layers), for a total of 576 water molecules. The *c* parameter of the simulation box, *i.e.* the non-periodic one, was set to 50 Å to avoid interactions among the fictitious slab replicas. The size of the slab model was chosen to avoid non-physical temperature increase due to the extremely large exothermic reaction (Pantaleone et al., 2020) (Chapter 11).

The amorphous model was obtained by performing a classical molecular dynamics (MD) simulation on the crystalline structure. The MD was carried out with the TIP3P force-field (Jorgensen et al., 1983) for 200 ps (with a timestep of 0.5 fs) at 300 K within the NVT (N = number of particles, V = volume, T = Temperature) ensemble. A second NVT simulation was performed at 10 K, to cool down the system at the temperature of cold molecular clouds. Finally, a geometry optimization and another NVT-MD simulation at 10 K were run using PBE, to recover the potential energy surface at the same theory level as described in the previous section.

H_2 vibrational state

To calculate the H_2 vibrational state during the AIMDs the anharmonic oscillator model was employed. As a first step, the PES (potential energy surface) of the H_2 isolated molecule was explored by performing a rigid scan of the H–H distance, ranging from 0.3 to 3.0 Å with a step of 0.01 Å. Computed data were fitted with the Morse equation to obtain the force constant of the oscillator, its dissociation energy and, hence, the vibrational levels of H_2. The H_2 turning points calculated with our model were compared with those of the AIMD simulations and the vibrational level was assigned at each H_2 oscillation during the AIMDs.

12.3 Results

Reactants plus product positions in the ice models

Figure 12.1 shows the structure of the used crystalline and ASW ice models as well as the starting positions of the center of mass of the two adsorbed H atoms before the reaction. The starting H–H distance, as well as its evolution during the AIMDs is shown in Figure 12.1 in appendix F. The ASW model presents a rugged morphology (e.g. holes, cavities, channels) in comparison to the crystalline one and, therefore, we carried out simulations in three positions, roughly representing different possible situations in terms of energetics and surface morphology. Position marked as Pos1 is the deepest one, within a cavity, while positions Pos2 and Pos3 are in the outermost parts of the surface.

As a first step, we optimized the geometries of reactants (the two H atoms) and product (the H_2 molecule) on the water ice surface in order to obtain the potential energy surface of the reaction. No search for transition state structures has been performed because AIMDs indicated this reaction is barrierless at 10 K. That is, the starting kinetic energy of the two H atoms provided by the 10 K is high enough to overcome

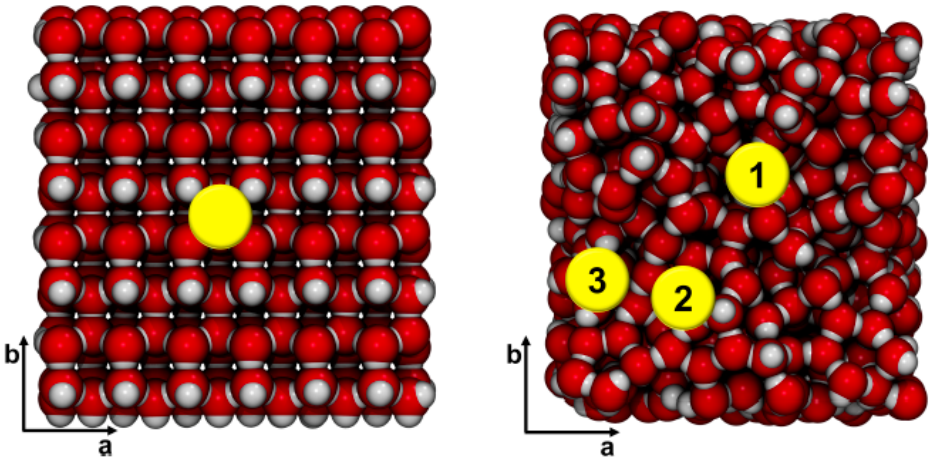

(a) Crystalline ice, top view – ab plane.

(b) ASW ice, top view – ab plane.

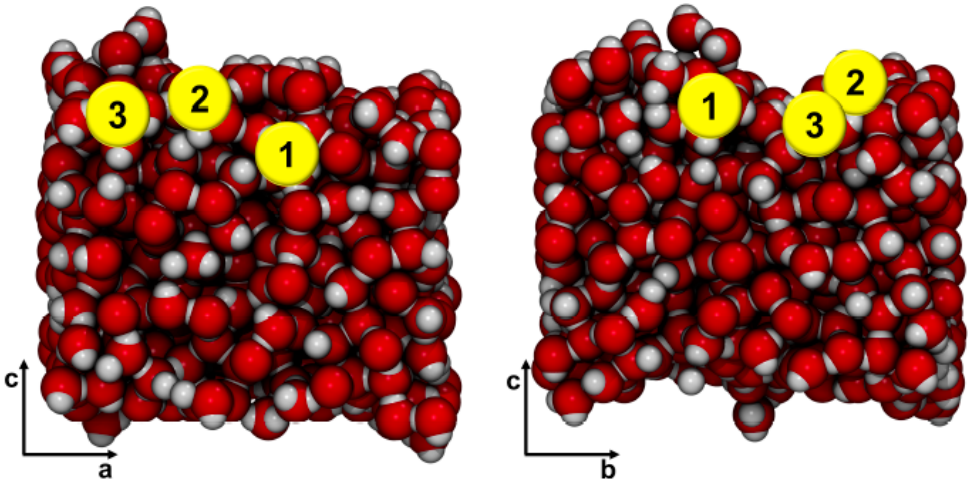

(c) ASW ice, side view – ac plane.

(d) ASW ice, side view – bc plane.

Figure 12.1: *Top view of the crystalline (a), and top (b) and side (c and d) views of the ASW ice models. The yellow circles represent the centers of mass of the two H atoms starting positions. In the case of ASW, the numbers mark the positions (Pos1, Pos2 and Pos3) discussed in the text. The initial H to H distance is about 4 Å (see Figure 12.1 in appendix F). O atoms are in red and H atoms of the ice are in white.*

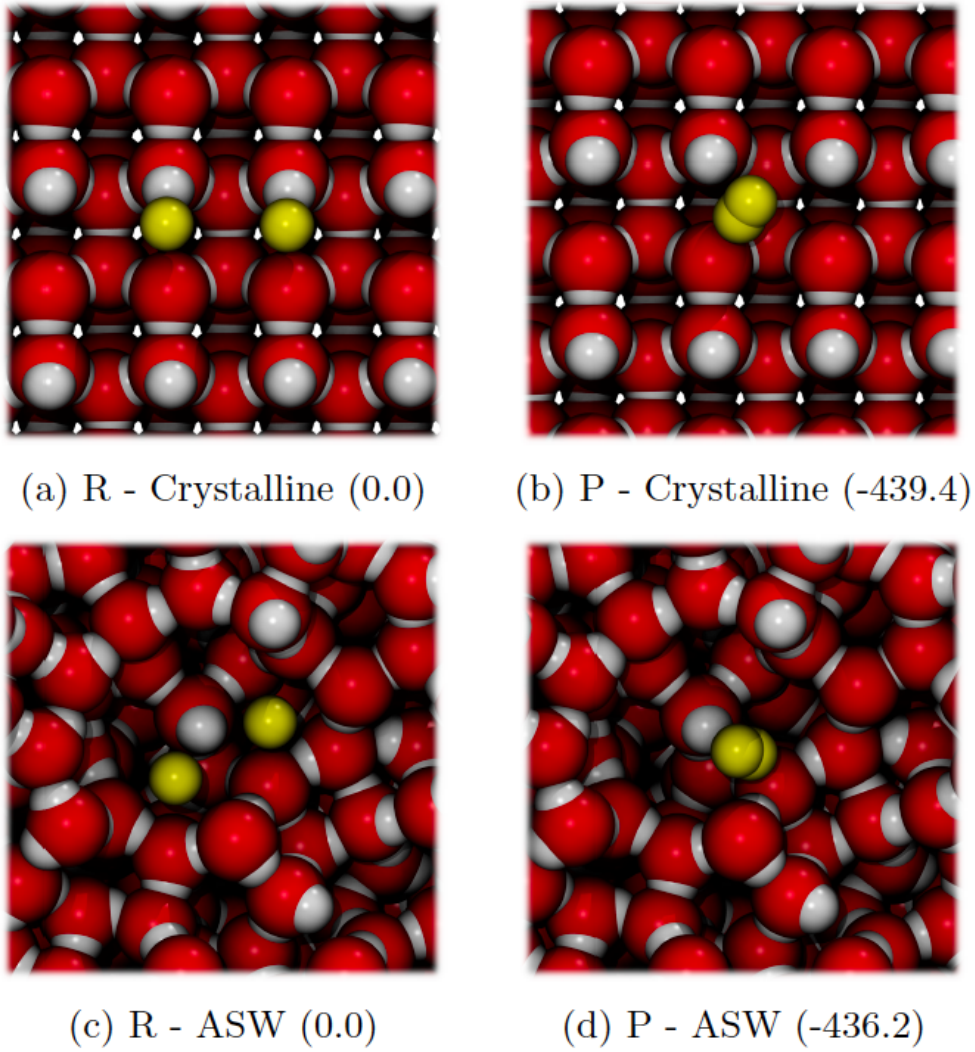

Figure 12.2: *PBE-D3/TZVP optimized geometries of reactants (left panels) and product (right panels) of the H_2 reaction formation on the crystalline (top) and ASW Pos1 (bottom) ice models. The numbers in parenthesis correspond to the relative energy in kJ/mol with respect to the reactants. The H atoms involved in the H + H $\longrightarrow$ H_2 reaction are in yellow, those belonging to surface water molecules are in white, and O atoms are in red.*

the eventually small potential energy barrier. The total energy to be dissipated is around 435-440 kJ/mol, depending on the surface and starting position.

Figure 12.2 provides a view of the two H atoms starting positions and H_2 position immediately after the reaction, on the crystalline and ASW (Pos1 as an example) models, respectively.

Molecular hydrogen desorption

AIMDs results are summarized in Table 12.2 and shown in Fig. 12.3. First, at least half of the kinetic energy is absorbed by the ice while the remaining one is kept by the newly formed H_2 molecule ($\sim$50–35%). These numbers are similar for both for the crystalline and ASW ice positions, suggesting they do no depend much on the surface structural details of the ice.

Second, after the H–H bond formation, the newly formed H_2 molecule diffuses over the surface, as it keeps a large kinetic energy, in both crystalline and ASW ice models. However, despite the energetics of the two processes are similar (Figs. 12.3 left panels) the H_2 diffusion (Figs. 12.3 right panels) is different.

On the crystalline surface, the diffusion of the newly formed H_2 over the ice surface is constrained in a specific direction, along the a-axis, parallel to the ice surface, whereas in the b-axis and c-axis directions the starting position does not change. This is because the crystalline model has alternated and opposite electrostatic potentials along the b-axis direction (see Figures F.2-a and F.2-c in appendix F), which constrains the H_2 diffusion to the perpendicular a-axis, within a channel-like structure created in between the two alternated potential regions. In contrast, on the ASW ice model, H_2 diffuses over all the three directions, also along the c-axis which corresponds to direction perpendicular to the ice surface. However, the movement is not the same in the three studied positions. In Pos1, H_2 achieves a maximum height of $\sim$10 Å over the surface in a timescale of 0.4 ps and does not come back (Fig. 12.3-d), this way leaving definitely the surface. In Pos2, on the contrary, H_2 slides and hops on the surface within the 1 ps of the simulation (Fig. 12.3-f). A similar behavior is observed for Pos3, but with wider hops and jumps (Fig. 12.3-h). However, and this is the key point of the simulations, the kinetic energy remains much larger ($\sim$ 150 kJ/mol) than the binding energy ($\sim$ 10 kJ/mol) in all cases: therefore, the nascent H_2 is likely doomed to leave the ice surface.

Energy dissipation towards the ice water molecules

Fig. 12.4 shows how the energy absorbed by the ice is first transmitted from reaction site to a neighbor water(i.e. at $\sim$4 Å) in $\sim$200–800 fs and, with time, to shells of water molecules with increasing distances. The neighbor water molecule acquires from $\sim$3 to $\sim$14 kJ/mol and stays with that energy for more than about 100–200 fs before the energy is dissipated towards more external water molecules. These timescales are in excellent agreement with previous studies of the sound speed in ices (see e.g. Ruocco et al., 1996).

H_2 vibrational state

The initial state of the H_2 formed on the crystalline ice is ν = 4–5 (obtained averaging over 0.2–1 ps) and then it decreases to ν = 1–2 (1–5 ps average) because of the H_2 energy dissipation. Conversely, at Pos1 of the ASW model, H_2 is formed with a low vibrational state (ν = 1–2, 0.2–1 ps average).

For the other two positions (Pos2 and Pos3), the vibrational state of the newly formed H_2 molecule lies in highly excited states, ν = 6 and ν = 5, respectively. However, our simulations stop at 1 ps and, likely, as on the crystalline ice, the vibrational state of the newly formed H_2 will lower to ν = 1–2. The difference in the behavior between the Pos1 and Pos2/3 is probably due to a transient chemical bond between one of the reacting H and one O atom of a neighboring water molecule (see Figure F.3 in appendix F.

12.4 Discussion

H_2 and other molecules desorption

While there were no doubts that, once formed on the icy surfaces, H_2 molecules will be released into the gas-phase, our new computations provide a quantitative and atomistic-view support to this theory. The newly formed H_2 molecules possess an energy much larger than their binding energy, by more than a factor ten, so that very likely H_2 will be injected into the gas-phase. Even in the worst case of crystalline ice, where

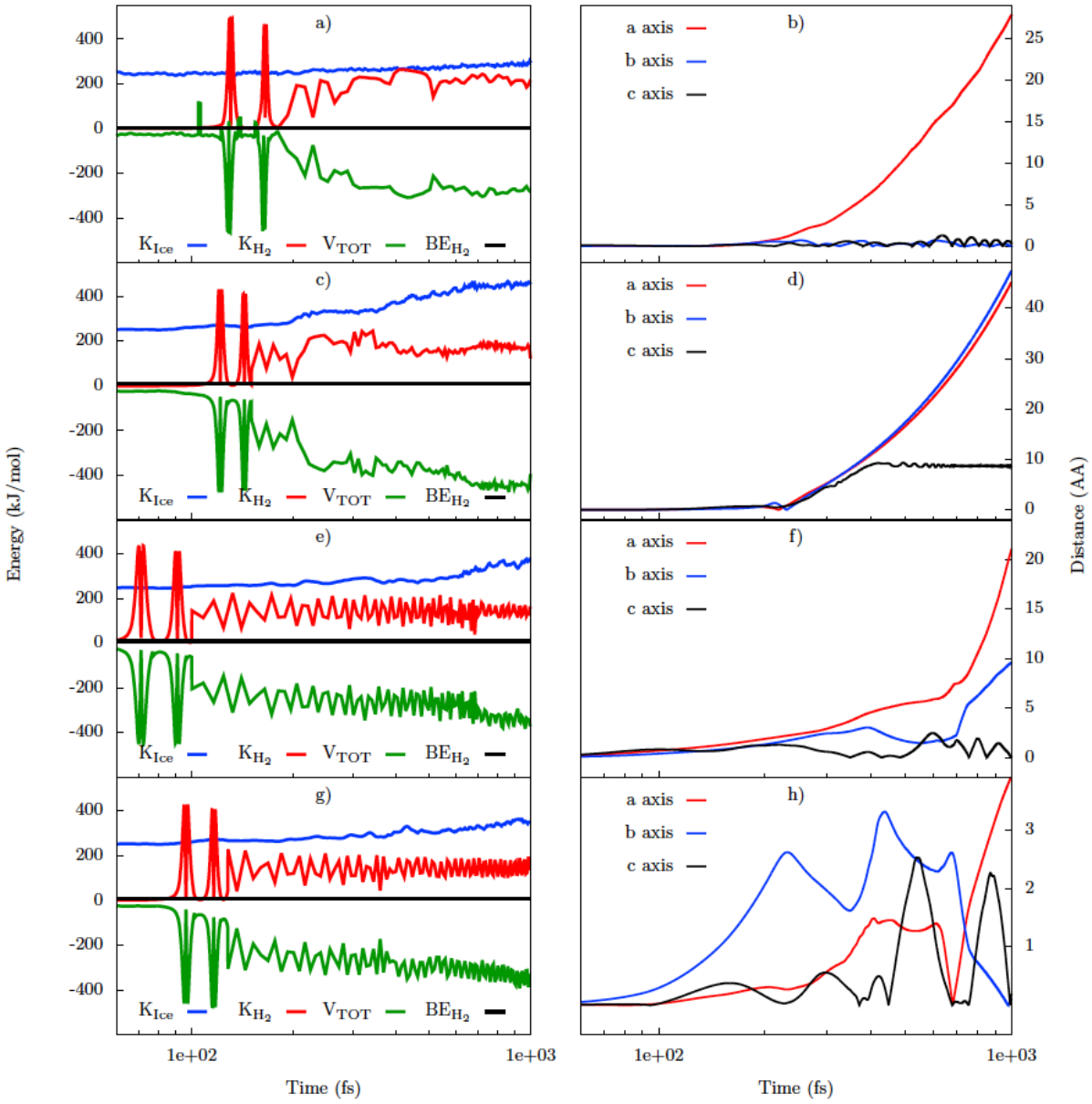

Figure 12.3: *Results of the AIMDs for the crystalline (top panels) and ASW Pos1, Pos2, Pos3 (panels on the second, third and bottom rows) models, respectively. Left panels: Evolution over time (in fs) of the most relevant energetic components (in kJ/mol) of the H_2/ice system for the crystalline (panel a) and ASW Pos1, Pos2 and Pos3 (panel c, e and g) models, respectively. V_{TOT} is the total potential energy (green lines), K_{H_2} and K_{Ice} are the kinetic energies of H_2 (red lines) and ice (blue lines), respectively, while BE_{H_2} (10 kJ/mol = 1200 K) is the binding energy of the H_2 (black lines). Right panels: Diffusion of the center of mass of the H_2 molecule split into the three cartesian components: c-axis is the direction perpendicular to the ice surface, while a-axis and b-axis are along the ice surface (§ 12.2).*

the simulations show H_2 sliding over the perfect ice surface, the newly formed H_2 will sooner or later stumble on an imperfection of the ice so that its trajectory would be deviated and the molecule escape into the gas. To have an estimation of the timescale of this phenomenon one could consider the timescale for the newly H_2 to scan the entire surface of an interstellar grain. Assuming its radius equal to 0.1 μm and each icy site size equal to 3 Å, the number of sites to scan are about 10^5. A first estimate of the time to scan all the sites can be directly obtained by our simulations by considering that about 15 sites of our crystalline ice are covered in less 1 ps: therefore, to scan the 10^5 it will take less than 10 ns. However, this is strictly true if the H_2 molecule does not loose energy in other minor impacts, so ~ 10 ns can be considered a lower limit. The upper limit can be computed by assuming that no residual energy is left to the H_2 molecule except the thermal one and, in this case, the velocity to scan is given by the hopping rate and the timescale for scanning the entire grain surface becomes:

$$t_{scan} = N_s \nu_0^{-1} e^{\frac{E_d}{k_B T_{dust}}} \tag{12.2}$$

where ν_0 is about 10^{12} s^{-1} and E_d is assumed to be 0.3 times the binding energy (about 400 K). Inserting the numbers, a rough estimate of the time that H_2 takes to leave a typical interstellar grain is ≤ 1000 yr. In laboratory analogues of interstellar grains, the timescale would be even larger, and, consequently, not observable. In conclusion, the newly formed H_2 will leave the surface in a timescale between a few ns to a max of about 1000 yr, which is still a very short lifetime with respect to the cloud life.

We want to highlight that the choice of using a proton order ice is just a matter of convenience to test our simulations, before going to the more realistic case of the amorphous surface. On a more realistic proton disordered crystalline ice we expect a more anisotropic behavior of the H_2 molecule, and, as a consequence, a faster H_2 desorption.

Our computations also show that the ice absorbs a significant fraction of the reaction energy, 45–65% (Tab. 12.2). This energy propagates like a wave from the point where the H + H reaction occurs (see Fig. 12.4 and also Pantaleone et al., 2020). In ASW ice, a water molecule close to reaction site acquires 7–43 kJ/mol, (840–5160 K), for more than 100-200 fs. Within the first shell of radius 4 Å, water molecules acquire energies from 3 to 14 kJ/mol (360 to 1680 K, average value counting all the water molecules within the first shell), and farther away the energy acquired by the ice-water molecules decreases to less than 1.6 kJ/mol. The energy acquired by the water ice molecules within a radius of 4 Å from the reaction site could, potentially, be enough to release into the gas-phase any molecule whose binding energy is lower than 3–14 kJ/mol. This could be the case of another H_2 molecule frozen on the ice, a possibility predicted by some astrochemical models (e.g. Hincelin et al., 2015). Indeed, since the binding energy of H_2 is less than $\sim$5 kJ/mol (e.g. Ferrero et al., 2020; Germán Molpeceres et al., 2020; Vidali, 2013), several H_2 molecules could be kicked into the gas-phase.

More interesting is the case of CO, the most abundant molecule after H_2 in galactic cold molecular clouds. It has a binding energy between 7 and 16 kJ/mol (e.g. Ferrero et al., 2020; He et al., 2016) so that frozen CO could potentially be liberated into the gas-phase by the formation of H_2. It has been long recognized that, in absence of a non-thermal desorption process, CO in molecular clouds should be entirely frozen onto the interstellar ices in $\sim 3 \times 10^5$ yr (e.g. Léger, 1983). Several mechanisms have been proposed to explain its presence in the gas (e.g. Duley et al., 1993; Ivlev et al., 2015; Leger et al., 1985; Schutte et al., 1991; Shen et al., 2004). They are all based on the idea that the grain is locally heated and that the frozen molecules are statistically desorbed on a time scale of a few thousands seconds (e.g. Tatsuhiko I. Hasegawa et al., 1993; Herbst et al., 2006), except when faster photodesorption processes are involved. In particular, Duley et al. (1993) and Takahashi et al. (2000) focused on the CO desorption caused by the H_2 formation. Using the results of classical MD simulations by Takahashi and colleagues (Takahashi, 1999; Takahashi et al., 2000, 1999c) and a statistical approach, these authors found that the surface within a radius of $\sim$4 Å from the reaction site is heated up to $\leq$40 K for a too short time (~ 10 fs) to allow CO to sublimate. However, despite the Takahashi's simulations are impressive considering that they were carried out more than 20 years ago, old force fields (like the TIP3P used by Takahashi et al.) have limitations in describing the actual intermolecular interactions and the energy transfer from one molecule to another, compared to our simulations treated at quantum mechanical level.

Our AIMDs show that the water molecules within a radius of 4 Å from the reaction site can be excited from 3 to 14 kJ/mol (depending on the position) for more than 100 fs (Fig. 12.4). Using the range of values in the literature for the CO binding energies (7–16 kJ/mol: Ferrero et al., 2020; He et al., 2016), and the usual

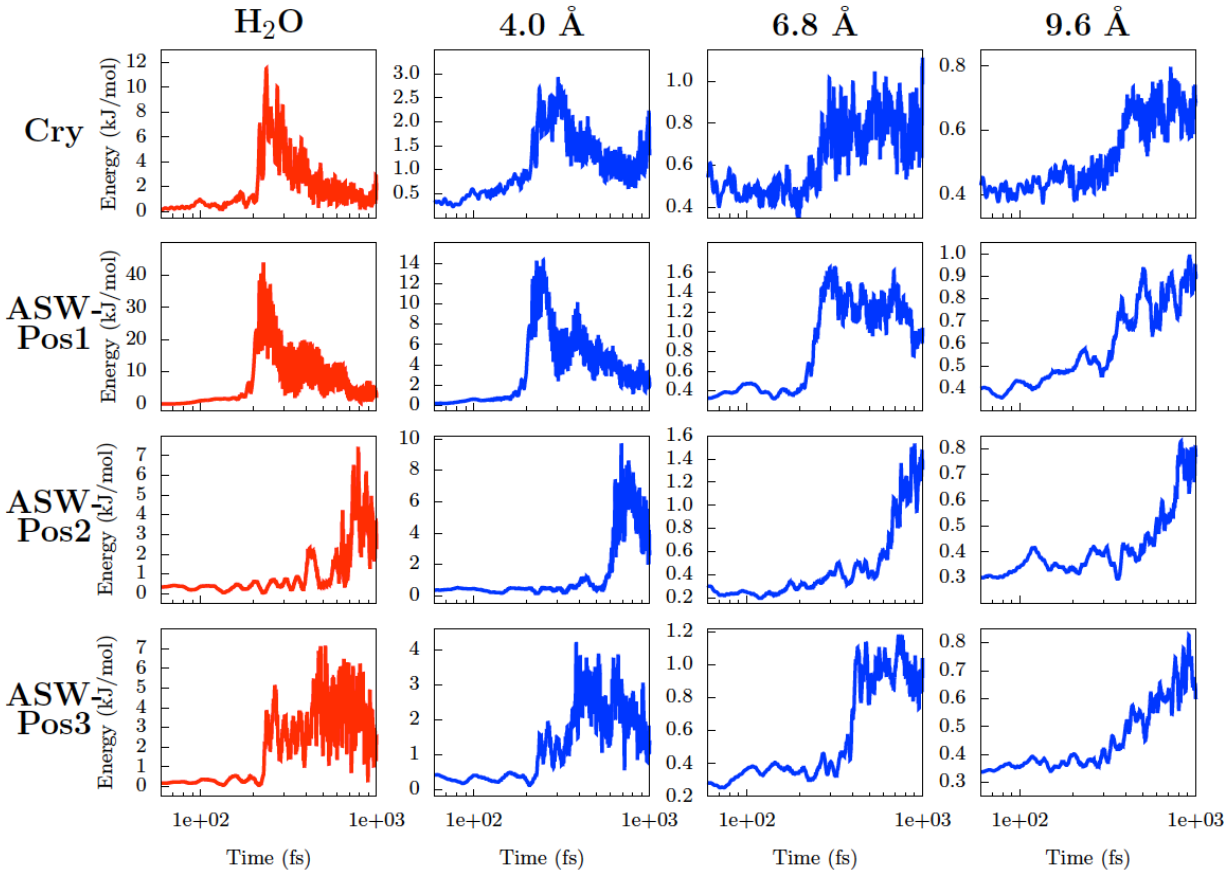

Figure 12.4: *Kinetic energy (in kJ/mol) acquired by the water ice molecules as a function of time for the crystalline (top first row panels) and ASW Pos1-3 (lower panels) ices, as marked by the left-hand labels. Left first column panels: Energy acquired by a single neighboring water ice molecule (i.e. at $\sim$ 3 Å) from the H_2 reaction site. Other column panels: Energy acquired by the ice surface divided in concentric shells (normalized by the number of water molecules per shell), centered at the reaction site. The labels on the top mark the shells radii.*

Eyring equation to estimate the half-life time of CO desorption, we obtain that a CO molecule within a radius of 4 Å from Pos1 would desorb in 33–62 fs, and 69–185 fs from Pos2. On the contrary, CO molecules close to Pos3 and on crystalline ice would not desorb. Therefore, based on this rough argument, the formation of H_2 can potentially desorb frozen CO molecules. Whether this hypothesis is realistic or not, it depends on (i) how many sites of the AWS ice water molecules are excited as in Pos1 and Pos2, (ii) the ratio of H_2 formation rate with respect to the CO freezing rate ($R = \frac{v(H_2)}{v(CO)}$), and (iii) the probability that CO and H_2 are adjacent.

While a more realistic model for the ASW ice is needed to estimate the first quantity (i), one can estimate the second one (ii) as follows. At steady state, assuming that the H + H reaction has efficiency 1 (e.g. Vidali, 2013), the ratio R of the H_2 formation rate with respect to the CO freezing rate is equal to the ratio between the rate of H atoms over CO molecules landing on the grain surface, divided by 2 (because two H atoms are needed for the H_2 formation). Considering an average Milky Way molecular cloud with H_2 density of $10^3 - 10^4$ cm^{-3}, temperature 10 K, a gaseous (undepleted) CO abundance with respect to H_2 equal to 2×10^{-4}, and a cosmic ray ionisation rate of 3×10^{-17} s^{-1}, one obtains $n_H \sim 2$ cm^{-3} and $R \sim 26 - 2.6$. That is, the H_2 formation rate dominates over the CO freezing one. Therefore, frozen CO molecules can potentially be desorbed by the energy released by the H_2 formation on the icy grain surfaces. This process, if confirmed, might naturally explain the presence of gaseous CO in not too dense ($n_H \lesssim 10^4$ cm^{-3}) molecular clouds and solve a decades long mystery. However, to put this affirmation on a solid ground, specific AIMDs showing the effective sublimation of the CO molecule as well as larger ASW ice models and dedicated astrochemical

modeling simulations that include this effect are mandatory. They will be the focus of forthcoming works.

H_2 vibrational state

Previous experimental and computational works on graphite surfaces show that after its formation, the H_2 molecule populates vibrational levels around ν = 3–4 (Casolo et al., 2013; Islam et al., 2010; Latimer et al., 2008). On crystalline and amorphous ice surfaces only a few studies were carried out. Based on classical MD simulations, Takahashi et al., 1999a, 2001 predicted that H_2 formed on amorphous ice would be vibrationally excited to ν = 7–8. In contrast, in some laboratory experiments Hama et al., 2012; Hornekær et al., 2003; Roser et al., 2003, the authors did not detect such excited states. Our new simulations confirm both findings: depending on the site where the formation occurs, H_2 can have large (up to 6) or low (1–2) ν (Tab. 12.2). For example, the case of ASW Pos1, which is the one in a cavity, shows the lowest ν. In the ISM, the vibrational state of the newly formed H_2 molecules will depend on the probability of H_2 leaving the grain surface before being "thermalised" by collisions with ice water molecules, as also found and discussed in Hama et al., 2012.

The vibrational state of the newly formed H_2 molecule, *i.e.* how much the molecule is vibrationally excited, has important consequences on two major astrophysical aspects: (i) to help gas-phase reactions with high activation energy barriers, some of which are the starting points of the entire chemistry in molecular clouds Agúndez et al., 2010; (ii) the possibility to detect newly formed H_2 with near-future JWST (James Webb Space Telescope) observations and, consequently, measure the rate of H_2 formation in molecular clouds and put constraints to theories.

12.5 Conclusions

We studied the energy dissipation of the H_2 formation reaction on both crystalline and amorphous (ASW) ice models by means of state-of-art *ab-initio* molecular dynamics simulations (AIMDs). In the ASW ice, we explored three formation sites meant to represent different situations in terms of energetics and surface morphology: one is in a cavity (Pos1) and two in the outermost parts of the surface (Pos2 and Pos3).

In all simulations, we found that about at least 30% of the reaction energy ($\sim$440 kJ/mol) is acquired by the newly formed H_2, namely more than ten times the H_2 binding energy ($\sim$10 kJ/mol), so that H_2 is likely doomed to leave the ice and to be injected into the gas. The remaining two thirds of the reaction energy are absorbed by the water ice in less than 1 ps. The water molecules nearby to the reaction site have energy peaks of 7–43 kJ/mol for more than 100–200 fs, while those within a 4.0 Å radius of 3–14 kJ/mol.

We showed that it is in principle possible that frozen CO molecules close to the H_2 formation site sublimate. If confirmed, this will be a simple explanation to the decades-long conundrum of why gaseous CO is present in cold molecular clouds. In order to quantify this effect new focused AIMDs adopting larger ASW ice models and dedicated astrochemical modeling will be necessary.

Finally, the nascent H_2 molecules have large ($\nu = 6$) vibrational states in the first ps and later decay to 1–2. This high vibrational state could help reactions with an activation barrier involving H_2 to occur also in cold gas and be observable by JWST.

Conclusions and Perspectives

Chapter 13
Conclusions and Perspectives

Outline

13.1 Conclusions

In this thesis I have investigated two important aspects of interstellar ice surface chemistry: the reactivity between radicals and the capacity of ices to absorb the nascent energy after a chemical reaction. More specifically, I have conducted static quantum chemistry calculations on several important radical–radical reactions, I have derived the kinetics for the case of CH_3 + HCO leading to either acetaldehye or CO + CH_4, and I have studied the fate of the energy released by the H + CO $\rightarrow$ HCO and H + H $\rightarrow$ H_2 reactions on the surface of water ices by means of *ab initio* molecular dynamics.

In this last chapter I shortly discuss the results obtained and their importance for the astrochemistry community.

Radical–radical reactivity I have studied radical–radical surface reactions between HCO + X and CH_3 + X, where X = CH_3, HCO, NH_2, CH_2OH, CH_3O, and additionally CH_3O + CH_3O and CH_2OH + CH_2OH. Based on the surface chemistry paradigm by R. T. Garrod et al. (2006), these radicals react in a Langmuir-Hinshelwood manner and form iCOMs on interstellar ices. In order to simulate the reactions, I have used two models of the amorphous solid water (ASW) consituted by clusters of water molecules. The largest one is composed of 33 water molecules and it is large enough to contain a cavity-like structure. The smallest one is made of 18 water molecules and it best describes a flat surface. According to the Garrod & Herbst scheme, radicals are formed by the photolysis of water, methanol and similar hydrogenated specie, when the ice is still growing. Therefore, they remain frozen within the structure of the ice until they are able to diffuse during the warm-up phase of the protostar (see Figure 1.7). Thus, the ice model that best represents this picture is our largest one because of the presence of a cavity. In this context, I will discuss the conclusions on radical–radical chemistry derived from the results obtained on the ASW 33w-ice model.

The first important result is that the radical–radical reactions listed above can proceed through two channels: (i) radical coupling, leading to iCOMs (e.g. CH_3 + CH_3O $\rightarrow$ CH_3OCH_3), and (ii) direct H-abstraction, which involves the transference of an H atom from one radical to the other (e.g. CH_3 + CH_3O $\rightarrow$ CH_4 + H_2CO).

The second important result is that, contrarily to what is usually assumed, we found that the radical-radical reactions can have activation energy barriers. These barriers can be quite large in some specific cases, like those involving the transference of an H atom from the –OH group in CH_2OH. In other cases, the reactions are actually barrierless or nearly barrierless, like it is the case of CH_3 + NH_2 that leads to CH_3NH_2. However, in general, these activation energy barriers are reaction, system, and surface dependent. Their origin is, in most cases, the interactions of radicals with the icy surface, which need to be broken in order for the two radicals to react.

The third major result is that there are cases in which competition between the radical coupling and the direct H-abstraction channels are important, for instance in many HCO + X reactions where HCO acts as an H-donor.

Finally, based on estimations of the efficiencies of the studied reactions, we provided suggestions on which iCOMs will be likely formed by the reaction between two radicals. We identified three major classes of reactions: a) Ethane (C_2H_6), methylamine (CH_3NH_2) and ethyleneglycol (CH_2OHCH_2OH) are likely formed with no competition from other channels; b) Glyoxal (HCOCHO), formamide (NH_2CHO), methyl formate (CH_3OCHO) and glycolaldehyde (CH_2OCHO) compete with the formation of CO + H_2CO, NH_3 + CO, CH_3OH + CO and again CH_3OH + CO, respectively; c) Acetaldehyde (CH_3CHO) and dimethyl peroxide (CH_3OOCH_3) will likely not be formed, becaus ethey have too high activation energy barriers.

In addition, there are some details that are worth commenting. The first one is related to the reactivity of CH_3, which can be highly suppressed due to “cavity effects”; in other words, CH_3 can get trapped in regions of the ices like cavities so that its mobility is highly reduced. The second one regards the mode in which CH_2OH interacts with the water surface, namely through its OH group, which leaves the C atom vulnerable to reactions (either with other radicals or with H atoms). Finally, the high barriers of CH_3O + CH_3O coupling, which are explained by the stabilization of this radical in the O atom of this radical due to H-bonding.

The ice model influence, namely whether the reaction takes place in the cavity of our largest ASE ice model or on the flat surface of our smallest one, on radical–radical reactions is evidenced in the values of the radical/surface binding energies. Radicals experience more intermolecular interactions in the cavity of our largest ice model, and as a consequence, binding energies are a $\sim$10–80% larger in the cavity than

on the flat surface. This has important consequences on the reaction efficiencies, as the latter depend on the diffusion and desorption kinetics which in turn depend on the binding energies. The reason is rather simple: lower binding energies imply faster diffusion and, therefore, less time to react when the reaction has an activation energy barrier.

As it was said above, many of the iCOM formation reactions studied have a competitive channel. This means that the relative orientation of radicals upon encounter is of paramount importance, as this will benefit more one channel over the other.

As a final comment, I want to stress out that, in our computations, we consider that the two radicals are close to each other (even sharing the same cavity for our largest ASW ice model). However, in a more realistic situation each radical would be stored in different cavities and thus the actual barriers to overcome would not only involve breaking the radical/ice inter-molecular interactions, but also surmounting the ice surface diffusional barriers, decreasing in this way the efficiency of radical–radical coupling and H-abstraction reactions, even if they were ultimately barrierless.

Acetaldehyde formation from CH_3 + HCO This is one of the systems that has a relatively high activation energy barrier for both the radical–radical coupling and direct H-abstraction channels in the cavity of our largest ASW ice model. In order to gain further insight on this radical–radical system we have carried out kinetics calculations by means of the RRKM theory, which includes an approximated description of quantum tunneling for the direct H-abstraction channel *via* the unsymmetric Eckart barrier.

The efficiencies of both reactions were calculated by following the same recipe used in astrochemical models, which accounts for the competition between the reaction, the diffusion and desorption processes. Diffusion and desorption depend on the binding energies of the radicals to the surface, which were also calculated. Given the (large) uncertainty on the diffusion energy barriers E_{dif} and their value with respect to the desorption energy E_{des} in the literature, we carried out the computations assuming three different values for E_{dif}/E_{des}: 0.5, 0.4 and 0.3 respectively. We find that the choice of the diffusion barrier strongly affects the conclusions. For E_{dif}/E_{des} ratios larger than 0.4 we find reaction efficiencies around unity for both channels (coupling and H-abstraction). On the contrary, for a ratio of 0.3, we find that the formation of acetaldehyde is highly suppressed, never going above values of 0.01, while that of CO + CH_4 is unity at low ($\leq$14 K) temperatures, thanks to quantum tunneling, and then it decreases down to $\sim$0.001 as temperature rises. The latest experiments on the CO diffusion in icy surfaces found a E_{dif}/E_{des} ratio close to 0.3 **Kouchi2020_diff_diff**. If the same value applies to the case of CH_3, the radical with lowest binding energy, then the formation on icy surfaces of acetaldehyde is unlikely and, therefore, alternative paths like its gas-phase formation could be required (see e.g. Dimitrios Skouteris et al., 2018; Vazart et al., 2020).

Reaction energy dissipation simulations The capacity of interstellar ices to dissipate the energy of chemical reactions has important consequences on our understanding of interstellar chemistry as it defines another way to connect the chemistry taking place on dust grains and that of the gas phase. Regarding the fate of the energy released by a bond forming reaction on surfaces, one can consider three scenarios: (i) the surface is very efficient at absorbing the chemical energy and the product remains attached to the surface, (ii) part of the energy is kept by the product which induces non-thermal diffusion/desorption, and (iii) the surface is a bad energy dissipator, and as a consequence the product breaks apart into simpler species, like it would happen in the gas phase in the absence of a third body.

We have studied the fate of the reaction energy for two cases of utmost importance in the ISM: the formation of HCO from the hydrogenation of CO and the formation of H_2 from two H atoms, by means of *ab initio* molecular dynamics (AIMD).

The HCO formation study served as a test case in which the surface was modeled by a crystalline water slab. In this study, no chemical desorption was observed, as the ice surface absorbs the nascent chemical energy very fast and the product HCO remains attached to the surface with a kinetic energy much lower than its binding energy to the surface. This is due to the capacity of HCO to establish H-bonds with the surface.

On the contrary, for H_2 formation (a system with much less binding energy to the surface and much more exothermic), both non-thermal desorption and non-thermal diffusion were observed, depending on the point at which the reaction takes place. In all cases the product H_2 molecule kept much more kinetic energy than its binding energy, which indicates that it is doomed to leave the surface sooner or later, with a possibly

high vibrational excitation ($\nu < 6$). In addition to this, the water molecules in the vicinity of the reaction site were observed to be kinetically excited forming a transient hot spot. This energy could be employed in desorbing weakly bound molecules like another H_2 molecule or potentially a CO molecule. If confirmed, this process could account for the presence of gaseous CO in molecular cloud, even in absence of desorption of cosmic-rays.

Conclusive remarks In this thesis, it has been shown that radical–radical surface chemistry on interstellar ices cannot be ruled out as a synthetic pathway towards iCOMs during the so called warm-up phase of protostars. However, we have shown that it is more complex than just a LEGO-like game. The radical/surface interaction, the relative orientation with which radicals meet, the diffusion activation energy of each radical on the surface, the region of the surface where the reaction takes place and the nature of the radicals themselves deeply affect their chemistry and the result of the reaction.

Concerning the capacity of ice surfaces to absorb and dissipate reaction energies, from the two cases that we have explored, HCO and H_2 formation, it is clear that the nature of the product affects the final result. This can be seen by comparing the two simulations on top of the crystalline slab model: HCO remains attached while H_2 diffuses over the surface in a non-thermal manner, keeping enough kinetic energy to eventually desorb. In the case of H_2 we have also seen that the surface morphology and surface site do not play such a strong role for this reaction since little differences are observed between the simulations on the crystalline and the amorphous surface models. In addition, the formation of H_2 could still provide a means for the desorption of nearby CO molecules.

In summary, nowadays it is clear that the interplay between gas-phase and grain-surface chemistry is much more complex than it was thought a decade ago. Surface chemistry products can become precursors for complex gas-phase reactions in warm ($>$100 K) and probably also in cold ($<$10 K) stages of the star formation process, setting the onset of complex molecules in space much earlier than it was supposed a few years ago. iCOM forming reactions in luke-warm conditions may also occur on the grain-surfaces, but the process is clearly much more complicated than it was assumed before this thesis.

13.2 Perspectives

My thesis has started to explore a number of issues related to the reaction between radical occurring on icy surfaces. We are far to have reached firm conclusions on how efficient and important they are in the growth of molecular complexity in star forming regions. In the following, I will discuss the perspective that I see in future similar studies and my short and long term plans.

Kinetic data on radical–radical reactions In my thesis work, I have shown that RRKM theory can be used in deriving kinetic data for reactions between radicals on the surface. This is a great asset for astrochemical models and, for this reason, I plan to use the information on the activation energy barriers of the radical–radical surface reactions studied in this thesis in order to derive their kinetic constants. In addition to complete the computations on the kinetics of radical–radical reactions, using the same methods and PES, I will investigate the kinetic isotopic effects due to deuterium substitutions on icy surfaces, a field that has been almost unexplored so far, despite the recent detection of deuterated iCOMs. In principle, the observed iCOMs deuteration could bring valuable information on their formation route, if theoretical predictions were available, a gap that I plan to fill up in the very short and long term.

AIMD simulations for radical–radical reactions In this thesis, I have shown that many radical–radical surface reactions have similar reaction energy barriers for radical coupling and direct H-abstraction reactions, something that evidences the importance of the relative orientation of radicals upon encounter. AIMD simulation of radicals–radical reactions are the key to better understand this point. On the same vein, the fate of the nascent chemical energy after reaction needs also to be investigated further. This can only be done by means of molecular dynamics studies, which, due to the particluar electronic structure of singlet electronic state biradical systems, can only be done with AIMD simulations. I, therefore, plan to tackle both issues by running AIMD simulations as we did for the formation of H_2. My idea is to run a limited number of simulations starting with the radicals in selected positions with different relative orientations and let them

evolve. If when running the simulation I find an energetic barrier, I will follow the same methodology as in the HCO formation simulation, namely searching the transition state (TS) and starting from there, with the radical orientation computed by the AIMD.

Can actually H_2 formation desorb a nearby CO molecule? In the work on the H_2 formation on icy surfaces, we have suggested the possibility that the energy dissipated could be used to kick into the gas-phase frozen CO molecules, which would solve a decades long riddle. In order to further check this possibility, I will run new AIMD simulations where H_2 is formed on amorphous water ice with nearby CO molecules, on a dedicated "dirty" ice model and on a pure CO ice, respectively. I plan to take the results from the H_2 formation simulations presented in this thesis and add a nearby CO molecule in order to check if our proposal is correct or not within the constrains of the employed methodology, namely the DFT method and the used ice models.

Other reactions where radicals act as a reactant Radical–radical reactions are but a small part of the possible reactivity of radicals. Radicals could, indeed, react with closed shell molecules like H_2, O_2 and even species where a carbon–carbon double bond is present. Such reactions would produce saturated closed shell species, oxidized organics and larger carbon-based radicals. In addition to this, the carbene and nitrene families (species containing a singlet/tripet open-shell electronic state localized on the same atom) could show very interesting surface chemistry. Such species can react with single electron radicals (e.g. CH_3), double-bonded carbon groups (e.g. C_2H_4), and can get inserted into C–H, O–H and N–H bonds (interstellar ices are thought to be rich in this kind of species thanks to hydrogenation reactions). Therefore, these reactions could be a great asset for surface astrochemistry worth studying. The simplest carbene and nitrene species one can think of are CH_2 and NH, both of which were proposed in Robin T. Garrod et al., 2008 as possible surface reactants, and which could be formed by the partial hydrogenation of C and N atoms on interstellar grains.

iCOM formation on ices without the requirement of surface diffusion Surface chemical reactions do not only regard hydrogenation, oxidation and radical–radical coupling reactions. The ice can also play a chemically active role and not just that of a third body. For example, Rimola et al. (2018) found that water molecules from the ice can readily react with the CN radical leading to formamide (NH_2CHO), if it is assumed that there are no significant energy losses during the reaction sequence, which has three steps: (i) reaction with a water molecule forming an imide acid radical (HNCOH) (ii) a rearrangement of this radical into NH_2CO radical thanks to a water assisted H-transfer, and finally (iii) barrierless hydrogenation into formamide. The very first step works thanks to the formation of a hemibond[1] between the C atom of CN and the O atom of a water molecule from the surface.

This kind of mechanism could also be at play for other systems able to form similar hemibond structures. We have identified another radical able to do so, CCH, which is very abundant in the ISM gas-phase of a variety of interstellar objects such as photon-dominated regions, diffuse clouds, prestellar cores, protoplanetary disks and high mass star formation regions Beuther et al., 2008; Cuadrado et al., 2015; Dutrey et al., 1997; Lucas et al., 2000; Padovani et al., 2009; Teyssier et al., 2004; Tucker et al., 1974a. We have started to investigate the reactivity of the CCH radical with water molecules leading to vinyl alcohol (CH_2CHOH), which could then yield ethanol in the solid phase, a molecule which is though to be crucial in the developement of some iCOMs in the gas-phase (Dimitrios Skouteris et al., 2018; Vazart et al., 2020). So far we have found that the formation of vinyl alcohol possesses a barrier $<$2 kJ mol^{-1}, so that this ethanol formation path is a possibility.

A similar reaction scheme has been experimentally investigated, effectively leading to ethanol. Indeed, Chuang et al. (2020) and Chuang et al. (2021) showed that the deposition of H atoms on C_2H_2:O_2 ices at 10 K and the irradiation of C_2H_2:H_2O ices with energetic protons at 17 K, respectively produce iCOMs like vinyl alcohol, acetaldehye, ketene and ethanol. The first step is C_2H_2 + OH $\rightarrow$ CHCHOH, which, after a barrierless hydrogenation step, yields vinyl alcohol[2], the same product as in our CCH + H_2O reaction. Vinyl

[1] A non-classical type of chemical bond that relates two nuclear centers and three electrons.
[2] Something already reported earlier on by the ion irradiation experiments of Hudson et al. (2003).

alcohol can then (i) isomerize into acetaldehyde (although the barriers are expected to be very high $>$49.5 kJ mol^{-1}), and (ii) produce ethanol after two hydrogenation steps.

The reaction scheme that we propose has the same capabilities, also at low temperatures, and does not require of the thermal diffusion of surface species. In fact its first step can be understood as an Eley-Rideal reaction, in which a gas phase CCH radical lands on a water-dominated interstellar ice.

Conclusions I think that my thesis has only scratched the tip of the iceberg that represents the surface chemistry in the ISM. There are plenty of issues that still await to be understood and I hope that in my near and distant future I will be able to further contribute to this young field of the astrochemistry, thanks to the availability of computational facilities more and more powerful and the methodology developments stimulated by them.

Whole Bibliography

References

Abe, Manabu (Sept. 2013). “Diradicals”. In: *Chem. Rev.* 113.9, pp. 7011–7088.

Acharyya, Kinsuk and Eric Herbst (2015). “Molecular Development in the Large Magellanic Cloud”. In: *Astrophys. J.* 812.2, p. 142.

Agúndez, M et al. (2010). “The chemistry of vibrationally excited H_2 in the interstellar medium”. In: *The Astrophysical Journal* 713.1, p. 662.

Aikawa, Yuri et al. (Feb. 2008). “Molecular Evolution and Star Formation: From Prestellar Cores to Protostellar Cores”. In: *Astrophys. J.* 674.2, pp. 984–996. DOI: 10.1086/524096. arXiv: 0710.0712 [astro-ph].

Aikawa, Yuri et al. (July 2020). “Chemical Variation among Protostellar Cores: Dependence on Prestellar Core Conditions”. In: *Astrophys. J.* 897.2, 110, p. 110. DOI: 10.3847/1538-4357/ab994a. arXiv: 2006.11696 [astro-ph.SR].

Allen, M. and G. W. Robinson (Mar. 1977). “The molecular composition of dense interstellar clouds.” In: *Astrophys. J.* 212, pp. 396–415. DOI: 10.1086/155059.

Álvarez-Barcia, S. et al. (Sept. 2018). “Hydrogen transfer reactions of interstellar complex organic molecules”. In: *Mon. Not. R. Astron. Soc.* 479.2, pp. 2007–2015. DOI: 10.1093/mnras/sty1478. arXiv: 1806.02062 [astro-ph.GA].

Andersson, Stefan, T. P. M. Goumans, and Andri Arnaldsson (Sept. 2011). “Tunneling in hydrogen and deuterium atom addition to CO at low temperatures”. In: *Chemical Physics Letters* 513.1-3, pp. 31–36.

Andersson, Stefan et al. (Feb. 2006). “Molecular-dynamics study of photodissociation of water in crystalline and amorphous ices”. In: *J. Chem. Phys.* 124.6, pp. 064715–064715. DOI: 10.1063/1.2162901.

André, Ph. et al. (July 2010). “From filamentary clouds to prestellar cores to the stellar IMF: Initial highlights from the Herschel Gould Belt Survey”. In: *Astron. Astrophys.* 518, L102, p. L102. DOI: 10.1051/0004-6361/201014666. arXiv: 1005.2618 [astro-ph.GA].

Aquilante, Francesco et al. (2010). “MOLCAS 7: The Next Generation”. In: *J. Comput. Chem.* 31.1, pp. 224–247. DOI: 10.1002/jcc.21318. URL: https://onlinelibrary.wiley.com/doi/abs/10.1002/jcc.21318.

Aquilante, Francesco et al. (2016). “Molcas 8: New capabilities for multiconfigurational quantum chemical calculations across the periodic table”. In: *J. Comput. Chem.* 37.5, pp. 506–541. DOI: 10.1002/jcc.24221. URL: https://onlinelibrary.wiley.com/doi/abs/10.1002/jcc.24221.

Arce, Héctor G. et al. (June 2008). “Complex Molecules in the L1157 Molecular Outflow”. en. In: *Astrophys. J. Lett.* 681.1, p. L21. ISSN: 1538-4357. DOI: 10.1086/590110. URL: https://iopscience.iop.org/article/10.1086/590110/meta (visited on 11/18/2019).

Ásgeirsson, V, H Jónsson, and KT Wikfeldt (2017). “Long-time scale simulations of tunneling-assisted diffusion of hydrogen on ice surfaces at low temperature”. In: *The Journal of Physical Chemistry C* 121.3, pp. 1648–1657.

Asplund, Martin et al. (Sept. 2009). “The Chemical Composition of the Sun”. In: *Annu. Rev. Astron. Astrophys.* 47.1, pp. 481–522. DOI: 10.1146/annurev.astro.46.060407.145222. arXiv: 0909.0948 [astro-ph.SR].

Atkins, P, J de Paula, and R Friedman (2013). *Physical Chemistry. Quanta, Matter, and Change*. Oxford University Press. ISBN: 9780199609819.

Awad, Zainab et al. (Oct. 2010). “Warm cores around regions of low-mass star formation”. In: *Mon. Not. R. Astron. Soc.* 407.4, pp. 2511–2518. DOI: 10.1111/j.1365-2966.2010.17077.x. arXiv: 1005.5265 [astro-ph.SR].

Bacmann, A. et al. (July 2002). “The degree of CO depletion in pre-stellar cores”. In: *Astron. Astrophys.* 389, pp. L6–L10. DOI: 10.1051/0004-6361:20020652. arXiv: astro-ph/0205154 [astro-ph].

Bacmann, A. et al. (Mar. 2003). “CO Depletion and Deuterium Fractionation in Prestellar Cores”. In: *Astrophys. J. Lett.* 585.1, pp. L55–L58. DOI: 10.1086/374263. arXiv: astro-ph/0301651 [astro-ph].

Bacmann, A. et al. (May 2012). “Detection of complex organic molecules in a prestellar core: a new challenge for astrochemical models”. In: *Astron. Astrophys.* 541, L12, p. L12. DOI: 10.1051/0004-6361/201219207.

Baer, Tomas and William L. Hase (1996). *Unimolecular Reaction Dynamics. Theory and Experiments*. International Series of Monographs on Chemistry. ISBN: 9780195074949.

Bahn, S. R. and K. W. Jacobsen (2002). “An object-oriented scripting interface to a legacy electronic structure code”. In: *Comput. Sci. Eng.* 4 (3), pp. 56–66. DOI: 10.1109/5992.998641.

Balucani, N., C. Ceccarelli, and V. Taquet (Apr. 2015). “Formation of complex organic molecules in cold objects: the role of gas-phase reactions.” In: *Mon. Not. R. Astron. Soc.* 449, pp. L16–L20. DOI: 10.1093/mnrasl/slv009. arXiv: 1501.03668 [astro-ph.SR].

Bar-Nun, A. et al. (Jan. 1987). “Amorphous water ice and its ability to trap gases”. In: *Phys. Rev. B* 35.5, pp. 2427–2435. DOI: 10.1103/PhysRevB.35.2427.

Baratta, G. A. et al. (Jan. 2004). “Ion irradiation of ices relevant to astrophysics”. In: *Memorie della Societa Astronomica Italiana Supplementi* 5, p. 33.

Barger, Christopher J. and Robin T. Garrod (Jan. 2020). “Constraining Cosmic-Ray Ionization Rates and Chemical Timescales in Massive Hot Cores”. In: *Astrophys. J.* 888.1, 38, p. 38. DOI: 10.3847/1538-4357/ab5b0d.

Barone, V. et al. (Oct. 2015). “Gas-phase formation of the prebiotic molecule formamide: insights from new quantum computations.” In: *Mon. Not. R. Astron. Soc.* 453, pp. L31–L35. DOI: 10.1093/mnrasl/slv094. arXiv: 1507.03741 [astro-ph.GA].

Barone, Vincenzo, Malgorzata Biczysko, and Cristina Puzzarini (2015). “Quantum Chemistry Meets Spectroscopy for Astrochemistry: Increasing Complexity toward Prebiotic Molecules”. In: *Accounts of Chemical Research* 48.5, pp. 1413–1422. DOI: 10.1021/ar5003285.

Becke, Axel D (1993a). “A new mixing of Hartree–Fock and local density-functional theories”. In: *J. Chem. Phys.* 98.2, pp. 1372–1377.

— (1993b). “Density-functional thermochemistry. III. The role of exact exchange”. In: *J. Chem. Phys.* 98.7, pp. 5648–5652.

Beichman, C. A. et al. (Aug. 1986). “Candidate Solar-Type Protostars in Nearby Molecular Cloud Cores”. In: *Astrophys. J.* 307, p. 337. DOI: 10.1086/164421.

Belloche, A. et al. (May 2017). “Rotational spectroscopy, tentative interstellar detection, and chemical modeling of N-methylformamide”. In: *Astron. Astrophys.* 601, A49. ISSN: 0004-6361, 1432-0746. DOI: 10.1051/0004-6361/201629724. URL: https://www.aanda.org/articles/aa/abs/2017/05/aa29724-16/aa29724-16.html (visited on 11/12/2019).

Bennett, Chris J. and Ralf I. Kaiser (June 2007). “On the Formation of Glycolaldehyde (HCOCH2OH) and Methyl Formate (HCOOCH3) in Interstellar Ice Analogs”. In: *Astrophys. J.* 661.2, pp. 899–909. DOI: 10.1086/516745.

Bennett, Chris J. et al. (Jan. 2005). “A combined experimental and theoretical study on the charged particle processing of low temperature ices”. In: *Astrochemistry: Recent Successes and Current Challenges*. Ed. by Dariusz C. Lis, Geoffrey A. Blake, and Eric Herbst. Vol. 231, p. 113.

Bergin, Edwin A. and Mario Tafalla (Sept. 2007). “Cold Dark Clouds: The Initial Conditions for Star Formation”. In: *Annu. Rev. Astron. Astrophys.* 45.1, pp. 339–396. DOI: 10.1146/annurev.astro.45.071206.100404. arXiv: 0705.3765 [astro-ph].

Bernstein, Max P. et al. (Mar. 2002). “Racemic amino acids from the ultraviolet photolysis of interstellar ice analogues”. In: *Nature* 416.6879, pp. 401–403. DOI: 10.1038/416401a.

Bertin, Mathieu et al. (Dec. 2013). “Indirect Ultraviolet Photodesorption from CO:N2 Binary Ices – an Efficient Grain-gas Process”. In: *Astrophys. J.* 779.2, 120, p. 120. DOI: 10.1088/0004-637X/779/2/120. arXiv: 1312.4571 [astro-ph.GA].

Bertin, Mathieu et al. (Feb. 2016). “UV Photodesorption of Methanol in Pure and CO-rich Ices: Desorption Rates of the Intact Molecule and of the Photofragments”. In: *Astrophys. J. Lett.* 817.2, L12, p. L12. DOI: 10.3847/2041-8205/817/2/L12. arXiv: 1601.07027 [astro-ph.GA].

Beuther, H. et al. (Mar. 2008). “Ethynyl (C_2H) in Massive Star formation: Tracing the Initial Conditions?” In: *Astrophys. J. Lett.* 675.1, p. L33. DOI: 10.1086/533412. arXiv: 0801.4493 [astro-ph].

Bianchi, E et al. (Nov. 2018). “The census of interstellar complex organic molecules in the Class I hot corino of SVS13-A”. In: *Mon. Not. R. Astron. Soc.* 483.2, pp. 1850–1861. ISSN: 0035-8711. DOI: 10.1093/mnras/sty2915. eprint: http://oup.prod.sis.lan/mnras/article-pdf/483/2/1850/27124262/sty2915.pdf. URL: https://doi.org/10.1093/mnras/sty2915.

Blake, Geoffrey A. et al. (Apr. 1987). “Molecular Abundances in OMC-1: The Chemical Composition of Interstellar Molecular Clouds and the Influence of Massive Star Formation”. In: *Astrophys. J.* 315, p. 621. DOI: 10.1086/165165.

Bockelée-Morvan, Dominique (2011). “An overview of comet composition”. In: *Proc. Int. Astron. Union* 7.S280, pp. 261–274.

Boogert, A. C. Adwin, Perry A. Gerakines, and Douglas C. B. Whittet (Aug. 2015). “Observations of the icy universe.” In: *Annu. Rev. Astron. Astrophys.* 53, pp. 541–581. DOI: 10.1146/annurev-astro-082214-122348. arXiv: 1501.05317 [astro-ph.GA].

Bovolenta, Giulia et al. (Dec. 2020). “High level ab initio binding energy distribution of molecules on interstellar ices: Hydrogen fluoride”. In: *Molecular Astrophysics* 21, 100095, p. 100095. DOI: 10.1016/j.molap.2020.100095. arXiv: 2010.09138 [astro-ph.GA].

Boys, S F_ and Fiorenza de Bernardi (1970). “The calculation of small molecular interactions by the differences of separate total energies. Some procedures with reduced errors”. In: *Mol. Phys.* 19.4, pp. 553–566.

Bredehöft, Jan H. et al. (Mar. 2017). “Electron-Induced Synthesis of Formamide in Condensed Mixtures of Carbon Monoxide and Ammonia”. In: *ACS Earth and Space Chemistry* 1.1, pp. 50–59. DOI: 10.1021/acsearthspacechem.6b00011.

Brown, P. D., S. B. Charnley, and T. J. Millar (Mar. 1988). “A model of the chemistry in hot molecular cores.” In: *Mon. Not. R. Astron. Soc.* 231, pp. 409–417. DOI: 10.1093/mnras/231.2.409.

Buch, V. and Q. Zhang (Oct. 1991). “Sticking Probability of H and D Atoms on Amorphous Ice: A Computational Study”. In: *Astrophys. J.* 379, p. 647. DOI: 10.1086/170537.

Burke, J. R. and D. J. Hollenbach (Feb. 1983). “The gas-grain interaction in the interstellar medium - Thermal accommodation and trapping”. In: *Astrophys. J.* 265, pp. 223–234. DOI: 10.1086/160667.

Burrows, Christopher J. et al. (Dec. 1996). “Hubble Space Telescope Observations of the Disk and Jet of HH 30”. In: *Astrophys. J.* 473, p. 437. DOI: 10.1086/178156.

Butscher, Teddy et al. (Jan. 2017). “Radical recombination in interstellar ices, a not so simple mechanism”. In: *Physical Chemistry Chemical Physics (Incorporating Faraday Transactions)* 19.4, pp. 2857–2866. DOI: 10.1039/C6CP07024H.

Caballol, R et al. (1976). “Theoretical interstellar and prebiotic organic chemistry: a tentative methodology.” In: *Origins of life* 7.3, pp. 163–173.

Caselli, P., T. W. Hartquist, and O. Havnes (June 1997). “Grain-grain collisions and sputtering in oblique C-type shocks.” In: *Astron. Astrophys.* 322, pp. 296–301.

Caselli, P. et al. (Oct. 1999). “CO Depletion in the Starless Cloud Core L1544”. In: *Astrophys. J. Lett.* 523.2, pp. L165–L169. DOI: 10.1086/312280.

Caselli, P. et al. (May 2003). “Abundant H2D+ in the pre-stellar core L1544”. In: *Astron. Astrophys.* 403, pp. L37–L41. DOI: 10.1051/0004-6361:20030526. arXiv: astro-ph/0304103 [astro-ph].

Caselli, P, TI Hasegawa, and Eric Herbst (1993). “Chemical differentiation between star-forming regions-The Orion hot core and compact ridge”. In: *The Astrophysical Journal* 408, pp. 548–558.

Caselli, Paola and Cecilia Ceccarelli (Oct. 2012). “Our astrochemical heritage”. en. In: *Astron. Astrophys. Rev.* 20.1, p. 56. ISSN: 1432-0754. DOI: 10.1007/s00159-012-0056-x. URL: https://doi.org/10.1007/s00159-012-0056-x (visited on 11/12/2019).

Casolo, Simone, Gian Franco Tantardini, and Rocco Martinazzo (2013). “Insights into H_2 formation in space from ab initio molecular dynamics”. In: *Proceedings of the National Academy of Sciences* 110.17, pp. 6674–6677.

Cazaux, S. et al. (Aug. 2003). “The Hot Core around the Low-mass Protostar IRAS 16293-2422: Scoundrels Rule!” In: *Astrophys. J. Lett.* 593.1, pp. L51–L55. DOI: 10.1086/378038.

Ceccarelli, C. (Dec. 2004). “The Hot Corinos of Solar Type Protostars”. In: *Star Formation in the Interstellar Medium: In Honor of David Hollenbach*. Ed. by D. Johnstone et al. Vol. 323. Astronomical Society of the Pacific Conference Series, p. 195.

Ceccarelli, C. et al. (May 2000). “The hot core of the solar-type protostar IRAS 16293-2422: H2CO emission”. In: *Astron. Astrophys.* 357, pp. L9–L12.

Ceccarelli, C. et al. (Jan. 2014). “Deuterium Fractionation: The Ariadne’s Thread from the Precollapse Phase to Meteorites and Comets Today”. In: *Protostars and Planets VI*. Ed. by Henrik Beuther et al., p. 859. DOI: 10.2458/azu_uapress_9780816531240-ch037. arXiv: 1403.7143 [astro-ph.EP].

Ceccarelli, C. et al. (Nov. 2017a). “Seeds Of Life In Space (SOLIS): The Organic Composition Diversity at 300–1000 au Scale in Solar-type Star-forming Regions”. In: *Astrophys. J.* 850.2, p. 176. DOI: 10.3847/1538-4357/aa961d.

Ceccarelli, C. et al. (Dec. 2017b). “Seeds Of Life In Space (SOLIS): The Organic Composition Diversity at 300-1000 au Scale in Solar-type Star-forming Regions”. In: *Astrophys. J.* 850.2, 176, p. 176. DOI: 10.3847/1538-4357/aa961d. arXiv: 1710.10437 [astro-ph.SR].

Cernicharo, J., M. Guélin, and C. Kahane (Mar. 2000). “A lambda 2 mm molecular line survey of the C-star envelope IRC+10216”. In: *A&ASS* 142.2, pp. 181–215. ISSN: 0365-0138, 1286-4846. DOI: 10.1051/aas:2000147. URL: https://aas.aanda.org/articles/aas/abs/2000/05/ds1723/ds1723.html (visited on 11/18/2019).

Cernicharo, J. et al. (Nov. 2012). “Discovery of the Methoxy Radical, CH3O, toward B1: Dust Grain and Gas-phase Chemistry in Cold Dark Clouds”. In: *Astrophys. J. Lett.* 759.2, L43, p. L43. DOI: 10.1088/2041-8205/759/2/L43.

Chaabouni, H. et al. (Dec. 2012). “Water formation through O2 + D pathway on cold silicate and amorphous water ice surfaces of interstellar interest”. In: *J. Chem. Phys.* 137.23, pp. 234706–234706. DOI: 10.1063/1.4771663.

Chalk, S. J. (2019). *IUPAC. Compendium of Chemical Terminology*. ISBN: 0967855098. International Union of Pure and Applied Chemistry (IUPAC): Research Triangle Park, NC.

Chang, Q., H. M. Cuppen, and E. Herbst (July 2007). “Gas-grain chemistry in cold interstellar cloud cores with a microscopic Monte Carlo approach to surface chemistry”. In: *Astron. Astrophys.* 469.3, pp. 973–983. DOI: 10.1051/0004-6361:20077423. arXiv: 0704.2704 [astro-ph].

Charnley, S. B. (Jan. 2004). “Acetaldehyde in star-forming regions”. In: *Advances in Space Research* 33.1, pp. 23–30. DOI: 10.1016/j.asr.2003.08.005.

Charnley, S. B., A. G. G. M. Tielens, and T. J. Millar (Nov. 1992). “On the Molecular Complexity of the Hot Cores in Orion A: Grain Surface Chemistry as “The Last Refuge of the Scoundrel””. In: *Astrophys. J. Lett.* 399, p. L71. DOI: 10.1086/186609.

Chevance, Mélanie et al. (Apr. 2020). “The Molecular Cloud Lifecycle”. In: *Space Sci. Rev.* 216.4, 50, p. 50. DOI: 10.1007/s11214-020-00674-x. arXiv: 2004.06113 [astro-ph.GA].

Choi, Minho (Sept. 2005). “Variability of the NGC 1333 IRAS 4A Outflow: Silicon Monoxide Observations”. In: *Astrophys. J.* 630.2, pp. 976–986. DOI: 10.1086/432113.

Chuang, K. -J. et al. (Jan. 2016). “H-atom addition and abstraction reactions in mixed CO, H2CO and CH3OH ices - an extended view on complex organic molecule formation”. In: *Mon. Not. R. Astron. Soc.* 455.2, pp. 1702–1712. DOI: 10.1093/mnras/stv2288. arXiv: 1606.01049 [astro-ph.GA].

Chuang, K. -J. et al. (Feb. 2018). “Reactive Desorption of CO Hydrogenation Products under Cold Prestellar Core Conditions”. In: *Astrophys. J.* 853.2, 102, p. 102. DOI: 10.3847/1538-4357/aaa24e. arXiv: 1806.06215 [astro-ph.GA].

Chuang, K. -J. et al. (Mar. 2020). “Formation of complex molecules in translucent clouds: acetaldehyde, vinyl alcohol, ketene, and ethanol via “nonenergetic” processing of C2H2 ice”. In: *Astron. Astrophys.* 635, A199, A199. DOI: 10.1051/0004-6361/201937302. arXiv: 2002.06971 [astro-ph.SR].

Chuang, K. -J. et al. (June 2021). “Formation of complex organic molecules in molecular clouds: acetaldehyde, vinyl alcohol, ketene, and ethanol via the “energetic” processing of C2H2 ice”. In: *Astron. Astrophys.* 650, A85, A85. DOI: 10.1051/0004-6361/202140780. arXiv: 2104.09434 [astro-ph.GA].

Codella, C. et al. (Sept. 2017). “Seeds of Life in Space (SOLIS). II. Formamide in protostellar shocks: Evidence for gas-phase formation”. In: *Astron. Astrophys.* 605, L3, p. L3. DOI: 10.1051/0004-6361/201731249. arXiv: 1708.04663 [astro-ph.EP].

Codella, C. et al. (Mar. 2020). “Seeds of Life in Space (SOLIS). V. Methanol and acetaldehyde in the protostellar jet-driven shocks L1157-B0 and B1”. In: *Astron. Astrophys.* 635, A17, A17. DOI: 10.1051/0004-6361/201936725. arXiv: 2001.00217 [astro-ph.SR].

Collings, Mark P. et al. (Nov. 2004). “A laboratory survey of the thermal desorption of astrophysically relevant molecules”. In: *Mon. Not. R. Astron. Soc.* 354.4, pp. 1133–1140. DOI: 10.1111/j.1365-2966.2004.08272.x.

Cooke, Ilsa R. et al. (Jan. 2018). “CO Diffusion and Desorption Kinetics in CO_2 Ices”. In: *Astrophys. J.* 852.2, 75, p. 75. DOI: 10.3847/1538-4357/aa9ce9. arXiv: 1711.09967 [astro-ph.GA].

Coutens, A. et al. (May 2016). “The ALMA-PILS survey: First detections of deuterated formamide and deuterated isocyanic acid in the interstellar medium”. In: *Astron. Astrophys.* 590, L6, p. L6. DOI: 10.1051/0004-6361/201628612. arXiv: 1605.02562 [astro-ph.SR].

Crapsi, A. et al. (Jan. 2005). “Probing the Evolutionary Status of Starless Cores through N2H+ and N2D+ Observations”. In: *Astrophys. J.* 619.1, pp. 379–406. DOI: 10.1086/426472. arXiv: astro-ph/0409529 [astro-ph].

Crapsi, A. et al. (July 2007). “Observing the gas temperature drop in the high-density nucleus of L 1544”. In: *Astron. Astrophys.* 470.1, pp. 221–230. DOI: 10.1051/0004-6361:20077613. arXiv: 0705.0471 [astro-ph].

Csengeri, T. et al. (Dec. 2019). “Search for high-mass protostars with ALMA revealed up to kilo-parsec scales (SPARKS). II. Complex organic molecules and heavy water in shocks around a young high-mass protostar”. In: *Astron. Astrophys.* 632, A57, A57. DOI: 10.1051/0004-6361/201935226.

Cuadrado, S. et al. (Mar. 2015). “The chemistry and spatial distribution of small hydrocarbons in UV-irradiated molecular clouds: the Orion Bar PDR”. In: *Astron. Astrophys.* 575, A82, A82. DOI: 10.1051/0004-6361/201424568. arXiv: 1412.0417 [astro-ph.GA].

Cuppen, H. M. et al. (Oct. 2017). “Grain Surface Models and Data for Astrochemistry”. In: *Space Sci. Rev.* 212.1-2, pp. 1–58. DOI: 10.1007/s11214-016-0319-3.

Dartois, E. et al. (Oct. 1998). “Detection of the “44 MU m” band of water ice in absorption in combined ISO SWS-LWS spectra”. In: *Astron. Astrophys.* 338, pp. L21–L24.

de Duve, C. (Feb. 2011). “Life as a cosmic imperative?” In: *Philosophical Transactions of the Royal Society of London Series A* 369.1936, pp. 620–623. DOI: 10.1098/rsta.2010.0312.

De Duve, Christian (2005). *Singularities: landmarks on the pathways of life*. Cambridge University Press.

De Simone, M. et al. (Aug. 2020). “Seeds of Life in Space (SOLIS). X. Interstellar complex organic molecules in the NGC 1333 IRAS 4A outflows”. In: *Astron. Astrophys.* 640, A75, A75. DOI: 10.1051/0004-6361/201937004. arXiv: 2006.09925 [astro-ph.SR].

Drozdovskaya, Maria N et al. (2016). “Cometary ices in forming protoplanetary disc midplanes”. In: *Mon. Not. R. Astron. Soc.* 462.1, pp. 977–993.

Duley, W. W. and D. A. Williams (Jan. 1993). “The formation of H2 on interstellar dust”. In: *Mon. Not. R. Astron. Soc.* 260.1, pp. 37–42. DOI: 10.1093/mnras/260.1.37.

Dulieu, F. et al. (Mar. 2010). “Experimental evidence for water formation on interstellar dust grains by hydrogen and oxygen atoms”. In: *Astron. Astrophys.* 512, A30, A30. DOI: 10.1051/0004-6361/200912079. arXiv: 0903.3120 [astro-ph.IM].

Dulieu, François et al. (Feb. 2013). “How micron-sized dust particles determine the chemistry of our Universe”. In: *Scientific Reports* 3, 1338, p. 1338. DOI: 10.1038/srep01338.

Dutrey, A., S. Guilloteau, and M. Guelin (Jan. 1997). “Chemistry of protosolar-like nebulae: The molecular content of the DM Tau and GG Tau disks.” In: *Astron. Astrophys.* 317, pp. L55–L58.

Eckart, Carl (June 1930). “The Penetration of a Potential Barrier by Electrons”. In: *Phys. Rev.* 35 (11), pp. 1303–1309.

Enrique-Romero, J. et al. (June 2016). “The (impossible?) formation of acetaldehyde on the grain surfaces: insights from quantum chemical calculations”. In: *Mon. Not. R. Astron. Soc.* 459.1, pp. L6–L10. DOI: 10.1093/mnrasl/slw031. arXiv: 1603.09096 [astro-ph.EP].

Enrique-Romero, J. et al. (Apr. 2020). “Revisiting the reactivity between HCO and CH3 on interstellar grain surfaces”. In: *Mon. Not. R. Astron. Soc.* 493.2, pp. 2523–2527. DOI: 10.1093/mnras/staa484. arXiv: 2002.06101 [astro-ph.GA].

Enrique-Romero, Joan et al. (Oct. 2019). “Reactivity of HCO with CH3 and NH2 on Water Ice Surfaces. A Comprehensive Accurate Quantum Chemistry Study”. In: *ACS Earth and Space Chemistry* 3.10, pp. 2158–2170. DOI: 10.1021/acsearthspacechem.9b00156. arXiv: 1909.12686 [astro-ph.SR].

— (2021a). “Radical-Radical chemistry on icy surfaces”. In: *In preparation* –, pp. –, –.

Enrique-Romero, Joan et al. (2021b). “Theoretical computations on the efficiency of acetaldehyde formation on interstellar icy grains”. In: *Submitted to Astronomy & Astrophysics* –, pp. –, –.

Fayolle, E. et al. (May 2011). “Photodesorption of interstellar ice analogues: a wavelength-dependent study.” In: *The Molecular Universe*. Ed. by José Cernicharo and Rafael Bachiller. Vol. 280, p. 157.

Fedoseev, G. et al. (Apr. 2015). “Experimental evidence for glycolaldehyde and ethylene glycol formation by surface hydrogenation of CO molecules under dense molecular cloud conditions”. In: *Mon. Not. R. Astron. Soc.* 448.2, pp. 1288–1297. DOI: 10.1093/mnras/stu2603. arXiv: 1705.09235 [astro-ph.GA].

Fedoseev, G. et al. (Aug. 2016). “Simultaneous hydrogenation and UV-photolysis experiments of NO in CO-rich interstellar ice analogues; linking HNCO, OCN-, NH2CHO, and NH2OH”. In: *Mon. Not. R. Astron. Soc.* 460.4, pp. 4297–4309. DOI: 10.1093/mnras/stw1028. arXiv: 1706.00736 [astro-ph.GA].

Fermann, Justin T. and Scott Auerbach (Apr. 2000). “Modeling proton mobility in acidic zeolite clusters: II. Room temperature tunneling effects from semiclassical rate theory”. In: *J. Chem. Phys.* 112.15, pp. 6787–6794. DOI: 10.1063/1.481318.

Fernandez Galván, Ignacio et al. (June 2019). *OpenMolcas: From Source Code to Insight*. DOI: 10.26434/chemrxiv.8234021.v1. URL: https://chemrxiv.org/articles/OpenMolcas_From_Source_Code_to_Insight/8234021/1.

Ferrero, Stefano et al. (Nov. 2020). “Binding Energies of Interstellar Molecules on Crystalline and Amorphous Models of Water Ice by Ab Initio Calculations”. In: *Astrophys. J.* 904.1, 11, p. 11. DOI: 10.3847/1538-4357/abb953. arXiv: 2009.09763 [astro-ph.GA].

Fiorentini, Vincenzo and Michael Methfessel (1996). “Extracting convergent surface energies from slab calculations”. In: *Journal of Physics: Condensed Matter* 8.36, p. 6525.

Flower, D. R. and G. Pineau des Forets (June 1994). “Grain/Mantle Erosion in Magnetohydrodynamic Shocks”. In: *Mon. Not. R. Astron. Soc.* 268, p. 724. DOI: 10.1093/mnras/268.3.724.

Fortenberry, Ryan C. (2017). “Quantum astrochemical spectroscopy”. In: *International Journal of Quantum Chemistry* 117.2, pp. 81–91. DOI: https://doi.org/10.1002/qua.25180. URL: https://onlinelibrary.wiley.com/doi/abs/10.1002/qua.25180.

Fredon, A. and H. M. Cuppen (Feb. 2018). “Molecular dynamics simulations of energy dissipation and non-thermal diffusion on amorphous solid water”. In: *Physical Chemistry Chemical Physics (Incorporating Faraday Transactions)* 20, pp. 5569–5577. DOI: 10.1039/C7CP06136F.

Fredon, A., T. Lamberts, and H. M. Cuppen (Nov. 2017). “Energy Dissipation and Nonthermal Diffusion on Interstellar Ice Grains”. In: *Astrophys. J.* 849.2, 125, p. 125. DOI: 10.3847/1538-4357/aa8c05.

Frisch, M. J. et al. (2009). *Gaussian09 Revision D.01*. Gaussian Inc. Wallingford CT 2009.

Frisch, M. J. et al. (2016). *Gaussian~16 Revision C.01*. Gaussian Inc. Wallingford CT.

Fuchs, G. W. et al. (Oct. 2009). “Hydrogenation reactions in interstellar CO ice analogues. A combined experimental/theoretical approach”. In: *Astron. Astrophys.* 505.2, pp. 629–639. DOI: 10.1051/0004-6361/200810784.

Garrod, R. T. and E. Herbst (Oct. 2006). “Formation of methyl formate and other organic species in the warm-up phase of hot molecular cores”. In: *Astron. Astrophys.* 457.3, pp. 927–936. DOI: 10.1051/0004-6361:20065560. arXiv: astro-ph/0607560 [astro-ph].

Garrod, R. T. and T. Pauly (July 2011). “On the Formation of CO2 and Other Interstellar Ices”. In: *Astrophys. J.* 735.1, 15, p. 15. DOI: 10.1088/0004-637X/735/1/15. arXiv: 1106.0540 [astro-ph.GA].

Garrod, R. T., V. Wakelam, and E. Herbst (June 2007). “Non-thermal desorption from interstellar dust grains via exothermic surface reactions”. In: *Astron. Astrophys.* 467.3, pp. 1103–1115. DOI: 10.1051/0004-6361:20066704. arXiv: astro-ph/0703188 [astro-ph].

Garrod, R. T. et al. (July 2009). “A New Modified-Rate Approach For Gas-Grain Chemistry: Comparison with a Unified Large-Scale Monte Carlo Simulation”. In: *Astrophys. J. Lett.* 700.1, pp. L43–L46. DOI: 10.1088/0004-637X/700/1/L43.

Garrod, Robin T. (Dec. 2013). “Three-dimensional, Off-lattice Monte Carlo Kinetics Simulations of Interstellar Grain Chemistry and Ice Structure”. In: *Astrophys. J.* 778.2, 158, p. 158. DOI: 10.1088/0004-637X/778/2/158. arXiv: 1310.2512 [astro-ph.IM].

Garrod, Robin T., Susanna L. Widicus Weaver, and Eric Herbst (July 2008). “Complex Chemistry in Star-forming Regions: An Expanded Gas-Grain Warm-up Chemical Model”. In: *Astrophys. J.* 682.1, pp. 283–302. DOI: 10.1086/588035. arXiv: 0803.1214 [astro-ph].

Garufi, A. et al. (Jan. 2021). “ALMA chemical survey of disk-outflow sources in Taurus (ALMA-DOT). V. Sample, overview, and demography of disk molecular emission”. In: *Astron. Astrophys.* 645, A145, A145. DOI: 10.1051/0004-6361/202039483. arXiv: 2012.07667 [astro-ph.GA].

Geppert, W. D. et al. (Aug. 2005). “Dissociative Recombination of CD3OD2+”. In: *Astrochemistry: Recent Successes and Current Challenges*. Ed. by Dariusz C. Lis, Geoffrey A. Blake, and Eric Herbst. Vol. 231, pp. 117–124. DOI: 10.1017/S1743921306007101.

Geppert, W. D. et al. (Jan. 2006). “Dissociative recombination of protonated methanol”. In: *Faraday Discussions* 133, p. 177. DOI: 10.1039/B516010C.

Ghesquière, P. et al. (Jan. 2015). “Diffusion of molecules in the bulk of a low density amorphous ice from molecular dynamics simulations”. In: *Physical Chemistry Chemical Physics (Incorporating Faraday Transactions)* 17.17, pp. 11455–11468. DOI: 10.1039/C5CP00558B.

Goddard, John D (1984). “The geometry of the propynol cation, HC3O+”. In: *Chemical physics letters* 109.2, pp. 170–174.

Goedecker, S, M Teter, and J. Hutter (1996). “Separable dual-space Gaussian pseudopotentials.” In: *Phys. Rev. B* 54 (3), pp. 1703–1710. DOI: 10.1103/PhysRevB.54.1703.

Goerigk, Lars and Nisha Mehta (2019). “A trip to the density functional theory zoo: warnings and recommendations for the user”. In: *Australian Journal of Chemistry* 72.8, pp. 563–573.

Goerigk, Lars et al. (Jan. 2017). “A look at the density functional theory zoo with the advanced GMTKN55 database for general main group thermochemistry, kinetics and noncovalent interactions”. In: *Physical Chemistry Chemical Physics (Incorporating Faraday Transactions)* 19.48, pp. 32184–32215. DOI: 10.1039/C7CP04913G.

Goldsmith, P. F. and W. D. Langer (June 1978). “Molecular cooling and thermal balance of dense interstellar clouds.” In: *Astrophys. J.* 222, pp. 881–895. DOI: 10.1086/156206.

Goumans, T. P. M., C. Richard A. Catlow, and Wendy A. Brown (Apr. 2008). “Hydrogenation of CO on a silica surface: An embedded cluster approach”. In: *J. Chem. Phys.* 128.13, pp. 134709–134709. DOI: 10.1063/1.2888933.

Goumans, T. P. M. et al. (Dec. 2007). “Silica grain catalysis of methanol formation”. In: *Mon. Not. R. Astron. Soc.* 382.4, pp. 1829–1832. DOI: 10.1111/j.1365-2966.2007.12491.x.

Gredel, R. et al. (Dec. 1989). “Cosmic-Ray–induced Photodissociation and Photoionization Rates of Interstellar Molecules”. In: *Astrophys. J.* 347, p. 289. DOI: 10.1086/168117.

Green, S., Jr. Montgomery J. A., and P. Thaddeus (Oct. 1974). “Tentative Identification of U93.174 as the Molecular Ion N2H+”. In: *Astrophys. J. Lett.* 193, p. L89. DOI: 10.1086/181639.

Green, Sheldon and Patrick Thaddeus (1976). “Rotational excitation of CO by collisions with He, H, and H2 under conditions in interstellar clouds”. In: *The Astrophysical Journal* 205, pp. 766–785.

Grimme, Stefan (2004). “Accurate description of van der Waals complexes by density functional theory including empirical corrections”. In: *Journal of computational chemistry* 25.12, pp. 1463–1473.

— (Nov. 2006). “Semiempirical GGA-type density functional constructed with a long-range dispersion correction”. In: *J. Comput. Chem.* 27.15, pp. 1787–1799. ISSN: 0192-8651. DOI: 10.1002/jcc.20495.

Grimme, Stefan, Stephan Ehrlich, and Lars Goerigk (2011). “Effect of the damping function in dispersion corrected density functional theory”. In: *Journal of Computational Chemistry* 32.7, pp. 1456–1465.

Grimme, Stefan et al. (2010). “A consistent and accurate ab initio parametrization of density functional dispersion correction (DFT-D) for the 94 elements H-Pu”. In: *The Journal of Chemical Physics* 132.15, p. 154104.

Gusdorf, A. et al. (May 2008a). “SiO line emission from C-type shock waves: interstellar jets and outflows”. In: *Astron. Astrophys.* 482.3, pp. 809–829. DOI: 10.1051/0004-6361:20078900. arXiv: 0803.2791 [astro-ph].

Gusdorf, A. et al. (Nov. 2008b). “SiO line emission from interstellar jets and outflows: silicon-containing mantles and non-stationary shock waves”. In: *Astron. Astrophys.* 490.2, pp. 695–706. DOI: 10.1051/0004-6361:200810443.

Hagen, W., L. J. Allamandola, and J. M. Greenberg (Sept. 1979). “Interstellar Molecule Formation in Grain Mantles: The Laboratory Analog Experiments, Results and Implications”. In: *Astrophys. Space Sci.* 65.1, pp. 215–240. DOI: 10.1007/BF00643502.

Al-Halabi, A. and E. F. van Dishoeck (Dec. 2007). “Hydrogen adsorption and diffusion on amorphous solid water ice”. In: *Mon. Not. R. Astron. Soc.* 382.4, pp. 1648–1656. DOI: 10.1111/j.1365-2966.2007.12415.x.

Al-Halabi, A. et al. (2002). “Sticking of Hydrogen Atoms to Crystalline Ice Surfaces: Dependence on Incidence Energy and Surface Temperature”. In: *The Journal of Physical Chemistry B* 106.25, pp. 6515–6522. DOI: 10.1021/jp020007y.

Hama, Tetsuya and Naoki Watanabe (Dec. 2013). “Surface Processes on Interstellar Amorphous Solid Water: Adsorption, Diffusion, Tunneling Reactions, and Nuclear-Spin Conversion”. In: *Chemical Reviews* 113.12, pp. 8783–8839. DOI: 10.1021/cr4000978.

Hama, Tetsuya et al. (Oct. 2012). “The Mechanism of Surface Diffusion of H and D Atoms on Amorphous Solid Water: Existence of Various Potential Sites”. In: *Astrophys. J.* 757.2, 185, p. 185. DOI: 10.1088/0004-637X/757/2/185.

Hariharan, P. C. and J. A. Pople (Sept. 1973). “The influence of polarization functions on molecular orbital hydrogenation energies”. en. In: *Theoret. Chim. Acta* 28.3, pp. 213–222. ISSN: 1432-2234. DOI: 10.1007/BF00533485. URL: https://doi.org/10.1007/BF00533485 (visited on 03/02/2021).

Hartwigsen, C, S Goedecker, and J. Hutter (1998). “Relativistic separable dual-space Gaussian pseudopotentials from H to Rn.” In: *Phys. Rev. B* 58 (7), pp. 3641–3662. DOI: 10.1103/PhysRevB.58.3641.

Hasegawa, T. I. and E. Herbst (Aug. 1993). “Three-Phase Chemical Models of Dense Interstellar Clouds - Gas Dust Particle Mantles and Dust Particle Surfaces”. In: *Mon. Not. R. Astron. Soc.* 263, p. 589. DOI: 10.1093/mnras/263.3.589.

Hasegawa, Tatsuhiko I. and Eric Herbst (Mar. 1993). “New gas–grain chemical models of quiescent dense interstellar clouds: the effects of H2 tunnelling reactions and cosmic ray induced desorption”. en. In: *Mon. Not. R. Astron. Soc.* 261.1, pp. 83–102. ISSN: 0035-8711. DOI: 10.1093/mnras/261.1.83. URL: https://academic.oup.com/mnras/article/261/1/83/1001106 (visited on 01/09/2020).

Hasegawa, Tatsuhiko I., Eric Herbst, and Chun M. Leung (Sept. 1992). “Models of Gas-Grain Chemistry in Dense Interstellar Clouds with Complex Organic Molecules”. In: *Astrophys. J., Suppl. Ser.* 82, p. 167. DOI: 10.1086/191713.

Hassel, George E., Nanase Harada, and Eric Herbst (Dec. 2011). “Carbon-chain Species in Warm-up Models”. In: *Astrophys. J.* 743.2, 182, p. 182. DOI: 10.1088/0004-637X/743/2/182. arXiv: 1112.1997 [astro-ph.SR].

Hassel, George E., Eric Herbst, and Robin T. Garrod (July 2008). “Modeling the Lukewarm Corino Phase: Is L1527 Unique?” In: *Astrophys. J.* 681.2, pp. 1385–1395. DOI: 10.1086/588185. arXiv: 0803.1805 [astro-ph].

Hayes, D. M. and K. Morokuma (Jan. 1972). “Theoretical studies of carbonyl photochemistry. I. ab initio potential energy surfaces for the photodissociation H2CO* to H + HCO”. In: *Chemical Physics Letters* 12.4, pp. 539–543. DOI: 10.1016/0009-2614(72)80003-4.

He, Jiao, Kinsuk Acharyya, and Gianfranco Vidali (July 2016). “Binding Energy of Molecules on Water Ice: Laboratory Measurements and Modeling”. In: *The Astrophysical Journal* 825.2, 89, p. 89. DOI: 10.3847/0004-637X/825/2/89. arXiv: 1603.02191 [astro-ph.IM].

He, Jiao, Shahnewaj M. Emtiaz, and Gianfranco Vidali (Dec. 2017). “Mechanism of Atomic Hydrogen Addition Reactions on np-ASW”. In: *Astrophys. J.* 851.2, 104, p. 104. DOI: 10.3847/1538-4357/aa9a3e. arXiv: 1711.03698 [astro-ph.IM].

He, Jiao, SM Emtiaz, and Gianfranco Vidali (Aug. 2018). “Measurements of Diffusion of Volatiles in Amorphous Solid Water: Application to Interstellar Medium Environments”. In: *Astrophys. J.* 863.2, 156, p. 156. DOI: 10.3847/1538-4357/aad227. arXiv: 1806.06980 [astro-ph.IM].

He, Jiao and Gianfranco Vidali (June 2014). “Experiments of Water Formation on Warm Silicates”. In: *Astrophys. J.* 788.1, 50, p. 50. DOI: 10.1088/0004-637X/788/1/50.

Hehre, W. J., R. Ditchfield, and J. A. Pople (Mar. 1972). “Self—Consistent Molecular Orbital Methods. XII. Further Extensions of Gaussian—Type Basis Sets for Use in Molecular Orbital Studies of Organic Molecules”. In: *J. Chem. Phys.* 56.5. Publisher: American Institute of Physics, pp. 2257–2261. ISSN:

0021-9606. DOI: 10.1063/1.1677527. URL: https://aip-scitation-org.gaelnomade-1.grenet.fr/doi/10.1063/1.1677527 (visited on 03/02/2021).

Henning, Thomas (Sept. 2010). "Cosmic Silicates". In: *Annu. Rev. Astron. Astrophys.* 48, pp. 21–46. DOI: 10.1146/annurev-astro-081309-130815.

Henning, Thomas and Dmitry Semenov (Dec. 2013). "Chemistry in Protoplanetary Disks". In: *Chemical Reviews* 113.12, pp. 9016–9042. DOI: 10.1021/cr400128p. arXiv: 1310.3151 [astro-ph.GA].

Henriksen, Niels E. and Flemming Y. Hansen (2018). *Theories of Molecular Reaction Dynamics, 2nd edition. The Microscopic Foundation of Chemical Kinetics*. Oxford Graduate Texts. ISBN: 9780198805014.

Herbst, Eric (2017). "The synthesis of large interstellar molecules". In: *International Reviews in Physical Chemistry* 36.2, pp. 287–331.

Herbst, Eric and Herma M Cuppen (2006). "Monte Carlo studies of surface chemistry and nonthermal desorption involving interstellar grains". In: *Proceedings of the National Academy of Sciences* 103.33, pp. 12257–12262.

Herbst, Eric and Ewine F. van Dishoeck (2009a). "Complex Organic Interstellar Molecules". In: *Annu. Rev. Astron. Astrophys.* 47.1, pp. 427–480. DOI: 10.1146/annurev-astro-082708-101654. URL: https://doi.org/10.1146/annurev-astro-082708-101654 (visited on 11/12/2019).

Herbst, Eric and William Klemperer (Oct. 1973). "The Formation and Depletion of Molecules in Dense Interstellar Clouds". In: *Astrophys. J.* 185, pp. 505–534. DOI: 10.1086/152436.

— (Mar. 1974). "Is X-Ogen HCO+?" In: *Astrophys. J.* 188, pp. 255–256. DOI: 10.1086/152712.

Herbst, Eric and Ewine F. van Dishoeck (Sept. 2009b). "Complex Organic Interstellar Molecules". In: *Annu. Rev. Astron. Astrophys.* 47.1, pp. 427–480. DOI: 10.1146/annurev-astro-082708-101654.

Hidaka, H. et al. (Oct. 2004). "Conversion of H2CO to CH3OH by Reactions of Cold Atomic Hydrogen on Ice Surfaces below 20 K". In: *Astrophys. J.* 614.2, pp. 1124–1131. DOI: 10.1086/423889.

Hincelin, Ugo, Qiang Chang, and Eric Herbst (2015). "A new and simple approach to determine the abundance of hydrogen molecules on interstellar ice mantles". In: *Astronomy & Astrophysics* 574, A24.

Hiraoka, K. and T. Sato (Jan. 2001). "Laboratory simulation of tunneling reactions in interstellar ices". In: *Radiation Physics and Chemistry* 60.4-5, pp. 389–393. DOI: 10.1016/S0969-806X(00)00414-X.

Hiraoka, Kenzo et al. (Nov. 1994). "Formation of formaldehyde and methanol from the reactions of H atoms with solid CO at 10-20 K". In: *Chemical Physics Letters* 229.4, pp. 408–414. DOI: 10.1016/0009-2614(94)01066-8.

Hiraoka, Kenzo et al. (May 1998). "Gas-Grain Processes for the Formation of CH4 and H2O: Reactions of H Atoms with C, O, and CO in the Solid Phase at 12 K". In: *Astrophys. J.* 498.2, pp. 710–715. DOI: 10.1086/305572.

Hiraoka, Kenzo et al. (Sept. 2002). "Formation of Formaldehyde by the Tunneling Reaction of H with Solid CO at 10 K Revisited". In: *The Astrophysical Journal* 577.1, pp. 265–270.

Hohenberg, P. and W. Kohn (Nov. 1964). "Inhomogeneous Electron Gas". In: *Phys. Rev.* 136 (3B), B864–B871.

Hollenbach, David and E. E. Salpeter (July 1970). "Surface Adsorption of Light Gas Atoms". In: *J. Chem. Phys.* 53.1, pp. 79–86. DOI: 10.1063/1.1673836.

— (Jan. 1971). "Surface Recombination of Hydrogen Molecules". In: *Astrophys. J.* 163, p. 155. DOI: 10.1086/150754.

Hollenbach, David et al. (Jan. 2009). "Water, O2, and Ice in Molecular Clouds". In: *Astrophys. J.* 690.2, pp. 1497–1521. DOI: 10.1088/0004-637X/690/2/1497. arXiv: 0809.1642 [astro-ph].

Horn, Anne et al. (Aug. 2004). "The Gas-Phase Formation of Methyl Formate in Hot Molecular Cores". In: *Astrophys. J.* 611.1, pp. 605–614. DOI: 10.1086/422137.

Hornekær, L. et al. (Dec. 2003). "Importance of Surface Morphology in Interstellar H2 Formation". In: *Science* 302.5652, pp. 1943–1946. DOI: 10.1126/science.1090820.

Huang, L. C. L. et al. (Nov. 2000). "Crossed beam reaction of cyano radicals with hydrocarbon molecules. IV. Chemical dynamics of cyanoacetylene (HCCCN; X1S+) formation from reaction of CN(X2S+) with acetylene, C2H2(X1S+g)". In: *J. Chem. Phys.* 113.19, pp. 8656–8666. DOI: 10.1063/1.1289530.

Hudson, R. L. and M. H. Moore (Mar. 1997). "NOTE: Hydrocarbon Radiation Chemistry in Ices of Cometary Relevance". In: *Icarus* 126.1, pp. 233–235. DOI: 10.1006/icar.1997.5678.

Hudson, R. L. and M. H. Moore (Aug. 1999). “Laboratory Studies of the Formation of Methanol and Other Organic Molecules by Water+Carbon Monoxide Radiolysis: Relevance to Comets, Icy Satellites, and Interstellar Ices”. In: *Icarus* 140.2, pp. 451–461. DOI: 10.1006/icar.1999.6144.

— (Dec. 2001). “Radiation chemical alterations in solar system ices: An overview”. In: *J. Geophys. Res.* 106.E12, pp. 33275–33284. DOI: 10.1029/2000JE001299.

— (Mar. 2003). “Solid-Phase Formation of Interstellar Vinyl Alcohol”. In: *Astrophys. J. Lett.* 586.1, pp. L107–L110. DOI: 10.1086/374580.

Hutter, J et al. (2014). “CP2K: atomistic simulations of condensed matter systems.” In: *WIREs Comput. Mol. Sci.* 4, pp. 15–25. DOI: 10.1002/wcms.1159.

Ioppolo, S. et al. (May 2011). “Surface formation of CO2 ice at low temperatures”. In: *Mon. Not. R. Astron. Soc.* 413.3, pp. 2281–2287. DOI: 10.1111/j.1365-2966.2011.18306.x.

Islam, Farahjabeen et al. (2010). “Formation pumping of molecular hydrogen in dark clouds”. In: *The Astrophysical Journal* 725.1, p. 1111.

Isokoski, K. et al. (Jan. 2014). “Porosity and thermal collapse measurements of H2O, CH3OH, CO2, and H2O:CO2 ices”. In: *Physical Chemistry Chemical Physics (Incorporating Faraday Transactions)* 16.8, p. 3456. DOI: 10.1039/C3CP54481H.

Ivlev, AV et al. (2015). “Impulsive spot heating and thermal explosion of interstellar grains revisited”. In: *The Astrophysical Journal* 805.1, p. 59.

Jaber, Ali A. et al. (Aug. 2014). “The Census of Complex Organic Molecules in the Solar-type Protostar IRAS16293-2422”. In: *Astrophys. J.* 791.1, 29, p. 29. DOI: 10.1088/0004-637X/791/1/29. arXiv: 1406.7195 [astro-ph.SR].

Jaffe, RL, DM Hayes, and Keiji Morokuma (1974). “Photodissociation of formaldehyde: Potential energy surfaces for H2CO to H2 + CO”. In: *The Journal of Chemical Physics* 60.12, pp. 5108–5109.

Jenkins, Edward B. (Aug. 2009). “A Unified Representation of Gas-Phase Element Depletions in the Interstellar Medium”. In: *Astrophys. J.* 700.2, pp. 1299–1348. DOI: 10.1088/0004-637X/700/2/1299. arXiv: 0905.3173 [astro-ph.GA].

Jensen, Frank (2017). *Introduction to Computational Chemistry, 3rd Edition*. John Wiley & Sons, Ltd. ISBN: 9781118825990.

Jensen, S. S. et al. (May 2021). “Modeling chemistry during star formation: water deuteration in dynamic star-forming regions”. In: *Astron. Astrophys.* 649, A66, A66. DOI: 10.1051/0004-6361/202040196. arXiv: 2103.12135 [astro-ph.GA].

Jiménez-Serra, Izaskun et al. (Oct. 2016). “The Spatial Distribution of Complex Organic Molecules in the L1544 Pre-stellar Core”. In: *Astrophys. J. Lett.* 830.1, L6, p. L6. DOI: 10.3847/2041-8205/830/1/L6. arXiv: 1609.05045 [astro-ph.SR].

Jin, Mihwa and Robin T. Garrod (Aug. 2020). “Formation of Complex Organic Molecules in Cold Interstellar Environments through Nondiffusive Grain-surface and Ice-mantle Chemistry”. In: *Astrophys. J., Suppl. Ser.* 249.2, 26, p. 26. DOI: 10.3847/1538-4365/ab9ec8. arXiv: 2006.11127 [astro-ph.GA].

Johnson, Jennifer A. (Feb. 2019). “Populating the periodic table: Nucleosynthesis of the elements”. In: *Science* 363.6426, pp. 474–478. DOI: 10.1126/science.aau9540.

Jones, A. P. et al. (June 2017). “The global dust modelling framework THEMIS”. In: *Astron. Astrophys.* 602, A46, A46. DOI: 10.1051/0004-6361/201630225. arXiv: 1703.00775 [astro-ph.GA].

Jørgensen, J. K. et al. (Nov. 2016). “The ALMA Protostellar Interferometric Line Survey (PILS). First results from an unbiased submillimeter wavelength line survey of the Class 0 protostellar binary IRAS 16293-2422 with ALMA”. In: *Astron. Astrophys.* 595, A117, A117. DOI: 10.1051/0004-6361/201628648. arXiv: 1607.08733 [astro-ph.SR].

Jørgensen, JK, FL Schöier, and EF Van Dishoeck (2005). “Molecular freeze-out as a tracer of the thermal and dynamical evolution of pre-and protostellar cores”. In: *Astronomy & Astrophysics* 435.1, pp. 177–182.

Jorgensen, W. L. et al. (1983). “Comparison of simple potential functions for simulating liquid water”. In: *J. Chem. Phys.* 79, pp. 926–935.

Kahane, C. et al. (Jan. 2013). “DETECTION OF FORMAMIDE, THE SIMPLEST BUT CRUCIAL AMIDE, IN A SOLAR-TYPE PROTOSTAR”. In: *Astrophys. J.* 763.2, p. L38. DOI: 10.1088/2041-8205/763/2/l38.

Kalvāns, J. (Aug. 2018). “The efficiency of photodissociation for molecules in interstellar ices”. In: *Mon. Not. R. Astron. Soc.* 478.2, pp. 2753–2765. DOI: 10.1093/mnras/sty1172. arXiv: 1805.03618 [astro-ph.GA].

Kalvāns, Juris (June 2016). “Temperature Spectra of Interstellar Dust Grains Heated by Cosmic Rays. I. Translucent Clouds”. In: *Astrophys. J., Suppl. Ser.* 224.2, 42, p. 42. DOI: 10.3847/0067-0049/224/2/42. arXiv: 1605.09120 [astro-ph.HE].

Karlström, Gunnar et al. (2003). “MOLCAS: a program package for computational chemistry”. In: *Comput. Mater. Sci.* 28.2. Proceedings of the Symposium on Software Development for Process and Materials Design, pp. 222–239. ISSN: 0927-0256. DOI: https://doi.org/10.1016/S0927-0256(03)00109-5. URL: http://www.sciencedirect.com/science/article/pii/S0927025603001095.

Karssemeijer, L. J. and H. M. Cuppen (Sept. 2014). “Diffusion-desorption ratio of adsorbed CO and CO2 on water ice”. In: *Astron. Astrophys.* 569, A107, A107. DOI: 10.1051/0004-6361/201424792. arXiv: 1409.3038 [astro-ph.GA].

Kassel, Louis S. (1928). “Studies in homogeneous gas reactions. I”. In: *The Journal of Physical Chemistry* 32.2, pp. 225–242.

Kayanuma, Megumi et al. (July 2019). “First-Principles Study of the Reaction Mechanism of CHO + H on Graphene Surface”. In: *Journal of Physical Chemistry A* 123.26, pp. 5633–5639. DOI: 10.1021/acs.jpca.9b02345.

Kayi, Hakan, Ralf I. Kaiser, and John D. Head (Jan. 2011). “A computational study on the structures of methylamine-carbon dioxide-water clusters: evidence for the barrier free formation of the methylcarbamic acid zwitterion (CH3NH2+COO-) in interstellar water ices”. In: *Physical Chemistry Chemical Physics (Incorporating Faraday Transactions)* 13.23, p. 11083. DOI: 10.1039/C0CP01962C.

Keane, J. V. et al. (Sept. 2001). “Ice absorption features in the 5-8 μm region toward embedded protostars”. In: *Astron. Astrophys.* 376, pp. 254–270. DOI: 10.1051/0004-6361:20010936.

Kemper, F., W. J. Vriend, and A. G. G. M. Tielens (July 2004). “The Absence of Crystalline Silicates in the Diffuse Interstellar Medium”. In: *Astrophys. J.* 609.2, pp. 826–837. DOI: 10.1086/421339. arXiv: astro-ph/0403609 [astro-ph].

Keto, Eric and Paola Caselli (Aug. 2008). “The Different Structures of the Two Classes of Starless Cores”. In: *Astrophys. J.* 683.1, pp. 238–247. DOI: 10.1086/589147. arXiv: 0804.0822 [astro-ph].

Kohn, W. and L. J. Sham (Nov. 1965). “Self-Consistent Equations Including Exchange and Correlation Effects”. In: *Phys. Rev.* 140 (4A), A1133–A1138.

Korchagina, Kseniia A., Fernand Spiegelman, and Jérôme Cuny (Dec. 2017). “Molecular Dynamics Study of the Collision-Induced Reaction of H with CO on Small Water Clusters”. In: *Journal of Physical Chemistry A* 121.49, pp. 9485–9494. DOI: 10.1021/acs.jpca.7b09217.

Kouchi, Akira et al. (Mar. 2020). “Direct Measurements of Activation Energies for Surface Diffusion of CO and CO2 on Amorphous Solid Water Using In Situ Transmission Electron Microscopy”. In: *Astrophys. J. Lett.* 891.1, L22, p. L22. DOI: 10.3847/2041-8213/ab78a2.

Krishnan, R. et al. (Jan. 1980). “Self-consistent molecular orbital methods. XX. A basis set for correlated wave functions”. In: *J. Chem. Phys.* 72.1. Publisher: American Institute of Physics, pp. 650–654. ISSN: 0021-9606. DOI: 10.1063/1.438955. URL: https://aip-scitation-org.gaelnomade-1.grenet.fr/doi/10.1063/1.438955 (visited on 03/02/2021).

Kuwahata, K. et al. (Sept. 2015). “Signatures of Quantum-Tunneling Diffusion of Hydrogen Atoms on Water Ice at 10 K”. In: *Phys. Rev. Lett.* 115.13, 133201, p. 133201. DOI: 10.1103/PhysRevLett.115.133201.

Lada, Charles J. et al. (Mar. 2003). “The Dynamical State of Barnard 68: A Thermally Supported, Pulsating Dark Cloud”. In: *Astrophys. J.* 586.1, pp. 286–295. DOI: 10.1086/367610. arXiv: astro-ph/0211507 [astro-ph].

Lamberts, Thanja and Johannes Kästner (Sept. 2017a). “Influence of Surface and Bulk Water Ice on the Reactivity of a Water-forming Reaction”. In: *Astrophys. J.* 846.1, 43, p. 43. DOI: 10.3847/1538-4357/aa8311. arXiv: 1708.05555 [astro-ph.GA].

— (Dec. 2017b). “Tunneling Reaction Kinetics for the Hydrogen Abstraction Reaction H + H2S to H2 + HS in the Interstellar Medium”. In: *Journal of Physical Chemistry A* 121.51, pp. 9736–9741. DOI: 10.1021/acs.jpca.7b10296. arXiv: 1712.02088 [astro-ph.GA].

Lamberts, Thanja et al. (Jan. 2016). “Quantum tunneling during interstellar surface-catalyzed formation of water: the reaction H + H2O2 to H2O + OH”. In: *Physical Chemistry Chemical Physics (Incorporating Faraday Transactions)* 18.48, pp. 33021–33030. DOI: 10.1039/C6CP06457D. arXiv: 1611.09188 [physics.chem-ph].

Lamberts, Thanja et al. (June 2019). “Formation of Acetaldehyde on CO-Rich Ices”. In: *ACS Earth Space Chem.* 3.6, pp. 958–963. DOI: 10.1021/acsearthspacechem.9b00029. URL: https://doi.org/10.1021/acsearthspacechem.9b00029 (visited on 11/06/2019).

Larsen, Ask Hjorth et al. (2017). “The atomic simulation environment—a Python library for working with atoms”. In: *J. Phys.: Condens. Matter* 29 (27), p. 273002. DOI: 10.1088/1361-648X/aa680e.

Latimer, Elspeth R, Farahjabeen Islam, and Stephen D Price (2008). “Studies of HD formed in excited vibrational states from atomic recombination on cold graphite surfaces”. In: *Chemical Physics Letters* 455.4-6, pp. 174–177.

Lauck, Trish et al. (Mar. 2015). “CO Diffusion into Amorphous H_2O Ices”. In: *Astrophys. J.* 801.2, 118, p. 118. DOI: 10.1088/0004-637X/801/2/118. arXiv: 1502.07772 [astro-ph.GA].

Lee, Chengteh, Weitao Yang, and Robert G. Parr (Jan.). “Development of the Colle-Salvetti correlation-energy formula into a functional of the electron density”. In: *Phys. Rev. B* 37.2, pp. 785–789. DOI: 10.1103/PhysRevB.37.785. URL: https://link.aps.org/doi/10.1103/PhysRevB.37.785.

Lee, Chin-Fei et al. (May 2019). “First Abundance Measurement of Organic Molecules in the Atmosphere of HH 212 Protostellar Disk”. In: *Astrophys. J.* 876.1, 63, p. 63. DOI: 10.3847/1538-4357/ab15db. arXiv: 1904.10572 [astro-ph.GA].

Lefloch, Bertrand et al. (July 2017). “L1157-B1, a factory of complex organic molecules in a solar-type star-forming region”. en. In: *Mon. Not. R. Astron. Soc.* 469.1, pp. L73–L77. ISSN: 1745-3925. DOI: 10.1093/mnrasl/slx050. URL: https://academic.oup.com/mnrasl/article/469/1/L73/3192219 (visited on 11/18/2019).

Léger, A (1983). “Does CO condense on dust in molecular clouds?” In: *Astronomy and Astrophysics* 123, pp. 271–278.

Leger, A., M. Jura, and A. Omont (Mar. 1985). “Desorption from interstellar grains”. In: *Astron. Astrophys.* 144.1, pp. 147–160.

Ligterink, N. F. W. et al. (Aug. 2017). “The ALMA-PILS survey: detection of CH3NCO towards the low-mass protostar IRAS 16293-2422 and laboratory constraints on its formation”. In: *Mon. Not. R. Astron. Soc.* 469.2, p. 2219. ISSN: 0035-8711. DOI: 10.1093/mnras/stx890. URL: https://ui.adsabs.harvard.edu/abs/2017MNRAS.469.2219L/abstract (visited on 11/13/2019).

Ligterink, N. F. W. et al. (Nov. 2018). “The formation of peptide-like molecules on interstellar dust grains”. In: *Mon. Not. R. Astron. Soc.* 480.3, pp. 3628–3643. DOI: 10.1093/mnras/sty2066. arXiv: 1808.00742 [astro-ph.SR].

Linnartz, Harold, Sergio Ioppolo, and Gleb Fedoseev (2015). “Atom addition reactions in interstellar ice analogues”. In: *International Reviews in Physical Chemistry* 34.2, pp. 205–237.

Lippert, G, J Hutter, and M. Parrinello (1997). “A hybrid Gaussian and plane wave density functional scheme.” In: *Mol. Phys.* 92 (3), pp. 477–487. DOI: 10.1080/002689797170220.

Loison, J. C. and K. M. Hickson (Aug. 2015). “Ab initio study of the C + HNC, N + C2H, H + C2N and H + CNC reactions”. In: *Chemical Physics Letters* 635, pp. 174–179. DOI: 10.1016/j.cplett.2015.05.060.

Loison, Jean-Christophe, Valentine Wakelam, and Kevin M. Hickson (Sept. 2014a). “The interstellar gas-phase chemistry of HCN and HNC”. In: *Mon. Not. R. Astron. Soc.* 443.1, pp. 398–410. DOI: 10.1093/mnras/stu1089. arXiv: 1406.1696 [astro-ph.GA].

Loison, Jean-Christophe et al. (Dec. 2010). “Gas-Phase Kinetics of Hydroxyl Radical Reactions with C3H6 and C4H8: Product Branching Ratios and OH Addition Site-Specificity”. In: *Journal of Physical Chemistry A* 114.51, pp. 13326–13336. DOI: 10.1021/jp107217w.

Loison, Jean-Christophe et al. (Dec. 2012). “Gas-Phase Reaction of Hydroxyl Radical with Hexamethylbenzene”. In: *Journal of Physical Chemistry A* 116.50, pp. 12189–12197. DOI: 10.1021/jp307568c.

Loison, Jean-Christophe et al. (Jan. 2014b). “An experimental and theoretical investigation of the N(4S) + C2(1 Sigma g+) reaction at low temperature”. In: *Physical Chemistry Chemical Physics (Incorporating Faraday Transactions)* 16.27, p. 14212. DOI: 10.1039/C4CP01801J. arXiv: 1406.1374 [astro-ph.GA].

López-Sepulcre, A. et al. (Dec. 2015). “Constraining the Abundances of Complex Organics in the Inner Regions of Solar-Type Protostars”. In: *Revolution in Astronomy with ALMA: The Third Year* 499, p. 223. ISSN: [’1050-3390’]. URL: https://ui.adsabs.harvard.edu/abs/2015ASPC..499..223L/abstract (visited on 11/12/2019).

López-Sepulcre, A. et al. (Oct. 2017). “Complex organics in IRAS 4A revisited with ALMA and PdBI: Striking contrast between two neighbouring protostellar cores”. In: *Astron. Astrophys.* 606, A121, A121. DOI: 10.1051/0004-6361/201630334. arXiv: 1707.03745 [astro-ph.GA].

López-Sepulcre, Ana et al. (Oct. 2019). “Interstellar Formamide (NH2CHO), a Key Prebiotic Precursor”. In: *ACS Earth and Space Chemistry* 3.10, pp. 2122–2137. DOI: 10.1021/acsearthspacechem.9b00154. arXiv: 1909.11770 [astro-ph.SR].

Lucas, R. and H. S. Liszt (June 2000). “Comparative chemistry of diffuse clouds. I. C_2H and C_3H_2”. In: *Astron. Astrophys.* 358, pp. 1069–1076.

Marcus, R. A. (1952). “Unimolecular Dissociations and Free Radical Recombination Reactions”. In: *The Journal of Chemical Physics* 20.3, pp. 359–364.

Mardirossian, Narbe and Martin Head-Gordon (2017). “Thirty years of density functional theory in computational chemistry: an overview and extensive assessment of 200 density functionals”. In: *Molecular Physics* 115.19, pp. 2315–2372.

Martin, Richard M. (2004). *Electronic Structure: Basic Theory and Practical Methods*. Cambridge University Press. ISBN: 9780521782852.

Martıín-Doménech, Rafael, Karin I. Öberg, and Mahesh Rajappan (May 2020). “Formation of NH_2CHO and CH_3CHO upon UV Photoprocessing of Interstellar Ice Analogs”. In: *Astrophys. J.* 894.2, 98, p. 98. DOI: 10.3847/1538-4357/ab84e8. arXiv: 2004.01151 [astro-ph.SR].

Martıínez-Bachs, Berta, Stefano Ferrero, and Albert Rimola (2020). “Binding Energies of N-Bearing Astrochemically-Relevant Molecules on Water Interstellar Ice Models. A Computational Study”. In: *International Conference on Computational Science and Its Applications*. Springer, pp. 683–692.

Marx, Dominik and Jürg Hutter (2009). *Ab Initio Molecular Dynamics: Basic Theory and Advanced Methods*. Cambridge University Press. ISBN: 9780511609633.

Masuda, Koichi, Junko Takahashi, and Tadashi Mukai (Feb. 1998). “Sticking probability and mobility of a hydrogen atom on icy mantle of dust grains”. In: *Astron. Astrophys.* 330, pp. 773–781.

Maté, Belén et al. (Nov. 2020). “Diffusion of CH_4 in amorphous solid water”. In: *Astron. Astrophys.* 643, A163, A163. DOI: 10.1051/0004-6361/202038705. arXiv: 2102.13357 [astro-ph.IM].

Mathis, J. S., W. Rumpl, and K. H. Nordsieck (Oct. 1977). “The size distribution of interstellar grains.” In: *Astrophys. J.* 217, pp. 425–433. DOI: 10.1086/155591.

McGuire, Brett A. et al. (Jan. 2018). “Detection of the aromatic molecule benzonitrile (c-C6H5CN) in the interstellar medium”. In: *Science* 359.6372, pp. 202–205. ISSN: 0036-8075, 1095-9203. DOI: 10.1126/science.aao4890. URL: https://science.sciencemag.org/content/359/6372/202 (visited on 11/13/2019).

McKee, C. F. and J. P. Ostriker (Nov. 1977). “A theory of the interstellar medium: three components regulated by supernova explosions in an inhomogeneous substrate.” In: *Astrophys. J.* 218, pp. 148–169. DOI: 10.1086/155667.

McQuarrie, D. (1976). *Statistical Mechanics*. New York: Harper and Row.

Meisner, Jan, Thanja Lamberts, and Johannes Kästner (Sept. 2017). “Atom Tunneling in the Water Formation Reaction H2 + OH to H2O + H on an Ice Surface”. In: *ACS Earth and Space Chemistry* 1.7, pp. 399–410. DOI: 10.1021/acsearthspacechem.7b00052. arXiv: 1708.05559 [astro-ph.GA].

Mendoza, Edgar et al. (Sept. 2014). “Molecules with a peptide link in protostellar shocks: a comprehensive study of L1157”. In: *Mon. Not. R. Astron. Soc.* 445.1, pp. 151–161. ISSN: 0035-8711. DOI: 10.1093/mnras/stu1718. URL: https://doi.org/10.1093/mnras/stu1718.

Millar, T. J., Eric Herbst, and S. B. Charnley (Mar. 1991). “The Formation of Oxygen-containing Organic Molecules in the Orion Compact Ridge”. In: *Astrophys. J.* 369, p. 147. DOI: 10.1086/169745.

Min, M. et al. (Feb. 2007). “The shape and composition of interstellar silicate grains”. In: *Astron. Astrophys.* 462.2, pp. 667–676. DOI: 10.1051/0004-6361:20065436. arXiv: astro-ph/0611329 [astro-ph].

— (Aug. 2008). “[Erratum] The shape and composition of interstellar silicate grains”. In: *Astron. Astrophys.* 486.3, pp. 779–780. DOI: 10.1051/0004-6361:20065436e.

Minissale, M., E. Congiu, and F. Dulieu (Feb. 2014a). “Oxygen diffusion and reactivity at low temperature on bare amorphous olivine-type silicate”. In: *J. Chem. Phys.* 140.7, 074705, p. 074705. DOI: 10.1063/1.4864657. arXiv: 1402.2211 [astro-ph.GA].

Minissale, M., E. Congiu, and F. Dulieu (Jan. 2016a). “Direct measurement of desorption and diffusion energies of O and N atoms physisorbed on amorphous surfaces”. In: *Astron. Astrophys.* 585, A146, A146. DOI: 10.1051/0004-6361/201526702. arXiv: 1603.02897 [astro-ph.SR].

Minissale, M. and F. Dulieu (July 2014b). “Influence of surface coverage on the chemical desorption process”. In: *J. Chem. Phys.* 141.1, 014304, p. 014304. DOI: 10.1063/1.4885847. arXiv: 1406.5594 [physics.chem-ph].

Minissale, M. et al. (Aug. 2013). “Quantum Tunneling of Oxygen Atoms on Very Cold Surfaces”. In: *Phys. Rev. Lett.* 111.5, 053201, p. 053201. DOI: 10.1103/PhysRevLett.111.053201. arXiv: 1402.3207 [cond-mat.mtrl-sci].

Minissale, M. et al. (Jan. 2016b). “Dust as interstellar catalyst. I. Quantifying the chemical desorption process”. In: *Astron. Astrophys.* 585, A24, A24. DOI: 10.1051/0004-6361/201525981. arXiv: 1510.03218 [astro-ph.SR].

Minissale, M. et al. (May 2016c). “Hydrogenation of CO-bearing species on grains: unexpected chemical desorption of CO”. In: *Mon. Not. R. Astron. Soc.* 458.3, pp. 2953–2961. DOI: 10.1093/mnras/stw373.

Mispelaer, F. et al. (July 2013). “Diffusion measurements of CO, HNCO, H_2CO, and NH_3 in amorphous water ice”. In: *Astron. Astrophys.* 555, A13, A13. DOI: 10.1051/0004-6361/201220691.

Molinari, Sergio et al. (Aug. 1999). “Detection of the 62 Micron Crystalline H_2O Ice Feature in Emission toward HH 7 with the Infrared Space Observatory Long-Wavelength Spectrometer”. In: *Astrophys. J. Lett.* 521.1, pp. L71–L74. DOI: 10.1086/312178.

Molpeceres, G. et al. (Nov. 2018). “Silicate-mediated interstellar water formation: a theoretical study”. In: *MNRAS* 482.4, pp. 5389–5400. DOI: 10.1093/mnras/sty3024.

Molpeceres, Germán and Johannes Kästner (Apr. 2020). “Adsorption of H_2 on amorphous solid water studied with molecular dynamics simulations”. In: *Physical Chemistry Chemical Physics (Incorporating Faraday Transactions)* 22.14, pp. 7552–7563. DOI: 10.1039/D0CP00250J. arXiv: 2003.08873 [physics.chem-ph].

Molpeceres, Germán et al. (2019). “Silicate-mediated interstellar water formation: a theoretical study”. In: *Monthly Notices of the Royal Astronomical Society* 482.4, pp. 5389–5400.

Müller, Holger S. P. et al. (Mar. 2016). “Exploring molecular complexity with ALMA (EMoCA): Alkanethiols and alkanols in Sagittarius B2(N2)”. In: *Astron. Astrophys.* 587, A92, A92. DOI: 10.1051/0004-6361/201527470. arXiv: 1512.05301 [astro-ph.GA].

Muller, S. et al. (Mar. 2013). “A precise and accurate determination of the cosmic microwave background temperature at z = 0.89”. In: *Astron. Astrophys.* 551, A109. ISSN: 0004-6361, 1432-0746. DOI: 10.1051/0004-6361/201220613. URL: https://www.aanda.org/articles/aa/abs/2013/03/aa20613-12/aa20613-12.html (visited on 11/12/2019).

Navarro-Ruiz, Javier et al. (2015). “Relevance of silicate surface morphology in interstellar H2 formation. Insights from quantum chemical calculations”. In: *Monthly Notices of the Royal Astronomical Society* 453.1, pp. 914–924.

Navarro-Ruiz, J et al. (2016). “Does Fe 2+ in olivine-based interstellar grains play any role in the formation of H 2? Atomistic insights from DFT periodic simulations”. In: *Chemical Communications* 52.42, pp. 6873–6876.

Neese, Frank (2004). “Definition of corresponding orbitals and the diradical character in broken symmetry DFT calculations on spin coupled systems”. In: *Journal of Physics and Chemistry of Solids* 65.4, pp. 781–785.

— (2009). “Prediction of molecular properties and molecular spectroscopy with density functional theory: From fundamental theory to exchange-coupling”. In: *Coordination Chemistry Reviews* 253.5, pp. 526–563.

Noble, J. A. et al. (July 2011). “CO2 Formation in Quiescent Clouds: An Experimental Study of the CO + OH Pathway”. In: *Astrophys. J.* 735.2, 121, p. 121. DOI: 10.1088/0004-637X/735/2/121. arXiv: 1104.0031 [astro-ph.SR].

Noble, J. A. et al. (Apr. 2015). “Hydrogenation at low temperatures does not always lead to saturation: the case of HNCO”. In: *Astron. Astrophys.* 576, A91, A91. DOI: 10.1051/0004-6361/201425403. arXiv: 1502.03282 [astro-ph.SR].

Noodleman, Louis (May 1981). “Valence bond description of antiferromagnetic coupling in transition metal dimers”. In: *J. Chem. Phys.* 74.10, pp. 5737–5743. ISSN: 0021-9606. DOI: 10.1063/1.440939. URL: https://aip.scitation.org/doi/10.1063/1.440939 (visited on 11/12/2019).

Noodleman, Louis and Evert Jan Baerends (1984). “Electronic structure, magnetic properties, ESR, and optical spectra for 2-iron ferredoxin models by LCAO-X.alpha. valence bond theory”. en. In: *J. Am. Chem. Soc.* 106.8, pp. 2316–2327. DOI: 10.1021/ja00320a017. URL: https://doi.org/10.1021/ja00320a017 (visited on 11/12/2019).

Oba, Y. et al. (Aug. 2009). “Formation of Compact Amorphous H_2O Ice by Codeposition of Hydrogen Atoms with Oxygen Molecules on Grain Surfaces”. In: *Astrophys. J.* 701.1, pp. 464–470. DOI: 10.1088/0004-637X/701/1/464.

Oba, Y. et al. (Apr. 2012). “Water Formation through a Quantum Tunneling Surface Reaction, OH + H2, at 10 K”. In: *Astrophys. J.* 749.1, 67, p. 67. DOI: 10.1088/0004-637X/749/1/67. arXiv: 1202.1035 [astro-ph.GA].

Oba, Y. et al. (Mar. 2018). “An infrared measurement of chemical desorption from interstellar ice analogues”. In: *Nature Astronomy* 2, pp. 228–232. DOI: 10.1038/s41550-018-0380-9. arXiv: 1810.04669 [astro-ph.GA].

Öberg, K. I. et al. (Sept. 2009). “Formation rates of complex organics in UV irradiated CH3OH-rich ices. I. Experiments”. In: *Astron. Astrophys.* 504.3, pp. 891–913. DOI: 10.1051/0004-6361/200912559. arXiv: 0908.1169 [astro-ph.GA].

Öberg, Karin I. and Edwin A. Bergin (Jan. 2021). “Astrochemistry and compositions of planetary systems”. In: *Physics Reports* 893, pp. 1–48. DOI: 10.1016/j.physrep.2020.09.004. arXiv: 2010.03529 [astro-ph.EP].

Öberg, Karin I. et al. (June 2010). “A Cold Complex Chemistry Toward the Low-mass Protostar B1-b: Evidence for Complex Molecule Production in Ices”. In: *Astrophys. J.* 716.1, pp. 825–834. DOI: 10.1088/0004-637X/716/1/825. arXiv: 1005.0637 [astro-ph.GA].

Padovani, M. et al. (Oct. 2009). “C{2}H in prestellar cores”. In: *Astron. Astrophys.* 505.3, pp. 1199–1211. DOI: 10.1051/0004-6361/200912547. arXiv: 0908.1176 [astro-ph.GA].

Palumbo, M. E. (July 2006). “Formation of compact solid water after ion irradiation at 15 K”. In: *Astron. Astrophys.* 453.3, pp. 903–909. DOI: 10.1051/0004-6361:20042382.

Palumbo, M. E. et al. (May 2010). “H bonds in astrophysical ices”. In: *Journal of Molecular Structure* 972, pp. 64–67. DOI: 10.1016/j.molstruc.2009.12.017.

Pantaleone, Stefano et al. (July 2020). “Chemical Desorption versus Energy Dissipation: Insights from Ab Initio Molecular Dynamics of HCO Formation”. In: *Astrophys. J.* 897.1, 56, p. 56. DOI: 10.3847/1538-4357/ab8a4b. arXiv: 2004.11758 [astro-ph.GA].

Pantaleone, Stefano et al. (May 2021). “H2 formation on interstellar grains and the fate of reaction energy”. In: *arXiv e-prints*, arXiv:2105.06843, arXiv:2105.06843. arXiv: 2105.06843 [astro-ph.GA].

Park, Jin-Young and David E. Woon (Aug. 2004). “Theoretical Investigation of OCN-Charge-Transfer Complexes in Condensed-Phase Media: Spectroscopic Properties in Amorphous Ice”. In: *Journal of Physical Chemistry A* 108.31, pp. 6589–6598. DOI: 10.1021/jp048763m.

— (Sept. 2006). “Theoretical Modeling of Formic Acid (HCOOH), Formate (HCOO-), and Ammonium (NH4+) Vibrational Spectra in Astrophysical Ices”. In: *Astrophys. J.* 648.2, pp. 1285–1290. DOI: 10.1086/506175.

Pearson, Peter K and Henry F Schaefer III (1974). “Some Properties of H2CN+: a Potentially Important Interstellar Species”. In: *The Astrophysical Journal* 192, pp. 33–36.

Pedersen, Andreas et al. (2015). “Long-time-scale simulations of h2o admolecule diffusion on ice ih (0001) surfaces”. In: *The Journal of Physical Chemistry C* 119.29, pp. 16528–16536.

Penteado, E. M., C. Walsh, and H. M. Cuppen (July 2017). “Sensitivity Analysis of Grain Surface Chemistry to Binding Energies of Ice Species”. In: *Astrophys. J.* 844.1, 71, p. 71. DOI: 10.3847/1538-4357/aa78f9. arXiv: 1708.01450 [astro-ph.GA].

Perdew, John P. and Karla Schmidt (2001). “Jacob’s ladder of density functional approximations for the exchange-correlation energy”. In: *AIP Conference Proceedings* 577.1, pp. 1–20.

Perdew, JP, K Burke, and M. Ernzerhof (1996). “Generalized gradient approximation made simple.” In: *Phys. Rev. Lett.* 77 (18), pp. 3865–3868. DOI: 10.1103/PhysRevLett.77.3865.

Persson, Magnus Vilhelm (Aug. 2014). *Current view of protostellar evolution (ENG)*. DOI: 10.6084/m9.figshare.654555.v7. URL: https://figshare.com/articles/Current_view_of_protostellar_evolution/654555/7.

Peters, P. P. et al. (July 2011). “Theoretical Investigation of the Isomerization of trans-HCOH to H2CO: An Example of a Water-Catalyzed Reaction”. In: *Journal of Physical Chemistry A* 115, pp. 8983–8989. DOI: 10.1021/jp202052h.

Pirim, C. and L. Krim (Jan. 2011). “A neon-matrix isolation study of the reaction of non-energetic H-atoms with CO molecules at 3 K”. In: *Physical Chemistry Chemical Physics (Incorporating Faraday Transactions)* 13.43, p. 19454. DOI: 10.1039/C1CP21835B.

Pirim, C. et al. (Mar. 2010). “Preliminary Study of the Influence of Environment Conditions on the Successive Hydrogenations of CO”. In: *Journal of Physical Chemistry A* 114.9, pp. 3320–3328. DOI: 10.1021/jp909600q.

Pisani, C, S Casassa, and P Ugliengo (1996). “Proton-ordered ice structures at zero pressure. A quantum-mechanical investigation”. In: *Chem. Phys. Lett.* 253, pp. 201–208. DOI: 10.1016/0009-2614(96)00228-X.

Planck Collaboration et al. (Nov. 2014a). “Planck 2013 results. I. Overview of products and scientific results”. In: *Astron. Astrophys.* 571, A1, A1. DOI: 10.1051/0004-6361/201321529. arXiv: 1303.5062 [astro-ph.CO].

Planck Collaboration et al. (Nov. 2014b). “Planck 2013 results. XVI. Cosmological parameters”. In: *Astron. Astrophys.* 571, A16, A16. DOI: 10.1051/0004-6361/201321591. arXiv: 1303.5076 [astro-ph.CO].

Planck Collaboration et al. (Sept. 2020). “Planck 2018 results. I. Overview and the cosmological legacy of Planck”. In: *Astron. Astrophys.* 641, A1, A1. DOI: 10.1051/0004-6361/201833880. arXiv: 1807.06205 [astro-ph.CO].

Potapov, Alexey and Martin McCoustra (May 2021). “Physics and Chemistry on the Surface of Cosmic Dust Grains: A Laboratory View”. In: *arXiv e-prints*, arXiv:2105.01387, arXiv:2105.01387. arXiv: 2105.01387 [astro-ph.GA].

Prasad, S. S. and S. P. Tarafdar (Apr. 1983). “UV radiation field inside dense clouds - Its possible existence and chemical implications”. In: *Astrophys. J.* 267, pp. 603–609. DOI: 10.1086/160896.

Redondo, Pilar, Carmen Barrientos, and Antonio Largo (2013). “Some insights into formamide formation through gas-phase reactions in the interstellar medium”. In: *The Astrophysical Journal* 780.2, p. 181.

Rice, Oscar Knefler and Herman C Ramsperger (1927). “Theories of unimolecular gas reactions at low pressures”. In: *Journal of the American Chemical Society* 49.7, pp. 1617–1629.

Rimola, Albert, Mariona Sodupe, and Piero Ugliengo (2010). “Deep-space glycine formation via Strecker-type reactions activated by ice water dust mantles. A computational approach”. In: *Phys. Chem. Chem. Phys.* 12 (20), pp. 5285–5294. DOI: 10.1039/B923439J. URL: http://dx.doi.org/10.1039/B923439J.

— (July 2012). “Computational Study of Interstellar Glycine Formation Occurring at Radical Surfaces of Water-ice Dust Particles”. In: *Astrophys. J.* 754.1, 24, p. 24. DOI: 10.1088/0004-637X/754/1/24.

Rimola, Albert et al. (Dec. 2014). “Combined quantum chemical and modeling study of CO hydrogenation on water ice”. In: *Astronomy & Astrophysics* 572, A70, A70.

Rimola, Albert et al. (July 2018). “Can Formamide Be Formed on Interstellar Ice? An Atomistic Perspective”. In: *ACS Earth and Space Chemistry* 2.7, pp. 720–734. DOI: 10.1021/acsearthspacechem.7b00156. arXiv: 1810.02965 [astro-ph.EP].

Rimola, Albert et al. (2021). “Interaction of HCO+ Cations With Interstellar Negative Grains. Quantum Chemical Investigation and Astrophysical Implications”. In: *Frontiers in Astronomy and Space Sciences* 8, p. 38. ISSN: 2296-987X. DOI: 10.3389/fspas.2021.655405. URL: https://www.frontiersin.org/article/10.3389/fspas.2021.655405.

Rodgers, S. D. and S. B. Charnley (Jan. 2001). “Chemical Differentiation in Regions of Massive Star Formation”. In: *Astrophys. J.* 546.1, pp. 324–329. DOI: 10.1086/318263.

Roser, J. E. et al. (Oct. 2003). “Measurement of the Kinetic Energy of Hydrogen Molecules Desorbing from Amorphous Water Ice”. In: *Astrophys. J. Lett.* 596.1, pp. L55–L58. DOI: 10.1086/379095.

Ruaud, M. et al. (Mar. 2015). “Modelling complex organic molecules in dense regions: Eley-Rideal and complex induced reaction”. In: *Mon. Not. R. Astron. Soc.* 447.4, pp. 4004–4017. DOI: 10.1093/mnras/stu2709. arXiv: 1412.6256 [astro-ph.SR].

Ruaud, Maxime, Valentine Wakelam, and Franck Hersant (2016). “Gas and grain chemical composition in cold cores as predicted by the Nautilus three-phase model”. In: *Monthly Notices of the Royal Astronomical Society* 459.4, pp. 3756–3767.

Rubin, R. H. et al. (Oct. 1971). “Microwave Detection of Interstellar Formamide”. In: *Astrophys. J.* 169, p. L39. ISSN: ['0004-637X']. DOI: 10.1086/180810. URL: https://ui.adsabs.harvard.edu/abs/1971ApJ...169L..39R/abstract (visited on 11/12/2019).

Ruffle, Deborah P. and Eric Herbst (Dec. 2000a). “New models of interstellar gas-grain chemistry - I. Surface diffusion rates”. In: *Mon. Not. R. Astron. Soc.* 319.3, pp. 837–850. DOI: 10.1046/j.1365-8711.2000.03911.x.

— (Dec. 2000b). “New models of interstellar gas-grain chemistry - I. Surface diffusion rates”. In: *Mon. Not. R. Astron. Soc.* 319.3, pp. 837–850. DOI: 10.1046/j.1365-8711.2000.03911.x.

Ruocco, G. et al. (Feb. 1996). “Equivalence of the sound velocity in water and ice at mesoscopic wavelengths”. en. In: *Nature* 379.6565, pp. 521–523. ISSN: 0028-0836, 1476-4687. DOI: 10.1038/379521a0. URL: http://www.nature.com/articles/379521a0 (visited on 09/08/2020).

Sakai, Nami et al. (2008). “Abundant carbon-chain molecules toward the low-mass protostar IRAS 04368+2557 in L1527”. In: *The Astrophysical Journal* 672.1, p. 371.

— (Oct. 2010a). “Distributions of Carbon-chain Molecules in L1527”. In: *Astrophys. J.* 722.2, pp. 1633–1643. DOI: 10.1088/0004-637X/722/2/1633.

Sakai, Nami et al. (Aug. 2010b). “Long Carbon-chain Molecules and Their Anions in the Starless Core, Lupus-1A”. In: *Astrophys. J. Lett.* 718.2, pp. L49–L52. DOI: 10.1088/2041-8205/718/2/L49.

Sakai, Takeshi et al. (Apr. 2018). “ALMA Observations of the IRDC Clump G34.43+00.24 MM3: Complex Organic and Deuterated Molecules”. In: *Astrophys. J.* 857.1, 35, p. 35. DOI: 10.3847/1538-4357/aaadfd.

Sameera, WMC et al. (2017). “ONIOM (QM: AMOEBA09) Study on binding energies and binding preference of OH, HCO, and CH3 radicals on hexagonal water ice (Ih)”. In: *The Journal of Physical Chemistry C* 121.28, pp. 15223–15232.

Schilke, P. et al. (May 1997). “SiO production in interstellar shocks.” In: *Astron. Astrophys.* 321, pp. 293–304.

Schutte, WA and JM Greenberg (1991). “Explosive desorption of icy grain mantles in dense clouds”. In: *Astronomy and Astrophysics* 244, pp. 190–204.

Scibelli, Samantha and Yancy Shirley (Mar. 2020). “Prevalence of Complex Organic Molecules in Starless and Prestellar Cores within the Taurus Molecular Cloud”. In: *Astrophys. J.* 891.1, 73, p. 73. DOI: 10.3847/1538-4357/ab7375. arXiv: 2002.02469 [astro-ph.GA].

Senevirathne, Bethmini et al. (Mar. 2017). “Hydrogen atom mobility, kinetic isotope effects and tunneling on interstellar ices (Ih and ASW)”. In: *Molecular Astrophysics* 6, pp. 59–69. DOI: 10.1016/j.molap.2017.01.005.

Shen, CJ et al. (2004). “Cosmic ray induced explosive chemical desorption in dense clouds”. In: *Astronomy & Astrophysics* 415.1, pp. 203–215.

Sherrill, C. David (Mar. 2010). “Frontiers in electronic structure theory”. In: *Journal of Chemical Physics* 132.11, pp. 110902–110902. DOI: 10.1063/1.3369628.

Shingledecker, Christopher N. and Eric Herbst (Feb. 2018a). “A general method for the inclusion of radiation chemistry in astrochemical models”. In: *Physical Chemistry Chemical Physics (Incorporating Faraday Transactions)* 20, pp. 5359–5367. DOI: 10.1039/C7CP05901A.

Shingledecker, Christopher N. et al. (July 2018b). “On Cosmic-Ray-driven Grain Chemistry in Cold Core Models”. In: *Astrophys. J.* 861.1, 20, p. 20. DOI: 10.3847/1538-4357/aac5ee. arXiv: 1805.05764 [astro-ph.GA].

Shu, F. H. (June 1977). “Self-similar collapse of isothermal spheres and star formation.” In: *Astrophys. J.* 214, pp. 488–497. DOI: 10.1086/155274.

Simons, M. A. J., T. Lamberts, and H. M. Cuppen (Feb. 2020). “Formation of COMs through CO hydrogenation on interstellar grains”. In: *Astron. Astrophys.* 634, A52, A52. DOI: 10.1051/0004-6361/201936522. arXiv: 2001.04895 [astro-ph.SR].

Skouteris, D. et al. (June 2017). “New quantum chemical computations of formamide deuteration support gas-phase formation of this prebiotic molecule”. In: *Mon. Not. R. Astron. Soc.* 468.1, pp. L1–L5. DOI: 10.1093/mnrasl/slx012. arXiv: 1701.06138 [astro-ph.SR].

Skouteris, Dimitrios et al. (Feb. 2018). “The Genealogical Tree of Ethanol: Gas-phase Formation of Glycolaldehyde, Acetic Acid, and Formic Acid”. In: *Astrophys. J.* 854.2, 135, p. 135. DOI: 10.3847/1538-4357/aaa41e. arXiv: 1712.08938 [astro-ph.SR].

Skouteris, D et al. (2017). “New quantum chemical computations of formamide deuteration support gas-phase formation of this prebiotic molecule”. In: *Monthly Notices of the Royal Astronomical Society: Letters* 468.1, pp. L1–L5.

Smith, Daniel GA et al. (2016). “Revised damping parameters for the D3 dispersion correction to density functional theory”. In: *The journal of physical chemistry letters* 7.12, pp. 2197–2203.

Smith, Robert G., K. Sellgren, and Alan T. Tokunaga (Sept. 1989). “Absorption Features in the 3 Micron Spectra of Protostars”. In: *Astrophys. J.* 344, p. 413. DOI: 10.1086/167809.

— (1988). “A study of H_2O ice in the 3 micron spectrum of OH 231.8+ 4.2 (OH 0739-14)”. In: *The Astrophysical Journal* 334, pp. 209–219.

Smoluchowski, R. (Jan. 1983). “Adsorption and mobility on amorphous surfaces. Application to astrophysical problems.” In: *Journal of Physical Chemistry* 87.21, pp. 4229–4233. DOI: 10.1021/j100244a050.

Song, Lei and Johannes Kästner (Jan. 2016). “Formation of the prebiotic molecule NH2CHO on astronomical amorphous solid water surfaces: accurate tunneling rate calculations”. In: *Physical Chemistry Chemical Physics (Incorporating Faraday Transactions)* 18.42, pp. 29278–29285. DOI: 10.1039/C6CP05727F. arXiv: 1610.01007 [physics.chem-ph].

— (Dec. 2017). “Tunneling Rate Constants for H2CO+H on Amorphous Solid Water Surfaces”. In: *Astrophys. J.* 850.2, 118, p. 118. DOI: 10.3847/1538-4357/aa943e. arXiv: 2009.05442 [astro-ph.GA].

Stahler, Steven W. and Francesco Palla (Nov. 2004). *The Formation of Stars*. Wiley. DOI: 10.1002/9783527618675. URL: https://doi.org/10.1002/9783527618675.

Strazzulla, G., L. Calcagno, and G. Foti (Aug. 1983). “Polymerization induced on interstellar grains by low-energy cosmic rays”. In: *Mon. Not. R. Astron. Soc.* 204, 59P–62P. DOI: 10.1093/mnras/204.1.59P.

Strazzulla, G., A. C. Castorina, and M. E. Palumbo (Feb. 1995). “Ion irradiation of astrophysical ices”. In: *Planet. Space Sci.* 43.10, pp. 1247–1251. DOI: 10.1016/0032-0633(95)00040-C.

Szabo, Attila and Neil S. Ostlund (1996). *Modern Quantum Chemistry. Introduction to Advanced Electronic Structure Theory*. Dover Publications, INC. ISBN: 9780486691862.

Tafalla, M. et al. (Mar. 2004). “On the internal structure of starless cores. I. Physical conditions and the distribution of CO, CS, N2H+, and NH3 in L1498 and L1517B”. In: *Astron. Astrophys.* 416, pp. 191–212. DOI: 10.1051/0004-6361:20031704.

Takahashi, Junko (Nov. 1999). “MD simulation for H2 formation on amorphous ice”. In: *Earth, Planets, and Space* 51, pp. 1215–1222. DOI: 10.1186/BF03351595.

Takahashi, Junko, Koichi Masuda, and Masataka Nagaoka (Aug. 1999a). “Product Energy Distribution of Molecular Hydrogen Formed on Icy Mantles of Interstellar Dust”. In: *Astrophys. J.* 520.2, pp. 724–731. DOI: 10.1086/307461.

— (June 1999b). “The formation mechanism of molecular hydrogen on icy mantles of interstellar dust”. In: *Mon. Not. R. Astron. Soc.* 306.1, pp. 22–30. DOI: 10.1046/j.1365-8711.1999.02480.x.

Takahashi, Junko and Hideya Uehara (2001). “H_2 Emission Spectra with New Formation Pumping Models”. In: *The Astrophysical Journal* 561.2, p. 843.

Takahashi, Junko and David A. Williams (May 2000). “Chemically driven desorption of CO from icy grains in dark clouds”. In: *Mon. Not. R. Astron. Soc.* 314.2, pp. 273–278. DOI: 10.1046/j.1365-8711.2000.03291.x.

— (Aug. 1999c). “Chemical Desorption of CO in the Vicinity of H2 Forming Sites on Dust”. In: *The Physics and Chemistry of the Interstellar Medium*. Ed. by V. Ossenkopf, J. Stutzki, and G. Winnewisser, p. 375.

Taquet, V., C. Ceccarelli, and C. Kahane (Feb. 2012). “Multilayer modeling of porous grain surface chemistry. I. The GRAINOBLE model”. In: *Astron. Astrophys.* 538, A42, A42. DOI: 10.1051/0004-6361/201117802. arXiv: 1111.4165 [astro-ph.GA].

Taquet, Vianney, Eva S. Wirström, and Steven B. Charnley (Apr. 2016). “Formation and Recondensation of Complex Organic Molecules during Protostellar Luminosity Outbursts”. In: *Astrophys. J.* 821.1, 46, p. 46. DOI: 10.3847/0004-637X/821/1/46. arXiv: 1602.05364 [astro-ph.GA].

Taquet, Vianney et al. (May 2015). “Constraining the Abundances of Complex Organics in the Inner Regions of Solar-type Protostars”. In: *Astrophys. J.* 804.2, 81, p. 81. DOI: 10.1088/0004-637X/804/2/81. arXiv: 1502.06427 [astro-ph.SR].

Terada, Hiroshi and Alan T Tokunaga (2012). “Discovery of Crystallized Water Ice in a Silhouette Disk in the M43 Region”. In: *The Astrophysical Journal* 753.1, p. 19.

Teyssier, D. et al. (Apr. 2004). “Carbon budget and carbon chemistry in Photon Dominated Regions”. In: *Astron. Astrophys.* 417, pp. 135–149. DOI: 10.1051/0004-6361:20034534. arXiv: astro-ph/0401309 [astro-ph].

Tielens, A. G. G. M. (May 1998). “Interstellar Depletions and the Life Cycle of Interstellar Dust”. In: *Astrophys. J.* 499.1, pp. 267–272. DOI: 10.1086/305640.

— (Sept. 2008). “Interstellar polycyclic aromatic hydrocarbon molecules.” In: *Annu. Rev. Astron. Astrophys.* 46, pp. 289–337. DOI: 10.1146/annurev.astro.46.060407.145211.

— (2010). *The Physics and Chemistry of the Interstellar Medium*.

— (July 2013). “The molecular universe”. In: *Reviews of Modern Physics* 85.3, pp. 1021–1081. DOI: 10.1103/RevModPhys.85.1021.

Tielens, A. G. G. M. and L. J. Allamandola (1987). “Composition, Structure, and Chemistry of Interstellar Dust”. In: *Interstellar Processes*. Ed. by David J. Hollenbach and Jr. Thronson Harley A. Vol. 134, p. 397. DOI: 10.1007/978-94-009-3861-8_16.

Tielens, A. G. G. M. and W. Hagen (Oct. 1982). “Model calculations of the molecular composition of interstellar grain mantles”. In: *Astron. Astrophys.* 114.2, pp. 245–260.

Tucker, K. D., M. L. Kutner, and P. Thaddeus (Nov. 1974a). “The Ethynyl Radical C_2H-A New Interstellar Molecule”. In: *Astrophys. J. Lett.* 193, p. L115. DOI: 10.1086/181646.

— (Nov. 1974b). “The Ethynyl Radical C2H – A New Interstellar Molecule”. In: *Astrophys. J. Lett.* 193, p. L115. DOI: 10.1086/181646.

van de Hulst, H. C. (Jan. 1946). “The solid particles in interstellar space”. In: *Recherches Astronomiques de l’Observatoire d’Utrecht* 11, pp. 2.i–2.

VandeVondele, J and J. Hutter (2003). “An efficient orbital transformation method for electronic structure calculations.” In: *J. Chem. Phys.* 118, p. 4365. DOI: 10.1063/1.1543154.

VandeVondele, J et al. (2005). “QUICKSTEP: Fast and accurate density functional calculations using a mixed Gaussian and plane waves approach.” In: *Comput. Phys. Commun.* 167, pp. 103–128. DOI: 10.1016/j.cpc.2004.12.014.

Vastel, C. et al. (Nov. 2014). “The Origin of Complex Organic Molecules in Prestellar Cores”. In: *Astrophys. J. Lett.* 795.1, L2, p. L2. DOI: 10.1088/2041-8205/795/1/L2. arXiv: 1409.6565 [astro-ph.SR].

Vasyunin, A. I. and Eric Herbst (May 2013). “Reactive Desorption and Radiative Association as Possible Drivers of Complex Molecule Formation in the Cold Interstellar Medium”. In: *Astrophys. J.* 769.1, 34, p. 34. DOI: 10.1088/0004-637X/769/1/34. arXiv: 1303.7266 [astro-ph.GA].

Vasyunin, A. I. et al. (June 2017). “Formation of Complex Molecules in Prestellar Cores: A Multilayer Approach”. In: *Astrophys. J.* 842.1, 33, p. 33. DOI: 10.3847/1538-4357/aa72ec. arXiv: 1705.04747 [astro-ph.GA].

Vazart, Fanny et al. (2016). “State-of-the-art thermochemical and kinetic computations for astrochemical complex organic molecules: formamide formation in cold interstellar clouds as a case study”. In: *Journal of chemical theory and computation* 12.11, pp. 5385–5397.

Vazart, Fanny et al. (Dec. 2020). “Gas-phase formation of acetaldehyde: review and new theoretical computations”. In: *Mon. Not. R. Astron. Soc.* 499.4, pp. 5547–5561. DOI: 10.1093/mnras/staa3060. arXiv: 2010.02718 [astro-ph.GA].

Veeraghattam, Vijay K. et al. (July 2014). “The Sticking of Atomic Hydrogen on Amorphous Water Ice”. In: *Astrophys. J.* 790.1, 4, p. 4. DOI: 10.1088/0004-637X/790/1/4.

Vidali, Gianfranco (Dec. 2013). “H2 Formation on Interstellar Grains”. In: *Chemical Reviews* 113.12, pp. 8752–8782. DOI: 10.1021/cr400156b.

Viti, Serena and David A. Williams (May 1999). “Time-dependent evaporation of icy mantles in hot cores”. In: *Mon. Not. R. Astron. Soc.* 305.4, pp. 755–762. DOI: 10.1046/j.1365-8711.1999.02447.x.

Viti, Serena et al. (Nov. 2004). “Evaporation of ices near massive stars: models based on laboratory temperature programmed desorption data”. In: *Mon. Not. R. Astron. Soc.* 354.4, pp. 1141–1145. DOI: 10.1111/j.1365-2966.2004.08273.x. arXiv: astro-ph/0406054 [astro-ph].

Vydrov, Oleg A. and Troy Van Voorhis (2010). “Nonlocal van der Waals density functional: The simpler the better”. In: *The Journal of Chemical Physics* 133.24, p. 244103.

Wakelam, V. et al. (Mar. 2017). “Binding energies: New values and impact on the efficiency of chemical desorption”. In: *Molecular Astrophysics* 6, pp. 22–35. DOI: 10.1016/j.molap.2017.01.002. arXiv: 1701.06492 [astro-ph.GA].

Wakelam, Valentine et al. (Dec. 2017). “H2 formation on interstellar dust grains: The viewpoints of theory, experiments, models and observations”. In: *Molecular Astrophysics* 9, pp. 1–36. DOI: 10.1016/j.molap.2017.11.001. arXiv: 1711.10568 [astro-ph.GA].

Walch, Stephen P et al. (2001). “On the reaction CH2O + NH3 to CH2NH + H2O”. In: *Chemical Physics Letters* 333.1, pp. 6–11. ISSN: 0009-2614. DOI: https://doi.org/10.1016/S0009-2614(00)01341-5.

Ward-Thompson, D., F. Motte, and P. Andre (May 1999). “The initial conditions of isolated star formation - III. Millimetre continuum mapping of pre-stellar cores”. In: *Mon. Not. R. Astron. Soc.* 305.1, pp. 143–150. DOI: 10.1046/j.1365-8711.1999.02412.x.

Watanabe, N. et al. (Oct. 2007). “Laboratory Simulation of Competition between Hydrogenation and Photolysis in the Chemical Evolution of H2O-CO Ice Mixtures”. In: *Astrophys. J.* 668.2, pp. 1001–1011. DOI: 10.1086/521421.

Watanabe, Naoki and Akira Kouchi (June 2002a). “Efficient Formation of Formaldehyde and Methanol by the Addition of Hydrogen Atoms to CO in H2O-CO Ice at 10 K”. In: *Astrophys. J. Lett.* 571.2, pp. L173–L176. DOI: 10.1086/341412.

— (June 2002b). “Efficient Formation of Formaldehyde and Methanol by the Addition of Hydrogen Atoms to CO in H2O-CO Ice at 10 K”. In: *Astrophys. J. Lett.* 571.2, pp. L173–L176. DOI: 10.1086/341412.

Watanabe, Naoki, Takahiro Shiraki, and Akira Kouchi (May 2003). “The Dependence of H2CO and CH3OH Formation on the Temperature and Thickness of H2O-CO Ice during the Successive Hydrogenation of CO”. In: *Astrophys. J. Lett.* 588.2, pp. L121–L124. DOI: 10.1086/375634.

Watanabe, Naoki et al. (May 2010). “Direct Measurements of Hydrogen Atom Diffusion and the Spin Temperature of Nascent H2 Molecule on Amorphous Solid Water”. In: *Astrophys. J. Lett.* 714.2, pp. L233–L237. DOI: 10.1088/2041-8205/714/2/L233.

Whittet, D. C. B. (1993). “Observations of Molecular Ices”. In: *Dust and Chemistry in Astronomy*. Ed. by T. J. Millar and D. A. Williams, p. 9.

Whittet, Doug CB (2002). *Dust in the galactic environment*. CRC press.

Wilson, S (1978). “Theoretical study of the thioformyl ion”. In: *The Astrophysical Journal* 220, pp. 739–741.

Woods, Paul M et al. (2013). “Glycolaldehyde formation via the dimerization of the formyl radical”. In: *The Astrophysical Journal* 777.2, p. 90.

Woon, David E (2002a). “Ab initio quantum chemical studies of reactions in astrophysical ices. 4. Reactions in ices involving HCOOH, CH2NH, HCN, HNC, NH3, and H2O”. In: *International journal of quantum chemistry* 88.1, pp. 226–235.

— (2012). “A quantum chemical study of the formation of cyanide (CN-) and acetate (CH3COO-) ions in astrophysical ices via proton transfer from HCN, HNC, or CH3COOH to NH3”. In: *Computational and Theoretical Chemistry* 984, pp. 108–112.

— (Dec. 1999). “Ab Initio Quantum Chemical Studies of Reactions in Astrophysical Ices. 1. Aminolysis, Hydrolysis, and Polymerization in H2CO/NH3/H2O Ices”. In: *Icarus* 142.2, pp. 550–556. DOI: 10.1006/icar.1999.6227.

— (Oct. 2001a). “Ab Initio Quantum Chemical Studies of Reactions in Astrophysical Ices 3. Reactions of HOCH2NH2 Formed in H2CO/NH3/H2O Ices”. In: *Journal of Physical Chemistry A* 105.41, pp. 9478–9481. DOI: 10.1021/jp011830h.

— (Jan. 2001b). “Ab Initio Quantum Chemical Studies of Reactions in Astrophysical Ices. 2. Reactions in H2CO/HCN/HNC/H2O Ices”. In: *Icarus* 149.1, pp. 277–284. DOI: 10.1006/icar.2000.6524.

— (Apr. 2002b). “Modeling Gas-Grain Chemistry with Quantum Chemical Cluster Calculations. I. Heterogeneous Hydrogenation of CO and H2CO on Icy Grain Mantles”. In: *Astrophys. J.* 569.1, pp. 541–548. DOI: 10.1086/339279.

— (June 2002c). “Pathways to Glycine and Other Amino Acids in Ultraviolet-irradiated Astrophysical Ices Determined via Quantum Chemical Modeling”. In: *Astrophys. J. Lett.* 571.2, pp. L177–L180. DOI: 10.1086/341227.

— (Feb. 2011). “Ion-Ice Astrochemistry: Barrierless Low-energy Deposition Pathways to HCOOH, CH3OH, and CO2 on Icy Grain Mantles from Precursor Cations”. In: *Astrophys. J.* 728.1, 44, p. 44. DOI: 10.1088/0004-637X/728/1/44.

Zamirri, Lorenzo et al. (Oct. 2018). “IR spectral fingerprint of carbon monoxide in interstellar water-ice models”. In: *Mon. Not. R. Astron. Soc.* 480.2, pp. 1427–1444. DOI: 10.1093/mnras/sty1927. arXiv: 1807.09494 [astro-ph.GA].

Zamirri, Lorenzo et al. (Aug. 2019). “Quantum Mechanical Investigations on the Formation of Complex Organic Molecules on Interstellar Ice Mantles. Review and Perspectives”. In: *ACS Earth and Space Chemistry* 3.8, pp. 1499–1523. DOI: 10.1021/acsearthspacechem.9b00082.

Zhao, Yan and Donald G Truhlar (2008). “The M06 suite of density functionals for main group thermochemistry, thermochemical kinetics, noncovalent interactions, excited states, and transition elements: two new functionals and systematic testing of four M06-class functionals and 12 other functionals”. In: *Theoretical Chemistry Accounts* 120.1-3, pp. 215–241.

— (Feb.). “Density Functionals with Broad Applicability in Chemistry”. In: *Acc. Chem. Res.* 41.2, pp. 157–167. DOI: 10.1021/ar700111a. URL: https://doi.org/10.1021/ar700111a.

Zhitnikov, R. A. and Yu. A. Dmitriev (May 2002). “Detection of free radicals in low-temperature gas-grain reactions of astrophysical interest”. In: *Astron. Astrophys.* 386, pp. 1129–1138. DOI: 10.1051/0004-6361:20020268.

Appendix

Chapter A
Supporting data for Chapter 5

Outline

A.1 Energetics

Gas phase

Table A.1: *Reaction energies of the C-C coupling and C-H abstraction barrierless reactions of CH_3 + HCO leading to CH_3CHO and CO + CH_4 respectively. Units are in kJ/mol.*

Gas phase	C-C coupling	C-H abstraction
Methods	E_{rx}	E_{rx}
(BS)UM062X	-430.8	-434.2
CASSCF(2,2)	-443.8	-451.9
CASPT2//CASSCF(2,2)	-399.5	-442.0
(BS)UBHLYP	-400.0	-403.9
(BS)UBHLYPD3	-403.0	-404.2
U/RM062X//(BS)UM062X	-664.4	-663.5

Table A.2: *Absolute energies of the C-C coupling and H-abstraction reactions of CH_3 + HCO giving CH_3HCO and CO + CH_4, respectively. Initial structures were built by putting the two radicals 5 Å away with the proper orientation to undergo C-C coupling or C-H abstraction reactions. Energy units are in a.u.*

Method	C-C coupling: CH_3 + HCO $\rightarrow$ CH_3COH	
	initial structure (sp)	CH_3COH
(BS)UM062X	-153.657227412	-153.821295382
CASSCF(2,2)	-152.79226156	-152.9612874
CASPT2//CASSCF(2,2)	-153.22690133	-153.37904434
(BS)UBHLYP	-153.6523389	-153.8046821
(BS)UBHLYPD3	-153.652683711	-153.80618633
U/RM062X//(BS)UM062X	-153.568221141	-153.821294693
Method	C-H abstraction: CH_3 + HCO $\rightarrow$ CH_4 + CO	
	initial structure (sp)	CO + CH_4
(BS)UM062X	-153.657946824	-153.823307135
CASSCF(2,2)	-152.79276915	-152.9648938
CASPT2//CASSCF(2,2)	-153.2277876	-153.39612934
(BS)UBHLYP	-153.652804076	-153.806623321
(BS)UBHLYPD3	-153.653251424	-153.80718911
U/RM062X//(BS)UM062X	-153.570968836	-153.823683981

Table A.3: *Energetics of the gas-phase C-O coupling of CH_3 + HCO. These energy values correspond to the PESs shown in Figure 1 of the manuscript. In order to obtain the single point energies on the triplet optimised energies we performed the optimisations at the corresponding level, which gave energies of: -152.81627741, -153.25105234, -153.670441964 and -153.6718638 a.u. at CASSCF(2,6), CASPT2//CASSCF(2,6), UBHLYP and UBHLYP-D3, respectively; the one for M062X is shown in the table. Cartesian coordinates of all structures can be found in the xyz section of the supporting information (SI) from the publication (here). Energy units are in a.u.*

Methods	C-O coupling: CH_3 + HCO $\rightarrow$ CH_3OCH					
	CH_3	HCO	PRE-R	CO + CH_4	TS	CH3OCH
(BS)UM062X	-39.82416785	-113.85091026	-153.67875153	-153.82368400	-153.66317488	-153.70838127
CASSCF(2,2)	-39.55963911	-113.25478481	-152.81636424	-152.96492461	-152.79429220	-152.83592053
CASPT2//CASSCF(2,2)	-39.69123819	-113.55502863	-153.25064832	-153.38681526	-153.24187342	-153.26590089
(BS)UBHLYP	-39.82904607	-113.84056775	-153.670428225	-153.80658565	-153.64806718	-153.68978117
(BS)UBHLYPD3	-39.82913519	-113.84071570	-153.671802764	-153.80761507	-153.65041271	-153.69127618
U/RM062X//(BS)UM062X	–	–	-153.608835136	-153.823684203	-153.657816312	-153.70838126
m_s=3 UM062X	–	–	-153.678715228	–	-153.657816312	–

In presence of a water molecule

Table A.4: *Absolute energies of the stationary points of the Rc, dHa and wHt reactions between CH_3 and HCO in the presence of a water molecule (W1). Cartesian coordinates of all structures can be found in the xyz section of the SI (here). Energy units are in a.u.*

Methods	Radical-radical coupling (Rc)		
	Reactants	TS	CH_3CHO + W1
(BS)UM062X	-230.114510658	–	-230.260744755
CASSCF(2,2)	-228.92083138	–	-228.99819759
CASPT2//CASSCF(2,2)	-229.48528085	–	-229.62105588
(BS)UBHLYP	-230.09923615	-230.098533436	-230.236562366
(BS)UBHLYPD3	-230.101441018	–	-230.240060042
U/RM062X//(BS)UM062X	-230.038551041	–	-230.260744755
Methods	Direct hydrogen-abstraction (dHa)		
	Reactants	TS	CH_4 + CO + W1
(BS)UM062X	-230.115421123	-230.114491293	-230.255624374
CASSCF(2,2)	-228.85043151	-228.84945529	-229.00215028
CASPT2//CASSCF(2,2)	-229.48687303	-229.4863605	-229.62869576
(BS)UBHLYP	-230.099692832	-230.097494612	-230.231286937
(BS)UBHLYPD3	-230.102986745	-230.101057485	-230.233397667
U/RM062X//(BS)UM062X	-230.038502991	-230.048153135	-230.255624374
Method	Water assisted H-transfer (wHt)		
	Reactants	TS	CH_4 + CO + W1
(BS)UM062X	-230.114782772	-230.092608209	-230.256418756
CASSCF(2,2)	-228.92624436	-228.86776384	-229.00096235
CASPT2//CASSCF(2,2)	-229.48250892	-229.46874458	-229.62795624
(BS)UBHLYP	-230.099449066	-230.071422797	-230.232347227
(BS)UBHLYPD3	-230.101871013	-230.073970512	-230.234810765
U/RM062X//(BS)UM062X	-230.018934144	-230.076076484	-230.256418756

A.2 Input examples:

Broken symmetry example in Gaussian

- Singlet broken symmetry, comments are preceded by an asterisk for the sake of clarity, bear in mind to remove them to use the input as a template. The option `guess=mix` requires HOMO and LUMO orbitals to be mixed so that the initial guess wave function (WF) is broken (spin) symmetry (referred to as BS).

```
%nprocshared=XX
%mem=YYgb
%chk=PATH/TO/CHK
#P CALC_TYPE int=ultrafine
UDFT/BASIS_SET
*empiricaldispersion=gd3    * Add dispersion if wanted
guess=(mix)                 * BS keyoword
stable=opt                  * to ensure actual ground state WF

MESSAGE

0 1
*GEOMETRY GOES HERE
*...
*...

-link1-
MORE CALCULATIONS
...
...
<last line in is empty>
```

OpenMolcas

- CASSCF(2,2) optimisation+freq. Asterisks are comments.

```
&gateway
  COORD=geom.xyz     * geometry
  BASIS=CC-PVDZ      * basis set
  GROUP=NoSymm       * symmetry

»EXPORT MOLCAS_MAXITER=350
»»»»»»» Do while «««««««     * starting OPT loop
&SEWARD
»»»» IF ( ITER = 1 ) «««««     * initialize WF
&SCF                 * HF (default) / DFT
spin=1               * ms, if ms!=1 UHF keyword is needed before spin
»»»>  ENDIF «««««««««««
&RASSCF              * will read HF WF and generate CASSCF(2,2)
  Charge
    0
  Spin
    1                * ms
  Nactel
    2 0 0            * 2 active electrons
  Ras2
    2                * 2 active orbitals
&SLAPAF              * Opt
*   TS               ** TS search, see the manual for more options
```

```
>>>>>>>  ENDDO  <<<<<<<    * end of loop

&MCKINLEY           * freqs
*
* see Mocas manual for more info
* www.molcas.org
*
```

- CASPT2//CASSCF(2,2) single point

```
&gateway
  COORD=geom.xyz
  BASIS=CC-PVDZ
  GROUP=NoSymm

&SEWARD
&SCF
spin=1

&SEWARD
&RASSCF
  Charge
    0
  Spin
    1
  Nactel
    2 0 0
  Ras2
    2

&CASPT2
  MaxIter=  200
```

A.3 CASSCF active space orbital selection example

In this section we wish to explain in an easy way how to choose the correct set of orbitals for a CASSCF(2,2) calculation (i.e. the active space has 2 electrons and 2 orbitals) for a singlet state. To do so we report the orbitals used in a single point calculation with Molcas (see input examples above) for the reactions between CH_3 and HCO to form CH_3CHO, CH_3OCH and CH_4 + HCO, hence the C-C, C-O, C-H bond formation reactions from Figure 1 in the main body text.
In the case of a singlet diradical system one requires the use an active space formed at least by two molecular orbitals (MOs) and two electrons, as one is concerned about the two unpaired electrons coming each from one of the radicals.
The process internally followed by OpenMolcas to generate a CASSCF(2,2) wave-function can be outlined as: (i) generate a set of initial guess orbitals (the *SEWARD* program takes care of this), (ii) use these guess orbitals as an input to the *SFC* program where a Hartree-Fock calculation generates a new set of orbitals, (iii) these new orbitals are the input for the *RAS2* program where the CASSCF(2,2) calculation is performed, which generates the last set of orbitals, this time with enough static correlation so as to better describe the singlet diradical. Hence, before running any optimisation or TS search... one must check that the guess, SCF and final CASSCF orbitals are chemically sound. The singlet CH_3 + HCO system has 24 electrons. In a closed-shell wave-function these would be allocated by pairs in 12 MOs. However, this would actually be a wrong description of the system, as diradicals are open-shell systems, i.e. there are orbitals containing unpaired electrons. These unpaired electrons will occupy two different orbitals and should be the two occupied orbitals with highest energy, i.e. instead of 12 doubly occupied MOs there shall be 11 doubly

and 2 singly occupied orbitals (13 in total). Hence, the orbitals of the active space will be the 12th and 13th orbitals from the *SCF* calculation, which are the so-called highest occupied and lowest unoccupied MOs (HOMO and LUMO, respectively) if they fullfil the following conditions.
The guess orbitals should spatially resemble the singly occupied MOs (SOMOs) of each radical so that after going though the SCF program they will spatially be similar to the bonding (σ) and anti-bonding ($\sigma*$) orbitals of the C-X bond to be formed (X=H,C,O from HCO), but with the wrong occupancy (the SCF gives a closed shell solution, and hence it will provide 12 doubly occupied orbitals). In the last step, the RAS2 calculation will take the HOMO and LUMO orbitals from the SCF calculation and use them as the active space, which will yield the acutal σ and $\sigma*$ orbitals. A representation of the concepts presented in the last few lines can be seen in in Figure A.1.

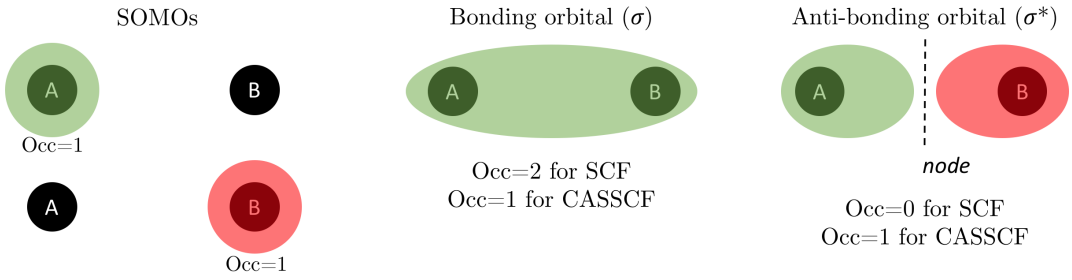

Figure A.1: *Simplistic representation of the SOMOs, bonding and anti-bonding orbitals in dummy systems represented by 2 radicals, A and B. We also report the expected occupancies for the bonding and anti-bonding orbitals depending on the method. Different colors represent different a phase of the MO.*

Having in mind the internal processes followed by Molcas and the expected MOs, we report the initial orbitals for: the initial structures leading to (i) C-C bond formation (producing CH_3CHO) and (ii) C-H bond formation (producing CH_4 + CO) and the transition state structure for the (iii) C-O bond formation (producing the CH_3OCH carbene-ether). For the two first cases (Figures A.2 and A.3), it is clear from our simplistic example above (Figure A.1) that the selection of the orbitals is good. For the last case (Figure A.4), the guess HOMO/LUMO already have a bit of $\sigma/\sigma*$ character which becomes stronger for the SCF ones. The CASSCF orbitals have the (qualitatively) the same shape as the SCF ones but now the occupancy changes and since it is a TS towards the C-O bond formation we can see that the σ orbital is more populated than the $\sigma*$.

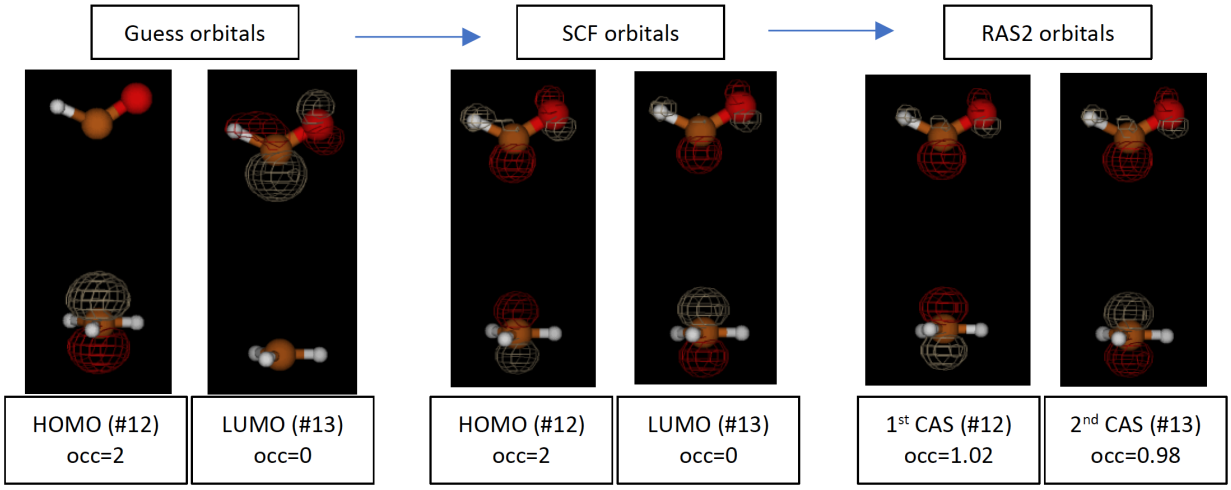

Figure A.2: *First orbitals for the C-C bond formation case.*

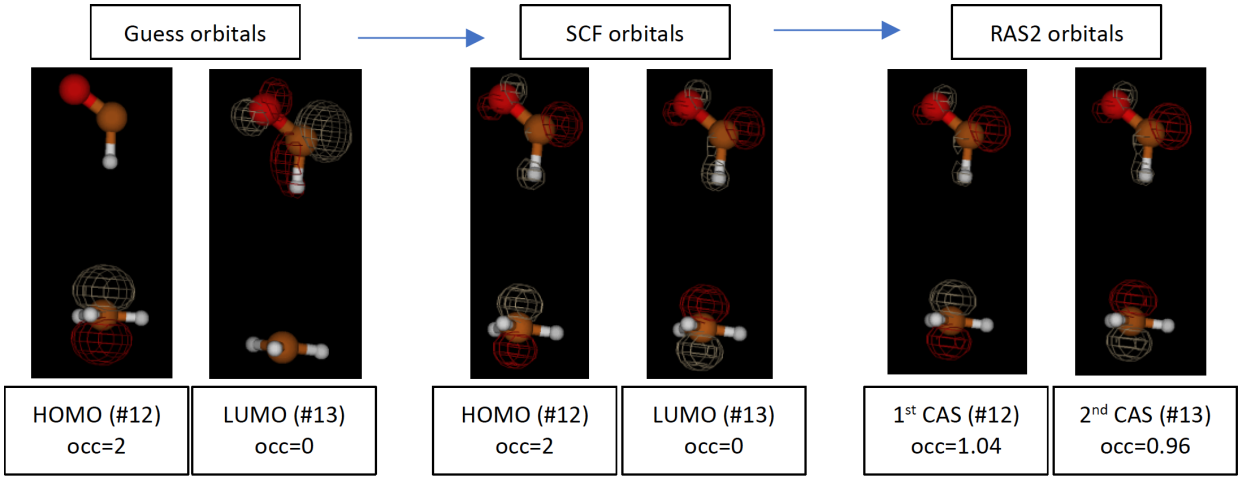

Figure A.3: *First orbitals for the C-H bond formation case.*

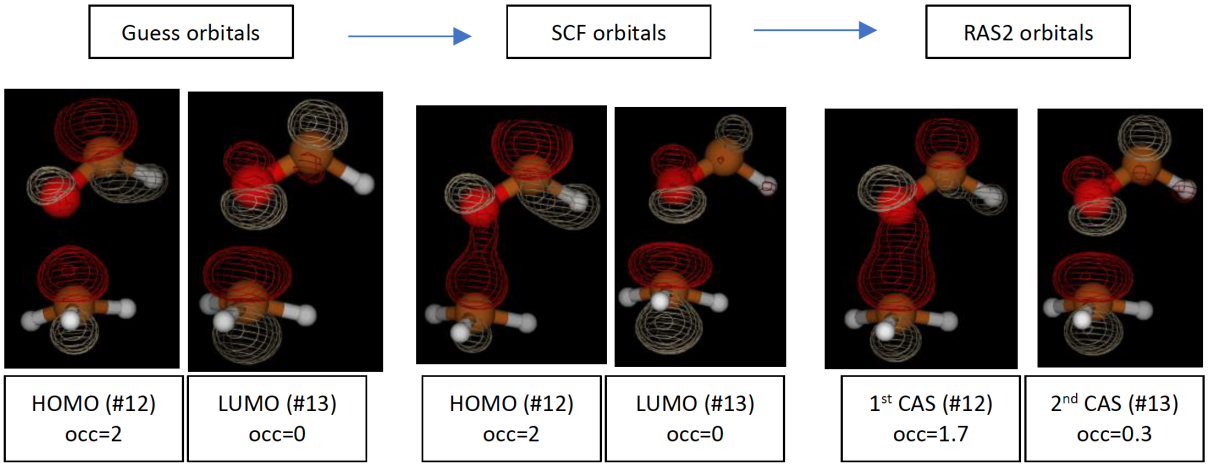

Figure A.4: *First orbitals for the C-O bond formation transition state.*

Chapter B
Supporting data for Chapter 6

Outline

B.1 Benchmark binding and activation energy geometries:

These geometries were optimised at B3LYP-D3/6-311++G(2df,2pd) level. Figure B.1 shows the structures used for the benchmark of interaction energies on 1 and 2 water molecules (Table 1 of main body). Figures B.2 and B.3 show the optimised structures used for the activation energy benchmark for HCO/CH_3 and HCO/NH_2, respectively, on 1 and 2 water molecules.

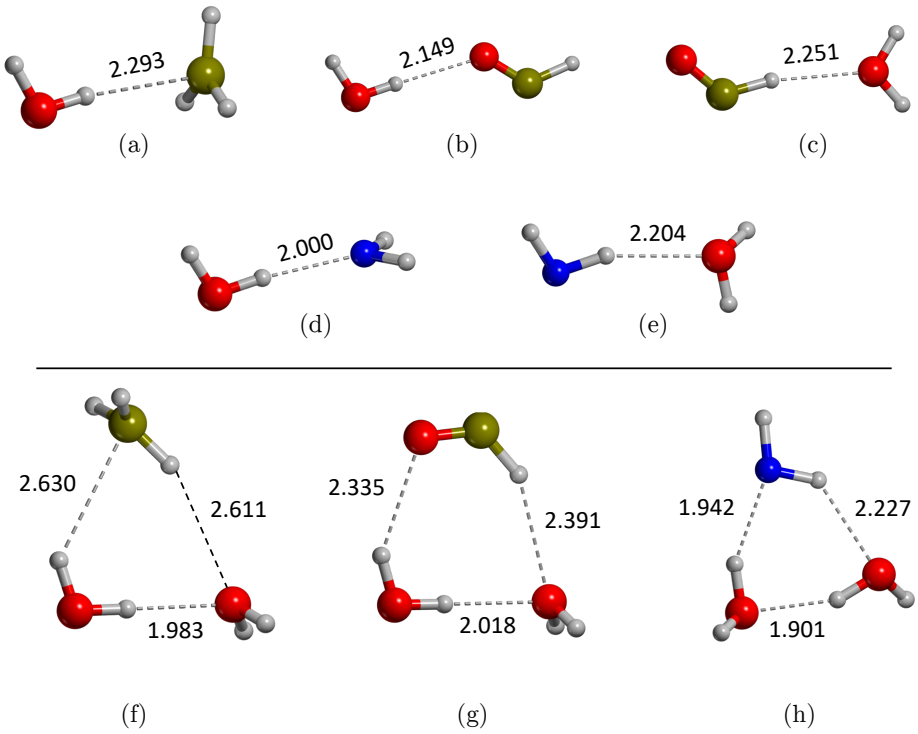

Figure B.1: *B3LYP-D3/6-311++G(2df,2pd)-optimised structures of each of the three radicals studied in this work (CH_3, NH_2 and HCO) interacting with 1, (a)-(e), and 2, (f)-(h), water molecules. Distances in Å.*

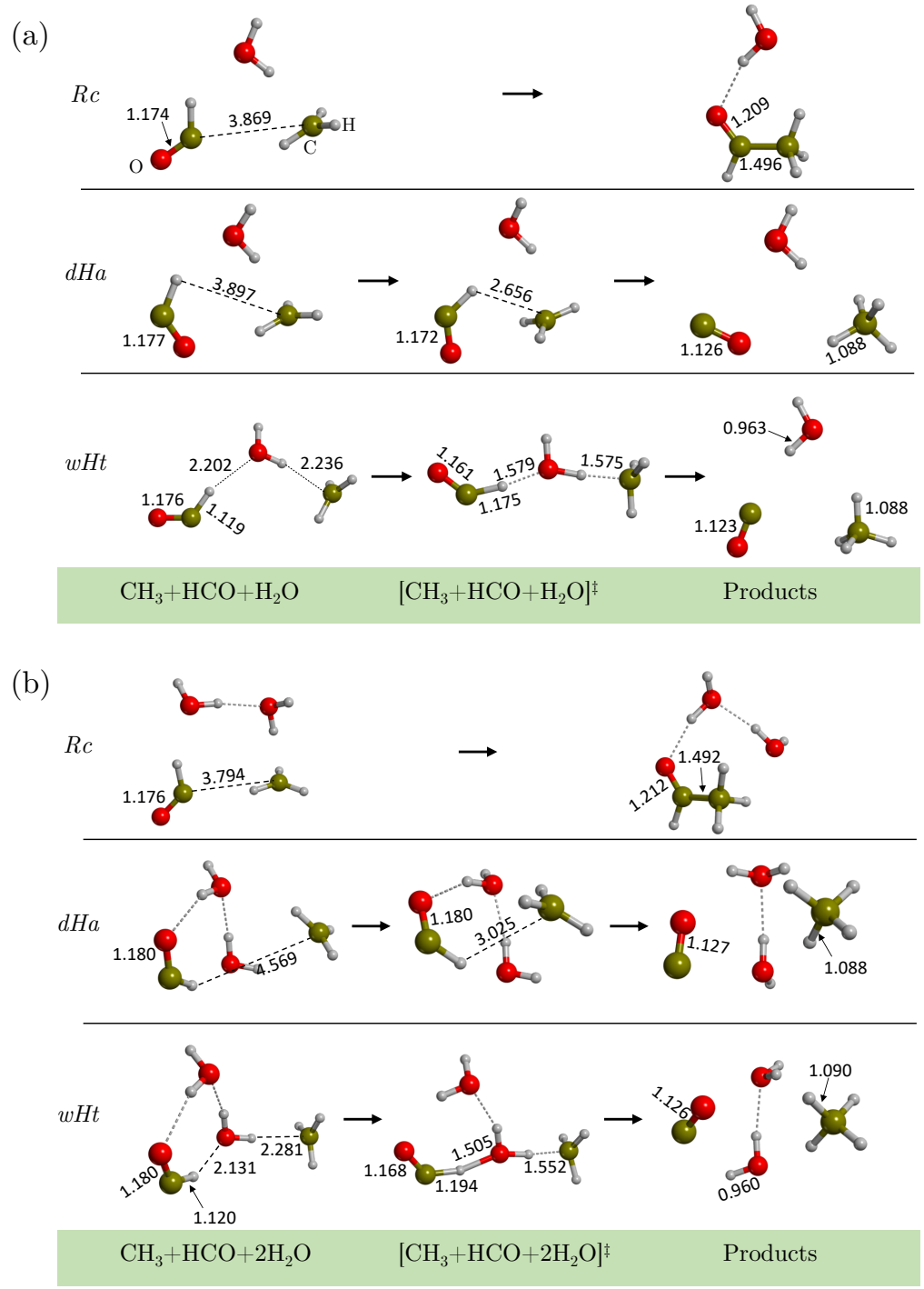

Figure B.2: *B3LYP-D3/6-311++G(2df,2pd)-optimized geometries of the stationary points for reactions between CH_3 and HCO in presence of (a) a single water molecule and (b) two water molecules. Distances are in Å.*

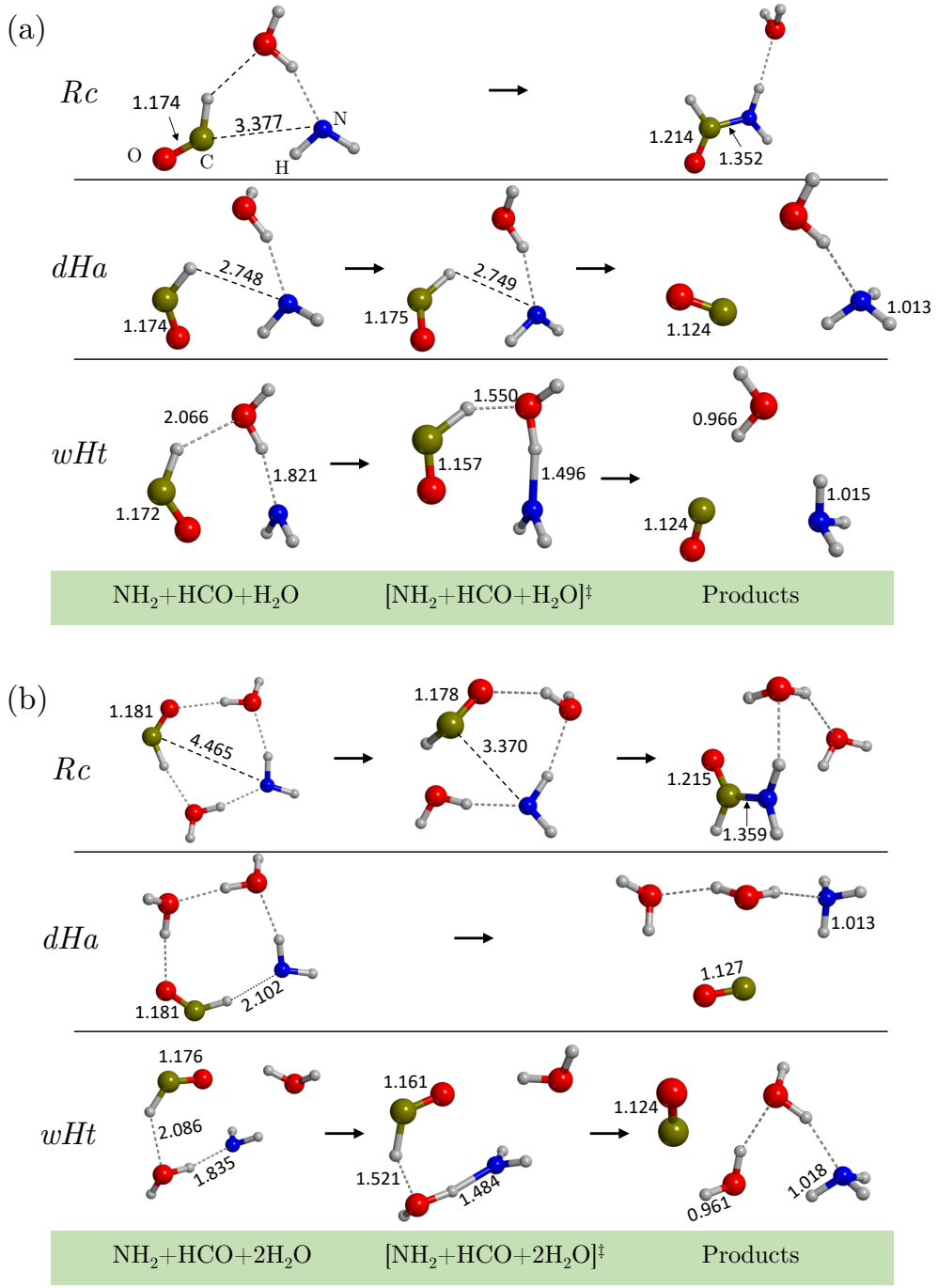

Figure B.3: *B3LYP-D3/6-311++G(2df,2pd)-optimized geometries of the stationary points for reactions between NH_2 and HCO in presence of (a) a single water molecule and (b) two water molecules. Distances are in Å.*

B.2 Benchmark binding and activation energy errors:

Figure B.4 shows the percentage relative errors of the binding energies shown in Table 6.1 of the main body with respect to CCSD(T) level of theory. Figure B.5 and B.6 contains the deviations of *Rc* and *dHa* activation energies and the percentage relative errors of *wHt* reactions, respectively, of the methods listed in Table 6.2 of the main body with respect to the reference values.

One can see that, for *Rc* and dHa, the best performances compared to CASPT2 are provided by B3LYP-D3 and BHLYP-D2, followed by BHLYP-D3. The worst results are given by pure BHLYP (without the inclusion of any dispersion correction term). On the other hand, however, B3LYP-D3 underestimates dramatically *wHt* energy barriers, presenting errors of about $\sim$ 40-78%, while BHLYP-based methods tend to moderately overestimate them, by $\sim$ 1-25%, BHLYP-D2 and BHLYP-D3 presenting similar results. Regarding CCSD(T), we can see that it performs similarly to the BHLYP-based methods, also presenting moderate energy barrier deviations compared to the CASPT2 values.

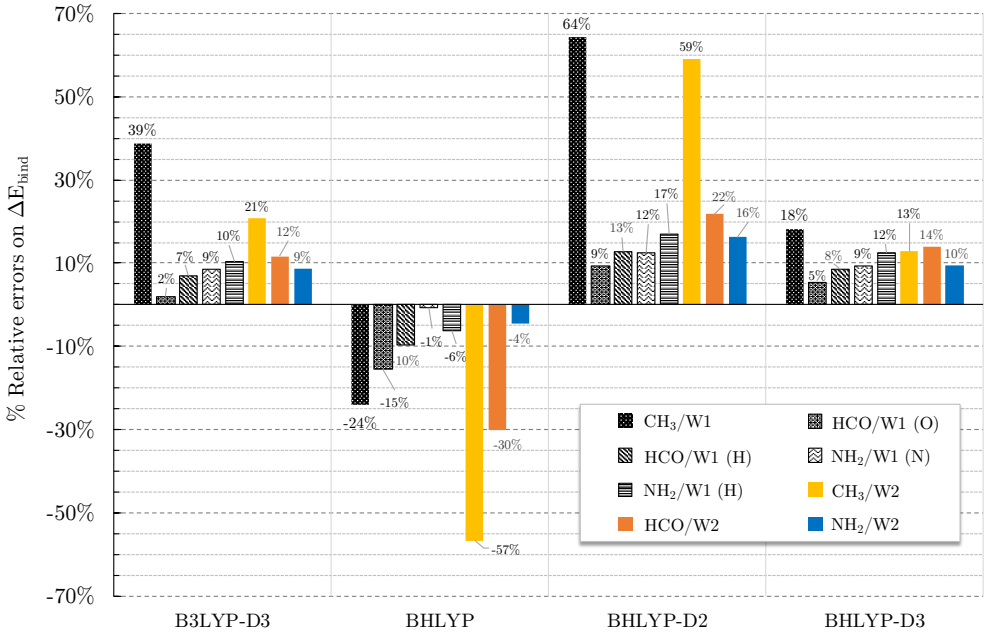

Figure B.4: *Percentage relative errors on the binding energies calculated at DFT level (Table 1 of main text) relative to CCSD(T) as reference.*

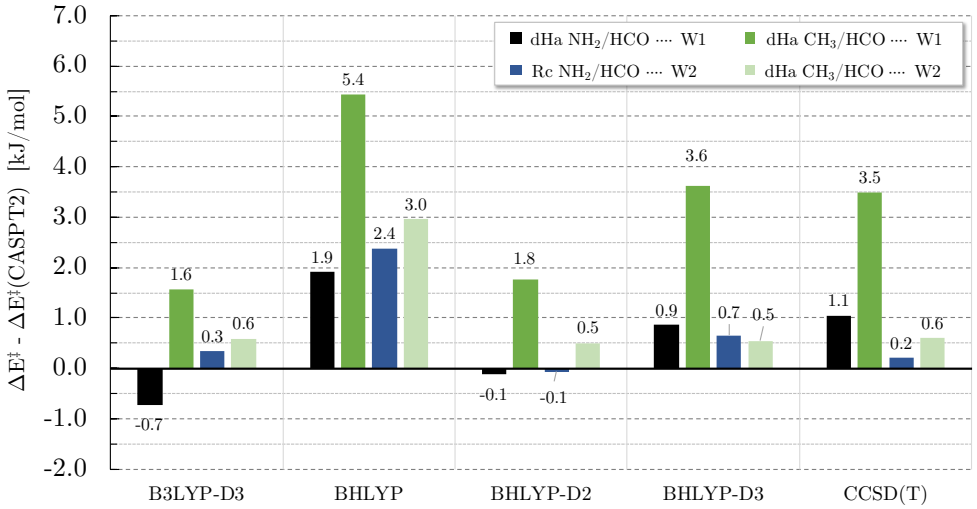

Figure B.5: *Differences between the energy energies calculated at DFT and CCSD(T) levels with respect to CASPT2 for Rc and dHa reactions (Table 2 of main text).*

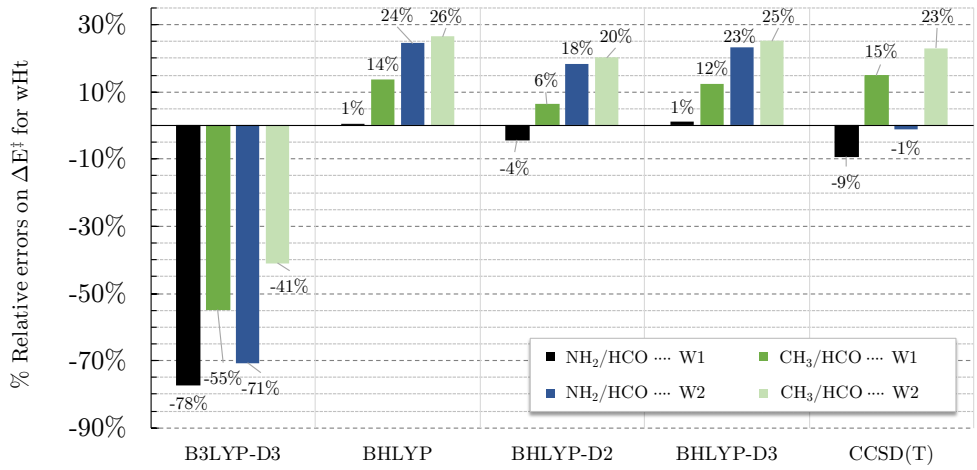

Figure B.6: *Percentage relative errors on the energy barriers calculated at DFT and CCSD(T) levels with respect to CASPT2 (Table 2 of main text).*

B.3 Binding energies at BHLYP-D2 and B3LYP-D3

Table B.1 contains the binding energies computed at BHLYP-D2 (on W18 and W33-side, W33-cav) and B3LYP-D3 (only on W18). The energy values were corrected for BSSE and ZPE.

Table B.1: *BSSE-corrected and ZPE-corrected binding energies of HCO, CH_3 and NH_2 on the W18 and W33 clusters at B3LYP-D3 and BHLYP-D2. Units are in kJ/mol.*

	W18 (B3LYP-D3)	W18 (BHLYP-D2)	W33-side (BHLYP-D2)	W33-cav (BHLYP-D2)
CH_3	7.5	8.7	5.8	10.2
HCO	12.8	16.8	17.4	22.5
NH_2	24.9	36.9	24.2	36.3

B.4 Water assisted H transfers at BHLYP-D3 on W18 and W33-cav

Figures B.7, B.8 and B.9 show the *wHt* PESs computed at BHLYP-D3 of HCO + CH_3 and HCO + NH_2 on W18, HCO + CH_3 on W33-cav and HCO + NH_2 on W33-cav, respectively. A main difference with respect to those with W1 and W2 (Figures B.2, B.3) is that, in general, they occur via a two-step process on W18 and W33-cav. In the first step, the CH_3/NH_2 radicals, which act as H-bond acceptors, receive a H atom from the water cluster, forming and intermediate species in which CH_4/NH_3 coexist with an OH radical of the ice surface. In the second step, the HCO transfers its H atom to the ice so that the OH transforms into H_2O, forming finally CO. In relation to the *wHt* HCO + NH_2 on W33-cav reaction (Figure B.9), in a previous work by us [23], we identified a path in which four water molecules assisted the H transfer with an energy barrier of 35.3 kJ/mol at BHLYP/6-311++G(d,p). The same path has been elucidated in this work (not shown here for the sake of clarity) with an energy barrier of $\sim$ 75 kJ/mol. In addition to the difference among the employed basis sets, the main reason for the energy barrier difference is essentially the inclusion of the dispersion forces, which were omitted in Rimola et al. [23]. Indeed, dispersion forces largely stabilize the binding of the radical species with the ice surface, which in this case is enhanced due to the cavity, and hence the energy barrier increase in the present work. additionally a path with a single step was found for HCO + NH_2 on W33-cav (Path A in Figure B.9).

The cavity structure does not influence the energy barriers significantly, when compared to W18, as the energy barriers are still very high (80-95 kJ/mol on W18 and 70-80 kJ/mol on W33-cav).

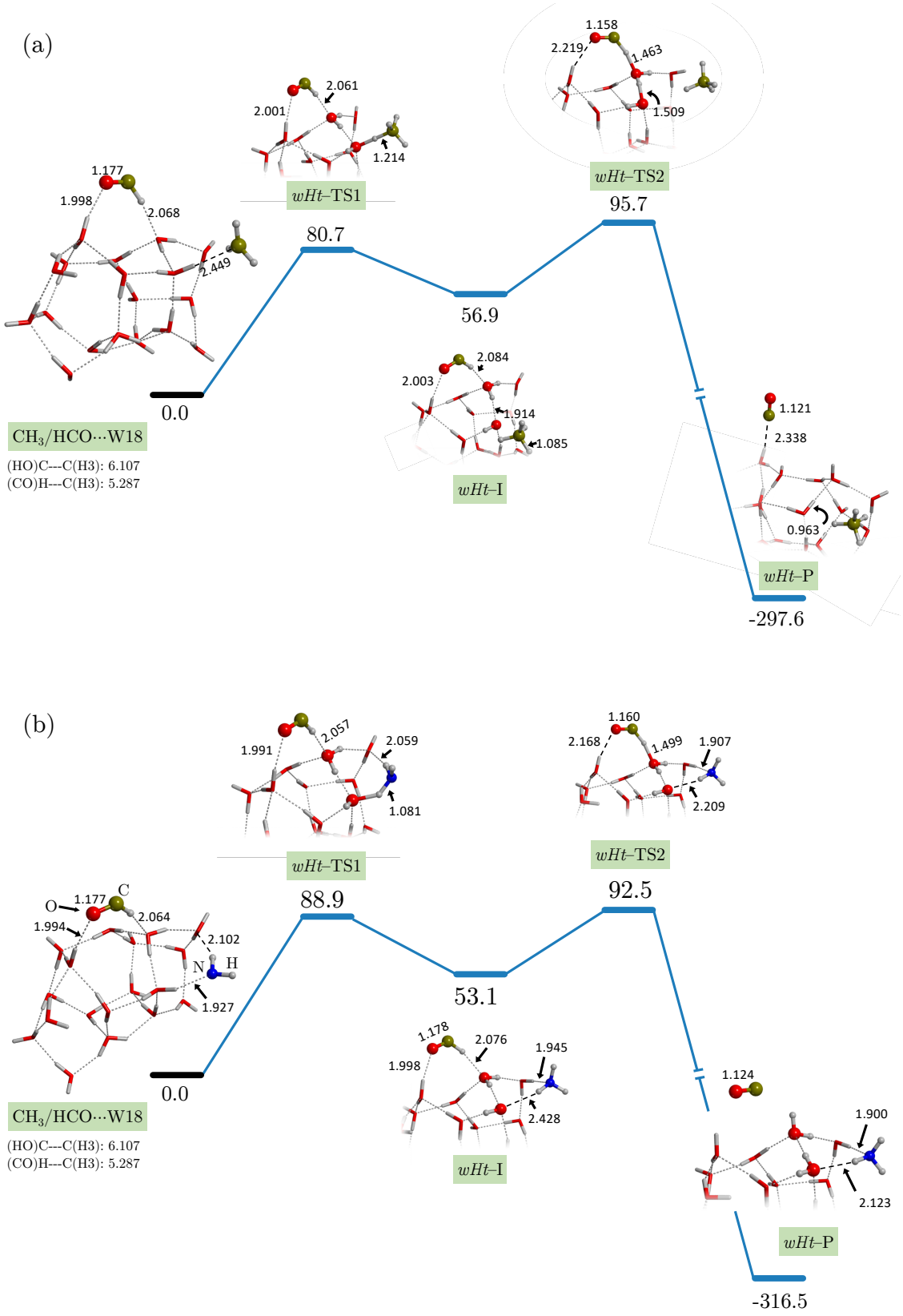

Figure B.7: *ZPE-corrected PESs for the wHt process at BHLYP-D3 of (a) CH_3 + HCO and (b) NH_2 + HCO on W18. Energy units are in kJ/mol and distances in Å.*

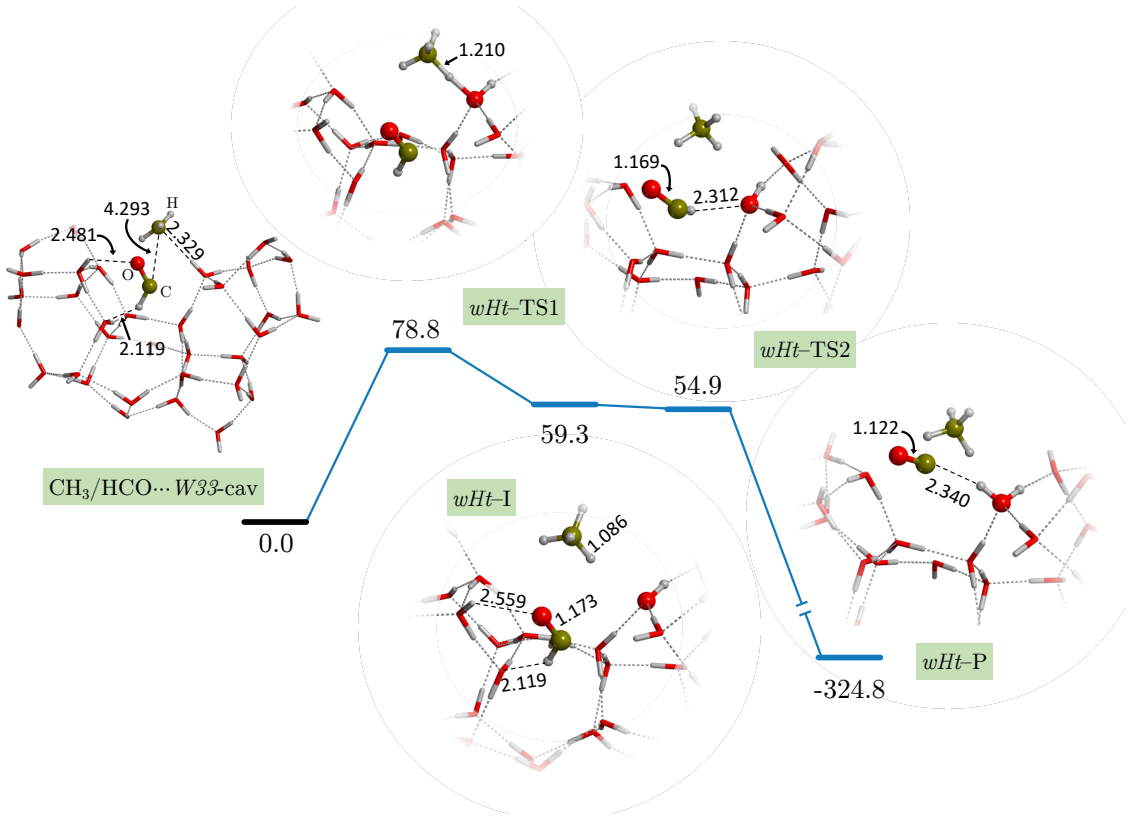

Figure B.8: *ZPE-corrected PES for the wHt process at BHLYP-D3 of HCO + CH_3 on W33-cav system. Energy units are in kJ/mol and distances in Å. wHt-TS2 lies below wHt-I due to the ZPE correction.*

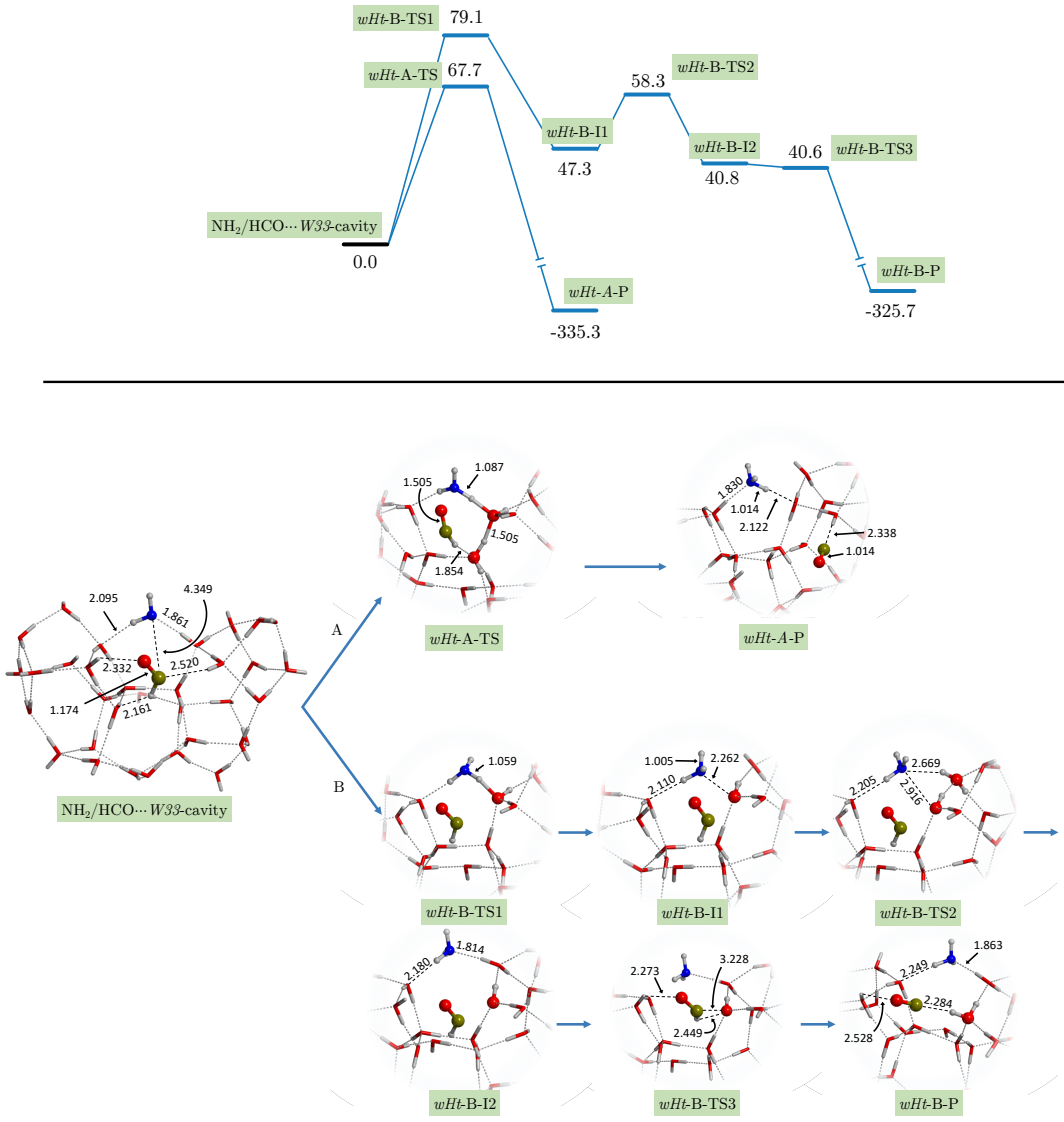

Figure B.9: *ZPE-corrected PES for the wHt process at BHLYP-D3 of HCO + NH_2 on W33-cav system. Energy units are in kJ/mol and distances in Å. wHt-B-TS3 lies below wHt-B-I2 due to the ZPE correction.*

B.5 Reactivity on W18 at B3LYP-D3

Figure B.10 shows the Rc, *dHa* and *wHt* PESs computed at B3LYP-D3 on W18 of both HCO + CH_3 and HCO + NH_2.

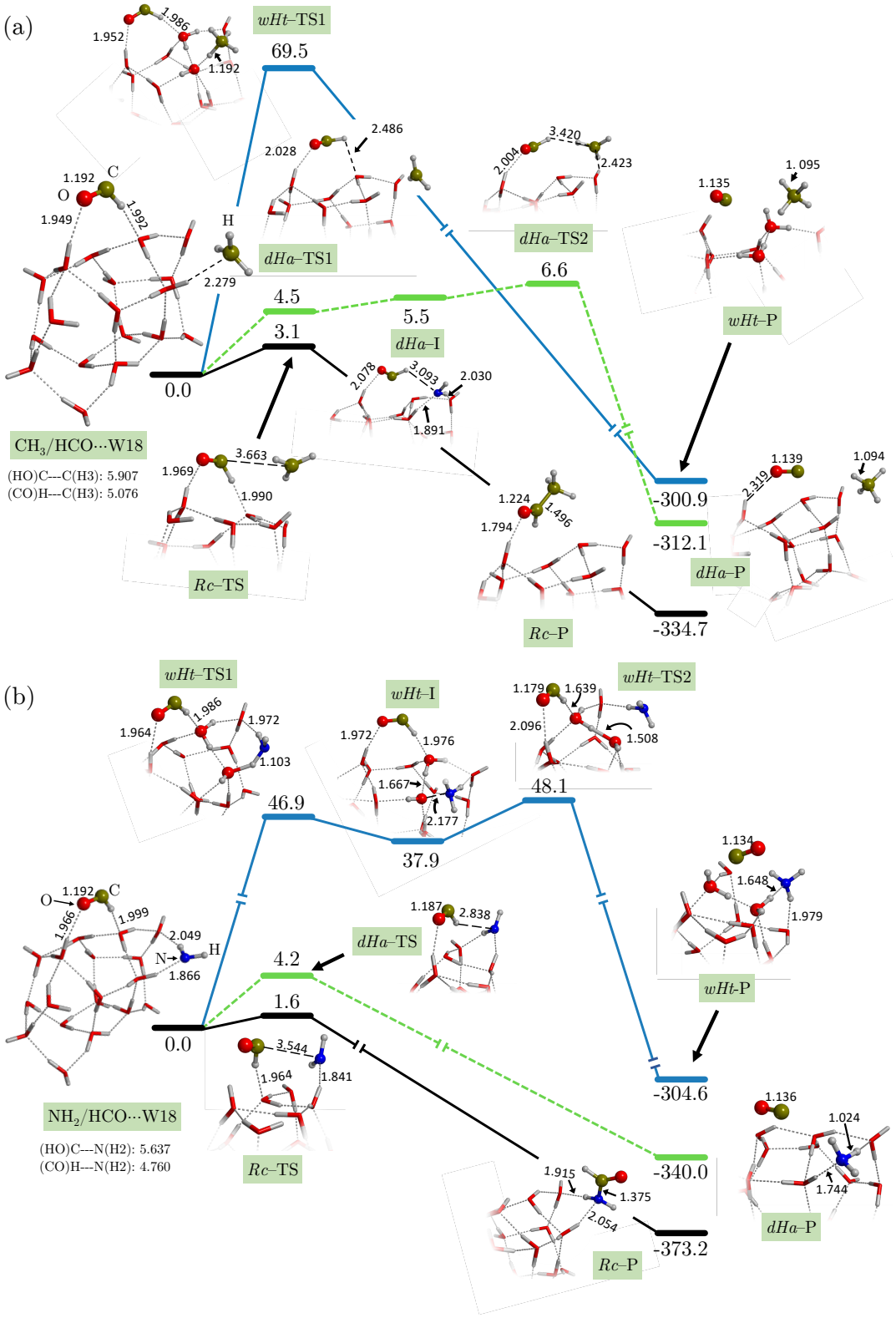

Figure B.10: *ZPE-corrected PESs on W18 at B3LYP-D3 level of (a) the HCO + CH_3 and (b) HCO + NH_2. Solid black lines correspond to radical coupling (Rc) reactions, dashed green lines to direct hydrogen abstraction (dHa) reactions and solid blue lines to water assisted hydrogen transfer (wHt) reactions. Energy units are in kJ/mol and distances in Å. For CH_3 + HCO, the transition state dHa-TS1 lies below dHa-I due to the ZPE energy correction.*

B.6 Reactivity on W18, W33-side and W33-cav at BHLYP-D2

Table B.2 and shows the PESs values of *Rc dHa* on W18, W33-side W33-cav and Table B.3 those for *wHt* on W18 and W33-cav for both, HCO + CH_3 and HCO + NH_2.

Table B.2: *BHLYP-D2 PESs values for the Rc and dHa reactions on W18, W33-side and W33-cav of both HCO + CH_3 and HCO + NH_2. Energy units are kJ/mol.*

	W18		w33-side		w33-cav	
	HCO/CH_3	HCO/NH_2	HCO/CH_3	HCO/NH_2	HCO/CH_3	HCO/NH_2
React	0.0	0.0	0.0	0.0	0.0	0.0
Rc-TS	-7.2	6.1	-0.8	3.3	6.0	1.9
Rc-P	-334.6	-365.3	-326.3	-386.3	-318.9	-388.5
dHa-TS1	-1.1	3.8	-0.7	4.4	7.8	0.8
dHa-I	-0.4					
dHa-TS2	2.5					
dHa-P	-319.6	-333.5	-310.0	-331.5	-314.8	-388.5

Table B.3: *BHLYP-D2 PESs values for wHt reactions on W18 and W33-cav of both HCO + CH_3 and HCO + NH_2. Energy units are kJ/mol.*

	W18		w33-cav		
	HCO/CH_3	HCO/NH_2	HCO/CH_3	HCO/NH_2	
React	0.00	0.00	0.00	React	0.00
wHt-TS1	75.90	88.80	79.20	*wHt*-A-TS1	63.1
wHt-I	55.80	54.10	61.90	*wHt*-A-P	-337.6
wHt-TS2	95.70	91.70	57.10	*wHt*-B-TS1	79.4
wHt-P	-313.10	-317.60	-323.50	*wHt*-B-I1	48.6
				wHt-B-TS2	60.2
				wHt-B-I2	43.4
				wHt-B-TS3	42.9
				wHt-B-P	-325.4

Chapter C
Supporting data for Chapter 7

Outline

C.1 Radical–water interactions

In order to trace the origin of CH_2OH and CH_3O binding energies we have run optimisations at BHLYP-D3-BJ/6-311++G(2df,2pd) level and single point calculations at CCSD(T)/aug-cc-pVTZ level, similarly to what we did for CH_3, HCO and NH_2 in Joan Enrique-Romero et al., 2019. For the three latter, the main differences are the bond distances (due to the change of DFT method) with minor changes in the interaction energies, smaller than 1 kJ mol^{-1} (comparing the new values to those computed at BHLYP-D3/6-311++G(2df,2pd)//B3LYP-D3/6-311++G(2df,2pd) level) and the NH–H$\cdots$$OH_2$ geometry from Joan Enrique-Romero et al., 2019 evolves into the $NH_2\cdots H_2O$ case shown in Figure C.1(d) during optimization. Regarding the two new radicals, CH_3O mainly interacts with the water molecules via a strong H-bond on its O atom while CH_2OH can interact *via* two strong H-bonds on the –OH group, one as an H-donor and another as H-acceptor. The resulting geometries and energetics are shown in Figure C.1. It is worth mentioning that different initial radical-water orientations were tried for CH_3O and CH2OH, which, after optimisation converged to the ones in Figure C.1. All in all, the differences between DFT and CCSD(T) values ie below 2.2 kJ mol^{-1}, corresponding to the $NH_2\cdots H_2O$ case (Figure C.1(d)).

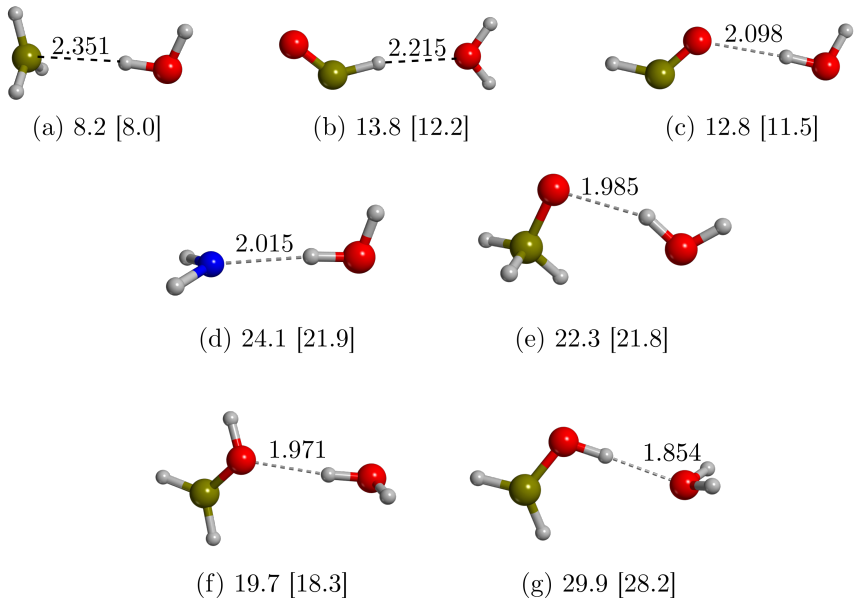

(a) 8.2 [8.0] (b) 13.8 [12.2] (c) 12.8 [11.5]

(d) 24.1 [21.9] (e) 22.3 [21.8]

(f) 19.7 [18.3] (g) 29.9 [28.2]

Figure C.1: *ZPE- and BSSE- non-corrected binding energies of CH_3 (a), HCO (b,c), NH_2 (d), CH_3O (e) and CH_2OH (f,g) with a single water molecule at BHLYP-D3(BJ)/6-311++G(2df,2pd) and CCSD(T)/aug-cc-pVTZ//BHLYP-D3(BJ)/6-311++G(2df,2pd) in brackets. Distances in Å.*

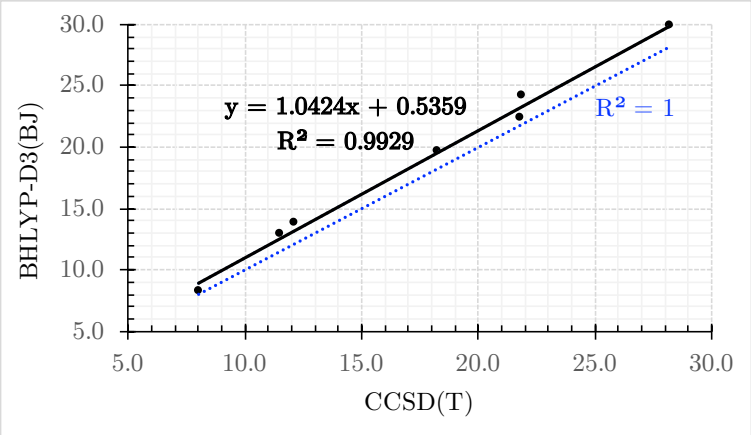

Figure C.2: *Correlation between ZPE- and BSSE- non-corrected binding energies of the radicals in Figure C.1 BHLYP-D3(BJ)/6-311++G(2df,2pd) and CCSD(T)/aug-cc-pVTZ//BHLYP-D3(BJ)/6-311++G(2df,2pd) (black-filled points) with their trend line, and for the sake of comparison, the line corresponding to a perfect correlation with CCSD(T) data.*

C.2 Adsorption geometries on W18

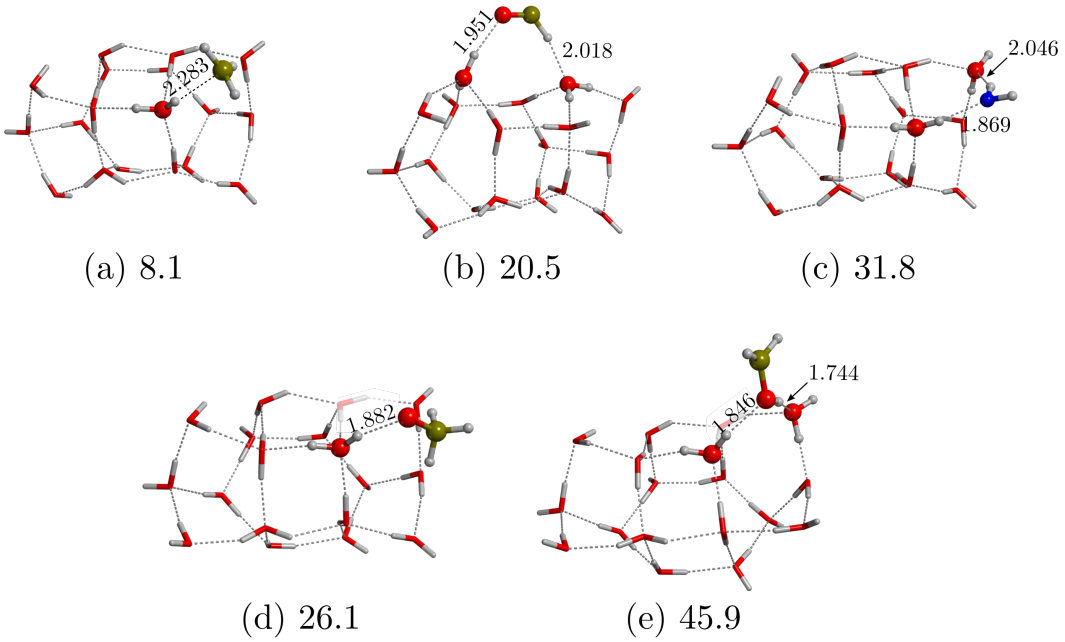

Figure C.3: *Geometries of the five studied radicals, CH_3 (a), HCO (b), NH_2 (c), CH_3O (d) and CH_2H (e); adsorbed on W18 fully optimized at the UBHLYP-D3(BJ)/6-31+G(d,p) theory level. Energy values in kJ mol^{-1} are those refined at UBHLYP-D3(BJ)/6-311++G(2df,2pd) level with the ZPE- (at 6-31+G(d,p) level) and BSSE- corrections. Distances in Å.*

C.3 Adsorption geometries of NH and OH on W18 and W33

We have calculated the binding energies (BE) of NH (ground triplet electronic state) and OH (doublet electronic state) radicals following the same methodology as for the other radicals in this works. As it can be seen from Figure C.4, we find again that the BE on the W18 amorphous solid water (ASW) ice model, 13.0 and 24.2 kJ mol^{-1} for NH and OH, are roughly half those on the cavity of W33, 32.5 and 44.7 kJ mol^{-1} for NH and OH. This values are in good agreement with those in the literature. There are several works reporting the BE for OH on water surfaces: Sameera et al., 2017 report a range of BEs in between 19.3 and 64.6 kJ mol^{-1} on top of a crystalline ice structure, V. Wakelam et al., 2017 recommend a value of 38.2 kJ mol^{-1} for astrochemical models and, most recently, Ferrero et al., 2020 report a range in between 12.9 and 44.2 kJ mol^{-1} on amorphous water ice. On the other hand, for NH V. Wakelam et al., 2017 recommends a value of 21.6 kJ mol^{-1}, which lies in between the values we report for this nitrene. On the other hand, Martıínez-Bachs et al., 2020 reported a binding energy of 35.1 kJ mol^{-1} on top of a crystalline water ice surface. On top of an ASW ice surface, the BE cover a wider range, from $\sim$ 11 to 45 kJ mol^{-1} (private communication), centered at around 20 kJ mol^{-1}, so that our BE values are well within the limits and close to this central value.

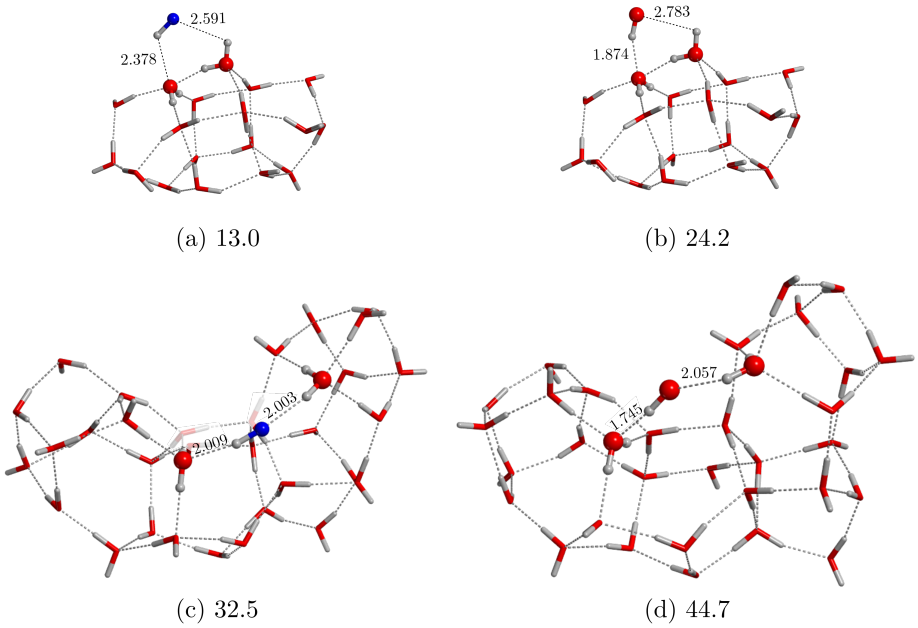

(a) 13.0 (b) 24.2

(c) 32.5 (d) 44.7

Figure C.4: *Geometries of NH (in its ground triplet electronic state) and OH (doublet electronic state) on W18 (a, b) and on the cavity of W33 (c, d). These geometries were fully optimized at the UBHLYP-D3(BJ)/6-31+G(d,p) theory level. Energy values in kJ mol^{-1} are those refined at UBHLYP-D3(BJ)/6-311++G(2df,2pd) level with the ZPE- (at 6-31+G(d,p) level) and BSSE- corrections. Distances in Å.*

C.4 Components of the binding energies

Here we report the components of the BEs. We recall that we define $\Delta E_{bind} = -\Delta E_{ads}$.

Table C.1: *Components of the adsorption energies energies. U are pure DFT energies, D are dispersion corrections, ZPE are zero point energies, BSSE are the basis set superposition error energies.Energy units are kJ mol^{-1}.*

W18	ΔU_{ads}	ΔD_{ads}	ΔZPE	BSSE
CH_3	-9.5	-6.7	7.3	0.8
HCO	-26.1	-2.8	6.2	2.3
NH_2	-40.0	-7.2	13.2	2.2
CH_3O	-26.8	-8.4	6.6	2.4
CH_2OH	-50.1	-7.0	8.0	3.2
NH	-14.5	-4.0	4.4	1.1
OH	-28.7	-3.7	6.0	2.2

W33-cav	ΔU_{ads}	ΔD_{ads}	ΔZPE	BSSE
CH_3	-15.3	-0.5	0.5	1.1
HCO	-28.6	-5.0	1.7	2.4
NH_2	-51.3	-2.8	7.0	2.7
CH_3O	-35.8	-14.9	8.9	3.7
CH_2OH	-38.6	-26.3	9.3	4.4
NH	-35.5	-10.3	10.8	2.5
OH	-49.3	-10.1	11.4	3.4

C.5 Radical-radical reaction energetics

Table C.2: *Energetics of the investigated radical-radical reactions on W18. DFT and dispersion energies were calculated at BHLYP-D3(BJ)/6-311++G(2df,2pd), while ZPE corrections were calculated at BHLYP-D3(BJ)/6-31+G(d,p) level. Column number 2 indicates the reaction type, and for dHa wether it is case 1 (dHa1) or 2 (dHa2). Some reactions have more than one step, as indicated by column number 3 (Step #). Energy units in kJ mol^{-1}.*

X + Y···W18	RX	Step #	$\Delta H^{\ddagger}$	ΔH_{rx}
CH_2OH + CH_2OH	Rc		4.4	-288.7
	dHa1		39.1	-223.7
	dHa2	1	20.6	14.9
	dHa2	2	27.6	-226.3
CH_3O + CH_3O	Rc		10.3	-64.1
	dHa1		15.9	-312.5
	dHa2		18.2	-296.0
CH_3 + CH_2OH	Rc		1.9	-320.4
	dHa1		23.9	24.2
	dHa2		32.2	-255.1
CH_3 + CH_3	Rc		-0.1	-333.4
CH_3 + CH_3O	Rc		0.2	-299.5
	dHa		1.0	-302.7
CH_3 + NH_2	Rc		1.6	-316.8
HCO + CH_2OH	Rc		1.6	-286.2
	dHa1		-0.6	-290.2
	dHa2		30.7	-182.9
HCO + CH_3O	Rc		5.1	-358.5
	dHa1		3.2	-323.4
	dHa2		9.6	-246.3
HCO + HCO	Rc		4.0	-260.3
	dHa1		2.7	-272.7
	dHa2		8.3	-273.3

Table C.3: *Energetics of the investigated radical-radical reactions on W33. DFT and dispersion energies were calculated at BHLYP-D3(BJ)/6-311++G(2df,2pd), while ZPE corrections were calculated at BHLYP-D3(BJ)/6-31+G(d,p) level. Column number 2 indicates the reaction type, and for dHa wether it is case 1 (dHa1) or 2 (dHa2). Some reactions have more than one step, as indicated by column number 3 (Step #). Energy units in kJ mol^{-1}.*

X + Y···W33	RX	Step #	$\Delta H^{\ddagger}$	ΔH_{rx}
CH_2OH + CH_2OH	Rc		2.6	-299.5
	dHa1	1	1.4	-10.2
	dHa1	2	11.6	7.2
	dHa1	3	9.1	8.0
	dHa1	4	24.9	25.4
	dHa1	5	29.1	-218.3
	dHa2	1	9.0	-0.7
	dHa2	2	7.4	-245.8
CH_3O + CH_3O	Rc		20.1	-58.3
	dHa1		11.7	-292.3
	dHa2		21.2	-298.6
CH_3 + CH_2OH	Rc	1	2.5	0.5
	Rc	2	0.4	-310.0
	dHa		39.0	-258.5
CH_3 + CH_3	Rc		4.6	-323.6
CH_3 + CH_3O	Rc		3.1	-290.1
	dHa		9.5	-301.9
CH_3 + NH_2	Rc		0.4	-319.2
HCO + CH_2OH	Rc		1.7	-288.6
	dHa1		0.8	-295.8
	dHa2	1	10.2	10.4
	dHa2	2	18.4	-228.6
HCO + CH_3O	Rc		3.5	-351.6
	dHa1	1	-0.5	0.4
	dHa1	2	2.0	-322.2
	dHa2		13.2	-242.4
HCO + HCO	Rc		4.1	-268.0
	dHa1		4.0	-279.5

C.6 W18 and W33 transition state energetics

Table C.4: *Data of the transition states found on the W18 cluster model at BHLYP-D3(BJ)/6-31+G(d,p) level. Pure DFT energies were refined at BHLYP-D3(BJ)/6-311++G(2df,2pd) level (TZ). U, D and ZPE stand for pure DFT, dispersion and zero point (vibrational) energies, H is the combination of them three (i.e. enthalpies at zero Kelvin).* T_c *is the tunneling crossover temperature. Column number 2 indicates the reaction type, and for dHa wether it is case 1 (dHa1) or 2 (dHa2). Some reactions have more than one step, as indicated by column number 3 (Step #). Energies kJ mol*$^{-1}$*.*

			ΔE_{TS}								
X/Y$\cdots$W18	RX	TS #	ΔU	ΔD	$\Delta U + D$	ΔZPE	ΔH	iν (cm^{-1})	ΔU (TZ)	ΔH (TZ)	T_c (K)
CH_2OH + CH_2OH	Rc		9.1	-4.8	4.3	0.3	**4.6**	-82.50	8.9	**4.4**	–
	dHa1		61.9	-7.7	54.2	-14.4	**39.8**	-1837.06	61.1	**39.1**	448.5
	dHa2	1	25.5	-0.8	24.7	-2.2	**22.5**	-60.69	23.6	**20.6**	–
	dHa2	2	26.8	-5.7	21.1	-11.4	**9.7**	-1461.84	44.4	**27.6**	394.3
CH_3O + CH_3O	Rc		16.2	-4.0	12.2	-0.5	**11.7**	-31.29	14.8	**10.3**	–
	dHa1		29.3	-3.6	25.7	-7.4	**18.3**	-863.13	26.9	**15.9**	212.9
	dHa2		33.6	-4.4	29.2	-8.2	**21.0**	-822.52	30.8	**18.2**	352.2
CH_3 + CH_2OH	Rc		2.8	-0.7	2.1	-0.1	**2.0**	-69.97	2.7	**1.9**	–
	dHa	1	28.2	-2.0	26.2	-0.6	**25.6**	-21.93	26.5	**23.9**	–
	dHa	2	47.0	-2.7	44.3	-11.7	**32.6**	-1226.28	46.6	**32.2**	295.7
CH_3 + CH_3	Rc		7.4	-5.4	2.1	-1.4	**0.7**	-36.520	6.6	**-0.1**	–
CH_3 + CH_3O	Rc		3.0	-1.5	1.5	-0.8	**0.7**	-88.820	2.5	**0.2**	–
	dHa		3.9	-1.9	2.0	-0.6	**1.3**	-129.30	3.5	**1.0**	36.1
CH_3 + NH_2	Rc		1.4	-1.0	0.4	-0.3	**0.0**	-19.83	1.2	**-0.1**	–
HCO + CH_2OH	Rc		6.8	-4.7	2.1	0.0	**2.2**	-55.33	6.3	**1.6**	–
	dHa1		5.0	-3.3	1.7	-1.6	**0.1**	-154.61	4.3	**-0.6**	26.2
	dHa2		46.9	-0.6	46.2	-13.7	**32.6**	-652.3997	45.0	**30.7**	153.7
HCO + CH_3O	Rc		8.9	-0.5	8.4	-2.1	**6.3**	-106.15	7.7	**5.1**	–
	dHa1		12.1	-5.3	6.8	-2.3	**4.5**	-228.50	10.8	**3.2**	57.8
	dHa2		23.0	-3.0	19.9	-6.6	**13.3**	-387.25	19.2	**9.6**	93.7
HCO + HCO	Rc		8.3	-2.7	5.6	-0.9	**4.7**	-75.94	7.6	**4.0**	–
	dHa1		6.3	-1.6	4.7	-1.4	**3.3**	-46.31	5.7	**2.7**	10.8
	dHa2		15.8	-0.9	14.9	-4.1	**10.8**	-102.29	13.3	**8.3**	8.3

Table C.5: *Summary of all the transition states found in this work at BHLYP-D3(BJ)/6-31+G(d.p) level, see the results section for the full PESs. Pure DFT energies were refined at BHLYP-D3(BJ)/6-311++G(2df,2pd) level (TZ). U, D and ZPE stand for pure DFT, dispersion and zero point (vibrational) energies, H is the combination of them three (i.e. enthalpies at zero Kelvin).* T_c *is the tunneling crossover temperature. Column number 2 indicates the reaction type, and for dHa wether it is case 1 (dHa1) or 2 (dHa2). Some reactions have more than one step, as indicated by column number 3 (Step #). Energies in kJ mol*$^{-1}$.

			Δ E TS								
X/Y···W33-cav	RX	# TS	ΔU	ΔD	Δ(U+D)	ΔZPE	ΔH	iν (cm^{-1})	ΔU (TZ)	ΔH (TZ)	T_c
CH_2OH + CH_2OH	Rc	-	0.5	4.4	4.9	-1.8	**3.1**	28.78	0.0	**2.6**	–
	dHa1	1	0.8	2.0	2.8	-1.5	**1.3**	71.45	1.0	**1.4**	–
	dHa1	2	1.3	13.3	14.5	-3.9	**10.7**	-46.04	2.1	**11.6**	–
	dHa1	3	-1.4	14.4	13.0	-3.7	**9.2**	79.17	-1.6	**9.1**	–
	dHa1	4	10.7	18.5	29.2	-3.4	**25.7**	68.37	9.8	**24.9**	–
	dHa1	5	23.8	15.2	39.0	-10.9	**28.1**	542.54	24.7	**29.1**	154.7
	dHa2	1	10.6	-1.3	9.3	-0.4	**8.9**	95.87	10.6	**9.0**	–
	dHa2	2	26.6	-8.9	17.7	-11.0	**6.7**	1068.76	27.3	**7.4**	296.2
CH_3O + CH_3O	Rc	-	20.4	-2.3	18.1	2.8	**21.0**	140.15	19.5	**20.1**	–
	dHa1	-	22.1	-3.0	19.1	-5.9	**13.2**	886.62	20.6	**11.7**	225.7
	dHa2	-	32.2	-1.6	30.6	-4.9	**25.7**	788.36	27.8	**21.2**	189.8
CH_3 + CH_2OH	Rc	1	-1.6	4.5	3.0	-0.6	**2.4**	27.48	-1.4	**2.5**	–
	Rc	2	-2.8	1.6	-1.2	1.6	**0.4**	59.97	-2.7	**0.4**	–
	dHa	-	52.1	-0.4	51.7	-11.8	**39.9**	1020.12	51.2	**39.0**	242.0
CH_3 + CH_3	Rc	-	9.8	-2.5	7.2	-1.3	**5.9**	110.49	8.4	**4.6**	–
CH_3 + CH_3O	Rc	-	8.1	-3.8	4.3	0.1	**4.4**	123.81	6.8	**3.1**	–
	dHa	-	17.1	-2.9	14.2	-2.3	**11.9**	200.13	14.7	**9.5**	47.1
CH_3 + NH_2	Rc	-	1.4	-0.3	1.1	-0.4	**0.7**	92.25	1.1	**0.4**	–
HCO + CH_2OH	Rc	-	0.2	2.8	3.0	-1.3	**1.7**	55.18	0.2	**1.7**	–
	dHa1	-	1.9	1.2	3.2	-1.6	**1.6**	90.00	1.2	**0.8**	24.2
	dHa2	1	13.6	3.8	17.4	-2.2	**15.2**	35.32	10.6	**10.2**	–
	dHa2	2	37.4	0.5	37.9	-16.1	**21.7**	1321.28	36.0	**18.4**	387.0
HCO + CH_3O	Rc	-	2.4	2.3	4.7	-0.2	**4.5**	27.20	1.4	**3.5**	–
	dHa1	-	13.3	-4.8	8.6	-4.6	**4.0**	137.45	11.4	**2.0**	34.6
	dHa2	-	15.4	3.4	18.8	-3.6	**15.1**	188.68	13.4	**13.2**	35.4
HCO + HCO	Rc	-	6.7	-1.0	5.7	-0.7	**4.9**	64.27	5.8	**4.1**	–
	dHa1	1	9.0	-1.2	7.8	-1.5	**6.3**	119.03	6.7	**4.0**	28.4
	dHa2*	2	1.5	0.0	1.5	-1.7	**-0.3**	164.89	0.9	**-0.8**	29.6

* The energy reference is point 24 from the backwards ICR calculation, see Figure C.16.

C.7 Potential energy surfaces on W18

In this section we report the PESs on W18 of the radical–radical reactions studied in Chapter 7.

- CH_3 + CH_3: Figure C.5
- CH_3 + NH_2: Figure C.6
- CH_3 + CH_2OH: Figure C.8
- CH_3 + CH_3O: Figure C.7
- HCO + CH_2OH: Figure C.11
- HCO + CH_3O: Figure C.10
- HCO + HCO: Figure C.9
- CH_2OH + CH_2OH: Figure C.13
- CH_3O + CH_3O: Figure C.12

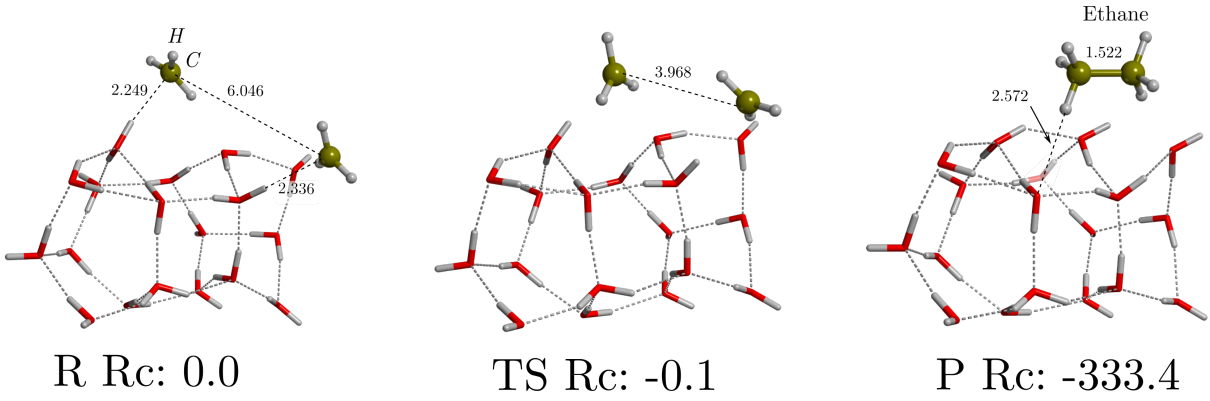

Figure C.5: *ZPE-corrected Rc PES for CH_3 + CH_3 on W18 fully optimized at the UBHLYP-D3(BJ)/6-31+G(d,p) theory level with the DFT energy refined to UBHLYP-D3(BJ)/6-311++G(2df,2pd). Energy units are in kJ/mol and distances in Å.*

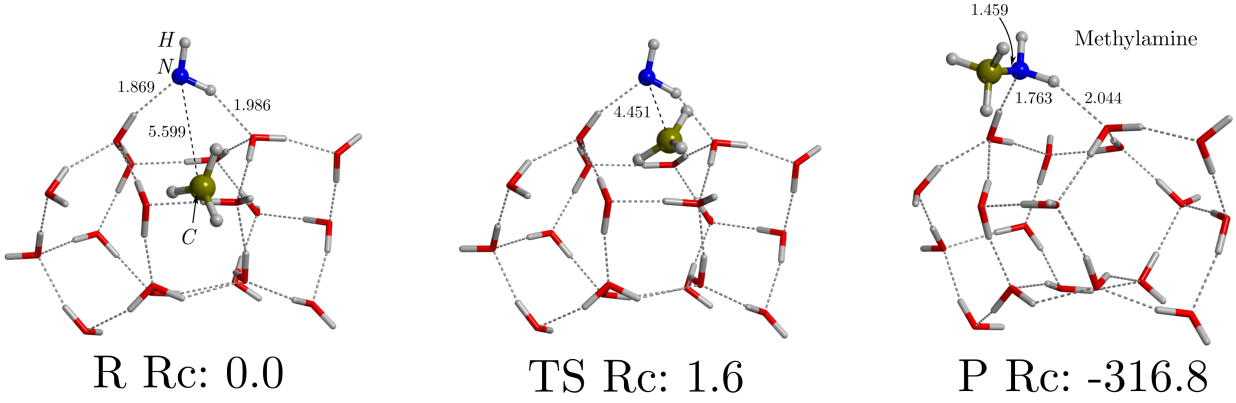

Figure C.6: *ZPE-corrected Rc PES for CH_3 + NH_2 on W18 fully optimized at the UBHLYP-D3(BJ)/6-31+G(d,p) theory level with the DFT energy refined to UBHLYP-D3(BJ)/6-311++G(2df,2pd). Energy units are in kJ/mol and distances in Å.*

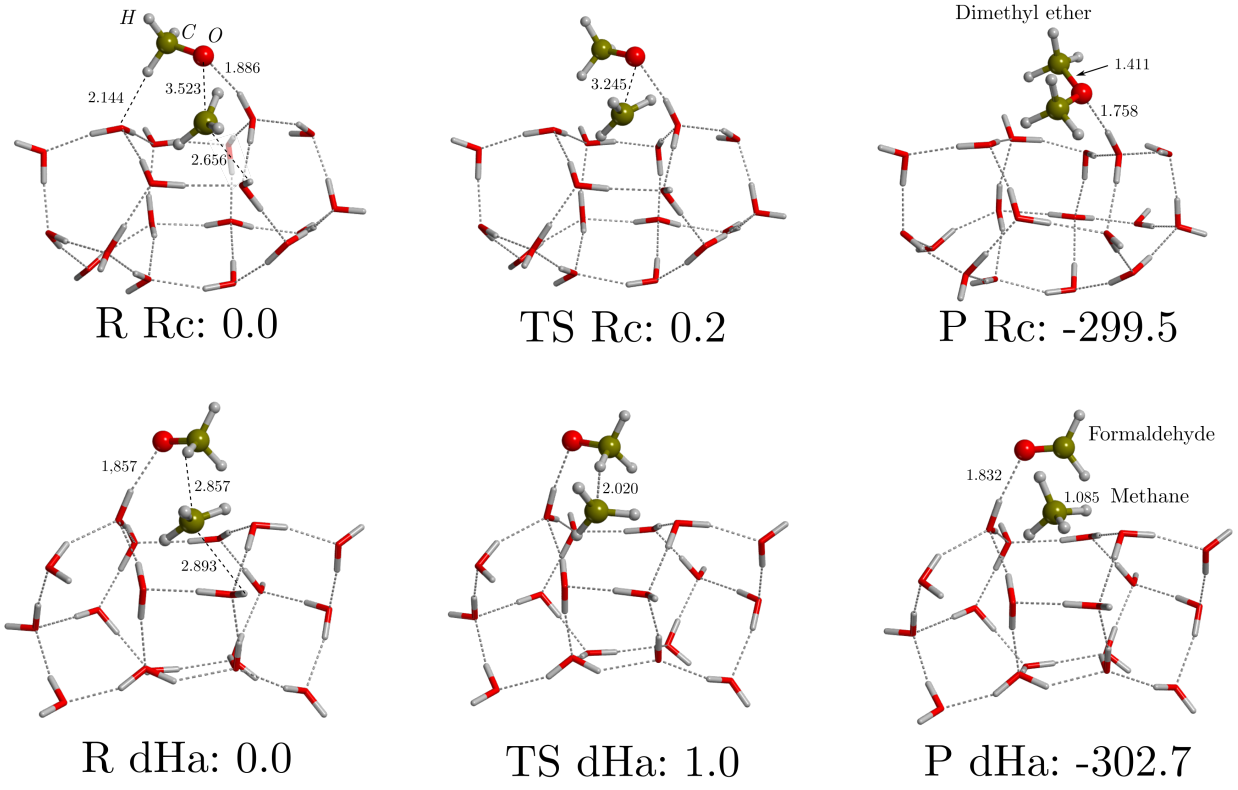

Figure C.7: *ZPE-corrected Rc PES for CH_3 + CH_3O on W18 fully optimized at the UBHLYP-D3(BJ)/6-31+G(d,p) theory level with the DFT energy refined to UBHLYP-D3(BJ)/6-311++G(2df,2pd). Energy units are in kJ/mol and distances in Å.*

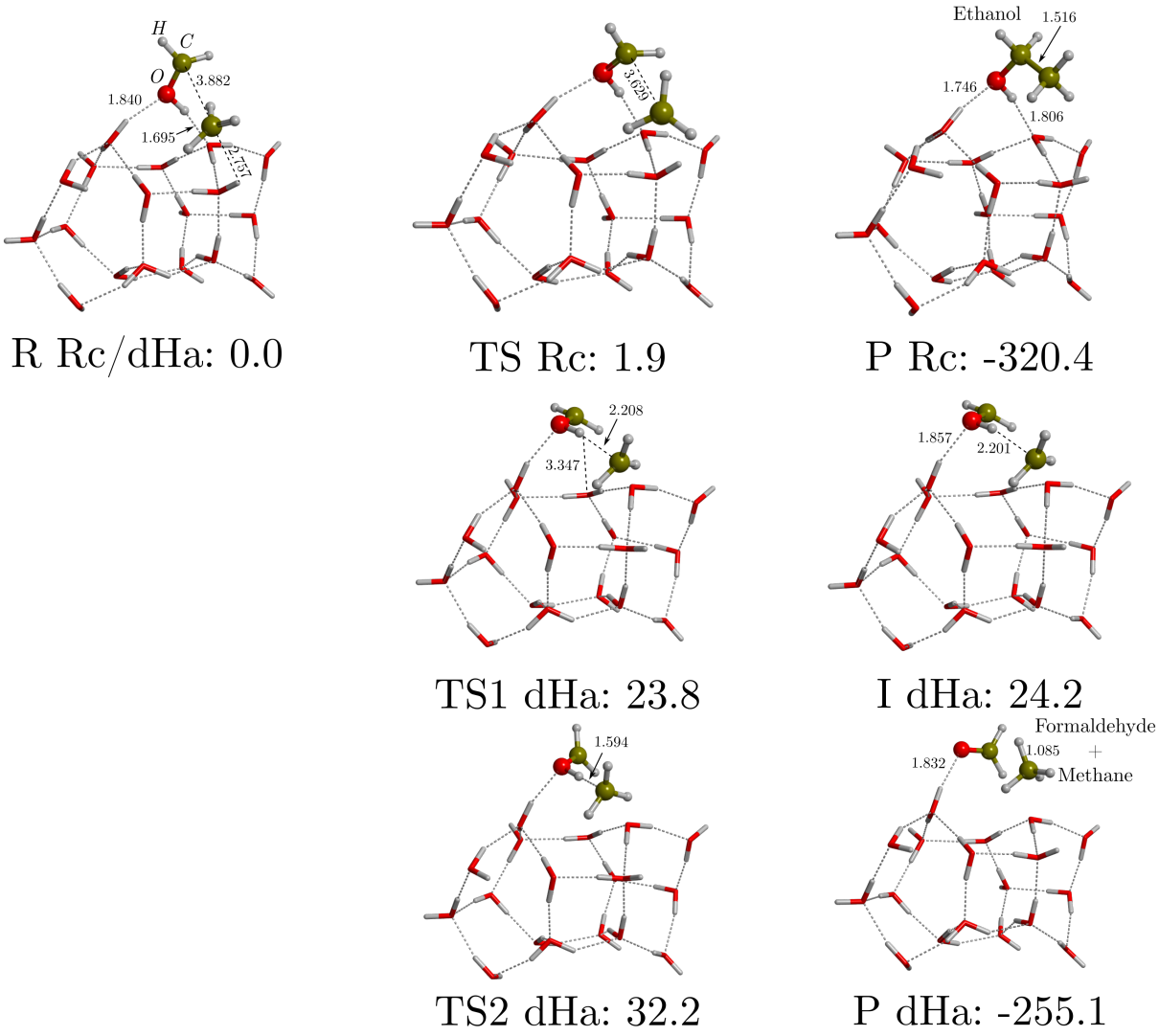

Figure C.8: *ZPE-corrected Rc PES for CH_3 + CH_2OH on W18 fully optimized at the UBHLYP-D3(BJ)/6-31+G(d,p) theory level with the DFT energy refined to UBHLYP-D3(BJ)/6-311++G(2df,2pd). Energy units are in kJ/mol and distances in Å.*

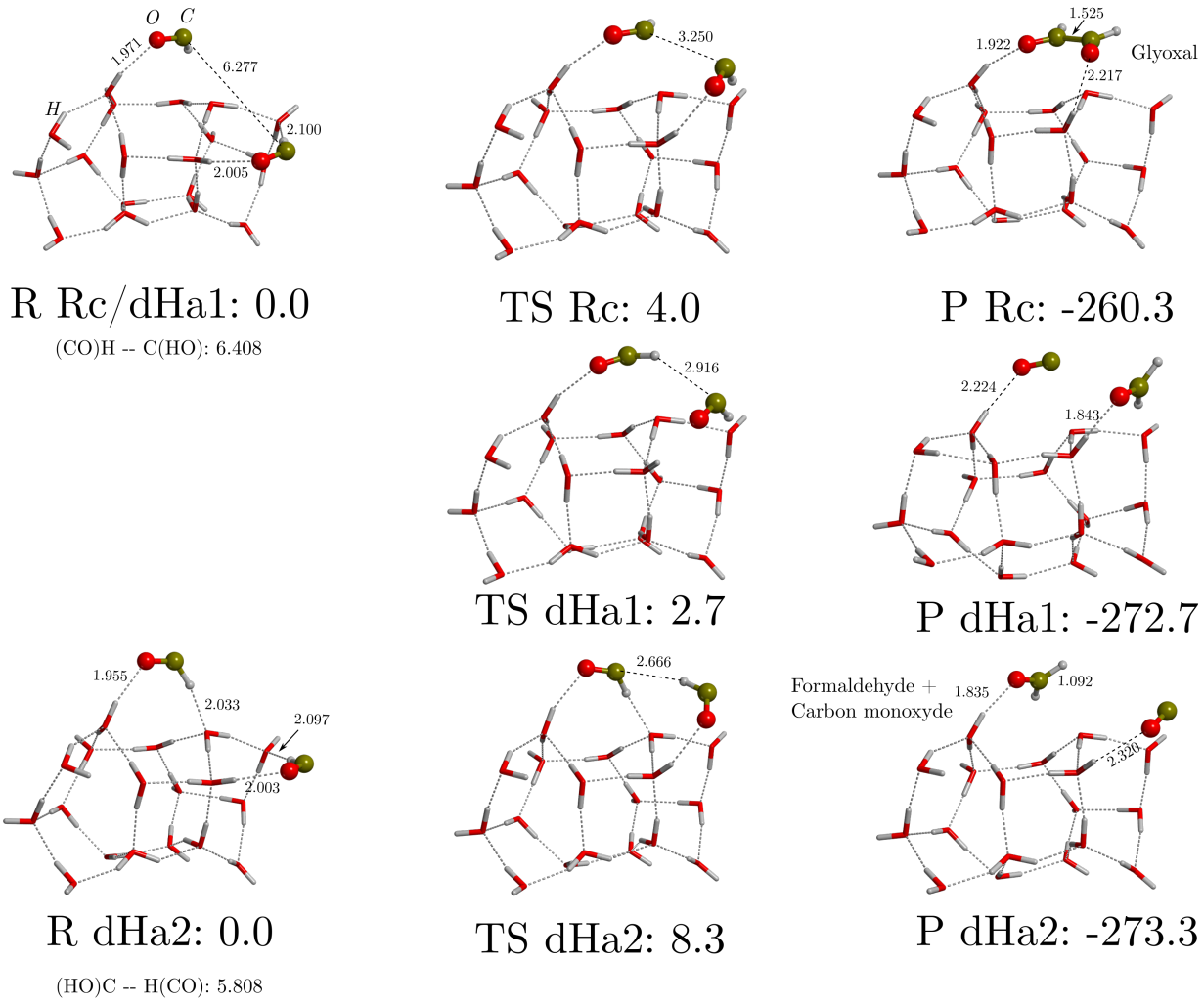

Figure C.9: *ZPE-corrected Rc PES for HCO + HCO on W18 fully optimized at the UBHLYP-D3(BJ)/6-31+G(d,p) theory level with the DFT energy refined to UBHLYP-D3(BJ)/6-311++G(2df,2pd). Energy units are in kJ/mol and distances in Å.*

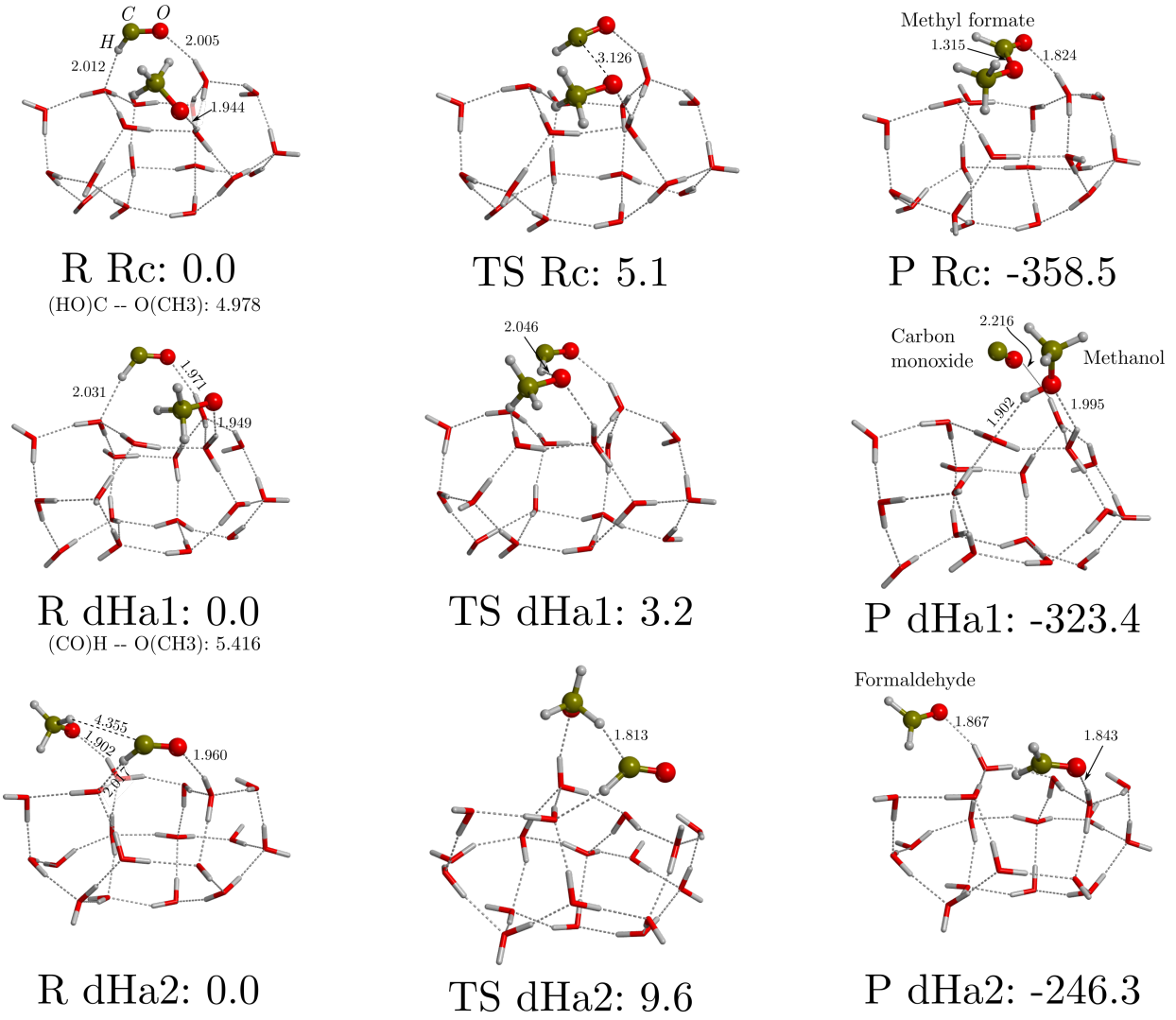

Figure C.10: *ZPE-corrected Rc PES for HCO + CH_3O on W18 fully optimized at the UBHLYP-D3(BJ)/6-31+G(d,p) theory level with the DFT energy refined to UBHLYP-D3(BJ)/6-311++G(2df,2pd). Energy units are in kJ/mol and distances in Å.*

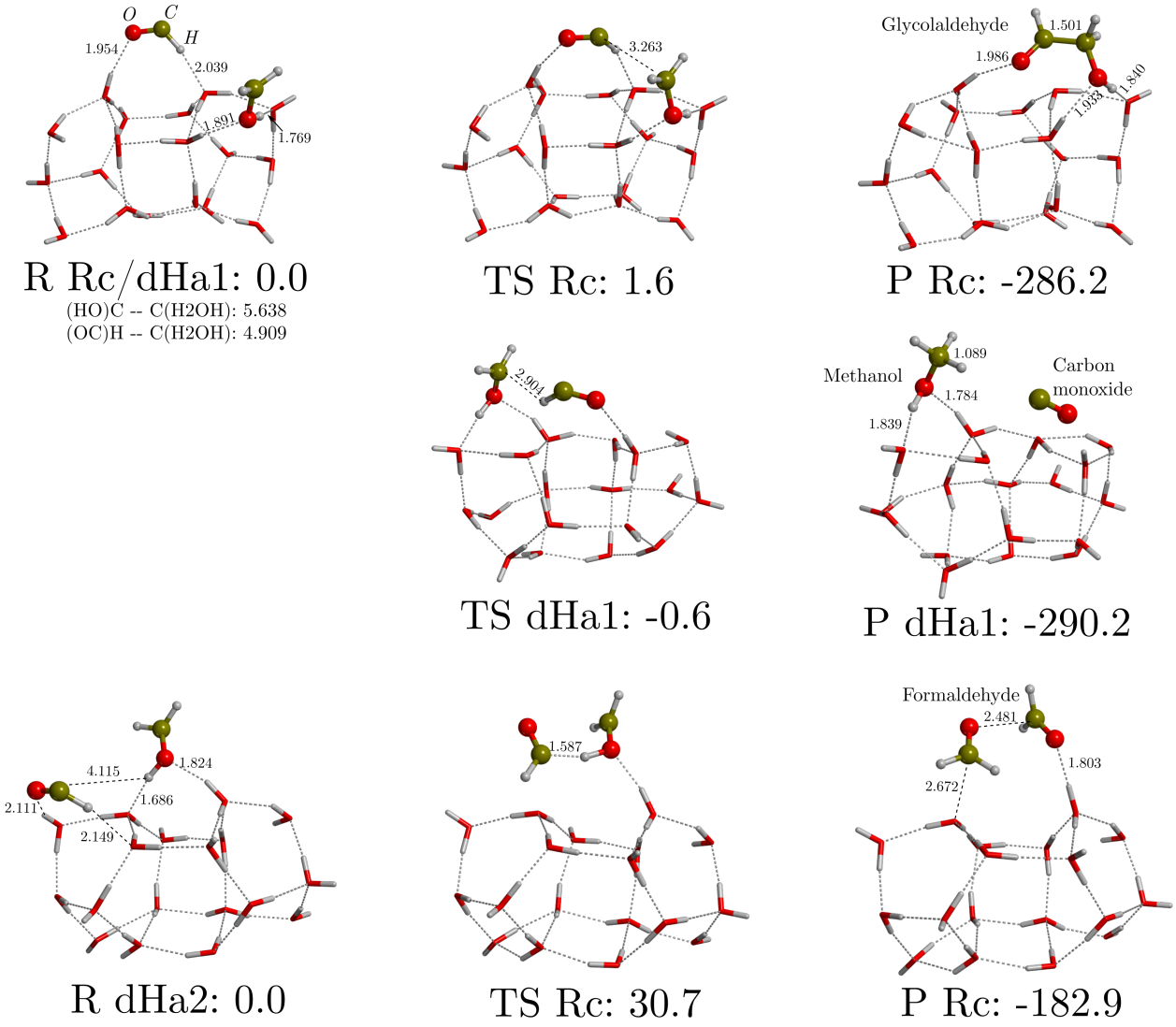

Figure C.11: *ZPE-corrected Rc PES for HCO + CH_2OH on W18 fully optimized at the UBHLYP-D3(BJ)/6-31+G(d,p) theory level with the DFT energy refined to UBHLYP-D3(BJ)/6-311++G(2df,2pd). Energy units are in kJ/mol and distances in Å.*

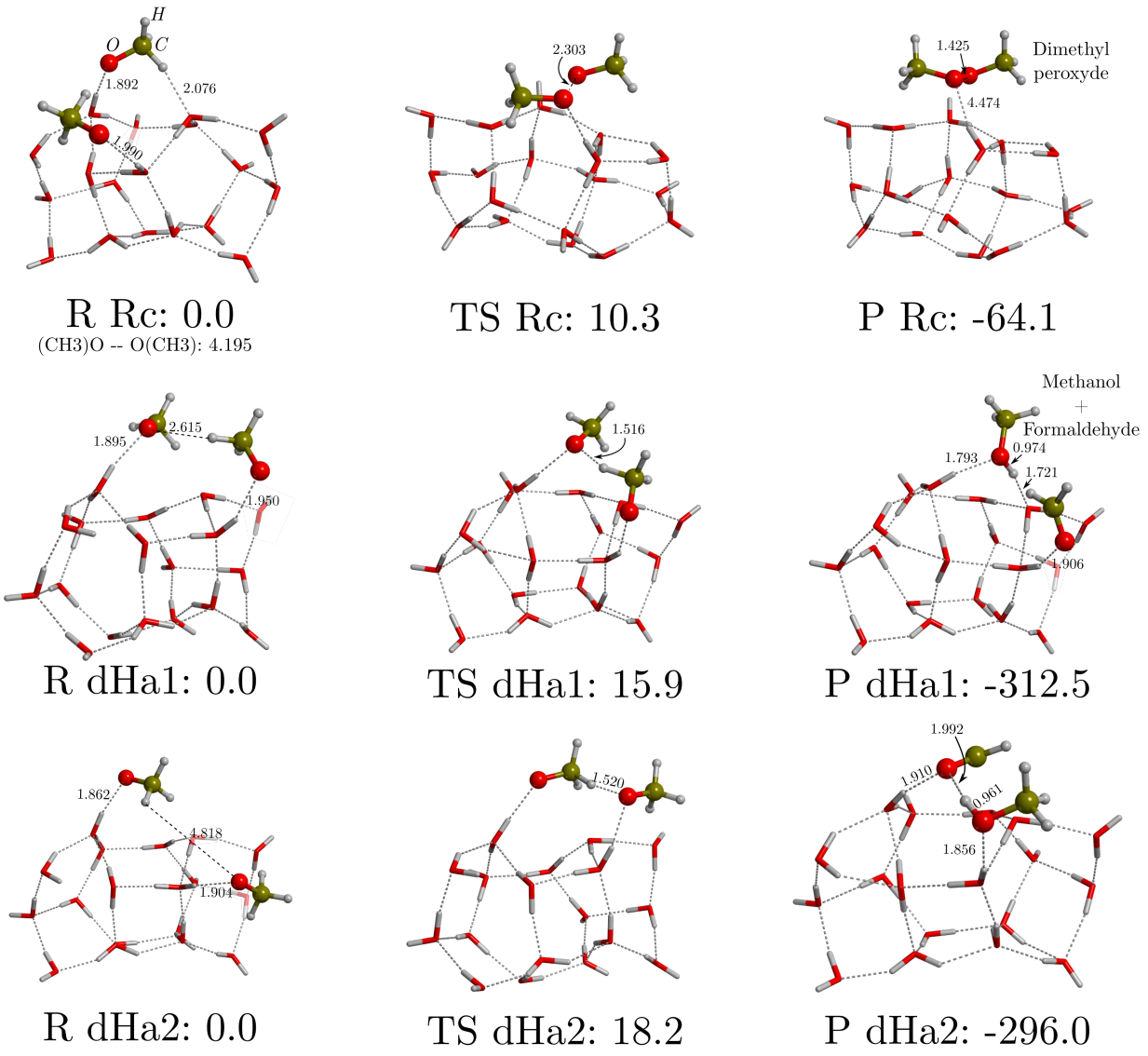

Figure C.12: *ZPE-corrected Rc PES for CH_3O + CH_3O on W18 fully optimized at the UBHLYP-D3(BJ)/6-31+G(d,p) theory level with the DFT energy refined to UBHLYP-D3(BJ)/6-311++G(2df,2pd). Energy units are in kJ/mol and distances in Å.*

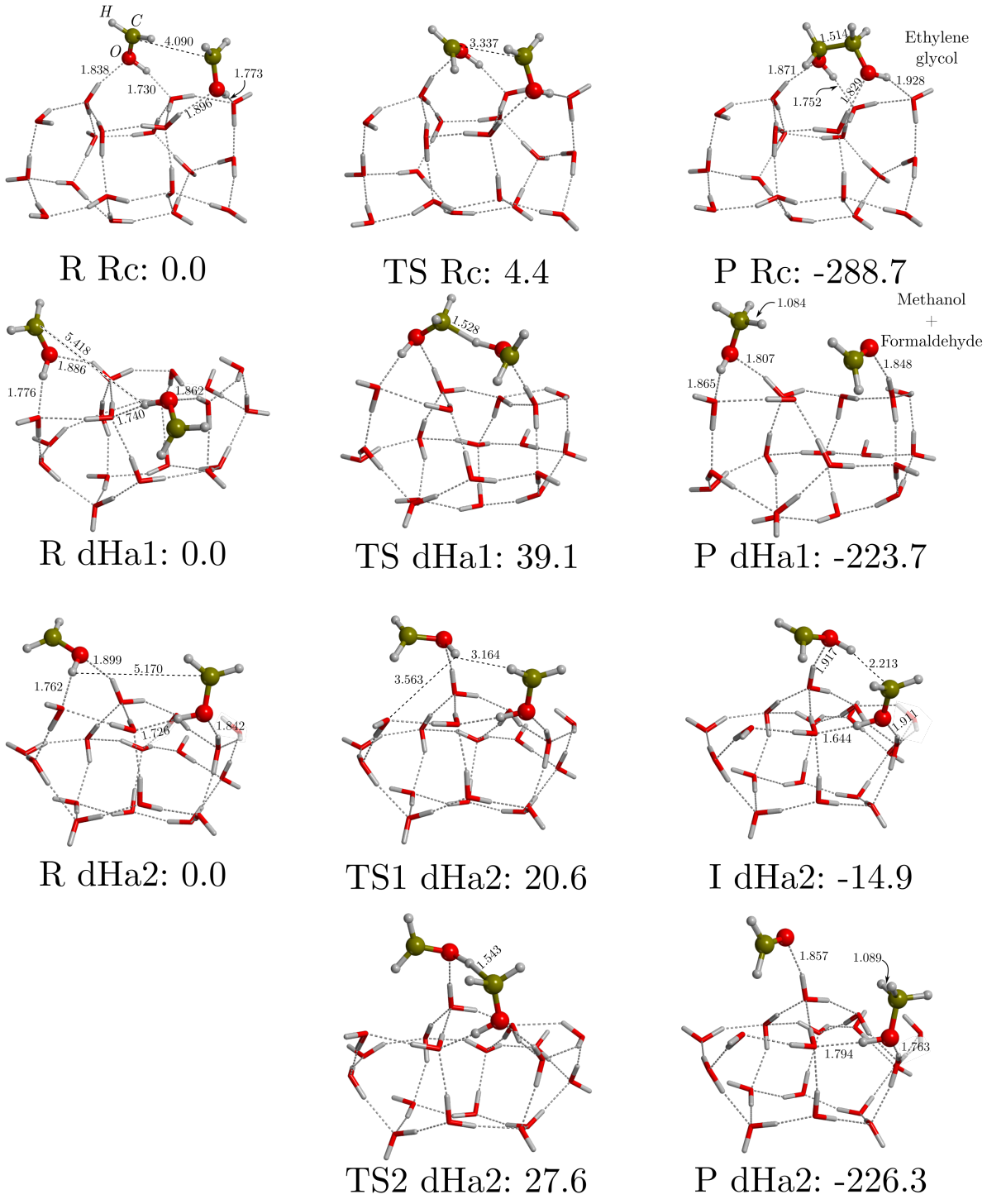

Figure C.13: *ZPE-corrected Rc PES for CH_2OH + CH_2OH on W18 fully optimized at the UBHLYP-D3(BJ)/6-31+G(d,p) theory level with the DFT energy refined to UBHLYP-D3(BJ)/6-311++G(2df,2pd). Energy units are in kJ/mol and distances in Å.*

C.8 Potential energy surfaces on W33

In this section we report the rest of PESs on W33 of the radical–radical reactions studied in Chapter 7.

- HCO + HCO dHa2: Figure C.16
- HCO + CH_3O dHa2: Figure C.14
- HCO + CH_2OH dHa2: Figure C.17
- CH_3O + CH_3O dHa2: Figure C.18
- CH_2OH + CH_2OH: Figure C.15

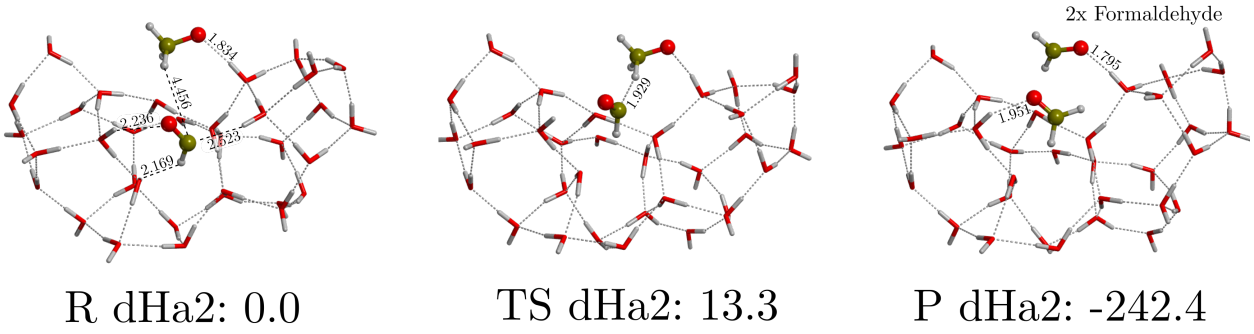

Figure C.14: *ZPE-corrected dHa2 PES for HCO/CH_3O· · · W33-cav fully optimized at the BHLYP-D3(BJ) theory level. For dHa we report the two possibilities, the transfer from HCO and the one from CH_3O. Energy units are in kJ/mol and distances in Å.*

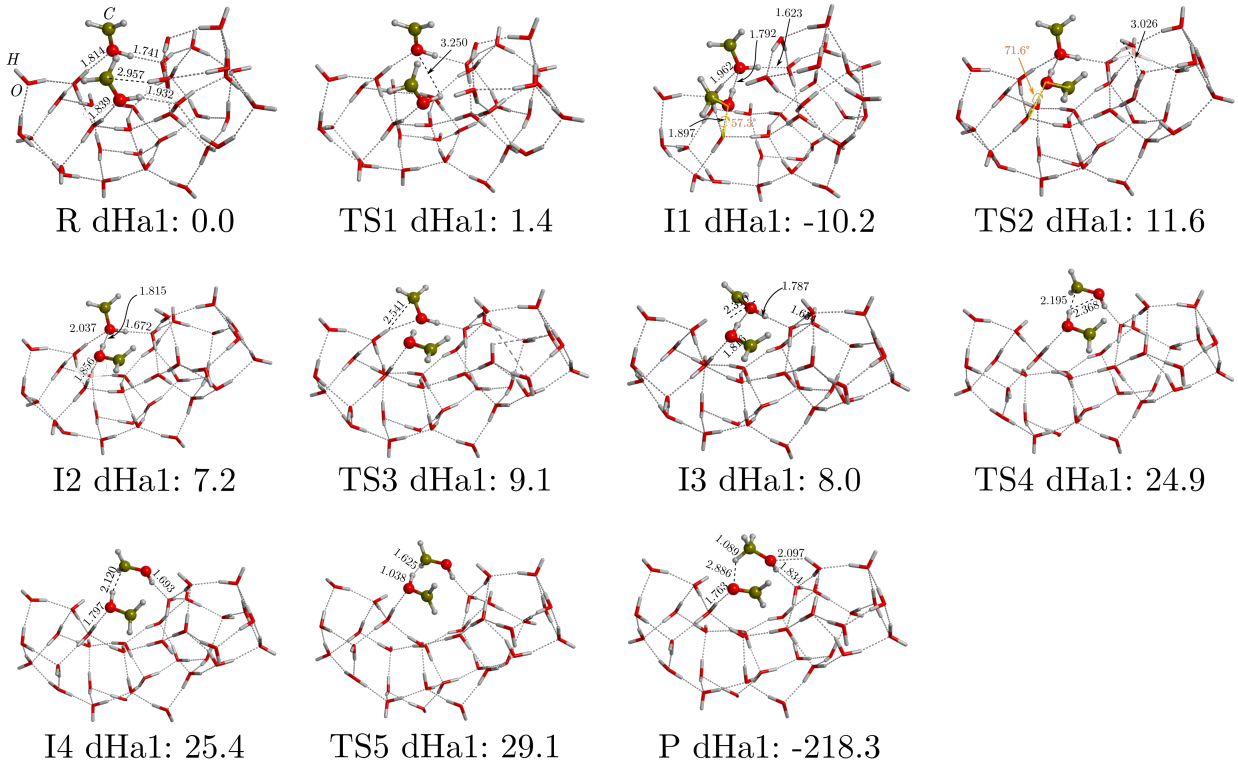

Figure C.15: *ZPE-corrected dHa from radical 1 to radical 2 PES for $CH_2OH/CH_2OH\cdot\cdot\cdot$ W33-cav fully optimized at the BHLYP-D3(BJ) theory level. Energy units are in kJ/mol and distances in Å.*

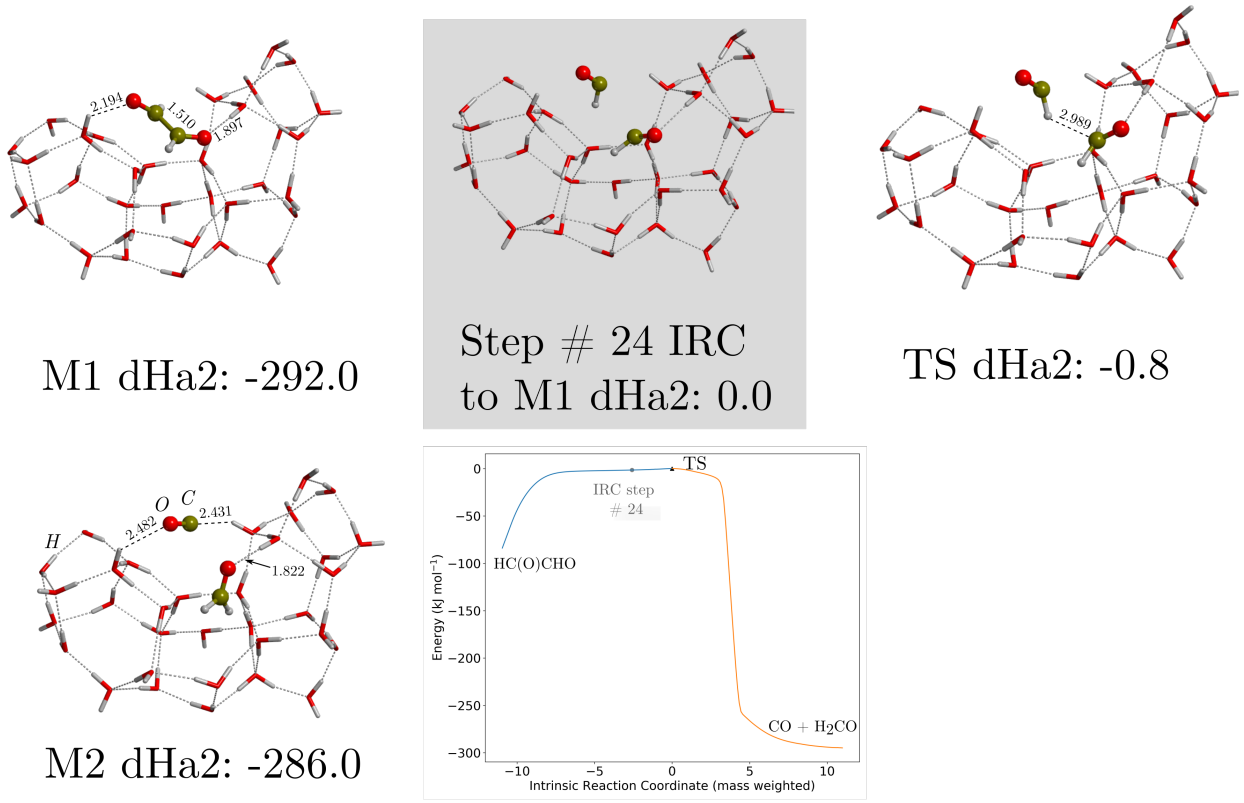

Figure C.16: *ZPE-corrected HCO/HCO· · · W33-cav PES for the dHa2 transition state, which in this case connects a Rc and a dHa-like paths. The grey-shaded structure corresponds to an intermediate position in the IRC path leading from the TS to the Rc minimum (M1). a plot with the IRC (not ZPE-corrected) can be found in the lower right side, in which the grey dot corresponds to the intermediate structure and the black one to the transition state. The minima and maxima of the TS were fully optimized at the BHLYP-D3(BJ) theory level. Energy units are in kJ mol*$^{-1}$ *and distances in Å.*

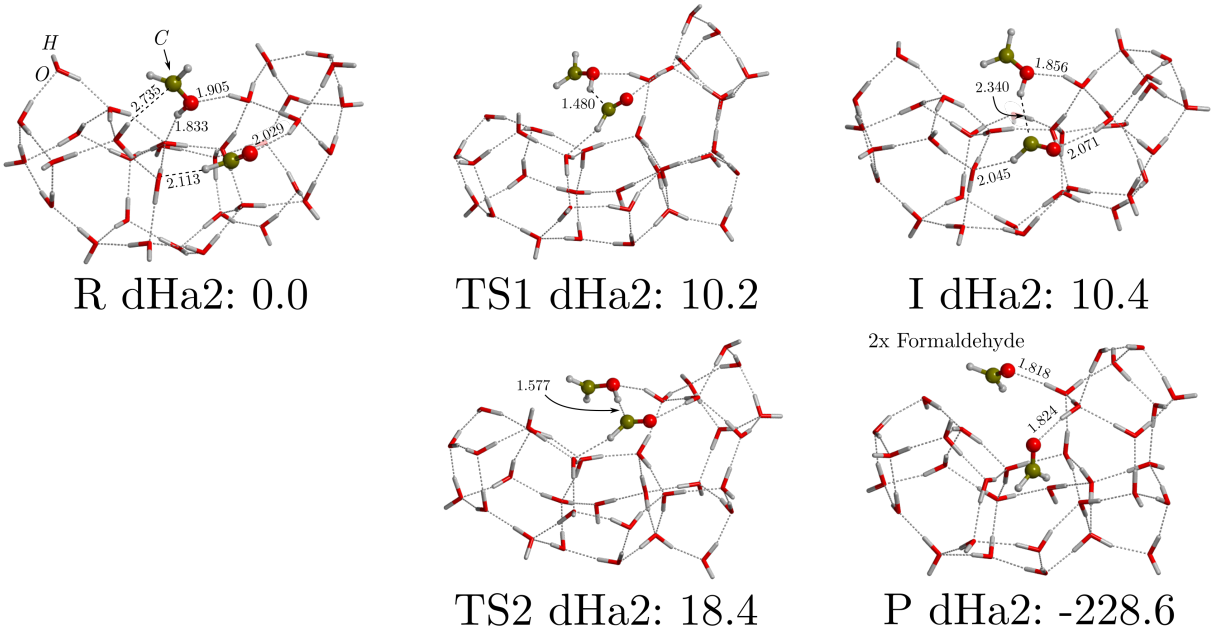

Figure C.17: *ZPE-corrected dHa2 PESs for HCO/CH_2OH· · · W33-cav fully optimized at the BHLYP-D3(BJ) theory level. Energy units are in kJ/mol and distances in Å.*

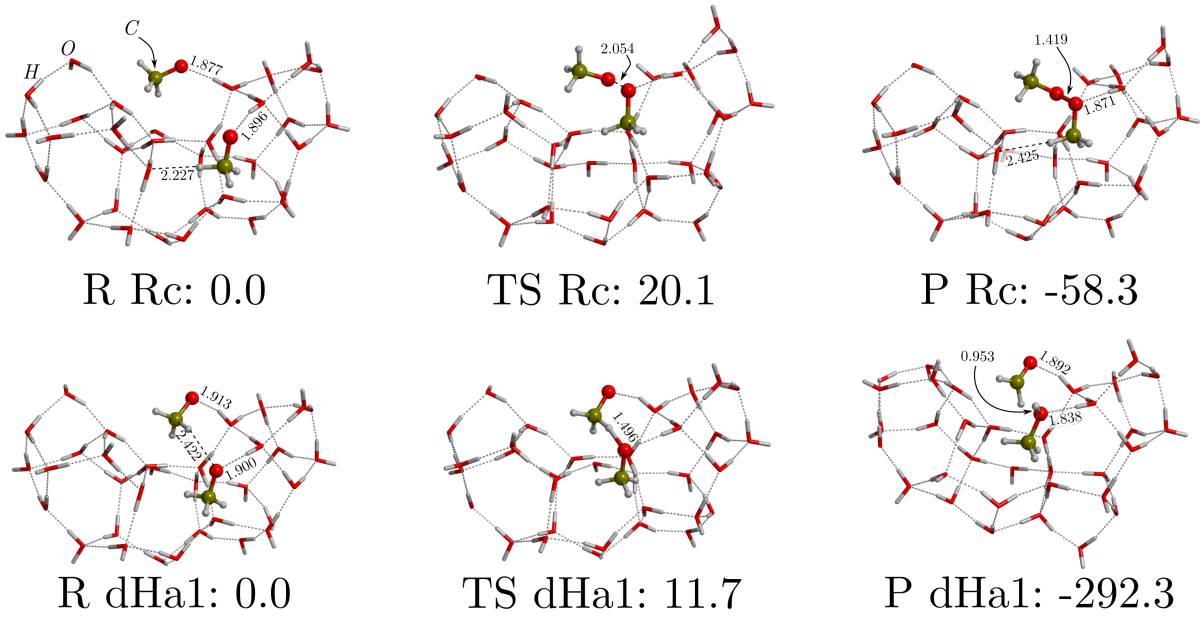

Figure C.18: *ZPE-corrected dHa from radical 2 to radical 1 and vice-versa PESs for $CH_3O/CH_3O\cdot\cdot\cdot$ W33-cav fully optimized at the BHLYP-D3(BJ) theory level. Energy units are in kJ/mol and distances in Å.*

C.9 Activation energy and temperature dependent efficiencies for those systems not explicitly studied in this work

In this section we present all the E_a and T dependent efficiencies for the systems: OH + CH_3/HCO/OH/NH_2/CH_3O/CH_2OH, NH + CH_3/HCO/OH/NH_2/CH_3O/CH_2OH, NH_2 + NH_2/CH_3O/CH_2OH and CH_3O + CH_2OH. More details can be found in the main body of the article.

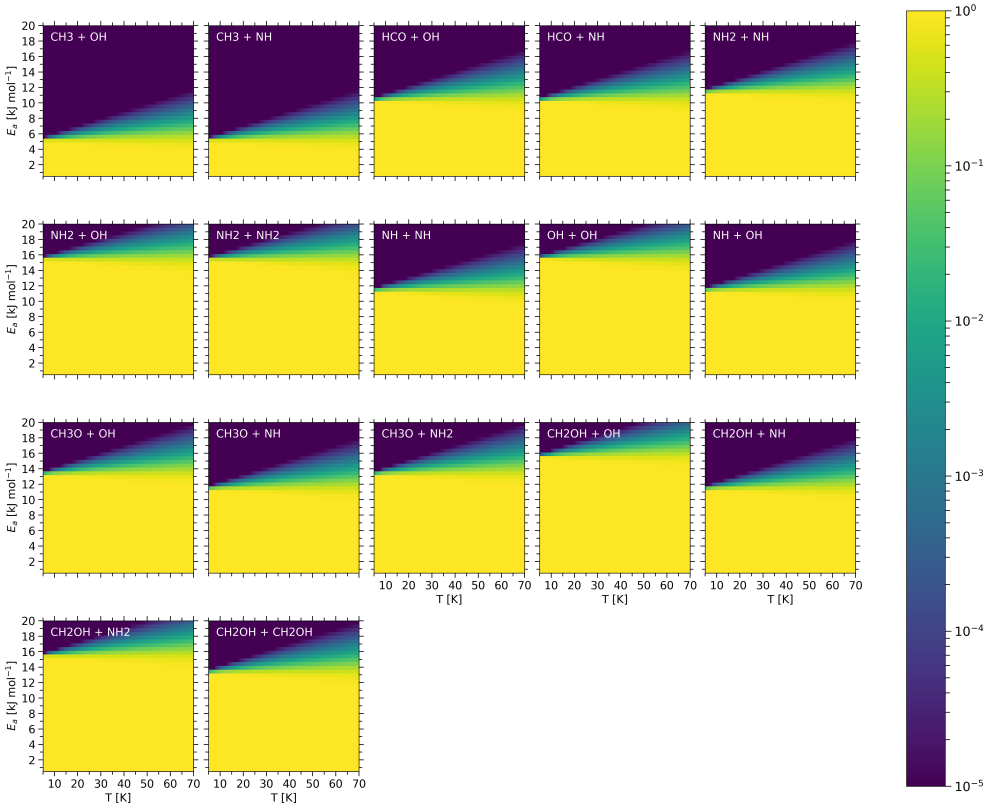

Figure C.19: *Reaction efficiencies on W33 as a function of activation energy and temperature of those radical–radical reactions in Robin T. Garrod et al., 2008 not explicitly studied in this work.*

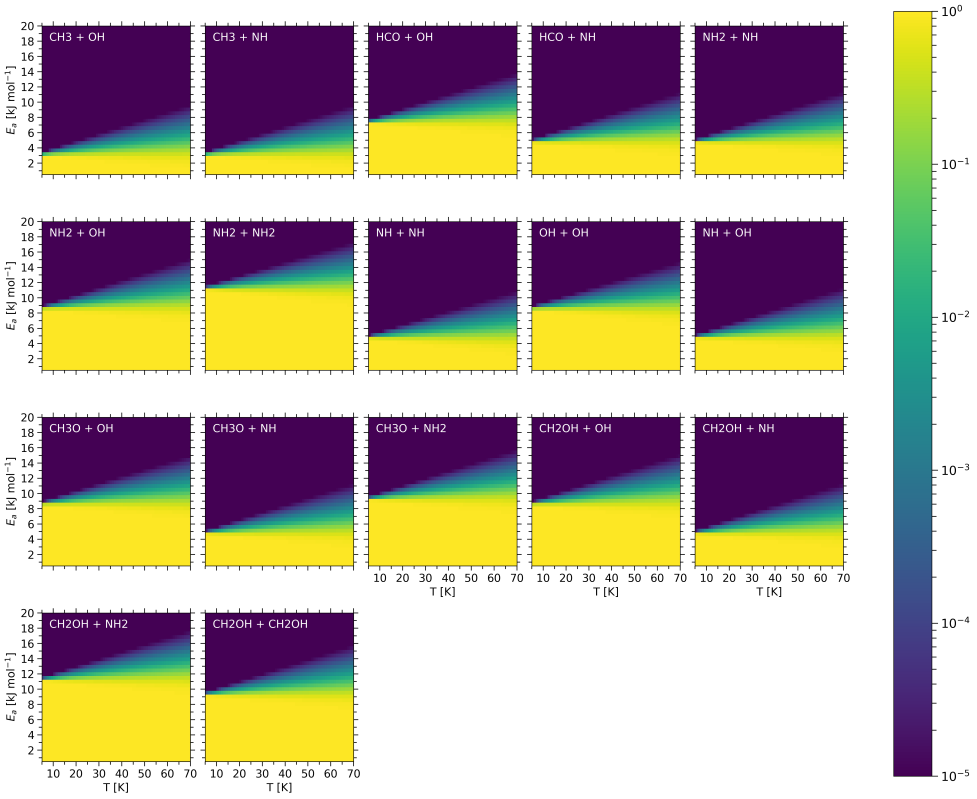

Figure C.20: *Reaction efficiencies on W18 as a function of activation energy and temperature of those radical–radical reactions in Robin T. Garrod et al., 2008 not explicitly studied in this work.*

C.10 Crossover temperature formula

In order to calculate the crossover temperatures (T_c), we have used equation C.1 (Fermann et al., 2000). At temperatures below T_c tunnelling effects become dominant, and above it tunnelling is negligible.

$$T_c = \frac{\hbar\omega^{\ddagger}\Delta H^{\ddagger}/k_B}{2\pi\Delta H^{\ddagger} - \hbar\omega^{\ddagger}\ln(2)} \tag{C.1}$$

where $\hbar$ is the reduced Plank constant, $\omega^{\ddagger} = 2\pi\nu^{\ddagger}$ with $\nu^{\ddagger}$ the frequency (in absolute value) associated to the transition state, $\Delta H^{\dagger}$ is the ZPE-corrected energy barrier at 0 K and k_B is the Boltzmann constant.

C.11 Spin densities of each radical in reactant structures

Table C.6: *Spin densities of the reactant radical radical structures. Computed employing natural bond population analysis.*

W18				
Reaction	R1	R2	SD R1	SD R2
Rc	CH3O	CH3O	-0.99655	1.00061
Rc	CH2OH	CH3	-0.99561	0.98991
Rc	CH3O	HCO	-1.00005	0.98816
Rc	CH2OH	CH2OH	-0.99358	0.99107
Rc	HCO	HCO	-0.99323	0.99112
Rc	CH3	CH3O	-0.99476	0.99810
Rc	HCO	CH2OH	-0.98802	0.99912
Rc	CH3	NH2	-0.99307	1.00575
dHa2	HCO	CH3O	-0.98813	1.00073
dHa	CH3	CH3O	-0.99352	0.99509
dHa2	HCO	CH2OH	-0.99078	0.99727
dHa2	CH3O	CH3O	-0.99985	0.99948
dHa2	CH3O	HCO	-0.99904	0.98953
dHa1	HCO	CH2OH	-0.98788	0.99898
dHa2	HCO	HCO	-0.98843	0.99094
dHa1	CH2OH	CH2OH	-0.99982	0.99592
dHa1	CH3O	CH3O	-1.00116	0.99809
dHa1	CH3O	HCO	-1.00104	0.98860

W33				
Reaction	R1	R2	SD R1	SD R2
Rc	CH3O	CH3O	-1.00019	1.00021
Rc	CH3O	HCO	-1.00020	0.99241
Rc	CH2OH	HCO	-0.98984	0.98981
Rc	CH2OH	CH2OH	-0.98789	0.99624
Rc	CH2OH	CH3	-0.99694	0.98891
Rc	CH2OH	CH3	-0.98978	0.98025
Rc	HCO	HCO	-0.97371	0.99443
Rc	CH3	CH3	-0.97903	0.98453
Rc	CH3	CH3O	-0.98658	0.99996
Rc	CH3	NH2	-0.98649	1.00420
dHa1	HCO	HCO	-0.97365	0.99442
dHa1	CH2OH	HCO	-0.98988	0.98980
dHa	CH3	CH3O	-0.98652	0.99999
dHa2	HCO	CH2OH	-0.98932	0.99573
dHa2	CH3O	CH3O	-0.99722	0.99942
dHa2	CH2OH	CH2OH	-0.99802	0.99996
dHa1	CH3O	HCO	-0.99924	0.97255
dHa1	CH3O	HCO	-0.99884	0.98571
dHa	CH2OH	CH3	-0.99693	0.98892
dHa1	CH2OH	CH2OH	-0.98764	0.99148
dHa1	CH3O	CH3O	-0.99668	0.99872
dHa2	HCO	CH3O	-0.98176	1.00135

Chapter D
Supporting data for Chapter 9

Outline

D.1 Benchmark study

The quality of BHLYP-D3(BJ) as an accurate, cost-effective method for the reactions studied in this work is shown in this section.

We have taken 5 hybrid DFT dispersion-corrected methods: MPWB1K-D3(BJ), M062X-D3, PW6B95-D3(BJ), wB97X-D3 and BHandHLYP-D3(BJ), recommended in Goerigk et al., 2017 for their good overall performance.

We have then compared their performance with respect to CASPT2 by studying reactions I and II on 2 water molecules. We proceeded in two steps: (i) we performed geometry optimised and run frequency calculations at BHLYP-D3(BJ)/6-311++G(d,p) for each reaction channel, finding and checking each stationary point (i.e. reactants, transition state and products); (ii) we then run single point calculations on top of these geometries at each DFT method combined with the 6-311++G(2df,2pd) basis set, and CASPT2/aug-cc-PVTZ for reference. The unrestricted broken symmetry scheme was adopted for all DFT calculations, and the CASPT2 guess wave function was generated using a CASSCF(2,2) calculation where the active space is formed by the two unpaired electrons and their molecular orbitals, starting from a triplet Hartree-Fock wave-function.

BHLYP-D3(BJ) gives the best overall performance with and average unsigned error of 3.0%, and a maximum of 5.0% with respect to CASPT2/aug-cc-PVTZ. The rest of DFT methods have average errors between 10 and 80% (Table D.1). The raw energy values are shown in Table D.3.

Table D.1: *DFT method benchmark results.*

	% Unsigned Error from CASPT2/aug-cc-PVTZ//BHLYP-D3(BJ)/6-311++G(d,p)				
System	BHLYP-D3(BJ)	MPWB1K-D3(BJ)	M062X-D3	PW6B95-D3(BJ)	wB97x-D3
TS dHa on W2	5.0	18.5	59.1	15.8	46.0
HCO + CH4 on W2	3.5	2.0	3.9	1.3	214.3
TS Rc on W2	2.2	3.9	250.4	17.9	18.0
CH3CHO on W2	1.1	8.7	6.5	6.1	6.5
Average	3.0	8.3	80.0	10.3	71.2

Table D.2: *Energetics (kJ mol^{-1}) of the stationary points optimised at BHLYP-D3(BJ)/6-311++G(d,p), together with the frequencies of the transition states (cm^{-1}).*

	OPT: BHLYP-D3(BJ)/6-311++G(d,p)	
	E	iv
React. I	-306.5101581	
TS I	-306.5101000	-26.1495
Prod. I	-306.6472250	
React. II	-306.5106910	
TS II	-306.5098973	-32.8207
Prod. II	-306.6377604	

Table D.3: *Raw data from the DFT method benchmark. Energies in kJ mol^{-1}.*

	DFT/6-311++G(2df,2pd)					Multi-reference methods	
	BHLYP-D3(BJ)	MPWB1K-D3(BJ)	M062X-D3	PW6B95-D3(BJ)	wB97X-D3	CASSCF(2,2)/aug-cc-PVTZ	CASPT2/aug-cc-PVTZ
React. I	-306.5278673	-306.5199277	-306.5443283	-307.0275371	-306.6077421	-304.99849	-306.092193
TS I	-306.5274906	-306.5195273	-306.5429782	-307.0270829	-306.6074261	-304.99793	-306.0918077
Prod. I	-306.6651096	-306.6673671	-306.6888795	-307.1714705	-306.7523061	-305.14355	-306.2278841
React. II	-306.5278665	-306.5199185	-306.5443285	-307.0275286	-306.6077403	-304.99849	-306.0921923
TS II	-306.5273893	-306.5195091	-306.5435295	-307.027106	-306.6074694	-304.9976	-306.0916902
Prod. II	-306.6561571	-306.6555907	-306.6825872	-307.1623168	-307.0257242	-305.14411	-306.2251986

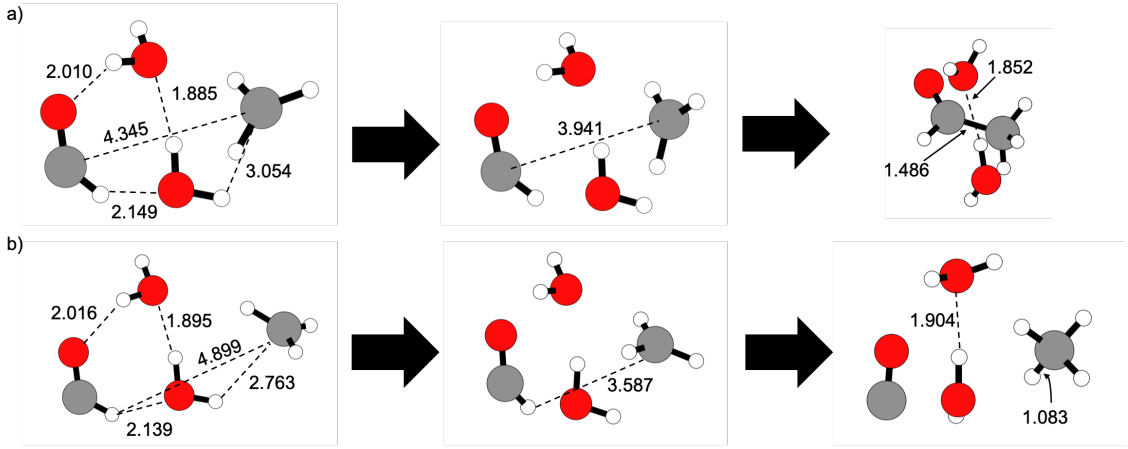

Figure D.1: *Geometries of the stationary points (reactants, transition state and products) of reactions a)* I *and b)* II *on top of two water molecules optimised at BHLYP-D3(BJ)/6-311++G(d,p) level. Distances in Å.*

D.2 Calculation of desorption and diffusion rate constants

In order to calculate the rates of diffusion/desorption we have used Eyring's equation (eq. 9.5), where entropy and thermal corrections to the enthalpy are accounted for since energy term in the exponential should be the Gibbs free energy ($G = H - TS$). In the astrochemistry community, desorption/diffusion rates consist of two parts, first the attempt frequency (i.e. the pre-exponential factor) and then the exponential with the binding energies. We define the attempt frequency within the Eyring equation as

$$\nu = \frac{k_B T}{h} \times \exp(\Delta S / k_B), \tag{D.1}$$

where h, k_B are the Planck and Boltzmann constants, T the temperature and S the entropy. For the ice model and the complex surface+radical the entropy contributions are $S = S_{vib}$, where the vibrational counterpart is (eq. D.2):

$$S_{vib} = k_B \sum_i \left[\frac{\theta_{v,i}/T}{e^{\theta_{v,i}/T} - 1} - \ln\left(1 - e^{-\theta_{v,i}/T}\right) \right] \tag{D.2}$$

where $\theta_{v,i} = hc\overline{\nu}_i / k_B$ with c the speed of light and $\overline{\nu}_i$ the ith vibrational mode frequency in cm^{-1}.

For the free radicals, additionally, we also take into account the rotational and translational contributions: $S = S_{vib} + S_{rot} + S_{trans}$, where the rotational and translational counterparts are given by eqs. D.3 and D.4 respectively:

$$S_{rot} = k_B \left[\ln\left(\frac{\pi^{1/2}}{\sigma_{rot}} \frac{T^{3/2}}{(\theta_{r,x}\theta_{r,y}\theta_{r,z})^{1/2}} \right) + \frac{3}{2} \right], \tag{D.3}$$

$$S_{trans} = k_B \left(\ln\left[\left(\frac{2\pi m k_B}{h^2} \right)^{3/2} \frac{k_B T}{P} \right] + \frac{5}{2} \right), \tag{D.4}$$

where σ_{rot} is the rotational symmetry number (6 for CH_3 and 1 for HCO), $\theta_{r,i} = B_i h / k_B$ with B_i the ith axis rotational constant (in s^{-1}), m is the mass of the radical and P the gas pressure, which was calculated assuming a density of 10^4 cm^{-3}.

The thermal corrections follow: $H = E_{DFT} + ZPE + E_{vib}(T) + k_B T$ for the surface and the surface + radical complex. Here E_{DFT} is the energy obtained from our DFT calculations, ZPE is the zero-point energy and $E_{vib}(T)$ is the thermal vibrational energy calculated with eq. D.5. In analogy to to the entropy, the rotational and translational contributions are also included for the free radicals: $H = E_{DFT} + ZPE + E_{vib}(T) + k_B T + H_{rot} + H_{trans}$ where $H_{rot} = H_{trans} = \frac{3}{2} k_B T$.

$$E_{vib}(T) = k_B \sum_i \frac{\theta_{v,i}}{e^{\theta_{v,i}/T} - 1} \tag{D.5}$$

The magnitude of these contributions is shown in Table D.4, where it can be seen that the most important contribution to the enthalpy comes from the vibrational modes, while for entropy all contributions are rather small:

Table D.4: *Corrections incorporated in the calculation of ΔG of binding. Quantities calculated at 20 K and 30 K. Energy and entropy units are kJ mol-1 and kJ mol-1 K^{-1}. See that Boltzmann's constant is about 0.0083 kJ mol^{-1}, therefore the $k_B T$ and $3k_B T/2$ terms are also very small.*

	T = 20 K				T = 30 K			
	ΔE_{vib}	ΔS_{vib}	S^{rad}_{rot}	S^{rad}_{trans}	ΔE_{vib}	ΔS_{vib}	S^{rad}_{rot}	S^{rad}_{trans}
CH_3	0.124	-0.007	0.010	0.005	0.293	-0.003	0.015	0.011
HCO	0.077	-0.012	0.034	0.011	0.228	-0.009	0.039	0.016

As it was explained in the introduction, we have adopted the assumption that the barrier for diffusion can be expressed as a fraction of that of desorption, therefore in this model we multiply the ΔG of desorption times these fractions (assumed to be 0.3, 0.4 and 0.5). With this, we get different attempt frequencies for

diffusion and desorption (see Table D.5), all around 10^8–10^{11} s^{-1}, smaller than the normally used approach of the harmonic oscillator[1] in astrochemical models (e.g. Tatsuhiko I. Hasegawa et al., 1992; Tielens et al., 1987) due to the use of Eyring's relation and the inclusion of entropy.

Table D.5: *Attempt frequencies for desorption and the different cases of diffusion considered in this work. Units in s^{-1}. See that at 20 K $k_BT/h \sim 4.2 \times 10^{11}$, so the effect of entropy at such low temperatures is very small.*

	Eyring equation (computed at 20 K)				Harmonic oscillator
	Desorption	Diffusion			
Diff-to-Des	–	0.5	0.4	0.3	–
$\nu(CH_3)$	4.7×10^8	1.1×10^{11}	1.4×10^{11}	1.9×10^{11}	1.5×10^{12}
ν(HCO)	2.9×10^{10}	1.4×10^{10}	2.8×10^{10}	5.4×10^{10}	1.5×10^{12}

[1] $\nu = \sqrt{2N_s E_{bind}/\pi^2 m}$, with N_S the density of sites, $\sim 10^{15}$ and m the mass of the particle.

D.3 Rate constant comparison

Figure D.2 compares the rates of the radical-radical reactions with the hopping and desorption rates for each radical species, using three different criteria for the diffusion barrier, namely making it 0.3, 0.4 and 0.5 times those of desorption.

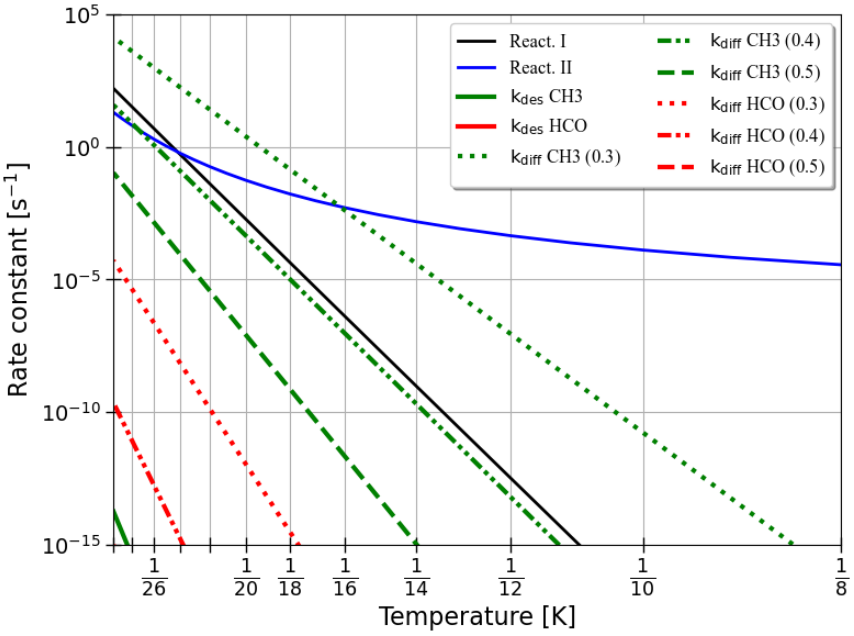

Figure D.2: *Comparison of reaction, diffusion and desorption rate constants involved in the CH_3 + HCO system. Notice that the desorption rate of HCO is not seen as it appears at very low rate constant values. Numbers in brackets indicate the diffusion-to-desorption energy barrier ratio.*

D.4 H + CO data

Table D.6: *H + CO $\rightarrow$ HCO energetic data, in Hartree, at UBHandHLYP-D3(BJ)/6-31+G(d,p) (double ζ) level. U is the DFT energy, D is the Dispersion energy and ZPE is the zero-point energy. DFT energies were refined by performing single point calculations on double ζ geometries at UBHandHLYP-D3(BJ)/6-311++G(2df,2pd) (triple ζ) level. Energy units are Hartree (1.0 Hartree are $\sim$ 2625.5 kJ mol^{-1}).*

$H + CO$	Reactant	TS	Product
U (double ζ)	-2558.84099479	-2558.83665194	-2558.88783666
D (double ζ)	-0.08428582	-0.08266012	-0.08407096
ZPE (double ζ)	0.86306000	0.86239000	0.872578000
U (triple ζ)	-2559.79323262	-2559.78741062	-2559.83765264

Table D.7: *H$\cdots$CO transition state data. Units are the usual for a* GAUSSIAN16 *output: frequencies in cm^{-1}, IR intensities in KM/Mole, reduced masses in AMU and force constants in mDyne/Å. At UBHandHLYP-D3(BJ)/6-31+G(d,p) level.*

	$i\nu$	red mass	F ctn	IR int
$H + CO$	605.7354	1.1042	0.2387	14.8487

D.5 Radical-radical TS data:

Table D.8: *CH_3 + HCO energetic data, in Hartree, at UBHandHLYP-D3(BJ)/6-31+G(d,p) level (double ζ). U is the DFT energy, D is the Dispersion energy and ZPE is the zero-point energy. DFT energies were refined by performing single point calculations on double ζ geometries at UBHandHLYP-D3(BJ)/6-311++G(2df,2pd) (triple ζ) level. Energy units are Hartree (1.0 Hartree are $\sim$ 2625.5 kJ mol^{-1}).*

React. I	Reactant	TS	Product
U (double ζ)	-2675.130087	-2675.127479	-2675.266272
D (double ζ)	-0.091309097	-0.091229233	-0.088094692
ZPE (double ζ)	0.933864	0.933528	0.94406
U (triple ζ)	-2676.122287	-2676.119848	-2676.253986
React. II	Reactant	TS	Product
U (double ζ)	-2675.130087	-2675.12475	-2675.255587
D (double ζ)	-0.091309097	-0.092369778	-0.091838262
ZPE (double ζ)	0.933864	0.933255	0.938711
U (triple ζ)	-2676.122287	-2676.118937	-2676.250317

Table D.9: *Features of the transition states studied in this work. Units are the usual for a* GAUSSIAN16 *output: frequencies in cm^{-1}, IR intensities in KM/Mole, reduced masses in AMU and force constants in mDyne/Å. At UBHandHLYP-D3(BJ)/6-31+G(d,p) level.*

	reaction I				reaction II			
	$i\nu$	red mass	F ctn	IR int	$i\nu$	red mass	F ctn	IR int
CH_3 + HCO	91.0685	4.7645	0.0233	0.5366	168.6488	1.8100	0.0303	16.6868

D.6 Efficiency figures, separated by E_{diff}/E_{des} ratios

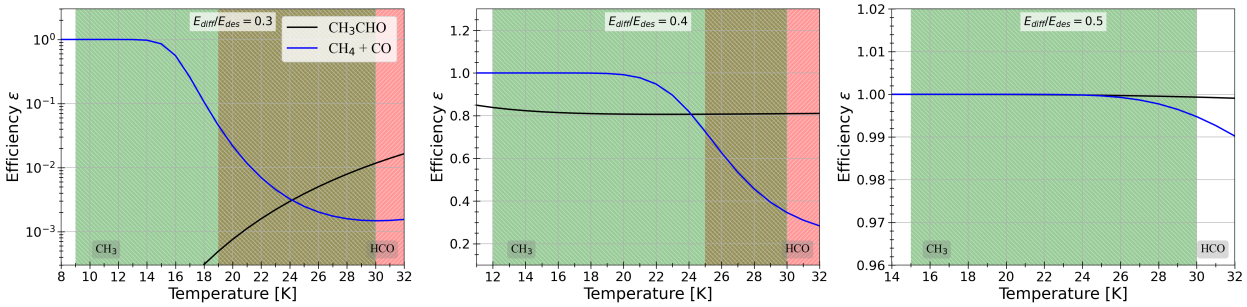

Figure D.3: *CH3 + HCO reaction efficiencies ε (Eq. 9.3), assuming diffusion barriers 0.3, 0.4 and 0.5 times those of desorption (panels from left to right). The green-colored regions indicate the diffusion and desorption temperatures limits of CH3, while the red ones are the same for HCO.*

D.7 Fittings to k_{aeb} and ε:

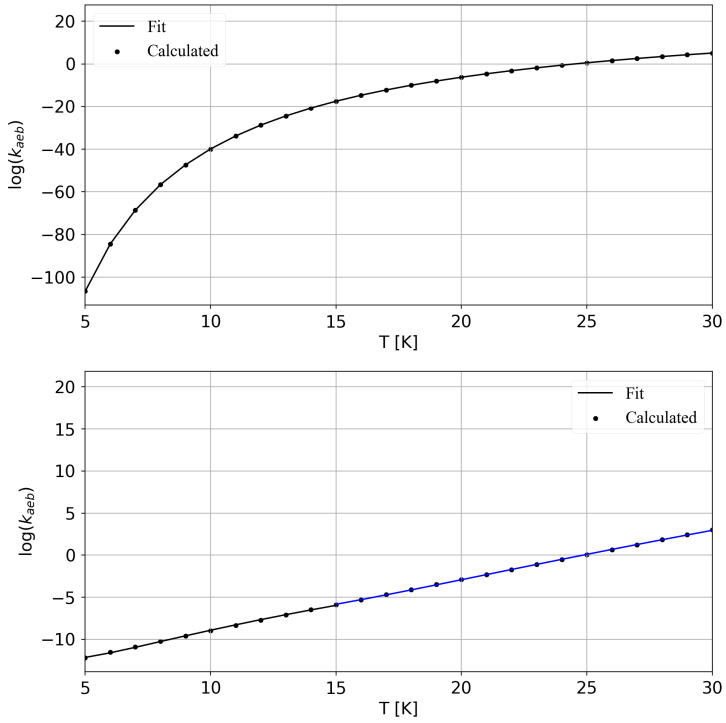

Figure D.4: *Fittings to the computed rate constants (Figure 9.3) with eq. 9.9 for reactions* I *(upper panel) and* II *(lower panel).*

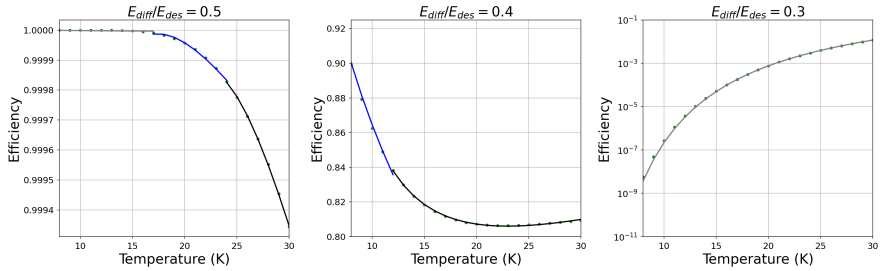

Figure D.5: *Fittings (solid lines) to the computed efficiency factors (points) using eq. 9.9 for acetaldehyde using* $E_{diff}/E_{des} = 0.5$, 0.4 *and* 0.3 *(left to right panels).*

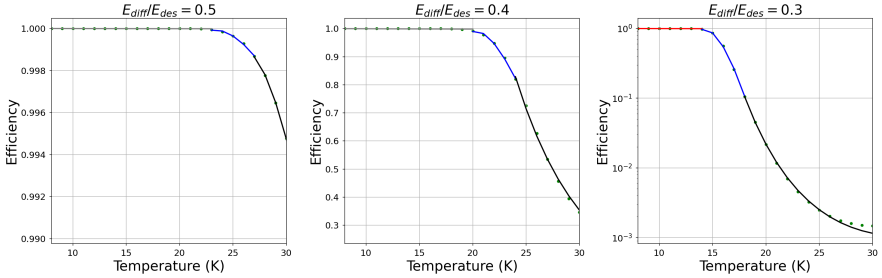

Figure D.6: *Fittings (solid lines) to the computed efficiency factors (points) using eq. 9.9 for CO + CH_4 formation using* $E_{diff}/E_{des} = 0.5$, 0.4 *and* 0.3 *(left to right panels).*

D.8 Calculation of diffusion and desorption temperatures

Half-lives are calculated from the rate constants (k_i, with i either diffusion of desorption of radicals) following

$$N_{1/2} = N_0 \exp(-k_i t) \qquad \Longrightarrow \qquad t_{1/2} = \frac{\ln(2)}{k_i},$$

and shown in Fig. D.7.

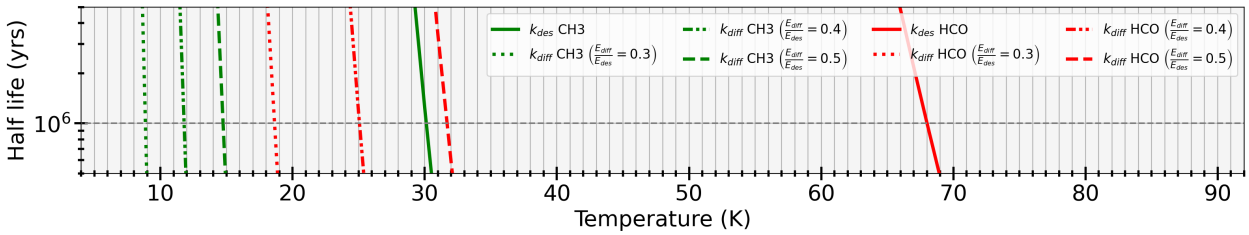

Figure D.7: *Diffusion and diffusion temperatures of CH_3 and HCO assuming a half-life of 1 Myrs for desorption.*

Chapter E
Supporting data for Chapter 11

Outline

E.1 Spin densities

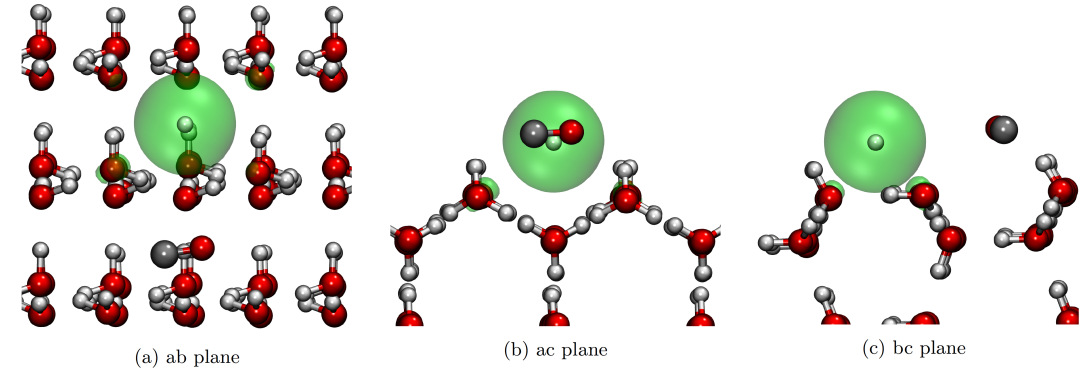

(a) ab plane (b) ac plane (c) bc plane

Figure E.1: *Spin density of the two reactants adsorbed on the (100) P-ice surface.*

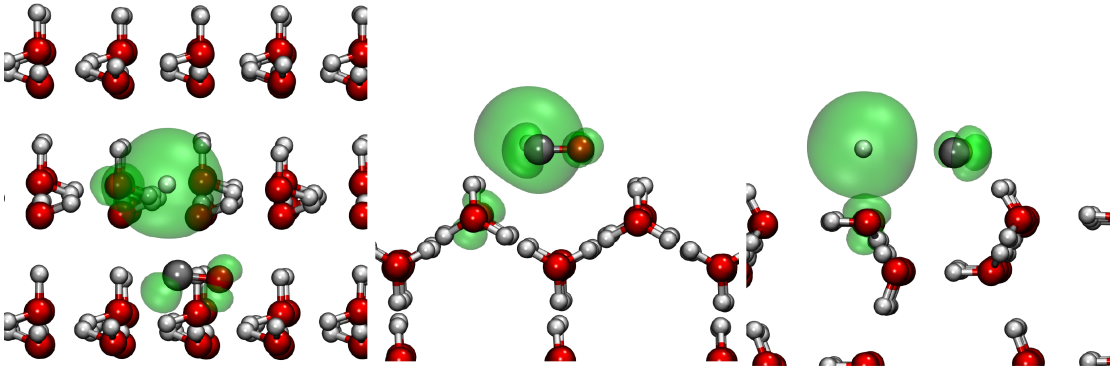

(a) ab plane (b) ac plane (c) bc plane

Figure E.2: *Spin density of the transition state adsorbed on the (100) P-ice surface.*

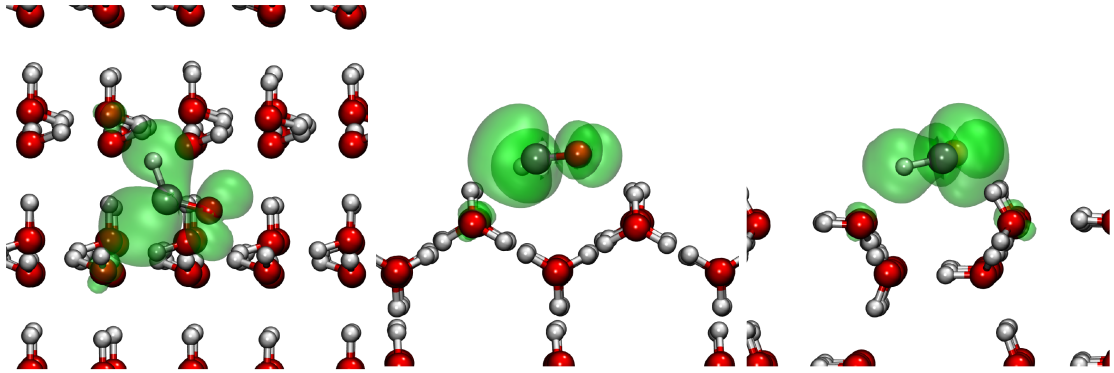

(a) ab plane (b) ac plane (c) bc plane

Figure E.3: *Spin density of the product adsorbed on the (100) P-ice surface.*

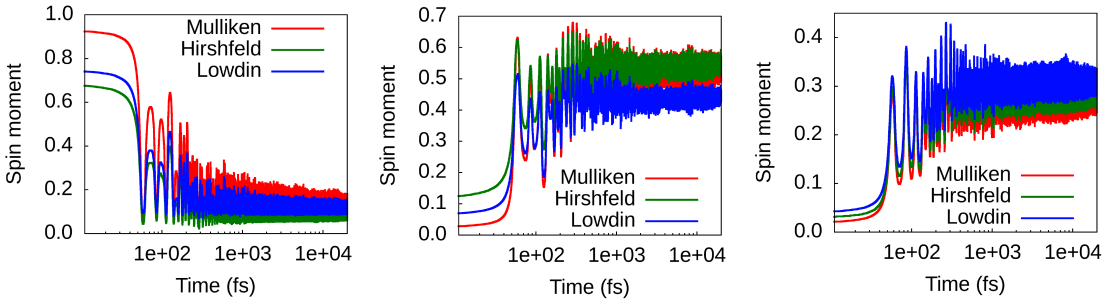

(a) ab plane (b) ac plane (c) bc plane

Figure E.4: *Spin density evolution of H, C and O atoms belonging to the HCO radical during the AIMD simulation.*

E.2 Extra positions, initial and final geometries

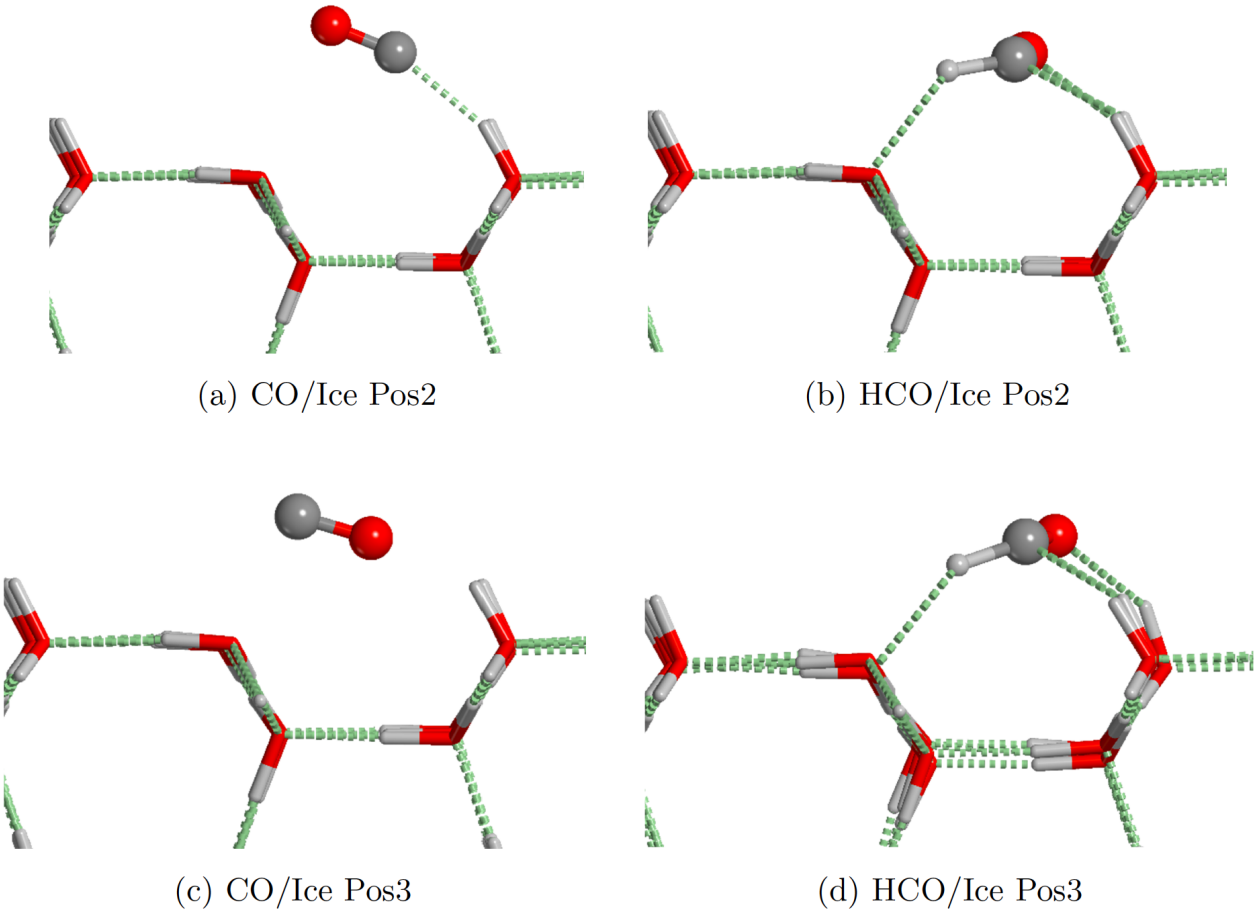

Figure E.5: *PBE-D3/TZV2P optimized structure of Pos2 reactant (a) and product (b) on the crystalline ice surface. PBE-D3/TZV2P optimized structure of the Pos3 reactant (c) and 2 picoseconds AIMD snapshot (d) on the crystalline ice surface.*

E.3 Temperature and Potential energy evolution

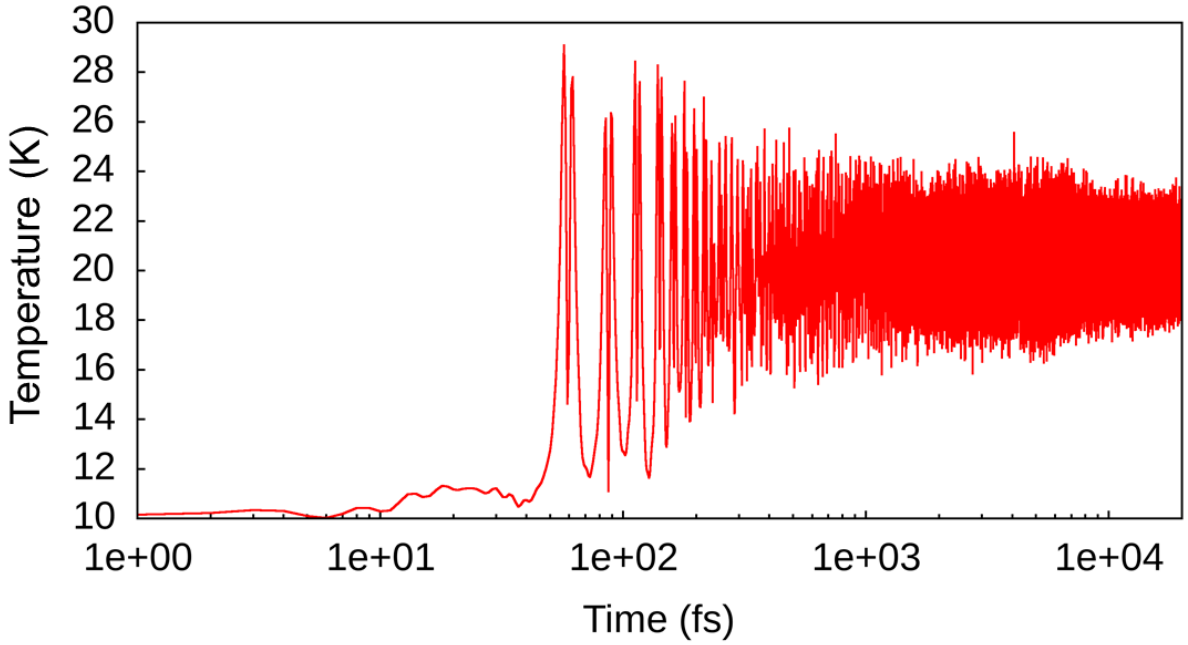

Figure E.6: *Evolution of the temperature during the AIMD simulation.*

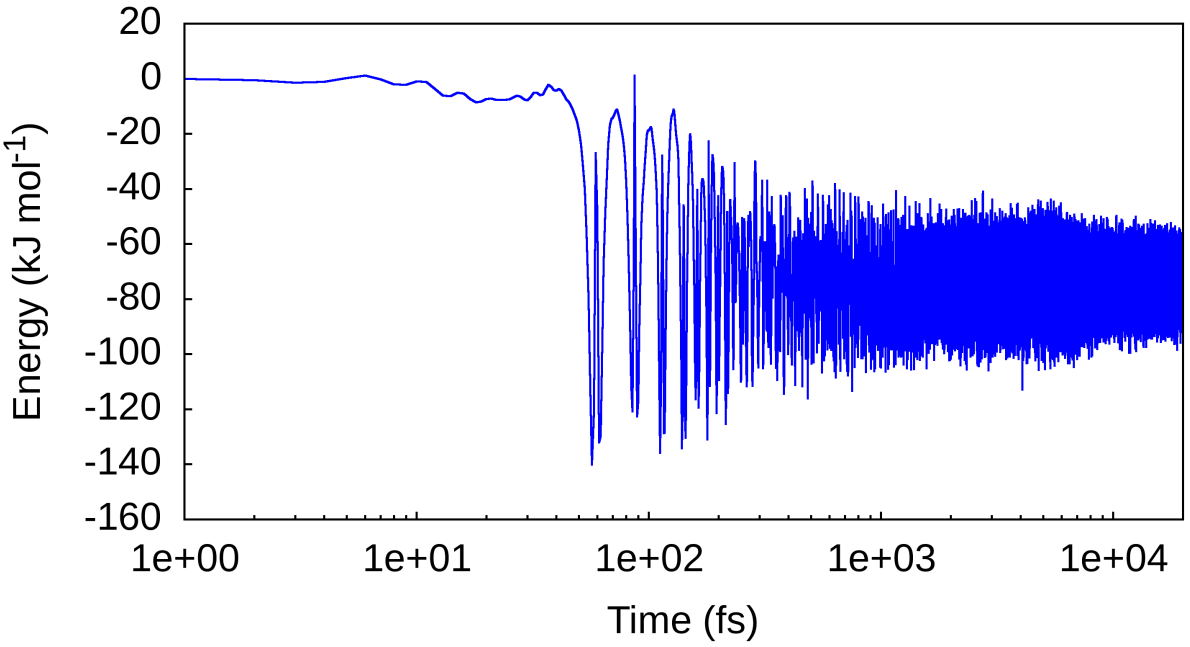

Figure E.7: *Evolution of the potential energy during the AIMD simulation.*

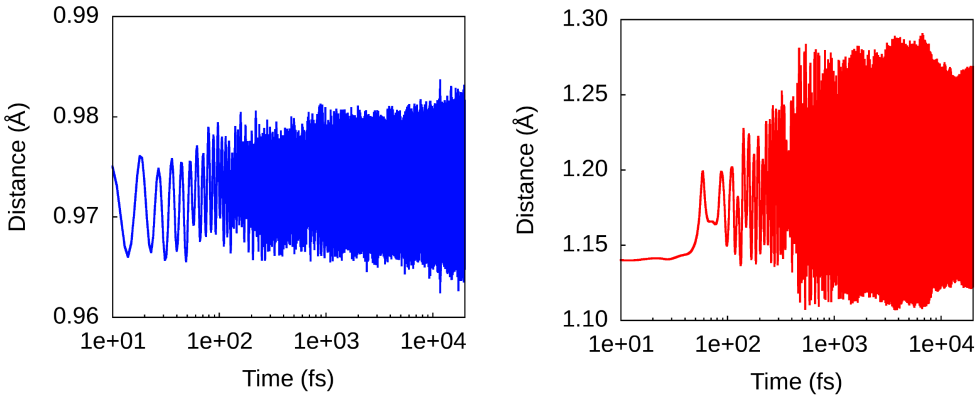

(c) OH bond

(b) CO bond

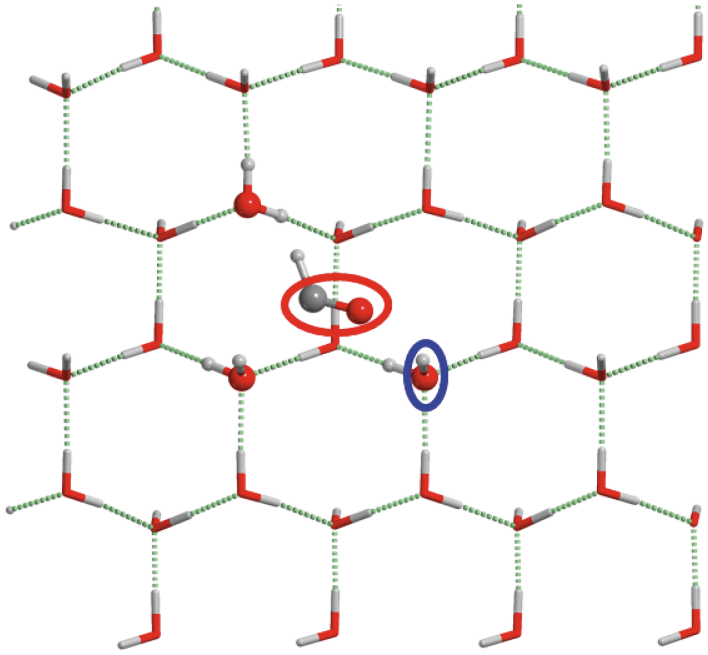

(a) HCO/Ice structure

Figure E.8: *CO and OH bonds evolution along the MD simulation. Colored lines in the graphs corresponds to the colored circles in the top view structure of the HCO/Ice system.*

E.4 Shell division

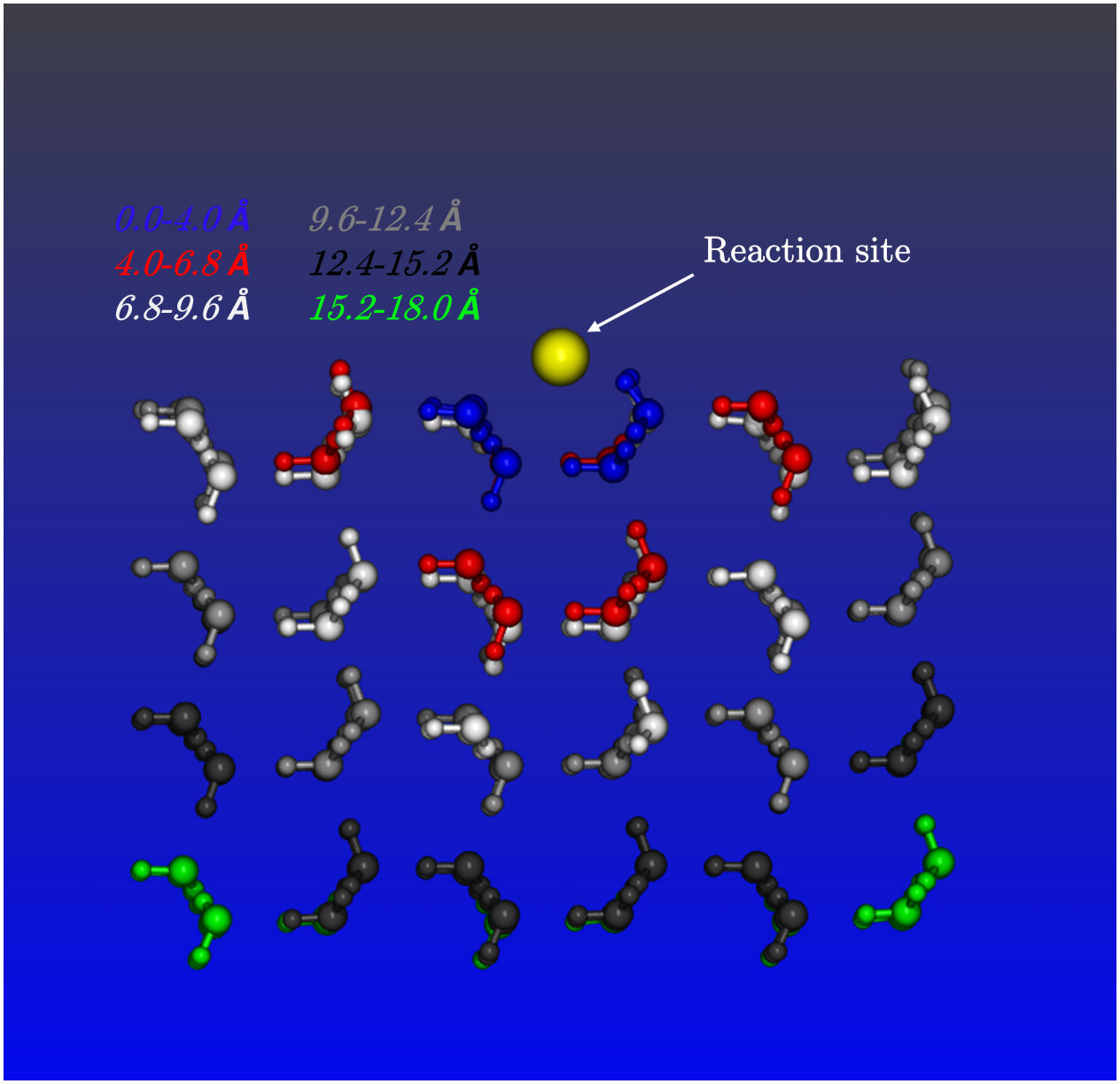

Figure E.9: *Graphic representation of the shell division of the water ice structure, each one in a different color. This is the shell structure used in the energy dissipation analysis. The reaction center, defined as the C atom of HCO at the first AIMD step, is highlighted in yellow. Note that the ice structure was cut in half for the sake of clarity.*

E.5 Kinetic energy evolution for each shell

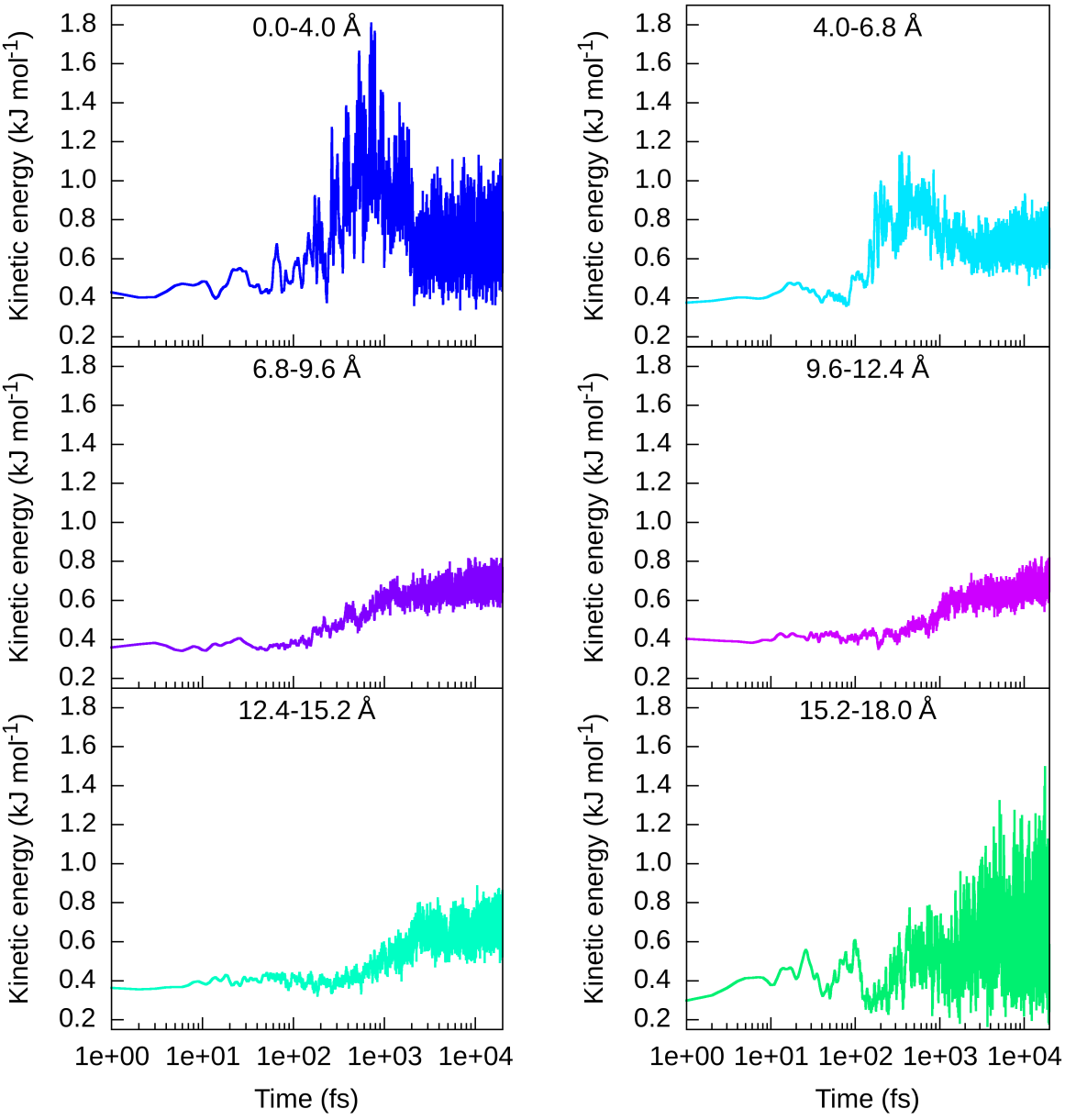

Figure E.10: *Kinetic energy evolution (in kJ mol^{-1}) of the ice surface. The ranges in the legend refer to the shells the water molecules belong to. The energy was normalized per water molecule.*

Chapter F
Supporting data for Chapter 12

Outline

F.1 H–H bond distance evolution during the simulations

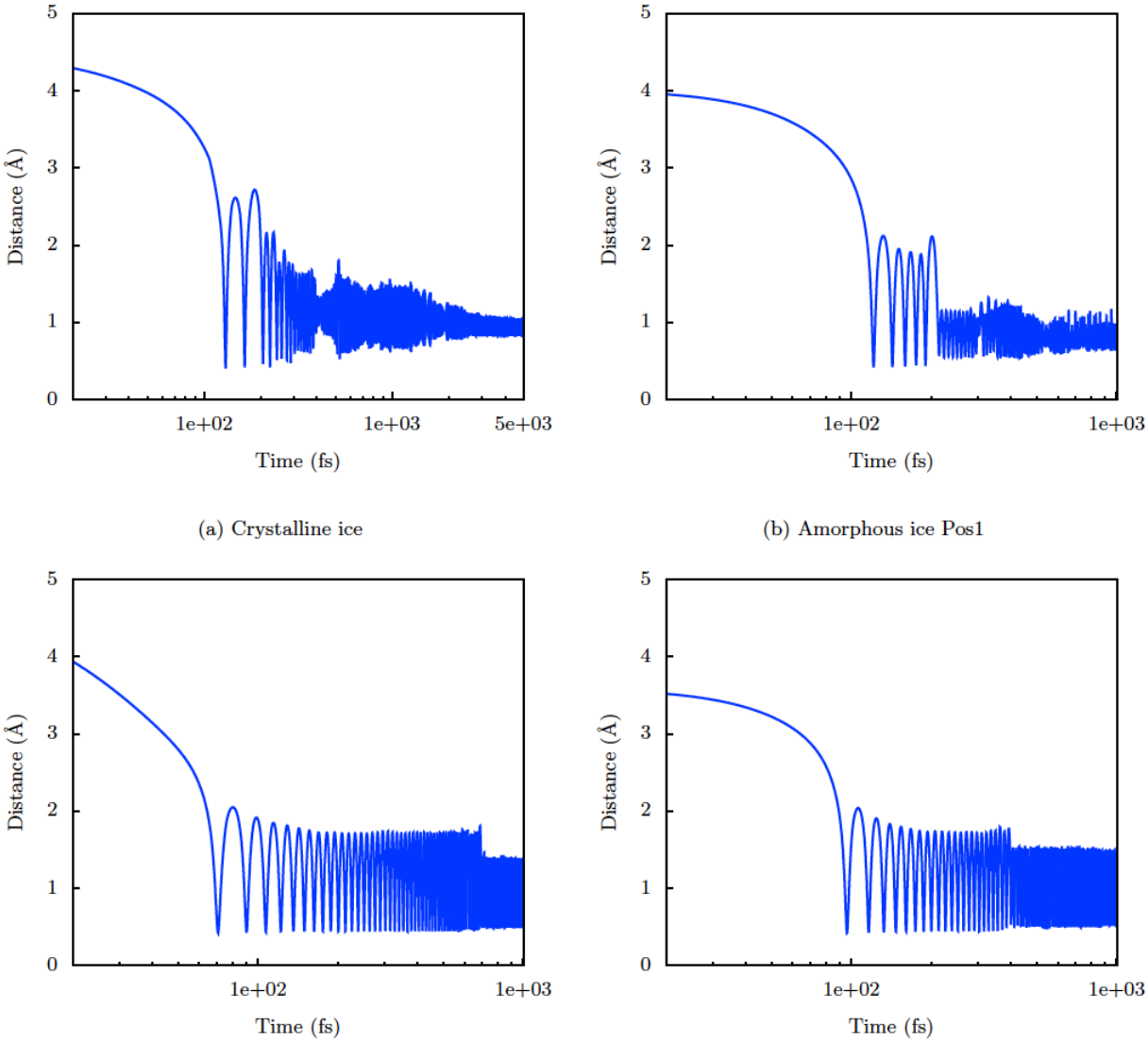

Figure F.1: *Evolution of the H–H bond distance during the AIMD simulations.*

F.2 Electrostatic potential maps

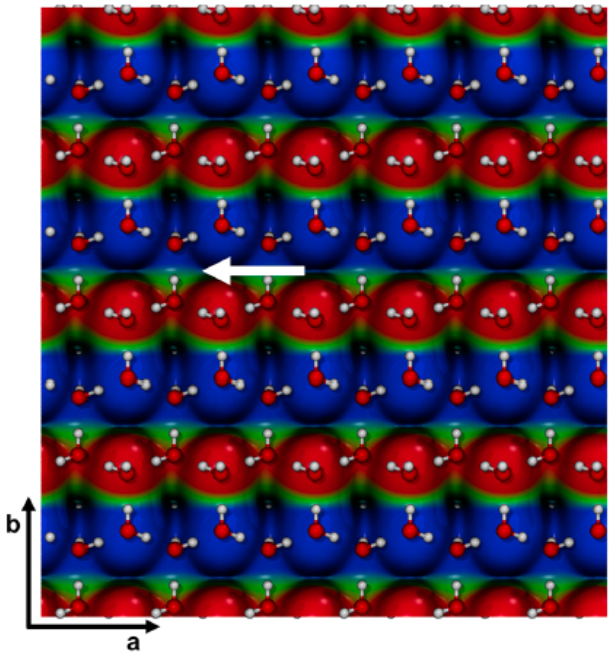

(a) Crystalline ice: top view

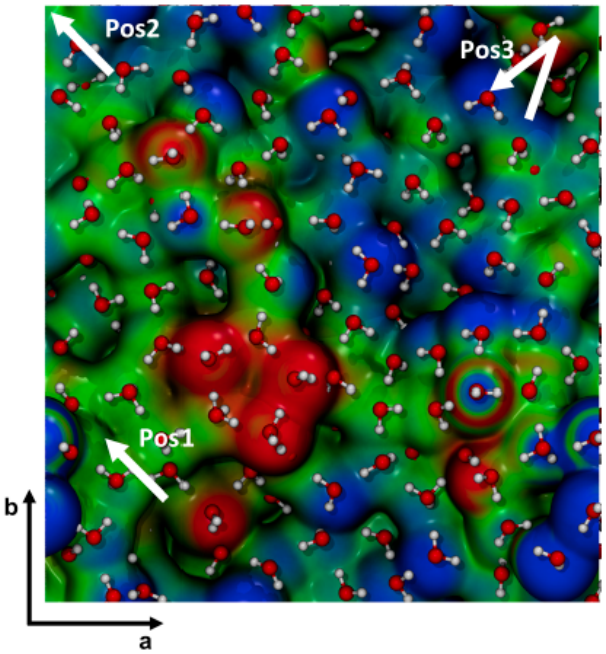

(b) Amorphous ice: top view

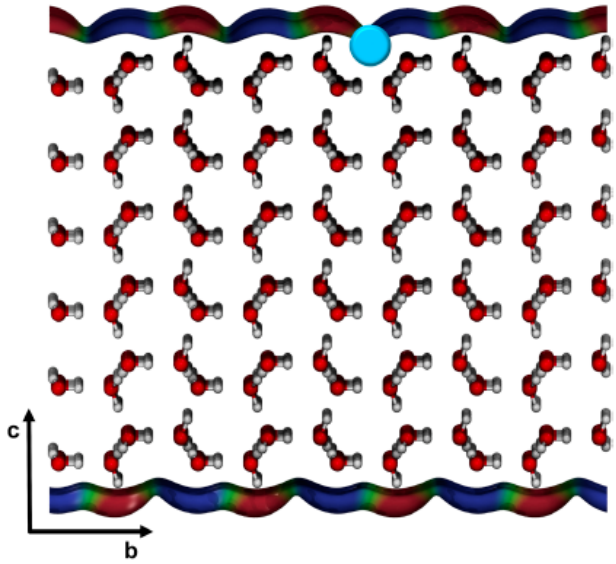

(c) Crystalline ice: lateral view

Figure F.2: *Top view of the electrostatic potential map of the crystalline (a) and amorphous (b) ice models. Lateral view of the crystalline ice model (c). White arrows represent the H_2 diffusion direction. The light blue circle in the bottom panel represents the cavity inside of which the H_2 diffuses over the crystalline ice model. Red and blue zones of the electrostatic maps correspond to positive and negative potentials. O atoms in red, H atoms in white.*

F.3 Kinetic energy evolution of H2 and a nearby water molecule on the amorphous ice model at Pos1

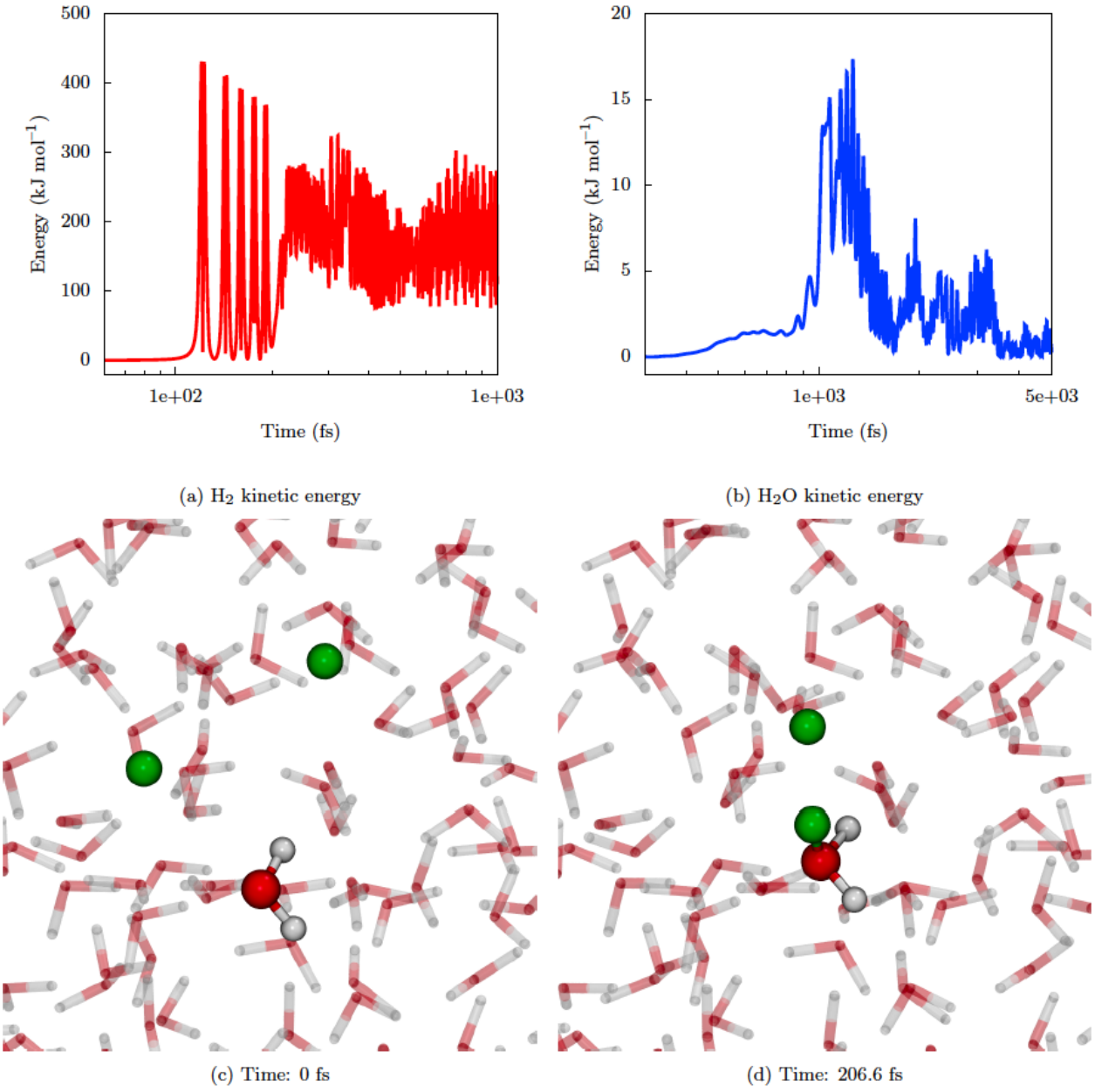

(a) H_2 kinetic energy

(b) H_2O kinetic energy

(c) Time: 0 fs

(d) Time: 206.6 fs

Figure F.3: *Evolution of the kinetic energy of H_2 (panel (a)) and a neighbor water molecule (panel (b)) for the amorphous Pos1 case. Starting position of the AIMD simulation (panel (c)) and formation of the H^-/H_3O^+ adduct after 0.2 picoseconds of simulation (panel (d)). O atoms in red, H atoms in white. The H atoms highlighted in green are the reactants.*

List of useful abbreviations

Find here a list of the most used abbreviations.

- AIMD: *Ab Initio* molecular dynamics
- AO: Atomic orbital
- ASW: Amorphous solid water
- AWS: Amorphous water surface
- BE: Binding energy
- BHLYP: Becke's half and half exchange DFT functional combined with the LYP correlation one
- BHLYP: Becke's 3 parameters DFT functional
- BO, BOA: Born Oppenheimer Approximation
- BS-DFT: Broken (spin) symmetry DFT
- BSSE: Basis set superposition error correction
- CASPT2: Complete active space self consistent field combined with second order perturbation theory
- CASSCF: Complete active space self consistent field
- CCSD(T): Coupled cluster singles and doubles corrected for triples with perturbation theory
- CI: Configuration interaction
- CISD: Configuration interaction with single and double excitations
- CP2K: Carr Parrinello 2000, a computational chemistry software used for AIMD calculations
- CR: Cosmic ray
- D3, D3(BJ): Grimme's three body dispersion term, whithout and with the Becke-Johnson dampin corrections
- dHa: Direct H-abstraction reaction
- ER: Eley Rideal surface reaction mechanism
- GGA: Generalized gradient approximation
- GPW: Gaussian and plane waves, a type of basis set for PBC calculations
- HF: Hartree Fock
- iCOM:Interstellar complex organic molecule
- ISM: Interstellar medium
- JWST: James Webb space telescope
- KS: Kohn Sham
- LH: Lamgmuir Hinshelwood, a surface reaction mechanism
- LSDA: Local spin density approximation
- MCSCF: Multiconfigurational self consistent field
- MD: Molecular dynamics
- MP2: Møller Plesset 2nd order perturbation theory method
- NVE: Microcanonical ensemble (N = number of particles, V = volume, E = total energy)
- NVT: Canonical ensemble (N = number of particles, V = volume, T = temperature)
- PBC: Periodic boundary conditions
- PES: Potential energy surface
- RAS: Restricted active space
- Rc: Radical coupling reaction
- RHF: Restricted Hartree-Fock
- RRKM: Rice–Ramsperger–Kassel–Marcus theory (a.k.a microcanonical TST)

- SCF: Self consistent field
- SD: Slater determinant
- TST: Transition state theory
- TZVP: Tripleζ quality basis set for valence electrons with polarization functions
- UHF: Unrestricted Hartree Fock
- W18: Our 18 molecules ASW model
- W33: Our 33 molecules ASW model
- wHt: Water assisted H-transfer
- ZPE: Zero point (vibrational) energy

List of Figures

List of Tables

Published and accepted articles

Monthly Notices
of the
ROYAL ASTRONOMICAL SOCIETY

MNRAS **493,** 2523–2527 (2020)
Advance Access publication 2020 February 20

doi:10.1093/mnras/staa484

Revisiting the reactivity between HCO and CH_3 on interstellar grain surfaces

J. Enrique-Romero,[1,2★] S. Álvarez-Barcia,[3] F. J. Kolb,[3] A. Rimola,[2★] C. Ceccarelli,[1] N. Balucani,[1,4,5] J. Meisner,[3,6,7] P. Ugliengo,[8] T. Lamberts[3,9] and J. Kästner[3]

[1]*Univ. Grenoble Alpes, CNRS, Institut de Planétologie et d'Astrophysique de Grenoble (IPAG), F-38000 Grenoble, France*
[2]*Departament de Química, Universitat Autònoma de Barcelona, E-08193 Bellaterra, Catalonia, Spain*
[3]*Institut für Theoretische Chemie, Universität Stuttgart, Pfaffenwaldring 55, D-70569 Stuttgart, Germany*
[4]*Dipartamento di Chimica, Biologia e Biotecnologie, Università degli Studi di Perugia, Via Elce di Sotto 8, I-06123 Perugia, Italy*
[5]*Osservatorio Astrofisico di Arcetri, Largo E. Fermi 5, I-50125 Firenze, Italy*
[6]*Department of Chemistry and The PULSE Institute, Stanford University, Stanford, CA 94305, USA*
[7]*SLAC National Accelerator Laboratory, Menlo Park, CA 94025, USA*
[8]*Dipartamento di Chimica and Nanostructured Interfaces and Surfaces (NIS), Università degli Studi di Torino, Via P. Giuria 7, I-10125 Torino, Italy*
[9]*Leiden Institute of Chemistry, Gorleaus Laboratories, Leiden University, PO Box 9502, NL-2300 RA Leiden, the Netherlands*

Accepted 2020 February 14. Received 2020 February 14; in original form 2019 December 11

ABSTRACT

The formation of interstellar complex organic molecules is currently thought to be dominated by the barrierless coupling between radicals on the interstellar icy grain surfaces. Previous standard density functional theory (DFT) results on the reactivity between CH_3 and HCO on amorphous water surfaces showed that the formation of CH_4 + CO by H transfer from HCO to CH_3 assisted by water molecules of the ice was the dominant channel. However, the adopted description of the electronic structure of the biradical (i.e. CH_3/HCO) system was inadequate [without the broken-symmetry (BS) approach]. In this work, we revisit the original results by means of BS-DFT both in gas phase and with one water molecule simulating the role of the ice. Results indicate that the adoption of BS-DFT is mandatory to describe properly biradical systems. In the presence of the single water molecule, the water-assisted H transfer exhibits a high energy barrier. In contrast, CH_3CHO formation is found to be barrierless. However, direct H transfer from HCO to CH_3 to give CO and CH_4 presents a very low energy barrier, hence being a potential competitive channel to the radical coupling and indicating, moreover, that the physical insights of the original work remain valid.

Key words: astrochemistry – molecular processes – ISM: clouds – ISM: molecules.

1 INTRODUCTION

Interstellar complex organic molecules (iCOMs) are usually defined as compounds of 6–13 atoms in which at least one is C (Herbst & van Dishoeck 2009; Ceccarelli et al. 2017; Herbst 2017). They are complex only from the astronomical point of view, while they are the simplest organic compounds according to terrestrial standards. Since terrestrial life is based on organic chemistry, the existence of iCOMs is of fundamental importance to ultimately understand the possible astrochemical origins of life.

iCOMs are widespread in the Universe. They have been detected in a great variety of astrophysical objects like star-forming regions (e.g. Rubin et al. 1971; Cazaux et al. 2003; Kahane et al. 2013; Mendoza et al. 2014; López-Sepulcre et al. 2015; Belloche et al. 2017; Ligterink et al. 2017; McGuire et al. 2018), in the circumstellar envelopes of AGB stars (Cernicharo, Guélin & Kahane 2000), shocked regions (Arce et al. 2008; Codella et al. 2017; Lefloch et al. 2017), and even in external galaxies (Muller et al. 2013). Despite their presence has been known for decades, how iCOMs are synthesized is still an open question and under debate (Herbst & van Dishoeck 2009; Caselli & Ceccarelli 2012; Woods et al. 2013; Balucani, Ceccarelli & Taquet 2015; Fedoseev et al. 2015; Enrique-Romero et al. 2016; Butscher et al. 2017; Gal et al. 2017; Rivilla et al. 2017; Vasyunin et al. 2017; Rimola et al. 2018; Butscher et al. 2019; Enrique-Romero et al. 2019; Lamberts et al. 2019). Two different paradigms have been proposed: (i) on the surfaces of grains (either during the cold pre-stellar or warmer collapse phase (e.g. Garrod & Herbst 2006; Woods et al. 2013; Fedoseev et al. 2015; Öberg 2016), and (ii) through reactions in the gas phase (e.g. Charnley, Tielens & Millar 1992; Balucani et al. 2015; Skouteris et al. 2018). The first paradigm assumes that whenever two radicals (e.g. created by UV photon and/or cosmic ray incidences) are in

★ E-mail: juan.enrique-romero@univ-grenoble-alpes.fr (JER); albert.rimola@uab.cat (AR)

close proximity (e.g. because of their diffusion) they can react to form iCOMs in a barrierless way. In the second one, iced simple hydrogenated molecules are released into the gas phase (e.g. due to thermal desorption), where they react to form iCOMs through gas-phase reactions. Interestingly, a review on the formation of iCOMs on interstellar grain surfaces investigated by means of quantum chemical calculations has recently appeared (Zamirri et al. 2019).

Currently, the 'on-surface' paradigm is the scheme mostly adopted in astrochemical models. However, a first theoretical study of the reactivity of HCO and CH_3 on an amorphous water surface (AWS), which is the bulk of the ices that envelope interstellar grains in cold objects, showed that the combination of these two radicals does not necessarily lead to the formation of the iCOM acetaldehyde (CH_3CHO) (Enrique-Romero et al. 2016). This unexpected result called for and was followed by other studies of different systems and with different computational methods. First, Rimola et al. (2018) and Enrique-Romero et al. (2019) studied the formation of formamide (NH_2CHO) and acetaldehyde by reactions between HCO and NH_2 and HCO and CH_3 on an AWS model by means of static quantum chemical calculations. Subsequently, Lamberts et al. (2019) studied the formation of acetaldehyde by reaction between HCO and CH_3 on a CO-pure ice model by means of *ab initio* molecular dynamics simulations. The three works confirmed the main finding by Enrique-Romero et al. (2016), namely that the reactivity between the radical pairs does not lead exclusively to the formation of the iCOMs, but the formation of CO + NH_3 and CO + CH_4 via direct H abstraction can also take place. In view of these results, the formation of iCOMs via the barrierless radical–radical combination scheme still needs to be validated.

In this article, we aim to revise the first calculations carried out on the CH_3 + HCO system (Enrique-Romero et al. 2016), which were based on the standard density functional theory (DFT) approach. Since then, it has become clear that an improved treatment of the radical spins is necessary (Rimola et al. 2018; Enrique-Romero et al. 2019). The article is organized as follows: In Section 2, we review the treatment of the spins of a biradical system, in Section 3 we provide the details of the new computations carried out in this article, in Section 4 we show the results, and in Section 5 we discuss the conclusions.

2 WHY A BETTER TREATMENT OF THE BIRADICAL WAVEFUNCTION IS NEEDED

In a previous work by some of us (Enrique-Romero et al. 2016), the reactivity between HCO and CH_3 in the gas phase and on AWS modelled by H_2O ice clusters was theoretically studied with standard DFT calculations. In the gas-phase model,[1] different synthetic channels were identified, namely the formation of acetaldehyde (CH_3CHO), CO + CH_4, and CH_3OCH, the occurrence of which being determined by the relative orientation of the radicals. In contrast, on the AWS models, a hydrogen-atom relay mechanism assisted by water molecules of the ice led to the exclusive formation of CO + CH_4.

The electronic ground state for the CH_3CHO, CO + CH_4, and CH_3OCH products is a singlet wavefunction as they are closed-shell systems. Conversely, the HCO and CH_3 radicals are open-shell doublet systems due to their unpaired electron, while a system consisting of the two radicals (i.e. HCO and CH_3 together) can be either in triplet or singlet electronic states (the spins of the unpaired electrons can be of the same sign or of opposite signs, respectively). The triplet state is electronically non-reactive due to the Pauli repulsion. In contrast, the singlet state (usually referred to as a biradical system) is reactive because of the opposite spin signs. The description of the electronic structure of biradical states requires a wavefunction composed of more than one Slater determinant to recover static correlation. In the wavefunction-based post-Hartree–Fock (post-HF) realm, this can be described by multiconfigurational self-consistent field (MCSCF) methods, such as the complete active space self-consistent field (CASSCF), or the so-called multireference methods like the complete active space perturbation theory (CASPTn) ones. In CASSCF, a particular number of electrons (N) are distributed between all possible (namely, ground and excited) configurations that can be constructed from M molecular orbitals, i.e. a (N, M) active space. It is worth mentioning that one has to pay special care when deciding the orbitals to include in the active space, since the resulting wavefunction could erroneously describe the system under study. CASPTn is an improvement over CASSCF(N, M) where a perturbative expansion is further performed in order to retrieve more dynamic electron correlation. On the other hand, such a multireference character cannot be obtained from normal Kohn–Sham DFT. Instead, the electronic structure of biradicals can be approximated by an unrestricted open-shell wavefunction with the broken-(spin)-symmetry *ansatz*, where a triplet state is mixed with a combination of ground and excited singlet states in order to obtain an electron-correlated wavefunction (Noodleman 1981; Noodleman & Baerends 1984; Neese 2004).

Calculations by Enrique-Romero et al. (2016) were performed in an open-shell formalism, but after publication we realized that the initial guess wavefunctions remained in a metastable, symmetric state with spin-up and spin-down orbitals being equally mixed (i.e. spin analysis indicated 50 per cent of spin-up and 50 per cent of spin-down in both radicals and the total spin density being zero), thus resembling a closed-shell solution. Compared to that, the actual broken-symmetry (BS) wavefunction leads to a significant stabilization of the reactants, which changes the results qualitatively. Thus, this work aims to revise some of the original results using the DFT BS solution, showing, moreover, that it agrees reasonably well with those at the CASPT2 level.

3 COMPUTATIONAL DETAILS

All DFT calculations were performed using the GAUSSIAN09 package (Frisch et al. 2009), while post-HF multiconfigurational and multireference calculations were carried out with the OPENMOLCAS 18.09 software (Karlström et al. 2003; Aquilante et al. 2010; Aquilante et al. 2016; Fernandez Galván et al. 2019).

DFT geometry optimizations and transition state searches were carried out with (i) the M06-2X (Zhao & Truhlar 2008) and (ii) BHLYP-D3 (i.e. BHLYP; Lee, Yang & Parr 1988; Becke 1993) including the Grimme's D3 dispersion correction (Grimme 2006; Grimme et al. 2010) functionals, in combination with a def2-TZVPD basis set. Structures with triplet electronic states were simulated with open-shell calculations based on an unrestricted formalism. Singlet biradical systems were calculated adopting an unrestricted BS approach. For the sake of comparison, for some cases, single point energy calculations adopting standard (i.e. non-BS) unrestricted (U) formalisms have also been carried out.

[1]We loosely use the term 'gas phase' to refer to systems where no water molecule is involved. The reader has to bear in mind that these reactions cannot take place in the ISM unless a third body (i.e. the grain) absorbs the released nascent energy.

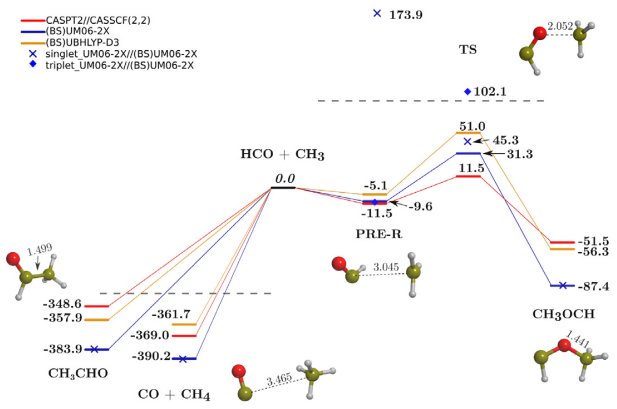

Figure 1. PESs at different DFT levels and at CASPT2 for the reactivity between CH_3 and HCO to form CH_3OCH (right side panel) or CO + CH_4 and CH_3CHO (left side panel). The energy reference 0.0 is the HCO + CH_3 asymptote. The dashed horizontal lines indicate broken vertical axis. PRE-R refers to the pre-reactant complexes and TS to the transition states. Single point energies at singlet and triplet UM06-2X levels on the (BS)UM06-2X optimized geometries are also shown. The presented structures correspond to the (BS)UM06-2X optimized geometries except for PRE-R, which is the triplet UM06-2X optimized geometry. Energy units are in kJ mol^{-1} and distances are in Å. We have also checked the triplet state of the CH_3OCH product resulting in 80 kJ mol^{-1} higher in energy than the singlet state and an energy barrier for its formation of about 55 kJ mol^{-1} higher than the singlet case (UM06-2X theory level).

CASSCF geometry optimizations and transition state searches were performed using a (2,2) active space, corresponding to the radical unpaired electrons in their respective orbitals. Reaction energetics were refined by performing CASPT2 single point energy calculations on the CASSCF(2,2) optimized geometries. In both cases, the cc-pVDZ basis set was employed. For the sake of clarity, here we only show the CASPT2 results, the CASSCF(2,2) ones being available as online supporting information (SI).

Since the scope of this work is to revise the electronic structure of the biradical systems, only electronic energy values are reported and accordingly zero-point energy corrections were not accounted for here.

Input file examples for this kind of calculations are provided in SI.

4 RESULTS

4.1 Reactions in the gas phase

In the gas phase, in agreement to the previous work Enrique-Romero et al. (2016), the nature of the final product depends on the relative initial orientations of the reactants. When the C atoms of the two radicals are pointing one to each other (i.e. $H_3C\cdots CHO$), they couple to form CH_3CHO; similarly, when the H atom of the HCO is pointing to the C atom of CH_3 (i.e. $OCH\cdots CH_3$), H is transferred to form CO + CH_4. Both processes have been found to be barrierless, irrespective of the method (i.e. BS-DFT and MCSCF; see the left-hand side of Fig. 1).

On the other hand, when the O atom of HCO points towards the C atom of CH_3 (i.e. $HCO\cdots CH_3$), the carbene CH_3OCH species can form. For this case, however, BS-DFT calculations indicate that the biradical system is metastable. Consequently, the formation of CH_3OCH is not spontaneous but it requires overcoming an energy barrier of 31.3 and 51.0 kJ mol^{-1} at the (BS)UM06-2X and (BS)UBHLYP-D3 levels, respectively. The same trend is found for CASPT2 calculations with an energy barrier of 11.5 kJ mol^{-1} (see the right-hand side of Fig. 1). It is worth mentioning that, for the formation of CH_3OCH, U single point calculations on the (BS)UM06-2X optimized geometries (without considering the BS approach) result in the spontaneous formation of CH_3OCH, leading to the same result as for the restricted situation (see singlet_UM06-2X energies in Fig. 1 represented by blue crosses). This is because the singlet UM06-2X initial guess wavefunction does not consider the reactant as an actual biradical system but the unpaired electrons are localized 50 per cent spin-up and 50 per cent spin-down in one radical and the same for the other radical, resembling an electronic closed-shell situation. This excited initial guess wavefunction is about 173.9 kJ mol^{-1} less stable than the asymptote (0.0 kJ mol^{-1}, corresponding to the situation where the radicals are infinitely separated) and hence the system rolls down to the most stable closed-shell situation. Similarly, single points at the triplet UM06-2X level on the (BS)UM06-2X optimized geometries are also shown in Fig. 1 (represented by blue diamonds). We want to stress out that triplet-state wavefunctions do not require the use of the BS *ansatz* as single-reference methods like UDFT already provide good descriptions of such open-shell systems, thanks to Pauli's exclusion principle.

4.2 Reactions in the presence of one water molecule

For the reactivity between CH_3 and HCO in the presence of one water molecule, we have studied the reactions of CH_3CHO formation through a radical–radical coupling (Rc) and the formation of CO + CH_4 through both a direct hydrogen abstraction (dHa), i.e. the H transfer is direct from HCO to CH_3, and a water-assisted hydrogen transfer (wHt), i.e. the H transfer is assisted by the water molecule, which allows a successive H-transfer mechanism $OC\cdot \cdot H\cdots HO\cdot \cdot H\cdots CH_3$.

In Enrique-Romero et al. (2016), it was shown that, in the presence of $(H_2O)_{18}$ and $(H_2O)_{33}$ water cluster models, the wHt was found to be barrierless, i.e. the assisted H transfer occurred spontaneously during the optimization process, a finding that led the authors to conclude that this channel was the dominant one over the others. However, we identified that such a spontaneous process is a consequence of the limitation of standard DFT to describe the electronic structure of biradical systems if the BS approach is not adopted.

By adopting BS-DFT, we have found here that for both the (BS)UM06-2X and (BS)UBHLYP-D3 methods, Rc is a barrierless process (see Fig. 2).

The PESs for the dHa and wHt processes at the different theory levels are shown in Fig. 3. At (BS)UM06-2X and (BS)UBHLYP-D3 levels, dHa presents a small energy barrier (2.4 and 5.1 kJ mol^{-1}, respectively). In contrast, wHt presents a high energy barrier (58.2 and 73.3 kJ mol^{-1}, respectively), indicating that it is not spontaneous. Similar findings are provided by CASPT2, which predicts energy barriers of 1.3 and 36.1 kJ mol^{-1} for dHa and wHt, respectively. In contrast, U single point energy calculations on the (BS)UM06-2X optimized geometries without considering the BS approach describe both dHa and wHt as spontaneous processes (see singlet_UM06-2X energies in Fig. 3 represented by blue crosses), in which the reactant structures lay above the actual reactants by more than 200 and 250 kJ mol^{-1}, respectively. This is because the singlet UM06-2X calculation starts from a non-symmetry broken initial guess wavefunction, hence yielding the same wavefunction as a restricted (i.e. closed-shell) M06-2X calculation. This calculated closed-shell wavefunction can be understood as an electronically excited state, in which the electronic structure has a significant contribution of an ionic state: a protonated CO molecule (HCO^+)

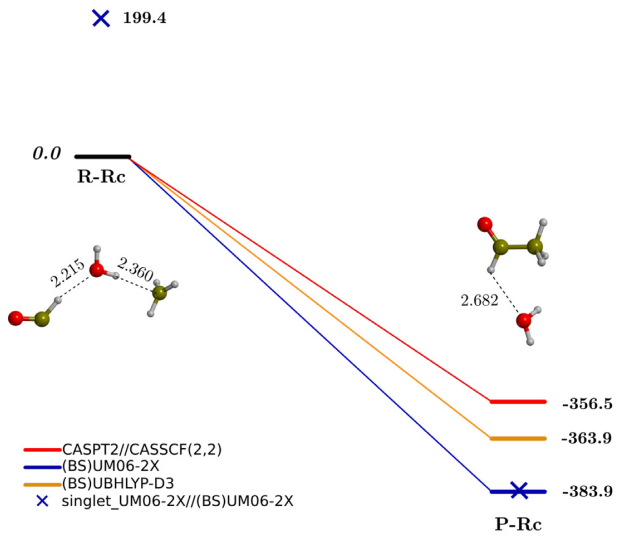

Figure 2. PESs at different DFT levels and at CASPT2 for the Rc reaction between CH_3 and HCO in the presence of one water molecule. The 0th energy reference corresponds to the pre-reactant complex (R-Rc). Single point energies at the singlet UM06-2X level on the (BS)UM06-2X optimized geometries are also shown. The structures presented in this figure are those corresponding to the (BS)UM06-2X optimized geometries. Energy units are in kJ mol^{-1} and distances are in Å.

and a negatively charged CH_3 species (CH_3^-). This ionic state is an ideal situation to trigger a Grotthus-like mechanism, in which the 'extra' proton of HCO^+ is transferred through the assisting water molecule to the 'proton-defective' CH_3^-. These results confirm again the need to use the BS-DFT approach to properly describe biradical systems.

5 CONCLUSIONS

This work is a revision note of a previous work by some of us (Enrique-Romero et al. 2016), in which the reactivity of the same system, i.e. CH_3 + HCO, has been studied using DFT methods adopting an unrestricted BS approach [i.e. (BS)UM06-2X and (BS)UBHLYP-D3] as well as post-HF multiconfigurational and multireference methods [i.e. CASSCF(2,2) and CASPT2]. In the original work, the DFT BS formalism was not adopted, hence seriously affecting the description of the electronic structure of the CH_3/HCO biradical system. The main conclusions of this work are summarized as follows:

(i) When the unrestricted DFT formalism is used without adopting the BS approach to describe the electronic structure of biradical systems, the initial guess wavefunction may collapse into a restricted closed-shell solution. If this occurs, the reactivity between two radicals is likely to be wrongly described. In the particular case of the CH_3 + HCO reactivity on water ice, calculations indicate that the water-assisted H transfer process is spontaneous.

(ii) Unrestricted BS DFT calculations for biradical systems show qualitatively similar results as those obtained at post-HF multiconfigurational and multireference levels, indicating the suitability of this DFT approach to describe the reactivity of biradical systems.

(iii) In the gas phase, both CH_3CHO and CO + CH_4 formations are found to be barrierless. In contrast, the formation of the carbene CH_3OCH species has a noticeable barrier.

(iv) In the presence of one water molecule, the wHt reaction is not spontaneous but, in contrast, it has a high energy [58 and 73 kJ mol^{-1} at the (BS)M06-2X and (BS)BHLYP-D3 levels]. Accordingly, its occurrence is unlikely under the interstellar conditions. In contrast, the radical–radical coupling is barrierless and the dHa presents a very small energy barrier (5 kJ mol^{-1} at the most). Similar results have been obtained using larger cluster models mimicking the surface of interstellar water ice (Enrique-Romero et al. 2019).

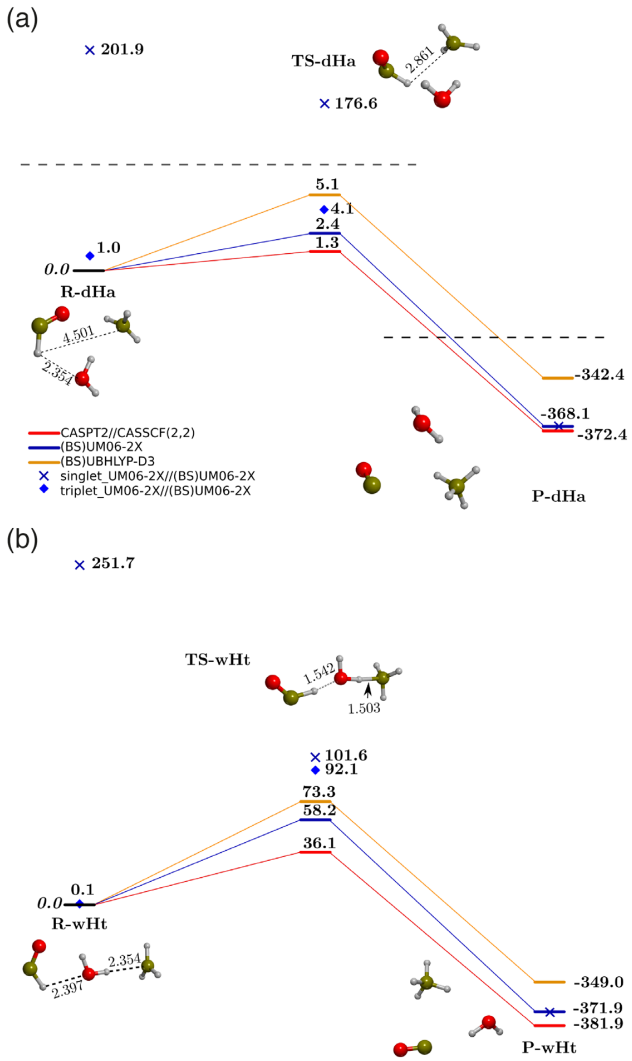

Figure 3. PESs at different DFT levels and at CASPT2 for the reactions of dHa (a) and wHt (b) between CH_3 and HCO in the presence of one water molecule. The 0th energy references are the pre-reactant complexes: R-dHA (a) and R-wHt (b). Single point energies at the singlet UM06-2X and triplet UM06-2X levels on the (BS)UM06-2X optimized geometries are also shown. The dashed horizontal lines indicate broken vertical axis. The presented structures correspond to the (BS)UM06-2X optimized geometries. Energy units are in kJ mol^{-1} and distances are in Å.

Finally, it is worth mentioning that, despite the limited description of the biradical system in Enrique-Romero et al. (2016), the physical insights provided by that work remain still valid, since it is shown that the biradical reactivity does not necessarily result in the radical–radical coupling product (i.e. the iCOM). Indeed, it is found here that the dHa can actually be a competitive channel, giving the same product as that for the wHt. This finding is in agreement with recent theoretical works dealing with the reactivity of biradical systems on interstellar ice surfaces (Rimola et al. 2018; Enrique-Romero et al. 2019; Lamberts et al. 2019).

ACKNOWLEDGEMENTS

JER and CC acknowledge funding from the European Research Council (ERC) under the European Union's Horizon 2020 research and innovation programme, for the Project 'the Dawn of Organic Chemistry' (DOC), grant agreement no. 741002. AR is indebted to the 'Ramón y Cajal' programme. Ministerio de Economía y Competitividad (MINECO, project CTQ2017-89132-P) and Agència de Gestió d'Ajuts Universitaris i de Recerca (AGAUR, project 2017SGR1323) are acknowledged. TL and JK acknowledge financial support by the European Union's Horizon 2020 research and innovation programme (grant agreement no. 646717, TUNNELCHEM), the Alexander von Humboldt Foundation, and the Netherlands Organisation for Scientific Research (NWO) via a VENI fellowship (722.017.008). We additionally acknowledge the Grenoble Alpes Recherche Infrastructure de Calcul Intensif et de Données (GRICAD, https://gricad.univ-grenoble-alpes.fr), which is partly supported by the Equip@Meso project (reference ANR-10-EQPX-29-01) of the programme Investissements d'Avenir supervised by the Agence Nationale pour la Recherche and the HPC resources of the Institut du Développement et des Ressources en Informatique Scientifique (IDRIS) under the allocation 2019-A0060810797 attributed by Grand Equipement National de Calcul Intensif (GENCI). PU and NB acknowledge Ministero dellIstruzione, dellUniversita' e della Ricerca (MIUR) and Scuola Normale Superiore (project PRIN 2015, STARS in the CAOS – Simulation Tools for Astrochemical Reactivity and Spectroscopy in the Cyberinfrastructure for Astrochemical Organic Species, cod. 2015F59J3R). This project has received funding from the European Union's Horizon 2020 research and innovation programme under the Marie Skodowska-Curie grant agreement no. 811312.

REFERENCES

Aquilante F. et al., 2010, J. Comput. Chem., 31, 224
Aquilante F. et al., 2016, J. Comput. Chem., 37, 506
Arce H. G., Santiago-García J., Jørgensen J. K., Tafalla M., Bachiller R., 2008, ApJ, 681, L21
Balucani N., Ceccarelli C., Taquet V., 2015, MNRAS, 449, L16
Becke A. D., 1993, J. Chem. Phys., 98, 1372
Belloche A. et al., 2017, A&A, 601, A49
Butscher T., Duvernay F., Rimola A., Segado-Centellas M., Chiavassa T., 2017, Phy. Chem. Chem. Phys., 19, 2857
Butscher T., Duvernay F., Danger G., Torro R., Lucas G., Carissan Y., Hagebaum-Reignier D., Chiavassa T., 2019, MNRAS, 486, 1953
Caselli P., Ceccarelli C., 2012, A&AR, 20, 56
Cazaux S., Tielens A. G. G. M., Ceccarelli C., Castets A., Wakelam V., Caux E., Parise B., Teyssier D., 2003, ApJ, 593, L51
Ceccarelli C. et al., 2017, ApJ, 850, 176
Cernicharo J., Guélin M., Kahane C., 2000, A&AS, 142, 181
Charnley S. B., Tielens A. G. G. M., Millar T. J., 1992, ApJ, 399, L71
Codella C. et al., 2017, A&A, 605, L3
Enrique-Romero J., Rimola A., Ceccarelli C., Balucani N., 2016, MNRAS, 459, L6
Enrique-Romero J., Rimola A., Ceccarelli C., Ugliengo P., Balucani N., Skouteris D., 2019, ACS Earth Space Chem., 3, 2158
Fedoseev G., Cuppen H. M., Ioppolo S., Lamberts T., Linnartz H., 2015, MNRAS, 448, 1288
Fernandez Galván I. et al., 2019, OpenMolcas: From Source Code to Insight. Available at: https://chemrxiv.org/articles/OpenMolcas_From_Source_Code_to_Insight/8234021/1
Frisch M. J. et al., 2009, Gaussian09, Revision D.01, Gaussian, Inc., Wallingford CT
Gal R. L., Herbst E., Dufour G., Gratier P., Ruaud M., Vidal T. H. G., Wakelam V., 2017, A&A, 605, A88
Garrod R. T., Herbst E., 2006, A&A, 457, 927
Grimme S., 2006, J. Comput. Chem., 27, 1787
Grimme S., Antony J., Ehrlich S., Krieg H., 2010, J. Chem. Phys., 132, 154104
Herbst E., 2017, Int. Rev. Phys. Chem., 36, 287
Herbst E., van Dishoeck E. F., 2009, ARA&A, 47, 427
Kahane C., Ceccarelli C., Faure A., Caux E., 2013, ApJ, 763, L38
Karlström G. et al., 2003, Comput. Mater. Sci., 28, 222
Lamberts T., Markmeyer M. N., Kolb F. J., Kästner J., 2019, ACS Earth Space Chem., 3, 958
Lee C., Yang W., Parr R. G., 1988, Phys. Rev. B, 37, 785
Lefloch B., Ceccarelli C., Codella C., Favre C., Podio L., Vastel C., Viti S., Bachiller R., 2017, MNRAS, 469, L73
Ligterink N. F. W. et al., 2017, MNRAS, 469, 2219
López-Sepulcre A., Taquet V., Ceccarelli C., Neri R., Kahane C., Charnley S. B., 2015, in Daisuke I., Ken-ichi T., Alwyn W., Leonardo T., eds, ASP Conf. Ser. Vol. 499, Revolution in Astronomy with ALMA: The Third Year. Astron. Soc. Pac., San Francisco, p. 223
McGuire B. A., Burkhardt A. M., Kalenskii S., Shingledecker C. N., Remijan A. J., Herbst E., McCarthy M. C., 2018, Science, 359, 202
Mendoza E., Lefloch B., López-Sepulcre A., Ceccarelli C., Codella C., Boechat-Roberty H. M., Bachiller R., 2014, MNRAS, 445, 151
Muller S. et al., 2013, A&A, 551, A109
Neese F., 2004, J. Phys. Chem. Solids, 65, 781
Noodleman L., 1981, J. Chem. Phys., 74, 5737
Noodleman L., Baerends E. J., 1984, J. Am. Chem. Soc., 106, 2316
Öberg K. I., 2016, Chem. Rev., 116, 9631
Rimola A., Skouteris D., Balucani N., Ceccarelli C., Enrique-Romero J., Taquet V., Ugliengo P., 2018, ACS Earth Space Chem., 2, 720
Rivilla V. M., Beltrán M. T., Cesaroni R., Fontani F., Codella C., Zhang Q., 2017, A&A, 598, A59
Rubin R. H., Swenson G. W., Benson R. C., Tigelaar H. L., Flygare W. H., 1971, ApJ, 169, L39
Skouteris D., Balucani N., Ceccarelli C., Vazart F., Puzzarini C., Barone V., Codella C., Lefloch B., 2018, ApJ, 854, 135
Vasyunin A. I., Caselli P., Dulieu F., Jiménez-Serra I., 2017, ApJ, 842, 33
Woods P. M., Slater B., Raza Z., Viti S., Brown W. A., Burke D. J., 2013, ApJ, 777, 90
Zamirri L., Ugliengo P., Ceccarelli C., Rimola A., 2019, ACS Earth Space Chem., 3, 1499
Zhao Y., Truhlar D. G., 2008, Acc. Chem. Res., 41, 157

SUPPORTING INFORMATION

Supplementary data are available at *MNRAS* online.

Appendix A.

Please note: Oxford University Press is not responsible for the content or functionality of any supporting materials supplied by the authors. Any queries (other than missing material) should be directed to the corresponding author for the article.

APPENDIX A: ONLINE MATERIAL

In the online material file, we provide: (i) the absolute energies (in Hartrees) of the reactions presented in this work, (ii) some input examples for GAUSSAIN and OPENMOLCAS calculations, and (iii) the *XYZ* Cartesian coordinates of the structures presented in the work.

This paper has been typeset from a TEX/LATEX file prepared by the author.

ACS EARTH AND SPACE CHEMISTRY

Article

Cite This: ACS Earth Space Chem. XXXX, XXX, XXX−XXX

http://pubs.acs.org/journal/aesccq

Reactivity of HCO with CH_3 and NH_2 on Water Ice Surfaces. A Comprehensive Accurate Quantum Chemistry Study

Joan Enrique-Romero,[†,‡] Albert Rimola,[*,‡] Cecilia Ceccarelli,[*,†] Piero Ugliengo,[§] Nadia Balucani,[†,∥,⊥] and Dimitrios Skouteris[▽]

[†]Univ. Grenoble Alpes, Institut de Planétologie et Astrophysique de Grenoble (IPAG), 38000 Grenoble, France

[‡]Departament de Química, Universitat Autònoma de Barcelona, 08193, Catalunya, Spain

[§]Dipartamento di Chimica and Nanostructured Interfaces and Surfaces (NIS), Università degli Studi di Torino, Via P. Giuria 7, 10125 Torino, Italy

[∥]Dipartamento di Chimica, Biologia e Biotecnologie, Università degli Studi di Perugia, Via Elce di Sotto 8, I-06123 Perugia, Italy

[⊥]Osservatorio Astrosico di Arcetri, Largo E. Fermi 5, 50125 Firenze, Italy

[▽]Master-Up, Strada Vicinale Sperandio 15, I-06123 Perugia, Italy

Supporting Information

ABSTRACT: Interstellar complex organic molecules (iCOMs) can be loosely defined as chemical compounds with at least six atoms in which at least one is carbon. The observations of iCOMs in star-forming regions have shown that they contain an important fraction of carbon in a molecular form, which can be used to synthesize more complexes, even biotic molecules. Hence, iCOMs are major actors in the increasing molecular complexity in space, and they might have played a role in the origin of terrestrial life. Understanding how iCOMs are formed is relevant for predicting the ultimate organic chemistry reached in the interstellar medium. One possibility is that they are synthesized on the interstellar grain icy surfaces, via recombination of previously formed radicals. The present work focuses on the reactivity of HCO with CH_3/NH_2 on the grain icy surfaces, investigated by means of quantum chemical simulations. The goal is to carry out a systematic study using different computational approaches and models for the icy surfaces. Specifically, DFT computations have been benchmarked with CASPT2 and CCSD(T) methods, and the ice mantles have been mimicked with cluster models of 1, 2, 18, and 33 H_2O molecules, in which different reaction sites have been considered. Our results indicate that the HCO + CH_3/NH_2 reactions, if they actually occur, have two major competitive channels: the formation of iCOMs CH_3CHO/NH_2CHO or the formation of CO + CH_4/NH_3. These two channels are either barrierless or present relatively low (≲10 kJ/mol equal to about 1200 K) energy barriers. Finally, we briefly discuss the astrophysical implications of these findings.

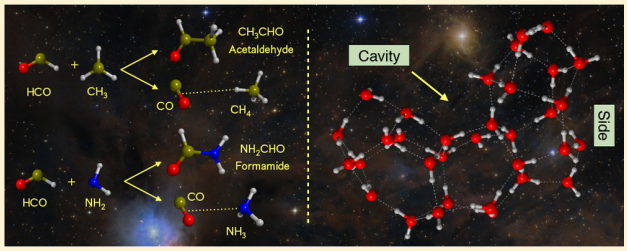

KEYWORDS: *interstellar medium, astrochemistry, DFT, iCOMs, grains*

1. INTRODUCTION

It has been long demonstrated that star forming regions are places with a rich organic chemistry (e.g., refs 1−6). Although there are no proofs that organic molecules formed in the interstellar medium (ISM) did play a role in the emergence of terrestrial life, there is mounting evidence that they were inherited by the small objects of the Solar System: for example, carbonaceous chondrites and comets contain a wide variety of organic molecules, some of them probably being a direct heritage of the ISM based on their relative abundances and ratio of deuterated versus hydrogenated species (e.g., refs 4 and 7−9).

Knowing how detected interstellar complex organic molecules (iCOMs: C-bearing molecules with at least six atoms[10]) are formed and destroyed is not only important per se but also because it is the only way to understand the ultimate organic complexity present in the ISM. Indeed, there is an intrinsic limit to the detection of large iCOMs (excluding linear chains), which is caused by the fact that the larger the molecule the larger the number of rotational transitions (because of the larger number of functional groups of the iCOM) and, consequently, the weaker the intensity of the lines. As a result, the numerous and weak lines of large iCOMs produce a "grass" of lines in the spectra, which makes the identification of a large molecule eventually impossible.

Special Issue: Complex Organic Molecules (COMs) in Star-Forming Regions

Received: June 3, 2019
Revised: September 13, 2019
Accepted: September 18, 2019
Published: September 18, 2019

Therefore, there is a limit to the largest detectable iCOM, and this has a direct consequence: we need to rely on our knowledge of the processes to predict which large molecules are synthesized in the ISM.

How iCOMs are formed is a question that has baffled astrochemists for decades. In the 90s it was thought that gas-phase reactions were the dominant formation processes (e.g., refs 11 and 12). However, subsequent astronomical observations (e.g., refs 2 and 13), laboratory experiments (e.g., ref 14), and theoretical calculations (e.g., ref 15) challenged this synthetic route model. As a result, a new paradigm was proposed, which assumes that most (if not all) iCOMs are formed on the surfaces of icy interstellar grains.[16,17] According to this paradigm, radicals are created by the UV photons impinging on the ice grain mantles, which are formed during the cold cloud/prestellar phase and contain simple hydrogenated species (mostly water but also other species, such as methanol and ammonia, in smaller quantities). With the warming up of the environment caused by the birth of a protostar, the radicals trapped in the ice can diffuse on the grain surfaces and react between them to form iCOMs. The reaction process is assumed to be a direct combination of radicals, which are considered as "lego-like" blocks.

This paradigm is usually assumed in current gas-grain astrochemical models (e.g., refs 18−22). However, there are still many uncertainties that make the paradigm not fully validated. First, it is not clear that the lego-like radical combination is actually an effective process (e.g. refs 23 and 24). Second, it appears that the role of gas-phase reactions has been underestimated in the past.[9,25−32] Finally, models based on the "exclusive grain-surface" paradigm are unable to reproduce the observed abundance of several iCOMs (e.g., refs 33−35).

The numerous laboratory experiments reported in the literature are extremely useful to study the possible processes occurring on ices illuminated by UV photons and/or irradiated by energetic particles (e.g., refs 36−47). However, investigating surface-induced iCOMs formation by means of experimental techniques is extremely difficult, if not impossible, since the actual interstellar conditions cannot exactly be reproduced in terrestrial laboratories. For example, the UV irradiation used in laboratory experiments is, for practical reasons, more than a million times larger than the one impinging on the interstellar grain mantles: this causes an instantaneous injection of energy of several orders of magnitude larger than that absorbed by the interstellar grain mantles and, consequently, likely introduces different reaction routes (e.g., energy barriers are probably overcome in laboratory experiments while they are not in the cold ISM). Similarly, the H-flux in experiments is also extremely larger compared with the actual ISM conditions, causing a dramatic amplification of the results toward a full saturation of the compounds. A suitable alternative, and certainly a complementary method for such investigations, is the use of theoretical simulations based on quantum chemical calculations. Indeed, these calculations provide a description of the surface reactions from an atomistic perspective, providing unique, relevant energetic information, and, accordingly, they can be useful to assess the validity of the "exclusive grain-surface" paradigm.

In this work, we focus on two reactions occurring on amorphous solid water (ASW) surfaces: HCO + CH_3 and HCO + NH_2. In the "exclusive grain-surface" paradigm mentioned above, it is expected that the radical coupling produces two iCOMs: CH_3CHO (acetaldehyde) and NH_2CHO (formamide). However, previous works by some of us[23,24] showed that other reactive channels can compete with the iCOM formation. Specifically, the two reactions can lead to the formation of CO + CH_4 and CO + NH_3, respectively, in which the H atom of HCO is transferred to the radical partner. Similar processes were identified computationally when HCO reacts with CH_3 on surfaces of CO-pure ices.[48]

The goal of the present work is to carry out a systematic study of two reactions, i.e., HCO + CH_3 and HCO + NH_2, considered here as prototype reactions for the formation of iCOMs, using different approximations for the calculations and models of ASW with the aim to (1) understand how the different methods and models affect the results, (2) individuate the most convenient methods and models to use in future calculations of other similar radical−radical systems, and (3) identify the products of the reactions for different conditions. To this end, the present work focuses on the following three points:

1. *Methodology benchmark:* (i) The energy barriers for reactions between the two couples of radicals in the presence of 1 and 2 water molecules are computed with two DFT methods (B3LYP and BHLYP) and compared to the values calculated with the multireference CASPT2 method; (ii) The interaction of the three radicals (CH_3, HCO, and NH_2) with 1 and 2 water molecules is studied and bench-marked taking as reference the binding energies computed at the CCSD(T) level.

2. *Radical-surface binding enthalpies:* We study the binding of the three radicals (CH_3, HCO, and NH_2) to an ASW cluster model of 18 water molecules and to a larger cluster of 33 water molecules sporting two different morphological sites, a cavity and its side.

3. *Radical−radical reactivity:* The reactivity of the two radical couples is studied (i) on the 18 water molecules cluster and (ii) on the two different morphological sites of the 33 water molecules cluster.

It is worth mentioning that the systems to deal with here sport an additional complexity from an electronic structure point of view. That is, two radicals interacting with water ice, in which the unpaired electrons have opposite signs, constitute a singlet biradical system. Describing this electronic situation with quantum chemistry calculations is delicate. Ab initio multireference methods are a good choice to describe biradical systems, but they are extremely expensive and, accordingly, unpractical for large systems. Alternatively, a good compromise between accuracy and computational cost is the DFT broken-symmetry approach.[49] By using this method, however, our own experience[23,24] indicates that one has to be sure that the initial guess wave function corresponds to the actual singlet biradical state (i.e., the unpaired electrons being localized on the corresponding radicals and with opposite spin signs), as it may well happen that the initial wave function represents wrongly a closed-shell-like situation, in which the unpaired electrons are 50% distributed among the two radicals. Results derived from one or the other situation are dramatically different.

This article is organized as follows. First the adopted methods are presented (section 2); then the results are provided following the three objectives described above (section 3); and finally a discussion, including the astrophysical

DOI: 10.1021/acsearthspacechem.9b00156
ACS Earth Space Chem. XXXX, XXX, XXX−XXX

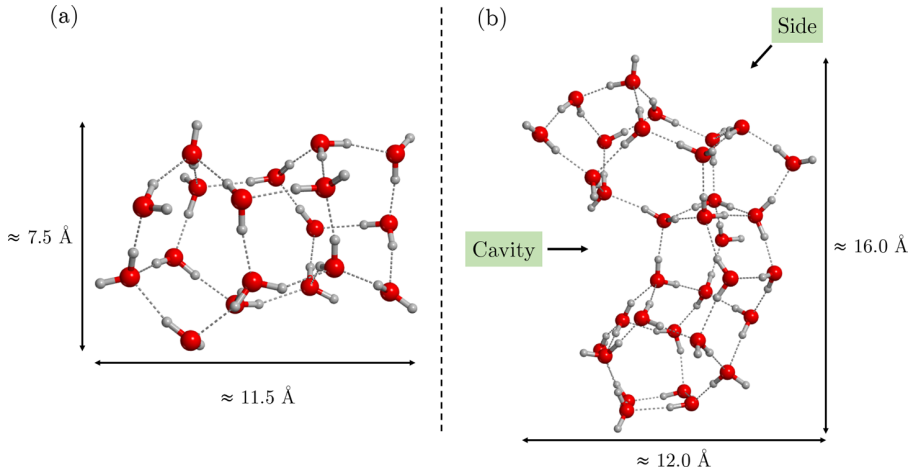

Figure 1. Structures of the 18 and 33 water molecules clusters, (a) and (b) respectively, optimized at the BHLYP/6-31+G(d,p) level.

implications, and the conclusions are presented in sections 4 and 5, respectively.

2. METHODS

All DFT and CCSD(T) calculations were performed using the GAUSSIAN09[50] software package, while the multireference calculations were carried out with the OpenMolcas 18.09[51−54] program.

Stationary points of the potential energy surfaces (PESs) were fully optimized using two hybrid density functional theory (DFT) methods: B3LYP and BHLYP. These methods have the same Lee, Yang, Parr correlation functional (LYP)[55] but differ on the exchange functionals: the Becke's three parameter (B3), which includes a 20% of exact exchange in its definition,[56] and the Becke's half-and-half (BH), which mixes the pure DFT and the exact exchange energy in a 1:1 ratio.[57] For B3LYP calculations, the Grimme's D3 dispersion term[58] was accounted for during the geometry optimizations. In contrast, for BHLYP, both the D2[59] and D3 dispersion terms were included in a posteriori way onto the pure BHLYP optimized geometries.

A calibration study was first carried out for (i) the NH_2 + HCO and CH_3 + HCO reactivities in the presence of 1 and 2 water molecules (W1 and W2, respectively) and (ii) the interaction of each radical with W1 and W2. For this calibration study, the DFT methods were combined with the Pople's 6-311++G(2df,2pd) basis set. As reference for the reactivity results we used single point energy calculations at the multireference CASPT2 level combined with the Dunnning's cc-pVTZ basis using as initial guess the orbitals generated at the CASSCF(2,2) level. In the same way, single point energy calculations at the CCSD(T)/aug-cc-pVTZ level were also carried out in order to compare them to CASPT2 values. Regarding the interaction energies, the same DFT methods were compared to the CCSD(T)/aug-cc-pVTZ level. All the single point energy calculations for this benchmark study were carried out on the B3LYP-D3 optimized geometries.

Radical−radical reactivity was also studied more realistically on two amorphous solid water (ASWs) ices modeled by molecular clusters consisting of 18 (W18) and 33 (W33) water molecules, which were also used in previous works.[23,24,60] The optimized structures are shown in Figure 1. Interestingly, W33 exhibits a hemispherical cavity and, accordingly, we studied the surface processes considering both this cavity and an extended side of the ice surface (see Figure 1(b)), as they exhibit different surface properties. In order to make the calculations computationally affordable, for these cases the DFT methods were combined with the Pople's 6-31+G(d,p) basis set.

All stationary points were characterized by the analytical calculation of the harmonic frequencies as minima (reactants, products, and intermediates) and saddle points (transition states). Intrinsic reaction coordinate (IRC) calculations at the same level of theory were carried out when needed to ensure that the transition states connect with the corresponding minima. Thermochemical corrections to the potential energy values were carried out using the standard rigid rotor/harmonic oscillator formulas[61] to compute the zero point energy (ZPE) corrections.

Adsorption energies of HCO, CH_3, and NH_2 on W18 and W33 were refined with single point energy calculations combining the DFT methods with the extended 6-311++G(2df,2pd) basis set and corrected for the basis set superposition error (BSSE). Considering A as the adsorbate and B as the surface cluster model, the BSSE-noncorrected adsorption energy was computed as $\Delta E_{ads} = E^{AB}_{AB}(AB) - E^{A}_{A}(A) - E^{B}_{B}(B)$, where superscripts denote the basis set used and the subscripts the geometry at which the calculation was done. BSSE-corrected energies were calculated as

$$\Delta E^{CP}_{ads}(AB) = \Delta E_{ads} + BSSE(A) + BSSE(B) + \delta^{A}(A) + \delta^{B}(B) \quad (1)$$

where the BSSE values were calculated following the Boys and Bernardi counterpoise correction method ($BSSE(A) = E^{AB}_{AB}(A) - E^{A}_{AB}(A)$),[62] and where the deformation of each monomer was also accounted for ($\delta^{A}(A) = E^{A}_{AB}(A) - E^{A}_{A}(A)$).

Inclusion of ZPE corrections allowed us to obtain adsorption enthalpies at 0 K:

$$\Delta H_{ads}(AB) = \Delta E^{CP}_{ads}(AB) + \Delta ZPE \quad (2)$$

In the sign convention followed in this work, the adsorption energy is the negative of the binding energy, i.e. $\Delta E_{ads} = -\Delta E_{bind}$.

The systems containing two radical species were first optimized in the triplet electronic state, which was then optimized in the singlet state to describe the biradical system. Structures with doublet and triplet electronic states were simulated with open-shell calculations based on the unre-

DOI: 10.1021/acsearthspacechem.9b00156
ACS Earth Space Chem. XXXX, XXX, XXX−XXX

Table 1. ZPE- and BSSE-Noncorrected Binding Energies Computed with Different Methods for the Interaction of CH_3, HCO and NH_2 with 1 and 2 Water Molecules (W1 and W2) at the B3LYP-D3 and BHLYP Levels[a]

	B3LYP-D3	BHLYP	BHLYP-D2	BHLYP-D3	CCSD(T)
CH_3/W1	9.5	5.2	11.3	8.1	6.9
HCO/W1 (H)	12.9	10.9	13.6	13.1	12.0
HCO/W1 (O)	11.7	9.7	12.5	12.1	11.5
NH_2/W1 (H)	14.1	12.0	14.9	14.4	12.8
NH_2/W1 (N)	23.4	21.5	24.3	23.6	21.6
CH_3/W2	8.6	3.1	11.3	8.0	7.1
HCO/W2	14.8	9.2	16.1	15.1	13.2
NH_2/W2	41.6	36.6	44.5	41.9	38.3

[a]None, D2 (accounting for 2-body interactions), and D3 (accounting for 2- and 3-body interactions) dispersion corrections were considered for the latter. BHLYP-based and CCSD(T) values were calculated as single points on the B3LYP-D3 optimized geometries. Energy units are in kJ/mol.

Table 2. ZPE-Noncorrected Energy Barriers ($\Delta E^{\ddagger}$), Computed with Different Methods, for Radical−Radical Coupling (*Rc*), Direct Hydrogen Abstraction (*dHa*), and Water Assisted Hydrogen Transfer (*wHt*) Reactions of NH_2 + HCO and CH_3 + HCO in the Presence of 1 and 2 Water Molecules Computed at the B3LYP-D3 and BHLYP-based Levels[a]

System	Process	B3LYP-D3	BHLYP	BHLYP-D2	BHLYP-D3	CCSD(T)	CASPT2
NH_2/HCO···W1	*Rc*	NB	NB	NB	NB	NB	NB
	dHa	3.5	6.1	4.1	5.1	5.3	4.2
	wHt	10.9	48.6	46.2	48.8	43.8	48.3
CH_3/HCO···W1	*Rc*	NB	NB	NB	NB	NB	NB
	dHa	3.1	6.9	3.3	5.1	5.0	1.5
	wHt	23.5	59.4	55.5	58.6	60.0	52.2
NH_2/HCO···W2	*Rc*	6.5	8.5	6.1	6.8	6.3	6.1
	dHa	NB	NB	NB	NB	NB	NB
	wHt	15.5	65.8	62.5	65.1	52.3	52.9
CH_3/HCO···W2	*Rc*	NB	NB	NB	NB	NB	NB
	dHa	1.6	4.0	1.5	1.6	1.6	1.0
	wHt	30.7	65.8	62.5	65.1	64.0	52.0

[a]For the latter two dispersion corrections have been considered: D2 (which considers all 2-body interactions) and D3 (which considers 2- and 3-body interactions). BHLYP-based, CCSD(T) and CASPT2 values were calculated as single point energy calculations on the B3LYP-D3 optimized geometries. Energy units are in kJ mol^{-1}. NB stands for "No Barrier" and means that the process is found to be barrierless.

stricted formalism. Singlet biradical systems were calculated adopting the unrestricted broken symmetry (BS) approach, in which the most stable initial wave function was found using the *stable = opt* keyword in Gaussian09.

Following the International System Units, all energy units are given in kJ mol^{-1}, whose conversion factor to K is 1 kJ mol^{-1} = 120.274 K.

3. RESULTS

In this section, results of the calibration study devoted to the reactivity and interaction of HCO with CH_3 and NH_2 in the presence of 1 and 2 water molecules are first presented. Then, results on adsorption properties and the radical−radical reactions on W18 and W33 are reported.

3.1. Methodology Benchmark. This section aims to be a calibration study to check the reliability of the B3LYP and BHLYP methods for (i) the radical−water interactions and (ii) the activation energy of the reactions of CH_3/HCO and NH_2/HCO, in both cases with one and two water molecules (W1 and W2 hereafter) as minimal models representing an ice surface. The references used for the study of the binding and activation energies are CCSD(T) and CASPT2, respectively. In all cases, single point energies were computed onto the B3LYP-D3 optimized geometries. In the Supporting Information (SI) section the reader can find these geometries as well as the relative errors of the data presented in the following.

Table 1 contains the binding energies for the three radicals involved in this study (namely CH_3, NH_2, and HCO) interacting with W1 and W2. The systems where a radical interacts with W1 have been based on those presented by Wakelam et al.,[63] where the initial structures were built in a chemical-wise manner following the ability of each component of the radical to establish a hydrogen bond to a single water molecule; e.g. in the cases where NH_2 and HCO interact with W1 two possibilities were considered: the radicals either acting as H-bond donors (through one of their H atoms) or acting as H-bond acceptors (through the N and O atoms, respectively). The initial geometries of the systems with W2 were built similarly, with the radicals having the maximum number of hydrogen bonds to the two water molecules.

It can be seen that CH_3 is the species having the weakest interaction with the water molecules (6.9−7.1 kJ/mol at the CCSD(T) level). HCO and NH_2, instead, can form intermediate and strong H-bonds, respectively, and, accordingly, they show higher binding energies (11.5−13.2 kJ/mol for the former and 12.8−38.3 kJ/mol for the latter at the CCSD(T) level). This trend is in agreement with that found by Wakelam et al.,[63] in which the binding energies of these

DOI: 10.1021/acsearthspacechem.9b00156
ACS Earth Space Chem. XXXX, XXX, XXX−XXX

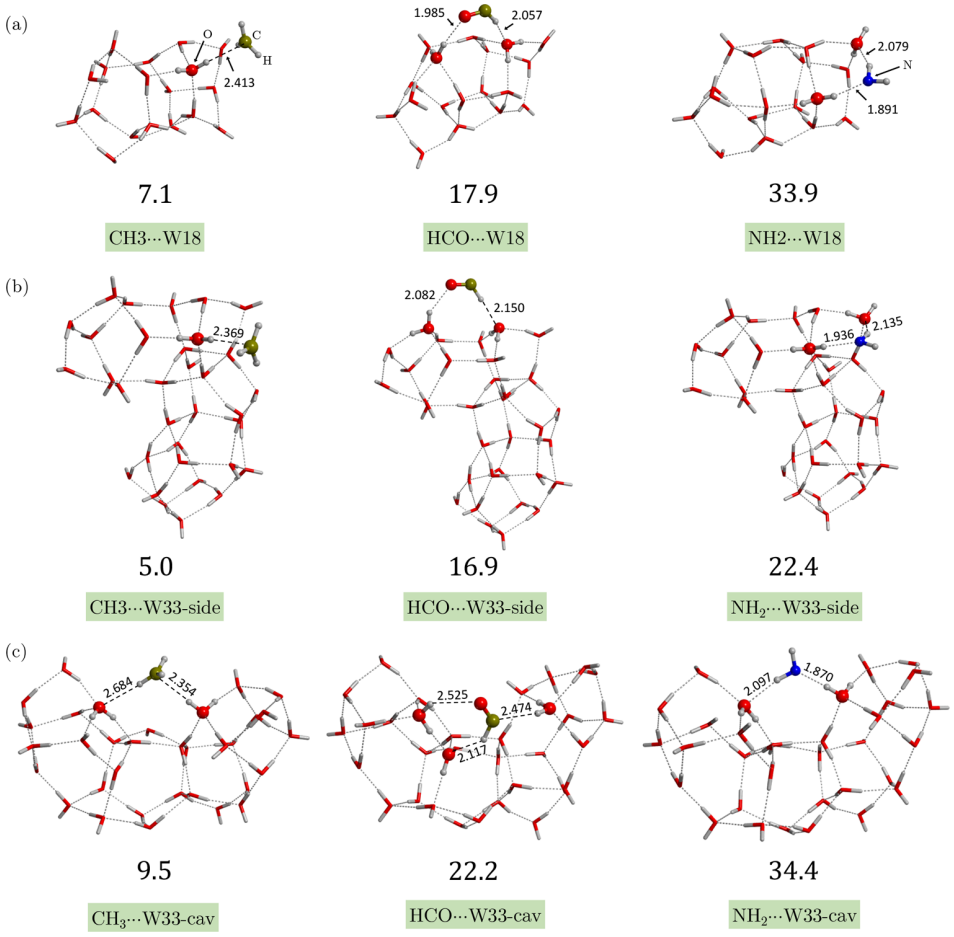

Figure 2. Fully optimized geometries for the binding of CH_3, HCO, and NH_2 on (a) W18, (b) W33-side, and (c) W33-cav at BHLYP/6-31+G(d,p). Bond distances are in Å. Binding enthalpies including the D3 correction (at 0 K) values (in kJ/mol) are corrected for BSSE and are shown below their respective structures.

species with W1 were 13, 19−23, and 23−38 kJ/mol for CH_3, HCO, and NH_2 respectively, computed at the M062X/aug-cc-PVTZ level. Note, however, that the quoted values are not the final values used in the model by Wakelam et al.,[63] as they also use binding energies from other sources in the literature in order to fit experimental data.

Regarding the performance of the methods, the best ones are B3LYP-D3 and BHLYP-D3, with relative errors of 2−39% and 5−18%, respectively (see SI section). The pure BHLYP method systematically underestimates the binding energies, providing strong deviations for CH_3 and HCO, especially on W2. BHLYP-D2 dramatically overestimates the binding energies of CH_3-containing systems (relative errors of ∼60%), indicating that the D2 term probably accounts for dispersion in excess for this kind of weakly bound complexes.

Table 2 shows the calculated energy barriers of CH_3/HCO and NH_2/HCO on W1 and W2. Three different possible reactions have been identified: (i) radical−radical coupling, leading to formation of the iCOMs (i.e., CH_3CHO and NH_2CHO); (ii) direct hydrogen abstraction, in which the H atom of HCO is transferred to the other radicals, forming CO + CH_4 and CO + NH_3, respectively; and (iii) water assisted hydrogen transfer, which is the same as (ii) but the H transfer is assisted by the water molecules adopting a H relay mechanism. These reactions will be referred to as *Rc*, *dHa*, and *wHt*, respectively, along the work.

According to these values, two general trends are observed: (i) *Rc* and *dHa* are either barrierless (meaning that the initial biradical structures were not stable) or have relatively low energy barriers (1.0−6.1 kJ/mol for CASPT2), and (ii) *wHt* are the processes presenting the highest energy barriers (around 50 kJ/mol for CASPT2).

For those *Rc* and *dHa* reactions having an energy barrier, one can see that the worst performance is given by the pure BHLYP method compared to CASPT2. The rest of the methods perform similarly, with BHLYP-D2 and B3LYP-D3 being the best ones, which are followed by BHLYP-D3. Regarding the wHt reactions, B3LYP-D3 dramatically underestimates the energy barriers (errors of ∼40−80%), while BHLYP-based methods perform reasonably well with errors below ∼25%. CCSD(T) performs similarly to the BHLYP-based methods, presenting moderate energy barrier deviations compared to the CASPT2 values. All errors can be found in the SI section.

In summary, BHLYP-D3 provides the most reliable binding energies, B3LYP-D3, BHLYP-D2, and BHLYP-D3 show good performances for energy barriers related to Rc and dHa processes, while BHLYP-D2 and BHLYP-D3 perform well for wHt energy barriers. Accordingly, and with the aim to be

DOI: 10.1021/acsearthspacechem.9b00156
ACS Earth Space Chem. XXXX, XXX, XXX−XXX

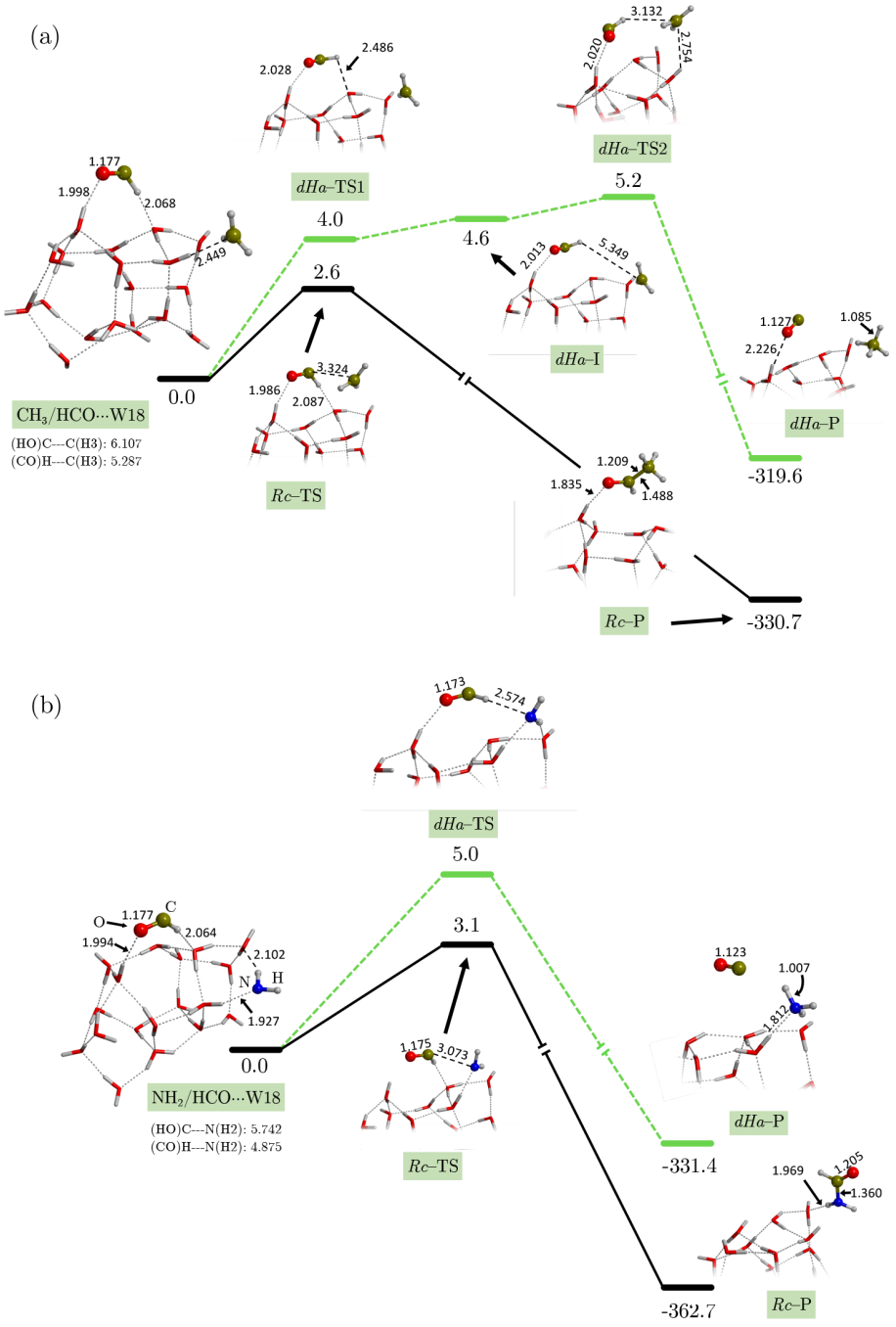

Figure 3. ZPE-corrected *Rc* (solid black line) and *dHa* (dashed green lines) PESs for (a) HCO/CH_3···W18 and (b) HCO/NH_2···W18 calculated at the BHLYP-D3/6-31+G(d,p). Energy units are in kJ/mol and distances in Å. Notice that dHa-TS1 for (a) HCO/CH_3 ···W18 lies below the intermediate dHa-I, due to the ZPE correction, setting effectively a single energy barrier: dHa-Ts2.

consistent, in the following sections (devoted to the binding and potential energy profiles on the W18 and W33 cluster models) we provide the results at the BHLYP-D3 level of theory, while results based on BHLYP-D2 (on both W18 and W33) and on B3LYP-D3 (on W18) are reported in the SI.

3.2. Radical-Surface Binding Enthalpies. Here we present the ZPE- and BSSE-corrected binding energies of the radicals on the *W18* and *W33* cluster models and their comparison with recent literature. These values are important because binding energies are essential parameters in astrochemical modeling studies.

As was stated in the previous section, the binding of the radicals on the water ice surfaces is mainly dictated by hydrogen bonds (H-bonds) and dispersion interactions. The clusters exhibit several potential binding sites (Figure 1), and accordingly, different radical/surface complexes can exist. Here, for the sake of simplicity, we choose those complexes in which the intermolecular interactions between the two partners are maximized. The underlying assumption is that radicals on the water ice surfaces have had enough time to thermalize and establish the largest number of intermolecular interactions with the surface, as very probably is the case in the

DOI: 10.1021/acsearthspacechem.9b00156
ACS Earth Space Chem. XXXX, XXX, XXX−XXX

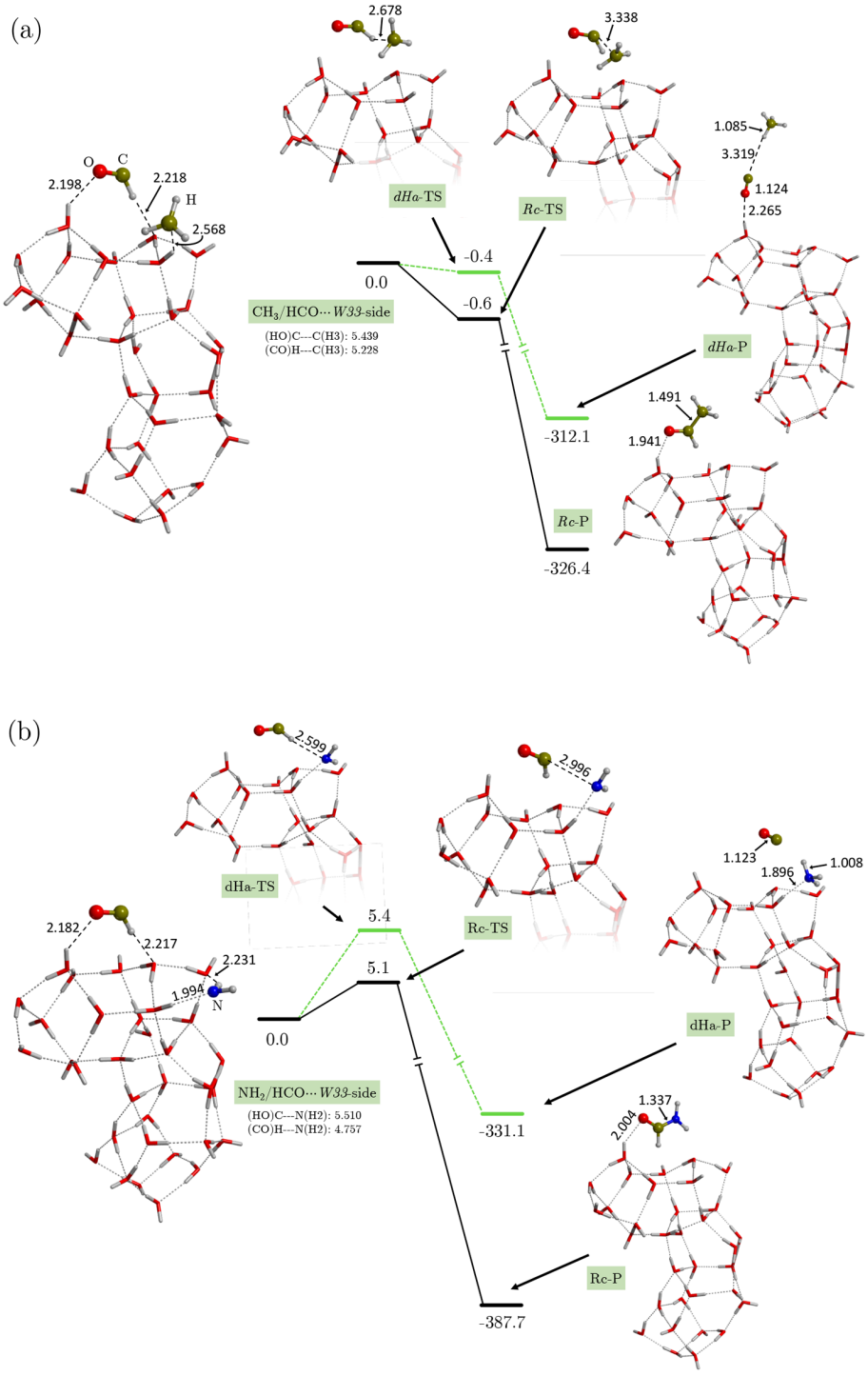

Figure 4. ZPE-corrected *Rc* (solid black lines) and *dHA* (green dashed lines) PES for the HCO/CH_3···W33-side (a) and HCO/NH_2···W33-side (b) systems optimized at the BHLYP-D3 theory level. Energy units are in kJ/mol and distances in Å. Notice that both Rc and dHa TS for CH_3/HCO lie below the energy of reactants due to the ZPE correction.

interstellar conditions. Figure 2 shows the BHLYP fully optimized complexes on W18 and on the two differentiated W33 sites: its side (W33-side) and its cavity (W33-cav). The corresponding BSSE-corrected binding enthalpies including the D3 correction (at 0 K) are also shown. The same information at BHLYP-D2 and B3LYP-D3 is available in the SI.

The binding enthalpy trend is NH_2 > HCO > CH_3, irrespective of the cluster model and surface morphology, in agreement with the results of the previous section. Specifically, the binding enthalpy ranges are 22.4−34.4, 16.9−22.2, and 5.0−9.5 kJ/mol for NH_2, HCO, and CH_3, respectively. These values compare well with those previously computed by Enrique-Romero et al.[24] for HCO and CH_3 on the W18 cluster (19 and 6 kJ/mol) and by Rimola et al.[23] for NH_2 and HCO

DOI: 10.1021/acsearthspacechem.9b00156
ACS Earth Space Chem. XXXX, XXX, XXX−XXX

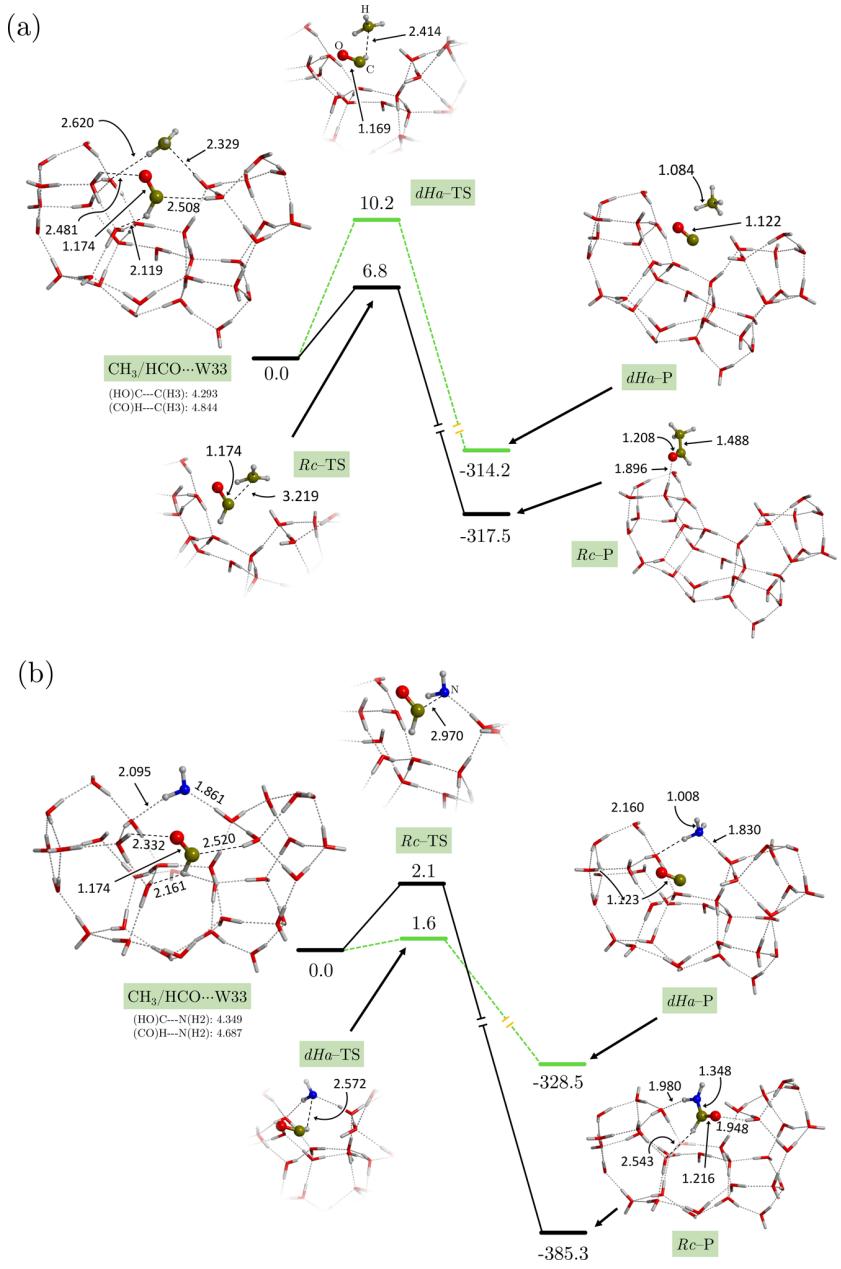

Figure 5. ZPE-corrected *Rc* (solid black lines) and *dHa* (green dashed lines) PESs for the HCO/CH_3···W33-cav (a) and HCO/NH_2···W33-cav (b) systems optimized at the BHLYP-D3 theory level. Energy units are in kJ/mol and distances in Å. BHLYP-D2 values can be found in the SI.

on the W33-cav cluster (33.5 and 17.5 kJ/mol). In the model presented in Wakelam et al.,[63] the authors reported binding energies of 27, 20, and 13 kJ/mol for NH_2, HCO, and CH_3, respectively, in rough agreement with our results. Sameera et al.[64] have recently computed the binding energies of HCO and CH_3 adsorbed on hexagonal ice slabs. (The authors used either full DFT with a double-ζ basis set or the ONIOM approach combining DFT with force fields. They reported several values owing to the different adsorption modes of these two species adopting the two computation approaches. This allowed them to report the wide range of binding energies reported here.) They found HCO binding energies ranging between 12−40 kJ/mol, and 11−25 kJ/mol for HCO and CH_3, respectively. These values are similar or moderately larger than the values found in our W33-cav cluster.

Finally, it is worth mentioning that these complexes do not present hemicovalent bonds, as was the case for CN in Rimola et al.[23] Attempts to identify this type of binding in the current systems have been made, but the initial structures collapsed to the complexes presented here upon geometry optimization. Therefore, for these systems, the interaction of the radicals with the ice surfaces is essentially dictated by H-bonds and dispersion forces.

3.3. Radical−Radical Reactivity. In this section, the reactivities of HCO with CH_3 and NH_2 on W18, W33-side, and W33-cav are investigated. Given that the chemical environment between W18 and W33-side is similar (note that the surface morphology of W33-side is very similar to that of W18 because W33 was built up by joining two W18 units[23]), the comparison of the results between these two

DOI: 10.1021/acsearthspacechem.9b00156
ACS Earth Space Chem. XXXX, XXX, XXX−XXX

Table 3. Highest Activation Enthalpies (at 0 K) for *Rc*, *dHa*, and *wHt* Reactions on W18, W33-side, and W33-cav at the BHLYP-D3 Level[a]

	W18			W33-side			W33-cav		
system	*Rc*	*dHa*	*wHt*	*Rc*	*dHa*	*wHt*	*Rc*	*dHa*	*wHt*
HCO + CH_3	2.6	5.2	100.6	NB	NB		6.8	10.2	78.8
HCO + NH_2	3.1	5.0	92.5	5.1	5.4		2.1	1.6	79.1

[a]Note that NB stands for "No Barrier". Units are in kJ/mol.

models will allow us to assess the effects introduced by the ASW model size. On the other hand, comparison between the reactivity on W33-side and W33-cav will allow us to assess the effects due to different surface environments, namely the presence of a higher number of radical/surface interactions. Please note that the cavity sites are probably more representative of the interstellar conditions than the side sites, as the vast majority of radicals are trapped in the bulk of the ice.

Figures 3, 4, and 5 show the PESs of the reactivity of CH_3/HCO and NH_2/HCO calculated at BHLYP-D3 on top of W18, W33-side, and W33-cav, respectively. Based on the results for the reactivity in the presence of W1 and W2 (see section 3.1), the same three reaction paths, i.e., *Rc*, *dHa*, and *wHt*, have been investigated. However, as the later processes are those exhibiting the highest activation enthalpies (as high as 100.6, 78.8, 92.5, and 79.1 kJ/mol for CH_3/HCO···W18, CH_3/HCO···W33-cav, NH_2/HCO···W18, and NH_2/HCO··· W33-cav, respectively), for the sake of clarity and with the aim of focusing only on the reactions that might play a role in interstellar chemistry, all results related to wHt can be found in the SI, with this section only showing the Rc and dHa reactions calculated at BHLYP-D3. In the same way, the reader can also find in the SI the results for all systems computed at BHLYP-D2 and, for W18, also at B3LYP-D3.

The initial structures of these systems were built according to the interaction patterns present in the single adsorbed radical complexes (see reactant structures of Figures 3−5). The *Rc* and *dHa* reactions, forming acetaldehyde or formamide and CO + CH_4 or CO + NH_3, respectively, both take place through a single step. That is, the bond formation between the two radicals for *Rc* and the H transfer for *dHa*. The only exception is the *dHa* reaction of CH_3/HCO···W18, which displays first a submerged activation energy step where HCO breaks its H-bonds with the surface to facilitate the H transfer (see *dHa*-TS1 of Figure 3(a)). By comparing the *Rc* and *dHa* reactions on these three cluster models, the general trend is that *Rc* activation enthalpies are lower than the *dHa* ones, between 0.5−4 kJ/mol lower. This was already observed in the presence of W1 and W2, where most of the *Rc* reactions are barrierless while the *dHa* present physical (although low) energy barriers. It should be noticed that the HCO/CH_3 reactions on the W33-side (Figure 4a) are barrierless due to the ZPE correction, as opposed to the W1 and W2 cases where the lack of barrier is because of the unstable singlet evolving directly toward products. Indeed, all the stationary points shown in Figure 4(a) have been identified as stable structures in the pure PESs (i.e., without ZPE corrections), but after introduction of ZPE corrections, the transition state becomes lower in energy than the reactants, and hence the barrierless character.

Another interesting point is that results for W18 and W33-side present some differences, particularly for the HCO + CH_3 reactions: on the W33-side, both *Rc* and *dHa* are barrierless while on W18 they present energy barriers. This is indicative of the fact that the size of the cluster for this radical−radical reactivity is important. Finally, no clear trends related to the effect of the ASW ice morphology can be obtained by comparing the W33-side results with the W33-cav. That is, for HCO + CH_3 reactions, activation enthalpies are higher on W33, while the opposite occurs for HCO + NH_2 ones.

In the following section, a comprehensive discussion of all these results is provided.

4. DISCUSSION

4.1. Reaction Channels and Competition to iCOMs Formation. Our computations show that if HCO + CH_3 and HCO + NH_2 react on top of an ASW ice, they have two sets of possible reaction products: (i) formation of iCOMs (*Rc* process), where the two radical species meet and couple, and (ii) the formation of the hydrogenated CH_4/NH_3 species, where the H atom of HCO migrates to CH_3/NH_2, which can happen either directly (*dHa* process) or through the ice water molecules adopting a H transfer relay mechanism (*wHt* process). The energetics associated with each process at the BHLYP-D3 level are summarized in Table 3.

The *Rc* and *dHa* reactions show, in all the studied systems, similar energetic features; that is, they are either barrierless or exhibit relatively low energy barriers. The highest pair of energy barriers concerns the HCO + CH_3 reactions on W33-cav, i.e., 6.8 and 10.2 kJ/mol for *Rc* and *dHa*, respectively. As a general trend, *dHa* reactions have slightly higher activation energies than *Rc* (by as much as 3.4 kJ/mol for HCO/CH_3 and 1.9 kJ/mol for HCO/NH_2). In some cases, like HCO/CH_3··· W33-side, HCO/NH_2···W33-side, and HCO/NH_2···W33-cav, both *Rc* and *dHa* can be considered as competitive reactions given the small activation energy differences. In contrast, the lowest energy barriers for *wHt* HCO + CH_3 and HCO + NH_2 reactions are ∼80 kJ/mol, respectively. These values are larger than any *Rc* and *dHa* energy barrier, and accordingly, *wHt* reactions cannot be considered by any means as competitive channels. The explanation of these energetic differences is provided by the reaction mechanisms. Rc and dHa reactions take place, in most of the cases, in a concerted way, in which the radicals, in essence, have to partly break the interactions with the surface to proceed with the reaction. In contrast, most of the *wHt* reactions adopt a multistep mechanism since the H transfer, which is assisted by different ice water molecules, involves different breaking/formation bonds. In these cases, high energy intermediates consisting of the coexistence of HCO and an OH radical are involved (see the SI).

In previous works by some of us, (e.g., ref 24) the *wHt* reactions between CH_3 + HCO on the W18 cluster model were observed to spontaneously occur during geometry optimization; that is, they were found to be barrierless. The difference with the computations presented in this work resides on the fact that, in the previous work,[24] the initial wave

DOI: 10.1021/acsearthspacechem.9b00156
ACS Earth Space Chem. XXXX, XXX, XXX−XXX

function did not describe a singlet biradical system but a metastable singlet closed-shell-like one, and hence the spontaneous evolution to form CO + CH_4. In this work, as well as in Rimola et al. (2018),[23] the initial wave function is actually describing a singlet biradical situation, which leads to a significant stabilization of the reactants and hence the presence of high energy barriers.

Finally, some words related to the chemical role played by the ice on these reactions are here provided. The *Rc* and *dHa* processes in the gas-phase (namely, in the absence of the icy grain) are, in both cases, barrierless. In contrast as explained above, in the presence of the surface, they exhibit, although low, energy barriers. Accordingly, from a rigorous chemical kinetics standpoint, the grains slow down the reactions. This leads us to think that a major role played by the grains is as that of third bodies, by quickly absorbing the nascent energy associated with the reactions, and hence stabilizing the products. This aspect is particularly appealing in the iCOMs formation processes via radical recombination since in the gas phase iCOMs can redissociate back to reactants if they are not stabilized through three-body reactions. As we will discuss below, the water morphology plays a role in the reaction energetics, although it does not change the essence of our conclusions.

4.2. Influence of the Water Ice Surface Model. Clear differences arise when comparing W33-side and W33-cav, as radicals on the latter exhibit more intermolecular interactions with the surface. This can be seen for example in the binding energies (higher on W33-cav than on W33-side, see Figure 2). But also on the *Rc* and *dHa* energy barriers, for which a different behavior is observed. Indeed, for HCO + CH_3 these reactions are barrierless on the W33-side, while on W33-cav they present energy barriers of 7 (*Rc*) and 10 (*dHa*) kJ/mol. On the other hand, for HCO + NH_2 the opposite behavior is observed: the energy barriers are higher on the W33-side than on W33-cav (see Table 3). This might be indicating that the different polarity of the radicals, i.e., CH_3/apolar and NH_2/polar, is important when several polar-based intermolecular interactions surround the reaction sites, as is the case of W33-cav.

Finally, the size difference between the W18 and W33 models does not seem to provide a consistent trend, neither for binding energies nor for the PESs. This is probably due to the modest energetics of reactions of interest, which are the result of many intermingled effects, i.e. H-bond and dispersion interaction strength, small charge transfer, and polarization. All these components are affected by the nature and size of the water adopted clusters without a definite and predictable structure−properties relationship.

4.3. Astrophysical Implications. A major goal of this study is to understand whether iCOMs can be formed on the icy grain surfaces by the direct combination of radicals, a process assumed to be efficient in the majority of current astrochemical models (see Introduction). The present computations show that (i) there is a feasible channel leading to iCOM formation through radical−radical combination, (ii) this channel may possess a barrier, and (iii) there is at least a competitive reaction where radicals exchange a hydrogen atom, the outcome of which is somewhat a step backward in chemical complexity as the products are simple hydrogenated species (CH_4 and NH_3 in the current work) and CO.

The present computational data does not allow us to definitively exclude the presence of a barrier in the radicals combination. Indeed, although common sense would indicate a lack of barrier, calculations show that the presence of the ice water molecules introduces an intermolecular interaction that depends on where the radicals are placed and on the radical polarity. This interaction probably necessitates energy to be broken: it is not obvious that this energy is available in the ISM environments. In fact, according to the Garrod et al. model,[16] once the radicals are formed, they remain frozen on the ice and subsequently more ice layers build up on top. The radicals remain imprisoned in cavity structures inside the mantle and once the temperature reaches ∼30 K due to the evolution of the central protostar, they diffuse and react. Among the three reactions sites discussed in this article (W18, W33-side, and W33-cav), the one best resembling this picture is given by W33-cav (see Figure 1) due to the larger number of intermolecular interactions. The Rc and dHa energy barriers in the cavity have been shown to be larger for HCO + CH_3 than for HCO + NH_2, due probably to the different polarities of CH_3 and NH_2. If converted to Kelvin, the *Rc* and *dHa* barriers for HCO + CH_3 and HCO + NH_2 on W33-cav are about 800, 1200, 250, and 190 K, respectively (see Table 3). Thus, the efficiency of these reactions is not expected to be very high, especially for HCO + CH_3.

It has also to be noted that the starting points from where we study the reactivity in W33-cav (see reactant geometries from Figure 5) contain both radicals very close by and in the same cavity site (given the computational cost of higher quality calculations, we cannot simulate much larger clusters). However, in a more realistic situation each radical would be stored in different cavities and thus the actual barriers to overcome would not only involve breaking the radical/ice intermolecular interactions but also surmounting the ice surface diffusional barriers, decreasing in this way the efficiency of Rc and dHa reactions, even if they were ultimately barrierless.

We conclude this part mentioning that astronomical observations can also bring useful constraints to the formation routes of iCOMs showing alternative routes to the ones explored in this study. For example, high spatial resolution observations of formamide line emission toward the protostellar shock site L1157-B1 have demonstrated that the formation of formamide is dominated by the gas-phase reaction NH_2 + H_2CO,[65] a reaction theoretically studied by some of us.[66,67] On the same line, observations of the deuterated forms of formamide (namely containing D rather than H atoms) also provide strong constraints on the formation route of this species in the hot corino of the solar-type protostar IRAS 16293-2422. The comparison of the measured $NHDHCO/NH_2CHO$ and NH_2CDO/NH_2CHO abundance ratios[33] with those predicted by theoretical quantum chemical calculations[67] strongly favors a gas-phase origin of formamide also in this source. Therefore, it is very likely that both grain-surface and gas-phase reactions contribute to the enrichment of iCOMs in the ISM, playing different roles in different environments.

5. CONCLUSIONS AND PERSPECTIVES

In this work, we have carried out an accurate study of the chemistry of two couples of radicals, HCO + CH_3 and HCO + NH_2, on icy surfaces. Our goal was to understand the possible reactions between the two radicals on water ice mantles and how the results depend on the accuracy of the employed quantum chemical methods and on the adopted surface

DOI: 10.1021/acsearthspacechem.9b00156
ACS Earth Space Chem. XXXX, XXX, XXX−XXX

models. To this end, we used different quantum chemistry methods, in particular two hybrid DFT methods, B3LYP and BHLYP, plus the wave function based CCSD(T) and multi reference-based CASPT2 ones. In addition, we adopted different cluster models simulating the water surfaces: we started with the simple cases of one and two water molecules to identify the basic processes and to test the methodology, and then using two different, large molecular cluster models for the ASW surfaces, of 18 and 33 water molecules, respectively.

The conclusions of this work are the following:

1. If the reaction occurs, two channels are possible: (i) the combination of radicals into acetaldehyde/formamide and (ii) the formation of CH_4/NH_3 plus CO, where the H atom of HCO is passed to CH_3/NH_2 via H abstraction.
2. The two reaction channels are either barrierless or have relatively low energy barriers, from about 2 to 10 kJ/mol, as summarized in Table 3.
3. Comparison of the results obtained with B3LYP-D3 and BHLYP (the latter in its pure definition and including both D2 and D3 dispersion corrections) with those provided by CASPT2 for activation energies and those provided by CCSD(T) for binding energies, using one and two water molecules plus the radicals as test systems, indicates that B3LYP-D3 underestimates the energy barriers, while BHLYP-based methods show a reasonably good performance. For the computations relative to the 18 and 33 water clusters, we adopted BHLYP-D3 as it has been found, in the test systems, to properly deal with both the radical/surface binding and the radical−radical activation energies.
4. The morphology of the water cluster used for the simulations definitely affects the results of the computations. In particular, radicals would interact differently depending on whether they sit on a cavity structure, where they can establish several weak intermolecular interactions with the icy water molecules, in addition to the H-bond.
5. Taking into account the results described in points 1, 2, and 4, the mechanism that radical combination necessarily produces iCOMs is still to be validated and should be taken with care in astrochemical models.

In order to make progress, more accurate computations would be needed, but they are not yet within the reach of the current computational capacities. On the other hand, dynamical simulations would help to understand the effect of the relative orientation of radicals upon encounter.

■ ASSOCIATED CONTENT

Supporting Information

The Supporting Information is available free of charge on the ACS Publications website at DOI: 10.1021/acsearthspacechem.9b00156.

Structures and errors of the benchmark study, PESs of water assisted H-transfer reactions on W18 and W33-cav, structures, binding energies, and PESs (of radical−radical coupling, direct H-abstraction, and water assisted H-transfer reactions) on the three analyzed surfaces (W18, W33-side, and W33-cav) at BHLYP-D2 and on W18 at B3LYP-D3, and optimized Cartesian coordinates of all the structures (PDF)

■ AUTHOR INFORMATION

Corresponding Authors

*E-mail: albert.rimola@uab.cat.

*E-mail: cecilia.ceccarelli@univ-grenoble-alpes.fr.

ORCID

Albert Rimola: 0000-0002-9637-4554

Piero Ugliengo: 0000-0001-8886-9832

Nadia Balucani: 0000-0001-5121-5683

Notes

The authors declare no competing financial interest.

■ ACKNOWLEDGMENTS

JER and CC acknowledge funding from the European Research Council (ERC) under the European Union's Horizon 2020 research and innovation program, for the Project "the Dawn of Organic Chemistry" (DOC), grant agreement No 741002. AR is indebted to the "Ramón y Cajal" program. MINECO (project CTQ2017-89132-P) and DIUE (project 2017SGR1323) are acknowledged. PU and NB acknowledge MIUR (Ministero dellIstruzione, dellUniversità e della Ricerca) and Scuola Normale Superiore (project PRIN 2015, STARS in the CAOS - Simulation Tools for Astrochemical Reactivity and Spectroscopy in the Cyberinfrastructure for Astrochemical Organic Species, cod. 2015F59J3R). This project has received funding from the European Unions Horizon 2020 research and innovation programme under the Marie Skodowska-Curie grant agreement No 811312. We thank Prof. Gretobape for fruitful and stimulating discussions. Most of the calculations presented in this paper were performed using the GRICAD infrastructure (https://gricad.univ-grenoble-alpes.fr), which is partly supported by the Equip@Meso project (reference ANR-10-EQPX-29-01) of the programme Investissements d'Avenir supervised by the Agence Nationale pour la Recherche. Additionally this work was granted access to the HPC resources of IDRIS under the allocation 2019-A0060810797 attributed by GENCI (Grand Equipement National de Calcul Intensif).

■ REFERENCES

(1) Rubin, R.; Swenson, G., Jr; Benson, R.; Tigelaar, H.; Flygare, W. Microwave detection of interstellar formamide. *Astrophys. J.* **1971**, *169*, L39.

(2) Cazaux, S.; Tielens, A.; Ceccarelli, C.; Castets, A.; Wakelam, V.; Caux, E.; Parise, B.; Teyssier, D. The Hot Core around the Low-Mass Protostar IRAS 16293−2422: Scoundrels Rule! *Astrophys. Astrophys. J.* **2003**, *593*, L51.

(3) Herbst, E.; Van Dishoeck, E. F. Complex organic interstellar molecules. *Annu. Rev. Astron. Astrophys.* **2009**, *47*, 427−480.

(4) Caselli, P.; Ceccarelli, C. Our astrochemical heritage. *Astron. Astrophys. Rev.* **2012**, *20*, 56.

(5) Belloche, A.; Meshcheryakov, A.; Garrod, R.; Ilyushin, V.; Alekseev, E.; Motiyenko, R.; Margulès, L.; Müller, H.; Menten, K. Rotational spectroscopy, tentative interstellar detection, and chemical modeling of N-methylformamide. *Astron. Astrophys.* **2017**, *601*, A49.

(6) McGuire, B. A. 2018 Census of Interstellar, Circumstellar, Extragalactic, Protoplanetary Disk, and Exoplanetary Molecules. *Astrophys. J. Suppl. Ser.* **2018**, *239*, 17.

(7) Bockelée-Morvan, D. An overview of comet composition. *Proc. Int. Astron. Union* **2011**, *7*, 261−274.

(8) Ceccarelli, C.; Caselli, P.; Bockelée-Morvan, D.; Mousis, O.; Pizzarello, S.; Robert, F.; Semenov, D. Deuterium Fractionation: The Ariadne's Thread from the Precollapse Phase to Meteorites and Comets Today. In *Protostars and Planets VI*; Beuther, H., Klessen, R. S., Dullemond, C. P., Henning, T. Eds.; University of Arizona Press:

DOI: 10.1021/acsearthspacechem.9b00156
ACS Earth Space Chem. XXXX, XXX, XXX−XXX

Tucson, 2014; pp 859−882. DOI: 10.2458/azu_uapress_9780816531240-ch037.
(9) Bianchi, E.; Codella, C.; Ceccarelli, C.; Vazart, F.; Bachiller, R.; Balucani, N.; Bouvier, M.; DeSimone, M.; Enrique-Romero, J.; Kahane, C.; Lefloch, B.; López-Sepulcre, A.; Ospina-Zamudio, J.; Podio, L.; Taquet, V. The census of interstellar complex organic molecules in the Class I hot corino of SVS13-A. *Mon. Not. R. Astron. Soc.* **2019**, *483*, 1850−1861.
(10) Ceccarelli, C.; et al. Seeds Of Life In Space (SOLIS): The Organic Composition Diversity at 300−1000 au Scale in Solar-type Star-forming Regions. *Astrophys. J.* **2017**, *850*, 176.
(11) Charnley, S.; Tielens, A.; Millar, T. On the molecular complexity of the hot cores in Orion A-Grain surface chemistry as 'The last refuge of the scoundrel'. *Astrophys. J.* **1992**, *399*, L71−L74.
(12) Caselli, P.; Hasegawa, T.; Herbst, E. Chemical differentiation between star-forming regions-The Orion hot core and compact ridge. *Astrophys. J.* **1993**, *408*, 548−558.
(13) Ceccarelli, C.; Loinard, L.; Castets, A.; Tielens, A.; Caux, E.; Lefloch, B.; Vastel, C. Extended D_2CO emission: The smoking gun of grain surface-chemistry. *Astron. Astrophys.* **2001**, *372*, 998−1004.
(14) Geppert, W. D.; Thomas, R. D.; Ehlerding, A.; Hellberg, F.; Österdahl, F.; Hamberg, M.; Semaniak, J.; Zhaunerchyk, V.; Kaminska, M.; Källberg, A.; Paal, A.; Larsson, M. Dissociative recombination branching ratios and their influence on interstellar clouds. *J. Phys.: Conf. Ser.* **2005**, *4*, 26−31.
(15) Horn, A.; Møllendal, H.; Sekiguchi, O.; Uggerud, E.; Roberts, H.; Herbst, E.; Viggiano, A.; Fridgen, T. D. The gas-phase formation of methyl formate in hot molecular cores. *Astrophys. J.* **2004**, *611*, 605.
(16) Garrod, R. T.; Herbst, E. Formation of methyl formate and other organic species in the warm-up phase of hot molecular cores. *Astron. Astrophys.* **2006**, *457*, 927−936.
(17) Herbst, E. The synthesis of large interstellar molecules. *Int. Rev. Phys. Chem.* **2017**, *36*, 287−331.
(18) Garrod, R. A new modified-rate approach for gas-grain chemical simulations. *Astron. Astrophys.* **2008**, *491*, 239−251.
(19) Acharyya, K.; Herbst, E. Molecular Development in the Large Magellanic Cloud. *Astrophys. J.* **2015**, *812*, 142.
(20) Ruaud, M.; Loison, J.; Hickson, K.; Gratier, P.; Hersant, F.; Wakelam, V. Modelling complex organic molecules in dense regions: Eley−Rideal and complex induced reaction. *Mon. Not. R. Astron. Soc.* **2015**, *447*, 4004−4017.
(21) Drozdovskaya, M. N.; Walsh, C.; Van Dishoeck, E. F.; Furuya, K.; Marboeuf, U.; Thiabaud, A.; Harsono, D.; Visser, R. Cometary ices in forming protoplanetary disc midplanes. *Mon. Not. R. Astron. Soc.* **2016**, *462*, 977−993.
(22) Vasyunin, A. I.; Caselli, P.; Dulieu, F.; Jiménez-Serra, I. Formation of complex molecules in prestellar cores: a multilayer approach. *Astrophys. J.* **2017**, *842*, 33.
(23) Rimola, A.; Skouteris, D.; Balucani, N.; Ceccarelli, C.; Enrique-Romero, J.; Taquet, V.; Ugliengo, P. Can Formamide Be Formed on Interstellar Ice? An Atomistic Perspective. *ACS Earth Space Chem.* **2018**, *2*, 720−734.
(24) Enrique-Romero, J.; Rimola, A.; Ceccarelli, C.; Balucani, N. The (impossible?) formation of acetaldehyde on the grain surfaces: insights from quantum chemical calculations. *Mon. Not. R. Astron. Soc.: Lett.* **2016**, *459*, L6−L10.
(25) Balucani, N.; Ceccarelli, C.; Taquet, V. Formation of complex organic molecules in cold objects: the role of gas-phase reactions. *Mon. Not. R. Astron. Soc.: Lett.* **2015**, *449*, L16−L20.
(26) Spezia, R.; Jeanvoine, Y.; Hase, W. L.; Song, K.; Largo, A. Synthesis of Formamide and Related Organic Species in the Interstellar Medium via Chemical Dynamics Simulations. *Astrophys. J.* **2016**, *826*, 107.
(27) Taquet, V.; Wirström, E. S.; Charnley, S. B. Formation and Recondensation of Complex Organic Molecules during Protostellar Luminosity Outbursts. *Astrophys. J.* **2016**, *821*, 46.
(28) Suzuki, T.; Ohishi, M.; Hirota, T.; Saito, M.; Majumdar, L.; Wakelam, V. Survey Observations of a Possible Glycine Precursor, Methanimine (CH_2NH). *Astrophys. J.* **2016**, *825*, 79.
(29) Codella, C.; et al. Seeds of Life in Space (SOLIS) - II. Formamide in protostellar shocks: Evidence for gas-phase formation. *Astron. Astrophys.* **2017**, *605*, L3.
(30) Skouteris, D.; Balucani, N.; Ceccarelli, C.; Faginas Lago, N.; Codella, C.; Falcinelli, S.; Rosi, M. Interstellar dimethyl ether gas-phase formation: a quantum chemistry and kinetics study. *Mon. Not. R. Astron. Soc.* **2019**, *482*, 3567−3575.
(31) Rosi, M.; Skouteris, D.; Casavecchia, P.; Falcinelli, S.; Ceccarelli, C.; Balucani, N. Formation of Nitrogen-Bearing Organic Molecules in the Reaction NH + C_2H_5: A Theoretical Investigation and Main Implications for Prebiotic Chemistry in Space. *Computational Science and Its Applications − ICCSA 2018 (Melbourne, Australia)*; Springer International Publishing: Cham (Switzerland), 2018; pp 773−782.
(32) Skouteris, D.; Balucani, N.; Ceccarelli, C.; Vazart, F.; Puzzarini, C.; Barone, V.; Codella, C.; Lefloch, B. The Genealogical Tree of Ethanol: Gas-phase Formation of Glycolaldehyde, Acetic Acid, and Formic Acid. *Astrophys. J.* **2018**, *854*, 135.
(33) Coutens, A.; et al. The ALMA-PILS survey: First detections of deuterated formamide and deuterated isocyanic acid in the interstellar medium. *Astron. Astrophys.* **2016**, *590*, L6.
(34) Müller, H. S. P.; Belloche, A.; Xu, L.-H.; Lees, R. M.; Garrod, R. T.; Walters, A.; van Wijngaarden, J.; Lewen, F.; Schlemmer, S.; Menten, K. M. Exploring molecular complexity with ALMA (EMoCA): Alkanethiols and alkanols in Sagittarius B2(N2). *Astron. Astrophys.* **2016**, *587*, A92.
(35) Ligterink, N. F. W.; Terwisscha van Scheltinga, J.; Taquet, V.; Jørgensen, J. K.; Cazaux, S.; van Dishoeck, E. F.; Linnartz, H. The formation of peptide-like molecules on interstellar dust grains. *Mon. Not. R. Astron. Soc.* **2018**, *480*, 3628−3643.
(36) Strazzulla, G.; Palumbo, M. Organics produced by ion irradiation of ices: Some recent results. *Adv. Space Res.* **2001**, *27*, 237−243.
(37) Palumbo, M. E.; Baratta, G. A.; Fulvio, D.; Garozzo, M.; Gomis, O.; Leto, G.; Spinella, F.; Strazzulla, G. Ion irradiation of astrophysical ices. *J. Phys. Conf. Ser.* **2008**, *101*, 012002.
(38) Woods, P. M.; Slater, B.; Raza, Z.; Viti, S.; Brown, W. A.; Burke, D. J. Glycolaldehyde formation via the dimerization of the formyl radical. *Astrophys. J.* **2013**, *777*, 90.
(39) Fedoseev, G.; Ioppolo, S.; Zhao, D.; Lamberts, T.; Linnartz, H. Low-temperature surface formation of NH_3 and HNCO: hydrogenation of nitrogen atoms in CO-rich interstellar ice analogues. *Mon. Not. R. Astron. Soc.* **2015**, *446*, 439−448.
(40) Fedoseev, G.; Cuppen, H. M.; Ioppolo, S.; Lamberts, T.; Linnartz, H. Experimental evidence for glycolaldehyde and ethylene glycol formation by surface hydrogenation of CO molecules under dense molecular cloud conditions. *Mon. Not. R. Astron. Soc.* **2015**, *448*, 1288−1297.
(41) Linnartz, H.; Ioppolo, S.; Fedoseev, G. Atom addition reactions in interstellar ice analogues. *Int. Rev. Phys. Chem.* **2015**, *34*, 205−237.
(42) de Barros, A. L. F.; da Silveira, E. F.; Fulvio, D.; Boduch, P.; Rothard, H. Formation of nitrogen- and oxygen-bearing molecules from radiolysis of nitrous oxide ices implications for Solar system and interstellar ices. *Mon. Not. R. Astron. Soc.* **2017**, *465*, 3281−3290.
(43) Butscher, T.; Duvernay, F.; Rimola, A.; Segado-Centellas, M.; Chiavassa, T. Radical recombination in interstellar ices, a not so simple mechanism. *Phys. Chem. Chem. Phys.* **2017**, *19*, 2857−2866.
(44) Fedoseev, G.; Chuang, K.-J.; Ioppolo, S.; Qasim, D.; van Dishoeck, E. F.; Linnartz, H. Formation of Glycerol through Hydrogenation of CO Ice under Prestellar Core Conditions. *Astrophys. J.* **2017**, *842*, 52.
(45) Arumainayagam, C. R.; Garrod, R. T.; Boyer, M. C.; Hay, A. K.; Bao, S. T.; Campbell, J. S.; Wang, J.; Nowak, C. M.; Arumainayagam, M. R.; Hodge, P. J. Extraterrestrial prebiotic molecules: photochemistry vs. radiation chemistry of interstellar ices. *Chem. Soc. Rev.* **2019**, *48*, 2293−2314.
(46) Dulieu, F.; Nguyen, T.; Congiu, E.; Baouche, S.; Taquet, V. Efficient formation route of the prebiotic molecule formamide on

DOI: 10.1021/acsearthspacechem.9b00156
ACS Earth Space Chem. XXXX, XXX, XXX−XXX

interstellar dust grains. *Mon. Not. R. Astron. Soc.: Lett.* **2019**, *484*, L119−L123.
(47) Pereira, R.; de Barros, A.; Fulvio, D.; Boduch, P.; Rothard, H.; da Silveira, E. NO bearing molecules produced by radiolysis of N_2O and N_2O:CO_2 ices. *Nucl. Instrum. Methods Phys. Res., Sect. B* **2019**, DOI: 10.1016/j.nimb.2019.03.048.
(48) Lamberts, T.; Markmeyer, M. N.; Kolb, F. J.; Kstner, J. Formation of Acetaldehyde on CO-Rich Ices. *ACS Earth Space Chem.* **2019**, *3*, 958−963.
(49) Abe, M. Diradicals. *Chem. Rev.* **2013**, *113*, 7011−7088.
(50) Frisch, M. J.; et al. *Gaussian09*, Revision D.01; Gaussian Inc.: Wallingford, CT, 2009.
(51) Karlström, G.; Lindh, R.; Malmqvist, P.-Å.; Roos, B. O.; Ryde, U.; Veryazov, V.; Widmark, P.-O.; Cossi, M.; Schimmelpfennig, B.; Neogrady, P.; Seijo, L. MOLCAS: a program package for computational chemistry. *Comput. Mater. Sci.* **2003**, *28*, 222−239 Proceedings of the Symposium on Software Development for Process and Materials Design. .
(52) Aquilante, F.; De Vico; Luca; Ferré, N.; Ghigo, G.; Malmqvist, P.; Neogrády, P.; Pedersen, T. B.; Pitoňák, M.; Reiher, M.; Roos, B. O.; Serrano-Andrés, L.; Urban, M.; Veryazov, V.; Lindh, R. MOLCAS 7: The Next Generation. *J. Comput. Chem.* **2010**, *31*, 224−247.
(53) Aquilante, F.; et al. Molcas 8: New capabilities for multiconfigurational quantum chemical calculations across the periodic table. *J. Comput. Chem.* **2016**, *37*, 506−541.
(54) Fernandez Galván, I.; Vacher, M.; Alavi, A.; Angeli, C.; Autschbach, J.; Bao, J. J.; Bokarev, S. I.; Bogdanov, N. A.; Carlson, R. K.; Chibotaru, L. F.; et al. *OpenMolcas: From Source Code to Insight*. 2019; https://chemrxiv.org/articles/OpenMolcas_From_Source_Code_to_Insight/8234021/1.
(55) Lee, C.; Yang, W.; Parr, R. G. Development of the Colle-Salvetti correlation-energy formula into a functional of the electron density. *Phys. Rev. B: Condens. Matter Mater. Phys.* **1988**, *37*, 785.
(56) Becke, A. D. Density-functional thermochemistry. III. The role of exact exchange. *J. Chem. Phys.* **1993**, *98*, 5648−5652.
(57) Becke, A. D. A new mixing of Hartree−Fock and local density-functional theories. *J. Chem. Phys.* **1993**, *98*, 1372−1377.
(58) Grimme, S.; Antony, J.; Ehrlich, S.; Krieg, H. A consistent and accurate ab initio parametrization of density functional dispersion correction (DFT-D) for the 94 elements H-Pu. *J. Chem. Phys.* **2010**, *132*, 154104.
(59) Grimme, S. Semiempirical GGA-type density functional constructed with a long-range dispersion correction. *J. Comput. Chem.* **2006**, *27*, 1787−1799.
(60) Rimola, A.; Taquet, V.; Ugliengo, P.; Balucani, N.; Ceccarelli, C. Combined quantum chemical and modeling study of CO hydrogenation on water ice. *Astron. Astrophys.* **2014**, *572*, A70.
(61) McQuarrie, D. *Statistical Mechanics*; Harper & Row: New York, 1976.
(62) Boys, S. F.; Bernardi, F. d. The calculation of small molecular interactions by the differences of separate total energies. Some procedures with reduced errors. *Mol. Phys.* **1970**, *19*, 553−566.
(63) Wakelam, V.; Loison, J.-C.; Mereau, R.; Ruaud, M. Binding energies: new values and impact on the efficiency of chemical desorption. *Mol. Astrophys.* **2017**, *6*, 22−35.
(64) Sameera, W. M. C.; Senevirathne, B.; Andersson, S.; Maseras, F.; Nyman, G. ONIOM(QM:AMOEBA09) Study on Binding Energies and Binding Preference of OH, HCO, and CH_3 Radicals on Hexagonal Water Ice (Ih). *J. Phys. Chem. C* **2017**, *121*, 15223−15232.
(65) Codella, C.; et al. Seeds of Life in Space (SOLIS). II. Formamide in protostellar shocks: Evidence for gas-phase formation. *Astron. Astrophys.* **2017**, *605*, L3.
(66) Barone, V.; Latouche, C.; Skouteris, D.; Vazart, F.; Balucani, N.; Ceccarelli, C.; Lefloch, B. Gas-phase formation of the prebiotic molecule formamide: insights from new quantum computations. *Mon. Not. R. Astron. Soc.: Lett.* **2015**, *453*, L31−L35.
(67) Skouteris, D.; Vazart, F.; Ceccarelli, C.; Balucani, N.; Puzzarini, C.; Barone, V. New quantum chemical computations of formamide deuteration support gas-phase formation of this prebiotic molecule. *Mon. Not. R. Astron. Soc.: Lett.* **2017**, *468*, L1−L5.

DOI: 10.1021/acsearthspacechem.9b00156
ACS Earth Space Chem. XXXX, XXX, XXX−XXX

Astronomy & Astrophysics manuscript no. output
August 25, 2021

Theoretical computations on the efficiency of acetaldehyde formation on interstellar icy grains

Joan Enrique-Romero[1,2], Cecilia Ceccarelli[1], Albert Rimola[2], Dimitrios Skouteris[3], Nadia Balucani[1,4,5], and Piero Ugliengo[6]

[1] Univ. Grenoble Alpes, CNRS, Institut de Planétologie et d'Astrophysique de Grenoble (IPAG), 38000 Grenoble, France
e-mail: juan.enrique-romero@univ-grenoble-alpes.fr
e-mail: cecilia.ceccarelli@univ-grenoble-alpes.fr
[2] Departament de Química, Universitat Autònoma de Barcelona, Bellaterra, 08193, Catalonia, Spain
e-mail: albert.rimola@uab.cat
[3] Master-Tech, I-06123 Perugia, Italy
[4] Dipartimento di Chimica, Biologia e Biotecnologie, Università di Perugia, Via Elce di Sotto 8, 06123 Perugia, Italy
[5] Osservatorio Astrofisico di Arcetri, Largo E. Fermi 5, 50125 Firenze, Italy
[6] Dipartimento di Chimica and Nanostructured Interfaces and Surfaces (NIS) Centre, Università degli Studi di Torino, via P. Giuria 7, 10125, Torino, Italy

Received –; accepted –

ABSTRACT

Context. Interstellar grains are known to be important actors in the formation of interstellar molecules such as H_2, water, ammonia, and methanol. It has been suggested that the so-called interstellar complex organic molecules (iCOMs) are also formed on the interstellar grain icy surfaces by the combination of radicals via reactions assumed to have an efficiency equal to unity.

Aims. In this work, we aim to investigate the robustness or weakness of this assumption. In particular, we consider the case of acetaldehyde (CH_3CHO), one of the most abundant and commonly identified iCOMs, as a starting study case. In the literature, it has been postulated that acetaldehyde is formed on the icy surfaces via the combination of HCO and CH_3. Here we report new theoretical computations on the efficiency of its formation.

Methods. To this end, we coupled quantum chemical calculations of the energetics and kinetics of the reaction CH_3 + HCO, which can lead to the formation of CH_3CHO or CO + CH_4. Specifically, we combined reaction kinetics computed with the Rice–Ramsperger–Kassel–Marcus (RRKM) theory (tunneling included) method with diffusion and desorption competitive channels. We provide the results of our computations in the format used by astrochemical models to facilitate their exploitation.

Results. Our new computations indicate that the efficiency of acetaldehyde formation on the icy surfaces is a complex function of the temperature and, more importantly, of the assumed diffusion over binding energy ratio f of the CH_3 radical. If the ratio f is ≥0.4, the efficiency is equal to unity in the range where the reaction can occur, namely between 12 and 30 K. However, if f is smaller, the efficiency dramatically crashes: with f=0.3, it is at most 0.01. In addition, the formation of acetaldehyde is always in competition with that of CO + CH_4.

Conclusions. Given the poor understanding of the diffusion over binding energy ratio f and the dramatic effect it has on the formation, or not, of acetaldehyde via the combination of HCO and CH_3 on icy surfaces, model predictions based on the formation efficiency equal to one should to be taken with precaution. The latest measurements of f suggest f=0.3 and, if confirmed for CH_3, this would rule out the formation of acetaldehyde on the interstellar icy surfaces. We recall the alternative possibility, which was recently reviewed, that acetaldehyde could be synthesized in the gas phase starting from ethanol. Finally, our computations show the paramount importance played by the micro-physics involved in the interstellar surface chemistry and call for extensive similar studies on different systems believed to form iCOMs on the interstellar icy surfaces.

Key words. Interstellar molecules — Interstellar dust processes — Dense interstellar clouds — Surface ices

1. Introduction

Interstellar dust grains are known to be an essential component of the interstellar medium (ISM) for a large variety of reasons. Among them, dust grains provide the surfaces for chemical reactions that are difficult (or impossible) to take place in the gas phase. An emblematic example is the formation of the most abundant molecule in the universe, H_2, which largely occurs on grain surfaces (e.g., Hollenbach & Salpeter 1970; Vidali 2013; Wakelam et al. 2017). Other important examples are the formation of water (e.g., Dulieu et al. 2010; He & Vidali 2014a; Lamberts & Kästner 2017; Molpeceres et al. 2018) and methanol (e.g., Tielens & Hagen 1982; Watanabe & Kouchi 2002; Rimola et al. 2014), which are also abundant molecules predominantly synthesized on grain surfaces. As a matter of fact, in cold regions, the refractory core of the grains, made up of silicate or carbonaceous material, are coated by icy mantles mostly formed by amorphous water ice synthesized on these surfaces (e.g., Boogert et al. 2015).

It has also been suggested that more complex molecules, the so-called interstellar complex organic molecules (hereinafter iCOMs: Ceccarelli et al. 2017), composed of at least six atoms and containing at least one heavy element other than C, can also be a grain-surface chemistry product (e.g., Garrod & Herbst 2006; Herbst & van Dishoeck 2009; Garrod et al. 2009; Ruaud

et al. 2015; Aikawa et al. 2020; Barger & Garrod 2020). One crucial step of this theory is the formation of iCOMs from the combination of two radicals when they meet on the grain icy surfaces. In the majority of the current astrochemical models, the reaction is assumed to proceed barrierless and without competitive channels.

However, previous theoretical works have shown that this is not necessarily the case (Rimola et al. 2018; Enrique-Romero et al. 2019, 2020). For example, theoretical calculations on the energetics showed that the formation of acetaldehyde (CH_3CHO) on the icy surfaces via HCO + CH_3 is in competition with the formation of CO + CH_4 via direct H-abstraction. In addition, both reactions present barriers, caused by the orientation of the species on the ices, which are governed by the interactions created between the surface water molecules and the two radicals. Indeed, the height of the barriers depends on the site where the reaction occurs, whether the two radicals are on a "plain" ice surface or in a "cavity", namely on the interactions between the radicals and the ice water molecules.

In the present work, we pursue the above theoretical studies and present new computations to evaluate the efficiency of the radical-radical combination and H-abstraction reactions as a function of the temperature of the icy surfaces with the goal to provide values that can be easily incorporated in astrochemical models. In particular, here we focus on acetaldehyde (CH_3CHO), one of the most abundant and common iCOMs (e.g., Blake et al. 1987; Cazaux et al. 2003; Vastel et al. 2014; Lefloch et al. 2017; Sakai et al. 2018; Bianchi et al. 2019; Csengeri et al. 2019; Lee et al. 2019; Scibelli & Shirley 2020), as a study case.

Following the works of Enrique-Romero et al. (2019, 2020), we here consider the two competing reactions that can arise from the reactivity between HCO and CH_3:

(1) $HCO + CH_3 \rightarrow CH_3HCO$
(2) $HCO + CH_3 \rightarrow CH_4 + CO$.

Our goal is to evaluate the efficiency of each of the two reactions occurring on the interstellar icy surfaces. To this end, we computed the kinetics of the two reactions, using the previous energetic calculations by Enrique-Romero et al. (2019) as a base and the models of amorphous solid water (ASW) for the ice described in Rimola et al. (2018) and Enrique-Romero et al. (2019). In our calculations, we assume that the two radicals are in the most stable energetic configuration prior to reaction, an assumption motivated by the long surface residence timescale (1–10 Myr, the molecular life timescale: e.g. Chevance et al. 2020) that radicals would experience before they become mobile and react with each other.

The article is organized as follows. The definition of the reaction efficiency and our choices for the various assumptions entering in the computations are discussed in Sect. 2. Sect. 3 describes the adopted methodology. The results are reported in Sect. 4 and we discuss the implications of our new calculations in Sect. 5.

2. Efficiency of radical-radical reaction products on icy surfaces

2.1. Surface-reaction rate definition

Generally, astrochemical models solve the time-dependent equations of the species densities by computing the formation and destruction rates of each species at a given time, both for species in the gas and on the grain surfaces. In particular, the rate R_{ij} of the formation reaction from two reactant species i and j is expressed as $R_{ij} = k_{ij} n_i n_j$, where n_i and n_j are the densities of species i and j, and k_{ij} is the rate constant at a given temperature. For surface reactions the latter is given by (Hasegawa et al. 1992):

$$k_{ij} = \varepsilon_{ij} \times \frac{R_{\mathrm{diff},i} + R_{\mathrm{diff},j}}{n_d}, \quad (1)$$

where ε_{ij} is an efficiency factor which accounts for chemical barriers, n_d is the dust grain density and $R_{\mathrm{diff},i}$ and $R_{\mathrm{diff},j}$ are the diffusion rates for species i and j, respectively. These diffusion rates are defined as $1/t_{\mathrm{diff},k}$, where $t_{\mathrm{diff},k}$ is the time it takes the species k to scan the whole grain (e.g., Garrod & Herbst 2006). Thus, the sum $R_{\mathrm{diff},i} + R_{\mathrm{diff},j}$ gives the rate at which species i and j meet on the surface.

Regarding the efficiency factor ε_{ij}, different approaches exist in order to derive it. Hasegawa et al. (1992) set it to either 1, in barrierless reactions, or to the tunnelling probability, if the reaction has an activation energy barrier and one of the reactants is light enough to tunnel through it. Later models include also the thermal probability for reaction, if there is an activation energy barrier (e.g., Garrod & Herbst 2006). However, in the presence of an activation energy barrier, reactants need to be close to each other for a certain amount of time for the reaction to occur (Tielens & Hagen 1982). In order to take this into account, Chang et al. (2007) redefined the efficiency taking into account the competition between diffusion and desorption of the most mobile species, as follows:

$$\varepsilon_{ij} = \frac{k_{aeb}(ij)}{k_{aeb}(ij) + k_{diff}(i) + k_{des}(i)}, \quad (2)$$

where $k_{aeb}(ij)$ is the rate constant accounting for the reaction activation energy barrier, which is described by either classical thermal kinetics or quantum tunnelling; (i.e., a frequency times a Boltzmann factor or the tunnelling probability); $k_{diff}(i)$ is the rate constant for the diffusion of the most mobile species and $k_{des}(i)$ is its desorption rate constant. Garrod & Pauly (2011) further modified Eq. (2) by removing the desorption term and adding the diffusion of the other reaction partner, j, in the denominator.

For reactions involving radicals, ε_{ij} is normally assumed equal to 1 (e.g., Garrod & Herbst 2006), as they are considered to react via barrierless exothermic channels.

In this work, we include diffusion and desorption rates of the two reactants, which takes into account both the Chang et al. (2007) and Garrod & Pauly (2011) recipes:

$$\varepsilon_{ij} = \frac{k_{aeb}(ij)}{k_{aeb}(ij) + k_{diff}(i) + k_{des}(i) + k_{diff}(j) + k_{des}(j)}. \quad (3)$$

In practice, the efficiency for the reaction is equal to unity only when the time scale for the reaction to occur ($1/k_{aeb}$) is shorter than the timescales at which reactants remain on the reaction site (the smallest between $1/k_{diff}$(i) and $1/k_{diff}$(j)).

2.2. A novel treatment of surface radical-radical reactions rate constants

The novelty of the present work is the estimate of the $k_{aeb}(ij)$ coefficient of radical-radical reactions via statistical kinetics calculations based on the Ramsperger-Rice-Kassel-Marcus (RRKM) microcanonical transition state theory. Briefly, RRKM computations provide unimolecular rate constants, namely the rate at which a system A becomes A′ passing through a transition state (only once). In our case, the system A is the ice-water molecules

plus the two adsorbed radicals, namely we consider the water-cluster plus the radicals as a super-molecule isolated from its surrounding. The system A′ is the product of the radical-radical reaction on the icy surface, namely the water-cluster plus either the radical-radical recombination (e.g., React. I) or the H-abstraction (e.g., React. II) products.

It is important to note that in order to apply the RRKM theory, we implicitly assume that the intra-molecular energy redistribution of the reaction energy is faster than the reaction itself. This assumption is supported by recent ab initio molecular dynamics (AIMD) computations that show that a large fraction ($\geq$ 50%) of the reaction energy is absorbed by the water ice in less than 1 ps (Pantaleone et al. 2020, 2021). We have checked a posteriori that the timescale of the reactions studied here is indeed longer that 1 ps. Finally, the specific computational details of our proposed RRKM method are reported in § 3.2.

2.3. Desorption and diffusion energies

Equation 3 shows that, in addition to the probability $k_{aeb}(ij)$ for radicals i and j to react when they meet on a surface site, the efficiency factor ε_{ij} also depends on k_{des}^{-1} and on k_{diff}^{-1}, which are related to the residence time of the radicals on the surface and on the diffusion timescale of the radicals on the ice, respectively. The diffusion and desorption timescales $t_{\rm diff/des}$ are given by the classical Eyring transition state theory (TST), in which $t_{\rm diff/des}$ is inversely proportional to their rate constant, $t_{\rm diff/des} \propto k_{\rm diff/des}^{-1}$. According to TST, the general expression of the rate constant k for a unimolecular reaction (like diffusion and desorption) is:

$$k = \frac{k_B T}{h} \frac{Q^{\neq}}{Q_R} \exp(-\Delta V^{\neq}/k_B T), \quad (4)$$

where $\Delta V^{\neq}$ is the zero point energy-corrected energy barrier, $Q^{\neq}$ and $Q_{\rm R}$ are the total partition functions of the transition state and the initial state (namely, the reactants), respectively, k_B is Boltzmann's constant, T is the surface temperature and h is Planck's constant. We note that we use the classical Eyring equation because, since we are not dealing with light atoms but molecular radicals, tunneling is negligible.

By proper manipulation of equation 4, the rate constant becomes expressed as a function of the free energy barrier $\Delta G^{\neq}$ (usually referred to as free energy of activation) at a given temperature:

$$k = \frac{k_B T}{h} \exp(-\Delta G^{\neq}/k_B T), \quad (5)$$

in which $\Delta G^{\neq} = \Delta H^{\neq}$ - T$\Delta S^{\neq}$ and where $\Delta H^{\neq}$ is the enthalpy of activation and $\Delta S^{\neq}$ the entropy of activation. These terms contain translational, rotational, vibrational and electronic contributions as they arise partly from the total partition functions Q.

With the adopted quantum chemical approach, the application of the Eyring TST allows us to compute desorption-related data (e.g., desorption activation energies and desorption rate constants) for each radical through the outcome of these calculations (electronic energies, vibrational frequencies, partition functions, energy contributions, etc.). It is worth mentioning that, since the radicals are physisorbed on the ice surfaces, the energy barriers of the desorption processes coincide with the desorption energies. In the present case, we only account for the electronic and vibrational contributions to both $\Delta H^{\neq}$ and $\Delta S^{\neq}$ to arrive at the radical desorption energies as follows:

$$\Delta H = \Delta E_{electronic} + \Delta ZPE + \Delta E_{vib}(T) + \Delta H_{rot} + \Delta H_{trans}, \quad (6)$$

and

$$\Delta S = \Delta S_{vib} + \Delta S_{rot} + \Delta S_{trans}, \quad (7)$$

where the terms are the energy difference between the desorbed and the adsorbed states for the total electronic energy ($\Delta E_{electronic}$), for the zero point vibrational energy corrections (ΔZPE), for the thermal vibrational energy corrections ($\Delta E_{vib}(T)$), for the vibrational entropy (ΔS_{vib}), and for the rotational and translational contributions to enthalpy (ΔH_{rot} and ΔH_{trans}, respectively) and entropy (ΔS_{rot} and ΔS_{trans}, respectively). In this case, since we are dealing with the desorption of the radicals, the translational and rotational contributions arise from only the desorbed (free) radicals. Specific details on the calculation of some of these terms are provided in Appendix B. For the sake of simplicity, we refer to this final desorption energy as E_{des}.

In contrast to desorption, obtaining diffusion-related data with the present calculations is a daunting task, as it requires localizing a large number of transition states for the radical hoping between the different binding sites. Moreover, the use of a relatively small cluster model dramatically constraints the validity of these results because of its limition in terms of size and surface morphology. Therefore, to obtain a value for the diffusion energy of each radicals, which by analogy we will refer to as E_{diff}, we resorted to what is usually done in astrochemical modeling, that is, E_{diff} is taken to be a fraction f of E_{des}. However, deriving the value of f has proven to be difficult, both theoretically and experimentally. In the published astrochemical models, one can find a quite wide range of adopted f values, from 0.3 to ∼0.8 (e.g., Hasegawa et al. 1992; Ruffle & Herbst 2000). Some authors have taken a middle point by setting this ratio to 0.5 (e.g., Garrod & Herbst 2006; Garrod et al. 2008; Garrod & Pauly 2011; Ruaud et al. 2015; Vasyunin et al. 2017; Jensen et al. 2021).

In the past few years, theoretical and experimental works on the diffusion process of species on ASW surfaces have provided constraints to the f value (see also the more extensive discussion in Sect. 5.3). In a theoretical work, Karssemeijer & Cuppen (2014) showed that the range for the E_{diff}/E_{des} ratio can be narrowed down to 0.3–0.4 for molecules like CO and CO_2. Minissale et al. (2016) experimentally found that the f ratio of atomic species like N and O is about 0.55, while He et al. (2018) showed that f is 0.3–0.6, being the lower values more suitable for surface coverage lower than one mono-layer.

Given the uncertainty on the E_{diff}/E_{des} ratio for CH_3 and HCO, we carried out our calculations for three values: 0.3, 0.4 and 0.5.

2.4. Ice model

Regarding the amorphous solid water (ASW) model, there is still little knowledge that constrains the actual internal structure of interstellar ices. Observations suggest that the interstellar water ice is predominantly in the amorphous form (e.g., Smith et al. 1989; Boogert et al. 2015) (with some exceptions: e.g. Molinari et al. 1999). Many laboratory studies have been carried out to characterize the possible porosity of the interstellar ices. Typically, laboratory experiments produce porous ices of different densities by condensation of water vapor, even though they probably do not reproduce the interstellar water ice, in which water is believed to form *in situ* by hydrogenation reactions of frozen O, O_2 and O_3 (e.g., Dulieu et al. 2010; Hama & Watanabe 2013; He & Vidali 2014b; Potapov & McCoustra 2021). In general, porous ices are detected in laboratory via the infrared (IR) signature of dangling

OH groups, which are, however, missing in interstellar samples (Bar-Nun et al. 1987; Keane et al. 2001), (see also the discussion in e.g. Hama & Watanabe 2013; Zamirri et al. 2018). Several hypothesis have been suggested to explain the absence of the OH dangling signature (Oba et al. 2009; Palumbo 2006; Palumbo et al. 2010), so that, at the end, there is consensus in the community that interstellar water ices are amorphous and porous in nature, even though many details are missing and we do not have a precise picture of the degree of porosity (e.g., Hama & Watanabe 2013; Isokoski et al. 2014; Potapov & McCoustra 2021).

In order to simulate the interstellar icy surfaces, Enrique-Romero et al. (2019) considered a cluster of 33 water molecules. This ice model possesses two major types of surface with respect to the binding capability: a cavity, where species are in general more strongly bonded to the surface, and an elongated side (Rimola et al. 2014, 2018; Enrique-Romero et al. 2019). In this work, we only report the analysis of the reaction occurring in the cavity for the following reason. In astrochemical models, the vast majority of radical-radical reactions take place inside the bulk of the ice (e.g., Garrod & Herbst 2006). Therefore, the cavity site is a better representation of the sites where radical-radical reactions occur than that on the elongated side, which would at best describe the ice layer exposed to the gas and where just a tiny fraction of the reactions can occur, considering that the ice is constituted by more than 100 layers (e.g., Taquet et al. 2012; Aikawa et al. 2020).

Therefore, in this work, we use the Enrique-Romero et al. (2019) ice model and methodology, but we improve the calculations for a better accuracy of the computed energetics, including dispersion, as described in detail in § 3.

3. Methodology

3.1. Electronic structure calculations

Given the importance of inter-molecular interactions in radical-radical reactions, we recomputed the stationary points of the potential energy surfaces (PES) previously reported by (Enrique-Romero et al. 2019) using the Grimme's D3 dispersion term including the Becke-Johnson damping (D3(BJ)) (Grimme et al. 2010, 2011), this way improving the description of the dispersion forces with respect to the previous work.

All DFT calculations were performed with the Gaussian16 program package (Frisch et al. 2016). A benchmark study showed that the BHLYP hybrid density functional method is the best suited DFT method to study these reactions, with an average error of 3%, and a maximum error of 5.0% with respect to benchmark multi-reference CASPT2(2,2) calculations using OpenMolcas 18.09 (see Annex). We have chosen CASPT2(2,2) as the minimum level of post-HF theory, aware of the fact that a CASPT2 inclusive of full valence states would have been much better. The latter is prevented, however, by the size of our system.

Thus, stationary points were fully optimized using BHLYP (Becke 1993; Lee et al. 1988) combined with the standard 6-31+G(d,p) Pople basis set alongside the D3(BJ) dispersion term (Grimme et al. 2010, 2011). When needed, intrinsic reaction coordinate (IRC) calculations at the optimization theory level were carried out to ensure that the transition states connect with the corresponding minima. To balance the computational cost and chemical accuracy, reaction energetics were then refined by performing full BHLYP-D3(BJ)/6-311++G(2df,2pd) single-point energy calculations on the BHLYP-D3(BJ)/6-31+G(d,p) optimized stationary points. Improving chemical accuracy is a fundamental aspect when aiming at providing kinetic calculations and rate constants (including tunneling effects) (Álvarez-Barcia et al. 2018), as in the present work. Additionally, as shown in (Rimola et al. 2018; Enrique-Romero et al. 2019, 2020), DFT is a cost-effective methodology with which a correct description of biradical systems can be achieved by using the unrestricted broken (spin)-symmetry approach (e.g., Neese 2004).

All optimized stationary points were characterized by the analytical calculation of the harmonic frequencies as minima and saddle points. Thermochemical corrections computed at BHLYP-D3(BJ)/6-31+G(d,p) were included to the single point BHLYP-D3(BJ)/6-311++G(2df,2pd) potential energy values using the standard rigid-rotor and harmonic oscillator formulae in order to obtain the zero-point vibrational energy (ZPE) corrections.

3.2. Kinetic calculations

In order to compute the rate constants for the chemical reactions between the radical pairs, we adapted our in-house kinetic code, based on the RRKM scheme for gas-phase reactions (Skouteris et al. 2018), to the surface plus adsorbed radicals case. First, we obtained the microcanonical rate constant $k_{aeb}(E)$ at a given energy E as:

$$k_{aeb}(E) = \frac{N(E)}{h\rho(E)}, \tag{8}$$

where $N(E)$ is the sum of states for the active degrees of freedom in the transition state, $\rho(E)$ is the density of states for the active degrees of freedom in the reactant, and h is the Planck constant. Since we aim to simulate a reaction taking place on a solid surface, only vibrational degrees of freedom are taken into account. Second, the obtained rate constants were Boltzmann-averaged in order to derive the rate constants as a function of the temperature.

For the H abstraction reaction, we took into account tunneling effects adopting the Eckart scheme via the unsymmetric potential energy barrier approach. In order to have a chemical system of reference to compare with, we applied the same method to the well studied reaction H + CO → HCO. In this case, the initial structures of the reaction were taken from the theoretical study by Rimola et al. (2014), which were re-optimized at the present work computational level. Here, from the optimized transition state, intrinsic reaction coordinate (IRC) calculations were run assuming a Langmuir-Hinshelwood (LH) like reaction, contrarily to the Rimola et al. (2014) original computations. All stationary points were characterized by frequency calculations, obtaining their (harmonic) vibrational modes and their zero-point energies. More details of these computations can be found in Appendix D.

4. Results

4.1. Energetics of the reactions

Table 1 presents the 0 K enthalpies (i.e., potential energies plus ZPE corrections) of the studied reactions. The improvement in the dispersion correction and the refinement of the DFT energy slightly decrease the energy barriers of each one of the reactions to form acetaldehyde and CO + CH_4 by less than 2.5 kJ mol^{-1} with respect to the values quoted by Enrique-Romero et al. (2019). Inversely, the H + CO → HCO reaction has a higher barrier, 13.5 kJ mol^{-1}, than that quoted by Rimola et al. (2014), 9.2

Table 1. Energetics and related parameters of the reactions and desorption and diffusion of the radicals. *Top half:* Activation ($\Delta H^{\ddagger}$) and reaction (ΔH^{RX}) enthalpies (in kJ/mol) at 0 K (i.e., sum of electronic energies at BHLYP-D3(BJ)/6-311+G(2df,2pd)//BHLYP-D3(BJ)/6-31+G(d,p) and ZPE at BHLYP-D3(BJ)/6-31+G(d,p)) for each radical-radical reaction. Values for the H + CO → HCO reference reaction are also shown. *Bottom half:* Desorption energies (E_{des}) and desorption (T_{des}) and diffusion (T_{diff}) temperatures (in K) derived using the E_{des} assuming diffusion-to-desorption energy ratios of 0.5, 0.4 and 0.3, see § 2.3.

Product	$\Delta H^{\ddagger}$	ΔH^{RX}
CH_3CHO	5.5	-324.5
CO + CH_4	7.2	-328.9
HCO	13.5	-91.6
Quantity [K]	CH_3	HCO
E_{des}	1715	3535
T_{des}	30	68
T_{diff} (0.5)	15	32
T_{diff} (0.4)	12	25
T_{diff} (0.3)	9	19

kJ mol^{-1}, for two reasons: (i) Rimola et al. assumed an Eley-Rideal reaction (namely, the H atom comes from the gas phase and reacts with frozen CO), while here we have considered a LH mechanism (§ 3.2), and (ii) they did not consider dispersion corrections.

4.2. Rate constants

Figure 1 shows the rate constants as a function of the temperature of the reactions that form CH_3CHO and CO + CH_4 from the coupling and direct H-abstraction of CH_3 + HCO, respectively. The figure also reports the case of HCO formation from H + CO, for the sake of reference.

The rate constants of the reactions leading to CO + H_2CO and HCO take tunneling into account, which is evidenced by their deviation from linearity. It is also evident the strong temperature dependence of the radical-radical reactions studied, as compared to HCO formation.

The rate constants of the acetaldehyde formation are larger than those of CO + CH_4 formation at temperatures above ∼24 K. This is due to its lower barrier and the almost negligible quantum tunnelling contribution to HCO + CH_3 → CO + CH_4 at such temperatures. However, as the temperature decreases the tunnelling probability takes over deviating the rate constant of CO + CH_4 formation from linearity, becoming faster than the formation of acetaldehyde. On the contrary, HCO formation has a much weaker temperature dependence and higher rate constants over the considered temperature range. This is the result of the dominant strong quantum tunnelling of the H atom through the reaction barrier, in agreement with the literature results (e.g., Andersson et al. 2011; Rimola et al. 2014).

In order to facilitate the introduction of the new rate constants in astrochemical models, we fit the reactions rate constants with the standard formula in Eq. 9. The values of α, β and γ are listed in Table 2.

$$k_{aeb}(T) = \alpha \left(\frac{T}{300K}\right)^{\beta} \exp(-\gamma/T). \quad (9)$$

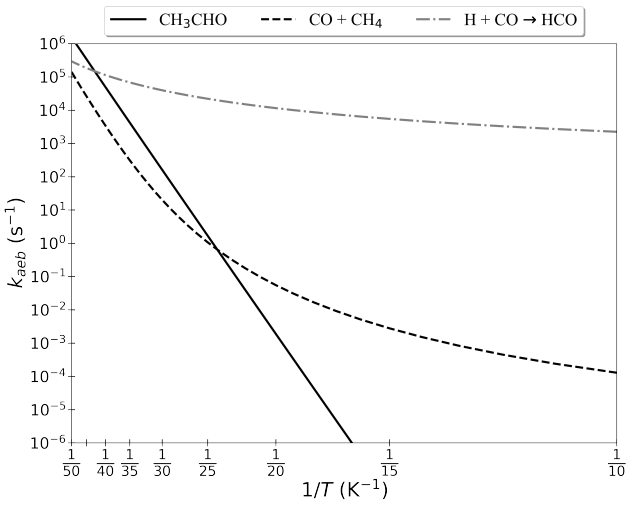

Fig. 1. Arrhenius plots, namely rate constants as a function of the inverse of temperature, for the reaction CH_3 + HCO forming acetaldehyde (black solid line) or CO + CH_4 (black dashed line), and for the reaction H + CO → HCO (gray dotted-dashed line), described in the main text.

4.3. Desorption and diffusion temperatures

Table 1 reports the computed E_{des} and the temperature for desorption T_{des} and diffusion T_{diff} derived assuming a half-life of 1 Myr. E_{des} values are obtained at BHLYP-D3(BJ)/6-311++G(2df,2pd)//BHLYP-D3(BJ)/6-31+G(d,p) level following the procedure explained in § 2.3, which moreover are corrected for deformation and basis set superposition energy. The T_{des} and T_{diff} values are obtained by using the standard equation for the half-life time, $t_{1/2}$=ln(2)/$k_{diff/des}$(T). These timescales provide an estimation of the characteristic temperatures for desorption and diffusion of the two radicals, CH_3 and HCO, involved in the formation of acetaldehyde on the icy surface.

Finally, we note that our E_{des} are consistent with those computed by Ferrero et al. (2020) on a substantially larger ASW ice model. Specifically, our E_{des} in Table 1 lies in the high end of the Ferrero et al. range. On the contrary, and as already discussed in Ferrero et al. (2020), our E_{des} are different than those reported in the astrochemical databases KIDA[1] and UMIST[2], often used by modellers. Unfortunately, no experimental data on the CH_3 and HCO E_{des} desorption energy exist, to our best knowledge.

5. Discussion

5.1. Formation of acetaldehyde versus CO + CH_4

We used the results of our new calculations (Sect. 4) of the CH_3 + HCO reaction kinetics, desorption and diffusion rate constants to compute the efficiency ε (Eq. 3) of the two channels leading to the formation of either CH_3CHO or CO + CH_4. As discussed in Sect. 2.3, given the uncertainty on its value, we considered three cases for the E_{diff}/E_{des} ratio f: 0.3, 0.4 and 0.5. Figure 2 shows the resulting ε as a function of the temperature and Table 2 reports the α, β and γ values obtained by fitting the ε curves with Eq. (9), for the three cases of f.

We note that, although we computed the efficiency of the reactions in the 5–100 K range, they will only take place as long

[1] http://kida.astrophy.u-bordeaux.fr/
[2] http://udfa.ajmarkwick.net/

Table 2. Rate constants k_{aeb} (in s^{-1}) and efficiency ε of the two possible reactions between HCO and CH_3. For each reaction, we report the values of α, β and γ of the rate constant k_{aeb} and the efficiency ε calculated assuming E_{diff}/E_{des} equal to 0.5, 0.4 and 0.3 (first column). The last three columns report the values of k_{aeb} and ε at 9, 20 and 30 K.

E_{diff}/E_{des}	Rate constant	Temperature [K]	α [s^{-1}]	β	γ [K]	9 K	20 K	30 K
Reaction (1): HCO + CH_3 → CH_3CHO								
	k_{aeb}					2.7×10^{-21}	1.9×10^{-3}	160.5
		9–30	3.1×10^{12}	0.70	663			
	ε					1.0	1.0	1.0
0.5		9–19	1.0	0.0	0.0			
		19–26	0.99	-3.4×10^{-3}	0.06			
		26–30	0.98	-0.01	0.28			
	ε					0.88	0.81	0.81
0.4		9–13	0.43	-0.21	0.28			
		13–30	1.0	0.14	-3.4			
	ε					4.9×10^{-8}	7.6×10^{-3}	0.01
0.3		9–30	3.3	0.12	161.2			
Reaction (2): HCO + CH_3 → CH_4 + CO								
	k_{aeb}					6.8×10^{-5}	0.05	20.1
		9–15	6.1×10^{9}	10.4	-39.7			
		15–30	1.7×10^{23}	25.9	-274			
	ε					1.0	1.0	1.0
0.5		9–24	1.0	0.0	0.0			
		24–28	0.83	-0.12	2.79			
		28–30	0.53	-0.44	11.4			
	ε					1.0	1.0	0.35
0.4		9–21	1.0	0.0	0.0			
		21–25	7.4×10^{-11}	-13.8	278.8			
		25–30	3.2×10^{-6}	-5.8	53.3			
	ε					1.0	0.02	1.5×10^{-3}
0.3		9–15	0.96	-0.01	0.02			
		15–19	2.4×10^{-76}	-84.9	1205.1			
		19–30	2.4×10^{7}	19.9	-660.4			

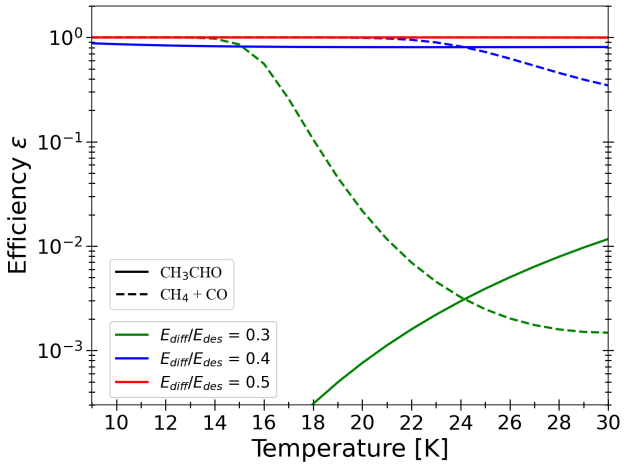

Fig. 2. Reaction efficiency ε (Eq. 3) of the reaction CH_3 + HCO leading to either CH_3CHO (solid lines) or CO + CH_4 (dashed lines) as a function of the temperature. The computations were obtained adopting three different E_{diff}/E_{des} ratios: 0.3 (green), 0.4 (blue) and 0.5 (red). We note that, for E_{diff}/E_{des}=0.5 the CH_3CHO and CO + CH_4 (red) curves overlap, namely they are constant and equal to 1.

as one of the two radicals can diffuse and scan the ASW sites and both radicals stay on the reaction site, namely they do not desorb (see Table 1). Consequently, the upper limit to the temperature where the CH_3CHO and CO + CH_4 formation reactions take place is set by the desorption of CH_3, as it has a lower desorption energy than HCO (30 and 68 K, respectively, see Table 1). Likewise, the lower limit is also set by the CH_3 diffusion energy only, which is equal to 15, 12 and 9 K for f equal to 0.5, 0.4 and 0.3, respectively. In the case of f equal to 0.5, HCO starts to be mobile when CH_3 has already sublimated, so that the efficiency of the reaction depends on CH_3 E_{diff} only. Conversely, for f equal to 0.4 and 0.3, the temperatures at which HCO and CH_3 can diffuse overlap, so that both species contribute to the denominator of Eq. (3).

Formation efficiency: For both reactions, formation of CH_3CHO and CO + CH_4, the efficiency ε is about 1 in the 9–15 K range regardless of the f value (between 0.3 and 0.5) with one exception, acetaldehyde formation with f=0.3, which starts at very low efficiency values and monotonically increases. For f=0.5, either reactions have efficiencies of about unity in the whole range of temperatures (up to 30 K). For f=0.4, formation of CO + CH_4 distances from unity at temperatures above ~ 22 K, going into lower values so that at 30 K it reaches ε ~0.3, while the efficiency of acetaldehyde formation stays about unity up to 30 K, where it takes a value of ~0.8. On the other hand, for f=0.3 things are very different. The efficiency of CO + CH_4

crashed at higher temperatures, reaching values of about 0.001 at 30 K, while that of acetaldehyde never goes above ~ 0.01.

This is because, for relatively large f values (≥0.4), the most mobile radical, CH_3, moves slowly and the two radicals have plenty of time to react when they meet before one of them moves away: ε is, therefore, close to unity. However, when the timescale for diffusion becomes smaller than the reaction timescale (i.e., $k_{diff} \gg k_{aeb}$), CH_3 moves away before having the time to react and the efficiency drops below unity. In practice, the smaller the E_{diff}/E_{des} ratio, the faster CH_3 moves and the smaller ε. However, since both k_{diff} and k_{aeb} have an exponential dependence on the temperature, a change in behavior occurs when the reaction activation energy γ (Eq. (9)) is similar to E_{diff} and the efficiency ε strongly depends on the temperature. For the formation of acetaldehyde, γ=663 K (Table 2) and, therefore, the change of behavior occurs when E_{diff}/E_{des} ~0.40. In these cases, the lower the temperature, the larger k_{diff} with respect to k_{aeb} and the smaller ε, as shown in Fig. 2. Similar arguments hold also for the HCO + CH_3 → CO + CH_4 reaction. The only difference is that, at low temperatures, k_{aeb} deviates from the exponential law because of the kicking in of the tunneling effect that greatly increases k_{aeb} (giving a negative γ values: see Table 2). Since the tunneling is more efficient for decreasing temperature, the k_{aeb}/k_{diff} ratio decreases at increasing temperatures and, consequently, ε decreases.

Branching ratio: Figure 3 shows the branching ratio BR of the formation rate of CH_3CHO over CO + CH_4 as a function of the temperature, for the three f values (0.5, 0.4 and 0.3). The BR is obtained integrating Eq. (1) from the temperature at which CH_3 starts to be mobile T_0, a value that depends on the assumed f (see above), to the temperature T. It holds:

$$\mathrm{BR}(T) = \frac{\int_{T_0}^{T} \mathrm{d}T' \, \varepsilon_{\mathrm{CH_3CHO}} \times (R_{\mathrm{diff,CH_3}} + R_{\mathrm{diff,HCO}})}{\int_{T_0}^{T} \mathrm{d}T' \, (\varepsilon_{\mathrm{CH_3CHO}} + \varepsilon_{\mathrm{CO+CH_4}}) \times (R_{\mathrm{diff,CH_3}} + R_{\mathrm{diff,HCO}})}. \quad (10)$$

The different effects commented above can be clearly seen in Fig. 3 and can be summarized as follows. For f = 0.5, the branching ratio BR is constant and equal to 0.5, namely the HCO + CH_3 reaction leads to acetaldehyde and CO + CH_4 in equal quantities. For f = 0.4, BR lies in the range 0.4–0.5 up to 25 K and then it becomes larger, because the tunneling gain in the CO + CH_4 production at low temperatures vanishes. For f = 0.3 (and, in general, ≤ 0.4), BR is <0.5 at temperatures less than ~25 K and rises to ~0.9 at 30 K.

In other words, for $f \geq 0.4$, acetaldehyde and CO + CH_4 are in approximately equal competition in the range of temperatures where the HCO + CH_3 reaction can occur. However, for $f < 0.4$, acetaldehyde is a very minor product for temperatures lower than about 25 K and flips to be a major product above it.

5.2. The experimental point of view

Experiments studying the formation of acetaldehyde from radical-radical coupling date back to the 1990s (Hudson & Moore 1997). They are mainly based on energetic (UV or particles) irradiation of different H_2O, CO, CH_3OH and CH_4 ice mixtures (e.g. Bennett et al. 2005; Öberg et al. 2010; Martín-Doménech et al. 2020). In relation to experimental acetaldehyde formation on grain surfaces, Bennett et al. (2005), after irradiation of a CO:CH_4 ice mixture, detected acetaldehyde and predicted that the orientation of the CH_3 and HCO radicals are crucial in the efficiency of the reaction. On the other hand, Martín-Doménech et al. (2020) conducted laboratory experiments on the formation of acetaldehyde via the CH_3 + HCO reaction, concluding that this channel is not efficient enough to reproduce the astronomical observations.

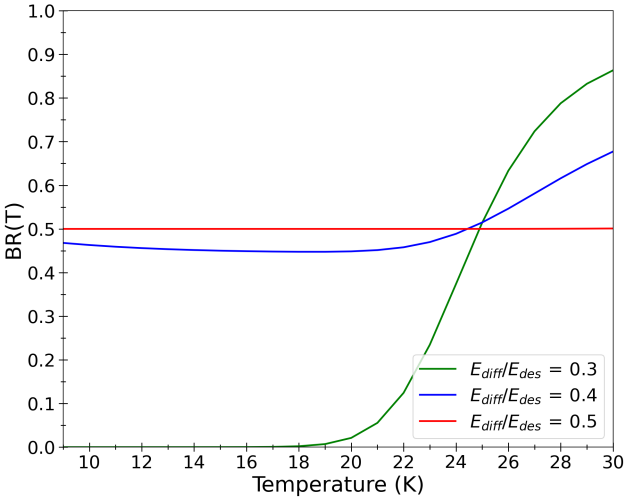

Fig. 3. Branching ratio $BR(T)$ of the formation rate of the CH_3CHO over CO + CH_4 (Eq. 10) as a function of the temperature in the range where the reactions can occur, namely below 30 K (see text), for E_{diff}/E_{des} equal to 0.3 (green), 0.4 (blue) and 0.5 (red).

As discussed by various authors, although laboratory experiments are primordial in suggesting possible mechanisms operating in the ISM and, specifically, the possible formation routes of molecules on the interstellar grain surfaces, they cannot provide the exact ISM conditions or a detailed description of the mechanisms at the atomic level. Despite this, the improvement of radical detection methods, such as the electron paramagnetic resonance (EPR) technique, will help to clarify the role of radicals generated in interstellar ice analogs (e.g., Zhitnikov & Dmitriev 2002). In this respect, therefore, theoretical computations as those reported in this work constitute a complementary, if not unique, tool to understand the interstellar surface chemistry.

5.3. Astrophysical implications

In astrochemical models, it is generally assumed that reactions between radicals on the surface of interstellar ices are barrierless and, consequently, that their efficiency is equal to 1 (Sect. 2). In addition, it is also often assumed that there are no competition channels to the production of iCOMs. At variance with these simple assumptions, our new calculations presented in Sect. 5.1, indicate that, at low (≤ 15 K) temperatures, the efficiency of the acetaldehyde formation is close to unity, for a E_{diff}/E_{des} ratio $f \geq$0.40. However, there is a competing channel leading to CO + CH_4, for which the efficiency is also equal to 1, so that, at low temperatures and for $f \geq$0.40 the two channels are equally probable. The acetaldehyde formation efficiency remains close to unity in the temperature range where the reaction can occur, namely at ≤ 30 K, for $f \geq$0.40. However, the situation drastically changes for f <0.40. Specifically, for f = 0.3, the efficiency of acetaldehyde formation crashes to very low values and increases with temperature to a maximum of 0.01 at 30 K. Similarly, the formation of CO + CH_4 drops to 1.5×10^{-3} at 30 K.

Therefore, two major messages come out from our calculations: (1) the efficiency of the formation of acetaldehyde from the HCO + CH_3 reaction on icy surfaces is a complex function of the temperature and of the CH_3 diffusion energy E_{diff} (Fig. 2) and (2) the acetaldehyde formation receives competition with CO + CH_4 formation, which cannot be neglected and whose efficiency is also a complex function of temperature and E_{diff} (Fig. 3).

While the dependence on the temperature and the importance of the competition of other products were already recognized (Enrique-Romero et al. 2019), the paramount importance of the diffusion energy E_{diff} in the radical-radical reactions efficiency was not appreciated, at least not at the extent indicated by this study (because of the assumption of astrochemical models that the efficiency of the radical-radical reactions on grains is 1). Penteado et al. (2017), for example, carried out an extensive study of the surface chemistry on the binding energies (namely, our E_{des}) showing how critical they are. Our new study suggests that E_{diff} is as much, or even more, crucial in the reactions involving two radicals on ASW.

What makes the situation actually critical is that, while studies of the binding energy of radicals can and have been estimated in experimental and theoretical works (e.g., see the recent works by Penteado et al. 2017; Ferrero et al. 2020), evaluating the diffusion energy of multi-atomic radicals on cold icy surfaces has proven to be extremely complicated and, to the best of our knowledge, no experimental or theoretical studies exist in the literature (see also e.g., Cuppen et al. 2017; Potapov & McCoustra 2021). Indeed, as mentioned above, obtaining E_{diff} experimentally is hitherto hampered by technical limitations on the instrumentation used to detect the radicals (i.e., EPR measurements). In relation to theoretical investigations, this lacking in bibliography is due to the convergence of methodological difficulties that make the study of diffusion with computational simulations intrinsically complex (but also compelling). Diffusion can currently be studied by means of molecular dynamics (MD) or kinetic Monte Carlo (kMC) simulations. With the first, to obtain a sufficient representativeness of the species diffusion, long simulation time-scales are mandatory. This in practice means to adopt classical force fields, in which the electronic structure of the systems is missing. However, radicals are open-shell species (with at least one unpaired electron) and accordingly electrons have to be accounted for. Thus MD simulations should be grounded within the quantum mechanics realm, which are much more expensive than the classical ones, making the MD simulations unfeasible. The alternative would be the adoption of kMC simulations. However, these simulations require building a complete network of the site-to-site radical hopping, in which for each hopping the corresponding rate constant has to be known a priori. This actually means to localize for each hopping the corresponding transition state structure (at a quantum chemical level), in which by using a realistic ASW model (i.e., large, amorphous and accordingly plenty of binding sites) makes the problem unpractical.

Usually, astrochemical models assume that the radical E_{diff} is a fraction f of E_{des} and the value f is derived from computations and experiments on species such as CO, CO_2, H_2O, CH_4 and NH_3 (e.g., Mispelaer et al. 2013; Karssemeijer & Cuppen 2014; Lauck et al. 2015; Ghesquière et al. 2015; He et al. 2017; Cooke et al. 2018; He et al. 2018; Maté et al. 2020; Kouchi et al. 2020). These studies give a value for f between 0.3 and 0.6, as mentioned in Sect. 2.3. However, rigorously speaking, the experiments do not necessarily measure the same diffusion processes as in interstellar conditions, for at least the reasons of the surface coverage (He et al. 2018) and its dependence of the nature of the ice, specifically its degree of porosity (Maté et al. 2020), which is poorly known in the case of interstellar ices. As a matter of fact, using experimental and a theoretical Monte Carlo code, Maté et al. (2020) found that "the microscopic diffusion is many times faster than the macroscopic diffusion measured experimentally". Most recently, Kouchi et al. (2020) obtained a direct measurement of the diffusion energy of CO and CO_2 on ASW, using the transmission electron microscopy (TEM) technique, which allows a direct measurement of the surface diffusion coefficients (against the often used technique of IR spectroscopy, which only indirectly estimates the diffusion energy). Kouchi and coworkers found an f ratio equal to 0.3.

We have seen that, in the case of acetaldehyde, this uncertainty on f has a dramatic effect. If f is >0.4, the efficiency of acetaldehyde formation is equal to 1 and it is about equal to that of the CO + CH_4 formation. On the contrary, if f is equal to 0.3, then the efficiency of acetaldehyde formation (and CO + CH_4) crashes, to a maximum value of 0.02. The most recent measurements by Kouchi et al. (2020) point out the latter case as the most probable. If the value f=0.3 is confirmed, then acetaldehyde is unlikely to be formed on the interstellar icy grain surfaces.

One could be tempted to use the astronomical observations against the astrochemical model predictions to add constraints to the f value in (real) interstellar ices. Of course, given the large number of parameters associated with the astrochemical models it could be a dangerous exercise. Nonetheless, we can analyze two cases, as illustrative examples. Barger & Garrod (2020) compared the predictions of their model, where the formation of acetaldehyde is dominated by the reaction CH_3 + HCO assumed to have ε=1, with the observations toward various hot cores and found that in two of them, NGC 7538 IRS 1 and W3(H_2O), their model overproduces the acetaldehyde column densities by more than a factor 10^3 with respect to the observed ones. If f is equal to 0.3, introducing our new values for ε could possibly cure this mismatch. On the contrary, Jørgensen et al. (2016) found a good agreement between the observed abundances of acetaldehyde in IRAS16293B and SgrB2(N) and those predicted by the Garrod (2013) model. In this case, the agreement would point to $f \geq 0.4$. In other words, our new computations might solve the mismatch observed toward NGC 7538 IRS 1 and W3(H_2O) if $f = 0.3$, but they would create a mismatch on the observations toward IRAS16293B and SgrB2(N), or viceversa. Alternatively, it is possible that f varies in different sources, belonging to different environments. For example, one could think that sources in cold quiescent regions have ices different, more or less porous, from those in warm and chaotic ones. The two examples discussed above, unfortunately, do not lead to a coherent behavior, as, for example, IRAS16293B and SgrB2(N) could not belong to more different environments.

In conclusion, the acetaldehyde formation by radical-radical recombination on the ices is such a strong function of the diffusion energy, likely linked to the nature of the ice, that a little variation of the E_{diff}/E_{des} (by 0.1) value can shift the efficiency from 1 to less than 0.01. The most recent estimates of E_{diff}/E_{des} suggest a value of 0.3 (Kouchi et al. 2020), which would make the formation of acetaldehyde on the grain surfaces unlikely. Anyway, the important message here is that astrochemical model predictions should be taken with a certain precaution. On the contrary, our new computations clearly show the huge importance of better knowing the microprocesses involved in the radical-radical chemistry on the icy interstellar grains and the urgent need of extensive studies, similar to the one presented here,

on different systems believed to form iCOMs on the interstellar icy surfaces.

For the sake of completeness, the formation of acetaldehyde via radical-radical reactions on surfaces with lower binding energies such as solid CO could have a higher efficiency, due to the low radical–surface interactions (Lamberts et al. 2019). Finally, it is worth reminding that acetaldehyde can alternatively be synthesized in the gas-phase (e.g., Charnley 2004; Vastel et al. 2014; De Simone et al. 2020). Recently, Vazart et al. (2020) reviewed the gas-phase routes leading to acetaldehyde and found that, very likely, the dominant one is that starting from ethanol, the so-called ethanol tree (Skouteris et al. 2018). In particular, the ethanol tree route reproduces quite well both the acetaldehyde and glycolaldehyde abundances in the sources where ethanol was also observed, including IRAS16293B (Vazart et al. 2020).

6. Conclusions

In this work, we report new computations on the energetics and kinetics of the reaction HCO + CH_3, which can lead to the formation of either acetaldehyde or CH_4 + CO. Specifically, we compute the rate constants of both reactions as a function of temperature as well as the efficiency of the formation of acetaldehyde and CH_4 + CO, respectively, combining reaction kinetics at RRKM (tunneling included) with diffusion and desorption competitive channels. We provide analytical formulae so that the computed rate constants and efficiency can be easily introduced in astrochemical models.

The main conclusions of our study are the following.

1- The HCO + CH_3 reaction can only occur when the surface temperature is lower than 30 K, because CH_3 desorbs at larger temperatures.

2- Our computations suggest that acetaldehyde is not the dominant product for the reaction HCO + CH_3. The efficiency ε of its formation strongly depends on the E_{diff}/E_{des} ratio, providing dramatic variations between 0.3-0.5 values, the most usually used values in astrochemical models.

3- At low ($\leq$ 15 K) temperatures, ε is close to unity for both the formation of acetaldehyde and its competing CO + CH_4 channel for $f \geq 0.4$, while only the efficiency of CO + CH_4 is unity at these temperatures for $f = 0.3$ thanks to quantum tunnelling. The efficiency of acetaldehyde formation remains unity in the range of temperatures where the reaction can occur ($\leq$30 K) for $E_{diff}/E_{des} \geq 0.40$. For lower E_{diff}/E_{des} ratios, ε becomes $\ll 1$ and increases with increasing temperature: in the case of E_{diff}/E_{des}=0.3, it reaches a maximum of ~0.01 at 30 K. Conversely, the efficiency of the formation of CO + CH_4 increases with decreasing temperature because of the tunneling.

4- These variant ε values as a function of E_{diff}/E_{des} go against the assumption made in many astrochemical models, in which ε is equal to 1. This might have a substantial impact on the acetaldehyde abundance predicted by these models, which may overestimate it by a few orders of magnitude.

5- We discussed the example of IRAS16293B and suggested that, in this object, acetaldehyde is likely synthesized by a gas-phase reaction route that starts from ethanol.

Finally, this new study calls for specific similar computations on the radical-radical reactions assumed to form iCOMs in astrochemical models as assuming that they have efficiency ε equal to 1 and are the only reaction product could be highly misleading.

Acknowledgements

This project has received funding within the European Union's Horizon 2020 research and innovation programme from the European Research Council (ERC) for the projects "The Dawn of Organic Chemistry" (DOC), grant agreement No 741002 and "Quantum Chemistry on Interstellar Grains" (QUANTUMGRAIN), grant agreement No 865657, and from the Marie Sklodowska-Curie for the project "Astro-Chemical Origins" (ACO), grant agreement No 811312. AR is indebted to "Ramón y Cajal" program. MINECO (project CTQ2017-89132-P) and DIUE (project 2017SGR1323) are acknowledged. Finally, we thank Prof. Gretobape for fruitful and stimulating discussions.

Most of the quantum chemistry calculations presented in this paper were performed using the GRICAD infrastructure (https://gricad.univ-grenoble-alpes.fr), which is partly supported by the Equip@Meso project (reference ANR-10-EQPX-29-01) of the programme Investissements d'Avenir supervized by the Agence Nationale pour la Recherche. Additionally this work was granted access to the HPC resources of IDRIS under the allocation 2019-A0060810797 attributed by GENCI (Grand Equipement National de Calcul Intensif). We thank prof. Gretobape for stimulating dicsussions, and J. Perrero for useful contributions.

References

Aikawa, Y., Furuya, K., Yamamoto, S., & Sakai, N. 2020, ApJ, 897, 110
Álvarez-Barcia, S., Russ, P., Kästner, J., & Lamberts, T. 2018, MNRAS, 479, 2007
Andersson, S., Goumans, T. P. M., & Arnaldsson, A. 2011, Chemical Physics Letters, 513, 31
Bar-Nun, A., Dror, J., Kochavi, E., & Laufer, D. 1987, Phys. Rev. B, 35, 2427
Barger, C. J. & Garrod, R. T. 2020, ApJ, 888, 38
Becke, A. D. 1993, J. Chem. Phys., 98, 1372
Bennett, C. J., Jamieson, C. S., Osamura, Y., & Kaiser, R. I. 2005, ApJ, 624, 1097
Bianchi, E., Codella, C., Ceccarelli, C., et al. 2019, MNRAS, 483, 1850
Blake, G. A., Sutton, E. C., Masson, C. R., & Phillips, T. G. 1987, ApJ, 315, 621
Boogert, A. C. A., Gerakines, P. A., & Whittet, D. C. B. 2015, ARA&A, 53, 541
Cazaux, S., Tielens, A. G. G. M., Ceccarelli, C., et al. 2003, The Astrophysical Journal, 593, L51
Ceccarelli, C., Caselli, P., Fontani, F., et al. 2017, ApJ, 850, 176
Chang, Q., Cuppen, H. M., & Herbst, E. 2007, A&A, 469, 973
Charnley, S. B. 2004, Advances in Space Research, 33, 23
Chevance, M., Kruijssen, J. M. D., Vazquez-Semadeni, E., et al. 2020, Space Sci. Rev., 216, 50
Cooke, I. R., Öberg, K. I., Fayolle, E. C., Peeler, Z., & Bergner, J. B. 2018, ApJ, 852, 75
Csengeri, T., Belloche, A., Bontemps, S., et al. 2019, A&A, 632, A57
Cuppen, H. M., Walsh, C., Lamberts, T., et al. 2017, Space Sci. Rev., 212, 1
De Simone, M., Codella, C., Ceccarelli, C., et al. 2020, A&A, 640, A75
Dulieu, F., Amiaud, L., Congiu, E., et al. 2010, A&A, 512, A30
Enrique-Romero, J., Álvarez-Barcia, S., Kolb, F. J., et al. 2020, MNRAS, 493, 2523
Enrique-Romero, J., Rimola, A., Ceccarelli, C., et al. 2019, ACS Earth and Space Chemistry, 3, 2158
Ferrero, S., Zamirri, L., Ceccarelli, C., et al. 2020, ApJ, 904, 11
Frisch, M. J., Trucks, G. W., Schlegel, H. B., et al. 2016, Gaussian~16 Revision C.01, gaussian Inc. Wallingford CT
Garrod, R. T. 2013, ApJ, 778, 158
Garrod, R. T. & Herbst, E. 2006, A&A, 457, 927
Garrod, R. T. & Pauly, T. 2011, ApJ, 735, 15
Garrod, R. T., Vasyunin, A. I., Semenov, D. A., Wiebe, D. S., & Henning, T. 2009, ApJ, 700, L43
Garrod, R. T., Widicus Weaver, S. L., & Herbst, E. 2008, ApJ, 682, 283
Ghesquière, P., Mineva, T., Talbi, D., et al. 2015, Physical Chemistry Chemical Physics (Incorporating Faraday Transactions), 17, 11455
Goerigk, L., Hansen, A., Bauer, C., et al. 2017, Physical Chemistry Chemical Physics (Incorporating Faraday Transactions), 19, 32184
Grimme, S., Antony, J., Ehrlich, S., & Krieg, H. 2010, J. Chem. Phys., 132, 154104

Grimme, S., Ehrlich, S., & Goerigk, L. 2011, Journal of Computational Chemistry, 32, 1456
Hama, T. & Watanabe, N. 2013, Chemical Reviews, 113, 8783
Hasegawa, T. I., Herbst, E., & Leung, C. M. 1992, ApJS, 82, 167
He, J., Emtiaz, S., & Vidali, G. 2018, ApJ, 863, 156
He, J., Emtiaz, S. M., & Vidali, G. 2017, ApJ, 837, 65
He, J. & Vidali, G. 2014a, ApJ, 788, 50
He, J. & Vidali, G. 2014b, ApJ, 788, 50
Herbst, E. & van Dishoeck, E. F. 2009, ARA&A, 47, 427
Hollenbach, D. & Salpeter, E. 1970, The Journal of Chemical Physics, 53, 79
Hudson, R. L. & Moore, M. H. 1997, Icarus, 126, 233
Isokoski, K., Bossa, J. B., Triemstra, T., & Linnartz, H. 2014, Physical Chemistry Chemical Physics (Incorporating Faraday Transactions), 16, 3456
Jensen, S. S., Jørgensen, J. K., Furuya, K., Haugbølle, T., & Aikawa, Y. 2021, A&A, 649, A66
Jørgensen, J. K., van der Wiel, M. H. D., Coutens, A., et al. 2016, A&A, 595, A117
Karssemeijer, L. J. & Cuppen, H. M. 2014, A&A, 569, A107
Keane, J. V., Tielens, A. G. G. M., Boogert, A. C. A., Schutte, W. A., & Whittet, D. C. B. 2001, A&A, 376, 254
Kouchi, A., Furuya, K., Hama, T., et al. 2020, ApJ, 891, L22
Lamberts, T. & Kästner, J. 2017, ApJ, 846, 43
Lamberts, T., Markmeyer, M. N., Kolb, F. J., & Kästner, J. 2019, ACS Earth and Space Chemistry, 3, 958
Lauck, T., Karssemeijer, L., Shulenberger, K., et al. 2015, ApJ, 801, 118
Lee, C., Yang, W., & Parr, R. G. 1988, Phys. Rev. B, 37, 785
Lee, C.-F., Codella, C., Li, Z.-Y., & Liu, S.-Y. 2019, ApJ, 876, 63
Lefloch, B., Ceccarelli, C., Codella, C., et al. 2017, Monthly Notices of the Royal Astronomical Society: Letters, 469, L73
Martín-Doménech, R., Öberg, K. I., & Rajappan, M. 2020, ApJ, 894, 98
Maté, B., Cazaux, S., Satorre, M. Á., et al. 2020, A&A, 643, A163
Minissale, M., Congiu, E., & Dulieu, F. 2016, A&A, 585, A146
Mispelaer, F., Theulé, P., Aouididi, H., et al. 2013, A&A, 555, A13
Molinari, S., Ceccarelli, C., White, G. J., et al. 1999, ApJ, 521, L71
Molpeceres, G., Rimola, A., Ceccarelli, C., et al. 2018, MNRAS, 482, 5389
Neese, F. 2004, Journal of Physics and Chemistry of Solids, 65, 781
Oba, Y., Miyauchi, N., Hidaka, H., et al. 2009, ApJ, 701, 464
Öberg, K. I., van Dishoeck, E. F., Linnartz, H., & Andersson, S. 2010, ApJ, 718, 832
Palumbo, M. E. 2006, A&A, 453, 903
Palumbo, M. E., Baratta, G. A., Leto, G., & Strazzulla, G. 2010, Journal of Molecular Structure, 972, 64
Pantaleone, S., Enrique-Romero, J., Ceccarelli, C., et al. 2021, ApJ, 917, 49
Pantaleone, S., Enrique-Romero, J., Ceccarelli, C., et al. 2020, ApJ, 897, 56
Penteado, E. M., Walsh, C., & Cuppen, H. M. 2017, ApJ, 844, 71
Potapov, A. & McCoustra, M. 2021, International Reviews in Physical Chemistry, 40, 299
Rimola, A., Skouteris, D., Balucani, N., et al. 2018, ACS Earth and Space Chemistry, 2, 720
Rimola, A., Taquet, V., Ugliengo, P., Balucani, N., & Ceccarelli, C. 2014, A&A, 572, A70
Ruaud, M., Loison, J. C., Hickson, K. M., et al. 2015, MNRAS, 447, 4004
Ruffle, D. P. & Herbst, E. 2000, MNRAS, 319, 837
Sakai, T., Yanagida, T., Furuya, K., et al. 2018, ApJ, 857, 35
Scibelli, S. & Shirley, Y. 2020, ApJ, 891, 73
Skouteris, D., Balucani, N., Ceccarelli, C., et al. 2018, ApJ, 854, 135
Smith, R. G., Sellgren, K., & Tokunaga, A. T. 1989, ApJ, 344, 413
Taquet, V., Ceccarelli, C., & Kahane, C. 2012, A&A, 538, A42
Tielens, A. G. G. M. & Allamandola, L. J. 1987, in Interstellar Processes, ed. D. J. Hollenbach & H. A. Thronson (Dordrecht: Springer Netherlands), 397–470
Tielens, A. G. G. M. & Hagen, W. 1982, A&A, 114, 245
Vastel, C., Ceccarelli, C., Lefloch, B., & Bachiller, R. 2014, ApJ, 795, L2
Vasyunin, A. I., Caselli, P., Dulieu, F., & Jiménez-Serra, I. 2017, ApJ, 842, 33
Vazart, F., Ceccarelli, C., Balucani, N., Bianchi, E., & Skouteris, D. 2020, MNRAS, 499, 5547
Vidali, G. 2013, Chemical Reviews, 113, 8752
Wakelam, V., Bron, E., Cazaux, S., et al. 2017, Molecular Astrophysics, 9, 1
Watanabe, N. & Kouchi, A. 2002, ApJ, 571, L173
Zamirri, L., Casassa, S., Rimola, A., et al. 2018, MNRAS, 480, 1427
Zhitnikov, R. A. & Dmitriev, Y. A. 2002, A&A, 386, 1129

Appendix A: Benchmark study

The quality of BHLYP-D3(BJ) as an accurate, cost-effective method for the reactions studied in this work is shown in this section.

We have taken five hybrid DFT dispersion-corrected methods: MPWB1K-D3(BJ), M062X-D3, PW6B95-D3(BJ), wB97X-D3 and BHandHLYP-D3(BJ), recommended in Goerigk et al. (2017) for their good overall performance.

We have then compared their performance with respect to CASPT2 by studying reactions I and II on 2 water molecules. We proceeded in two steps: (i) we performed geometry optimized and run frequency calculations at BHLYP-D3(BJ)/6-311++G(d,p) for each reaction channel, finding and checking each stationary point (i.e., reactants, transition state and products); (ii) we then run single point calculations on top of these geometries at each DFT method combined with the 6-311++G(2df,2pd) basis set, and CASPT2/aug-cc-PVTZ for reference. The unrestricted broken symmetry scheme was adopted for all DFT calculations, and the CASPT2 guess wave function was generated using a CASSCF(2,2) calculation where the active space is formed by the two unpaired electrons and their molecular orbitals, starting from a triplet Hartree-Fock wave-function.

BHLYP-D3(BJ) gives the best overall performance with and average unsigned error of 3.0%, and a maximum of 5.0% with respect to CASPT2/aug-cc-PVTZ. The rest of DFT methods have average errors between 10 and 80% (Table A.1). The raw energy values are shown in Table A.3.

Table A.1. DFT method benchmark results. % Unsigned Error from CASPT2/aug-cc-PVTZ//BHLYP-D3(BJ)/6-311++G(d,p). Methods are: (1) BHLYP-D3(BJ), (2) MPWB1K-D3(BJ), (3) M062X-D3, (4) PW6B95-D3(BJ) and (5) wB97x-D3.

System / Method	1	2	3	4	5
TS dHa on W2	5.0	18.5	59.1	15.8	46.0
HCO + CH4 on W2	3.5	2.0	3.9	1.3	214.3
TS Rc on W2	2.2	3.9	250.4	17.9	18.0
CH3CHO on W2	1.1	8.7	6.5	6.1	6.5
Average	3.0	8.3	80.0	10.3	71.2

Table A.2. Energetics (kJ mol^{-1}) of the stationary points optimized at BHLYP-D3(BJ)/6-311++G(d,p), together with the frequencies of the transition states (cm^{-1}).

	OPT: BHLYP-D3(BJ)/6-311++G(d,p)	
	E	iv
React. I	-306.5101581	
TS I	-306.5101000	-26.1495
Prod. I	-306.6472250	
React. II	-306.5106910	
TS II	-306.5098973	-32.8207
Prod. II	-306.6377604	

Table A.3. Raw data from the DFT method benchmark. Energies in kJ mol^{-1}.

	DFT/6-311++G(2df,2pd)				
	BHLYP-D3(BJ)	MPWB1K-D3(BJ)	M062X-D3	PW6B95-D3(BJ)	wB97X-D3
React. I	-306.5278673	-306.5199277	-306.5443283	-307.0275371	-306.6077421
TS I	-306.5274906	-306.5195273	-306.5429782	-307.0270829	-306.6074261
Prod. I	-306.6651096	-306.6673671	-306.6888795	-307.1714705	-306.7523061
React. II	-306.5278665	-306.5199185	-306.5443285	-307.0275286	-306.6077403
TS II	-306.5273893	-306.5195091	-306.5435295	-307.027106	-306.6074694
Prod. II	-306.6561571	-306.6555907	-306.6825872	-307.1623168	-307.0257242

	Multi-reference methods	
	CASSCF(2,2)/aug-cc-PVTZ	CASPT2/aug-cc-PVTZ
React. I	-304.99849	-306.092193
TS I	-304.99793	-306.0918077
Prod. I	-305.14355	-306.2278841
React. II	-304.99849	-306.0921923
TS II	-304.9976	-306.0916902
Prod. II	-305.14411	-306.2251986

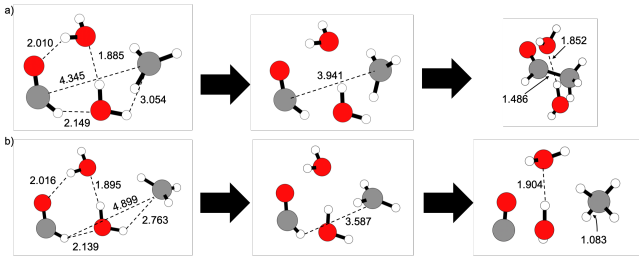

Fig. A.1. Geometries of the stationary points (reactants, transition state and products) of reactions a) I and b) II on top of two water molecules optimized at BHLYP-D3(BJ)/6-311++G(d,p) level. Distances in Å.

Appendix B: Calculation of desorption and diffusion rate constants

In order to calculate the rates of diffusion and desorption we have used Eyring's equation (Eq. 5), where entropy and thermal corrections to the enthalpy are accounted for since energy term in the exponential should be the Gibbs free energy ($G = H - TS$). In the astrochemistry community, desorption and diffusion rates consist of two parts, first the attempt frequency (i.e., the pre-exponential factor) and then the exponential with the binding energies. We define the attempt frequency within the Eyring equation as

$$\nu = \frac{k_B T}{h} \times \exp(\Delta S / k_B), \tag{B.1}$$

where h, k_B are the Planck and Boltzmann constants, T the temperature and S the entropy. For the ice model and the complex surface+radical the entropy contributions are $S = S_{vib}$, where the vibrational counterpart is (Eq. B.2):

$$S_{vib} = k_B \sum_i \left[\frac{\theta_{v,i}/T}{e^{\theta_{v,i}/T} - 1} - \ln\left(1 - e^{-\theta_{v,i}/T}\right) \right] \tag{B.2}$$

where $\theta_{v,i} = hc\bar{\nu}_i/k_B$ with c the speed of light and $\bar{\nu}_i$ the ith vibrational mode frequency in cm^{-1}.

For the free radicals, additionally, we also take into account the rotational and translational contributions: $S = S_{vib} + S_{rot} + S_{trans}$, where the rotational and translational counterparts are given by eqs. B.3 and B.4 respectively:

$$S_{rot} = k_B \left[\ln\left(\frac{\pi^{1/2}}{\sigma_{rot}} \frac{T^{3/2}}{(\theta_{r,x}\theta_{r,y}\theta_{r,z})^{1/2}} \right) + \frac{3}{2} \right], \tag{B.3}$$

$$S_{trans} = k_B \left(\ln \left[\left(\frac{2\pi m k_B}{h^2} \right)^{3/2} \frac{k_B T}{P} \right] + \frac{5}{2} \right), \quad \text{(B.4)}$$

where σ_{rot} is the rotational symmetry number (6 for CH_3 and 1 for HCO), $\theta_{r,i} = B_i h/k_B$ with B_i the ith axis rotational constant (in s^{-1}), m is the mass of the radical and P the gas pressure, which was calculated assuming a density of 10^4 cm^{-3}.

The thermal corrections follow: $H = E_{DFT} + ZPE + E_{vib}(T) + k_B T$ for the surface and the surface + radical complex. Here E_{DFT} is the energy obtained from our DFT calculations, ZPE is the zero-point energy and $E_{vib}(T)$ is the thermal vibrational energy calculated with Eq. B.5. In analogy to to the entropy, the rotational and translational contributions are also included for the free radicals: $H = E_{DFT} + ZPE + E_{vib}(T) + k_B T + H_{rot} + H_{trans}$ where $H_{rot} = H_{trans} = \frac{3}{2} k_B T$.

$$E_{vib}(T) = k_B \sum_i \frac{\theta_{v,i}}{e^{\theta_{v,i}/T} - 1} \quad \text{(B.5)}$$

The magnitude of these contributions is shown in Table B.1, where it can be seen that the most important contribution to the enthalpy comes from the vibrational modes, while for entropy all contributions are rather small:

Table B.1. Corrections incorporated in the calculation of ΔG of binding. Quantities calculated at 20 K and 30 K. Energy and entropy units are kJ mol−1 and kJ mol−1 K^{-1}. See that Boltzmann's constant is about 0.0083 kJ mol^{-1}, therefore the $k_B T$ and $3k_B T/2$ terms are also very small.

	T = 20 K				T = 30 K			
	ΔE_{vib}	ΔS_{vib}	S^{rad}_{rot}	S^{rad}_{trans}	ΔE_{vib}	ΔS_{vib}	S^{rad}_{rot}	S^{rad}_{trans}
CH_3	0.124	-0.007	0.010	0.005	0.293	-0.003	0.015	0.011
HCO	0.077	-0.012	0.034	0.011	0.228	-0.009	0.039	0.016

As it was explained in the introduction, we have adopted the assumption that the barrier for diffusion can be expressed as a fraction of that of desorption, therefore in this model we multiply the ΔG of desorption times these fractions (assumed to be 0.3, 0.4 and 0.5). With this, we get different attempt frequencies for diffusion and desorption (see Table B.2), all around 10^8–10^{11} s^{-1}, smaller than the normally used approach of the harmonic oscillator[3] in astrochemical models (e.g., Tielens & Allamandola (1987); Hasegawa et al. (1992)) due to the use of Eyring's relation and the inclusion of entropy.

Table B.2. Attempt frequencies for desorption and the different cases of diffusion considered in this work. Units in s^{-1}. See that at 20 K $k_B T/h \sim 4.2\times10^{11}$, so the effect of entropy at such low temperatures is very small.

	Eyring equation (computed at 20 K)				Harmonic oscillator
	Desorption	Diffusion			
Diff-to-Des	–	0.5	0.4	0.3	–
$\nu(CH_3)$	4.7×10^{8}	1.1×10^{11}	1.4×10^{11}	1.9×10^{11}	1.5×10^{12}
ν(HCO)	2.9×10^{10}	1.4×10^{10}	2.8×10^{10}	5.4×10^{10}	1.5×10^{12}

Appendix C: Rate constant comparison

Figure C.1 compares the rates of the radical-radical reactions with the hopping and desorption rates for each radical species, using three different criteria for the diffusion barrier, namely making it 0.3, 0.4 and 0.5 times those of desorption.

[3] $\nu = \sqrt{2N_s E_{bind}/\pi^2 m}$, with N_S the density of sites, ~10^{15} and m the mass of the particle.

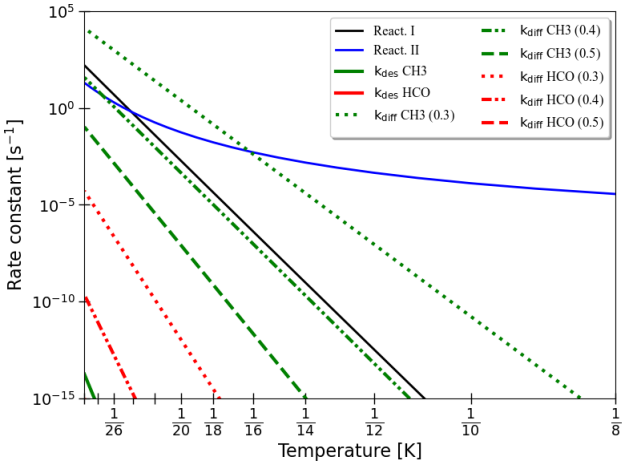

Fig. C.1. Comparison of reaction, diffusion and desorption rate constants involved in the CH_3 + HCO system. Notice that the desorption rate of HCO is not seen as it appears at very low rate constant values. Numbers in brackets indicate the diffusion-to-desorption energy barrier ratio.

Appendix D: H + CO PES and data

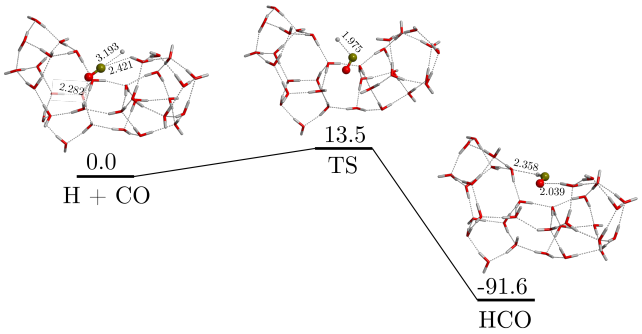

Fig. D.1. Potential energy surface of the H + CO → HCO reaction, in kJ mol^{-1}. Energies are corrected for dispersion and ZPE. Geometries and ZPE energies were obtained at UBHandHLYP-D3(BJ)/6-31+G(d,p) level and DFT energies were refined at UBHandHLYP-D3(BJ)/6-311++G(2df,2pd) level. Reactants and products were obtained by running intrinsic reaction coordinate calculations.

Table D.1. H + CO → HCO energetic data, in Hartree, at UBHandHLYP-D3(BJ)/6-31+G(d,p) (double ζ) level. U is the DFT energy, D is the Dispersion energy and ZPE is the zero-point energy. DFT energies were refined by performing single point calculations on double ζ geometries at UBHandHLYP-D3(BJ)/6-311++G(2df,2pd) (triple ζ) level. Energy units are Hartree (1.0 Hartree are ~ 2625.5 kJ mol^{-1}).

$H + CO$	Reactant	TS	Product
U (double ζ)	-2558.84099479	-2558.83665194	-2558.88783666
D (double ζ)	-0.08428582	-0.08266012	-0.08407096
ZPE (double ζ)	0.86306000	0.86239000	0.872578000
U (triple ζ)	-2559.79323262	-2559.78741062	-2559.83765264

Table D.2. H$\cdots$CO transition state data. Units are the usual for a Gaussian16 output: frequencies in cm^{-1}, IR intensities in KM/Mole, reduced masses in AMU and force constants in mDyne/Å. At UBHandHLYP-D3(BJ)/6-31+G(d,p) level.

	$i\nu$	red mass	F ctn	IR int
$H + CO$	605.7354	1.1042	0.2387	14.8487

Appendix E: Radical-radical TS data and PES:

Table E.1. CH_3 + HCO energetic data, in Hartree, at UBHandHLYP-D3(BJ)/6-31+G(d,p) level (double ζ). U is the DFT energy, D is the Dispersion energy and ZPE is the zero-point energy. DFT energies were refined by performing single point calculations on double ζ geometries at UBHandHLYP-D3(BJ)/6-311++G(2df,2pd) (triple ζ) level. Energy units are Hartree (1.0 Hartree are $\sim$ 2625.5 kJ mol^{-1}).

React. I	Reactant	TS	Product
U (double ζ)	-2675.130087	-2675.127479	-2675.266272
D (double ζ)	-0.091309097	-0.091229233	-0.088094692
ZPE (double ζ)	0.933864	0.933528	0.94406
U (triple ζ)	-2676.122287	-2676.119848	-2676.253986
React. II	Reactant	TS	Product
U (double ζ)	-2675.130087	-2675.12475	-2675.255587
D (double ζ)	-0.091309097	-0.092369778	-0.091838262
ZPE (double ζ)	0.933864	0.933255	0.938711
U (triple ζ)	-2676.122287	-2676.118937	-2676.250317

Table E.2. Features of the transition states studied in this work. Units are the usual for a Gaussian16 output: frequencies in cm^{-1}, IR intensities in KM/Mole, reduced masses in AMU and force constants in mDyne/Å. At UBHandHLYP-D3(BJ)/6-31+G(d,p) level.

	reaction I				reaction II			
	$i\nu$	red mass	F ctn	IR int	$i\nu$	red mass	F ctn	IR int
CH_3 + HCO	91.0685	4.7645	0.0233	0.5366	168.6488	1.8100	0.0303	16.6868

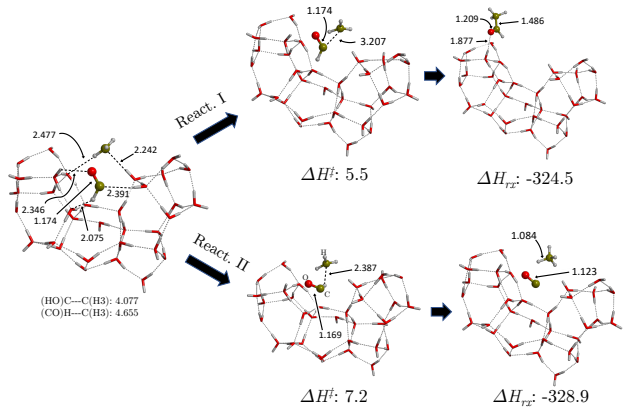

Fig. E.1. Potential energy surfaces Reacts. I and II. Geometries and ZPE energy correction was obtained at UBHandHLYP-D3(BJ)/6-31+G(d,p) level, DFT energy was refined at UBHandHLYP-D3(BJ)/6-311++G(2df,2pd) level. Energy units are in kJ mol^{-1}.

Appendix F: Efficiency figures, separated by E_{diff}/E_{des} ratios

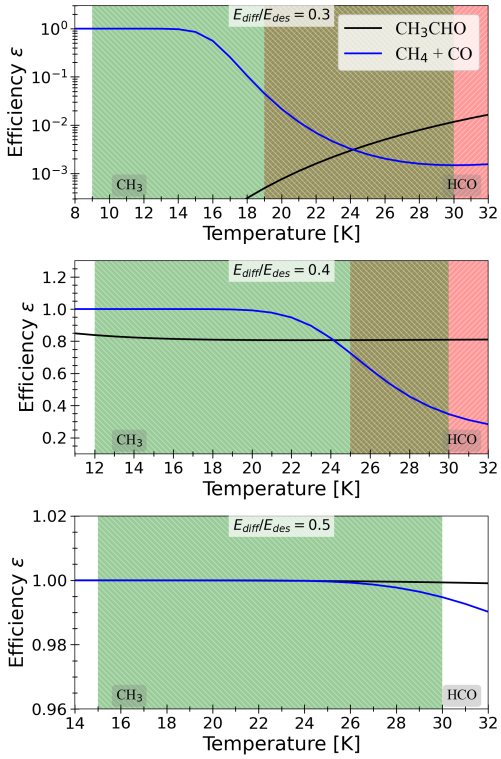

Fig. F.1. CH3 + HCO reaction efficiencies ε (Eq. 3), assuming diffusion barriers 0.3, 0.4 and 0.5 times those of desorption (panels from top to bottom). The green-colored regions indicate the diffusion and desorption temperatures limits of CH3, while the red ones are the same for HCO.

Appendix G: Calculation of diffusion and desorption temperatures

Half-lives are calculated from the rate constants (k_i, with i being either the diffusion or desorption of radicals) following

$$N_{1/2} = N_0 \exp(-k_i t) \quad \Longrightarrow \quad t_{1/2} = \frac{\ln(2)}{k_i},$$

and shown in Fig. G.1.

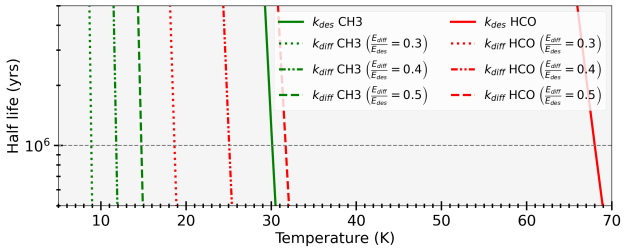

Fig. G.1. Diffusion and diffusion temperatures of CH_3 and HCO assuming a half-life of 1 Myrs for desorption.

Appendix H: Fittings to k_{aeb} and ε:

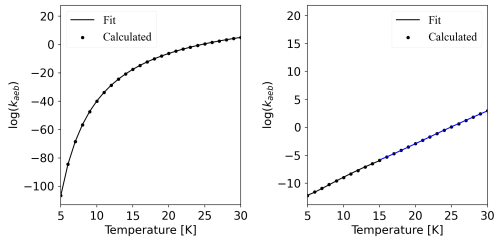

Fig. H.1. Fittings to the computed rate constants (Figure 1) with Eq. 9 for reactions I (left hand side panel) and II (left hand side panel).

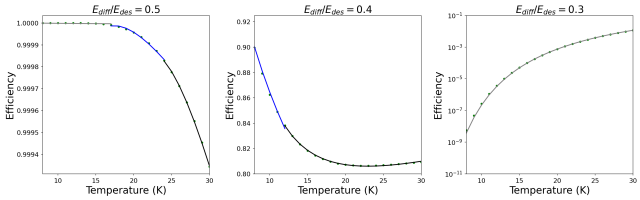

Fig. H.2. Fittings (solid lines) to the computed efficiency factors (points) using Eq. 9 for acetaldehyde using E_{diff}/E_{des} = 0.5, 0.4 and 0.3 (left to right panels).

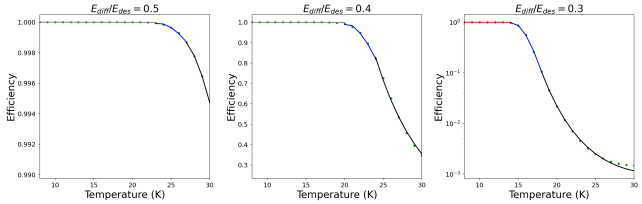

Fig. H.3. Fittings (solid lines) to the computed efficiency factors (points) using Eq. 9 for CO + CH_4 formation using E_{diff}/E_{des} = 0.5, 0.4 and 0.3 (left to right panels).

The Astrophysical Journal, 897:56 (13pp), 2020 July 1 https://doi.org/10.3847/1538-4357/ab8a4b

Chemical Desorption versus Energy Dissipation: Insights from Ab Initio Molecular Dynamics of HCO● Formation

Stefano Pantaleone[1], Joan Enrique-Romero[1,2], Cecilia Ceccarelli[1], Piero Ugliengo[3], Nadia Balucani[1,4,5], and Albert Rimola[2]

[1] Université Grenoble Alpes, CNRS, Institut de Planétologie et d'Astrophysique de Grenoble (IPAG), F-38000 Grenoble, France
stefano.pantaleone@univ-grenoble-alpes.fr
[2] Departament de Química, Universitat Autònoma de Barcelona, Bellaterra, E-08193, Catalonia, Spain; juan.enrique-romero@univ-grenoble-alpes.fr
[3] Dipartimento di Chimica and Nanostructured Interfaces and Surfaces (NIS) Centre, Università degli Studi di Torino, via P. Giuria 7, I-10125, Torino, Italy
piero.ugliengo@unito.it
[4] Dipartimento di Chimica, Biologia e Biotecnologie, Università degli Studi di Perugia, Via Elce di Sotto 8, I-06123 Perugia, Italy
[5] Osservatorio Astrofisico di Arcetri, Largo E. Fermi 5, I-50125 Firenze, Italy
Received 2020 January 10; revised 2020 March 26; accepted 2020 April 15; published 2020 July 1

Abstract

Molecular clouds are the cold regions of the Milky Way where stars form. They are enriched by rather complex molecules. Many of these molecules are believed to be synthesized on the icy surfaces of the interstellar submicron-sized dust grains that permeate the Galaxy. At 10 K thermal desorption is inefficient and, therefore, why these molecules are found in the cold gas has tantalized astronomers for years. The assumption of the current models, called chemical desorption, is that the molecule formation energy released by the chemical reactions at the grain surface is partially absorbed by the grain and the remaining energy causes the ejection of the newly formed molecules into the gas. Here we report accurate ab initio molecular dynamics simulations aimed at studying the fate of the energy released by the first reaction of the H· addition chain to CO, H· + CO → HCO·, occurring on a crystalline ice surface model. We show that about 90% of the HCO· formation energy is injected toward the ice in the first picosecond, leaving HCO· with an energy content (10–15 kJ mol^{-1}) of less than half its binding energy (30 kJ mol^{-1}). As a result, in agreement with laboratory experiments, we conclude that chemical desorption is inefficient for this specific system, namely H· + CO on crystalline ice. We suspect this behavior to be quite general when dealing with hydrogen bonds, which are responsible for both the cohesive energy of the ice mantle and the interaction with adsorbates, as HCO·, even though ad hoc simulations are needed to draw specific conclusions on other systems.

Unified Astronomy Thesaurus concepts: Astrochemistry (75); Pre-biotic astrochemistry (2079); Interstellar dust processes (838); Solid matter physics (2090)

Supporting material: tar.gz file

1. Introduction

To date, more than 200 types of molecules have been detected in the interstellar medium (ISM) (e.g., McGuire 2018). Of these, all molecules with more than five atoms contain carbon. These are the so-called interstellar complex organic molecules (iCOMs; Herbst & van Dishoeck 2009; Ceccarelli et al. 2017). iCOMs are most commonly observed in galactic star-forming regions (e.g., Rubin et al. 1971; Blake et al. 1986; Cazaux et al. 2003; Belloche et al. 2017; Lefloch et al. 2017; Bianchi et al. 2019) and external galaxies (e.g., Muller et al. 2013; Sewiło et al. 2018). Besides these, iCOMs are also detected toward cold (∼10 K) sources (e.g., Bacmann et al. 2012; Cernicharo et al. 2012; Vastel et al. 2014; Jiménez-Serra et al. 2016). These latter detections are important for (at least) two reasons: first, they challenge the idea that iCOMs are synthesized on lukewarm (30–40 K) grain surfaces by radical–radical combination (Garrod & Herbst 2006; Öberg et al. 2009; Ruaud et al. 2015), and, second, if for whatever reason they are formed on grain surfaces, the mechanism that lifts them off into the gas (where they are detected) must be nonthermal. Different nonthermal mechanisms have been invoked in the literature to explain the presence of gaseous iCOMs in cold environments: cosmic-ray spot heating (Léger et al. 1985; Hasegawa & Herbst 1993) or sputtering (e.g., Dartois et al. 2019), UV-induced photodesorption (e.g., Dominik et al. 2005; Fayolle et al. 2011; Bertin et al. 2013, 2016), codesorption of ices (e.g., Sandford & Allamandola 1988; Ligterink et al. 2018), and chemical (or reactive) desorption (Duley & Williams 1993; Garrod et al. 2007; Minissale & Dulieu 2014; Minissale et al. 2016).

Here, we focus on the last mechanism, the chemical desorption (CD). The underlying idea is that the energy released by strongly exothermic chemical reactions occurring on grain surfaces is only partly absorbed by the grains, while the remaining energy is used to break the bonds between the newly formed species and the surfaces, so that a fraction of the synthesized species is injected into the gas phase. Therefore, CD and the dissipation of the surface-reaction energy are two sides of the same coin, intrinsically linked.

From an experimental point of view, it is extremely difficult, if not impossible, to quantify the energy dissipation. Overall, laboratory experiments showed that CD can be more or less efficient depending on the adsorbate and the substrate. For example, Oba et al. (2018) found high CD efficiencies (∼60%) for H_2S formation on amorphous solid water. On the contrary, lower CD efficiencies for different systems were observed by other authors: Dulieu et al. (2013) found a CD efficiency for the O_2 + D reaction lower than 10%, He et al. (2017) showed that the H· addition to O_3 causes the desorption of the product O_2 by no more than 11%, and Chuang et al. (2018) found a CD

efficiency lower than 2% per hydrogen-atom-induced reaction in the hydrogenation of CO toward methanol. In a systematic study of CD in several reactions on different substrates, Minissale et al. (2016) showed that the CD efficiency does indeed depend on three major factors: the reaction formation energy, the binding energy of the adsorbate, and the nature of the substrate. They proposed a general formalism to estimate the CD probability, based on the idea that the energy dissipation can be approximately treated as an elastic collision.

Theoretical calculations are, in principle, capable of simultaneously studying the energy dissipation and CD. Various techniques have been so far used for different systems. Fredon et al. (2017) and Fredon & Cuppen (2018) simulated the relaxation of translationally excited admolecules (CO_2, H_2O, and CH_4) on crystalline and amorphous ice models, via classical molecular dynamics (MD) simulations. They ran thousands of simulations using approximate interaction potentials where the admolecules were given large (0.5–5 eV, equal to 50–500 kJ mol^{-1}) translational energies in random directions. Therefore, in these studies, all the chemical reaction energy is assumed to be canalized into translational motion of the admolecules and, for this reason, a statistical analysis was necessary to understand the fate of the energy for different injected trajectories. Thus, each simulation follows the evolution of the energy of the species, recording whether the molecule is desorbed, penetrates in the surface, or is adsorbed on the surface. Based on their large number of simulations, Fredon et al. (2017) and Fredon & Cuppen (2018) found that the desorption probability depends on the injected kinetic energy and binding energy of the species. Additionally, they provided a formula to estimate the CD probability, which depends on those two quantities. Despite careful and exhaustive statistical analysis on the simulations, there are some weaknesses to be pointed out: (i) the limits of force-field-based methods in dealing with chemical reactions; (ii) the injected energy of the admolecule which is only translational, while, after a reaction occurs, the energy should be partitioned also into vibrational and rotational levels; (iii) the relatively small size of the used water clusters, whose temperature may rise for high energy injections (∼5 eV), thus resulting in an overestimation of the admolecule mobility.

Korchagina et al. (2017) studied the energy dissipation of the hydrogenation reaction of CO (producing HCO·) under the Eley–Rideal model at temperatures of 70 K. They used MD simulations at the self-consistent-charge density functional tight binding theory level, which is an approximation of classical density functional theory, based on parameterized integrals and charges. They used small molecular clusters, 1–10 water molecules, to simulate the ice surfaces and showed that the energy released after HCO· formation can be dissipated (i.e., the reaction gives a stable HCO·) on clusters with $N \geqslant 1$ water molecules, and that the product remains adsorbed on the clusters (i.e., no CD) for clusters with $N \geqslant 3$. Such behavior is linked to the capacity of water to redistribute the reaction energy excess into vibrational excitation. However, such small clusters cannot represent the ice mantle when dynamical effects are taken into account, because, although very small clusters can stabilize the product by absorbing efficiently the nascent energy, the mobility of the molecule is strongly overestimated. Indeed, the cluster's temperature increase linearly depends on the number of water molecules on the surface model: it should be large enough to be able to harness the reaction energy while restraining the temperature increase.

Kayanuma et al. (2019) studied the reaction of H· with adsorbed HCO· on a graphene surface by means of ab initio molecular dynamics (AIMD) simulations, showing that in the case of HCO· chemisorption (i.e., a chemical bond between the adsorbate and the surface), the products H_2 + CO are desorbed, while in the case of HCO· physisorption (the interaction with the surface is of a dispersive nature), formaldehyde is formed without chemical desorption.

Here we present new AIMD simulations of the reaction H· + CO on a large periodic crystalline water-ice surface assuming the Langmuir–Hinshelwood (LH) mechanism. This reaction is the first step toward the formation of methanol on the grain surfaces, frequently studied both theoretically and experimentally (e.g., Hiraoka et al. 2002; Watanabe & Kouchi 2002; Woon 2002; Watanabe et al. 2007; Andersson et al. 2011; Rimola et al. 2014); therefore, in this context, it can be considered as one of the most important reactions in astrochemical studies. In addition, it is representative of the class of reactions with a relatively low reaction energy (less than 2 eV) needed to dissipate. Our scope is to understand from an atomic point of view how the energy released by the HCO· formation is transferred toward the water surface, without any a priori assumption on how the reaction energy is distributed over the system. We emphasize that our approach is substantially different from the one used by Fredon et al. (2017) and Fredon & Cuppen (2018), described above. In our case, we do not need to address a statistical behavior (depending on the species trajectory), because we simulate the reaction itself and how its energy is dissipated by the formed HCO·. This does not depend on the initial H· trajectory because the energy of the H atom is thermal (at 10 K, specifically) and, therefore, negligible with respect to the energy released by the reaction (about 1.4 eV). The result could, in principle, depend on the initial position of the CO on the crystalline ice, for which there are a few possibilities, and we will discuss this point in the article. In summary, our AIMD simulations allow us to quantify whether the newly formed species has enough energy to break its interactions with the water surface and, consequently, to be injected into the gas phase.

Finally, although it is well known that interstellar ice is often amorphous, we chose a crystalline model because tuning the computational setup is easier. Once the system is carefully tested, our future works will focus on amorphous ice models. It is important to notice, however, that crystalline water ice has been detected in the ISM (Molinari et al. 1999) and, particularly relevant for planet formation studies, in protoplanetary disks (Terada & Tokunaga 2012), so therefore our simulations will be directly applicable in those environments.

The article is organized as follows. In Section 2 we present the computational methodology, in Section 3 the results and in Section 4 we discuss these results in view of astrochemical implications. Finally, in Section 5, we summarize the most important conclusions.

2. Computational Details

2.1. Methods

All the calculations have been carried out with the CP2K package (Goedecker et al. 1996; Lippert et al. 1997; Hartwigsen et al. 1998; VandeVondele & Hutter 2003; VandeVondele et al. 2005; Hutter et al. 2014). The atoms have been treated as follows:

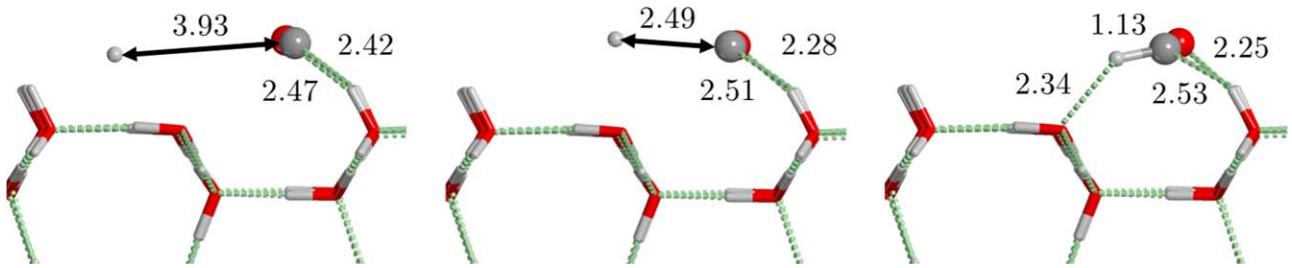

(a) Reactant (0.0) (b) Transition state (5.2) (c) Product (-132.5)

Figure 1. PBE-D3 optimized geometries of the reactant, TS, and product of the HCO· reaction formation on the ice surface. The numbers in parenthesis correspond to the relative energy in kJ mol^{-1} with respect to the reactant. Distances are in Å. H atoms in white, C atoms in gray, O atoms in red.

core electrons have been described with the Goedecker–Teter–Hutter pseudopotentials (Goedecker et al. 1996; Hartwigsen et al. 1998), while valence electrons with a mixed Gaussian and plane wave approach (Lippert et al. 1997). The Perdew–Burke-Ernzerhof (PBE) functional has been used for all the calculations (Perdew et al. 1996) combined with a triple-ζ basis set for valence electrons plus two polarization functions (TZV2P). The cutoff for plane waves has been set to 600 Ry. The a posteriori D3 Grimme correction has been applied to the PBE functional to account for dispersion forces (Grimme et al. 2010, 2011). During the optimization procedure, only the H, C, and O atoms (the ones belonging to the HCO·) were free to move, while the atoms belonging to the ice surface have been kept fixed to their thermalized positions. All calculations were carried out within the unrestricted formalism as we deal with open-shell systems. The spin density was checked for reactants, transition state (TS), and product and it always remains well localized either on a H atom (reactant) or on HCO· (product). No spread of spin density through the ice was detected (see Figures A2–A4). The binding energy (BE) of HCO· was calculated according to the following formula:

$$BE_{\mathrm{HCO}\cdot} = (\mathrm{E_{ice}} + \mathrm{E_{HCO}}\cdot) - \mathrm{E_{CPLX}} \quad (1)$$

where E_{CPLX} is the energy of the HCO·/ice system, E_{ice} that of the bare ice surface, and E_{HCO} the energy of the HCO· alone, each one optimized at its own minimum. The $BE_{\mathrm{HCO}\cdot}$ will be used later on for comparison with the residual kinetic energy of the HCO· formation.

In order to reproduce the ISM conditions, the reaction was carried out in the microcanonical ensemble (NVE), where the total energy (i.e., potential + kinetic) is conserved. Moreover, we run an equilibration AIMD in the NVT ensemble (using the canonical sampling through velocity rescaling, CSVR, thermostat, with a time constant of 20 fs) at 10 K for 1 ps (with a timestep of 1 fs) for the bare ice surface to obtain a thermally equilibrated ice. Accordingly, the equilibrated velocities of the ice surface were used as starting ones for the NVE production, while the H and C velocities of HCO· were manually set according to the H–C bond formation. The evolution of the system was followed for 20 ps, using a timestep of 1 fs.

In addition, in the Appendix, we present results obtained from a benchmark study on the reaction of HCO· formation on a small cluster of three H_2O molecules (H· + CO/3H_2O ⟶ HCO·/3H_2O, see Figure A1), similar to the work by Rimola et al. (2014). The results show that PBE overestimates the energetics of the reaction (132 kJ mol^{-1} versus 91 kJ mol^{-1}, provided by the CCSD(T) method, see Table A1). By contrast, frequency calculations, which are responsible for the vibrational coupling of the water molecules with the HCO· and, accordingly, of the kinetic energy dissipation efficiency, are in good agreement to those calculated at a higher level of theory (see Table A2).

2.2. Ice Model

Ordinary ice is proton disordered and, accordingly, its crystal structure cannot be simply modeled by adopting relatively small unit cells. A possible alternative is to adopt P-ice, a proton-ordered ice already successfully used in the past to simulate ice features (Pisani et al. 1996). P-ice bulk belongs to the $Pna2_1$ space group, and from the bulk we cut out a slab to simulate the (100) surface, shown in Figure A5. The size of the surface was chosen according to the amount of energy to be dissipated. Given that the HCO· radical formation is strongly exothermic (132.5 kJ mol^{-1}; see Figure 1(c)), a sufficiently large water-ice slab is needed to absorb most of the nascent energy (see more details in Section 3). Therefore, the periodic cell parameters have been set to $a = 17.544$ Å and $b = 21.2475$ Å with a slab thickness of ∼13 Å (which corresponds to four water layers). The model consists of 192 water molecules in total. In the CP2K code, the electron density is described by plane waves, and, accordingly, the surface is replicated also along the nonperiodic direction. To avoid interactions between the fictitious slab replicas, the c parameter (i.e., the nonperiodic one) was set to 35 Å.

3. Results

To study the CO hydrogenation on the ice surface, we simulated the reaction adopting a LH surface mechanism, i.e., with both the reactants (H· and CO) adsorbed on the surface. Accordingly, we first optimized the geometries of the reactants (H· + CO), TS (H···CO), and product (HCO·) in order to obtain the potential energy surface of the reaction. As reported in Figure 1, the activation barrier (5.2 kJ mol^{-1}, 622.1 K) is quite high if we consider the sources of energy available in the ISM. Indeed, it is well known that this reaction proceeds mostly through H tunneling (Hiraoka et al. 2002; Andersson et al. 2011; Rimola et al. 2014). However, as AIMD operates within the Born–Oppenheimer approximation, i.e., the nuclei motion is driven by classical equations, the quantum phenomena of atoms (such as the tunneling effect) cannot be taken into account. Since our aim is not to simulate the reaction itself, but to understand where the liberated energy goes, we run the simulation starting from the TS structure (Figure 1(b)). In this way, we force the system to evolve in the direction of the product. Therefore, the total energy to be dissipated is the sum of the energy barrier and of the reaction energy (5.2 + 132.5) kJ mol^{-1} = 137.7 kJ mol^{-1}. It is possible to estimate the

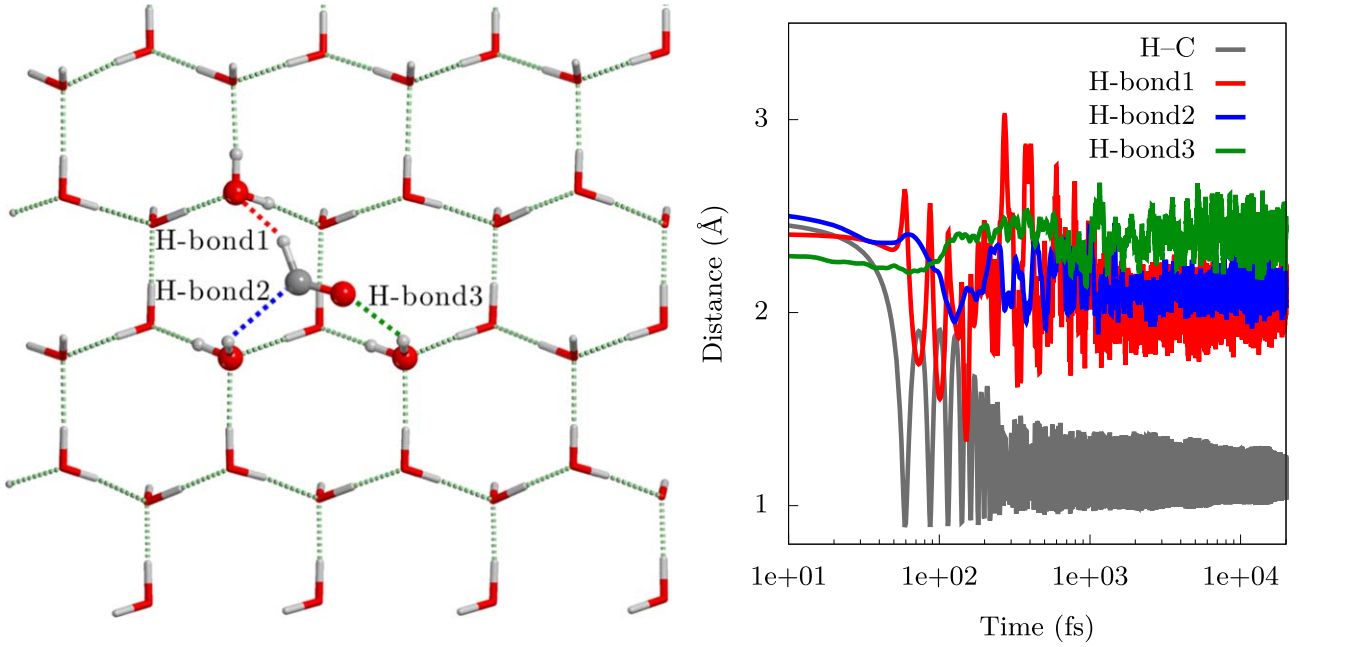

Figure 2. Structure of HCO· adsorbed on the ice surface at the last point of the AIMD simulation (left) and evolution of the most relevant geometrical parameters during the AIMD simulation (right). H-bond colors in the chart correspond to the H -bonds in the figure depicted as dotted lines. H atoms in white, C atom in gray, O atoms in red.

expected temperature increase of the whole system after the reaction by invoking the equipartition theorem:

$$T = \frac{2}{3}\frac{E_{\rm nasc}}{R\,N_{\rm at}}, \tag{2}$$

where $E_{\rm nasc}$ is the nascent energy due to the H–C bond formation (i.e., 137.7 kJ mol^{-1}), $N_{\rm at}$ is the number of atoms in the whole system (3 for HCO· and 3 × 192 for the ice), and R the gas constant. Thus, the energy dissipation through an ice slab containing 192 water molecules should produce a global temperature increase of about 19 K (which is in perfect agreement with the very first spike in T of Figure A6, reaching 29 K = (10 K + 19 K) where 10 K is the starting temperature). Then, when the simulation equilibrates, the temperature oscillates around 20 K. This very simple calculation is useful so as to have an idea of the number of atoms needed to avoid the nascent energy artificially rising to the total temperature.

Figure 2 shows the most interesting geometrical parameters of the system during the AIMD simulation (other geometrical parameters are shown in Figure A7). Both the temperature and potential energy oscillate around a stable value and they reach the equilibrium within 1 ps (see also Figures A6 and A8). As one can see in Figure 2, the H–C bond forms in the first tens of femtoseconds of the simulation (keeping in mind that we are starting from the TS). This is confirmed by the spin density evolution. At the beginning of the simulation, the unpaired electron is localized on H·; once the H–C bond is formed the spin density is spread on the HCO·, with a higher percentage on the C atom (see Figure A9). After the H–C bond formation, the HCO· moves on the surface in the sense of maximizing the H-bond contacts with the surrounding water molecules (Figure 2) and it lies in its most stable position after 1 ps, which corresponds to the equilibration of both the potential energy and the temperature. After this period, HCO· stays in this stable position, without diffusing anywhere.

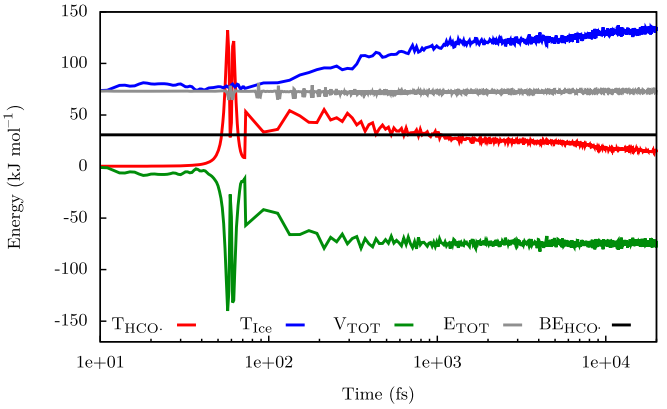

Figure 3. Evolution of the most relevant energetic components (in kJ mol^{-1}) of the HCO·/ice system during the AIMD simulation. $E_{\rm TOT}$ is the total energy (i.e., potential + kinetic, gray line). $V_{\rm TOT}$ is the potential energy (green line). $T_{\rm HCO·}$ and $T_{\rm ice}$ are the kinetic energies of HCO· (red line) and ice (blue line), respectively. $BE_{\rm HCO·}$ is the binding energy of the HCO· (black line). The gray line shows very good energy conservation.

In Figure 3, the kinetic energy dissipation due to the H–C bond formation is reported. As expected, the kinetic energy released from the H–C bond formation rapidly drops (in less than 100 fs) and it is, simultaneously, absorbed by the water molecules of the surface. As one can see, at the beginning of the simulation, before 200 fs, the red line ($T_{\rm HCO·}$) is complementary with the green line ($V_{\rm TOT}$). As the AIMD was executed in the NVE ensemble, when the kinetic energy drops, the potential rises by the same amount. However, after 300 fs, when the HCO· starts to exchange energy with the surface, the red ($T_{\rm HCO·}$) and blue ($T_{\rm ice}$) lines become symmetric, i.e., the energy loss of HCO· is equal to the energy gain of the surface, in terms of kinetic energy. The most important message from Figure 3 is that, within the first picosecond, HCO· loses 90% of its initial kinetic energy, which is immediately

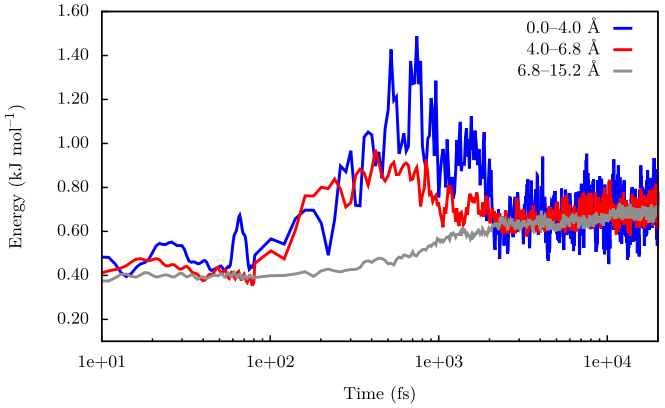

Figure 4. Kinetic energy evolution (in kJ mol^{-1} per water molecule) of the ice surface. The ranges in the legend refer to the shells the water molecules belong to.

transferred to the ice. Later, further along the simulation, HCO· continues to transfer energy to the ice at a slower rate. After 20 ps, its kinetic energy is around 15 kJ mol^{-1}, at least twice as low as its binding energy. Therefore, it is unlikely that the HCO· will desorb. This is corroborated by Figure 2, where the H-bonds linking HCO· to the surface lie in a rather steady fashion after its formation (they essentially vibrate around their equilibrium position).

In order to give a detailed analysis of the energy dissipation on the ice surface, we used the atomic simulation environment (ASE) python module (Bahn & Jacobsen 2002; Larsen et al. 2017). The energy dissipation was analyzed by dividing the slab of water molecules in concentric shells centered on the reaction center (i.e., the C atom). Note that HCO· has been excluded from this analysis because we are interested in the dissipation across the ice itself. The concentric shells were defined as follows: (i) the first one is a hemisphere of 4 Å radius containing the closest water molecules to the CO molecule; (ii) the other shells are equally spaced from each other by 2.8 Å (average closest O–O distance between water molecules), up to a distance of 18 Å in order to also include the farthest water molecules from the reaction center. We emphasize that only a single unit cell was used for this analysis, which means that no water molecules from periodic replicas are included in the energy dissipation analysis. The sketch showing the water shells is given in Figure A10.

The results of the energy dissipation analysis are shown in Figure 4. The kinetic energy was normalized per water molecule, in order to remove the dependence on the number of water molecules (as each shell contains a different number of water molecules). One can see from the two first shells (0.0–4.0 and 4.0–6.8 Å) that the energy is rapidly transferred from HCO· to the ice, which is later uniformly distributed to the outer shells: within ∼2 ps all shells have the same kinetic energy (in Figure A11, each panel reports the evolution of the kinetic energy for each water shell).

4. Discussion

In the present work, the HCO· formation reaction on an ice surface model has been used as a test case in order to study the kinetic energy dissipation due to the formation of a chemical bond (in this specific case, the H–C bond). This is particularly important because the energy released by the formation of a chemical bond may be a hot spot that makes other processes possible, like the desorption of the newly formed molecule or other molecules nearby. A crucial parameter is the timescale of the process: the main question is whether the released energy is available (and if so, for how long) and whether it can be used by other adsorbed species, or, in contrast, whether it is immediately dissipated through the ice surface. From Figure 3, the answer is very clear: the slab of water molecules absorbs ∼90% of the nascent energy, which is equally distributed among all the water molecules of the ice surface within the first picosecond after the bond formation, and it is no longer available to assist other processes. In particular, and most importantly, the residual HCO· kinetic energy after 1 ps is almost half of the HCO· binding energy, which implies that HCO· will remain stuck on the surface and will not desorb.

Our simulations are based on three assumptions: (i) the starting position of the CO adsorbed on the ice is the most energetically favorable one, (ii) the surface of the ice is crystalline, and (iii) the reaction follows a LH mechanism. In the following, we discuss the validity limits of each assumption.

(i) CO position: The first assumption is based on the fact that, as molecules in cold molecular clouds move at low thermal (∼10 K) velocities, landing on grain surfaces is slow enough for them to feel the electrostatic potential generated by the surface. Consequently, they have sufficient time to accommodate on the icy mantle, maximizing their interactions with the ice surface itself. In other words, the main driving forces of the adsorption process in cold molecular clouds are long range forces. Nonetheless, a few other starting positions may exist with respect to the one that was chosen for this study. For this reason, we have explored two other starting configurations, namely Pos2 and Pos3, reported in Figure A12. Both of them, after either geometry optimization (Figures A12(a) and (b)) or AIMD simulation (Figures A12(c) and (d)), lead to HCO· in the same position that is reported in Figures 1(c) and 2. In other words, whether CO is in the position we chose for the full AIMD simulations or in the other two positions, HCO· ends up having the same position, which means the same bonds with the surface and, consequently, the evolution of the system is the same.

(ii) Crystalline ice: As already mentioned in the Introduction, the major reason for choosing the crystalline ice structure is a computational one. In this respect, we should be cautious about the role of crystalline versus amorphous ice, because of the possibility that the symmetric electrostatic potential of the crystalline case can hinder the escape of the formed species from the surface and, in crystalline systems, the vibrational coupling might be more efficient than in amorphous ones, thus allowing a faster dissipation of the energy and, consequently, underestimating the desorption rate. Further studies need to be carried out in order to understand if the crystalline nature of the ice affects how the formed species behave because of the crystal symmetry compared to the random nature of the amorphous ice. Having said that, our simulations are valid and applicable in the environments where crystalline ice has been detected (e.g., Molinari et al. 1999; Terada & Tokunaga 2012).

(iii) LH mechanism: It is possible, and even probable, that the H atom will not arrive directly from the gas but rather is an atom that randomly grazes the ice surface. In this case, since the velocity of hydrogen is even smaller than if it landed from the gas, the results of our simulations would

not change. So, this choice is, after all, irrelevant for the purposes of our study.

In summary, we conclude that chemical desorption is not efficient in the H· + CO reaction on crystalline ice, and this is a robust result. Laboratory experiments have proven to be difficult to obtain for this specific reaction. To the best of our knowledge, no experiment simulates it on crystalline ices. Minissale et al. (2016) obtained a measure of the H· + CO CD when the reaction occurs on oxidized graphite. They found a CD efficiency equal to 10% ± 8%. Chuang et al. (2018) studied the CO hydrogenation process using a gold substrate, over which CO was deposited forming a thick layer of solid CO, which was subsequently bombarded with H atoms. They found that the global CD efficiency of the whole process up to the formation of CH_3OH is low, $\leqslant$0.07 per hydrogenation step, assuming an identical efficiency for each reaction in the hydrogenation process (Chuang et al. 2018). As already mentioned, the surface where the CO is adsorbed and the reaction occurs is certainly of paramount importance, so a direct comparison between our computations and the above experiments is not obviously made. Yet, it seems that the latter agree on a small CD efficiency, if any, like our computations predict.

Finally, it is possible that for more exothermic reactions (like for example the last step to CH_3OH, which is much more exothermic than H· + CO) and weakly bound systems (like H_2), CD can take place. This could also be the case for reactions occurring on grain surfaces of a different nature, such as silicates or carbonaceous materials, as their heat capacities are very different from those of H_2O-dominated ices. Dedicated simulations should be carried out to assess it in these systems.

5. Conclusions

We studied the first step of the hydrogenation of CO on the interstellar grain icy surfaces by means of AIMD simulation. We studied the H· + CO reaction occurring on a crystalline ice. Our goal was to understand it from an atomistic point of view and to quantify the possibility that the energy released in the reaction is only partially dispersed on the crystalline substrate and the residual energy is used to desorb the product, HCO·.

The main conclusions of the present study are:

(i) The reaction energy dissipation through thermal excitation of water molecules is extremely fast: after the first picosecond most of the reaction energy (137.7 kJ mol^{-1}) is dissipated away through the ice, leaving HCO· with a kinetic energy of 10–15 kJ mol^{-1}, more than twice as small as its binding energy (30 kJ mol^{-1}).
(ii) As a consequence, the HCO· product is doomed to remain attached to the crystalline ice and no desorption can occur.

The astrophysical implications are that, in the environments where crystalline ices are present, like for example some protoplanetary disks, chemical desorption does not occur for the reaction H· + CO. We suspect that this may be a general behavior for reactions dealing with hydrogen bonds, as they are responsible for both the cohesive energy and the interaction with the crystalline ice. However, in order to assess whether this is true, ad hoc simulations similar to those presented here are mandatory.

The authors acknowledge funding from European Union's Horizon 2020 research and innovation program, the European Research Council (ERC) Project "the Dawn of Organic Chemistry" grant agreement No. 741002, and the Marie Skodowska-Curie project "Astro-Chemical Origins" (ACO), grant agreement No. 811312. P.U. and N.B. acknowledge MIUR (Ministero dell' Istruzione, dell' Università e della Ricerca) and Scuola Normale Superiore (project PRIN 2015, STARS in the CAOS—Simulation Tools for Astrochemical Reactivity and Spectroscopy in the Cyberinfrastructure for Astrochemical Organic Species, cod. 2015F59J3R). A.R. is indebted to the "Ramón y Cajal" program. MINECO (project CTQ2017-89132-P) and DIUE (project 2017SGR1323) are acknowledged. BSC-MN and OCCIGEN HPCs are kindly acknowledged for the generous allowance of supercomputing time through the QS-2019-2-0028 and 2019-A0060810797 projects, respectively.

Appendix

A.1. Computational Details

Two sets of convergence criteria were used: (i) for geometry optimizations to energy minima the energy threshold of the self-consistent field (SCF) procedure was set to $\Delta E = 10^{-7}$ au, while the thresholds on gradients and displacements were set to their default values (4.5×10^{-4} Ha $Bohr^{-1}$ and 3.0×10^{-3} Ha $Bohr^{-1}$, respectively), and (ii) for the TS search tighter parameters were adopted ($\Delta E = 10^{-10}$ for the SCF and 4.5×10^{-5} Ha $Bohr^{-1}$ and 3.0×10^{-4} for gradients and displacements, respectively). These choices ensured good starting geometries for the AIMD simulation.

A benchmark study was performed using the same reaction on a smaller surface model, formed of three water molecules, in order to check the reliability of our results. The structures are shown in Figure A1, while energetic values and harmonic frequencies are reported in Tables A1 and A2, respectively. It is clear that PBE energies are quite far from those calculated at higher levels of theory, in particular with respect to the B2PLYPD3 and CCSD(T) methods. Hence, PBE results overestimate the chemical desorption, which in any case is not observed in our simulations. Harmonic frequencies computed at the PBE level, on the other hand, show very good agreement with those calculated at the B2PLYPD3 level (∼10% difference), which is the most accurate method used in

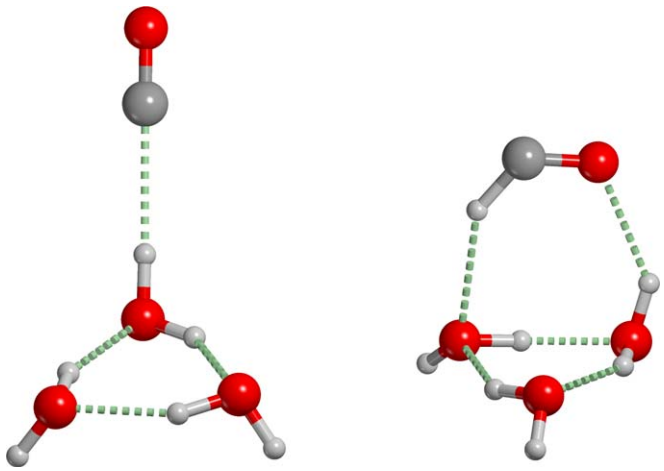

(a) $CO/3H_2O$ (b) $HCO·/3H_2O$

Figure A1. PBE-D3/TZV2P optimized structures of reactant (a) and product (b) of the H· + $CO/3H_2O \longrightarrow HCO·/3H_2O$ reaction.

the frequency-calculation benchmark (CCSD(T) is excluded here because frequency calculations are computationally too expensive and we cannot perform them). This means that the vibrational coupling of HCO· with the water molecules is correctly described, and hence, also the energy dissipation.

A.2. XYZ *Files*

We report the PBE/TZV2P optimized geometries of reactant, TS and product adsorbed on the ice surface, and the starting velocities of the AIMD simulation as *XYZ* files. These are available in the data.tar.gz package.

A.3. *Tables*

Tables A1 and A2 (reaction energy and vibrational frequencies, respectively) reports the results on the benchmark calculations we performed on the cluster models.

A.4. *Figures*

Figures A2–A4 show the spin density of reactants (H· + CO), TS (H···CO), and product (HCO·), respectively. Figure A1 shows the cluster model used in the benchmark calculations. Figure A5 shows the bulk structure of P-ice, and the surface model used for all the calculation in the present work. Figure A6 shows the evolution of the temperature during the AIMD simulation. Figure A7 shows the evolution of some geometrical parameters (namely, the C-O bond of HCO·, and the O-H bond of a neighbor water molecule). Figure A8 shows the evolution of the potential energy during the AIMD simulation. Figure A9 shows the spin density evolution on H, C, and O atoms of HCO· during the AIMD simulation. Figure A10 shows a schematic representation of the water shells used for calculating the kinetic energy spreading. Figure A11 shown the kinetic energy evolution of each water shell. Figure A12 shows other possible staring configurations for the HCO· formation.

Table A1
Energetic Data of the Reaction (H· + $CO/3H_2O \longrightarrow HCO·/3H_2O$) Calculated at Different Levels of Theory

Method	1	2	3	4	5	6	7
Energy (kJ mol^{-1})	−132.1	−122.6	−121.0	−108.0	−45.5	−91.3	−90.9

Note. 1: CP2K: PBE-D3/TZV2P, 2: Gaussian: PBE-D3/6-311++G(d,p), 3: Gaussian: BHLYP-D3/6-311++G(d,p), 4: Gaussian: BHLYP/6-311++G(d,p), 5: Gaussian: MP2/aug-cc-pvtz, 6: Gaussian: B2PLYPD3/aug-cc-pvtz, 7: Gaussian: CCSD(T)/aug-cc-pvtz//B2PLYPD3/aug-cc-pvtz.

Table A2
Harmonic Frequencies of the Reaction H· + $CO/3H_2O \longrightarrow HCO·/3H_2O$ Calculated at Different Levels of Theory, with Their Percentage Differences with Respect to the Method Adopted in the Present Work

Method	1	2	3	4	5	6	Diff% (1–2)	Diff% (1–3)	Diff% (1–4)	Diff% (1–5)	Diff% (1–6)
Frequencies (cm^{-1})											
	450	434	388	406	386	395	−4	−14	−10	−14	−12
	473	443	431	434	411	422	−6	−9	−8	−13	−11
	536	509	471	483	471	481	−5	−12	−10	−12	−10
	624	601	588	562	573	572	−4	−6	−10	−8	−8
	753	753	721	716	677	684	0	−4	−5	−10	−9
	994	974	877	915	880	891	−2	−12	−8	−11	−10
	1115	1108	1183	1183	1137	1146	−1	6	6	2	3
	1611	1583	1667	1670	1635	1640	−2	4	4	1	2
	1627	1593	1683	1686	1648	1655	−2	3	4	1	2
	1641	1623	1718	1712	1668	1673	−1	5	4	2	2
	1841	1847	2011	2014	1904	1871	0	9	9	3	2
	2690	2643	2897	2867	2858	2804	−2	8	7	6	4
	3196	3232	3707	3680	3509	3480	1	16	15	10	9
	3425	3474	3843	3846	3658	3643	1	12	12	7	6
	3465	3507	3876	3869	3698	3683	1	12	12	7	6
	3676	3703	4011	3996	3846	3821	1	9	9	5	4
	3762	3785	4060	4051	3899	3885	1	8	8	4	3
	3772	3795	4065	4063	3906	3892	1	8	8	4	3

Note. 1: CP2K: PBE-D3/TZV2P, 2: Gaussian: PBE-D3/6-311++G(d,p), 3: Gaussian: BHLYP-D3/6-311++G(d,p), 4: Gaussian: BHLYP/6-311++G(d,p), 5: Gaussian: MP2/aug-cc-pvtz, 6: Gaussian: B2PLYPD3/aug-cc-pvtz.

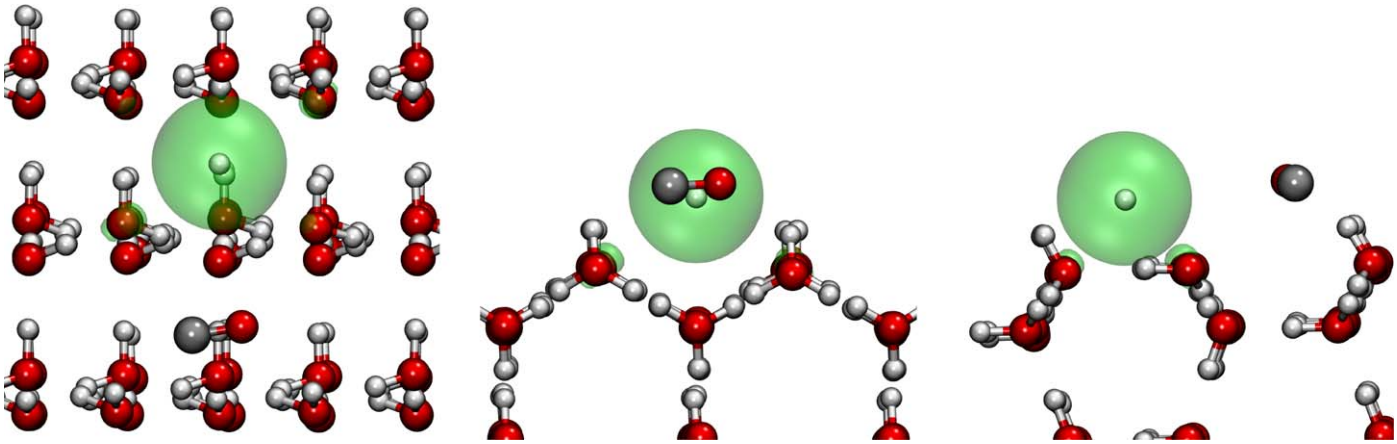

(a) ab plane (b) ac plane (c) bc plane

Figure A2. Spin density of the two reactants adsorbed on the (100) P-ice surface.

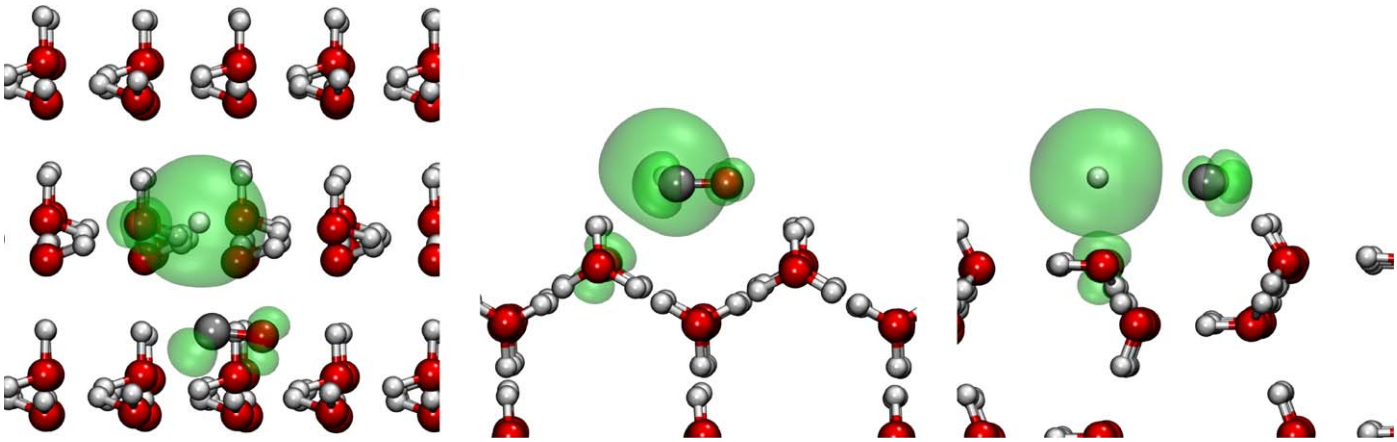

(a) ab plane (b) ac plane (c) bc plane

Figure A3. Spin density of the TS adsorbed on the (100) P-ice surface.

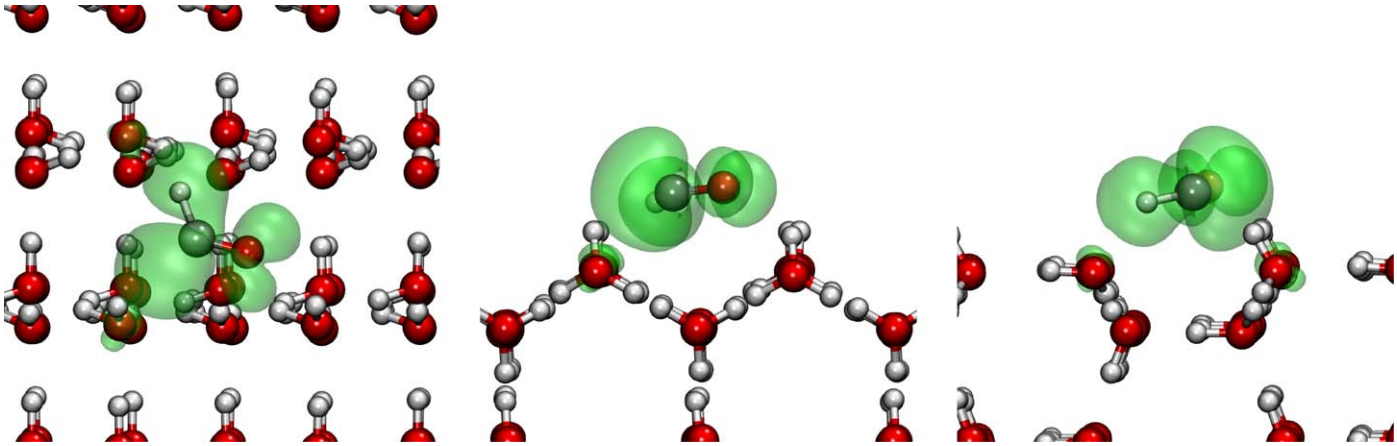

(a) ab plane (b) ac plane (c) bc plane

Figure A4. Spin density of the product adsorbed on the (100) P-ice surface.

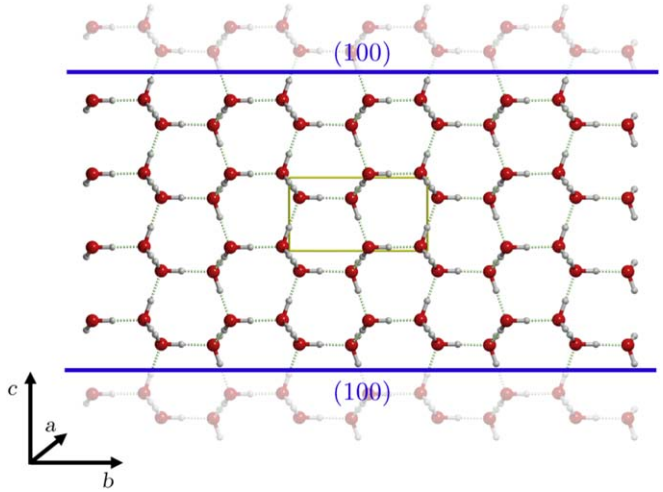

Figure A5. PBE-D3/TZV2P optimized structure of the hexagonal ice bulk. The blue lines correspond to the bulk cut along the (100) plane.

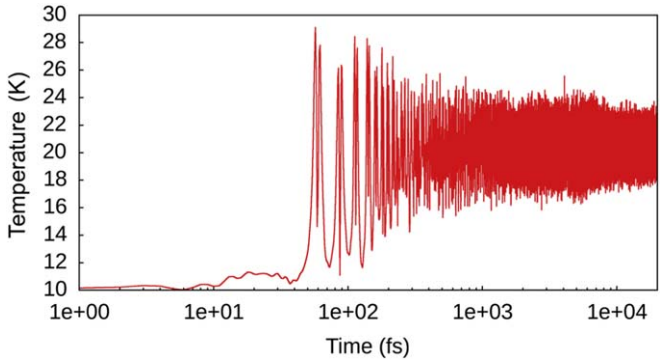

Figure A6. Evolution of the temperature during the AIMD simulation.

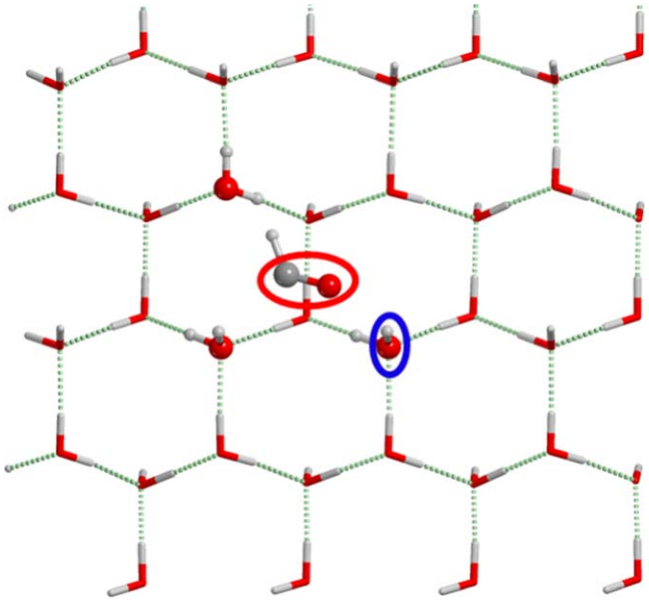

(a) HCO·/Ice structure

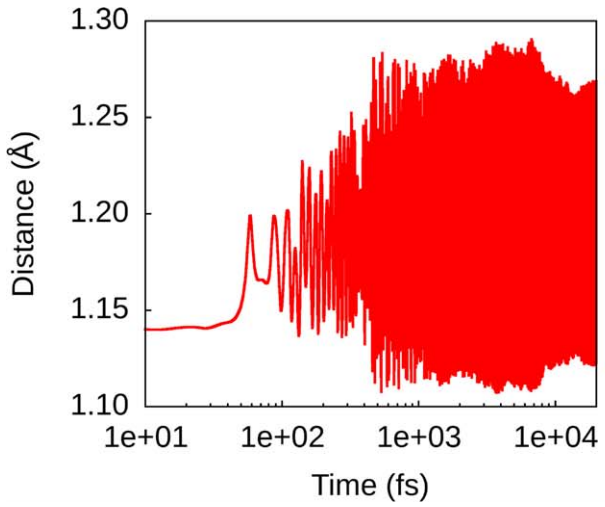

(b) CO bond

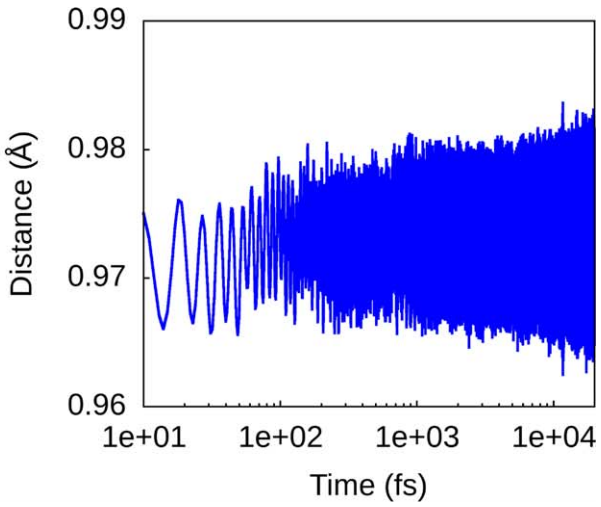

(c) OH bond

Figure A7. Evolution of CO and OH bonds along the MD simulation. Colored lines in the graphs correspond to the colored circles in the top view structure of the HCO·/ice system.

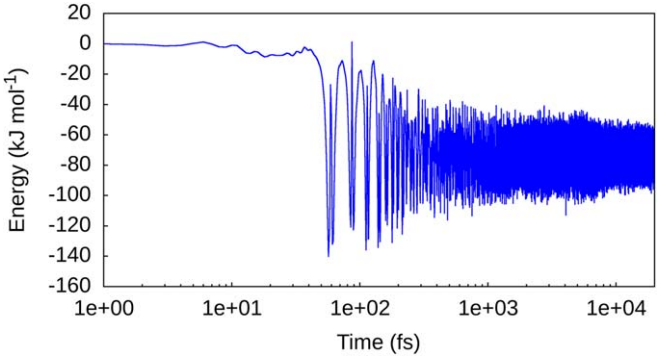

Figure A8. Evolution of the potential energy during the AIMD simulation.

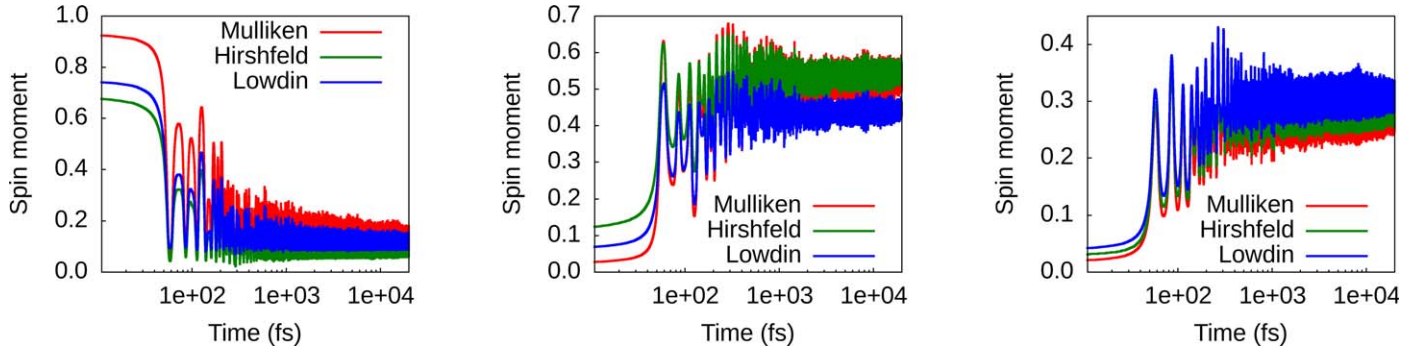

(a) ab plane (b) ac plane (c) bc plane

Figure A9. Spin density evolution of H, C, and O atoms belonging to the HCO· during the AIMD simulation.

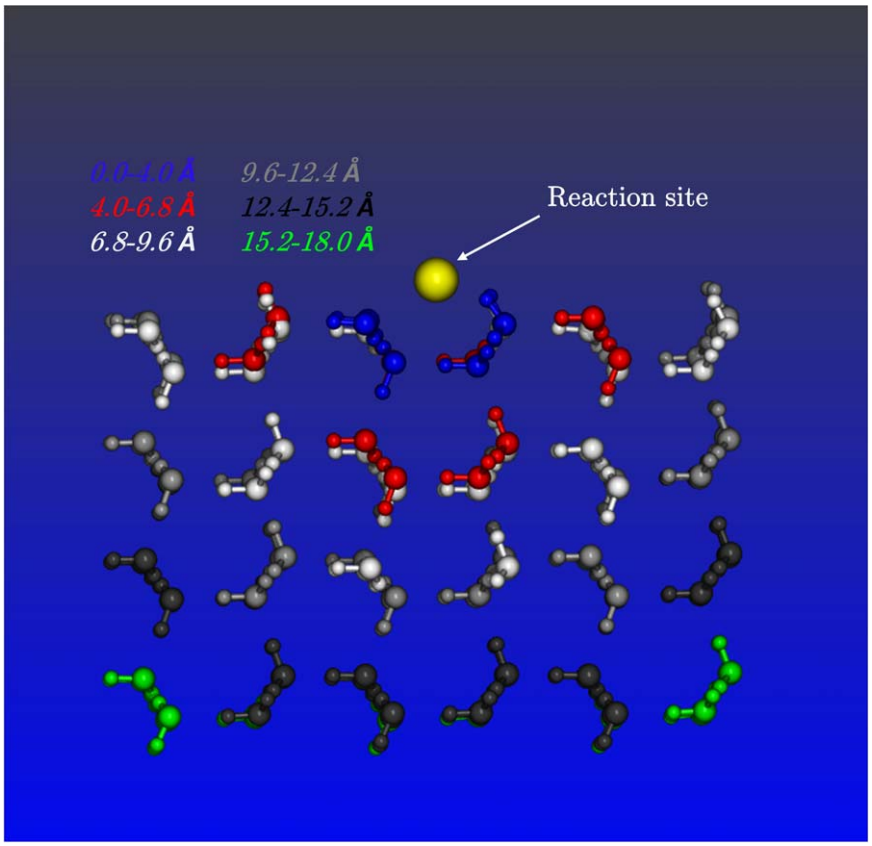

Figure A10. Graphic representation of the shell division of the water-ice structure, each one in a different color. This is the shell structure used in the energy dissipation analysis. The reaction center, defined as the C atom of HCO· at the first AIMD step, is highlighted in yellow. Note that the ice structure was cut in half for the sake of clarity.

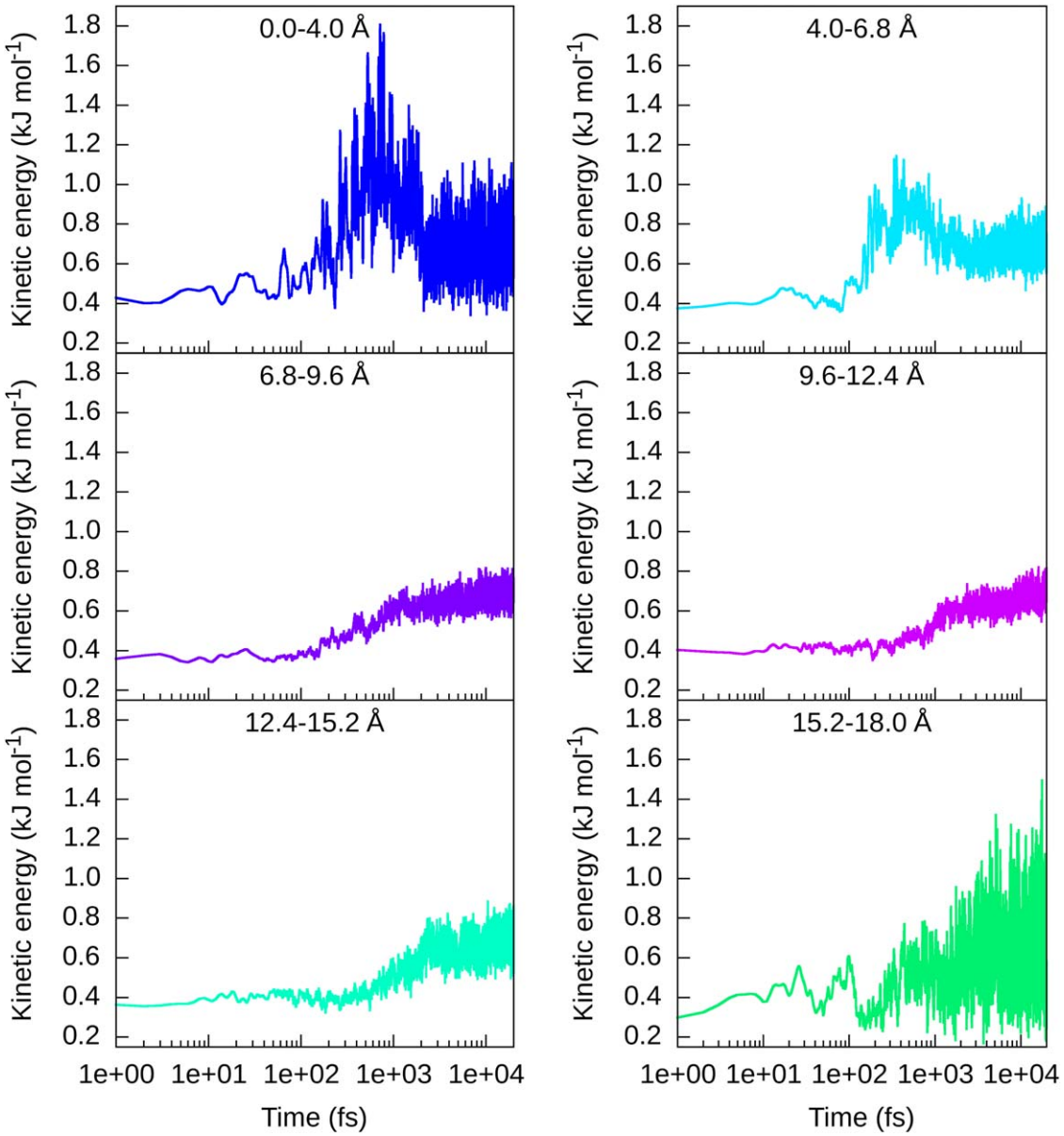

Figure A11. Kinetic energy evolution (in kilojoules per mole) of the ice surface. The ranges in the legend refer to the shells the water molecules belong to. The energy was normalized per water molecule.

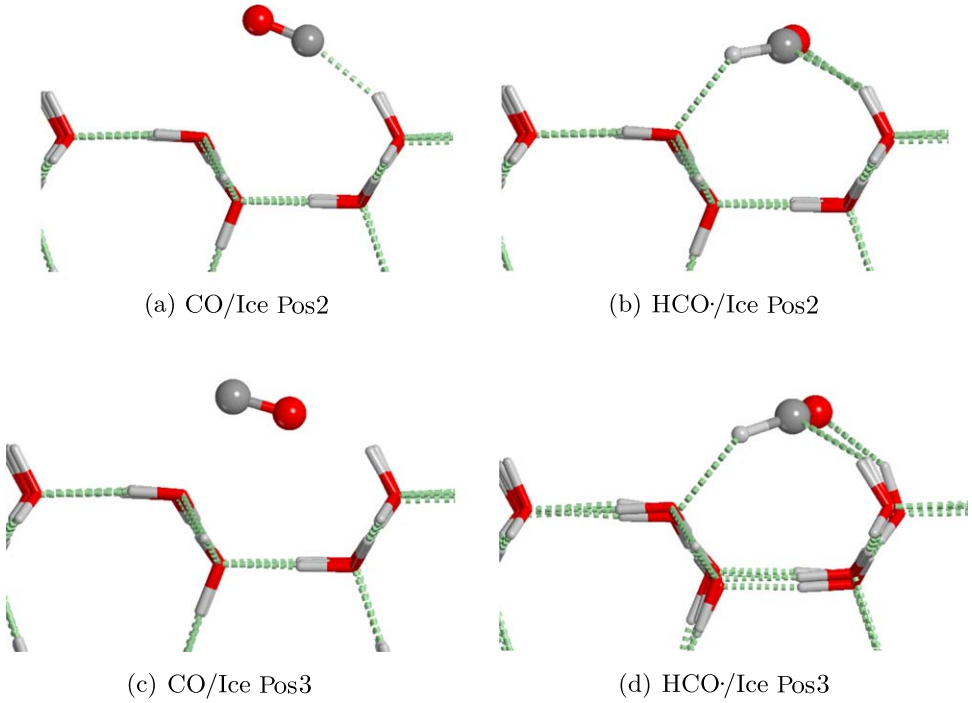

(a) CO/Ice Pos2 (b) HCO·/Ice Pos2

(c) CO/Ice Pos3 (d) HCO·/Ice Pos3

Figure A12. PBE-D3/TZV2P optimized structure of Pos2 reactant (a) and product (b) on the crystalline ice surface. PBE-D3/TZV2P optimized structure of the Pos3 reactant (c) and 2 ps AIMD snapshot (d) on the crystalline ice surface.

ORCID iDs

Stefano Pantaleone https://orcid.org/0000-0002-2457-1065
Joan Enrique-Romero https://orcid.org/0000-0002-2147-7735
Cecilia Ceccarelli https://orcid.org/0000-0001-9664-6292
Piero Ugliengo https://orcid.org/0000-0001-8886-9832
Nadia Balucani https://orcid.org/0000-0001-5121-5683
Albert Rimola https://orcid.org/0000-0002-9637-4554

References

Andersson, S., Goumans, T., & Arnaldsson, A. 2011, CPL, 513, 31
Bacmann, A., Taquet, V., Faure, A., Kahane, C., & Ceccarelli, C. 2012, A&A, 541, L12
Bahn, S. R., & Jacobsen, K. W. 2002, CSE, 4, 56
Belloche, A., Meshcheryakov, A., Garrod, R., et al. 2017, A&A, 601, A49
Bertin, M., Fayolle, E. C., Romanzin, C., et al. 2013, ApJ, 779, 120
Bertin, M., Romanzin, C., Doronin, M., et al. 2016, ApJL, 817, L12
Bianchi, E., Ceccarelli, C., Codella, C., et al. 2019, ESC, 3, 2659
Blake, G. A., Masson, C. R., Phillips, T. G., & Sutton, E. C. 1986, ApJS, 60, 357
Cazaux, S., Tielens, A., Ceccarelli, C., et al. 2003, ApJL, 593, L51
Ceccarelli, C., Caselli, P., Fontani, F., et al. 2017, ApJ, 850, 176
Cernicharo, J., Marcelino, N., Roueff, E., et al. 2012, ApJL, 759, L43
Chuang, K.-J., Fedoseev, G., Qasim, D., et al. 2018, ApJ, 853, 102
Dartois, E., Chabot, M., Barkach, T. I., et al. 2019, A&A, 627, A55
Dominik, C., Ceccarelli, C., Hollenbach, D., & Kaufman, M. 2005, ApJL, 635, L85
Duley, W. W., & Williams, D. A. 1993, MNRAS, 260, 37
Dulieu, F., Congiu, E., Noble, J., et al. 2013, NatSR, 3, 1338
Fayolle, E. C., Bertin, M., Romanzin, C., et al. 2011, ApJL, 739, L36
Fredon, A., & Cuppen, H. M. 2018, PCCP, 20, 5569
Fredon, A., Lamberts, T., & Cuppen, H. M. 2017, ApJ, 849, 125
Garrod, R. T., & Herbst, E. 2006, A&A, 457, 927
Garrod, R. T., Wakelam, V., & Herbst, E. 2007, A&A, 467, 1103
Goedecker, S., Teter, M., & Hutter, J. 1996, PhRvB, 54, 1703
Grimme, S., Antony, J., Ehrlich, S., & Krieg, H. 2010, JChPh, 132, 154104
Grimme, S., Ehrlich, S., & Goerigk, L. 2011, JCoCh, 32, 1456
Hartwigsen, C., Goedecker, S., & Hutter, J. 1998, PhRvB, 58, 3641
Hasegawa, T. I., & Herbst, E. 1993, MNRAS, 261, 83
He, J., Emtiaz, S. M., & Vidali, G. 2017, ApJ, 851, 104
Herbst, E., & van Dishoeck, E. F. 2009, ARA&A, 47, 427
Hiraoka, K., Sato, T., Sato, S., et al. 2002, ApJ, 577, 265
Hutter, J., Iannuzzi, M., Schiffmann, F., & VandeVondele, J. 2014, WIREs Comput. Mol. Sci., 4, 15
Jiménez-Serra, I., Vasyunin, A. I., Caselli, P., et al. 2016, ApJL, 830, L6
Kayanuma, M., Shoji, M., & Shigeta, Y. 2019, JPCA, 123, 2497
Korchagina, K. A., Spiegelman, F., & Cuny, J. 2017, JPCA, 121, 9485
Larsen, A. H., Mortensen, J. J., Blomqvist, J., et al. 2017, JPCM, 29, 273002
Lefloch, B., Ceccarelli, C., Codella, C., et al. 2017, MNRAS, 469, L73
Léger, A., Jura, M., & Omont, A. 1985, in Molecular Astrophysics: State of the Art and Future Directions, ed. G. H. F. Diercksen, W. F. Huebner, & P. W. Langhoff (Dordrecht: Springer), 701
Ligterink, N. F. W., Terwisscha van Scheltinga, J., Taquet, V., et al. 2018, MNRAS, 480, 3628
Lippert, G., Hutter, J., & Parrinello, M. 1997, MolPh, 92, 477
McGuire, B. A. 2018, ApJS, 239, 17
Minissale, M., & Dulieu, F. 2014, JChPh, 141, 014304
Minissale, M., Dulieu, F., Cazaux, S., & Hocuk, S. 2016, A&A, 585, A24
Molinari, S., Ceccarelli, C., White, G. J., et al. 1999, ApJL, 521, L71
Muller, S., Beelen, A., Black, J. H., et al. 2013, A&A, 551, A109
Oba, Y., Tomaru, T., Lamberts, T., Kouchi, A., & Watanabe, N. 2018, NatAs, 2, 228
Öberg, K. I., Garrod, R. T., Dishoeck, E. F. v., & Linnartz, H. 2009, A&A, 504, 891
Perdew, J., Burke, K., & Ernzerhof, M. 1996, PhRvL, 77, 3865
Pisani, C., Casassa, S., & Ugliengo, P. 1996, CPL, 253, 201
Rimola, A., Taquet, V., Ugliengo, P., Balucani, N., & Ceccarelli, C. 2014, A&A, 572, A70
Ruaud, M., Loison, J. C., Hickson, K. M., et al. 2015, MNRAS, 447, 4004
Rubin, J., Swenson, R., Jr, Benson, R., & Flygare, W. 1971, ApJL, 169, L39
Sandford, S. A., & Allamandola, L. J. 1988, Icar, 76, 201
Sewiło, M., Indebetouw, R., Charnley, S. B., et al. 2018, ApJL, 853, L19
Terada, H., & Tokunaga, A. T. 2012, ApJ, 753, 19
VandeVondele, J., & Hutter, J. 2003, JChPh, 118, 4365
VandeVondele, J., Krack, M., Mohamed, F., et al. 2005, CoPhC, 167, 103
Vastel, C., Ceccarelli, C., Lefloch, B., & Bachiller, R. 2014, ApJL, 795, L2
Watanabe, N., Hidaka, H., Nagaoka, A., & Kouchi, A. 2007, in Molecules in Space and Laboratory, ed. J. L. Lemaire & F. Combes (Paris: S. Diana), 52
Watanabe, N., & Kouchi, A. 2002, ApJL, 571, L173
Woon, D. E. 2002, ApJ, 569, 541

The Astrophysical Journal, 917:49 (11pp), 2021 August 10 https://doi.org/10.3847/1538-4357/ac0142

H_2 Formation on Interstellar Grains and the Fate of Reaction Energy

Stefano Pantaleone[1,6], Joan Enrique-Romero[1,2], Cecilia Ceccarelli[1], Stefano Ferrero[2], Nadia Balucani[1,3,4], Albert Rimola[2], and Piero Ugliengo[5]
[1] Université Grenoble Alpes, CNRS, Institut de Planétologie et d'Astrophysique de Grenoble (IPAG), F-38000 Grenoble, France
stefano.pantaleone@univ-grenoble-alpes.fr
[2] Departament de Química, Universitat Autònoma de Barcelona, Bellaterra, E-08193, Catalonia, Spain
[3] Dipartimento di Chimica, Biologia e Biotecnologie, Università di Perugia, Via Elce di Sotto 8, I-06123 Perugia, Italy
[4] Osservatorio Astrofisico di Arcetri, Largo E. Fermi 5, 50125 Firenze, Italy
[5] Dipartimento di Chimica and Nanostructured Interfaces and Surfaces (NIS) Centre, Università degli Studi di Torino, via P. Giuria 7, I-10125, Torino, Italy
Received 2021 March 26; revised 2021 April 27; accepted 2021 May 12; published 2021 August 16

Abstract

Molecular hydrogen is the most abundant molecular species in the universe. While no doubts exist that it is mainly formed on the interstellar dust grain surfaces, many details of this process remain poorly known. In this work, we focus on the fate of the energy released by the H_2 formation on the dust icy mantles: how it is partitioned between the substrate and the newly formed H_2, a process that has a profound impact on the interstellar medium. We carried out state-of-the-art ab initio molecular dynamics simulations of H_2 formation on periodic crystalline and amorphous ice surface models. Our calculations show that up to two-thirds of the energy liberated in the reaction ($\sim$300 kJ mol^{-1} $\sim$3.1 eV) is absorbed by the ice in less than 1 ps. The remaining energy ($\sim$140 kJ mol^{-1} $\sim$1.5 eV) is kept by the newly born H_2. Since it is 10 times larger than the H_2 binding energy on the ice, the new H_2 molecule will eventually be released into the gas phase. The ice water molecules within $\sim$4 Å from the reaction site acquire enough energy, between 3 and 14 kJ mol^{-1} (360–1560 K), to potentially liberate other frozen H_2 and, perhaps, frozen CO molecules. If confirmed, the latter process would solve the long standing conundrum of the presence of gaseous CO in molecular clouds. Finally, the vibrational state of the newly formed H_2 drops from highly excited states ($\nu = 6$) to low ($\nu \leqslant 2$) vibrational levels in a timescale of the order of picoseconds.

Unified Astronomy Thesaurus concepts: Astrochemistry (75)

1. Introduction

Molecular hydrogen is the most abundant molecule in the universe. Its formation is also the first step of the interstellar chemistry and, therefore, a fundamental reaction. In molecular clouds, H_2 is mainly formed via the H + H association reaction on the interstellar dust grain surfaces, which act as a third body capable of partially absorbing the energy ($\sim$440 kJ mol^{-1} $\sim$4.56 eV) released by the chemical reaction and, consequently, stabilize the newly formed H_2 molecule (e.g., van de Hulst 1946; Hollenbach & Salpeter 1970, 1971; Smoluchowski 1983). Although no doubts exist regarding the occurrence of this process, many specific details remain poorly known (see, e.g., Vidali 2013; Wakelam et al. 2017).

Here, we focus on the fate of the energy released by the reaction, which has been a source of debate for decades. Specifically, how much of the reaction energy is absorbed by the dust grain and in what timescale? What fraction of the chemical energy does go into the kinetic energy of the newly formed H_2? Is this energy large enough as H_2 breaks the interaction with the surface and proceeds into the gas phase? How much energy does the H_2 molecule possess when it leaves the grain surface and in what rovibrational state? And, finally, is the energy transmitted to the dust grain enough to locally warm it up and make adjacent frozen molecules sublimate? These points have a profound impact on several aspects of astrochemistry and, more generally, the physics and chemistry of the interstellar medium (ISM; Duley & Williams 1993).

Answers to the above questions largely depend on the nature of the substrate, namely the specific dust grain surface or, in practice, the interstellar environment where H_2 forms. Here we focus on cold ($\sim$10 K) molecular clouds. In these environments, the grain refractory cores are coated by water-dominated icy mantles either in polycrystalline or amorphous (ASW for amorphous solid water) phases, the latter dominating over the former (Smith et al. 1988; Whittet 1993; Boogert et al. 2015).

Unfortunately, laboratory experiments cannot entirely reproduce the interstellar conditions so that, while they can suggest routes and processes, they cannot provide definitive answers to the above-exposed questions (see, e.g., Vidali 2013). For example, obtaining experimentally how the H_2 formation nascent energy is partitioned is very difficult (Hornekær et al. 2003; Roser et al. 2003; Watanabe et al. 2010; Hama et al. 2012). Computational chemistry methods can be regarded as a complementary tool and, sometimes, as a unique alternative to laboratory experiments. So far, a limited number of studies devoted to the energy dissipation of the H_2 formation reaction on icy grains has appeared in the literature (Takahashi et al. 1999a; Takahashi & Uehara 2001; Herbst & Cuppen 2006).

Here, we present a new theoretical study on the dissipation of the energy released by the $H + H \rightarrow H_2$ reaction on water ice using ab initio molecular dynamics simulations (AIMDs). We simulated the reaction adopting a Langmuir–Hinshelwood mechanism (i.e., both reactants are adsorbed on the surface in neighboring sites) both on amorphous and crystalline periodic models of interstellar icy mantles.

[6] Present addresses: Dipartimento di Chimica and Nanostructured Interfaces and Surfaces (NIS) Centre, Università degli Studi di Torino, via P. Giuria 7, I-10125 Torino, Italy and Dipartimento di Chimica, Biologia e Biotecnologie, Università di Perugia, Via Elce di Sotto 8, I-06123 Perugia, Italy.

2. Computational Details

2.1. Methods

All our calculations were carried out with the CP2K package (Hutter et al. 2014). Core electrons were described with the Goedecker–Teter–Hutter pseudopotentials (Goedecker et al. 1996) and valence ones with a mixed Gaussian and plane-wave (GPW) approach (Lippert et al. 1997). The density functional theory (DFT) Perdew–Burke–Ernzerhof (PBE) method was adopted (Perdew et al. 1996), combined with a triple-ζ basis set for valence electrons with a single polarization function (TZVP), and the a posteriori D3 Grimme correction to account for dispersion forces (Grimme et al. 2010, 2011). The plane-wave cutoff was set to 600 Ry. Ice surfaces were thermalized (see Section 2.2), and during the geometry optimization only the reacting H atoms (those forming H_2) were allowed to move, keeping the water molecules fixed at their thermalized positions. All calculations were carried out within the unrestricted formalism as we deal with open-shell systems (see the Appendix for more details). The binding energy (BE) of H_2 was calculated as:

$$\mathrm{BE}_{H_2} = E_{\mathrm{CPLX}} - (E_{\mathrm{Ice}} + E_{H_2}), \quad (1)$$

where E_{CPLX} is the energy of the H_2/ice system, E_{Ice} is the energy of the bare ice surface, and E_{H_2} is the energy of the H_2 alone.

AIMDs were carried out within the NVE (N = number of particles, V = volume, E = energy) ensemble, where the total energy V_{TOT} (i.e., potential + kinetic) is conserved. The evolution of the system was followed for 5 ps for the crystalline model and for 1 ps for the amorphous model, using time steps of 0.2 fs.

2.2. Ice Models

For the crystalline ice model, a periodic slab cut from the hexagonal ice bulk structure was used. The periodic cell parameters defining the system are $a = 26.318$ Å and $b = 28.330$ Å, while the slab thickness is ~21 Å (corresponding to seven layers), for a total of 576 water molecules. The c parameter of the simulation box, i.e., the nonperiodic one, was set to 50 Å to avoid interactions among the fictitious slab replicas. The size of the slab model was chosen to avoid nonphysical temperature increase due to the extremely large exothermic reaction (Pantaleone et al. 2020).

The amorphous model was obtained by performing a classical molecular dynamics (MD) simulation on the crystalline structure. The MD was carried out with the TIP3P force field (Jorgensen et al. 1983) for 200 ps (with a time step of 0.5 fs) at 300 K within the NVT (N = number of particles, V = volume, T = Temperature) ensemble. A second NVT simulation was performed at 10 K to cool down the system at the temperature of cold molecular clouds. Finally, a geometry optimization and another NVT-MD simulation at 10 K were run using PBE to recover the potential energy surface at the same theory level as described in the previous section.

2.3. H_2 Vibrational State

To calculate the H_2 vibrational state during the AIMDs the anharmonic oscillator model was employed. As a first step, the potential energy surface (PES) of the H_2 isolated molecule was explored by performing a rigid scan of the H–H distance, ranging from 0.3 to 3.0 Å with a step of 0.01 Å. Computed data were fitted with the Morse equation to obtain the force constant of the oscillator, its dissociation energy and, hence, the vibrational levels of H_2. The H_2 turning points calculated with our model were compared with those of the AIMD simulations and the vibrational level was assigned at each H_2 oscillation during the AIMDs.

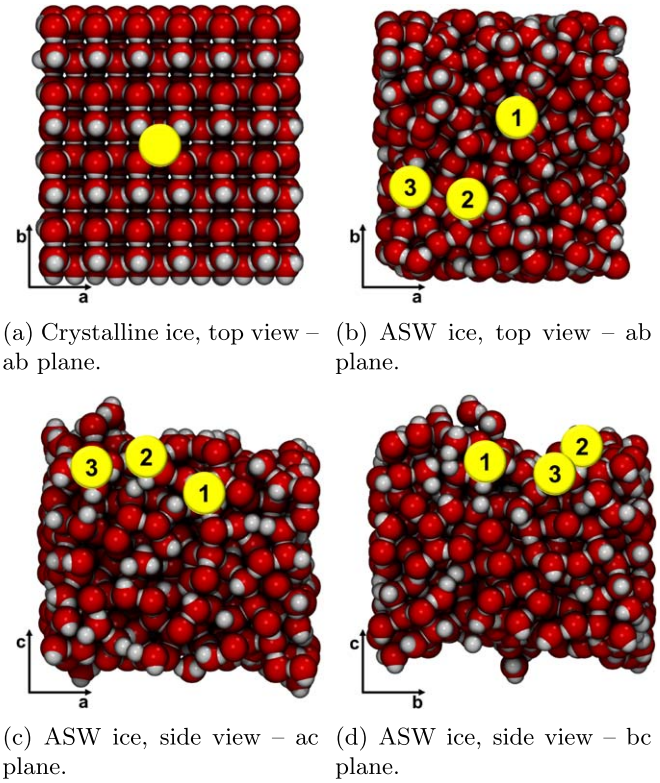

(a) Crystalline ice, top view – ab plane. (b) ASW ice, top view – ab plane. (c) ASW ice, side view – ac plane. (d) ASW ice, side view – bc plane.

Figure 1. Top view of the crystalline ice model (a), and top (b) and side ((c) and (d)) views of the ASW ice models. The yellow circles represent the centers of mass of the two H atoms' starting positions. In the case of ASW, the numbers mark the positions (Pos1, Pos2, and Pos3) discussed in the text. The initial H to H distance is about 4 Å (see Figure A1). O atoms are in red and H atoms of the ice are in white.

3. Results

3.1. Reactants Plus Product Positions in the Ice Models

Figure 1 shows the structure of the used crystalline and ASW ice models as well as the starting positions of the center of mass of the two adsorbed H atoms before the reaction. The starting H–H distance, as well as its evolution during the AIMDs is shown in Figure A1. The ASW model presents a rugged morphology (e.g., holes, cavities, and channels) in comparison to the crystalline one and, therefore, we carried out simulations in three positions, roughly representing different possible situations in terms of energetics and surface morphology. The position marked as Pos1 is the deepest one, within a cavity, while positions Pos2 and Pos3 are in the outermost parts of the surface.

As a first step, we optimized the geometries of reactants (the two H atoms) and product (the H_2 molecule) on the water ice surface in order to obtain the potential energy surface of the reaction. No search for transition state structures has been performed because AIMDs indicated this reaction is barrierless at 10 K. That is, the starting kinetic energy of the two H atoms

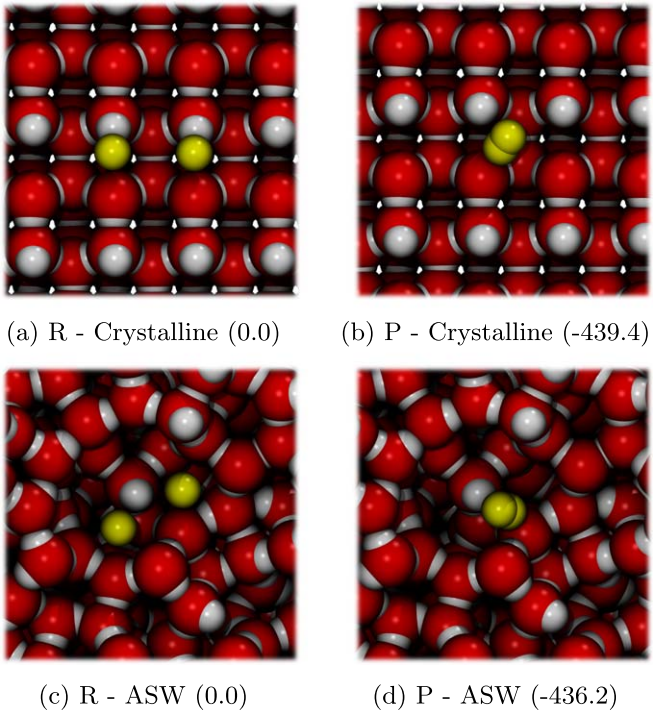

(a) R - Crystalline (0.0) (b) P - Crystalline (-439.4)

(c) R - ASW (0.0) (d) P - ASW (-436.2)

Figure 2. PBE-D3/TZVP optimized geometries of reactants (left panels) and product (right panels) of the H_2 reaction formation on the crystalline (top) and ASW Pos1 (bottom) ice models. The numbers in parentheses correspond to the relative energy in kJ mol^{-1} with respect to the reactants. The H atoms involved in the H+H $\rightarrow$ H_2 reaction are in yellow, those belonging to surface water molecules are in white, and O atoms are in red.

provided by the 10 K is high enough to overcome the eventually small potential energy barrier. The total energy to be dissipated is around 435–440 kJ mol^{-1}, depending on the surface and starting position.

Figure 2 provides a view of the two H atoms' starting positions and H_2 position immediately after the reaction, on the crystalline and ASW (Pos1 as an example) models, respectively.

3.2. Molecular Hydrogen Desorption

AIMDs results are summarized in Table 1 and shown in Figure 3. First, at least half of the kinetic energy is absorbed by the ice while the remaining one is kept by the newly formed H_2 molecule (∼50%–35%). These numbers are similar for both for the crystalline and ASW ice positions, suggesting they do no depend much on the surface structural details of the ice.

Second, after the H–H bond formation, the newly formed H_2 molecule diffuses over the surface, as it keeps a large kinetic energy, in both crystalline and ASW ice models. However, despite the energetics of the two processes being similar (Figure 3, left panels) the H_2 diffusion (Figure 3, right panels) is different.

On the crystalline surface, the diffusion of the newly formed H_2 over the ice surface is constrained in a specific direction, along the *a*-axis, parallel to the ice surface, whereas in the *b*-axis and *c*-axis directions the starting position does not change. This is because the crystalline model has alternated and opposite electrostatic potentials along the *b*-axis direction (see Figure A2, which constrains the H_2 diffusion to the perpendicular *a*-axis, within a channel-like structure created in between the two alternated potential regions (panels (a) and (c)). In contrast, on the ASW ice model, H_2 diffuses over all three directions, also along the *c*-axis, which corresponds to direction perpendicular to the ice surface. However, the movement is not the same in the three studied positions. In Pos1, H_2 achieves a maximum height of ∼10 Å over the surface in a timescale of 0.4 ps and does not come back (Figure 3(d)), thus definitely leaving the surface. On the contrary, in Pos2 H_2 slides and hops on the surface within the 1 ps of the simulation (Figure 3(f)). A similar behavior is observed for Pos3, but with wider hops and jumps (Figure 3(h)). This is the key point of the simulations: the kinetic energy remains much larger (∼150 kJ mol^{-1}) than the binding energy (∼10 kJ mol^{-1}) in all cases; therefore, the nascent H_2 is likely doomed to leave the ice surface.

Table 1
Results of the AIMD for the H_2 Formation on the Crystalline (First Row) and the ASW Three Position (Figure 1; Bottom Three Rows) Ices

Model	$\frac{K_{ice}}{K_{ice}+K_{H_2}}$	$\frac{K_{H_2}}{K_{ice}+K_{H_2}}$	BE_{H_2} (kJ mol^{-1})	$\nu^{0.2-1}$	ν^{1-5}	E_{peak} (kJ mol^{-1})
Crys.	0.45	0.55	9.0	4–5	1–2	12.0
Pos1	0.65	0.35	9.7	1–2	⋯	43.0
Pos2	0.46	0.54	10.6	6	⋯	7.0
Pos3	0.47	0.53	12.4	5	⋯	7.0

Note. Second and third columns report the fraction of kinetic energy of the ice and the newly formed H_2, respectively, at the end of the simulation (5 and 1 ps for crystalline and ASW ices, respectively). Fourth column reports the H_2 binding energy (in kilojoules per mole) at the reaction site. Fifth and sixth columns report the vibrational state averaged over 0.2–1 ps and 1–5 ps, respectively (the latter can be computed only for the crystalline case). Last column reports the peak energy (in kilojoules per mole) of an ice-molecule neighbor (i.e., at ∼3 Å) to where the reaction occurs.

3.3. Energy Dissipation toward the Ice Water Molecules

Figure 4 shows how the energy absorbed by the ice is first transmitted from the reaction site to a neighbor water (i.e., at ∼4 Å) in ∼200–800 fs and, with time, to shells of water molecules with increasing distances. The neighbor water molecule acquires from ∼3 to ∼14 kJ mol^{-1} and stays with that energy for more than about 100–200 fs before the energy is dissipated toward more external water molecules. These timescales are in excellent agreement with previous studies of the sound speed in ices (see, e.g., Ruocco et al. 1996).

3.4. H_2 Vibrational State

The initial state of the H_2 formed on the crystalline ice is $\nu = 4$–5 (obtained averaging over 0.2–1 ps) and then it decreases to $\nu = 1$–2 (1–5 ps average) because of the H_2 energy dissipation. Conversely, at Pos1 of the ASW model, H_2 is formed with a low vibrational state ($\nu = 1$–2, 0.2–1 ps average).

For the other two positions (Pos2 and Pos3), the vibrational state of the newly formed H_2 molecule lies in highly excited states, $\nu = 6$ and $\nu = 5$, respectively. However, our simulations stop at 1 ps and, likely, as on the crystalline ice, the vibrational state of the newly formed H_2 will lower to $\nu = 1$–2. The difference in the behavior between the Pos1 and Pos2/3 is probably due to a transient chemical bond between one of the reacting H and one O atom of a neighboring water molecule (see Figure A3).

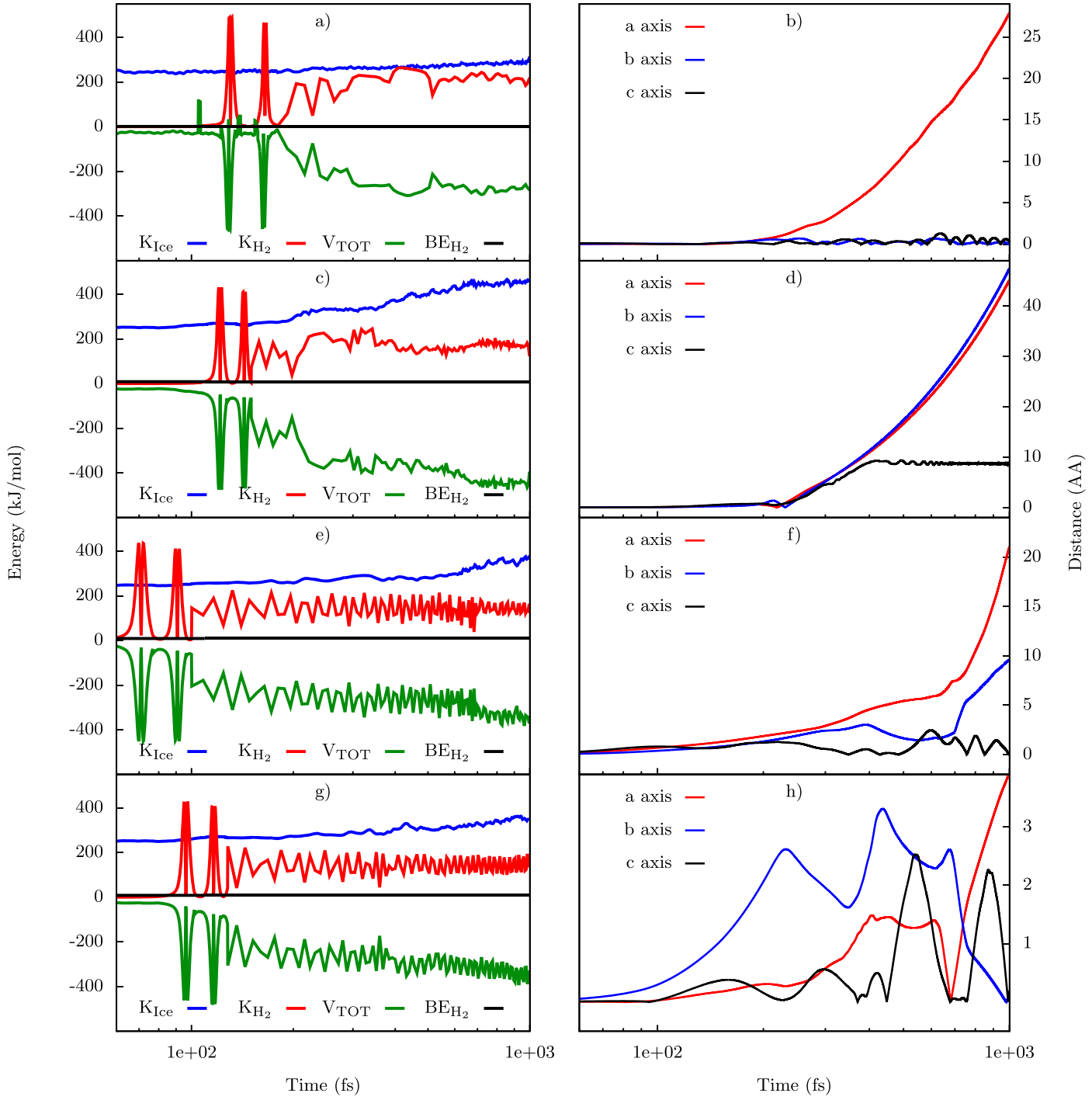

Figure 3. Results of the AIMDs for the crystalline (top panels) and ASW Pos1, Pos2, and Pos3 (panels on the second, third, and bottom rows) models, respectively. Left panels: evolution over time (in fs) of the most relevant energetic components (in kilojoules per mole) of the H_2/ice system for the crystalline (panel (a)) and ASW Pos1, Pos2, and Pos3 (panels (c), (e), and (g)) models, respectively. V_{TOT} is the total potential energy (green lines), K_{H_2} and K_{Ice} are the kinetic energies of H_2 (red lines) and ice (blue lines), respectively, while BE_{H_2} (10 kJ mol^{-1} = 1200 K) is the binding energy of the H_2 (black lines). Right panels: diffusion of the center of mass of the H_2 molecule split into the three Cartesian components—*c*-axis is the direction perpendicular to the ice surface, while the *a*- and *b*-axes are along the ice surface (Section 2).

4. Discussion

4.1. H_2 and Other Molecule Desorption

While there are no doubts that, once formed on the icy surfaces, H_2 molecules will be released into the gas phase, our new computations provide a quantitative and atomistic-view support to this theory. The newly formed H_2 molecules possess an energy much larger than their binding energy, by more than a factor of 10, so that H_2 will very likely be injected into the gas phase. Even in the worst case of crystalline ice, where the simulations show H_2 sliding over the perfect ice surface, the newly formed H_2 will sooner or later stumble onto an imperfection of the ice, and thus its trajectory will be deviated and the molecule will escape into the gas. To have an estimation of the timescale of this phenomenon one could consider the timescale for the newly H_2 to scan the entire

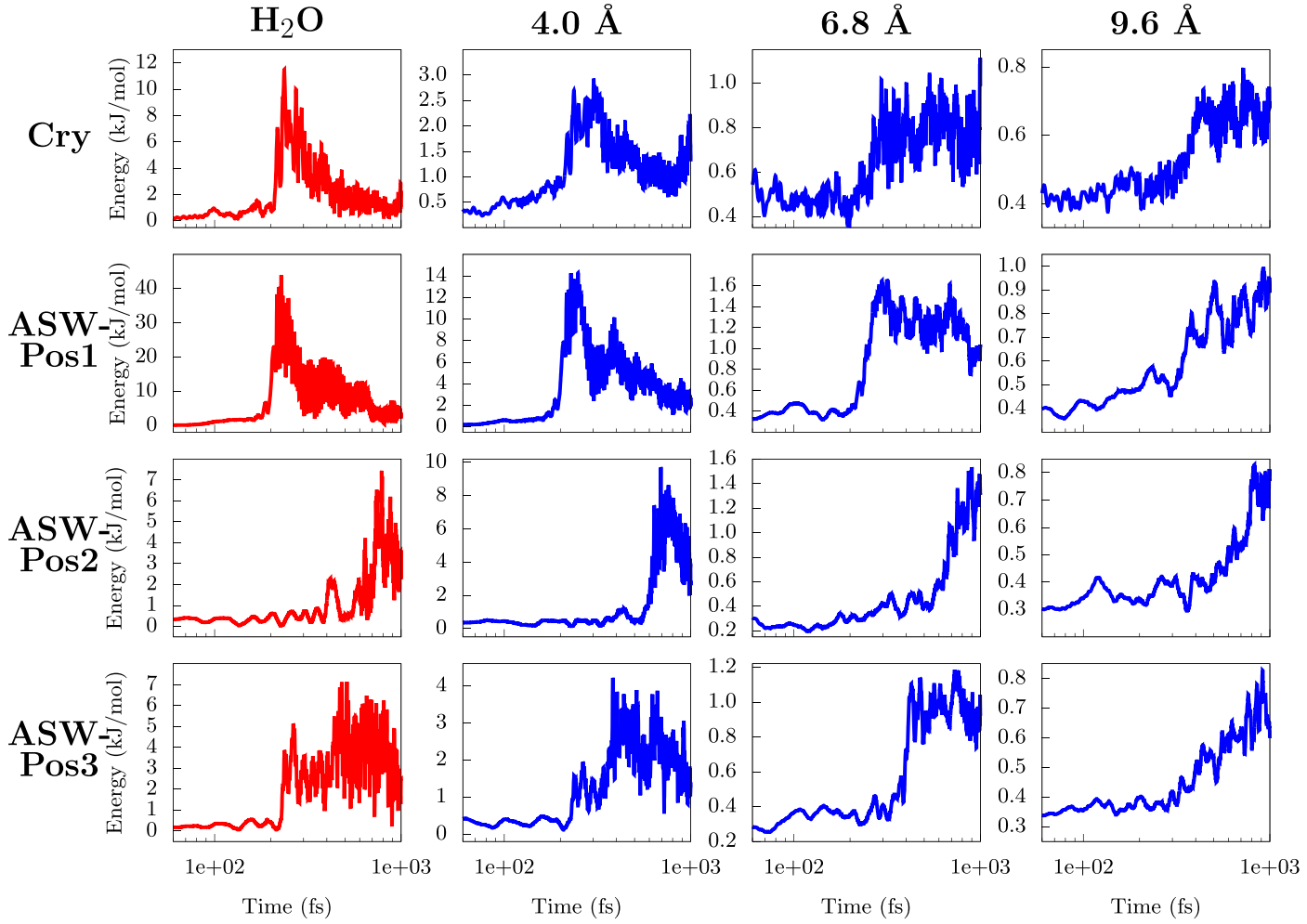

Figure 4. Kinetic energy (in kilojoules per mole) acquired by the water ice molecules as a function of time for the crystalline (top first row panels) and ASW Pos1-3 (lower panels) ices, as marked by the left-hand labels. Left first column panels: energy acquired by a single neighboring water ice molecule (i.e., at ∼3 Å) from the H_2 reaction site. Other column panels: energy acquired by the ice surface divided in concentric shells (normalized by the number of water molecules per shell), centered at the reaction site. The labels on the top mark the shells' radii.

surface of an interstellar grain. Assuming its radius is equal to 0.1 μm and each icy site size is equal to 3 Å the number of sites to scan is about 10^5. A first estimate of the time to scan all the sites can be directly obtained by our simulations by considering that about 15 sites of our crystalline ice are covered in less than 1 ps; therefore, to scan the 10^5 it will take less than 10 ns. However, this is strictly true if the H_2 molecule does not loose energy in other minor impacts, so ∼10 ns can be considered a lower limit. The upper limit can be computed by assuming that no residual energy is left to the H_2 molecule except the thermal one and, in this case, the velocity to scan is given by the hopping rate and the timescale for scanning the entire grain surface becomes:

$$t_{\rm scan} = N_s \nu_0^{-1} e^{\frac{E_d}{k_B T_{\rm dust}}}, \quad (2)$$

where ν_0 is about 10^{12} s^{-1} and E_d is assumed to be 0.3 times the binding energy (about 400 K). Inserting the numbers, a rough estimate of the time that H_2 takes to leave a typical interstellar grain is $\leqslant 1000$ yr. In laboratory analogs of interstellar grains, the timescale would be even larger, and, consequently, not observable. In conclusion, the newly formed H_2 will leave the surface in a timescale between a few nanoseconds to a max of about 1000 yr, which is still a very short lifetime with respect to the cloud life.

We want to highlight that the choice of using a proton order ice is just a matter of convenience to test our simulations before going to the more realistic case of the amorphous surface. On a more realistic proton disordered crystalline ice we expect a more anisotropic behavior of the H_2 molecule, and, as a consequence, a faster H_2 desorption.

Our computations also show that the ice absorbs a significant fraction of the reaction energy, 45%–65% (Table 1). This energy propagates like a wave from the point where the H + H reaction occurs (see Figure 4 and also Pantaleone et al. 2020). In ASW ice, a water molecule close to the reaction site acquires 7–43 kJ mol^{-1} (840–5160 K), for more than 100-200 fs. Within the first shell of radius 4 Å, water molecules acquire energies from 3 to 14 kJ mol^{-1} (360–1680 K, average value counting all the water molecules within the first shell). Farther away the energy acquired by the ice-water molecules decreases to less than 1.6 kJ mol^{-1}. The energy acquired by the water ice molecules within a radius of 4 Å from the reaction site could, potentially, be enough to release into the gas phase any molecule whose binding energy is lower than 3–14 kJ mol^{-1}. This could be the case of another H_2 molecule frozen on the ice, a possibility predicted by some astrochemical models (see,

e.g., Hincelin et al. 2015). Indeed, since the binding energy of H_2 is less than $\sim$5 kJ mol^{-1} (e.g., Vidali 2013; Ferrero et al. 2020; Molpeceres & Kästner 2020), several H_2 molecules could be kicked into the gas phase.

More interesting is the case of CO, the most abundant molecule after H_2 in galactic cold molecular clouds. It has a binding energy between 7 and 16 kJ mol^{-1} (e.g., He et al. 2016; Ferrero et al. 2020) so that frozen CO could potentially be liberated into the gas-phase by the formation of H_2. It has been long recognized that, in absence of a nonthermal desorption process, CO in molecular clouds should be entirely frozen onto the interstellar ices in $\sim 3 \times 10^5$ yr (see, e.g., Léger 1983). Several mechanisms have been proposed to explain its presence in the gas (see, e.g., Leger et al. 1985; Schutte & Greenberg 1991; Duley & Williams 1993; Shen et al. 2004; Ivlev et al. 2015). They are all based on the idea that the grain is locally heated and that the frozen molecules are statistically desorbed on a timescale of a few thousands seconds (see, e.g., Hasegawa & Herbst 1993; Herbst & Cuppen 2006), except when faster photodesorption processes are involved. In particular, Duley & Williams (1993) and Takahashi & Williams (2000) focused on the CO desorption caused by the H_2 formation. Using the results of classical MD simulations by Takahashi and colleagues (Takahashi 1999; Takahashi et al. 1999b; Takahashi & Williams 2000) and a statistical approach, these authors found that the surface within a radius of $\sim$4 Å from the reaction site is heated up to $\leqslant$ 40 K for a time too short ($\sim$10 fs) to allow CO to sublimate. However, despite the fact that Takahashi's simulations are impressive considering that they were carried out more than 20 yr ago, old force fields (like the TIP3P used by Takahashi et al.) have limitations in describing the actual intermolecular interactions and the energy transfer from one molecule to another, compared to our simulations treated at the quantum mechanical level.

Our AIMDs show that the water molecules within a radius of 4 Å from the reaction site can be excited from 3 to 14 kJ mol^{-1} (depending on the position) for more than 100 fs (Figure 4). Using the range of values in the literature for the CO binding energies (7–16 kJ mol^{-1}: He et al. 2016; Ferrero et al. 2020), and the usual Eyring equation to estimate the half-life time of CO desorption, we obtain that a CO molecule within a radius of 4 Å from Pos1 would desorb in 33–62 fs, and 69–185 fs from Pos2. On the contrary, CO molecules close to Pos3 and on crystalline ice would not desorb. Therefore, based on this rough argument, the formation of H_2 can potentially desorb frozen CO molecules. Whether this hypothesis is realistic or not depends on (i) how many sites of the AWS ice water molecules are excited as in Pos1 and Pos2, (ii) the ratio of H_2 formation rate with respect to the CO freezing rate ($R = \frac{\nu(H_2)}{\nu(CO)}$), and (iii) the probability that CO and H_2 are adjacent.

While a more realistic model for the ASW ice is needed to estimate the first quantity (i), one can estimate the second one (ii) as follows. At steady state, assuming that the H + H reaction has efficiency 1 (e.g., Vidali 2013), the ratio R of the H_2 formation rate with respect to the CO freezing rate is equal to the ratio between the rate of H atoms over CO molecules landing on the grain surface, divided by 2 (because two H atoms are needed for the H_2 formation). Considering an average Milky Way molecular cloud with H_2 density of 10^3–10^4 cm^{-3}, temperature 10 K, a gaseous (undepleted) CO abundance with respect to H_2 equal to 2×10^{-4}, and a cosmic-ray ionization rate of 3×10^{-17} s^{-1}, one obtains $n_H \sim 2$ cm^{-3} and $R \sim 26$–2.6. That is, the H_2 formation rate dominates over the CO freezing one. Therefore, frozen CO molecules can potentially be desorbed by the energy released by the H_2 formation on the icy grain surfaces. This process, if confirmed, might naturally explain the presence of gaseous CO in not too dense ($n_H \lesssim 10^4$ cm^{-3}) molecular clouds and solve a decades-long mystery. However, to put this affirmation on solid ground, specific AIMDs showing the effective sublimation of the CO molecule as well as larger ASW ice models and dedicated astrochemical modeling simulations that include this effect are mandatory. They will be the focus of forthcoming works.

4.2. H_2 Vibrational State

Previous experimental and computational works on graphite surfaces show that after its formation, the H_2 molecule populates vibrational levels around $\nu = 3$–4 (Latimer et al. 2008; Islam et al. 2010; Casolo et al. 2013). On crystalline and amorphous ice surfaces only a few studies were carried out. Based on classical MD simulations, Takahashi et al. (1999a) and Takahashi & Uehara (2001) predicted that H_2 formed on amorphous ice would be vibrationally excited to $\nu = 7$–8. In contrast, in some laboratory experiments (Hornekær et al. 2003; Roser et al. 2003; Hama et al. 2012), the authors did not detect such excited states. Our new simulations confirm both findings: depending on the site where the formation occurs, H_2 can have large (up to 6) or low (1–2) ν (Table 1). For example, the case of ASW Pos1, which is the one in a cavity, shows the lowest ν. In the ISM, the vibrational state of the newly formed H_2 molecules will depend on the probability of H_2 leaving the grain surface before being "thermalized" by collisions with ice water molecules, as also found and discussed in Watanabe et al. (2010).

The vibrational state of the newly formed H_2 molecule, i.e., how much the molecule is vibrationally excited, has important consequences on two major astrophysical aspects:

(i) to help gas-phase reactions with high activation energy barriers, some of which are the starting points of the entire chemistry in molecular clouds (Agúndez et al. (2010); and
(ii) the possibility to detect newly formed H_2 with near-future James Webb Space Telescope (JWST) observations and, consequently, measure the rate of H_2 formation in molecular clouds and put constraints to theories.

5. Summary

We studied the energy dissipation of the H_2 formation reaction on both crystalline and amorphous (ASW) ice models by means of state-of-the-art ab initio molecular dynamics simulations (AIMDs). In the ASW ice, we explored three formation sites meant to represent different situations in terms of energetics and surface morphology: one is in a cavity (Pos1) and the other two are in the outermost parts of the surface (Pos2 and Pos3).

In all simulations, we found that about at least 30% of the reaction energy ($\sim$440 kJ mol^{-1}) is acquired by the newly formed H_2, namely more than 10 times the H_2 binding energy ($\sim$10 kJ mol^{-1}), so that H_2 is likely doomed to leave the ice and to be injected into the gas. The remaining two-thirds of the reaction energy are absorbed by the water ice in less than 1 ps. The water molecules nearby the reaction site have energy peaks

of 7–43 kJ mol^{-1} for more than 100–200 fs, while those within a 4.0 Å radius of 3–14 kJ mol^{-1}.

We showed that it is in principle possible that frozen CO molecules close to the H_2 formation site sublimate. If confirmed, this will be a simple explanation to the decades-long conundrum of why gaseous CO is present in cold molecular clouds. In order to quantify this effect, new focused AIMDs, adopting larger ASW ice models and dedicated astrochemical modeling, will be necessary.

Finally, the nascent H_2 molecules have large ($\nu = 6$) vibrational states in the first picosecond and later decay to 1–2. This high vibrational state could help reactions with an activation barrier involving H_2 to occur also in cold gas and be observable by JWST.

The authors acknowledge funding from the European Union's Horizon 2020 research and innovation program, the European Research Council (ERC) Project "the Dawn of Organic Chemistry," grant agreement No. 741002, the European Research Council (ERC) Project "Quantum Chemistry on Interstellar Grains," grant agreement No 865657, and the Marie Skodowska-Curie project "Astro-Chemical Origins" (ACO), grant agreement No. 811312. A.R. is indebted to the "Ramón y Cajal" program. MINECO (project CTQ2017-89132-P) and DIUE (project 2017SGR1323) are acknowledged. BSC-MN and OCCIGEN HPCs are kindly acknowledged for the generous allowance of supercomputing time through the QS-2019-2-0028 and 2019-A0060810797 projects, respectively. S.P., N.B., and P.U. acknowledge the Italian Space Agency for cofunding the Life in Space Project (ASI N. 2019-3-U.O)

Appendix
Computational Details

Proper reactant spin localization is achieved by relying on the unrestricted-DFT broken (spin) symmetry approach. This is mandatory when dealing with diradical systems in singlet electronic state. In the H + H specific case, despite the total spin moment on the global system being 0, the unpaired electrons on the two H atoms are expected to have spin α (i.e. +1) and β (i.e. −1) each.

In order to check the quality of our results, in Table A1 a comparison between the H_2 formation energy in the gas phase calculated at PBE and CCSD(T) levels is presented. Moreover, the interaction between H_2 and one H_2O molecule was also

Table A1
Adsorption and Reaction ($H + H \rightarrow H_2$) Energy Data

	Reaction Energy (kJ mol^{-1})
Crystalline	−438.9
Pos1	−436.2
Pos2	−435.9
Pos3	−440.3
H_2 CP2K[a]	−440.6
H_2 Gaussian[b]	−457.4
	Binding Energy (kJ mol^{-1})
CP2K[a]	4.1
Gaussian[b]	2.6

Notes.
[a] H_2 gas-phase reaction energy calculated at PBE-D3/TZVP level.
[b] H_2 gas-phase reaction energy calculated at CCSD(T)/aug-cc-pv5z level.

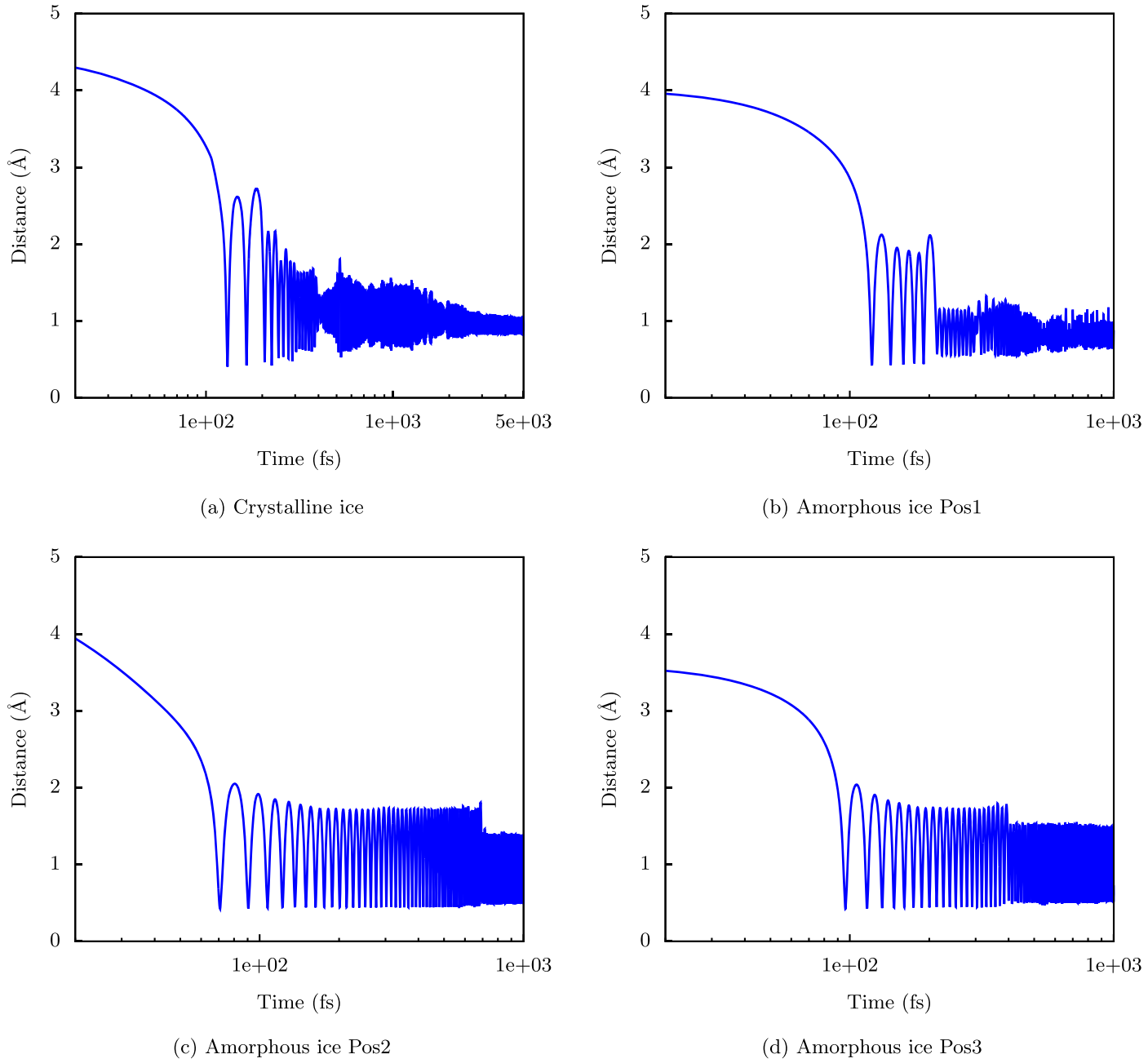

(a) Crystalline ice

(b) Amorphous ice Pos1

(c) Amorphous ice Pos2

(d) Amorphous ice Pos3

Figure A1. Evolution of the H–H bond distance during the AIMD simulations.

evaluated at the same levels of theory, giving results in good agreement. Additionally, the interaction between H_2 and one H_2O molecule was also evaluated at the same levels of theory, giving results in good agreement. The difference between the two methodologies is acceptable, considering the energy released by the reaction.

Regarding the AIMD simulations, we run an equilibration AIMD in the NVT ensemble (using the CSVR thermostat, with a time constant of 20 femtoseconds) at 10 K for 1 ps (with a time step of 1 fs) only for the bare ice surface. This ensures an initial thermally equilibrated ice. Then the velocities of the equilibrated ice surfaces are used as input for the NVE production runs. Those velocities correspond to the initial kinetic energy of the ice, as presented in Figure 3. The H velocities, instead, were manually set to favor the H–H bond formation respecting the 10 K limitation. In Figures A1–A3 the evolution of the H–H distance, the electrostatic potential map of the bare surface, and the snapshot of the adduct (H_3O^+–H^-) are reported, respectively.

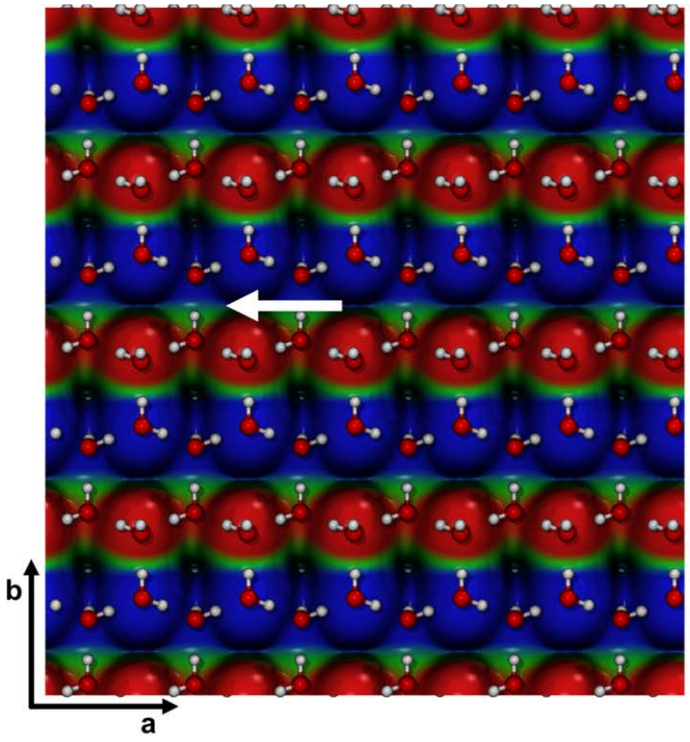

(a) Crystalline ice: top view

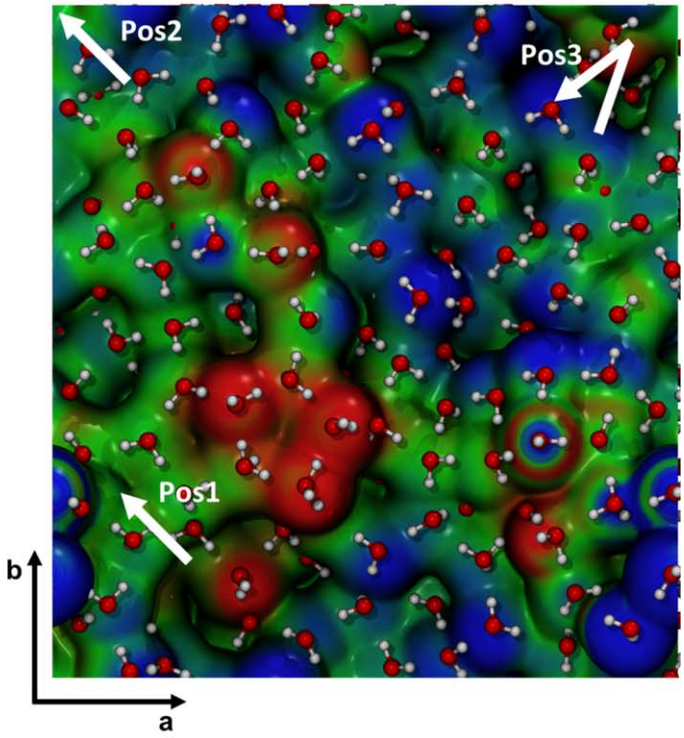

(b) Amorphous ice: top view

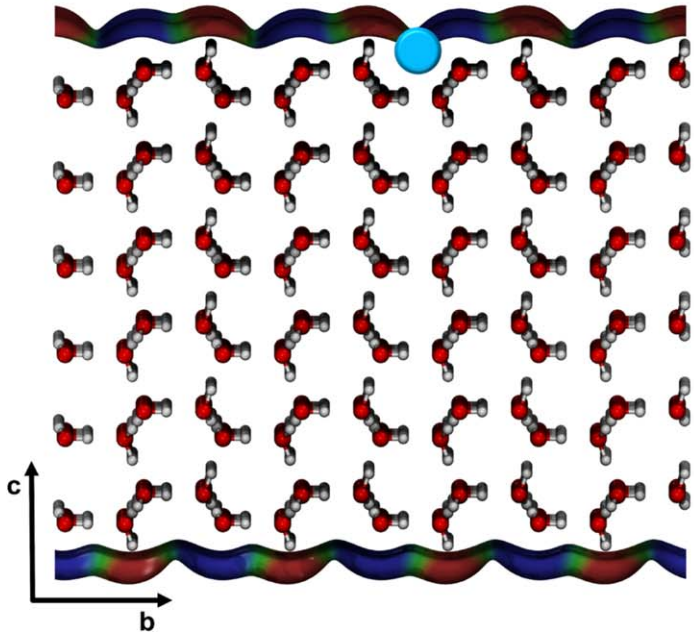

(c) Crystalline ice: lateral view

Figure A2. Top view of the electrostatic potential map of the crystalline (a) and amorphous (b) ice models. Lateral view of the crystalline ice model (c). White arrows represent the H_2 diffusion direction. The light blue circle in the bottom panel represents the cavity inside of which the H_2 diffuses over the crystalline ice model. Red and blue zones of the electrostatic maps correspond to positive and negative potentials. O atoms in red, H atoms in white.

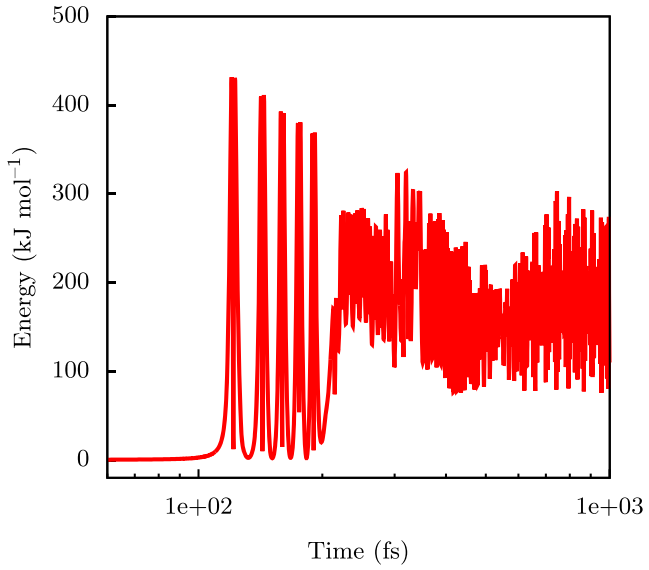

(a) H_2 kinetic energy

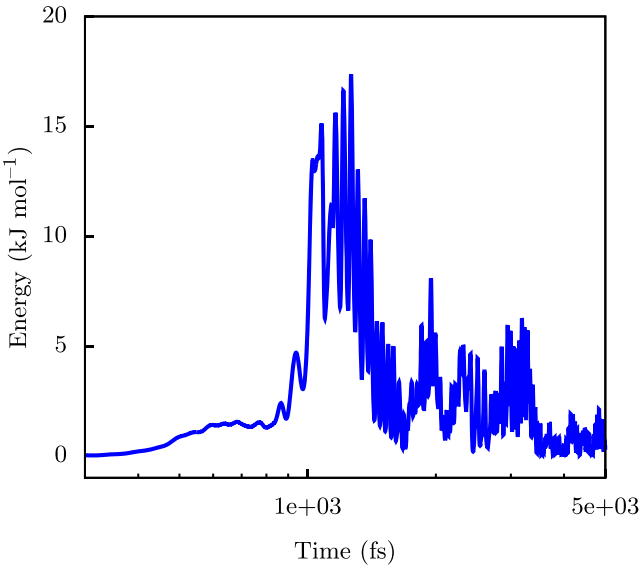

(b) H_2O kinetic energy

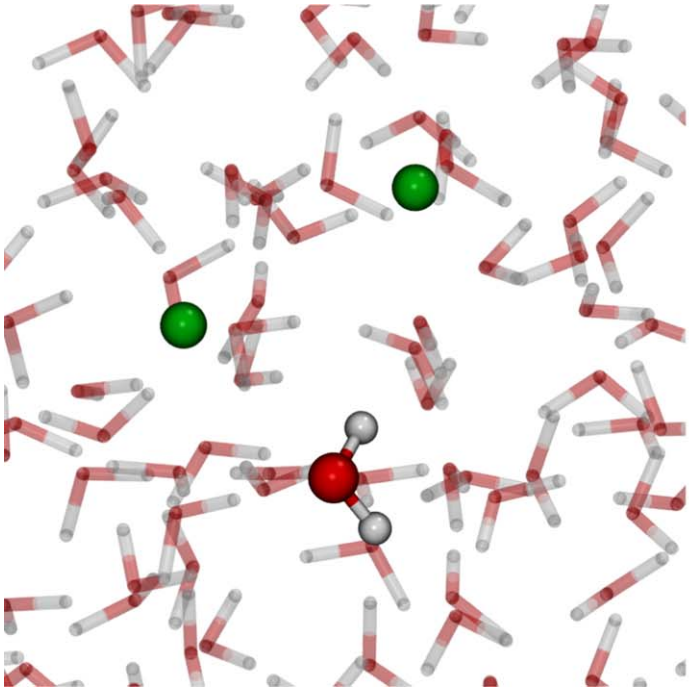

(c) Time: 0 fs

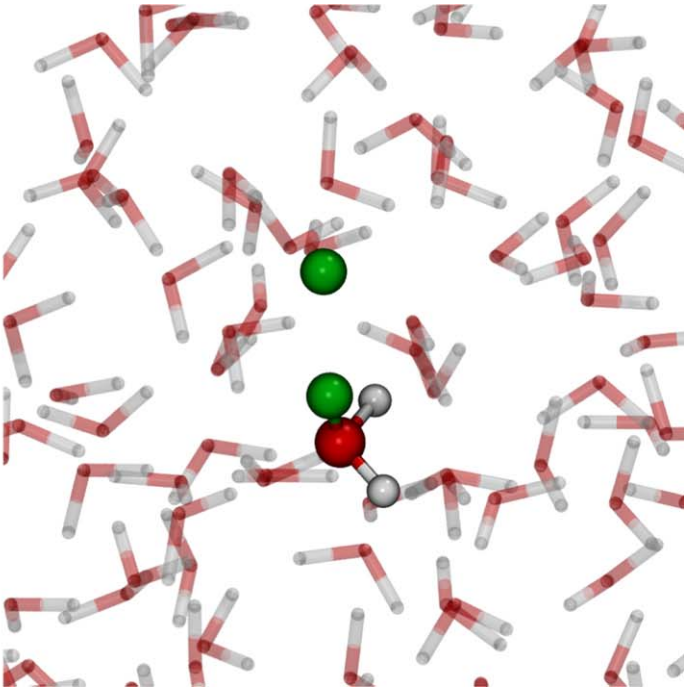

(d) Time: 206.6 fs

Figure A3. Evolution of the kinetic energy of H_2 (panel (a)) and a neighbor water molecule (panel (b)) for the amorphous Pos1 case. Starting position of the AIMD simulation (panel (c)) and formation of the H^-/H_3O^+ adduct after 0.2 ps of simulation (panel (d)). O atoms are in red, and H atoms are in white. The H atoms highlighted in green are the reactants.

ORCID iDs

Stefano Pantaleone https://orcid.org/0000-0002-2457-1065
Joan Enrique-Romero https://orcid.org/0000-0002-2147-7735
Cecilia Ceccarelli https://orcid.org/0000-0001-9664-6292
Stefano Ferrero https://orcid.org/0000-0001-7819-7657
Nadia Balucani https://orcid.org/0000-0001-5121-5683
Albert Rimola https://orcid.org/0000-0002-9637-4554
Piero Ugliengo https://orcid.org/0000-0001-8886-9832

References

Agúndez, M., Goicoechea, J., Cernicharo, J., Faure, A., & Roueff, E. 2010, ApJ, 713, 662
Boogert, A. C. A., Gerakines, P. A., & Whittet, D. C. B. 2015, ARA&A, 53, 541
Casolo, S., Tantardini, G. F., & Martinazzo, R. 2013, PNAS, 110, 6674
Duley, W. W., & Williams, D. A. 1993, MNRAS, 260, 37
Ferrero, S., Zamirri, L., Ceccarelli, C., et al. 2020, ApJ, 904, 11
Goedecker, S., Teter, M., & Hutter, J. 1996, PhRvB, 54, 1703
Grimme, S., Antony, J., Ehrlich, S., & Krieg, H. 2010, JChPh, 132, 154104
Grimme, S., Ehrlich, S., & Goerigk, L. 2011, JCoCh, 32, 1456
Hama, T., Kuwahata, K., Watanabe, N., et al. 2012, ApJ, 757, 185

Hasegawa, T. I., & Herbst, E. 1993, MNRAS, 261, 83
He, J., Acharyya, K., & Vidali, G. 2016, ApJ, 825, 89
Herbst, E., & Cuppen, H. M. 2006, PNAS, 103, 12257
Hincelin, U., Chang, Q., & Herbst, E. 2015, A&A, 574, A24
Hollenbach, D., & Salpeter, E. 1970, JChPh, 53, 79
Hollenbach, D., & Salpeter, E. 1971, ApJ, 163, 155
Hornekær, L., Baurichter, A., Petrunin, V., Field, D., & Luntz, A. 2003, Sci, 302, 1943
Hutter, J., Iannuzzi, M., Schiffmann, F., & VandeVondele, J. 2014, WIREs Comput. Mol. Sci, 4, 15
Islam, F., Cecchi-Pestellini, C., Viti, S., & Casu, S. 2010, ApJ, 725, 1111
Ivlev, A., Röcker, T., Vasyunin, A., & Caselli, P. 2015, ApJ, 805, 59
Jorgensen, W. L., Chandrasekhar, J., Madura, J. D., Impey, R. W., & Klein, M. L. 1983, JChPh, 79, 926
Latimer, E. R., Islam, F., & Price, S. D. 2008, CPL, 455, 174
Léger, A. 1983, A&A, 123, 271
Leger, A., Jura, M., & Omont, A. 1985, A&A, 144, 147
Lippert, G., Hutter, J., & Parrinello, M. 1997, MolPh, 92, 477
Molpeceres, G., & Kästner, J. 2020, PCCP, 22, 7552
Pantaleone, S., Enrique-Romero, J., Ceccarelli, C., et al. 2020, ApJ, 897, 56
Perdew, J., Burke, K., & Ernzerhof, M. 1996, PhRvL, 77, 3865
Roser, J., Swords, S., Vidali, G., Manico, G., & Pirronello, V. 2003, ApJL, 596, L55
Ruocco, G., Sette, F., Bergmann, U., et al. 1996, Natur, 379, 521
Schutte, W., & Greenberg, J. 1991, A&A, 244, 190
Shen, C., Greenberg, J., Schutte, W., & Van Dishoeck, E. 2004, A&A, 415, 203
Smith, R. G., Sellgren, K., & Tokunaga, A. T. 1988, ApJ, 334, 209
Smoluchowski, R. 1983, JPhCh, 87, 4229
Takahashi, J. 1999, EP&S, 51, 1215
Takahashi, J., Masuda, K., & Nagaoka, M. 1999a, ApJ, 520, 724
Takahashi, J., Masuda, K., & Nagaoka, M. 1999b, MNRAS, 306, 22
Takahashi, J., & Uehara, H. 2001, ApJ, 561, 843
Takahashi, J., & Williams, D. A. 2000, MNRAS, 314, 273
van de Hulst, H. C. 1946, RAOU, 11, 2
Vidali, G. 2013, ChRv, 113, 8762
Wakelam, V., Bron, E., Cazaux, S., et al. 2017, MolAs, 9, 1
Watanabe, N., Kimura, Y., Kouchi, A., et al. 2010, ApJL, 714, L233
Whittet, D. C. B. 1993, in Dust and Chemistry in Astronomy, ed. T. J. Millar & D. A. Williams (Boca Raton, FL: Routledge), 9

Résumées en Français des parties de résultats

Résumée en Français: Part I

Contexte

Dans les années 1990, on pensait que l'évolution des molécules organiques complexes interstellaires (iCOMs) dans les noyaux chauds/corinos était principalement pilotée par des réactions en phase gazeuse (par ex. Caselli et al., 1993; Charnley et al., 1992; Millar et al., 1991, paradigme 1 de la figure 1.7), dans lequel les espèces formant les couches de glace des grains de poussière s'évaporeraient rapidement une fois la proto-étoile chauffée, stimulant une chimie riche (Brown et al., 1988; Charnley et al., 1992). Cependant, l'inefficacité de réactions clés dans la voie vers les iCOMs (Geppert et al., 2005, 2006; Horn et al., 2004) a révélé la nécessité d'autres mécanismes de synthèse menant à des composés organiques complexes dans l'ISM. Dans les années 1960-1970, plusieurs études expérimentales ont proposé la possibilité que des radicaux puissent être formés dans les glaces interstellaires suite à l'exposition aux photons UV et aux rayons cosmiques (CR) (Hagen et al., 1979; Strazzulla et al., 1983; Tielens et al., 1987). Dans ce contexte, Allen et al. (1977) ont fourni une liste de réactions exothermiques plausibles qui pourraient avoir lieu sur les grains de poussière recouverts de glace et qui comprenaient des réactions de couplage radical-radical. Plus tard, R. T. Garrod et al. (2006) a proposé un modèle astrochimique qui prédit de grandes quantités de formate de méthyle, d'acide formique et d'éther diméthylique pendant la phase de *échauffement* protostellaire à partir de OH, HCO, CH_3 et CH_3O. Ce modèle a été inspiré par les travaux de Viti et de ses collaborateurs Collings et al., 2004; Viti et al., 1999, 2004 qui ont introduit pour la première fois le concept de "warm-up" et avec cette information, R. T. Garrod et al., 2006 a introduit la diffusion dépendante de l'espèce des radicaux lourds (par exemple HCO, CH_3O...) dans leur modèle lorsque la température est supérieure à environ 20–30 K. Ces auteurs ont également intégré le phototraitement des glaces comme source d'espèces radicalaires, en dehors de l'hydrogénation partielle des composants simples de la glace V. Taquet et al., 2012, dont les sources de photons sont le champ de rayonnement UV interstellaire fortement éteint, et surtout, le champ de rayonnement UV induit par les rayons cosmiques (CR) Gredel et al., 1989; Prasad et al., 1983. Leur modèle physique consistait en deux phases physiques successives, l'effondrement d'un nuage diffus (phase froide), suivi de l'allumage de la proto-étoile (phase chaude). Ce travail a donc proposé que les réactions radicalaires sur les glaces interstellaires pourraient être une voie très efficace vers la formation des iCOMs.

Des travaux de suivi tels que Robin T. Garrod et al. (2008) ont étendu le réseau réactionnel en incorporant des réactions de couplage entre H, OH, HCO, CH_3, CH_3O, CH_2OH, NH, et NH_2 (radicaux primaires, voir figure 13.4). Ils ont également inclus d'autres réactions entre radicaux impliquant différentes générations de radicaux ainsi que des réactions entre radicaux et aldéhydes (contenant le groupe -COH). Ils ont constaté que les radicaux de deuxième génération ont peu d'importance étant donné les abondances comparativement faibles de leurs espèces parentes et leurs plus grandes énergies de liaison, ce qui implique que les réactions d'hydrogénation peuvent avoir lieu en premier.

Malgré le succès de ces travaux dans la communauté, ce paradigme de formation de l'iCOM présente quelques problèmes. Le premier est lié à la réactivité des espèces radicales sur les surfaces de glace. Il est supposé que les réactions de surface radicales-radicalaires ont lieu en l'absence d'énergies d'activation, comme si les radicaux étaient en phase gazeuse, et de plus il est supposé qu'il y a un seul canal de produit menant à la formation d'iCOMs. Cette hypothèse est motivée par des expériences où la formation d'iCOMs est observée après le traitement énergétique d'analogues de glace interstellaire cultivés en lab-

E_b(K)	225	557	588	800	1189	1250	1425	1978	2254
Radical	**H**	**CO**	**CH_3**	**HCO**	**NH**	**CH_3O**	**OH**	**NH_2**	**CH_2OH**
H	H_2								
CO	HCO	x							
CH_3	CH_4	CH_3CO	C_2H_6						
HCO	H_2CO	x	CH_3CHO	OHCCHO					
NH	NH2	HNCO	CH_3NH	HNCHO	N_2H_2				
CH_3O	CH_3OH	CH_3OCO	CH_3OCH_3	$HCOOCH_3$	CH_3ONH	$(CH_3O)_2$			
OH	H_2O	COOH (CO_2 + H)	CH_3OH	HCOOH	HNOH	CH_3OOH	H_2O_2		
NH_2	NH_3	NH_2CO	CH_3NH_2	NH_2CHO	$HNNH_2$	CH_3ONH_2	NH_2OH	$(NH_2)_2$	
CH_2OH	CH_3OH	$CH_2(OH)CO$	C_2H_5OH	$CH_2(OH)CHO$	$CH_2(OH)NH$	CH_3OCH_2OH	$CH_2(OH)_2$	$CH_2(OH)NH_2$	$(CH_2OH)_2$
E_A (K)	2500	1500 (80)							

Figure 13.4: *Tableau tiré de Robin T. Garrod et al., 2008. En combinant un radical de gauche avec un autre de droite, on obtient un nouvel iCOM. Dans l'article original, ils ont inclus le CO dans la liste des radicaux même s'il ne l'est pas. Remarquez les énergies d'activation (ligne du bas, liées aux cases sombres) et les énergies de liaison (ligne du haut), deux paramètres très importants dans les modèles astrochimiques. Les croix signifient "non inclus" dans l'ensemble des réactions du modèle.*

oratoire. Cependant, ces expériences ne peuvent pas dire grand-chose sur les processus élémentaires qui se déroulent au niveau atomique. De plus, elles sont loin des conditions rencontrées dans le milieu interstellaire étant donné qu'elles travaillent à des pressions, des couvertures de surface et des flux de particules/photons beaucoup plus élevés que ceux rencontrés dans le ISM afin de reproduire des événements chimiques et physiques dans des échelles de temps de laboratoire (Tielens, 2013). Le deuxième problème concerne la mobilité des espèces sur les surfaces. Afin de simuler la diffusion et la sublimation en surface des espèces gelées, les modèles astrochimiques ont besoin d'une quantité clé : le BE de l'espèce à la surface. Cette quantité est généralement mal définie (car elle dépend de la molécule et du site de la surface) et dans de nombreux cas, elle est simplement extrapolée en fonction des groupes fonctionnels présents dans chaque espèce chimique. L'énergie de diffusion est généralement considérée comme une fraction de celle de la désorption, c'est-à-dire l'EB (par exemple : R. T. Garrod et al., 2006; Robin T. Garrod et al., 2008; Tatsuhiko I. Hasegawa et al., 1992; S. S. Jensen et al., 2021; M. Ruaud et al., 2015; Ruffle et al., 2000a; Vasyunin et al., 2017). Enfin, les taux, les rapports d'embranchement et les rendements des processus de photodissociation formant des radicaux sont également définis de manière vague : les taux de photodissociation sont généralement supposés être égaux à ceux de la phase gazeuse et les flux UV induits par les CR dépendent fortement du spectre d'énergie des CR et de la pénétration des photons UV dans les glaces [voir] [et les références qui y figurent] Taquet2012.

Il convient de mentionner qu'avec le temps, plusieurs améliorations ont été apportées à ces modèles "grain de gaz". Aikawa et al. (2008) a intégré la distribution spatiale et Awad et al. (2010) l'évolution du nuage en effondrement. V. Taquet et al. (2012) ont introduit la structure multicouche et poreuse des glaces interstellaires dans leur modèle, en supposant que seule la couche la plus externe est chimiquement active, tandis que la masse agit comme un stockage chimique. Ils ont prédit (i) une glace structurée avec la présence de dérivés CO relativement complexes (H_2CO et CH_3OH) plus abondants dans les couches supérieures, (ii) un effet important de la structure en couches des glaces, dans lequel certains des radicaux produits (formés par des réactions d'hydrogénation partielle plutôt que par des processus photolytiques) restent piégés dans le manteau avec un rôle réduit de la photolyse et (iii) un petit effet sur la chimie globale dû à la structure poreuse.

Avec la découverte d'iCOMs dans des noyaux prestellaires froids ($\leq$ 10 K) (e.g. Bacmann et al., 2012; Cernicharo et al., 2012; Jiménez-Serra et al., 2016; Vastel et al., 2014), de nouvelles voies ont été proposées pour tenter d'expliquer ces observations. Ces résultats remettent en cause le paradigme grain-surface de la formation de l'iCOM, car ce dernier nécessite le réchauffement des grains interstellaires à $\geq$ 20 K afin de permettre la diffusion des radicaux. Dans ce contexte, Vasyunin et al. (2013) ont utilisé le concept de désorption réactive comme un processus possible pour libérer les molécules précurseurs dans la phase gazeuse. Dans leur modèle, CH_3O est libéré dans la phase gazeuse par ce mécanisme où il peut subir, entre autres réactions de destruction, une association radiative avec CH_3 à des températures aussi

basses que 10 K en formant de l'éther diméthylique (cependant, ils ont utilisé une voie que des travaux antérieurs (Duley et al., 1993) ont montré comme étant inefficace, voir Balucani et al., 2015). De plus, l'efficacité de la désorption réactive est hideuse et plus complexe qu'il n'y paraissait initialement (voir §10). Sur une autre ligne de front, M. Ruaud et al. (2015) a intégré le mécanisme d'Eley-Rideal dans lequel les atomes de C atterrissant réagissent avec les espèces gelées via la formation de complexes de Van der Waals dans les cas où une barrière d'énergie d'activation élevée existe. Cependant, ce mécanisme ne peut pas rendre compte des grandes abondances d'éther diméthylique et de formiate de méthyle dans les noyaux froids : (Herbst, 2017). Comme alternative à la chimie de surface, des réactions neutres–neutres en phase gazeuse "froide" ont également été proposées par Balucani et al. (2015), qui a également supposé que le méthoxy se forme à la surface des grains.

Récemment, des voies alternatives invoquant la collision de CR avec des glaces interstellaires ont été proposées à l'aide de simulations de Monte Carlo Herbst, 2017; Shingledecker et al., 2018a,b. Ce nouveau paradigme n'est pas réellement nouveau dans la communauté, puisque des expériences caractérisant les produits d'irradiation de glaces de laboratoire analogues représentant les conditions des milieux interstellaires et du système solaire étaient déjà explorées depuis des décennies (e.g. Baratta et al., 2004; Bennett et al., 2007, 2005; Hudson et al., 1999, 2001; Strazzulla et al., 1983, 1995). Cependant, ce sont les premiers modèles astrochimiques à fournir une méthode pour prendre en compte l'irradiation des glaces par les CR. Dans ce modèle, les CR sont responsables de la formation d'ions et d'électrons au sein de la structure de la glace, qui peuvent devenir une source d'espèces de glace excitées électroniquement. Ces espèces excitées sont capables de subir des réactions chimiques avec une énergie d'activation substantielle, conduisant à la formation de plusieurs espèces chimiques, y compris les iCOMs. Par conséquent, ce modèle propose que le CR serait non seulement crucial pour les réactions en phase gazeuse, puisqu'elles constituent le principal mécanisme de formation du H_3^+ gazeux (Herbst et al., 1973), et la formation du champ UV secondaire dans les parties les plus denses de l'ISM, mais aussi pour la formation des iCOMs dans les glaces *via* la formation de ces ions et/ou électrons secondaires.

L'hypothèse cruciale et le problème commun à tous les modèles susmentionnés de formation d'iCOMs par la chimie des grains est que les radicaux à la surface se combinent sans barrière, c'est-à-dire avec une efficacité égale à l'unité. Cette hypothèse est-elle correcte ?

Buts, méthodes et nouveauté de la recherche dans cette part

Dans cette partie, je présente les résultats obtenus dans J. Enrique-Romero et al. (2020) and Joan Enrique-Romero et al. (2019, 2021a) (chapitres 6, 5 et 7, respectivement). Le premier chapitre (5) présente l'importance de l'utilisation de la symétrie brisée en DFT, le second (6) est une étude de "preuve de concept" dans laquelle la formation d'acétaldéhyde et de formamide à partir de HCO + CH_3 et de HCO + NH_2 sur des glaces ASW[1] est étudiée, et la troisième (7) est une étude systématique de différentes réactions radicalaires.

Les objectifs de cette recherche sont (i) de déterminer si les réactions radicales-radicalaires sur les surfaces de glace ASW sont réellement sans barrière ou non, (ii) de comprendre si ces réactions ont un seul canal de produit, (iii) dans le cas où il y a différents canaux de réaction, s'ils sont en compétition directe, et (iv) de comprendre comment l'environnement de surface affecte la réactivité.

L'ensemble des réactions radicalaires à étudier a été tiré de la Fig. 1 de Robin T. Garrod et al., 2008 (reproduit ici dans la Figure 13.4), de sorte que nous étudions un sous-ensemble d'entre elles, à savoir certaines des réactions entre CH_3, HCO, NH_2, CH_3O et CH_2OH, marquées en rouge dans la Figure 13.4. Deux modèles de glace ASW de tailles différentes ont été utilisés (tirés de Rimola et al., 2014). Le plus petit présente une surface externe plutôt plate et se compose de 18 molécules d'eau. Le plus grand, composé de 33 molécules d'eau, présente une structure en cavité où les radicaux peuvent établir davantage d'interactions intermoléculaires. Ces deux modèles sont illustrés dans la figure 13.5. Avec ce dernier modèle, nous cherchons à mieux représenter les surfaces des glaces interstellaires. Il comporte également une région plate qui s'est avérée ne pas convenir à notre étude systématique (Joan Enrique-Romero et al., 2021a) car certaines réactions radicales-radicalaires se sont avérées aboutir à l'effondrement de l'ensemble du modèle de surface.

[1] Amorphous solid water.

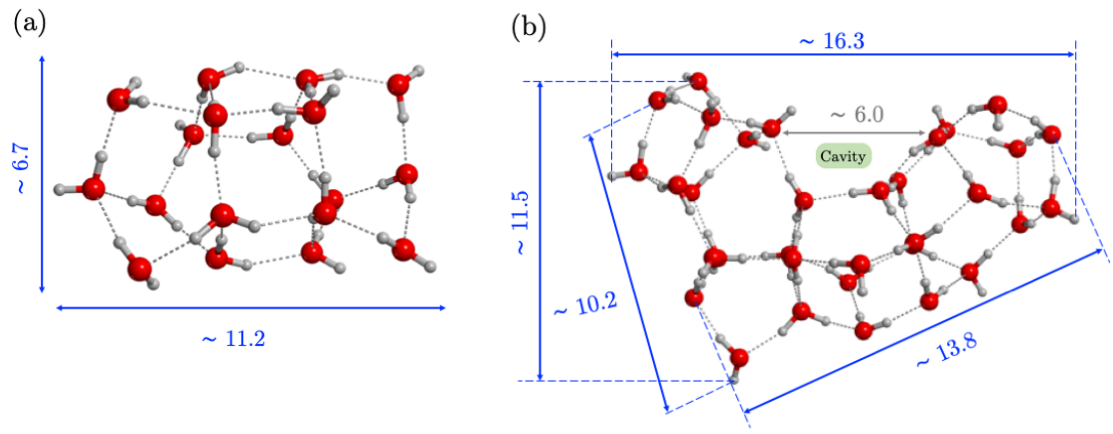

Figure 13.5: *Les deux principaux modèles ASW utilisés dans cette thèse, celui de gauche est constitué de 18 molécules d'eau (W18), et celui de droite de 33 molécules d'eau (W33). Les géométries moléculaires présentées dans cette figure ont été minimisées au niveau de théorie BHLYP-D3(BJ)/6-31+(d,p). Les distances sont en Å. Remarquez la structure de la cavité hémisphérique dans le plus grand modèle de glace du côté droit.*

La nouveauté de mes travaux présentés dans ce chapitre par rapport aux études précédentes réside dans le fait qu'il s'agit des toutes premières études de la réactivité radicalaire sur les glaces ASW à une échelle atomique et au moyen de simulations de chimie computationnelle. Ce type d'études n'a jamais été abordé auparavant : [2] pour plusieurs raisons. L'une d'elles est la croyance générale selon laquelle les réactions radicalaires sont sans barrière, ce qui, comme nous le verrons, n'est pas toujours vrai, en particulier sur les surfaces moléculaires polaires comme les glaces ASW. Une autre raison est la complexité intrinsèque de l'exécution de ces calculs : d'un point de vue technologique, on ne peut pas se permettre d'exécuter les calculs très précis et exigeants nécessaires pour décrire les systèmes à coquille ouverte singlet (par exemple deux espèces radicales sur la surface prêtes à réagir) sur des surfaces explicites, et l'autre raison est le manque de travaux théoriques employant l'approximation de symétrie brisée dans la communauté astrochimique.

À cette fin, nous avons utilisé la théorie DFT combinée aux approches de symétrie non restreinte et brisée (spin) afin de décrire correctement l'état biradical singulet des réactifs et des états de transition. Cette approche de symétrie brisée repose sur le mélange partiel de certains triplets afin d'obtenir une solution de fonction d'onde physiquement valable pour le système singulet (voir § 2.4), avec l'inconvénient d'être plus longue que la DFT normale en raison (i) de l'utilisation du schéma non restreint obligatoire et (ii) de la nécessité de s'assurer que la fonction d'onde initiale est un état singulet [3], et que c'est la solution d'énergie minimale. En ce qui concerne la fonctionnelle de densité, nous nous sommes appuyés sur BHLYP combiné avec la correction de dispersion de Grimme "D3" [4] car elle fournit des énergies de liaison précises et permet un mélange 1:1 des contributions de DFT pur et d'échange exact. Ces deux facteurs sont importants pour nous car (i) les barrières d'énergie d'activation des réactions radicalaires de surface proviennent principalement de l'interaction radicalaire-surface et (ii) parce qu'un rapport d'échange DFT/exact aussi élevé atténue les effets de l'erreur d'auto-interaction des électrons inhérente aux calculs DFT.

Dans nos calculs, tous les électrons et atomes du système sont traités au même niveau de théorie. Les minima et maxima des PES ont été caractérisés par des calculs de fréquence. Les énergies vibrationnelles du point zéro ont été calculées, et des calculs de coordonnées de réaction intrinsèques ont été effectués

[2] Avec deux exceptions: J. Enrique-Romero et al. (2016) et Rimola et al. (2018).

[3] La couche ouverte signifie que tous les électrons ne sont pas appariés. Le cas des biradicaux est clair, avec des états de couche ouverte singlet ou triplet, c'est-à-dire qu'il y a deux électrons non appariés avec des spins antiparallèles/parallèles.

[4] Voir plus de détails dans chaque article puisque l'introduction de cette correction a varié de notre premier travail Joan Enrique-Romero et al., 2019, dans lequel elle a été introduite sous forme d'énergies en un seul point au-dessus des structures moléculaires optimisées par BHLYP, au plus récent Joan Enrique-Romero et al., 2021a, dans lequel les énergies pendant le processus d'optimisation sont également corrigées, et de plus nous utilisons une implémentation plus moderne, à savoir celle avec l'amortissement Becke-Johnson. Voir § 2.3 pour plus de détails sur les corrections de dispersion.

lorsque cela était nécessaire (ou possible) afin d'assurer la connexion entre les réactifs et les produits à l'état de transition. Nous avons utilisé des ensembles de bases doubles et triples de la famille Pople, en fonction de la nature du calcul. Par exemple, les calculs d'optimisation et de fréquence prennent plus de temps que les calculs d'énergie au point zéro, c'est pourquoi l'ensemble de base le plus petit a été utilisé dans les premiers cas.

Des calculs d'énergie de liaison pour chaque radical sur chaque modèle de surface ont également été effectués. Dans ce cas, les énergies finales ont été corrigées pour la dispersion, les déformations, les erreurs de superposition de l'ensemble de base et les énergies du point zéro.

Résumé des résultats

On constate que les réactions radicalaires ont très souvent des barrières énergétiques typiquement inférieures à $\sim$7 kJ mol^{-1} (équivalent à 840 K), bien que certains cas spécifiques puissent avoir des barrières énergétiques beaucoup plus élevées. En général, ces barrières sont une conséquence de l'interaction des radicaux avec la surface de la glace, c'est-à-dire qu'elles proviennent de la rupture des interactions radicaux-surface.

Deux voies de réaction possibles sont envisageables : (i) le couplage des radicaux, c'est-à-dire la formation d'une liaison chimique entre les deux radicaux conduisant aux iCOM, et (ii) les réactions directes d'absorption de H, où l'un des radicaux transfère un atome de H à l'autre. Ces deux réactions présentent souvent des barrières d'énergie d'activation similaires, et sont donc probablement en compétition. Par conséquent, l'hypothèse selon laquelle une réaction entre deux radicaux donnés produira nécessairement des iCOM n'est pas justifiée et doit être prise avec précaution dans la modélisation astrochimique.

Les effets des surfaces sont mieux représentés par les valeurs des énergies de liaison (BE). Pour les deux modèles de surface, l'ordre des BE est le même : $CH_3 < HCO < NH_2 < CH_3O < CH_2OH$. Cependant, les BE dans la cavité de notre plus grand modèle s'avèrent être plus élevés que sur la surface du modèle à 18 molécules d'eau. Ces différences sont la conséquence d'un environnement chimique différent, étant donné que le nombre d'interactions dans la cavité est plus important.
En ce qui concerne les aspects plus spécifiques, certaines conclusions peuvent être tirées pour chaque radical :

- Nous avons constaté que le HCO est un donneur d'H très efficace dans les réactions directes d'absorption de l'H et, par conséquent, ce canal entre en concurrence avec les réactions de couplage radicalaire, établissant probablement un rapport de branchement de 1:1 pour chaque processus.

- En raison du faible BE de CH_3 à la surface ASW adoptée, dans de nombreux cas, ses mécanismes réactionnels comprennent une torsion de faible énergie, de sorte qu'il est fréquent de trouver des réactions avec ce radical sans barrière (ou presque). Il existe quelques exceptions sur la cavité de notre grand modèle, où la mobilité de CH_3 est beaucoup plus restreinte, de sorte que les barrières d'énergie d'activation peuvent s'élever jusqu'à $\sim$7 kJ mol^{-1}.

- La forte interaction du groupe OH de CH_2OH avec les molécules d'eau de la surface fait que ce radical présente un schéma d'interaction particulier, dans lequel son groupe OH est verrouillé par des liaisons H, tandis que son atome C (contenant le radical) est éloigné de la surface et libre de réagir. Ce radical présente donc des barrières d'énergie d'activation très faibles pour les réactions sur son atome C, mais très élevées pour les réactions directes de transfert d'hydrogène où CH_2OH est le donneur d'hydrogène.

  Le modèle de liaison de CH_2OH impliquerait que ce radical est efficacement détruit par des réactions avec d'autres radicaux moléculaires ou atomes d'hydrogène.

- CH_3O a son électron radical sur l'atome O, qui à son tour établit des liaisons H avec les molécules d'eau de surface. Ce radical est donc légèrement moins réactif que prévu et des barrières énergétiques élevées apparaissent donc pour les réactions CH_3O + CH_3O. D'autre part, il peut toujours effectuer des réactions d'extraction directe de H en tant que donneur, mais les barrières énergétiques élevées dues à la stabilité intrinsèque de sa liaison H–C (et pour la cavité, le nombre plus élevé

d'interactions intermoléculaires) indiquent qu'elles ne sont efficaces que si l'on considère les effets de tunnel quantique.

Enfin, dans notre dernier travail (Joan Enrique-Romero et al., 2021a, chapitre 7), nous discutons des iCOMs de notre échantillon qui pourraient effectivement être formés, ceux qui seront en compétition avec les produits d'absorption directe de H, et ceux qui ne peuvent pas être formés, sur la base d'une estimation approximative de leur efficacité de réaction. Cette efficacité nous renseigne sur la compétition entre la réaction et la diffusion/désorption loin du site de réaction (voir les chapitres 8 et 9 pour sa définition).

Les iCOM qui peuvent être formés sont : l'éthane (C_2H_6), la méthylamine (CH_3NH_2) et l'éthylène glycol (CH_2OHCH_2OH). Ceux qui devront entrer en compétition avec le canal d'absorption directe de l'hydrogène sont : le glyoxal (HCOCHO, contre CO + H_2CO), le formamide (NH_2CHO, contre NH_3 + CO), le méthylformate (CH_3OCHO, contre CH_3OH + CO) et le glycolaldéhyde (CH_2OCHO, contre CH_3OH + CO). Et ceux qui ne seront pas formés sont : l'acétaldéhyde (CH_3CHO) et le peroxyde de diméthyle (CH_3OOCH_3).

Résumée en Français: Part II

Contexte

Les modèles astrochimiques supposent généralement que les réactions de couplage radical-radical sur les grains de poussière glacés sont sans barrière, ce qui signifie que leur efficacité de réaction lors de leur rencontre sur la surface de la glace est unitaire (c'est-à-dire que s'ils se rencontrent, ils se coupleront pour former la molécule) R. T. Garrod et al., 2006; Robin T. Garrod et al., 2008. Cependant, comme nous l'avons vu dans la partie I, des barrières d'énergie d'activation peuvent exister et, de plus, le couplage radical-radical n'est pas le seul canal de réaction, mais des réactions directes d'absorption de H sont également possibles. Un de ces cas est la réaction entre CH_3 + HCO, présentée dans la partie I au moyen de calculs quantiques statiques.

Le fait d'avoir des efficacités de réaction unitaires dans les réactions de surface entre radicaux signifie que la vitesse à laquelle les radicaux se rencontrent sur la surface contrôle la vitesse de réaction. Afin de calculer l'échelle de temps de rencontre, on suppose généralement que les deux réactifs doivent balayer toute la surface avant de se rencontrer (Tatsuhiko I. Hasegawa et al., 1992). Par conséquent, les taux de rencontre dépendent des barrières de diffusion, et celles-ci sont supposées être une fraction f des barrières de désorption.

Dans la littérature, on peut trouver des valeurs de f (rapport entre les barrières de diffusion et de désorption) allant de 0,3 à $\sim$0,8 (par exemple (Tatsuhiko I. Hasegawa et al., 1992; Ruffle et al., 2000b)), de sorte que certains auteurs utilisent la valeur moyenne f=0,5 (R. T. Garrod et al., 2006, 2011; Robin T. Garrod et al., 2008; S. S. Jensen et al., 2021; M. Ruaud et al., 2015; Vasyunin et al., 2017). Cependant, ces dernières années, des travaux théoriques et expérimentaux sur la diffusion sur les glaces ont apporté des contraintes à la valeur de f. Par exemple, Karssemeijer et al. (2014) ont montré théoriquement que la plage pour f peut être réduite à 0,3-0,4 pour des molécules comme le CO et le CO2. Minissale et al. (2016a) a constaté expérimentalement que le rapport f des espèces atomiques comme N et O est d'environ 0,55, tandis que He et al. (2018) a montré que f est de 0,3-0,6, les valeurs inférieures étant plus appropriées pour une couverture de surface inférieure à une monocouche, et récemment Kouchi et al. (2020) a mesuré la fraction f de CO à environ 0,3 sur l'eau solide amorphe. Par conséquent, des valeurs de l'ordre de 0,3 à 0,4 pourraient être plus appropriées pour les espèces moléculaires.

Buts, méthodes et nouveauté de la recherche dans cette part

Dans ce chapitre, je présente les résultats obtenus dans Joan Enrique-Romero et al. (2021b). Les objectifs de cette recherche sont (i) de faire un pas en avant dans la formation d'acétaldéhyde/CO + CH_4 à partir de réactions de couplage radicalaire CH_3 + HCO et d'abstraction directe de H en étudiant ces réactions d'un point de vue cinétique, (ii) d'évaluer les efficacités de ces deux réactions, et (iii) de comprendre l'effet de la modification du rapport diffusion/désorption (f) sur ces efficacités.

La principale nouveauté de ce travail a été la production de données de cinétique chimique pour les réactions radicalaires, pour lesquelles nous avons utilisé la théorie RRKM (voir §2.6). Dans la théorie RRKM, l'ensemble du système, surface + radicaux, est considéré comme une "supermolécule" subissant une réaction unimoléculaire (par exemple Rimola et al., 2018), comme si la réaction était comprise comme

un changement de conformation de la supermolécule. Cette méthodologie inclut également les effets tunnel *via* le potentiel d'Eckart non symétrique pour les réactions d'absorption de l'hydrogène.

Comme base, nous utilisons nos résultats précédents sur la formation d'acétaldéhyde/CO + CH_4 dans Joan Enrique-Romero et al. (2019) la cavité du grand modèle de glace composé de 33 molécules d'eau, car c'est le site d'adsorption le plus stable dans nos modèles et nous supposons que les radicaux réagiront dans des sites stables comme celui-ci.

Les calculs cinétiques nécessitent des données énergétiques de chimie quantique aussi précises que possible, car les barrières énergétiques entrent dans une exponentielle et, par conséquent, toute erreur sur ce point sera amplifiée. Pour cette raison, nous avons réalisé une étude comparative afin de choisir la méthode fonctionnelle de densité la plus performante en utilisant comme référence les calculs CASPT2. La fonction BHLYP-D3(BJ) combinée à un ensemble de base de qualité triple-ζ s'est avérée être la meilleure méthode, avec des erreurs inférieures à 5 Par conséquent, par rapport à Joan Enrique-Romero et al. (2019), nous avons amélioré (i) la correction de la dispersion, en passant de la fonction D3 avec amortissement nul à la fonction D3 avec amortissement Becke-Johnson (BJ), et (ii) les énergies électroniques brutes en effectuant des calculs d'énergie à point unique au niveau de l'ensemble de base triple-ζ sur les géométries optimisées double-ζ pour des raisons de coût de calcul.

Nous avons également recalculé les énergies de liaison radical-surface et les avons utilisées pour calculer les taux de désorption et de diffusion. En ce qui concerne ces derniers, nous avons supposé que les barrières de diffusion étaient une fraction (f) de celles de la désorption. Etant donné l'incertitude sur le choix de cette fraction, trois valeurs pour f ont été utilisées : 0,3, 0,4 et 0,5$\times$E$_{des}$.

La cinétique de désorption a été calculée à l'aide de la formule d'Eyring (voir eq. 2.39 dans §2.6). Afin d'inclure les effets entropiques, les fonctions de partition du processus de désorption ont été calculées : pour la situation *prior* à la désorption, seuls les degrés de liberté vibrationnels ont été pris en compte, tandis que pour la situation *post* à la désorption, les degrés de liberté vibrationnels ont été inclus pour la surface et le radical, et les degrés rotationnels et translationnels ont été pris en compte uniquement pour le radical en phase gazeuse. Des corrections thermiques suivant ce même schéma ont également été incluses pour les enthalpies. Ces entropies et enthalpies ont été multipliées par la fraction de diffusion-désorption f lors du calcul des constantes de vitesse de diffusion.

Enfin, nous avons calculé les efficacités de réaction (ϵ) selon l'éq. 13.1 comme suit (voir §9) :

$$\epsilon = \frac{k_{aeb}}{k_{aeb} + k_{diff}(i) + k_{des}(i) + k_{diff}(j) + k_{des}(j)}, \tag{13.1}$$

où k_{aeb} est la constante de vitesse de réaction calculée avec la théorie RRKM (aeb représente la barrière d'énergie d'activation) et $k_{diff}(i)$ et $k_{des}(i)$ sont les constantes de vitesse de diffusion et de désorption des espèces i. Cette équation tient compte de la compétition entre l'événement réactionnel et la possibilité que les réactifs se diffusent ou soient désorbés.

Résumé des résultats

La réaction de couplage radicalaire CH_3 + HCO présente une barrière légèrement inférieure (5,5 kJ mol^{-1}) à celle de l'absorption directe de H (7,2 kJ mol^{-1}). En traduisant cela en termes cinétiques, nous trouvons des valeurs de constantes de vitesse plus élevées pour la seconde réaction à des températures plus élevées, tandis qu'à des températures plus basses, l'effet tunnel pour l'extraction de H prend le dessus et cette réaction devient beaucoup plus rapide que celle du couplage.

Les contraintes des températures les plus élevées auxquelles ces deux réactions peuvent avoir lieu sont dérivées en utilisant les échelles de temps de désorption. Nous dérivons la température à laquelle chaque radical se désorberait, en supposant une échelle de temps de 10^6 ans pour le processus (mais notez que cela change très peu pour des temps plus longs). Puisque CH_3 a une énergie de liaison beaucoup plus faible que HCO ($\sim$14,2 et $\sim$29,4 kJ mol^{-1}), CH_3 a une température limite de 30 K alors que HCO a 68 K. Cela signifie que les réactions de formation d'acétaldéhyde/CO + CH_4 à partir de CH_3 + HCO ne peuvent être opérationnelles qu'à des températures inférieures à 30 K.

En ce qui concerne les efficacités, le choix du rapport diffusion/désorption f a des conséquences dramatiques pour les deux réactions :

- Pour f=0,5, nous avons des valeurs constantes de ϵ=1,0 pour les deux réactions.
- Pour f=0,4, le rendement de la réaction de couplage se situe entre $\sim$0,8–0,9, et celui du transfert direct de H est égal à 1,0 jusqu'à $\sim$22 K, où il commence à diminuer.
- Enfin, pour f=0,3, les efficacités des deux réactions dépendent fortement de la température. À basse température et en raison de l'effet tunnel quantique sur la constante de vitesse de la réaction d'abstraction directe de l'H, son efficacité est unitaire sous $\sim$14 K et elle diminue à mesure que la température augmente, jusqu'à $\sim 10^{-3}$ à 30 K. D'autre part, l'efficacité de la réaction de couplage radicalaire est négligeable à basse température, et à 30 K elle augmente jusqu'à une valeur maximale d'environ 0,01.

En résumé, les efficacités des réactions de couplage radicalaire et d'extraction directe de H sur notre modèle de glace sont une fonction complexe de la température, de l'énergie de diffusion de CH_3 et du facteur f. Pour $f \geq$0.4 les efficacités sont proches de l'unité, résultant donc avec une compétition $\sim$1:1 entre la formation d'acétaldéhyde et de CO + CH_4. En revanche, pour f=0,3, la formation d'acétaldéhyde présente un $\epsilon \leq$0,01 et la formation de CO + CH_4 un ϵ situé entre l'unité et 0,001. Par conséquent, des mécanismes alternatifs vers l'acétaldéhyde sont nécessaires. Ces résultats ont également des conséquences importantes pour la modélisation astrochimique.

Résumée en Français: Part III

Contexte

La détection d'iCOMs dans des corps froids ($\sim$ 10 K) de l'ISM (Bacmann et al., 2012; Cernicharo et al., 2012; Jaber et al., 2014; Jiménez-Serra et al., 2016; Vastel et al., 2014) a remis en question le paradigme de la chimie de surface pour la formations d'iCOMs (mécanisme 2 de la figure 1.7) car il nécessite des conditions chaudes ($\sim$ 30 K) afin de permettre la diffusion de radicaux sur les surfaces de glace (R. T. Garrod et al., 2006). Une des alternatives proposées est que les composants simples de la glace, comme le méthanol, sont libérés dans la phase gazeuse, où ils participent à la chimie de la phase gazeuse froide, grâce à un mécanisme non thermique (Balucani et al., 2015; Vasyunin et al., 2013).

L'un de ces mécanismes est la désorption chimique (DC) (Duley et al., 1993; R. T. Garrod et al., 2007; Minissale et al., 2014b, 2016c; Takahashi et al., 2000), qui est proposée pour jouer un rôle majeur dans la chimie complexe du noyau froid par rapport à d'autres mécanismes de désorption non thermiques. Les autres mécanismes non thermiques sont le chauffage ponctuel du CR (Tatsuhiko I. Hasegawa et al., 1992; Leger et al., 1985) et la photodésorption induite par les UV (Bertin et al., 2013, 2016; Fayolle et al., 2011). (Vasyunin et al., 2017). L'idée est assez simple : l'énergie libérée par une réaction exothermique peut induire la désorption du produit nouvellement formé. Les surfaces de glace peuvent agir comme des corps tiers, et donc absorber et dissiper une partie de l'énergie de la réaction naissante, en laissant une partie qui pourrait être utilisée pour rompre les liens de la nouvelle molécule avec la surface. Cependant, si la surface de la glace absorbe trop d'énergie, cela pourrait entraver la désorption de l'espèce formée ou pourrait induire la désorption de molécules volatiles appartenant à la glace se trouvant à proximité du site de réaction. En d'autres termes, l'énergie de la réaction est généralement répartie entre le produit et la surface, et le degré de cette répartition peut éventuellement déterminer la CD des espèces formées. Les modèles astrochimiques utilisent généralement des efficacités de CD (c'est-à-dire la fraction de molécules non thermiquement désorbées par réaction chimique) comprises entre 1 et 10% (par exemple, R. T. Garrod et al., 2007; Vasyunin et al., 2013, 2017), bien que les valeurs de ces efficacités soient très controversées.

Le CD a été caractérisé expérimentalement sur un certain nombre de surfaces et pour un certain nombre de réactions, réalisant que son efficacité dépend de la nature du produit et de la surface où il est formé. En effet, dans certains cas, cette efficacité s'est avérée élevée. Par exemple, Oba et al. (2018) a trouvé des efficacités de désorption CD de $\sim$60% pour la formation de H_2S sur des glaces ASW et François Dulieu et al. (2013) a trouvé des efficacités CD très élevées pour la formation d'eau *via* l'hydrogénation de radicaux OH sur des surfaces de silice ($<$90%). Au contraire, d'autres études montrent que la CD peut en fait être très inefficace. Par exemple, François Dulieu et al. (2013) ont également trouvé des efficacités de désorption chimique très faibles ($<$ 10%) pour d'autres réactions d'hydrogénation dans la séquence de réaction de formation d'eau sur la silice : O_2 + D $\rightarrow$ DO_2, DO_2 + D $\rightarrow$ D_2O_2, D_2O_2 + D $\rightarrow$ D_2O + OD. De même, He et al. (2017) ont constaté que la réaction d'addition de H à O_3 produisant OH et O_2 sur des glaces ASW non poreuses entraîne une faible désorption de O_2 ($\leq$11%). En ce qui concerne la formation de formaldéhyde et de méthanol par l'hydrogénation successive de CO, Chuang et al. (2018) n'a trouvé presque aucun CD par atome H incident (inférieur à 2%) sur les glaces de CO, H_2CO et CH_3OH.

Minissale et al. (2016b) ont examiné et réalisé des expériences sur le CD d'un certain nombre de réactions, y compris O + O_2 $\rightarrow$ O_3 Minissale et al., 2014a,b, 2013, 2016b, les différentes étapes de la formation de l'eau (Chaabouni et al., 2012; François Dulieu et al., 2013), N + N $\rightarrow$ N_2, entre autres, en explorant

différentes surfaces (lorsque cela est possible) comme la glace d'eau solide amorphe non poreuse, les silicates amorphes et le graphite oxydé. Ils ont montré que l'efficacité du CD dépend de trois facteurs principaux : l'énergie de formation de la réaction, l'énergie de liaison de l'adsorbat et la nature du substrat. Le CD est plus efficace pour les petites molécules ayant une faible énergie de liaison. De plus, la CD sur des surfaces dures comme le graphite oxydé peut être comprise qualitativement comme une collision élastique entre le produit excité et la surface, alors que sur la glace d'eau, elle est beaucoup plus complexe et moins efficace. La CD réduite sur la glace d'eau est attribuée au transport rapide de l'énergie de l'eau grâce à son réseau de liaisons H, pour lequel le modèle des collisions élastiques ne peut pas être appliqué.

Moins de travaux théoriques ont étudié la dissipation et le processus de CD. Fredon et al. (2018, 2017) ont étudié la relaxation de molécules de CO_2, d'eau et de méthane excitées par translation (50–500 kJ mol^{-1}) sur des glaces d'eau cristallines et amorphes, afin d'étudier la désorption chimique et la diffusion non-thermique de ces espèces. On a supposé que ces molécules cinétiquement excitées étaient facilement formées, de sorte que l'énergie de réaction a été entièrement canalisée dans les degrés de liberté de translation. Ces auteurs ont constaté que la probabilité de désorption dépend de l'énergie injectée et des énergies de liaison des espèces (voir également §3.5), et non de la masse des espèces comme le suggère Minissale et al. (2016b).

Takahashi et al. (1999a,b) ont étudié la formation de H_2 sur les glaces ASW au moyen de la dynamique moléculaire classique. Ils ont simulé de nombreux processus impliqués dans la formation d'hydrogène moléculaire sur les surfaces, y compris la probabilité d'adhérence des atomes H, leur diffusion, leur réaction et leur désorption en conséquence de l'énergie libérée (c'est-à-dire après la CD). Les atomes H de la phase gazeuse peuvent diffuser pendant environ 60–140 Å, et s'ils perdent suffisamment d'énergie cinétique, ils peuvent rester piégés dans des puits de liaison profonds. Dans les cas où H_2 a été formé, on a observé que le produit était éjecté dans la phase gazeuse rapidement (en 400–600 fs) avec des états vibrationnels élevés (6–9 niveaux vibrationnels pour des températures de glace de 10 K) car on a constaté que la surface de la glace dissipait peu d'énergie ($\sim$3–5% de l'énergie totale de formation de H_2, environ 458,1 kJ mol^{-1} dans leur simulation). Plus tard, les mêmes auteurs (Takahashi et al., 2000) ont étudié la possibilité qu'une molécule de CO puisse être désorbée de manière non thermique suite à la formation d'une molécule de H_2 à proximité. Ils ont constaté que le voisinage le plus proche du site de réaction (distances inférieures à 4 Å) augmente sa température d'environ 20 K et d'environ 10 K pour les distances de 4–6 Å. Cependant, on a observé que ce gain de température était trop faible par rapport au temps nécessaire à la désorption du CO sur les gros grains (rayon de 0,1 μm). Par conséquent, il a été constaté que ce processus n'était pas efficace à moins de considérer un très petit grain, pour lequel des températures plus élevées pourraient être atteintes.

Korchagina et al. (2017) ont étudié l'hydrogénation du CO sur des amas moléculaires de glace d'eau composés de $\leq$5 et 10 molécules d'eau par le mécanisme Eley-Rideal à 70 K. Ils ont découvert que l'énergie de formation du HCO peut être dissipée par l'amas d'eau, ce qui conduit à une molécule de HCO stable pour les amas de plus de 3 molécules d'eau. Ce travail présente cependant deux faiblesses principales, la première étant les petits modèles de glace d'eau, et l'autre étant liée à la faible précision des méthodes employées. Plus récemment, Kayanuma et al. (2019) ont étudié le CD pour la réaction HCO + H par le mécanisme d'Eley-Rideal, où HCO est adsorbé sur le graphène. Ils ont trouvé un CD efficace pour les produits (H_2 et CO) lorsque le HCO est chimisorbé, alors qu'ils n'ont trouvé aucun CD lorsqu'il est physisorbé (dans ce cas, H_2CO est produit).

Dans cette partie, je me concentre sur la capacité des surfaces de glace d'eau à dissiper l'énergie naissante de deux réactions de surface clés en astrochimie : H + CO $\rightarrow$ HCO et H + H $\rightarrow$ H_2. Deux réactions largement étudiées à la fois expérimentalement (par exemple, Kenzo Hiraoka et al., 2002; Naoki Watanabe et al., 2002b pour HCO et Hama et al., 2012; Hornekær et al., 2003; Roser et al., 2003; Naoki Watanabe et al., 2010 pour H_2) et théoriquement (voir §3.2 et §3.1).

Buts, méthodes et nouveauté de la recherche dans cette partie

Dans cette partie, je présente les résultats obtenus dans Pantaleone et al. (2020) et Pantaleone et al. (2021), dans lesquels le devenir de l'énergie de formation de HCO et H_2 est étudié avec des simulations de dynamique moléculaire *ab initio* (AIMD) (chapitres 11 et 12, respectivement). Ce travail a été réalisé en collaboration avec S. Pantaleone, qui a eu un post-doc dans notre équipe de Grenoble. Nous avons travaillé

main dans la main pour exécuter les simulations, et j'ai ensuite conçu un code python afin d'analyser les résultats. Nous avons obtenu deux projets dans le réseau national français de supercalculateurs, GENCI, avec les numéros de dossier A0060810797 et A0080811498, de 1,7 et 6 millions d'heures respectivement. Enfin, nous avons rédigé les deux articles ensemble, et partagé nos travaux.

Les objectifs de cette recherche sont (i) de comprendre d'un point de vue atomistique comment l'énergie libérée par la formation de HCO et H_2 est transférée vers la surface de l'eau et de la quantifier, (ii) de comprendre si le produit quitte ou quittera la surface, (iii) dans le cas où il le fait, de quantifier la quantité d'énergie retenue dans le produit (HCO ou H_2) et, pour la formation de H_2 (iv) de quantifier si la glace est localement suffisamment réchauffée pour permettre la désorption d'une molécule de H_2 et de CO à proximité.

La nouveauté de ce travail est que (i) nous simulons le processus en tenant compte de la réaction réelle (au lieu de, par exemple, supposer une certaine quantité d'énergie initiale une fois que les produits sont déjà formés comme cela a souvent été fait dans des travaux similaires précédents ; voir §10.1) et (ii) nous le faisons au moyen de simulations AIMD en utilisant de grands modèles de surface de glace d'eau (contenant 192 et 576 molécules d'eau pour la formation de HCO et de H_2, respectivement), ce qui est fondamental pour représenter de manière fiable la dissipation d'énergie. Pour le premier travail (Pantaleone et al., 2020), nous avons utilisé un modèle de glace d'eau cristalline Ih ordonnée en protons, car il limite le nombre de modes de liaison et de sites possibles, ce qui rend le processus d'analyse global beaucoup plus facile. Pour la seconde Pantaleone et al., 2021, nous avons utilisé à la fois une glace cristalline et une glace amorphe.

Les calculs ont été effectués à l'aide du progiciel CP2K avec la fonctionnelle de densité PBE-D3 combinée à un ensemble de base de qualité triple-ζ avec des fonctions de polarisation pour les électrons de valence. Dans le cas de la formation de HCO, le PES H + CO $\rightarrow$ HCO a été préalablement caractérisé afin que la simulation ne parte pas des réactifs mais de la structure de l'état de transition (TS). La structure TS a été trouvée en utilisant la méthode Dimer, dans laquelle une géométrie initiale appropriée est donnée au code, et celui-ci localise un point de selle proche. En revanche, pour la formation de H_2, la simulation commence avec les deux atomes de H situés à proximité immédiate et, comme la réaction s'avère sans barrière à ces positions initiales à la température considérée (10 K), aucune recherche de TS n'a été nécessaire.

Les surfaces cristallines ont été dérivées de la structure hexagonale de la glace en vrac ordonnée par les protons (glace XI). Des coupes ont été effectuées le long de la direction [001] afin de générer des modèles de dalles avec un faible moment dipolaire et de nombreux sites de liaison (par exemple Zamirri et al., 2018). Les dalles ont ensuite été thermalisées à 10 K en exécutant une simulation dans l'ensemble canonique (NVT, c'est-à-dire que le nombre de particules, N, le volume, V, et la température, T, sont des grandeurs constantes).

Le modèle amorphe a été obtenu en effectuant une simulation classique de dynamique moléculaire (MD) à 300 K sur le modèle cristallin, puis en abaissant brusquement la température à 10 K, suivie d'une optimisation de la géométrie et d'une thermalisation à 10 K.[5].

Les tailles des boîtes périodiques pour les simulations de formation de HCO et H_2 sont : 17,544 $\times$ 21,2475 $\times$ 35,0 et 26,318 $\times$ 28,330 $\times$ 50,0 Å, où les épaisseurs des plaques sont d'environ 13 et 21 Å (correspondant à 4 et 7 couches de glace cristalline, c'est-à-dire 192 et 576 molécules d'eau), respectivement[6].

Les simulations de dissipation d'énergie ont été effectuées dans l'ensemble microcanonique (NVE, c'est-à-dire que le nombre de particules, N, le volume, V, et l'énergie totale, E, sont des grandeurs constantes). Afin de maintenir l'énergie totale constante (dans l'ensemble canonique, le bain thermique enlèverait artificiellement de l'énergie au système). Un seul site de surface initial a été utilisé pour la formation de HCO, tandis que pour H_2 nous avons pris un site sur le cristallin et trois sur l'amorphe.

Afin d'analyser le processus de dissipation d'énergie, j'ai utilisé mon propre code python. Dans ce code, la dalle de surface est séparée en différentes régions dans lesquelles le contenu énergétique de chaque région peut être mesuré en fonction du temps. De même, le contenu énergétique des produits HCO ou H_2 peut être séparé du reste du système.

[5]Crédit à Stefano Ferrero, membre de l'ITN "AstroChemical Origins", accord de subvention ITN-ACO numéro 811312. Ce projet européen est le "frère" des projets dans lesquels j'ai travaillé pendant mon doctorat, le ERC "Dawn of Organic Chemistry", P.I, C. Ceccarelli et le ERC QUANTUMGRAIN, P.I. A. Rimola, subventions numéro 741002 et 865657, respectivement

[6]Le code que nous avons utilisé nous contraint à utiliser des conditions limites périodiques le long des 3 dimensions de l'espace. Afin de simuler une surface, un espace vide dans la direction Z a été laissé afin d'éviter l'interaction entre les répliques verticales ($\sim$ 20 Å pour HCO et $\sim$ 30 Å pour H_2).

Résumé des résultats

Cette section est divisée en deux parties, une pour le HCO et une pour la formation de H_2.

Formation de HCO

Concernant la formation de HCO, nous n'avons pas observé de désorption chimique, en accord avec les preuves expérimentales (Chuang et al., 2018; Minissale et al., 2016c). En effet, nous avons constaté que la glace d'eau cristalline dissipe la majeure partie ($\sim$90%) de l'énergie naissante (c'est-à-dire l'énergie potentielle de la réaction + TS, puisque le point initial est la structure TS) en moins d'une picoseconde. Nous avons constaté qu'à la fin de la simulation, le HCO reste attaché à la surface en établissant 3 interactions non liantes avec les molécules d'eau de la surface, et son énergie cinétique totale ($\sim$15 kJ mol^{-1}) est bien inférieure à son énergie de liaison (30 kJ mol^{-1}). Cette configuration s'est avérée indépendante de l'orientation initiale de H + CO sur la surface de la glace. Tout ceci indique que, pour notre système, le HCO est condamné à rester sur la surface grâce à son couplage avec la surface dû à sa capacité à établir des liaisons H.

Le processus de dissipation d'énergie à travers la structure de la glace a été suivi dans l'espace en divisant la dalle de glace en coquilles concentriques et régulièrement espacées (de 2,8 Å). La première est un hémisphère de 4 Å de rayon centré sur le site de réaction (l'atome C de HCO) qui contient 6 molécules d'eau. Cette première région subit une excitation cinétique du fait de la réaction avec des pics de $\sim$ 1 kJ mol^{-1} ($\sim$120 K) par molécule d'eau au-dessus de l'énergie initiale, pendant environ 1 ps. La deuxième coquille (contenant 20 molécules d'eau) présente un pic d'excitation plus faible, environ la moitié du précédent, de $\sim$ 0,4 kJ mol^{-1} par molécule d'eau au-dessus de l'énergie initiale, et pour environ la même échelle de temps. À la fin de la simulation (à t=20 ps), toute la glace a la même énergie cinétique, ce qui indique que le système a atteint l'équilibre.

Formation de H2

La formation de H_2 à partir de deux atomes de H est une réaction beaucoup plus exothermique que celle de HCO ($\sim$440 et $\sim$132 kJ mol^{-1} dans nos calculs, respectivement) et, de plus H_2 a une énergie de liaison beaucoup plus faible (environ 10 kJ mol^{-1} dans nos calculs). Cette réaction est étudiée sur une glace cristalline ordonnée en protons, comme pour la formation de HCO, mais aussi sur une glace amophile, dans laquelle trois positions initiales Pos1–3 sont explorées.

Nous avons trouvé que, indépendamment du modèle de glace ou de la position initiale des deux atomes H, la glace absorbe jusqu'à 50% de l'énergie libérée (à la différence de Takahashi et al. (1999a,b), qui ont rapporté une capacité de dissipation d'énergie de $<$5%), montrant une faible dépendance de l'environnement de surface. On constate que la molécule de H_2 se désorbe ou diffuse de manière non thermique suite à la réaction, en conservant toujours plus d'énergie cinétique que son énergie de liaison à la surface. Par conséquent, H_2 est condamné à être désorbé tôt ou tard.

Sur la glace cristalline, on constate que H_2 commence à se diffuser en suivant les "canaux" de potentiel électrostatique de la surface[7] Dans les cas amorphes, par contre, nous avons trouvé soit une diffusion non-thermique (Pos2 et Pos3, cette fois-ci non contrainte à une direction, mais sur toute la surface), soit une désorption directe (Pos1). Dans les simulations Pos1 amorphes, il y a une forte collision contre une des molécules d'eau de la glace, ce qui permet de déduire que cette molécule d'eau est excitée jusqu'à 40 kJ mol^{-1} pendant une période de 100–200 fs. En conséquence de cette collision, la molécule de H_2 est expulsée dans la phase gazeuse (elle atteint 10 de distance par rapport à la surface).

En faisant la même analyse de la dissipation d'énergie que pour la formation de HCO, nous avons trouvé que les molécules d'eau dans le voisinage le plus proche du site de formation de H_2 ($<$ 4 Å) peuvent être excitées entre 3 et 14 kJ mol^{-1}. Nous soutenons que cette énergie pourrait potentiellement être utilisée pour désorber de manière non-thermique une autre molécule de H_2 et, plus intéressant, une molécule de CO. Enfin, l'état vibrationnel de la molécule de H_2 lors de sa formation est élevé ($\nu < 6$), sauf dans le cas

[7] La surface possède des atomes de O et de H pendants en alternance, ce qui rend son potentiel électrostatique périodique dans une direction.

de la glace amorphe Pos1 qui, après sa forte collision avec la molécule d'eau de surface, quitte la surface avec un état vibrationnel bas (ν=1–2).

Surface chemistry of astrophysical interest: theory and simulations

In this thesis I have investigated some of the critical points towards the formation of iCOMs on interstellar icy dust. In particular I have tackled the problem of the synthesis of iCOMs on the surfaces of interstellar dust grains from a theoretical point of view with quantum chemistry calculations. Such calculations have shown that radical—radical reactions on interstellar ice are (i) can have activation energy barriers mainly due to the radical—surface interaction, (ii) can have competitive channels other than the formation of iCOMs like that of direct hydrogen abstraction, in which one radical takes an H atom from the other and (iii) the occurrence of one channel or the other may entirely depend on their orientation upon encounter. These results have a strong impact in the astrochemistry community since in most cases it is usually assumed that radical–radical reactions are barrierless and that can only produce iCOMs. Another point that we have tackled in this thesis is the importance of binding energies when computing the efficiencies of radical—radical reactions, which strongly depend on the diffusion timescales, which in turn depend on the binding energies and on the diffusion-to-desorption activation energy ratio. We have shown for the formation of acetaldehyde from the coupling of CH_3 and HCO radicals the choice of the diffusion-to-desorption activation energy ratio strongly affects the conclusions, and that tunneling effects in direct H-abstraction reactions (in this case HCO + $CH_3 \rightarrow$ CO + CH_4) can be of great importance at low temperatures. The reaction rates related to the activation energies were obtained by means of the Rice-Rampsberger-Kassel-Marcus (RRKM) theory, i.e. the microcanonical counterpart of the classical transition state theory, while the desorption and diffusion rate constants were simulating using Eyring's equation. Finally, we have also tackled the problem of the fate of the energy after a chemical reaction on top interstellar ices. We have studied how does the energy released by H + CO $\rightarrow$ HCO and H + H $\rightarrow$ H_2 partition in between the product molecule and the surface by means of ab initio molecular dynamics. For the former reaction, the surface was modelled by a proton ordered Ih crystalline ice in order to limit the complexity of the system (in such an ordered surface, the number of binding sites is drastically reduced to a few that periodically repeat). We found that the energy released is very efficiently absorbed and dissipated by the ice structure in about 1 ps, so that the HCO product remains frozen on the ice surface. In the case of H_2, we have studied the reaction on crystalline and on three different spots on an amorphous ice model. In all cases the ice structure absorbs about one half of the energy released upon H_2 formation, which is still not enough for H_2 to remain frozen, so that its fate is probably leave into the gas phase with a certain amount of vibrational excitation (they were found to be vibrationally excited during the first ps). The region where the H_2 molecule was formed was observed to remain energized for about 100-200 fs, so that we cannot reject the idea that the energy released by such reactions might be used by other species with low binding energies to be ejected into the gas.

Keywords: *Interstellar medium, Surface chemistry, Computational chemistry, Theory, Simulations, Astrochemistry*

Joan Enrique-Romero